# Electron acceleration and loss caused by wave-particle interactions in the Van Allen radiation belts

## Thesis

# ELECTRON ACCELERATION AND LOSS CAUSED BY WAVE-PARTICLE INTERACTIONS IN THE VAN ALLEN RADIATION BELTS

By

Dipl.-Phys.
**Tobias Kersten**

British Antarctic Survey
Space Weather and Atmosphere Group

A thesis submitted to the Open University for the degree of

**Doctor of Philosophy**

In the discipline of Physical Sciences

May 2016

# Abstract

Modern society relies substantially on satellite technology as it is involved in vital services like telecommunication services, Earth observation, navigation, and many more. There are more than 1000 operational satellites in Earth orbit and most of these spend at least some of their time in the harsh environment of the Van Allen radiation belts. The radiation belts are usually split into two regions, the inner and the outer radiation belt. While the inner belt is considered stable, the flux of electrons in the outer belt can vary over several orders of magnitude, reaching levels that may disrupt satellite operations. It is therefore important to understand the variability of the outer belt and ultimately to predict its behaviour.

In this thesis, the radiation belts are described by the BAS Radiation Belt Model (BAS-RBM) which solves a 3D diffusion equation. The BAS-RBM requires accurate diffusion coefficients that describe the interaction between electrons and plasma waves. The most important plasma waves are chorus, plasmaspheric hiss, and EMIC waves. Here, new statistical models of the diffusion coefficients for these waves are presented, which considerably improve existing models. Among others, they benefit from better global wave models due to improved satellite coverage, and revised wave normal angle and plasma density models.

The results show that chorus waves are an important acceleration and loss mechanism at energies up to about 1 MeV and for all pitch-angles, while plasmaspheric hiss is found to be an essential loss process in the same energy and pitch-angle range. In contrast, EMIC waves proved to be a relevant loss process for ultrarelativistic electrons, but only at lower pitch-angles. The work presented here has led to a better understanding of the variability of the outer radiation belt and has considerably improved the accuracy and reliability of the modelling and forecasting capabilities.

# Preface

The work described in this thesis was carried out in the Space Weather and Atmosphere Group at the British Antarctic Survey under the supervision of Professor Richard B. Horne and Dr. Sarah A. Glauert. This thesis is the result of my own work and to the best of my knowledge and belief does not contain material previously published or written by other authors, except where due reference is indicated in the text. This thesis does not contain any material which has been previously submitted for the award of a degree or other qualification to any university or institution.
Parts of the work presented in this thesis were published in the following peer reviewed publications (in chronological order):

- Horne, R. B., T. Kersten, S. A. Glauert, N. P. Meredith, D. Boscher, A. Sicard-Piet, R. M. Thorne, and W. Li (2013), "A new diffusion matrix for whistler mode chorus waves", *J. Geophys. Res. Space Physics*, 118, 6302 - 6318

- Meredith, N. P., R. B. Horne, T. Kersten, B. J. Fraser, and R. S. Grew (2014), "Global morphology and spectral properties of EMIC waves derived from CRRES observations", *J. Geophys. Res. Space Physics*, 119, 5328 - 5342

- Kersten, T., R. B. Horne, S. A. Glauert, N. P. Meredith, B. J. Fraser, and R. S. Grew (2014), "Electron losses from the radiation belts caused by EMIC waves", *J. Geophys. Res. Space Physics*, 119, 8820 - 8837

The first publication contains preliminary results of the work presented in Chapter 4. The second and third publications act as companion papers and form the basis of the work presented in Chapter 5.

# Acknowledgements

I would like to thank Richard Horne, Sarah Glauert, and Nigel Meredith for their guidance, advice, and valuable feedback, as well as all the productive discussions we had, that considerably improved my knowledge of space plasma physics. I would also like to thank my colleague Hayley for all the great and fun conversations we had in our office, making it a lovely place to work at. Furthermore, I would like to thank all of my friends for the numerous enjoyable pub nights and evening gatherings. I want to express my gratitude to the British Antarctic Survey for funding my PhD and Alison Teague for taking care of all the administrative tasks related to it.
I would also like to thank my family for always being helpful, amusing and entertaining, in particular my Mom, without whose support I would have not been able to pursue an academic career at all. And most importantly, I would like to thank my wife Jennifer for being the most amazing person I know and of course her unconditional support all these years.

The results of this thesis are part of the British Antarctic Survey Polar Science for Planet Earth Programme. It was funded by the Natural Environment Research Council and additionally received funding from the European Union Seventh Framework Programme (FP7/2007-2013) under grant agreements 284520 (MAARBLE), 262468 (SPACECAST), and 606716 (SPACESTORM).

# Table of Contents

**Abstract** . . . . . **i**

**Preface** . . . . . **iii**

**Acknowledgements** . . . . . **v**

**Table of Contents** . . . . . **vii**

**List of Figures** . . . . . **xiii**

**Introduction** . . . . . **1**

**Chapter 1: Theoretical Background** . . . . . **3**

1.1 Introduction . . . . . 3

1.2 Solar-Terrestrial Environment . . . . . 3

1.2.1 The Sun and Interplanetary Space . . . . . 3

1.2.2 The Earth's Magnetic Field . . . . . 4

1.2.3 The Earth's Magnetosphere . . . . . 5

1.2.4 The Earth's Plasmasphere . . . . . 6

1.2.5 Van Allen Radiation Belts . . . . . 11

1.2.6 Geomagnetic Storms . . . . . 12

1.2.7 Substorms . . . . . 12

1.2.8 Magnetic Indices . . . . . 13

1.3 Motion of a Charged Particle in Electromagnetic Fields . . . . . 15

1.3.1 Uniform Magnetic Field . . . . . 16

1.3.2 Uniform Electric and Magnetic Field . . . . . 19

1.3.3 Inhomogeneous Electric and Magnetic Field . . . . . 21

1.3.4 Adiabatic Invariants . . . . . 28

1.3.5 Summary of the Particle Motion . . . . . 38

1.4 Electromagnetic Waves in a Plasma . . . . . 39
1.4.1 Definition of a Plasma . . . . . 39
1.4.2 Wave Propagation . . . . . 40
1.4.3 Plasma as a Conductive Medium . . . . . 41
1.4.4 Plasma as a Dielectric Medium . . . . . 47
1.4.5 Equivalence of the Conductive and Dielectric Characterisation of a Plasma . . . . . 49
1.5 Dispersion Relation . . . . . 50
1.5.1 Solutions of the Dispersion Relation . . . . . 56
1.5.2 Phase Velocity . . . . . 61
1.5.3 Group Velocity . . . . . 62
1.6 Wave-Particle Interaction . . . . . 62
1.6.1 The Resonance Condition . . . . . 62
1.6.2 Resonance Cone . . . . . 68
1.6.3 Resonance Ellipse . . . . . 70
1.7 Electron flux . . . . . 73

**Chapter 2: Modelling the Radiation Belts . . . . . 77**
2.1 Introduction . . . . . 77
2.2 PADIE Diffusion Code . . . . . 79
2.2.1 Power Spectral Density Distribution . . . . . 80
2.2.2 Definition of the Diffusion Coefficients . . . . . 82
2.2.3 Method of Calculation . . . . . 83
2.3 British Antarctic Survey Radiation Belt Model . . . . . 87
2.3.1 Radial Diffusion Coefficients . . . . . 89
2.3.2 Numerical Method . . . . . 90

**Chapter 3: Plasma Waves - A Review . . . . . 95**
3.1 Introduction . . . . . 95
3.2 Whistler Mode Chorus Waves . . . . . 96
3.3 EMIC Waves . . . . . 99

3.4 Plasmaspheric Hiss . . . . . 101

**Chapter 4: Whistler Mode Chorus Waves . . . . . 105**

4.1 Introduction . . . . . 105

4.2 Whistler Mode Wave Database . . . . . 106

4.2.1 Instrumentation and Data Analysis . . . . . 106

4.2.2 Chorus Wave Database . . . . . 108

4.2.3 Separating Chorus from Hiss . . . . . 109

4.3 Chorus Wave Models . . . . . 110

4.3.1 Fitted Chorus Wave Model . . . . . 110

4.3.2 Improved Chorus Models . . . . . 120

4.4 The Ratio of $f_{pe}/f_{ce}$ . . . . . 123

4.5 Bounce Averaged Diffusion Rates . . . . . 125

4.5.1 Comparison of the Chorus Models . . . . . 129

4.6 Drift and Bounce Averaged Diffusion Rates . . . . . 136

4.6.1 Latitudinal Distribution . . . . . 137

4.6.2 Combined Lower and Upper Band Diffusion Rates . . . . . 139

4.7 Global Simulations of the Electron Flux . . . . . 142

4.8 Discussion . . . . . 147

4.9 Conclusions . . . . . 148

**Chapter 5: Electromagnetic Ion Cyclotron Waves . . . . . 151**

5.1 Introduction . . . . . 151

5.2 EMIC Wave Data Analysis . . . . . 152

5.2.1 EMIC Wave Database . . . . . 152

5.2.2 Spectral Properties and Nominal Wave Model . . . . . 155

5.2.3 Wave Power . . . . . 161

5.3 Diffusion Rates . . . . . 164

5.3.1 Bounce Averaged Diffusion Rates . . . . . 164

5.3.2 Drift and Bounce Averaged Diffusion Rates . . . . . 167

5.3.3 Parameter Studies . . . . . 169

5.4 Global Simulations of the Electron Flux . . . . . 179
5.4.1 Temporal Distribution . . . . . 180
5.4.2 Pitch-angle Distribution . . . . . 184
5.5 Discussion . . . . . 187
5.6 Conclusions . . . . . 188

**Chapter 6: Plasmaspheric Hiss . . . . . 191**
6.1 Introduction . . . . . 191
6.2 Plasmaspheric Hiss Wave Database . . . . . 192
6.2.1 Separating Hiss from Chorus . . . . . 192
6.3 Wave Model . . . . . 200
6.3.1 Spectral Properties . . . . . 201
6.3.2 Wave Power . . . . . 203
6.3.3 Wave Normal Angle Model . . . . . 204
6.3.4 Comparison with the Glauert et al. [2014] Hiss Model . . . . . 206
6.4 The Ratio of $f_{pe}/f_{ce}$ . . . . . 207
6.5 Bounce Averaged Diffusion Rates . . . . . 209
6.5.1 Included Number of Resonances . . . . . 212
6.6 Drift and Bounce Averaged Diffusion Rates . . . . . 214
6.6.1 Latitudinal Distribution . . . . . 215
6.6.2 Comparison of the G14 and the New Hiss Model . . . . . 217
6.7 Global Simulation of the Electron Flux . . . . . 222
6.8 Discussion . . . . . 230
6.9 Conclusions . . . . . 231

**Chapter 7: Model Evaluation . . . . . 235**
7.1 Introduction . . . . . 235
7.2 The BAS Van Allen Probes Database . . . . . 236
7.3 Boundary and Initial Conditions . . . . . 238
7.3.1 Minimum and Maximum $L^*$ Boundary Conditions . . . . . 238
7.3.2 Minimum Energy Boundary Condition . . . . . 242

7.3.3 Initial Condition . . . . . 244
7.4 Results . . . . . 246
7.4.1 VAP Electron Flux . . . . . 246
7.4.2 Model Results . . . . . 251
7.5 Evaluation . . . . . 254
7.5.1 Chorus Waves . . . . . 255
7.5.2 Plasmaspheric Hiss . . . . . 264
7.5.3 Radial Diffusion . . . . . 273
7.6 Discussion . . . . . 286
7.7 Conclusion . . . . . 289

**Chapter 8: Summary and Conclusions . . . . . 291**

**References . . . . . 297**

# List of Figures

**Chapter 1: Theoretical Background**


Figure 1.1: Snapshot of the main magnetic field strength at Earth's surface . . 6

Figure 1.2: Artists representation of the Earth's magnetosphere . . . . . 7

Figure 1.3: Sketch of the convection and corotation electric field . . . . . 9

Figure 1.4: Plasmapause location for selected times after a sudden increase of the convection electric field . . . . . 10

Figure 1.5: Helical motion of a charged particle in an uniform magnetic field . 18

Figure 1.6: Cyclotron frequency as a function of L-shell . . . . . 19

Figure 1.7: $E \times B$ drift motion as observed in a stationary frame of reference . 21

Figure 1.8: Geometry of the mirror force . . . . . 23

Figure 1.9: Geometry of the gradient B drift . . . . . 25

Figure 1.10: Sketch illustrating the ring current as a result of the combined gradient B drift and curvature drift velocity . . . . . 26

Figure 1.11: Bounce and drift periods for electrons with an equatorial pitch-angle of 90° as a function of energy . . . . . 28

Figure 1.12: Illustration of the definition of the pitch-angle . . . . . 31

Figure 1.13: Schematic summary of the bounce and drift motion of a charged particle drifting around the Earth . . . . . 39

Figure 1.14: Geometry of the $x$-$z$ plane . . . . . 57

Figure 1.15: Dispersion relations for field aligned waves and oblique waves . . . 60

Figure 1.16: Dispersion relation of the whistler mode branch and the resonance condition for $n = 0, ..., 10$ . . . . . 67

Figure 1.17: Geometry of the resonance cone . . . . . 69

Figure 1.18: Contour plot of the electron phase space density together with resonance ellipses and diffusion surfaces . . . . . 73

Figure 1.19: Artists representation of the electron fluxes around the Earth forming the Van Allen electron radiation belts . . . . . 75

**Chapter 2: Modelling the Radiation Belts**

Figure 2.1: Illustration of the ($\alpha$-$E$) computational grid . . . . . 91

**Chapter 3: Plasma Waves - A Review**

Figure 3.1: Typical spectrogram of plasma waves . . . . . 96

**Chapter 4: Whistler Mode Chorus Waves**

Figure 4.1: Comparison of observed and fitted power spectral density for lower band and upper band chorus waves . . . . . 114

Figure 4.2: Fitted wave power of lower and upper band chorus waves . . . . . 115

Figure 4.3: Example for parameters derived from fitting the power spectra of lower band chorus waves . . . . . 117

Figure 4.4: Example for parameters derived from fitting the power spectra of upper band chorus waves . . . . . 118

Figure 4.5: Ratio of the fitted wave power and the integrated wave power for lower and upper band chorus . . . . . 121

Figure 4.6: Comparison of $f_{pe}/f_{ce}$ derived from satellites and the final $f_{pe}/f_{ce}$ model at the equator . . . . . 126

Figure 4.7: Bounce averaged pitch-angle and energy diffusion rates for lower band chorus (fitted model) . . . . . 127

Figure 4.8: Bounce averaged pitch-angle and energy diffusion rates for upper band chorus (fitted model) . . . . . 129

Figure 4.9: Bounce average pitch-angle and energy diffusion rates of combined lower and upper band chorus waves (fitted model) . . . . . 130

Figure 4.10: Bounce average pitch-angle and energy diffusion rates of combined lower and upper band chorus waves (data driven model, $\delta\psi = 30°$) and comparison with fitted model . . . . . 131

Figure 4.11: Bounce average pitch-angle and energy diffusion rates of combined lower and upper band chorus waves (data driven model, $\delta\psi = 15°$) and comparison with data driven model, $\delta\psi = 30°$ . . . . . 133

Figure 4.12: Dispersion relation and resonance condition for upper band chorus waves . . . . . 134

Figure 4.13: Bounce average pitch-angle and energy diffusion rates of combined lower and upper band chorus waves (lower frequency chorus model) and comparison with data driven model ($\delta\psi = 15°$) . . . . . 135

Figure 4.14: Latitudinal distribution of the drift and bounce averaged pitch-angle and energy diffusion rates of the lower band chorus . . . . . 137

Figure 4.15: Latitudinal distribution of the drift and bounce averaged pitch-angle and energy diffusion rates of upper band chorus . . . . . 138

Figure 4.16: Drift and bounce averaged pitch-angle and energy diffusion rates for combined lower and upper band chorus . . . . . 141

Figure 4.17: Contour plots comparing the electron flux measured by CRRES with the flux calculated by the `BAS-RBM` for the lower frequency chorus model and the data driven chorus model . . . . . 145

Figure 4.18: Line plots comparing the electron flux measured by CRRES with the flux calculated by the `BAS-RBM` for the lower frequency chorus model and the data driven chorus model at constant values of $L^*$ . 146

**Chapter 5: Electromagnetic Ion Cyclotron Waves**

Figure 5.1: Wave power spectral density from 12:30 - 15:30 UT on 30/Aug/1991 during CRRES orbit 968 as a function of frequency and UT . . . . 153

Figure 5.2: Time-averaged wave power of hydrogen band EMIC waves as measured by the CRRES satellite . . . . . 154

Figure 5.3: Time-averaged wave power of helium band EMIC waves as measured by the CRRES satellite . . . . . 155

Figure 5.4: Scatterplots of the normalised peak frequency, normalised frequency width, and the ratio $f_{pe}/f_{ce}$ for hydrogen band and helium band EMIC wave events . . . . . 156

Figure 5.5: EMIC waves dispersion relation for field aligned waves . . . . . 160

Figure 5.6: Average wave intensity used to model the EMIC waves . . . . . 163

Figure 5.7: Bounce averaged pitch-angle diffusion rates of hydrogen band and helium band EMIC waves . . . . . 164
Figure 5.8: Comparison of the bounce averaged pitch-angle diffusion rates and energy diffusion rates . . . . . 166
Figure 5.9: Bounce averaged energy diffusion rates of hydrogen band and helium band EMIC waves . . . . . 166
Figure 5.10: Drift and Bounce averaged pitch-angle diffusion rates for hydrogen band and helium band EMIC waves . . . . . 167
Figure 5.11: Drift and Bounce averaged energy diffusion rates for hydrogen band and helium band EMIC waves . . . . . 169
Figure 5.12: Bounce-averaged pitch-angle diffusion rates of EMIC waves for a variable peak frequency . . . . . 172
Figure 5.13: Energy dependence of the bounce-averaged pitch-angle diffusion rates at large peak frequencies . . . . . 173
Figure 5.14: Bounce-averaged pitch-angle diffusion rates of EMIC waves for a variable frequency width . . . . . 174
Figure 5.15: Energy dependence of the bounce-averaged pitch-angle diffusion rates at large frequency width . . . . . 175
Figure 5.16: Energy dependence of the bounce-averaged pitch-angle diffusion rates at large peak frequencies and large frequency width . . . . . 176
Figure 5.17: Bounce-averaged pitch-angle diffusion rates of EMIC waves for a variable upper cut-off frequency . . . . . 177
Figure 5.18: Bounce-averaged pitch-angle diffusion rates of EMIC waves for various values of $f_{pe}/f_{ce}$ . . . . . 178
Figure 5.19: Energy dependence of the bounce-averaged pitch-angle diffusion rates at large $f_{pe}/f_{ce}$ . . . . . 179
Figure 5.20: Comparison of the 90° electron flux calculated using the `BAS-RBM` with and without EMIC waves . . . . . 182
Figure 5.21: Comparison of the 45° electron flux calculated using the `BAS-RBM` with and without EMIC waves . . . . . 183

Figure 5.22: Comparison of the pitch-angle distribution of the electron flux calculated using the `BAS-RBM` with and without EMIC waves . . . . . 185

Figure 5.23: Comparison of the pitch-angle dependence of the flux at $L^* = 4.00$ calculated using the `BAS-RBM` with and without EMIC waves for different electron energies . . . . . 186

**Chapter 6: Plasmaspheric Hiss**

Figure 6.1: Average wave intensity of whistler mode waves in the frequency range of 200 Hz - 500 Hz and 1 kHz - 2 kHz . . . . . 194

Figure 6.2: Examples for the Gaussian fits to the $L^*$ distribution of the average wave intensity . . . . . 197

Figure 6.3: Average wave intensity of whistler mode waves in the frequency range of 200 Hz - 500 Hz and 1 kHz - 2 kHz together with the derived hiss boundary . . . . . 199

Figure 6.4: Frequency distribution of the power spectral density of plasmaspheric hiss at various $L^*$ and MLT . . . . . 201

Figure 6.5: Global maps of the frequency distribution of the average intensity of plasmaspheric hiss . . . . . 202

Figure 6.6: Latitudinal distribution of the average intensity in the frequency band 200 Hz - 500 Hz of plasmaspheric hiss . . . . . 203

Figure 6.7: Integrated wave power of plasmaspheric hiss . . . . . 204

Figure 6.8: Interpolated model for the ratio $f_{pe}/f_{ce}$ . . . . . 209

Figure 6.9: Bounce average pitch-angle and energy diffusion rates of plasmaspheric hiss . . . . . 211

Figure 6.10: Influence of the number of resonances on the bounce average pitch-angle and energy diffusion rates of plasmaspheric hiss . . . . . 213

Figure 6.11: Latitudinal distribution of the drift and bounce averaged pitch-angle and energy diffusion rates of plasmaspheric hiss . . . . . 216

Figure 6.12: Comparison of the drift and bounce averaged pitch-angle and energy diffusion rates of the new hiss model and the G14 hiss model at $L^* = 3.5$ . . . . . 218

Figure 6.13: Comparison of the drift and bounce averaged pitch-angle and energy diffusion rates of the new hiss model and the G14 hiss model at $L^* = 4.0$ . . . . . 219

Figure 6.14: Comparison of the drift and bounce averaged pitch-angle and energy diffusion rates of the new hiss model and the G14 hiss model at $L^* = 5.5$ . . . . . 220

Figure 6.15: Contour plots comparing the electron flux measured by CRRES with the flux calculated by the `BAS-RBM` for the G14 and the new hiss model at $E = 418\,\text{keV}$ . . . . . 226

Figure 6.16: Line plots comparing the electron flux measured by CRRES with the flux calculated by the `BAS-RBM` for the G14 and the new hiss model at constant values of $L^*$ and at $E = 418\,\text{keV}$ . . . . . 227

Figure 6.17: Contour plots comparing the electron flux measured by CRRES with the flux calculated by the `BAS-RBM` for the G14 and the new hiss model at $E = 976\,\text{keV}$ . . . . . 228

Figure 6.18: Line plots comparing the electron flux measured by CRRES with the flux calculated by the `BAS-RBM` for the G14 and the new hiss model at constant values of $L^*$ and at $E = 976\,\text{keV}$ . . . . . 229

**Chapter 7: Model Evaluation**

Figure 7.1: Illustration of the method used to define the times at which the $L^*_{min}$ and $L^*_{max}$ boundary condition are derived . . . . . 241

Figure 7.2: Electron flux at the minimum and maximum $L^*$ boundary derived from the Van Allen Probes data . . . . . 242

Figure 7.3: Illustration of the method to derive the $E_{min}$ boundary condition . 243

Figure 7.4: Electron flux at minimum energy boundary derived from the Van Allen Probes data . . . . . 244

Figure 7.5: Electron flux of the initial condition on 3 March 2015 (midnight) . 245
Figure 7.6: Flux of 593 keV electrons measured by RBSP compared with model results . . . . . 248
Figure 7.7: Flux of 1547 keV electrons measured by RBSP compared with model results . . . . . 249
Figure 7.8: Flux of 4200 keV electrons measured by RBSP compared with model results . . . . . 250
Figure 7.9: Comparison of the 593 keV electron flux with and without chorus waves . . . . . 258
Figure 7.10: Comparison of the 593 keV electron flux with and without chorus waves at constant values of $L^*$ . . . . . 259
Figure 7.11: Comparison of the 1547 keV electron flux with and without chorus waves . . . . . 260
Figure 7.12: Comparison of the 1547 keV electron flux with and without chorus waves at constant values of $L^*$ . . . . . 261
Figure 7.13: Comparison of the 4200 keV electron flux with and without chorus waves . . . . . 262
Figure 7.14: Comparison of the 4200 keV electron flux with and without chorus waves at constant values of $L^*$ . . . . . 263
Figure 7.15: Comparison of the 593 keV electron flux with and without hiss . . . 267
Figure 7.16: Comparison of the 593 keV electron flux with and without hiss at constant values of $L^*$ . . . . . 268
Figure 7.17: Comparison of the 1547 keV electron flux with and without hiss . . 269
Figure 7.18: Comparison of the 1547 keV electron flux with and without hiss at constant values of $L^*$ . . . . . 270
Figure 7.19: Comparison of the 4200 keV electron flux with and without hiss . . 271
Figure 7.20: Comparison of the 4200 keV electron flux with and without hiss at constant values of $L^*$ . . . . . 272
Figure 7.21: Electron PSD at $\mu = 400$ MeV/G measured by RBSP compared with model results . . . . . 274

Figure 7.22: Electron PSD at $\mu = 1000\,\mathrm{MeV/G}$ measured by RBSP compared with model results . . . . . 275
Figure 7.23: Electron PSD at $\mu = 3000\,\mathrm{MeV/G}$ measured by RBSP compared with model results . . . . . 276
Figure 7.24: Electron PSD measured by RBSP compared with model results at constant timesteps . . . . . 277
Figure 7.25: Comparison of the Brautigam & Albert and THEMIS radial diffusion rates . . . . . 279
Figure 7.26: Comparison of the 593 keV electron flux calculated with the Brautigam & Albert and THEMIS radial diffusion rates . . . . . 282
Figure 7.27: Comparison of the 1547 keV electron flux calculated with the Brautigam & Albert and THEMIS radial diffusion rates . . . . . 283
Figure 7.28: Comparison of the 4200 keV electron flux calculated with the Brautigam & Albert and THEMIS radial diffusion rates . . . . . 284
Figure 7.29: Comparison of the 4200 keV electron flux calculated with the Brautigam & Albert and THEMIS radial diffusion rates starting just before the main storm . . . . . 285

# Introduction

Modern human society relies considerably on satellite technology, which provides essential services like communication, the Internet, GPS, and the timing signal for the stock markets. Unfortunately, most satellites operate in a region of space with a high risk of natural hazard, namely the *Van Allen Radiation Belts*. In this region, the concentration and energies of protons and electrons can reach levels that can damage the electronic components on a satellite by causing internal or surface charging, leading to deterioration, which will cause disruption of services and in exceptional cases a total loss of the satellite. It is therefore imperative to be able to describe and forecast the temporal and spatial variability of the conditions in the near Earth environment, which are the fundamental principles of *space weather* research. Due to the danger posed to society, space weather became a concern at government level when it was added to the UK national risk register in 2012.

The Van Allen Belts were the first major discovery of the space age in 1958. They consist of energetic protons and electrons that are trapped by the Earth's magnetic field. The charged particles bounce back and forth between the northern and southern hemisphere on the timescale of seconds, while they slowly drift around the Earth on a timescale between tens of minutes and a few hours. While there is one proton belt that has a peak proton flux near about 1.7 Earth radii (Re) at the geomagnetic equator, the electron belt is split into two regions, the so-called inner and outer electron radiation belts. In the equatorial region the inner belt is located between about 1.2 and 2 Re and is generally considered stable, while the outer belt is located between about 3 and 7 Re (in the equatorial region) and is highly variable. The flux of electrons with energies ranging between about 100 keV up to several MeV inside the outer electron belt can vary over several orders of magnitudes on a timescale of hours. Since most satellites operate or pass through the region of the outer electron belt, they are in danger of malfunctions caused by the electrons.

One of the most important processes for the variability of the outer electron belt is the

electron acceleration and loss caused by wave-particle interactions between electrons and plasma waves. Over the last decade various computational models were developed in order to simulate the (outer) electron radiation belt including the effect of wave-particle interactions. There are many different types of plasma waves, characterised by their frequency range, location in space relative to the plasmapause, and their polarisation. The most important among them are whistler mode chorus waves, plasmaspheric hiss, and Electromagnetic Ion Cyclotron (EMIC) waves. These three types of plasma waves are well studied, but usually only for exemplary case studies based on few data. Furthermore, their effect on the radiation belt variability still needs to be quantified on a global scale. Therefore, the focus of this thesis is to develop considerably improved models for the wave-particle interactions with plasmaspheric hiss, chorus and EMIC waves and to study their effect on the radiation belts on a global scale.

At the British Antarctic Survey a large database was developed, that contains statistical information about the various types of plasma waves from up to seven different satellites covering a wide spatial and temporal range. Based on this database, novel statistical models for whistler mode chorus, EMIC waves, and plasmaspheric hiss were developed, considerably improving existing wave models. This thesis presents these new wave models in individual chapters and discusses the improvements made, as well as their impact on the global electron acceleration and loss rates. The necessary theoretical background and the computational tools used in this thesis are presented in Chapter 1 and Chapter 2, while an overview of previously published work on plasma waves is given in Chapter 3. The new wave models and their effects are presented in Chapter 4 for chorus waves, in Chapter 5 for EMIC waves, and in Chapter 6 for plasmaspheric hiss. The thesis concludes in Chapter 7 with an evaluation of the computational model and the presented three wave models. This is performed by a comparison of the simulation and the data for a selected period of the Van Allen Probes satellite mission, which provides the most recent and most detailed measurements of the Van Allen radiation belts.

# CHAPTER 1
# *Theoretical Background*

## 1.1 Introduction

The aim of this chapter is to present the theoretical background needed to understand the physical processes that enable electromagnetic waves to interact with electrons inside the Van Allen radiation belts. This is a complex process that includes three components, namely the trapping of electrons inside the radiation belts, the propagation of electromagnetic waves in the radiation belts, and the interaction between these waves and the trapped electrons. The chapter begins with a short introduction of the solar-terrestrial environment, including the interaction of Earth's magnetic field with particles emitted by the Sun. This is followed by the theoretical description of the motion of charged particles trapped inside magnetic and electric fields, such as the Earth's. Then, the theoretical description of the plasma surrounding the Earth is given. This plasma acts as a guiding medium for electromagnetic waves, whose characteristics and propagation inside the plasma are also described. The interaction between these waves and the trapped particles gives rise to acceleration and loss processes. The theoretical framework for this interaction concludes this chapter.
The derivations in this chapter loosely follow the books of *Walt* [1994], *Chen* [1984], and *Bittencourt* [2004], if not explicitly stated otherwise. All equations are derived in SI-units.

## 1.2 Solar-Terrestrial Environment

### 1.2.1 The Sun and Interplanetary Space

The environment of the Sun and the Earth form a coupled system that is linked through dynamic electromagnetic effects and charged particle interactions, which drive the space weather effects found at the Earth. The Sun is a nearly perfect spherical ball of hot plasma, composed primarily of hydrogen (73 %) and helium (25 %), with trace amounts

of heavier elements, such as oxygen, carbon, and iron [*Kivelson and Russell*, 1995].
The Sun is divided into several layers, separated by their density and temperature. From the outer layer, called the corona, there is a continuous outflow, expanding radially through the solar system. This so-called *solar wind* is a plasma primarily composed of protons and electrons, whose energy is high enough to escape the Sun's gravity. The solar magnetic field carried by the solar wind is the *interplanetary magnetic field* (IMF) [*Parker*, 1965]. The solar wind is usually separated into two components, the slow and the fast solar wind, which are defined by their velocity. The slow solar wind typically has a speed of about $400\,\mathrm{kms}^{-1}$, while fast solar wind streams can reach a speed of about $750\,\mathrm{kms}^{-1}$ [*Kivelson and Russell*, 1995]. The fast solar wind originates in large coronal holes, which are regions where the Sun's magnetic field does not reconnect to the Sun, creating open field lines. This allows plasma to escape more easily and hence at higher speeds. As a consequence, the coronal density and temperature are reduced in this region, further increasing the release of plasma. Coronal holes can last multiple rotations of the Sun, and they are associated with geomagnetic storms (See Section 1.2.6) that reoccur on a period equivalent to the sum of the solar rotation, which is 25.4 days, and the movement of the Earth in its orbit around the sun, adding up to about 27 days. Fast solar wind streams can cause an increase of the high energy electron flux trapped by the Earth's magnetic field.
In addition to the constant flow of solar wind there are the so-called coronal mass ejections (CMEs), which are a release of large quantities of coronal matter into space, usually accompanied by electromagnetic radiation. CMEs are associated with non-recurring geomagnetic storms, that can potentially cause an increase or decrease of the electron flux.

### 1.2.2 The Earth's Magnetic Field

The Earth's magnetic field, also known as the geomagnetic field, is believed to be generated by electric currents in the conductive material of the Earth's core. If the Earth was isolated in space, its field could be approximated as a dipole field that is tilted away from the Earth's rotational axis by about 11°. The rotational axis itself is

tilted about 23.5° from the vertical to the Sun's ecliptic plane [*Kivelson and Russell*, 1995]. Assuming a dipole field, the magnetic field $B_0$ of the Earth at a point in space defined by the radial distance $R$ to the surface of the Earth (in units of Earth radii) and the geomagnetic latitude $\lambda_m$ can be calculated by:

$$B_0 = \frac{B_d}{R^3} \cdot \sqrt{1 + 3\sin^2(\lambda_m)} \tag{1.1}$$

where $B_d = 3.12 \cdot 10^{-5}\,\mathrm{T}$ is the mean value of the Earth's dipole magnetic field at the magnetic equator on the Earth's surface.

If the geomagnetic field was a perfect dipole, the contours of constant magnetic field strength would be constant with geomagnetic latitude. However, early geological surveys showed that this is not the case and instead, asymmetries in the Earth's interior currents introduce higher order terms. Figure 1.1 shows measurements of the geomagnetic field taken in June 2014 by the SWARM satellite [*ESA/DTU Space*, 2014], showing the distorted geomagnetic field. One particular feature is the so-called South Atlantic anomaly, where the Earth's magnetic field is much weaker than at other longitudes, with consequences for the shape of the Van Allen Radiation belts (see Section 1.2.5).

### 1.2.3 The Earth's Magnetosphere

The Earth's *magnetosphere* is the region of space where the Earth's magnetic field is able to control the movement of charged particles. On the dayside the Earth's magnetic field, as approximated in the previous section, is compressed by the Sun's solar wind. The solar wind is diverted by the Earth's magnetic field, flowing around the Earth and thereby extending the magnetic field on the nightside. This so-called *magnetotail* can extend up to several hundred Earth radii [*Dungey*, 1965] and is comprised of two lobes, the northern and the southern lobe, which are separated by an area of weaker magnetic fields where the density of charged particles is higher, the so-called *plasma sheet*. The region where the pressure from the solar wind is balanced by the pressure created from the Earth's magnetic field is called the *magnetopause*. This boundary

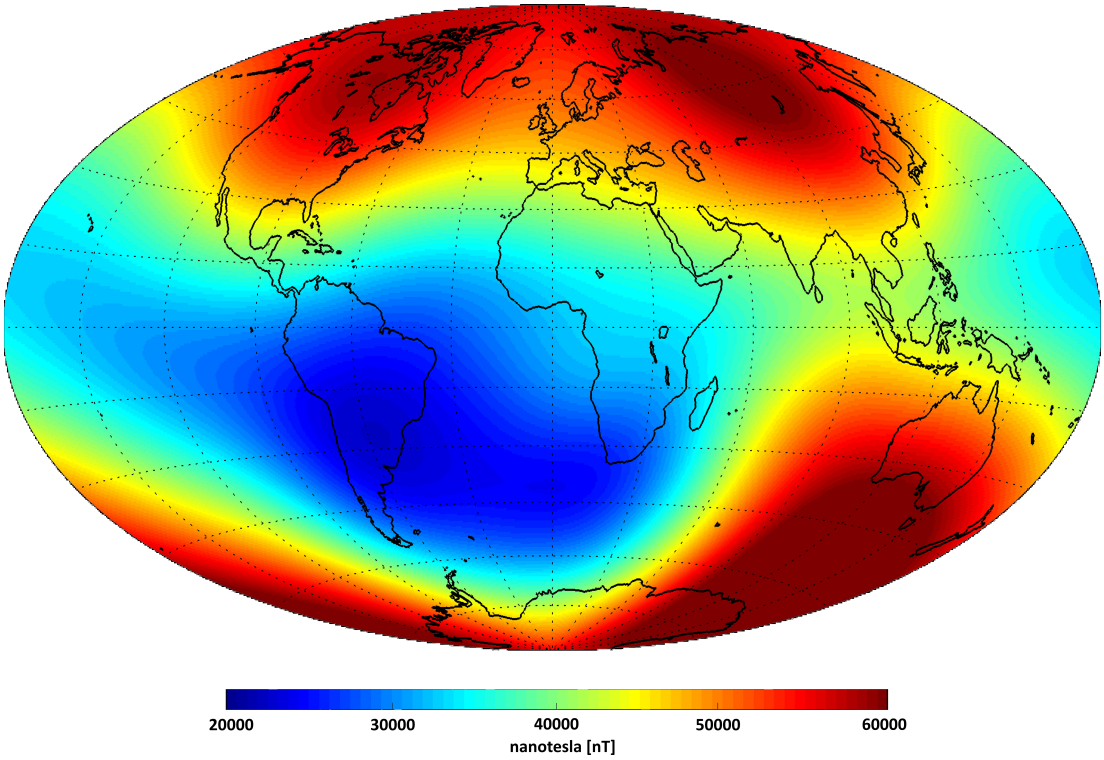


Figure 1.1: Snapshot of the main magnetic field at Earth's surface as of June 2014 based on Swarm data. Taken from *ESA/DTU Space* [2014].

effectively separates the charged particles that are moving inside the Earth's magnetic field from the charged particles forming the solar wind. Since the solar wind pressure varies, the location of the magnetopause is not fixed in space and hence constantly changes size and shape. The solar wind that flows around the Earth also gives rise to an electric field that points from dawn to dusk, the so-called *convection electric field*. Its magnitude is proportional to the magnetic field strength and more importantly to the solar wind velocity. A schematic representation of the Earth's magnetosphere is given in Figure 1.2.

### 1.2.4 The Earth's Plasmasphere

One important part of the magnetosphere is the so-called *plasmasphere*, the region that contains a larger concentration of low-energy charged particles. The plasmasphere is mainly composed of hydrogen, helium and oxygen ions, which form a cold ($\approx 1\,\mathrm{eV}$), dense ($10 - 10000\,\mathrm{cm}^{-3}$) plasma, co-rotating with the Earth. The source of the plasma in the plasmasphere is mainly the continuous outflow of ions streaming upward from

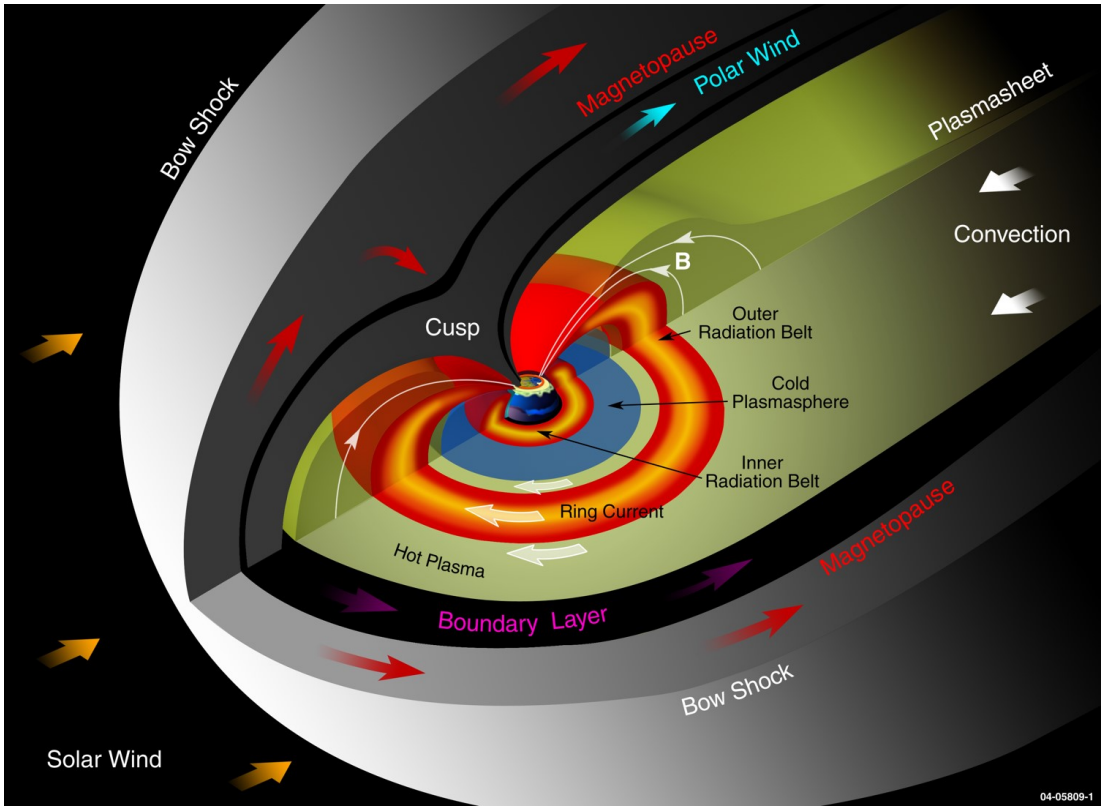


Figure 1.2: Artists representation of the Earth's magnetosphere. From [*Robert DeMajistre*, 2014].

the Earth's ionosphere along the Earth's magnetic field [e.g. *Hargreaves*, 1979; *Gallagher and Comfort*, 2016]. These ions remain trapped inside closed field lines and under the assumption of diffusive equilibrium they will fill up the plasmasphere. The plasmasphere begins at an altitude of about 90 km and extends up to about 4-8 Earth radii, depending on geomagnetic conditions [*Darrouzet et al.*, 2009]. During quiet geomagnetic conditions the plasmasphere is in the shape of a torus, while during disturbed times the plasmasphere can get deformed by sunward plasma convection leading to the so-called plasmaspheric plumes [*Lemaire and Gringauz*, 1998]. The outer boundary of the plasmasphere is called the *plasmapause*, which is defined as the region where the plasma density rapidly decreases by more than one decade. The location of the plasmapause depends on geomagnetic activity and can typically be found between about 6 $R_E$ during geomagnetically quiet times and about 3 $R_E$ during active periods [*Carpenter and Anderson*, 1992].

The cold and dense plasma of mainly ionospheric origin that constitutes the plasma-

sphere is usually confined inside the plasmapause and is not lost to the outer magnetosphere. Furthermore, the plasma inside the plasmasphere is isolated from the hotter magnetospheric plasma found outside the plasmapause. These two effects are the consequence of the motion of the plasma due to a total electric field $\underline{E}$, which is mainly comprised of two components. The first one is the convection electric field $E_c$ described in Section 1.2.3. It points from dawn to dusk and is proportional to the magnetic field strength and the solar wind velocity. In addition, the total electric field includes a contribution associated with the rotation of the Earth, the so-called *corotation electric field* $E_r$. This component points radially inwards and is proportional to the magnetic field strength, but independent of the solar wind velocity. The configuration of the convection and corotation electric field, as well as the resulting total electric field are illustrated in Figure 1.3.

We can see that the total electric potential is compressed on the dawn side and stretched on the dusk side. The lines of constant electric potential close to the Earth are closed and nearly circular, while they become tear-drop shaped at larger radial distances. They eventually progress to open equipotential lines at even larger radial distances. The transition between the open and closed equipotential configuration describes the location of the plasmapause. The point where $E_c$ and $E_r$ are equal and of opposite sign is the so-called *stagnation point*. It was shown by *Lyons and Williams* [1984] that this location moves radially inwards as the corotation electric field increases. Since $E_c$ is proportional to the solar wind velocity, we can directly infer that the last closed electric equipotential moves closer to the Earth if the geomagnetic activity increases.

#### Dynamics of The Plasmasphere

The motion of the cold plasma particles inside the plasmasphere is dominated by the so-called $E \times B$ drift (See Section 1.3.2). If we assume that the magnetic field lines are equipotentials, the $E \times B$ drift velocity has to lie along lines of constant electric potential $\varphi$, with $\underline{E} = -\underline{\nabla}\varphi$. The shape of the plasmasphere is therefore determined by the configuration of the electric field described before. As the charged particles of the plasma follow the lines of constant electric potential shown in Figure 1.3 they are trapped in the region of closed electric equipotentials close to the Earth. At larger

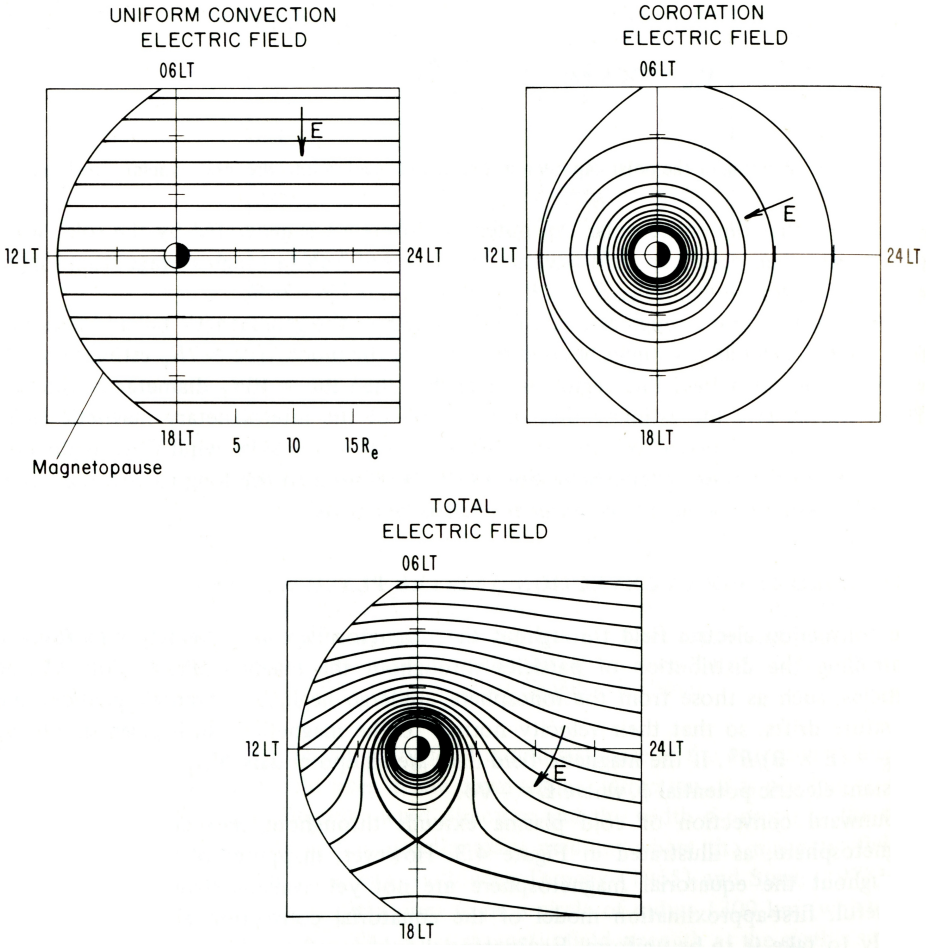


Figure 1.3: Sketch of the electric field equipotentials of the uniform convection electric field (top left), corotation electric field (top right) and the resulting total electric field (bottom). From *Lyons and Williams* [1984].

radial distances the particles' drift paths become open and the plasma is transported away from the inner magnetosphere. The plasmapause is hence expected to be tear-drop shaped with a bulge around 18 MLT.

The plasmasphere is created by the continuous outflow of ions streaming upward from the Earth's ionosphere which are slowly being transported to larger radial distances up to the plasmapause. Let us now assume that the plasmapause was fully formed due to a sufficiently long geomagnetically quiet period. If this quiet period was followed by a geomagnetically active time with larger solar wind velocity, the convection electric field will increase and hence, the closed drift paths move closer to the Earth. If this happens on a short timescale compared to the drift times of the cold, dense plasma, the

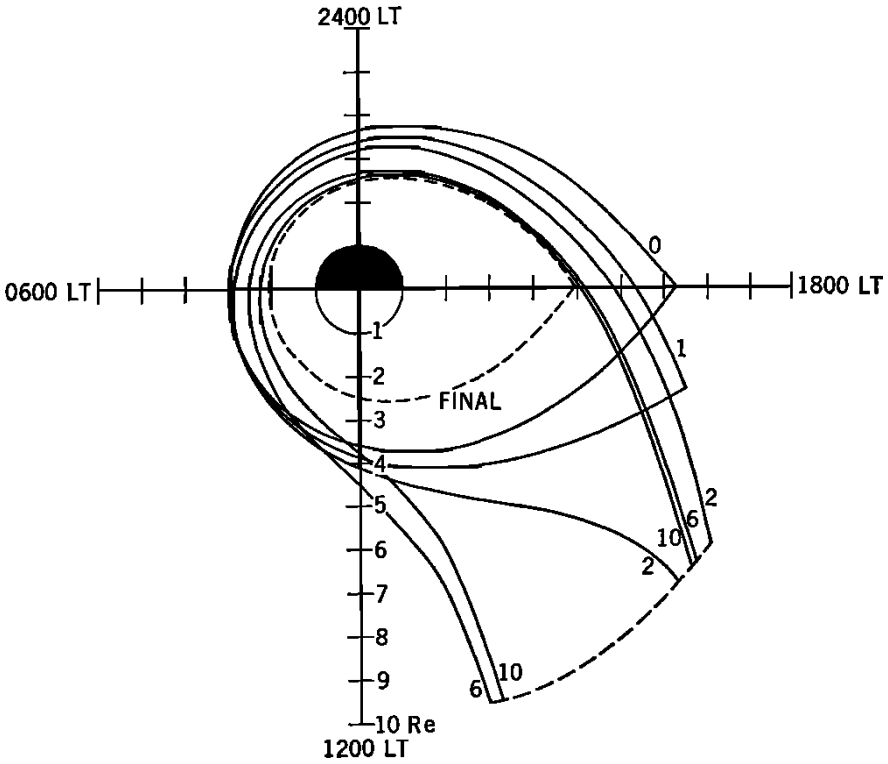


Figure 1.4: Plasmapause location for selected times after a sudden increase of the convection electric field. From *Grebowsky* [1970].

outermost plasma that was previously on closed drift paths will now be on open drift paths that are dominated by the convective electric field. This part of the plasma is therefore convected sunward, creating a tail-like structure of the plasmasphere on the dusk side pointing towards the sun [e.g. *Chen and Wolf*, 1972]. This region is called a *plasmaspheric plume*. If the active condition persists, the plume will be rapidly eroded on a timescale of about one day or less [*Park*, 1974], until the plasmasphere reaches the tear-drop shape determined by the total electric field configuration. The time evolution of the plasmasphere including the formation of a plume after a sudden increase of the convection electric field is depicted in Figure 1.4.

Once the geomagnetic storm ceases, the plasmasphere slowly refills, since the stagnation point will move to larger Earth radii. Measurements have shown that the timescale for the refilling depends on L-shell, ranging from around one day at $L = 2.5$ up to about 8 days at $L = 4$ [*Park*, 1974].

### 1.2.5 Van Allen Radiation Belts

The *Van Allen radiation belts* are a doughnut-shaped region, where the geomagnetic field has trapped high energy electrons and protons, that circulate around the Earth. While protons form one single belt ranging from about $1.2 - 7.0$ Earth radii ($R_E$), with a peak near about $1.7\,R_E$, two separate electron radiation belts were discovered at the beginning of the space age, over 50 years ago [*Van Allen and Frank*, 1959; *Van Allen*, 1959]. They were named the inner and the outer Van Allen (electron) radiation belts. The inner electron belt is located close to the Earth ranging from about $1.2 - 2.0\,R_E$ and the outer radiation belt is located from about 3 to $7\,R_E$ and beyond. The shape of the radiation belts is distorted, since the Earth's magnetic field is not a dipole field. For instance, the inner radiation belt is located closest to the Earth above the South Atlantic anomaly.

The proton belt is characterised by protons with an energy ranging from a few tens of keV up to several tens of MeV close to the Earth, while the proton energies are much lower in the outer regions [*Gusev et al.*, 2003]. The majority of the electrons characterising both the inner and the outer electron belt cover energies from about 100 keV extending to several MeV. Quantifying the upper limit of the electron energies of the inner radiation belt proves to be rather difficult, due to the background noise created by high-energy protons that exist in the inner radiation belt zone.

While the inner belt is considered as stable, except during the most intense geomagnetic storms [*Baker et al.*, 2007], the electron fluxes in the outer radiation belt are highly variable, dependent on the geomagnetic conditions [*Paulikas and Blake*, 1979; *Baker et al.*, 1986]. It was suggested that the outer belt forms during geomagnetically quiet conditions as a result of radial diffusion of trapped electrons towards the Earth and losses to the atmosphere due to wave-particle interactions [*Lyons and Thorne*, 1973]. During geomagnetically active periods however, the flux of high energy electrons can vary significantly on timescales of a few hours [*Baker et al.*, 1986, 1994; *Li et al.*, 1997]. It is believed that these variations are due to enhanced radial transport and electron acceleration and loss caused by wave-particle interaction [*Li et al.*, 2001; *Friedel et al.*, 2002; *Horne*, 2002].

Recent measurements taken by the Van Allen Probes satellites have shown that the electron fluxes at energies greater than about 800 keV are very low or non-existent in the inner belt, while there were significant electron fluxes at lower energies during the same periods [*Fennell et al.*, 2014]. Recently it was discovered that the outer radiation belt can split into two belts, effectively creating a narrow third radiation belt. This third belt consisted of ultrarelativistic electrons with energies as high as 5.6 MeV and persisted for about 4 weeks [*Baker et al.*, 2013].

### 1.2.6 Geomagnetic Storms

A geomagnetic storm is caused by a prolonged coupling between the solar wind and the magnetosphere, during which large amounts of energy are transferred into the magnetosphere. A geomagnetic storm can usually be separated into three different phases. The first phase causes an increase in the horizontal component (H-component) of the low latitude geomagnetic field and is called the storm sudden commencement (SSC). This phase is caused by a compression of the magnetosphere, caused by a rapid increase of the solar wind pressure. The SSC is followed by the main phase, where the H-component rapidly decreases, as the result of a sudden injection of charged particles from the magnetotail into the magnetosphere. This phase typically lasts less than a day and results in a very disturbed magnetosphere. It is usually accompanied by a large number of plasma waves. The last phase of a geomagnetic storm is the recovery phase, where the geomagnetic conditions gradually return to the state before the storm. The recovery phase can last between 1 and 7 days.

### 1.2.7 Substorms

In contrast to the long lasting geomagnetic storms, substorms are short disturbances of the geomagnetic field, lasting for a few hours, during which energy is transferred into the magnetotail and eventually quickly released into the high latitude ionosphere. Substorms are hence primarily observed in the polar regions and they are accompanied by enhanced aurora. A substorm consists of three phases, with the first one being the growth phase, during which the dayside reconnection between the solar wind and

the magnetosphere creates open field lines, which have one end connected to the solar wind and the other connected to the Earth. The flow of the solar wind thereby carries magnetic flux towards the magnetotail and as a consequence additional energy is stored in the expanded tail lobes. Furthermore, the magnetopause is eroded by this process. During the second phase, the so-called substorm expansion phase, the stretched field lines in the magnetotail reconnect to close the open field lines. The now closed field lines relax and snap back to their original state, releasing the energy stored in the tail lobes into the ionosphere. The last phase of a substorm is the recovery phase, during which the magnetosphere returns to its initial state before the substorm.

During geomagnetic storms and substorms electrons and ions are injected into the magnetosphere. The injection of mainly electrons and ions in the energy range of tens of keV significantly enhances the so-called ring current [*Gonzalez et al.*, 1989] and in turn considerably affects the generation of plasma waves as well as the motion of charged particles.

### 1.2.8 Magnetic Indices

Since the geomagnetic conditions have a great impact on the shape of the Earth's magnetic field and hence the resulting particle distributions inside the Van Allen radiation belts, it is imperative to have a measure of (sub)storm activity. Measuring the various corresponding parameters directly in space requires satellites to be present. Since these are unable to provide measurements at many locations in space at all times, we must rely on ground based measurements. There are a variety of indices available that aim to provide measurements that represent the geomagnetic conditions based on data from a worldwide distribution of observatories. In the following, the most commonly used indices will be discussed.

#### Auroral Electrojet Index $AE$

The *Auroral Electrojet index* ($AE$) provides a measurement of the auroral zone component of electric currents, which are often diverted along field lines during magnetic storms, in particular during substorms. The $AE$ index is derived from the one minute

readings of the H-component of the geomagnetic field, measured by a number of observatories in the northern and southern hemisphere, close to the auroral ovals. From all these individual measurements at the various observatories, the average intensity during the five geomagnetically quietest days of the preceding month is subtracted and the lowest and highest value of the H-component among all observatories is stored at the one minute resolution of the measurements, defining the $AL$ and $AU$ index, respectively. The $AE$ index is then defined as the difference between $AL$ and $AU$ in nT [*Davis and Sugiura*, 1966] and stored as a function of Universal Time, providing a measurement of substorm activity on a one minute time resolution. Since the $AE$ index is related to substorm activity and hence associated with the generation of various types of plasma waves, it provides a comparably good index for wave-particle interactions.

#### Planetary K Index $Kp$

The K-index is used to quantify disturbances in the horizontal component of the geomagnetic field during irregular and rapid storm-time magnetic activity [*Bartels et al.*, 1939]. It is an integer value on a quasi-logarithmic scale in the range of 0-9 with values of 0.0, 0.3, 0.7, 1.0, 1.3, ..., where 0 represents absolutely quiet conditions and 5 and above represent a geomagnetic storm. The K-index is derived from the maximum fluctuations of the horizontal components at each observatory individually and scaled in such a way that the historical rate of occurrence of certain levels of K are about the same at all observatories. This is necessary since the maximum fluctuation of the H-component depends on latitude, with larger fluctuations at higher latitudes during the same geomagnetic conditions. The K-index is determined at the end of a predefined three hour interval as the sum of the maximum positive and negative deviations from the average horizontal component of the field.
The *planetary K index* ($Kp$) is derived as the weighted average of all K-indices from all geomagnetic observatories around the world.

#### Disturbance Storm Time Index $Dst$

The *disturbance storm time* index ($Dst$) was designed to measure the enhancement of the westward magnetospheric equatorial ring current due to injections of magneto-

tail protons and electrons [*Sugiura and Hendricks*, 1967]. The ring current exhibits a magnetic field and hence, the enhancement of the ring current around the Earth is associated with a reduction of the Earth magnetic field, as the two magnetic fields are opposed. The calculation of the $Dst$ index is similar to that of the $AE$ index, but more refined. The horizontal component data from low-latitudinal observatories are used at the one minute time resolution and diurnal and secular variation baselines are subtracted. In order to map all measurements from all latitudes onto the equator, a geometric normalisation is performed. The average of all the data then defines the $Dst$ index, where a negative value of $Dst$ describes the presence of the ring current, and is often used as a measure of the strength of a magnetic storm.

## 1.3 Motion of a Charged Particle in Electromagnetic Fields

In order to understand the physical processes that allow the Earth's magnetic field to trap charged particles, we need to study the underlying fundamental physics of the motion of a charged particle in an electromagnetic field. The complex motion will be derived step by step, starting with the motion in an easy to understand uniform magnetic field. The complexity of the electromagnetic field will be increased and the resulting particle motions will be introduced, along with fundamental parameters and constants of space plasma physics.

If a charged particle with charge $q$ and velocity $\underline{v}$ travels through an electromagnetic field the motion of the particle is described by the *Lorentz equation*:

$$\underline{F}_L = \frac{\mathrm{d}\underline{p}}{\mathrm{d}t} = q(\underline{E} + \underline{v} \times \underline{B}) \,, \tag{1.2}$$

where $\underline{F}_L$ is the Lorentz Force acting on the particle and $\underline{p}$ the resulting particle momentum. The electric field is denoted by $\underline{E}$ and the magnetic field by $\underline{B}$. For simple geometries and simple electromagnetic fields the Lorentz equation can easily be solved analytically. Since the electromagnetic condition of the Earth fulfils neither of these conditions, a complex analysis is needed to describe the motion of a particle in Earth's

magnetic field. Here, we will build up the physical properties of the electromagnetic field step by step starting with simple geometries and arriving at geometries close to a realistic description of the Earth's field. We will thereby explain the resulting key consequences for a charged particle. The derivations will aim to describe general particles but might focus on electrons, as these are the topic of this thesis. It will be shown, that charged particles in Earth's magnetic field rotate around a magnetic field line, and will get trapped and guided by the magnetic field, forcing them to bounce between the magnetic poles and drift around the Earth.

The Lorentz Force (Eq. 1.2) can be separated into components that are parallel $\underline{F}_{L,\shortparallel}$ or perpendicular $\underline{F}_{L,\perp}$ to the acting magnetic field $\underline{B}$:

$$\underline{F}_{L,\perp} = \left(\frac{\mathrm{d}\underline{p}}{\mathrm{d}t}\right)_{\perp} = q(\underline{E}_{\perp} + \underline{v}_{\perp} \times \underline{B}) \tag{1.3}$$

and

$$\underline{F}_{L,\shortparallel} = \left(\frac{\mathrm{d}\underline{p}}{\mathrm{d}t}\right)_{\shortparallel} = q\underline{E}_{\shortparallel}\,. \tag{1.4}$$

The parallel component of the Lorentz Force does not therefore depend on $\underline{B}$, since the resulting vector of a cross product is always perpendicular to the two creating vectors.

### 1.3.1 Uniform Magnetic Field

If we assume that there is no external electric field ($\underline{E} = 0$) and the magnetic field is *uniform*, i.e. the intensity (or strength) of the magnetic field is constant in time and space, the parallel component of the Lorentz Force (Eq. 1.4) becomes:

$$\left(\frac{\mathrm{d}\underline{p}}{\mathrm{d}t}\right)_{\shortparallel} = 0\,. \tag{1.5}$$

This means that $\underline{p}_{\shortparallel} = \text{const}$, and hence movement of the particle parallel to the magnetic field will be of constant speed.

The perpendicular component of the Lorentz Force (Eq. 1.3) becomes:

$$\underline{F}_{L,\perp} = \left(\frac{\mathrm{d}\underline{p}}{\mathrm{d}t}\right)_{\perp} = q(\underline{v}_{\perp} \times \underline{B})\,. \tag{1.6}$$

Hence, $\underline{F}_{L,\perp}$ is perpendicular to $\underline{v}_{\perp}$ and the magnetic field $B$. This means that a charged particle that moves across a magnetic field line will be forced onto a circular trajectory around this field line. The Lorentz Force hence acts as a centripetal force, i.e.

$$\frac{mv_{\perp}^2}{\rho} = qv_{\perp}B\,, \tag{1.7}$$

where $\rho$ is the radius of the circular trajectory of the charged particle around the field line. This radius is commonly called the *gyroradius* or *cyclotron radius* and its definition can be obtained by solving Eq. 1.7 for $\rho$:

$$\rho = \frac{mv_{\perp}}{qB} = \frac{p_{\perp}}{qB}\,. \tag{1.8}$$

We can see that the sign of the charge determines the orientation of the motion around the magnetic field. Furthermore, the cyclotron radius is directly proportional to the particle's mass, which means that a proton moving at the same speed as an electron will have a cyclotron radius that is about 1836 times larger than the one of the electron, but at the same time its kinetic energy would be significantly larger. For a mildly relativistic electron ($E_{kin} \approx 150\,\mathrm{keV}$) at a radial distance of $6\,R_E$ the electron cyclotron radius decreases from about 10 km near the equator to about 5 km at a latitude of 60°. Overall, a charged particle in an uniform magnetic field therefore rotates around a magnetic field line and moves along the field line at constant speed, and hence displays helical motion. In Earth's magnetic field, the non-uniformities of $\underline{B}$ happen on a scale much larger than the cyclotron radius, which means that the primary motion of a charged particle in Earth's magnetic field is the helical motion around a field line as depicted in Figure 1.5.

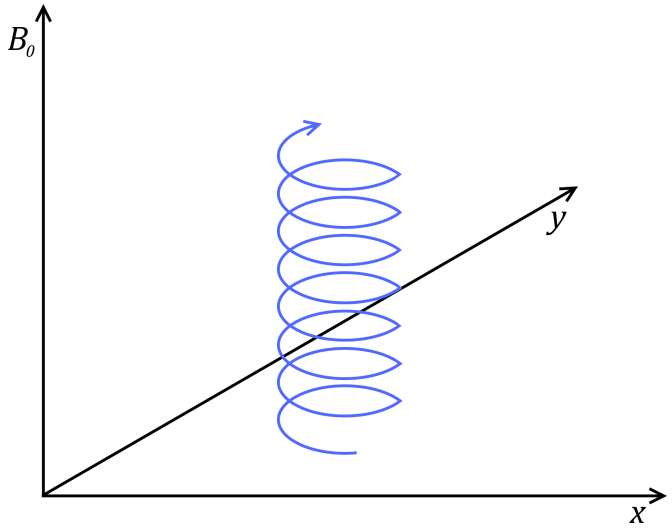


Figure 1.5: Helical motion of a charged particle in an uniform magnetic field.

### Cyclotron Frequency

A fundamental parameter in space plasma physics is the *(angular) cyclotron frequency* or *gyrofrequency* $\Omega_\sigma$, since spectral properties of waves in plasmas often show a dependence on frequency bands that are relative to the cyclotron frequency of specific ions or an electron. For instance, chorus waves are separated into two bands that are relative to the electron cyclotron frequency, while EMIC waves are separated by their frequency relative to the hydrogen, helium, and oxygen ion cyclotron frequencies (details are presented in the corresponding chapters). The cyclotron frequency is the angular frequency (in radians per second) of the circular motion of a charged particle (ion or electron) and can be defined using the cyclotron radius (Eq. 1.8). Generalising for a charged particle (electron or ion) of species $\sigma$, which is affected by the Earth's magnetic field $B_0$, the cyclotron frequency becomes:

$$\Omega_\sigma = \frac{v_\perp}{\rho_\sigma} = \frac{q_\sigma B_0}{m_\sigma} \,. \tag{1.9}$$

Note that $\Omega_\sigma$ includes the sign of the charge.

In keeping with convention, the angular cyclotron frequency (in radians per second) will be used in all the following derivations. However, in recent publications, results are

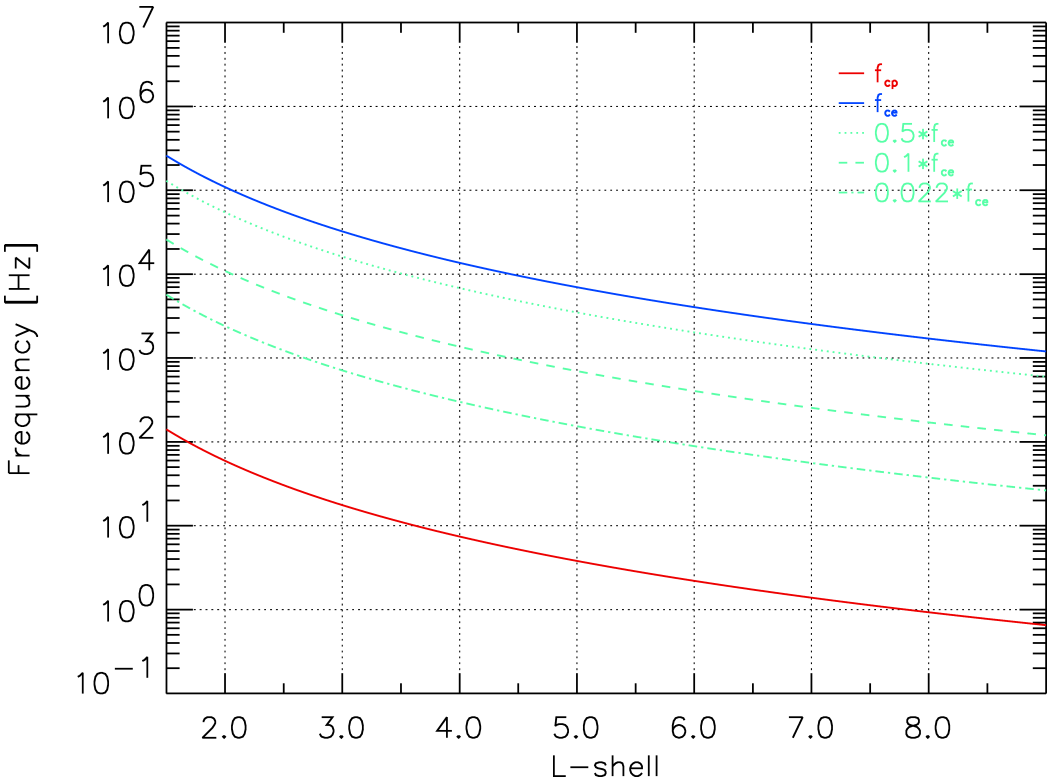


Figure 1.6: Cyclotron frequency of an electron (blue line) and proton (red line) as a function of L-shell. The dashed and dotted green lines show frequently used multiples of the electron cyclotron frequency.

usually presented using the non-angular cyclotron frequency (in Hz) denoted by $f_{c\sigma}$:

$$f_{c\sigma} = \frac{\Omega_\sigma}{2\pi} = \frac{v_\perp}{\rho_\sigma} = \frac{q_\sigma B_0}{2\pi m_\sigma} \,. \tag{1.10}$$

The *electron cyclotron frequency* $f_{ce}$ as well as the *hydrogen ion cyclotron frequency* $f_{cp}$ are shown in Figure 1.6 as a function of the McIlwain $L$-shell parameter (See section 1.3.4).

### 1.3.2 Uniform Electric and Magnetic Field

If we introduce an uniform electric field in addition to the uniform magnetic field described in the previous section, the parallel component of the Lorentz force (Eq. 1.4) becomes

$$\underline{F}_{L,\shortparallel} = q\underline{E}_{\shortparallel} \,, \tag{1.11}$$

which would lead to an acceleration (or deceleration) of the particle along the Earth's magnetic field, resulting in a larger (or smaller) pitch of the helical movement. Although electric fields parallel to the magnetic field of the Earth play an important role in accelerating particles in the aurora, they are rarely found in the region of the magnetosphere where charged particles are trapped [*Walt*, 1994]. This means that they can usually be neglected.

### E x B Drift

The component of the Lorentz force perpendicular to the Earth's magnetic field (Eq. 1.3) in an uniform electric field becomes:

$$\underline{F}_{L,\perp} = \left(\frac{\mathrm{d}\underline{p}}{\mathrm{d}t}\right)_{\perp} = q(\underline{E}_{\perp} + \underline{v}_{\perp} \times \underline{B})\,. \tag{1.12}$$

We can directly see that the introduction of an uniform electric field will cause an additional acceleration of the particle compared to the case without an electric field. In order to describe this additional motion, we will perform a Lorentz coordinate transformation, which allows us to separate the velocity $\underline{v}_{\perp}$ caused by $\underline{F}_{L,\perp}$ into a component that is identical to the one seen by an observer without any electric field ($\underline{v}'_{\perp}$) and into the remaining component only caused by the electric field ($\underline{v}_E$). This means that in the frame of reference moving at $\underline{v}_E$ the effects of the electric field vanish and only the helical motion is observed. Hence:

$$\underline{v}_{\perp} = \underline{v}'_{\perp} + \underline{v}_E\,. \tag{1.13}$$

The component of the electric field perpendicular to $\underline{B}$ can be expressed as [*Bittencourt*, 2004]:

$$\underline{E}_{\perp} = -\left(\frac{\underline{E} \times \underline{B}}{B^2}\right) \times \underline{B}\,. \tag{1.14}$$

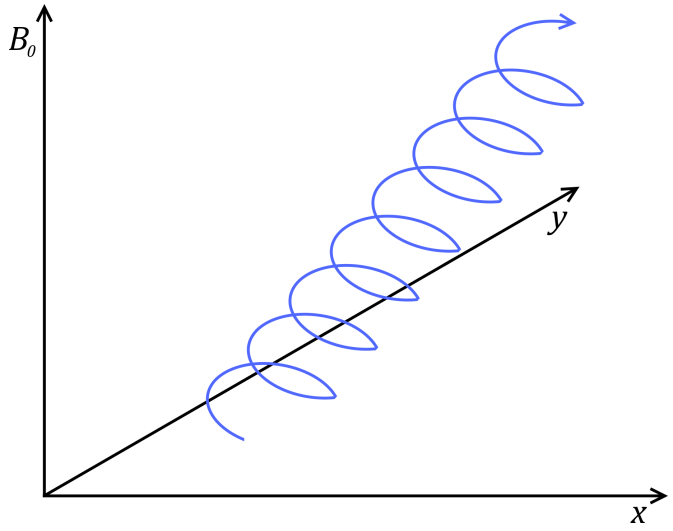


Figure 1.7: $E \times B$ drift motion as observed in a stationary frame of reference.

Using this expression for $\underline{E}_\perp$ and Eq. 1.13 we can rewrite the perpendicular component of the Lorentz force (Eq. 1.12) as:

$$\underline{F}_{L,\perp} = q\left(\underline{v}'_\perp + \underline{v}_E - \frac{\underline{E}_\perp \times \underline{B}}{B^2}\right) \times \underline{B}\,. \tag{1.15}$$

We can now directly see that if the observer moved with the velocity

$$\underline{v}_E = \frac{\underline{E}_\perp \times \underline{B}}{B^2}\,, \tag{1.16}$$

the motion of the particle would seem to be unaffected by any electrical field. Going back to the frame of reference of an external observer, the uniform electric field will therefore introduce an additional force acting on the charged particle, resulting in an additional velocity $\underline{v}_E$, which is called the $E \times B$ *drift*. The resulting motion is illustrated in Figure 1.7.

### 1.3.3 Inhomogeneous Electric and Magnetic Field

So far we have only considered the effects of uniform electric and magnetic fields on charged particles. While the equations of motions for these cases are relatively easy to derive and thereby allow the explanation of some of the fundamental effects for charged particles in these fields, a complete understanding of the motion of charged particles in

the radiation belts can only be obtained by analysing fields that are representative for the Earth's electromagnetic field. First of all, the Earth's magnetic field has a strong gradient pointing along the magnetic field ($z$-axis), which is fundamental to trap a charged particle inside the field. Additionally there are further slight differences of the electric and magnetic field of the Earth, causing inhomogeneities. Although the fields experienced by even a charged relativistic particle are nearly uniform during one gyration, the slight inhomogeneities accumulate over time and create a deviation from the helical motion derived for uniform fields.
Since the mathematical description of these problems is quite extensive, it is not useful to derive all the equations here. Instead, a concise summary of important effects for the particle motion, as well as underlying assumptions and restrictions will be presented.

### Mirror Force

As discussed in the previous sections, a charged particle moving perpendicular to a homogeneous magnetic field rotates around the magnetic field due to the Lorentz force. The cyclotron radius of this motion is inversely proportional to the strength of the magnetic field, which means that as the magnetic field increases, the cyclotron radius decreases. Let us now assume that the particle is moving inside an inhomogeneous magnetic field, which is cylindrically symmetric around the $z$-axis with a gradient of the field along the $z$-axis. If the particle is moving towards the stronger magnetic field, the radius of its helical motion will decrease. As the magnetic field increases, the orientation of the field lines change and therefore a component of $B$ that is not perpendicular to the cyclotron motion will arise. This will in return create a component $F_m$ of the Lorentz force that points against the gradient of the magnetic field, decelerating the particle along the $z$-axis towards the point of weakest magnetic field, as depicted in Fig. 1.8. Since $F_m$ will act on the charged particle as long as there is a gradient in the magnetic field, the $z$ component of the particle's velocity will eventually decrease to zero. Then $F_m$ will accelerate the particle towards the weaker field, effectively mirroring the particle. The particle will then be accelerated further until it reaches the point of weakest field, where the particle will pass into the region of opposite magnetic field

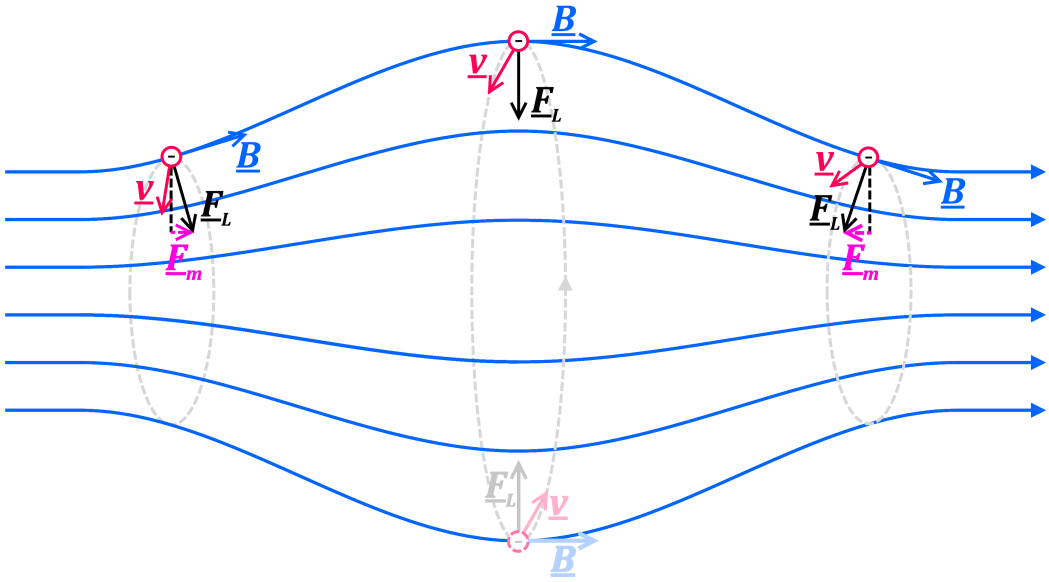


Figure 1.8: Geometry of the mirror force in an inhomogeneous magnetic field along the $z$-axis.

gradient. From here on, the direction of $F_m$ will reverse, again pointing back to weaker field, and hence decelerating the charged particle again. The charged particle will therefore bounce back and force between the mirror points and due to this behaviour, the component $F_m$ of the Lorentz force due to the gradient of the magnetic field along the $z$-axis is called the *mirror force*. Mathematically $F_m$ is given by:

$$\begin{aligned} \underline{F}_m &= -\frac{mv_\perp^2}{2B_0} \cdot \frac{\partial B}{\partial z} \cdot \underline{\hat{e}}_z \\ &= -\mu \cdot \frac{\partial B}{\partial z} \cdot \underline{\hat{e}}_z \,. \end{aligned} \tag{1.17}$$

The quantity $\mu$ is called the *magnetic moment* and is defined as:

$$\mu = \frac{mv_\perp^2}{2B_0} \,. \tag{1.18}$$

We can see that the location of the mirror point depends on the gradient of the magnetic field and most importantly on the particle's kinetic energy perpendicular to $B_0$. It is furthermore determined by the particle's initial velocity parallel to $B_0$, which means that $v_\perp$ has to be sufficiently large compared to $v_{\shortparallel}$ in order to provide enough space for the particle to be mirrored instead of hitting the Earth's atmosphere. This idea gives

rise of the concept of the loss cone, which is discussed in detail in Section 1.3.4.
Note that if a particle is injected in a region where the field has no defined gradient and the particle's velocity doesn't have any component parallel to the magnetic field, the particle won't experience any mirror force and therefore it will be trapped gyrating at this location. Assuming a perfect dipole field for the Earth's magnetic field, this would allow particles to be trapped at the equator, as long as their velocity did not have any component parallel to the magnetic field during the injection.

#### Gradient B Drift

Let us now consider the effects of a magnetic field that is inhomogeneous in the $x$-$y$-plane, i.e. perpendicular to $B$, where $\nabla B$ is in the $y$-direction. If a charged particle moves through this inhomogeneous magnetic field, the Lorentz force, which is forcing the particle to gyrate around the field line, will be affected by the changes of the magnetic field. Due to the gradient of the magnetic field during the gyration orbit, the gyroradius of the particle would be reduced or increased depending on the strength of the magnetic field in each region of the orbit, as illustrated in Fig. 1.9. The particle is decelerated, when it moves into a region where the magnetic field becomes weaker, and accelerated, when the field becomes stronger. The particle therefore experiences a drift that depends on the gradient of the magnetic field and of course on the charge of the particle. The *gradient B drift* velocity $\underline{v}_\nabla$ is given by:

$$\underline{v}_\nabla = \frac{m v_\perp^2}{2qB^3}(\underline{B} \times \nabla B)\,. \tag{1.19}$$

It can be seen that the gradient B drift is perpendicular to the gradient of the magnetic field $\nabla B$ and to the magnetic field itself. Furthermore, the gradient B drift depends on the particle's kinetic energy perpendicular to $B$, which is different to the energy independent E x B drift.
The presented expressions for the gradient drift employed a Taylor series expansion of the magnetic field around the spatial coordinate, and only the first terms of the Taylor series was used to derive the given equation. This means that the expression for the

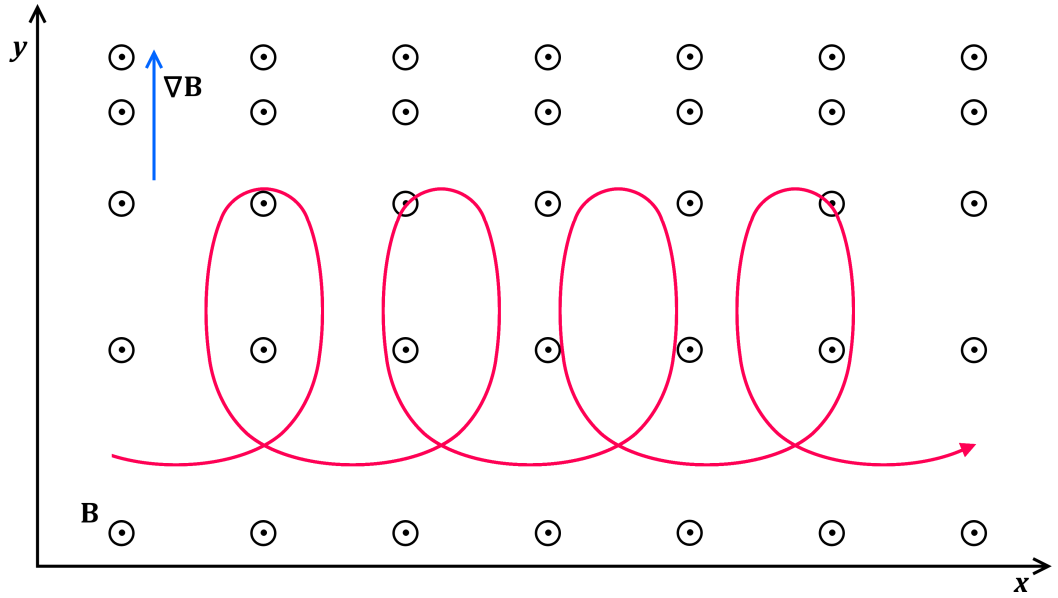


Figure 1.9: Geometry of the gradient B drift of an electron in an inhomogeneous magnetic field pointing out of the paper.

gradient drift become less valid for larger spatial differences, i.e. a larger gyroradius or magnetic field gradient.

Here, we will use the convention that the direction of a gradient points towards higher fields, or in other words 'up the slope'.

### Curvature Drift

The curvature drift is caused by the centripetal force acting on a charged particle moving along a curved field line. This drift therefore has to be proportional to the particle's velocity (and hence energy) parallel to the field line. The centripetal force is then defined as:

$$\underline{F_z} = \frac{m v_{\parallel}^2}{R_c} \cdot \frac{\underline{R_c}}{R_c}\,, \tag{1.20}$$

where $\underline{R_c}$ is the vector pointing from the centre of the Earth towards the charged particle, moving with velocity $v_{\parallel}$. In analogy to the E x B drift (Eq. 1.16), the curvature drift velocity is defined as:

$$\underline{v_c} = \frac{\underline{F_z} \times \underline{B}}{qB^2} \tag{1.21}$$

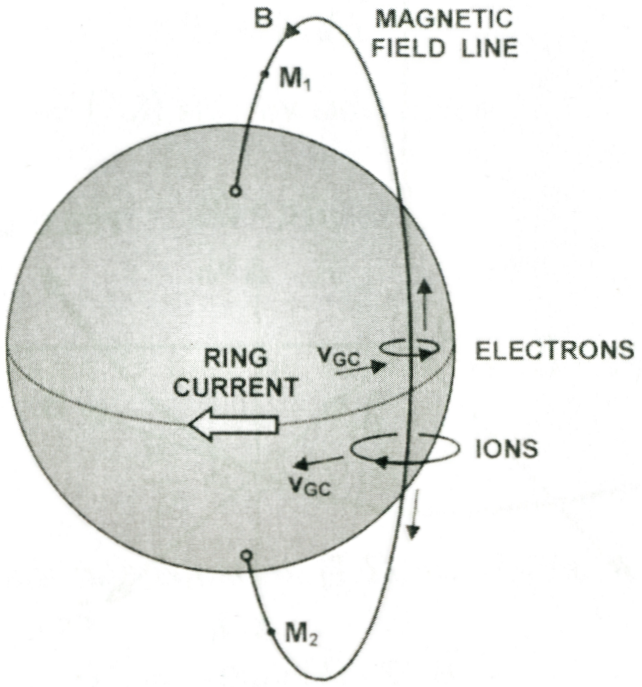


Figure 1.10: Sketch (not on scale) illustrating the ring current as a result of the combined gradient B drift and curvature drift velocity $v_{GC}$. From [*Bittencourt*, 2004].

Inserting the definition of $\underline{F}_z$ yields for the *curvature drift* velocity $\underline{v}_c$:

$$\underline{v}_c = \frac{m v_{\parallel}^2}{q} \cdot \frac{\underline{R}_c \times \underline{B}}{R_c^2 B^2} \tag{1.22}$$

### Ring Current

Since both the curvature and the gradient B drift depend on the sign of the charge, opposite charges will drift in opposite directions. Thereby charges of the (neutral) plasma will be separated, effectively creating a current. In Earth's magnetic field, both drifts will cause negatively charged particles to drift eastward and positively charged particles to drift westward, which can easily be understood for the curvature drift. For the direction of the gradient B drift we have to consider that Earth's magnetic field decreases with altitude, and hence $\nabla B$ points towards the Earth. The resulting net current is known as the *ring current*. An illustration of the combined gradient B drift and curvature drift velocity leading to the ring current is given in Figure 1.10.

### Bounce and Drift Periods

As we have just seen, the mirror force will cause a particle to bounce between the mirror points, and the curvature and gradient B drift will cause the particle to drift around the Earth. The periods of the bounce and drift motions of a charged particle were approximated in *Walt* [1994]. Under the assumption of a dipole field, the *bounce period* $\tau_b$ [in seconds] is given with an error of about 0.5 % by

$$\tau_b = 0.117 \left(\frac{R_0}{R_E}\right) \frac{c}{v} \left[1 - 0.4635(\sin\alpha_{eq})^{3/4}\right] , \tag{1.23}$$

where $R_0$ is the radial distance at which the charged particle crosses the equator, $R_E$ is the radius of the Earth, $v$ is the particle's speed, $\alpha_{eq}$ its equatorial pitch-angle (see next section), and $c$ is the speed of light.
Using the same assumptions, the *drift period* $\tau_d$ [in seconds] is given with an error of about 0.5 % by [*Walt*, 1994]:

$$\tau_d = C_d * \left(\frac{R_E}{R_0}\right) \frac{1}{\gamma - 1/\gamma} \left[1 - 0.3333(\sin\alpha_{eq})^{0.62}\right] , \tag{1.24}$$

with the constant factor $C_d = 1.557 \cdot 10^4$ (for electrons). The Lorentz factor $\gamma$ is defined as:

$$\gamma = \frac{1}{\sqrt{1 - \frac{v^2}{c^2}}} . \tag{1.25}$$

The Lorentz factor can be used to relate the relativistic kinetic energy $E_{kin,r}$ to the rest energy $E_0 = m_0 c^2$:

$$E_{kin,r} = (\gamma - 1) E_0 . \tag{1.26}$$

The bounce and drift periods calculated using these expressions are shown in Figure 1.11.

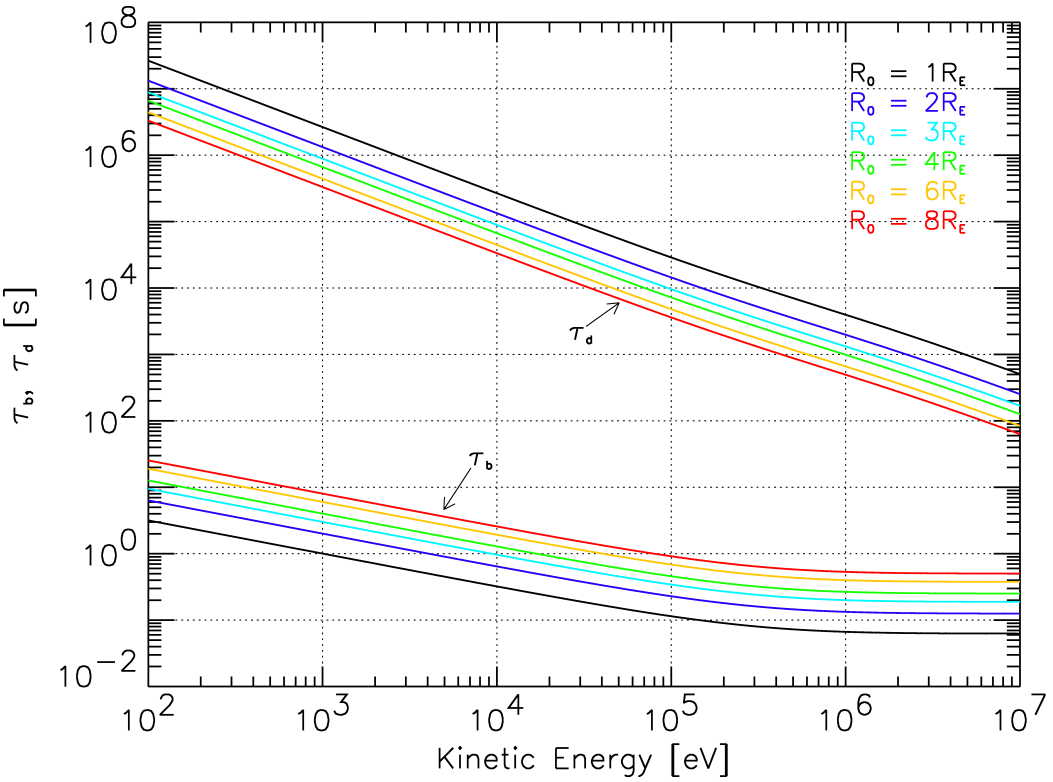


Figure 1.11: Bounce periods $\tau_b$ and drift periods $\tau_d$ as a function of kinetic energy for electrons with an equatorial pitch-angle of 90° at different radial distances.

### 1.3.4 Adiabatic Invariants

So far we have developed the theory to describe the short-term motion of a charged particle that is trapped in Earth's electromagnetic field. However, as we lack constants of motion, it is not possible to describe the long-term behaviour without introducing errors. The role of these constants of motion are filled by the *adiabatic invariants*, which stay constant, as long as changes of the system occur much slower than the associated quantity. In Lagrangian mechanics, the action integral taken over a closed path is a constant of motion if the system has a periodic motion alongside the closed path. Hamilton-Jacobi theory allows us to define the so-called action-angle variables for the periodic motion. The action integral then becomes:

$$J_i = \oint \underline{p}_i \mathrm{d}\underline{q}_i \,, \tag{1.27}$$

where $\underline{p}_i = \partial\mathcal{L}(x_i, v_i, t)/\partial v_i$ are the canonical momenta and $\underline{q}_i$ are their conjugate coordinates.

The Lagrangian function $\mathcal{L}(x_i, v_i, t)$ for a charged particle of species $\sigma$ in an electromagnetic field is defined as:

$$\mathcal{L}(\underline{r}, \underline{v}, t) = \frac{1}{2} m_\sigma \underline{v}^2 - q_\sigma \cdot \phi(\underline{r}, t) + q_\sigma \cdot \underline{v} \cdot \underline{A}(\underline{r}, t)\,, \tag{1.28}$$

with the particle's mass $m_\sigma$, velocity $\underline{v}$, charge $q$, electric potential $\phi$, and the magnetic vector potential $\underline{A}$. Hence the canonical momentum becomes:

$$\underline{p} = \frac{\partial\mathcal{L}(\underline{r}, \underline{v}, t)}{\partial v} = m_\sigma \underline{v} + q_\sigma \cdot \underline{A}(\underline{r}, t)\,. \tag{1.29}$$

As derived earlier, a charged particle trapped in Earth's electromagnetic field exhibits three periodic motions along a closed path: the rapid gyration around a field line, the bouncing between the two magnetic mirror points, and the longitudinal drift around the Earth. The physical properties of the system only change on timescales much larger than the corresponding periodicity of each of these motions and there are therefore three adiabatic invariants associated with these periodic motions. In order to determine the three adiabatic invariants, we hence have to calculate the action integral for each of these periodic motions.

### First Adiabatic Invariant

The first adiabatic invariant can be obtained by solving the action integral (Eq. 1.27) for the canonical momentum as defined in Eq. 1.29 along the closed path of the gyration orbit. As long as the spatial or temporal changes of the system are slower than the particle's cyclotron frequency, the action integral describes an adiabatic invariant. Denoting an element of the gyration orbit with $\mathrm{d}\underline{l}$ we get:

$$\begin{aligned} J_1 &= \oint [m_\sigma \underline{v} + q_\sigma \underline{A}] \cdot \mathrm{d}\underline{l} \\ &= \oint m_\sigma \underline{v} \cdot \mathrm{d}\underline{l} + q_\sigma \oint \underline{A} \cdot \mathrm{d}\underline{l}\,. \end{aligned} \tag{1.30}$$

For the integration of the first term in Eq. 1.30 we can exploit the fact that the integration path is always perpendicular to the guiding external magnetic field line and hence only components of the velocity $v_\perp$ perpendicular to the external magnetic field remain. For the second term of Eq. 1.30 we will use Stokes' theorem

$$\oint \underline{A} \cdot \mathrm{d}\underline{l} = \oint (\nabla \times \underline{A}) \cdot \mathrm{d}\underline{S}\,, \tag{1.31}$$

to change from a line integral to a surface integral over the area $S$ enclosed by the path described by $\mathrm{d}l$. Furthermore, we will use the relation between the magnetic vector potential and the magnetic field:

$$\underline{B} = \nabla \times \underline{A}\,. \tag{1.32}$$

Hence, Eq. 1.30 becomes:

$$\begin{aligned}
J_1 &\overset{Eq.1.31}{=} m_\sigma v_\perp \cdot 2\pi\rho_\sigma + q_\sigma \oint (\nabla \times \underline{A}) \cdot \mathrm{d}\underline{S} \\
&\overset{Eq.1.32}{=} m_\sigma v_\perp \cdot 2\pi\rho_\sigma + q_\sigma \oint \underline{B} \cdot \mathrm{d}\underline{S} \\
&= \quad m_\sigma v_\perp \cdot 2\pi\rho_\sigma - q_\sigma B_0 \pi \rho_\sigma^2 \\
&\overset{Eq.1.9}{=} m_\sigma v_\perp \cdot 2\pi \frac{m_\sigma v_\perp}{q_\sigma B_0} - q_\sigma B_0 \pi \frac{m_\sigma^2 v_\perp^2}{q_\sigma^2 B_0^2} \\
&= \quad \frac{\pi m_\sigma^2 v_\perp^2}{q_\sigma B_0} \\
J_1 &\overset{Eq.1.18}{=} \frac{2\pi m_\sigma}{q_\sigma} \cdot \mu\,.
\end{aligned} \tag{1.33}$$

Hence, the *first adiabatic invariant* is the magnetic moment $\mu$, except for a constant factor, where the magnetic moment is defined as (See Equation 1.18):

$$\mu = \frac{m v_\perp^2}{2B_0}\,.$$

Using this definition, it directly follows that

$$\frac{p_\perp^2}{B_0} = \mathrm{const}\,, \tag{1.34}$$

which leads to the useful and frequently used relations derived in the following subsection.

### Pitch-Angle

The magnetic moment is invariant even if a particle moves through a gradient of the magnetic field, particularly when it follows a field line, where the first invariant is most useful. If we define the *pitch-angle* $\alpha$ as the angle between the particle's velocity and the Earth's magnetic field $B_0$, we directly get (see Figure 1.12):

$$\tan \alpha = \frac{v_\perp}{v_{\shortparallel}} \,. \tag{1.35}$$

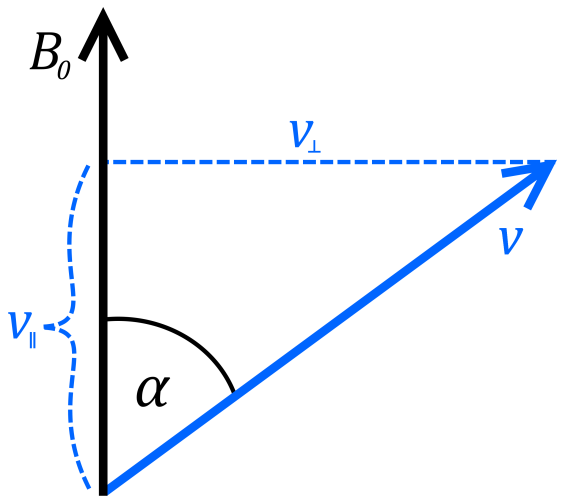


Figure 1.12: Illustration of the definition of the pitch-angle $\alpha$ as the angle between the particle velocity $v$ and the Earth's magnetic field $B_0$.

Using the definition of the pitch-angle we can rewrite Eq. 1.34 as:

$$\frac{p_\perp^2}{B_0} = \frac{p^2 \sin^2 \alpha}{B_0} = \text{const} \,. \tag{1.36}$$

This relation now allows us to derive a commonly used expression for $\mu$. Using $p_\perp = m_\sigma v_\perp$ and combining Equations 1.18 and 1.36 we get:

$$\mu = \frac{p^2 \sin^2 \alpha}{2 m_\sigma B_0} \,. \tag{1.37}$$

### The Loss Cone

Relations 1.35 and 1.36 are frequently used to describe the mirroring motion of a particle due to the mirror force (see section 1.3.3) in terms of the pitch-angle of a particle and furthermore to define the mirror points. If we investigate the particle at two different locations in space, it will experience a different magnetic field and differ in pitch-angle. From Eq. 1.36 it directly follows that

$$\frac{p^2 \sin^2 \alpha_1}{B_{0,1}} = \frac{p^2 \sin^2 \alpha_2}{B_{0,2}} \,. \tag{1.38}$$

As discussed in section 1.3.3, a particle will be mirrored when its velocity $v_{\shortparallel}$ parallel to the magnetic field is equal to zero. Using the definition of the pitch-angle (Eq. 1.36) and letting $v_{\shortparallel} \to \pm 0$ this is equivalent to a pitch-angle of 90°. If we denote the magnetic field at the mirror point by $B_m$ we get for Eq. 1.38:

$$\frac{p^2 \sin^2 90^\circ}{B_m} = \frac{p^2 \sin^2 \alpha}{B_0} \,, \tag{1.39}$$

and hence:

$$B_m = \frac{B_0}{\sin^2 \alpha} \,. \tag{1.40}$$

If a particle is injected at the equator with a pitch-angle $\alpha_{eq}$ it experiences the field $B_0 = B_{eq}$. If its pitch-angle is not equal to 90° it will move towards the stronger magnetic field, increasing its pitch-angle until it reaches a pitch-angle of 90°. At this point, it experiences the magnetic field $B_0 = B_m$ and will be reflected and move towards the equator. At the equator it will have the same pitch-angle (with different sign) as when it was injected. From there on the previously described motion will repeat in the other hemisphere, leading to a bouncing motion of the particle.

As explained, Eq. 1.40 shows that a particle with an equatorial pitch-angle of $\alpha_{eq}$ will be reflected at the point where the intensity of the magnetic field becomes $B_m$. However, the intensity of the field can not increase infinitely, and hence, a particle is not necessarily reflected. Instead, the charged particle reaches the atmosphere, where the

overall density of particles becomes large enough for the charged particle to be lost due to collisions with other particles, breaking the first invariant. If we denote the magnetic field at the altitude below which particles can be scattered into the atmosphere with $B_l$, we can rearrange Eq. 1.40 to identify the equatorial pitch-angle $\alpha_l$ which corresponds to this limit, i.e.:

$$\alpha_l = \arcsin\left(\frac{B_0}{B_l}\right)^{1/2} \tag{1.41}$$

This means that a particle that has an equatorial pitch-angle greater than $\alpha_l$ will be reflected at a higher altitude than the one defined by $B_l$. More importantly, a particle with an pitch-angle less than $\alpha_l$ will move beyond this point and enter the atmosphere, where it is lost due to collisions. The pitch-angle $\alpha_l$ is known as the *loss cone angle*.

### Second Adiabatic Invariant

The second adiabatic invariant is related to the bouncing of a particle trapped by Earth's magnetic field between the two magnetic mirror points. The action integral (Eq. 1.27) will again be solved for the canonical momentum as defined in Eq. 1.29, this time along the closed path of a full bounce between the mirror points. Denoting an element of the bounce path along a field line with $\mathrm{d}\underline{s}$ we get:

$$\begin{aligned} J_2 &= \oint [m_\sigma \underline{v} + q_\sigma \underline{A}] \cdot \mathrm{d}\underline{s} \\ &\overset{Eq.1.31}{=} \oint m_\sigma \underline{v} \cdot \mathrm{d}\underline{s} + q_\sigma \oint (\nabla \times \underline{A}) \cdot \mathrm{d}\underline{S} \\ &\overset{Eq.1.32}{=} \oint m_\sigma \underline{v} \cdot \mathrm{d}\underline{s} + q_\sigma \oint \underline{B} \cdot \mathrm{d}\underline{S}\,. \end{aligned}$$

The second integral describes the magnetic flux $\Phi$ enclosed by the area of the bounce path. Since the particle moves along a single field line, the magnetic field encountered by the particle will always be parallel to the area spanned by the bounce path. Hence,

the second integral becomes zero, i.e.:

$$\begin{aligned} J_2 &= \oint m_\sigma \underline{v} \cdot \mathrm{d}\underline{s} + 0 \\ &= \oint m_\sigma v_{\shortparallel} \, \mathrm{d}s \\ &= \text{const}\,. \end{aligned} \tag{1.42}$$

As long as the longitudinal drift of the particle around the Earth is small during the period of the bouncing between the mirror points, Eq. 1.42 describes the *second adiabatic invariant*. Conventionally, the second adiabatic invariant is usually called the *integral invariant* and it is designated by $J$ to highlight its relation to the action integral.
It is common to express $J$ as a quantity that is independent of the particle momentum $p = m_\sigma v$ and hence only depends on the geometry of the magnetic field. This leads to the introduction of the related quantity $I = J/2p$ or

$$I = \int_{s_m}^{s'_m} \sqrt{\left[1 - \frac{B(s)}{B_m}\right]} \mathrm{d}s\,, \tag{1.43}$$

where $s_m$ and $s'_m$ denote the mirror points of the charged particle moving along a field line.

### Third Adiabatic Invariant

To find an expression for the third adiabatic invariant, we solve the action integral (Eq. 1.27) once more for the canonical momentum as defined in Eq. 1.29, now along the longitudinal drift path of the charged particle around the Earth. Denoting an element of the drift path with $\mathrm{d}\underline{l}$ we get:

$$\begin{aligned} J_3 &= \oint [m_\sigma \underline{v} + q_\sigma \underline{A}] \cdot \mathrm{d}\underline{l} \\ &\overset{Eq.1.31}{=} \oint m_\sigma v_d \, \mathrm{d}l + q_\sigma \oint (\nabla \times \underline{A}) \cdot \mathrm{d}\underline{S} \\ &\overset{Eq.1.32}{=} \oint m_\sigma v_d \, \mathrm{d}l + q_\sigma \oint \underline{B} \cdot \mathrm{d}\underline{S} \\ &= \oint m_\sigma v_d \, \mathrm{d}l + q_\sigma \Phi\,. \end{aligned} \tag{1.44}$$

Here, $v_d$ is the drift velocity of the particle along its longitudinal drift path, and $\Phi$ denotes the magnetic flux through the surface area spanned by $\mathrm{d}\underline{S}$. A comparison of the magnitude of the first and second summand in Eq. 1.44 shows that it is possible to neglect the first term.

Assuming a drift period of about 1000 s, which roughly corresponds to an 1 MeV electron, as shown in Figure 1.11, the integral can be evaluated to the order of about $10^{-18}$ Kg m$^2$ s$^{-1}$.

In order to find a value for the second summand in Eq. 1.44, we assume a dipole field for the Earth's magnetic field and that the particle is moving at the equator. This allows us to approximate the magnetic flux as [*Roederer and Zhang*, 2014]:

$$\Phi = 2\pi B_d \cdot \frac{R_E^2}{R}\,, \tag{1.45}$$

where $R$ is the radial, equatorial distance of the charged particle orbiting the Earth in Earth radii, $R_E$ is the radius of the Earth, and $B_d$ is the mean value of the Earth's dipole magnetic field at the magnetic equator on the Earth's surface. Since the magnetic flux is inversely proportional to $R$, we will calculate the approximation of $\Phi$ for a particle that drifts around the Earth at a distance of 10 Earth radii. Inserting the values for $B_d$ and $R_E$ into Eq. 1.45 and multiplying with the electron charge, results in a value of about $10^{-10}$ Kg m$^2$ s$^{-1}$ as the lower boundary for the second term of $J_3$. This is much larger than the value of the first term, therefore we can neglect the first term of Eq. 1.44 and the action integral becomes:

$$J_3 = q_\sigma \oint \underline{B} \cdot \mathrm{d}\underline{S} = q_\sigma \Phi\,, \tag{1.46}$$

which is the definition of the *third adiabatic invariant*. In order for $J_3$ to be an invariant, the flux enclosed by the surface formed by the drift path needs to be conserved. Hence, the magnetic field of the Earth needs to be constant during one drift orbit period. Since changes of the magnetic field can happen rather quickly, $J_3$ is often not conserved, especially during disturbed periods.

### McIlwain L-shell Parameter

In space plasma physics scientists are usually interested in studying spatial changes of the charged particle fluxes that are trapped by Earth's magnetic field. As we have shown in the previous sections, these changes are caused by the magnetic field, which is irregular in Cartesian coordinates, even if we assumed a simple dipole field for the Earth's magnetic field. Therefore, a coordinate system that follows the trapped particle movement will be of great value, as it allows us to easily gain insight into changes of the fluxes as a function of position.

Such a coordinate system can be derived based on the adiabatic invariants. For instance, the first adiabatic invariant suggests that the magnitude of the magnetic field $B_m$ at a mirror point defines a constant latitudinal mirror point for a charged particle along a longitudinal drift orbit. Hence, using the magnetic field as a parameter for a coordinate system would allow us to simplify the longitudinal dependence for the particle motion, by exploiting this symmetry. Together with the quantity $I$ (Eq. 1.43) that is related to the second adiabatic invariant, this has led to the introduction of a coordinate system based on the coordinate pair $(B_m, I)$. This uniquely defines a particle *drift shell*, which is the surface that is formed by the intersection of $B_m$ and $I$. The drift shell is therefore different to the magnetic shell, which is defined by the strength of the magnetic field at the equator. As the drift shell is formed by $B_m$, different drift shells will hence not terminate at the same location.

If the magnetic field of the Earth was assumed to be a dipole field, which is axisymmetric with respect to the magnetic axis, the drift shells would be axisymmetric as well. Based on this, the parameter $L_m$ was introduced by *McIlwain* [1961], which corresponds to the equatorial radius of a drift shell assuming a dipole field for Earth's magnetic field. Since the geometry is axisymmetric, the particle drift orbit is independent of the particle's pitch-angle. Based on the particle's location in space defined by its radial distance $r$ to the Earth and its latitude $\lambda$, we can define $L_m$ for a dipole field as [*Roederer and Zhang*, 2014]:

$$L_m = \frac{r}{R_E} \cdot \frac{1}{\cos^2\lambda} = R \cdot \frac{1}{\cos^2\lambda} \,. \tag{1.47}$$

In order to capture the non-dipole nature of the Earth's magnetic field, McIlwain extended this definition to non-dipole fields, which led to the introduction of the *McIlwain L-shell parameter* $L$. In order to capture realistic fields, $L$ and $R_E$ are now linked by a analytical function $f$ that depends on the quantity $I$ (which is related to the second adiabatic invariant), the magnetic field $B$, and the dipole term $M_E$ of the Earth's magnetic field [*Walt*, 1994]:

$$LR_E = f(I, B, M_E)\,. \tag{1.48}$$

#### Roederer $L^*$ Parameter

Based on the fact that all trapped particles return to their initial drift shells as long as changes of the system are adiabatic, Roederer introduced an invariant reference presentation for stably trapped particles in realistic representations of the Earth's magnetic field. The *Roederer $L^*$ parameter* is based on the third adiabatic invariant $\Phi$, and is found by slowly turning off all external field sources in a realistic field model, allowing for an adiabatic change of the trapped particle from a realistic magnetic field to a dipole field. The $L^*$ parameter then represents the radial distance to the equatorial location of the particle, where it would be found if the adiabatic change of the magnetic field was performed. The $L^*$ parameter can hence be expressed as a function of the Earth's dipole magnetic field $B_d$ at the magnetic equator on the Earth's surface and the third adiabatic invariant $\Phi$ as [*Roederer and Zhang*, 2014]:

$$L^* = \frac{2\pi B_d R_E^2}{\Phi}\,. \tag{1.49}$$

Note that a $L^*$ value does not represent a particle drift shell or magnetic field lines and there is usually no simple transformation from the McIlwain L parameter to $L^*$. However, in a dipole field only and at the equator, we can directly see that $L^* = L$, using Equations 1.45 and 1.47. As a general rule of thumb, the difference between $L$ and $L^*$ increases as $L^*$ increases. At low values of $L^*$, the difference between $L$ and $L^*$ is relatively small, with $L^* = 2$ mapping to about $L = 2.05 - 2.10$, while $L^* = 5$ maps to about $L = 5.3 - 5.6$, and $L^* = 8$ maps to $L = 8.5 - 9.0$ [*Meredith et al.*, 2012].

In this thesis all data is given in dependence of the Roederer $L^*$ parameter, which was computed using the ONERA-DESP library V4.2 [*Boscher and Bourdarie*, 2004], with the IGRF field at the middle of the appropriate year. As a model for Earth's magnetic field, the Olson-Pfitzer quiet time model [*Olson et al.*, 1977] was chosen, which is based on quiet geomagnetic conditions. There are several models for the magnetic field that represent geomagnetically active conditions, but they still have large uncertainties during very disturbed times [e.g. *McCollough et al.*, 2008]. Furthermore, most of them require solar wind parameters which are usually not fully available for all the data periods that will be studied. The Olson-Pfitzer quiet time model has shown to be a reliable average magnetic field model when compared to measurements [*Friedel et al.*, 2005] and it was furthermore recently adopted by the Panel for Radiation Belt Environment Modelling for improving space radiation models. The ONERA-DESP library was designed for particles, which means that in the cases where it is utilised for electromagnetic waves in a plasma, a local pitch-angle of 90° had to be assumed.

### 1.3.5 Summary of the Particle Motion

In this section the complex motion of a charged particle trapped by the Earth's magnetic field was derived. It was found that the charged particle rotates around a field line, while it bounces back and forth between defined mirror points in the northern and southern hemisphere. The gradient B drift and the curvature drift will cause the particle to slowly drift around the Earth creating the so-called ring current. A summary of the bounce and drift motion of the particles is depicted in Figure 1.13.

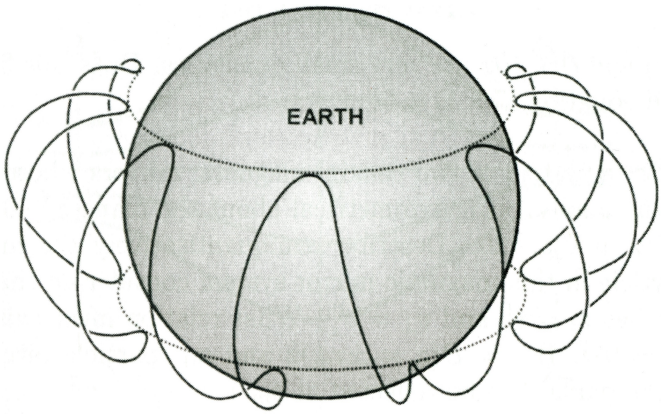


Figure 1.13: Schematic summary of the bounce and drift motion of a charged particle drifting around the Earth. From [*Bittencourt*, 2004].

## 1.4 Electromagnetic Waves in a Plasma

So far we have derived the theoretical framework for charged particle motion in the electromagnetic fields of the Earth. The second vital part to describe the interaction between electromagnetic waves in a plasma and the trapped particles in the radiation belts, is the propagation of electromagnetic waves in the plasma that surrounds the Earth. Therefore, a short description of a plasma will be given in this section followed by the theoretical description of the propagation of electromagnetic waves inside a plasma. It will be shown that the plasma can fundamentally be characterised as either a conductive medium or a dielectric medium. Additionally, it will be shown that, although these two characterisations seem to contradict each other, conductive and dielectric effects can be found for wave propagation in a plasma. The equivalency of both characterisations will be demonstrated.

### 1.4.1 Definition of a Plasma

Plasma is commonly referred to as the fourth fundamental state of matter, with the other three being the solid, liquid, and gaseous state. The state of a given substance is primarily defined by the strengths of the bonds between its molecules and atoms. In order to change the phase of substance the thermal energy of the molecules or atoms has to be increased, resulting in a phase transition. In the gaseous state, these forces are nearly absent and a further increase in energy will result in a gradual ionisation (by

collision) of the atoms in the gas, resulting in an ionised gas, or *plasma*. However, this transition into a plasma is not a phase transition, since it occurs gradually. A plasma is therefore a collection of particles that are at least partly ionised and hence is able to conduct electric currents.

#### Plasma Frequency

When the charged ions and electrons in a plasma are disturbed from their equilibrium position, electric fields between the displaced charged particles and the uniform neutral background of ions and electrons will build up. These electric fields pull back the charged particles towards their equilibrium state, but because of their inertia, the charged particles will start to oscillate around their original position. The oscillation frequency is known as the (angular) plasma frequency $\omega_{p,\sigma}$ and is defined as:

$$\omega_{p,\sigma}^2 = \frac{n_\sigma q_\sigma^2}{\varepsilon_0 m_\sigma}\,, \tag{1.50}$$

where $n_\sigma$ is the number density (in $\mathrm{m}^{-3}$) of the particle of species $\sigma$ with the charge $q$ (including the sign of the charge), $m_\sigma$ the mass of the particle, and $\epsilon_0$ the vacuum permittivity.

Similarly to the definition of the cyclotron frequency, it is common to specify a non-angular plasma frequency (in Hz) denoted by $f_{p,\sigma}$:

$$f_{p,\sigma} = \frac{\omega_{p,\sigma}}{2\pi} = \frac{1}{2\pi}\cdot\sqrt{\frac{n_\sigma q_\sigma^2}{\varepsilon_0 m_\sigma}}\,. \tag{1.51}$$

### 1.4.2 Wave Propagation

Electromagnetic waves that propagate inside a plasma, where the plasma acts as a guiding, dispersive medium, are commonly referred to as *plasma waves*. There is usually a multitude of plasma waves, which form a superposition of infinite plane waves (i.e. wave packets). Although the term plasma waves is also used to describe the translational periodic motion of the charged particles inside the plasma, described by the plasma frequency, we will use this short hand in the rest of this thesis and try to clarify if cases of the translational motion are meant rather than electromagnetic waves in a

plasma.

Electromagnetic waves, propagating in an infinite, uniform, collisionless, and magnetised plasma have to fulfil the Maxwell equations:

$$\underline{\nabla} \times \underline{E} = -\frac{\partial \underline{B}}{\partial t} \tag{1.52}$$

$$\underline{\nabla} \times \underline{B} = \mu_0 \underline{j} + \mu_0 \varepsilon_0 \frac{\partial \underline{E}}{\partial t} \tag{1.53}$$

$$\underline{\nabla} \cdot \underline{E} = \frac{1}{\varepsilon_0} (\rho + \rho_{ext}) \tag{1.54}$$

$$\underline{\nabla} \cdot \underline{B} = 0\,, \tag{1.55}$$

where $\underline{E}$ is the electric field, $\underline{B}$ the magnetic field, $\mu_0$ the vacuum permeability, $\varepsilon_0$ the vacuum permittivity, and $\rho_{(ext)}$ the (external) charge density. The total current density $\underline{j}$ is composed of the free current density $\underline{j}_f$, the displacement current density $\underline{j}_d$ and the current density of external currents $\underline{j}_{ext}$, which, in space plasma physics, is usually neglected. In order to be able to describe the wave propagation in a plasma, i.e. plasma waves, we need to find expressions for the free current density and the displacement current density.

A plasma can be either characterised as a conductive medium, where the displacement current density is equal to zero, or as a dielectric medium consisting of dipoles, where the free current density is zero. Hence, depending on the characterisation of the plasma, only one of the current densities needs to be specified in order to describe plasma waves. Both cases will be discussed in the following subsections, showing that it is merely a matter of taste which characterisation to choose. All following derivations assume a cold plasma, which means that the thermal velocity of the charged particles is considered very small.

### 1.4.3 Plasma as a Conductive Medium

If a plasma is characterised as a conductive medium, one assumes that the plasma consists of (free) charged particles, i.e. electrons and the corresponding ions. The total

free current density $\underline{j}_f$ considering all particles of all species $\sigma$ is defined as:

$$\underline{j}_f := \sum_\sigma n_\sigma q_\sigma \underline{v}_\sigma \,, \tag{1.56}$$

where $n_\sigma$ is the particle number density, $\underline{v}_\sigma$ is the velocity of the particle, and $q_\sigma$ is the charge of the particle of species $\sigma$ including the sign of the charge. The motion of an individual particle is determined by the forces of its surrounding electromagnetic field, described by the Lorentz force:

$$\underline{F}_{L,\sigma} = m_\sigma \frac{\mathrm{d}\underline{v}_\sigma}{\mathrm{d}t} = q_\sigma(\underline{E} + \underline{v}_\sigma \times \underline{B}) \,, \tag{1.57}$$

where $\underline{B} = \underline{B}_0 + \underline{B}_w$ is the total magnetic field, composed of the background magnetic field $\underline{B}_0$ and the magnetic field caused by a plasma wave $\underline{B}_w$. In order to solve the equation of motion for $\underline{v}_\sigma$ we need to assume that the plasma waves are infinite plane waves and hence the motion caused by the plasma waves is also oscillating, i.e.:

$$\underline{E} = \underline{E}_0 \cdot \exp[i(\underline{k} \cdot \underline{r} - \omega t)] \tag{1.58}$$

$$\underline{B}_w = \underline{B}_{w,0} \cdot \exp[i(\underline{k} \cdot \underline{r} - \omega t)] \tag{1.59}$$

$$\underline{v}_\sigma = \underline{v}_{\sigma,0} \cdot \exp[i(\underline{k} \cdot \underline{r} - \omega t)] \,. \tag{1.60}$$

Furthermore, if we assume small wave amplitude, i.e. $\underline{B}_w \ll \underline{B}_0 \Rightarrow \underline{B} \approx \underline{B}_0$, the equation of motion for a single particle (Eq. 1.57) can then be rewritten as:

$$\begin{aligned} & m_\sigma \frac{\mathrm{d}\underline{v}_\sigma}{\mathrm{d}t} = q_\sigma(\underline{E} + \underline{v}_\sigma \times \underline{B}_0) \\ \overset{\text{Eq.1.60}}{\Rightarrow} \quad & -m_\sigma i\omega \underline{v}_\sigma = q_\sigma(\underline{E} + \underline{v}_\sigma \times \underline{B}_0) \\ \Leftrightarrow \quad & \underline{v}_\sigma = \frac{iq_\sigma}{m_\sigma \omega}(\underline{E} + \underline{v}_\sigma \times \underline{B}_0) \,. \end{aligned} \tag{1.61}$$

In order to solve Eq. 1.61 for $\underline{v}_\sigma$ we will first separate Eq. 1.61 into its $x$, $y$, and $z$ components. Without loss of generality, we hereby choose our coordinate system in a way that the background magnetic field is aligned in the z direction and hence

$\underline{B}_0 = [0, 0, B_0]$.

$$v_{\sigma,x} = \frac{iq_\sigma}{m_\sigma \omega} \left[E_x + v_{\sigma,y} B_0\right] \tag{1.62}$$

$$v_{\sigma,y} = \frac{iq_\sigma}{m_\sigma \omega} \left[E_y - v_{\sigma,x} B_0\right] \tag{1.63}$$

$$v_{\sigma,z} = \frac{iq_\sigma}{m_\sigma \omega} E_z \tag{1.64}$$

Note, that the equations for $v_{\sigma,x}$ and $v_{\sigma,y}$ depend on each other. To find independent expressions, we will first insert Eq. 1.63 into Eq. 1.62. Furthermore, to find an expression that depends on basic plasma parameters, we will use the definition of the cyclotron frequency (Eq. 1.9) as well:

$$\begin{aligned}
& v_{\sigma,x} = \frac{iq_\sigma}{m_\sigma \omega} \left[E_x + v_{\sigma,y} B_0\right] \\
\overset{\text{Eq.1.63}}{\Rightarrow} \quad & v_{\sigma,x} = \frac{iq_\sigma}{m_\sigma \omega} E_x - \frac{q_\sigma^2 B_0}{m_\sigma^2 \omega^2} E_y + \frac{q_\sigma^2 B_0^2}{m_\sigma^2 \omega^2} v_{\sigma,x} \\
\overset{\text{Eq.1.9}}{\Rightarrow} \quad & v_{\sigma,x} = \frac{i\Omega_\sigma}{B_0 \omega} E_x - \frac{\Omega_\sigma^2}{B_0 \omega^2} E_y + \frac{\Omega_\sigma^2}{\omega^2} v_{\sigma,x} \\
\Leftrightarrow \quad & v_{\sigma,x} \left(1 - \frac{\Omega_\sigma^2}{\omega^2}\right) = \frac{i\Omega_\sigma}{B_0 \omega} E_x - \frac{\Omega_\sigma^2}{B_0 \omega^2} E_y \\
\Leftrightarrow \quad & v_{\sigma,x} = \frac{\omega^2}{B_0(\omega^2 - \Omega_\sigma^2)} \left[\frac{i\Omega_\sigma}{\omega} E_x - \frac{\Omega_\sigma^2}{\omega^2} E_y\right] .
\end{aligned} \tag{1.65}$$

By inserting Eq. 1.62 into Eq. 1.63 and performing the same operations, we get for $v_{\sigma,y}$:

$$v_{\sigma,y} = \frac{\omega^2}{B_0(\omega^2 - \Omega_\sigma^2)} \left[\frac{\Omega_\sigma^2}{\omega^2} E_x + \frac{i\Omega_\sigma}{\omega} E_y\right] . \tag{1.66}$$

Using the definition of the cyclotron frequency in Eq. 1.64, we get for $v_{\sigma,z}$:

$$v_{\sigma,z} = \frac{i\Omega_\sigma}{B_0 \omega} E_z \, . \tag{1.67}$$

We can now use the expressions for the components of the velocity of the particles of species $\sigma$ to calculate the $x$, $y$, and $z$ component of the free current density (Eq. 1.56) individually. We will again bring the expression into a form that only depends on characteristic plasma parameters by using the definition of the plasma frequency (Eq. 1.50):

$$\begin{aligned}
j_{f,x} &= \sum_\sigma n_\sigma q_\sigma v_{\sigma,x} \\
&\overset{\text{Eq.1.65}}{=} \sum_\sigma n_\sigma q_\sigma \frac{\omega^2}{B_0(\omega^2-\Omega_\sigma^2)}\left[\frac{i\Omega_\sigma}{\omega}E_x - \frac{\Omega_\sigma^2}{\omega^2}E_y\right] \\
&\overset{\text{Eq.1.9}}{=} \varepsilon_0 \sum_\sigma \frac{1}{\varepsilon_0}\frac{q_\sigma}{m_\sigma\Omega_\sigma}\frac{n_\sigma q_\sigma \omega^2}{(\omega^2-\Omega_\sigma^2)}\left[\frac{i\Omega_\sigma}{\omega}E_x - \frac{\Omega_\sigma^2}{\omega^2}E_y\right] \\
&\overset{\text{Eq.1.50}}{=} \varepsilon_0 \sum_\sigma \frac{\omega^2}{\Omega_\sigma}\frac{\omega_{p,\sigma}^2}{(\omega^2-\Omega_\sigma^2)}\left[\frac{i\Omega_\sigma}{\omega}E_x - \frac{\Omega_\sigma^2}{\omega^2}E_y\right] \\
&= -i\omega\varepsilon_0 \sum_\sigma -\frac{\omega_{p,\sigma}^2}{(\omega^2-\Omega_\sigma^2)}E_x - i\frac{\omega_{p,\sigma}^2\Omega_\sigma}{\omega(\omega^2-\Omega_\sigma^2)}E_y \\
\Leftrightarrow \quad \boxed{j_{f,x} &= -i\omega\varepsilon_0 \sum_\sigma -\frac{\omega_{p,\sigma}^2}{\omega^2}\cdot\frac{\omega^2}{(\omega^2-\Omega_\sigma^2)}E_x - i\frac{\omega_{p,\sigma}^2}{\omega^2}\cdot\frac{\omega\Omega_\sigma}{(\omega^2-\Omega_\sigma^2)}E_y} \qquad (1.68)
\end{aligned}$$

Similarly, for the $y$ component of the free current density we get:

$$\begin{aligned}
j_{f,y} &= \sum_\sigma n_\sigma q_\sigma v_{\sigma,y} \\
&\overset{\text{Eq.1.66}}{=} \sum_\sigma n_\sigma q_\sigma \frac{\omega^2}{B_0(\omega^2-\Omega_\sigma^2)}\left[\frac{\Omega_\sigma^2}{\omega^2}E_x + \frac{i\Omega_\sigma}{\omega}E_y\right] \\
&\overset{\text{Eq.1.50,1.9}}{=} \varepsilon_0 \sum_\sigma \frac{\omega^2}{\Omega_\sigma}\frac{\omega_{p,\sigma}^2}{(\omega^2-\Omega_\sigma^2)}\left[\frac{\Omega_\sigma^2}{\omega^2}E_x + \frac{i\Omega_\sigma}{\omega}E_y\right] \\
\Leftrightarrow \quad \boxed{j_{f,y} &= -i\omega\varepsilon_0 \sum_\sigma i\frac{\omega_{p,\sigma}^2}{\omega^2}\cdot\frac{\omega\Omega_\sigma}{(\omega^2-\Omega_\sigma^2)}E_x - \frac{\omega_{p,\sigma}^2}{\omega^2}\cdot\frac{\omega^2}{(\omega^2-\Omega_\sigma^2)}E_y} \qquad (1.69)
\end{aligned}$$

And for the $z$ component of the free current density we get:

$$\begin{aligned} j_{f,z} &= \sum_\sigma n_\sigma q_\sigma v_{\sigma,x} \\ &\overset{\text{Eq.1.66}}{=} \sum_\sigma n_\sigma q_\sigma \frac{i\Omega_\sigma}{B_0\omega} E_z \\ &\overset{\text{Eq.1.9}}{=} \sum_\sigma n_\sigma q_\sigma \frac{iq_\sigma}{m_\sigma\omega} E_z \\ \overset{\text{Eq.1.50}}{\Rightarrow} \quad \boxed{j_{f,z} &= -i\omega\varepsilon_0 \sum_\sigma -\frac{\omega_{p,\sigma}^2}{\omega^2} E_z} \end{aligned} \tag{1.70}$$

We have now derived expressions for each component of the free current density completely based on previously defined fundamental plasma parameters. This allows us to solve the Maxwell equations for the propagation of an electromagnetic wave in a plasma. It is common to simplify these expression by introducing short-hand notations, which are presented in the following paragraph.

Using vector notation, we can combine the components of the free current density (Eq. 1.68, 1.69, 1.70 to:

$$\begin{bmatrix} j_{f,x} \\ j_{f,y} \\ j_{f,z} \end{bmatrix} = -i\omega\varepsilon_0 \begin{bmatrix} \sum_\sigma -\frac{\omega_{p,\sigma}^2}{\omega^2} \cdot \frac{\omega^2}{(\omega^2-\Omega_\sigma^2)} & \sum_\sigma -i\frac{\omega_{p,\sigma}^2}{\omega^2} \cdot \frac{\omega\Omega_\sigma}{(\omega^2-\Omega_\sigma^2)} & 0 \\ \sum_\sigma i\frac{\omega_{p,\sigma}^2}{\omega^2} \cdot \frac{\omega\Omega_\sigma}{(\omega^2-\Omega_\sigma^2)} & \sum_\sigma -\frac{\omega_{p,\sigma}^2}{\omega^2} \cdot \frac{\omega^2}{(\omega^2-\Omega_\sigma^2)} & 0 \\ 0 & 0 & \sum_\sigma -\frac{\omega_{p,\sigma}^2}{\omega^2} \end{bmatrix} \cdot \begin{bmatrix} E_x \\ E_y \\ E_z \end{bmatrix} \tag{1.71}$$

The free current density can be related to the electric field $\underline{E}$ by:

$$\underline{j}_f := \underline{\underline{\sigma}} \cdot \underline{E}\,, \tag{1.72}$$

where, $\underline{\underline{\sigma}}$ is the *conductivity tensor*. Comparing Eq. 1.72 with Eq. 1.71, allows us to specify the conductivity tensor $\underline{\underline{\sigma}}$ directly as:

$$\underline{\underline{\sigma}} = -i\omega\varepsilon_0 \cdot \begin{bmatrix} \kappa_1 - 1 & i\kappa_2 & 0 \\ -i\kappa_2 & \kappa_1 - 1 & 0 \\ 0 & 0 & \kappa_3 - 1 \end{bmatrix}, \tag{1.73}$$

where we use the short-hand notations:

$$\kappa_1 = 1 - \sum_\sigma \frac{\omega_{p,\sigma}^2}{\omega^2} \cdot \frac{\omega^2}{(\omega^2 - \Omega_\sigma^2)} \tag{1.74}$$

$$\kappa_2 = -\sum_\sigma \frac{\omega_{p,\sigma}^2}{\omega^2} \cdot \frac{\omega\Omega_\sigma}{(\omega^2 - \Omega_\sigma^2)} \tag{1.75}$$

$$\kappa_3 = 1 - \sum_\sigma \frac{\omega_{p,\sigma}^2}{\omega^2} \tag{1.76}$$

In cold plasma theory the conductivity tensor is often written using the *Stix Parameters* (**L**)eft, (**R**)ight, (**S**)um, (**D**)ifference, and **P**, which are defined as:

$$L := \kappa_1 - \kappa_2 \tag{1.77}$$

$$R := \kappa_1 + \kappa_2 \tag{1.78}$$

$$P := \kappa_3 \tag{1.79}$$

$$S := \frac{1}{2}(R + L) = \kappa_1 \tag{1.80}$$

$$D := \frac{1}{2}(R - L) = \kappa_2 \tag{1.81}$$

and hence, using the Stix parameters, the conductivity tensor can be written as:

$$\underline{\underline{\sigma}} = -i\omega\varepsilon_0 \cdot \begin{bmatrix} S - 1 & iD & 0 \\ -iD & S - 1 & 0 \\ 0 & 0 & P - 1 \end{bmatrix}. \tag{1.82}$$

We now have derived the short-hand expression for the free current density for a plasma characterised as a conductive medium. This allows us to solve the Maxwell equations

in order to describe the propagation of plasma waves.

### 1.4.4 Plasma as a Dielectric Medium

Instead of a conductive medium, a plasma can also be described as a dielectric medium, consisting only of electric dipoles instead of individual charged particles. In this characterisation, an electromagnetic field will polarise the dipoles, displacing them from their equilibrium positions. This will cause a net polarisation current $\underline{j}_p$, which is defined as:

$$\underline{j}_p := \frac{\partial \underline{P}}{\partial t}\,, \tag{1.83}$$

where $\underline{P}$ is the polarisation, which is related to the *dielectric displacement* $\underline{D}$ by

$$\underline{D} := \varepsilon_0 \underline{E} + \underline{P}\,. \tag{1.84}$$

As the plasma is characterised as a dielectric medium, there is no free current density and hence, the total current density in Ampere's Law (Eq. 1.53) becomes $\underline{j} = \underline{j}_p + \underline{j}_{ext}$. It is common to describe plasma waves in a dielectric medium using the dielectric displacement. Using the relation between the polarisation and the dielectric displacement, we can rewrite Ampere's Law as:

$$\begin{aligned}
\underline{\nabla} \times \underline{B} &= \mu_0 \underline{j} + \mu_0 \varepsilon_0 \frac{\partial \underline{E}}{\partial t} \\
\underline{\nabla} \times \underline{B} &= \mu_0 \underline{j}_p + \mu_0 \varepsilon_0 \frac{\partial \underline{E}}{\partial t} + \mu_0 \underline{j}_{ext} \\
\underline{\nabla} \times \underline{B} &= \mu_0 \frac{\partial \underline{P}}{\partial t} + \mu_0 \varepsilon_0 \frac{\partial \underline{E}}{\partial t} + \mu_0 \underline{j}_{ext} \\
\underline{\nabla} \times \underline{B} &\overset{\text{Eq.1.84}}{=} \mu_0 \frac{\partial \underline{D}}{\partial t} - \mu_0 \varepsilon_0 \frac{\partial \underline{E}}{\partial t} + \mu_0 \varepsilon_0 \frac{\partial \underline{E}}{\partial t} + \mu_0 \underline{j}_{ext} \\
\underline{\nabla} \times \underline{B} &= \mu_0 \frac{\partial \underline{D}}{\partial t} + \mu_0 \underline{j}_{ext}\,.
\end{aligned} \tag{1.85}$$

In order to describe the propagation of a plasma wave in a plasma characterised as dielectric medium, we therefore need to find an expression for the dielectric displacement (Eq. 1.84). In particular we need to derive an expression for the polarisation $\underline{P}$. The

polarisation is generally defined as:

$$\underline{P} := \sum_{\sigma} n_\sigma q_\sigma \underline{r}_\sigma \,, \tag{1.86}$$

where $n_\sigma$ is the particle number density and $q_\sigma$ is the charge of the particle of species $\sigma$ including the sign of the charge. $\underline{r}_\sigma$ describes the displacement of the particle $\sigma$ from its equilibrium position caused by external and internal electromagnetic fields.
The motion of the charged particle, and hence its displacement is determined by the Lorentz force (Eq. 1.57). If we assume small amplitude waves as seen in Section 1.4.3, the displacement of the particles can be related to the (oscillating) particle velocity by a simple integration over time, i.e.

$$\underline{r}_\sigma = \int \underline{v}_\sigma \mathrm{d}t \,. \tag{1.87}$$

A close look at the derivations of $\underline{v}_\sigma$ shows that in each component of $\underline{v}_\sigma$ (Eqs. 1.65, 1.66, and 1.67) only the electric field is time dependent and of the form $\underline{E} \sim \exp(-i\omega t)$ (Eq. 1.58). Therefore, the integration of $\underline{v}_\sigma$ over t will only yield an additional factor of $i/\omega$. Hence:

$$\underline{r}_\sigma = \int \underline{v}_\sigma \mathrm{d}t = \frac{i}{\omega} \cdot \underline{v}_\sigma \,, \tag{1.88}$$

and therefore the polarisation (Eq. 1.86) becomes:

$$\begin{aligned} & \underline{P} \overset{\text{Eq.1.88}}{=} \sum_{\sigma} n_\sigma q_\sigma \frac{i}{\omega} \cdot \underline{v}_\sigma \\ \overset{\text{Eq.1.56}}{\Rightarrow} \quad & \underline{P} = \frac{i}{\omega} \cdot \underline{j}_f \\ \overset{\text{Eq.1.72}}{\Rightarrow} \quad & \underline{P} = \frac{i}{\omega} \cdot \underline{\underline{\sigma}} \cdot \underline{E} \end{aligned} \tag{1.89}$$

Inserting Eq. 1.89 into the definition of the electric displacement (Eq. 1.84) yields:

$$\begin{aligned} \underline{D} &= \varepsilon_0 \underline{E} + \frac{i}{\omega} \cdot \underline{\underline{\sigma}} \cdot \underline{E} \\ &= \varepsilon_0 \left( \underline{\underline{\mathbf{1}}} + \frac{i}{\omega \varepsilon_0} \underline{\underline{\sigma}} \right) \cdot \underline{E} \end{aligned} \tag{1.90}$$

The electric displacement $\underline{D}$ can also be related to the electric field $\underline{E}$ by the *dielectric tensor* $\underline{\underline{\varepsilon_{\mathbf{r}}}}$ (also known as the relative permittivity) by:

$$\underline{D} = \varepsilon_0 \underline{\underline{\varepsilon_{\mathbf{r}}}} \cdot \underline{E} \,. \tag{1.91}$$

By comparing Eq. 1.90 and 1.91 we can now define the dielectric tensor $\underline{\underline{\varepsilon_{\mathbf{r}}}}$ of a plasma as:

$$\underline{\underline{\varepsilon_{\mathbf{r}}}} = \left( \underline{\underline{\mathbf{1}}} + \frac{i}{\omega \varepsilon_0} \underline{\underline{\sigma}} \right) , \tag{1.92}$$

where $\underline{\underline{\sigma}}$ is the conductivity tensor as defined by Eq. 1.73. Again, it is common to write the dielectric tensor in terms of the Stix parameter (Eq. 1.77 - 1.81):

$$\underline{\underline{\epsilon_{\mathbf{r}}}} = \begin{bmatrix} S & iD & 0 \\ -iD & S & 0 \\ 0 & 0 & P \end{bmatrix} . \tag{1.93}$$

We now have derived an expression for the electric displacement in terms of the previously defined plasma parameters, which allows us to solve the Maxwell equations in order to describe the propagation of a plasma wave in a plasma characterised as a dielectric medium.

### 1.4.5 Equivalence of the Conductive and Dielectric Characterisation of a Plasma

Wave propagation of electromagnetic waves in a plasma is determined by the Maxwell Equations. Whether a plasma is characterised as a conductive medium or dielectric medium only directly affects the current densities in Ampere's Law (Eq. 1.53). If the

plasma is characterised as a conductive medium, the total current density is composed of the total free current density $\underline{j}_f$ and the external current density, and hence Ampere's law can be written as:

$$\begin{aligned} \underline{\nabla} \times \underline{B} &= \mu_0 \underline{j}_f + \mu_0 \varepsilon_0 \frac{\partial \underline{E}}{\partial t} + \mu_0 \underline{j}_{ext} \\ &\overset{\text{Eq.1.72}}{=} \mu_0 \underline{\underline{\sigma}} \cdot \underline{E} + \mu_0 \varepsilon_0 \frac{\partial \underline{E}}{\partial t} + \mu_0 \underline{j}_{ext} \end{aligned} \tag{1.94}$$

If the plasma is instead characterised as a dielectric medium, the total current density in Ampere's Law is composed of the polarisation current density $\underline{j}_p := \partial \underline{P}/\partial t$ and the external current density, and hence Ampere's law can be written as:

$$\begin{aligned} \underline{\nabla} \times \underline{B} &= \mu_0 \underline{j}_p + \mu_0 \varepsilon_0 \frac{\partial \underline{E}}{\partial t} + \mu_0 \underline{j}_{ext} \\ &= \mu_0 \frac{\partial \underline{P}}{\partial t} + \mu_0 \varepsilon_0 \frac{\partial \underline{E}}{\partial t} + \mu_0 \underline{j}_{ext} \\ &\overset{\text{Eq.1.84}}{=} \mu_0 \frac{\partial \underline{D}}{\partial t} - \mu_0 \varepsilon_0 \frac{\partial \underline{E}}{\partial t} + \mu_0 \varepsilon_0 \frac{\partial \underline{E}}{\partial t} + \mu_0 \underline{j}_{ext} \\ &= \mu_0 \frac{\partial \underline{D}}{\partial t} + \mu_0 \underline{j}_{ext} \\ &\overset{\text{Eq.1.90}}{=} \mu_0 \varepsilon_0 \frac{\partial \underline{E}}{\partial t} + \mu_0 \frac{\partial}{\partial t} \left( \frac{i}{\omega} \underline{\underline{\sigma}} \right) \cdot \underline{E} + \mu_0 \underline{j}_{ext} \\ &\overset{\text{Eq.1.58}}{=} \mu_0 \underline{\underline{\sigma}} \cdot \underline{E} + \mu_0 \varepsilon_0 \frac{\partial \underline{E}}{\partial t} + \mu_0 \underline{j}_{ext} \end{aligned} \tag{1.95}$$

Therefore, the representation of Ampere's law for a plasma characterised as a conductive medium (Eq. 1.94) and for a plasma characterised as a dielectric medium (Eq. 1.95) are identical. These equations were derived using the assumptions that the plasma waves are infinite plane waves, and that the $z$-axis of our coordinate system is oriented along the background magnetic field. Furthermore, it was assumed that the plasma is uniform, homogeneous, and anisotropic, and thermal effects were neglected.

## 1.5 Dispersion Relation

If electromagnetic waves of different frequencies propagate through a (dispersive) medium, they travel with different velocities. The *dispersion relation* describes the relation

of the (angular) wave frequency $\omega$ of a wave and the wave vector $\underline{k}$, which are used to define the phase and group velocity of the wave. Solving the dispersion relation allows us to specify the frequency range of the modes for the waves that can propagate in a plasma. Thereby their polarisation, phase velocity and group velocity can be defined. Furthermore, cut-off frequencies, where $k \to 0$, and resonances, where $k \to \infty$, can be derived from the dispersion relation. In the former case, the waves are reflected, while the latter describes the case where interaction between plasma waves and particles are strong, resulting in particle acceleration and loss.

To obtain a dispersion relation for a plasma, we will use the definition of the *refractive index* $\eta$ which is defined as

$$\eta = \frac{ck}{\omega}\,, \tag{1.96}$$

where $k$ is the wave number (magnitude of the wave vector $\underline{k}$), $\omega$ the (angular) wave frequency, and $c$ is the speed of light, which can be related to the vacuum permeability $\mu_0$ and vacuum permittivity $\varepsilon_0$ by:

$$c = \frac{1}{\sqrt{\mu_0 \varepsilon_0}}\,. \tag{1.97}$$

In the following, we will rewrite Ampere's Law (Eq. 1.53) into a form that allows us to use the definition of the refractive index to derive the dispersion relation. The final form of the dispersion relation will be a quadratic expression for the refractive index, which relates $\omega$ and $k$. We start by combining Gauss' Law (Eq. 1.52) with Ampere's Law (Eq. 1.53). To do this, we exploit that for infinite plane waves, we can rewrite the operators in the Maxwell equations as:

$$\underline{\nabla} \longrightarrow i\underline{k} \tag{1.98}$$

$$\frac{\partial}{\partial t} \longrightarrow -i\omega \tag{1.99}$$

Using these, Gauss' Law and Ampere's Law become:

$$i\underline{k} \times \underline{E} = i\omega \underline{B} \tag{1.100}$$

$$i\underline{k} \times \underline{B} = \mu_0 \underline{j} - i\omega\mu_0\varepsilon_0 \underline{E} \tag{1.101}$$

Characterising the plasma as a conductor and neglecting external currents ($\underline{j} = \underline{j}_f$), inserting Eq. 1.100 into Eq. 1.101 gives:

$$\begin{aligned} \underline{k} \times (\underline{k} \times \underline{E}) &= -i\omega(\mu_0 \underline{j}_f - i\omega\mu_0\varepsilon_0 \underline{E}) \\ &\overset{Eq.1.72}{=} -i\omega\mu_0 \underline{\underline{\sigma}} \cdot \underline{E} - \omega^2 \mu_0 \varepsilon_0 \underline{E}) \\ &\overset{Eq.1.97}{=} -\frac{\omega^2}{c^2}\left(\frac{i}{\omega\varepsilon_0}\underline{\underline{\sigma}} + \underline{\underline{\mathbf{1}}}\right) \cdot \underline{E} \\ &\overset{Eq.1.92}{=} -\frac{\omega^2}{c^2}\underline{\underline{\varepsilon_{\mathbf{r}}}} \cdot \underline{E} \\ \Leftrightarrow \quad \underline{k} \times (\underline{k} \times \underline{E}) + \frac{\omega^2}{c^2}\underline{\underline{\varepsilon_{\mathbf{r}}}} \cdot \underline{E} &= 0 \end{aligned} \tag{1.102}$$

Which is known as the *Helmholtz Equation* (neglecting external currents).
Remember that the equations used to derive these expressions assumed that the (cartesian) coordinate system was chosen in a way that the external magnetic field was aligned along the $z$-axis (i.e. $\underline{B}_0 = [0, 0, B_0]$). There is cylindrical symmetry around the $z$-axis and hence, we can choose that $\underline{k}$ lies within the $x$-$z$ plane without loss of generality. If we furthermore denote the angle between $\underline{k}$ and the background magnetic field $\underline{B}_0$ with $\psi$, known as the *wave normal angle*, we get for the components of $\underline{k}$:

$$k_x = |\underline{k}| \cdot \sin(\psi) \qquad k_y = 0 \qquad k_z = |\underline{k}| \cdot \cos(\psi) \tag{1.103}$$

Using these and the vector identity

$$\underline{a} \times (\underline{b} \times \underline{c}) = \underline{b}(\underline{a} \cdot \underline{c}) - \underline{c}(\underline{a} \cdot \underline{b}) \tag{1.104}$$

$$\rightarrow \quad \underline{k} \times (\underline{k} \times \underline{E}) = \underline{k}(\underline{k} \cdot \underline{E}) - |\underline{k}|^2 \underline{E}\,, \tag{1.105}$$

we can rewrite the Helmholtz Equation (Eq. 1.102) as:

$$0 = \underline{k}(\underline{k} \cdot \underline{E}) - |\underline{k}|^2 \underline{E} + \frac{\omega^2}{c^2} \underline{\underline{\varepsilon}}_{\mathbf{r}} \cdot \underline{E} \tag{1.106}$$

Using the previously mentioned identities, allows us to further rewrite this equation:

$$\begin{aligned}
& 0 = \underline{k}(k_x E_x + k_y E_y + k_z E_z) - |\underline{k}|^2 \underline{E} + \frac{\omega^2}{c^2} \underline{\underline{\varepsilon}}_{\mathbf{r}} \cdot \underline{E} \\
\overset{Eq.1.103}{\Rightarrow} \quad & 0 = \underline{k}(|\underline{k}| \cdot \sin(\psi) \cdot E_x + 0 + |\underline{k}| \cdot \cos(\psi) \cdot E_z) - |\underline{k}|^2 \underline{E} + \frac{\omega^2}{c^2} \underline{\underline{\varepsilon}}_{\mathbf{r}} \cdot \underline{E} \\
\Leftrightarrow \quad & 0 = \begin{bmatrix} k_x \cdot |\underline{k}| \cdot \sin(\psi) \cdot E_x + k_x \cdot |\underline{k}| \cdot \cos(\psi) \cdot E_z \\ k_y \cdot |\underline{k}| \cdot \sin(\psi) \cdot E_x + k_y \cdot |\underline{k}| \cdot \cos(\psi) \cdot E_z \\ k_y \cdot |\underline{k}| \cdot \sin(\psi) \cdot E_x + k_y \cdot |\underline{k}| \cdot \cos(\psi) \cdot E_z \end{bmatrix} - |\underline{k}|^2 \begin{bmatrix} E_x \\ E_y \\ E_z \end{bmatrix} + \frac{\omega^2}{c^2} \underline{\underline{\varepsilon}}_{\mathbf{r}} \cdot \underline{E} \\
\overset{Eq.1.103}{\Rightarrow} \quad & 0 = \begin{bmatrix} |\underline{k}|^2 \cdot \sin^2(\psi) \cdot E_x + |\underline{k}|^2 \cdot \sin(\psi)\cos(\psi) \cdot E_z - |\underline{k}|^2 E_x \\ -|\underline{k}|^2 E_y \\ |\underline{k}|^2 \cdot \sin(\psi)\cos(\psi) \cdot E_x + |\underline{k}|^2 \cdot \cos^2(\psi) \cdot E_z - |\underline{k}|^2 E_z \end{bmatrix} + \frac{\omega^2}{c^2} \underline{\underline{\varepsilon}}_{\mathbf{r}} \cdot \underline{E} \\
\Leftrightarrow \quad & 0 = |\underline{k}|^2 \begin{bmatrix} \left(\sin^2(\psi) - 1\right) \cdot E_x + \sin(\psi)\cos(\psi) \cdot E_z \\ -E_y \\ \sin(\psi)\cos(\psi) \cdot E_x + \left(\cos^2(\psi) - 1\right) \cdot E_z \end{bmatrix} + \frac{\omega^2}{c^2} \underline{\underline{\varepsilon}}_{\mathbf{r}} \cdot \underline{E} \\
\overset{Eq.1.96}{\Rightarrow} \quad & 0 = \eta^2 \begin{bmatrix} -\cos^2(\psi) & 0 & \sin(\psi)\cos(\psi) \\ 0 & -1 & 0 \\ \sin(\psi)\cos(\psi) & 0 & -\sin^2(\psi) \end{bmatrix} \cdot \begin{bmatrix} E_x \\ E_y \\ E_z \end{bmatrix} + \underline{\underline{\varepsilon}}_{\mathbf{r}} \cdot \underline{E} \\
\overset{Eq.1.93}{\Rightarrow} \quad & 0 = \eta^2 \begin{bmatrix} -\cos^2(\psi) & 0 & \sin(\psi)\cos(\psi) \\ 0 & -1 & 0 \\ \sin(\psi)\cos(\psi) & 0 & -\sin^2(\psi) \end{bmatrix} \cdot \underline{E} + \begin{bmatrix} S & iD & 0 \\ -iD & S & 0 \\ 0 & 0 & P \end{bmatrix} \cdot \underline{E}
\end{aligned}$$

Combining the sum of the two products into one, we get:

$$\boxed{\begin{bmatrix} S - \eta^2\cos^2(\psi) & iD & \eta^2\sin(\psi)\cos(\psi) \\ -iD & S - \eta^2 & 0 \\ \eta^2\sin(\psi)\cos(\psi) & 0 & P - \eta^2\sin^2(\psi) \end{bmatrix} \cdot \begin{bmatrix} E_x \\ E_y \\ E_z \end{bmatrix} = 0} \tag{1.107}$$

This equation is of the form $\underline{\underline{\mathbf{A}}} \cdot \underline{E} = 0$, which only has nontrivial solutions ($\underline{E} \neq 0$) if the determinant of $\underline{\underline{\mathbf{A}}}$ is zero, i.e.

$$\det \begin{bmatrix} S - \eta^2 \cos^2(\psi) & iD & \eta^2 \sin(\psi)\cos(\psi) \\ -iD & S - \eta^2 & 0 \\ \eta^2 \sin(\psi)\cos(\psi) & 0 & P - \eta^2 \sin^2(\psi) \end{bmatrix} = 0 \tag{1.108}$$

Evaluating this equation yields:

$$\begin{aligned}
0 &= [S - \eta^2\cos^2(\psi)] \cdot [S - \eta^2] \cdot [P - \eta^2\sin^2(\psi)] \\
&\quad - [\eta^2\sin(\psi)\cos(\psi)] \cdot [S - \eta^2] \cdot [\eta^2\sin(\psi)\cos(\psi)] \\
&\quad - [iD] \cdot [-iD] \cdot [P - \eta^2\sin^2(\psi)] \\
\Leftrightarrow \quad 0 &= [S^2 - S\eta^2 - S\eta^2\cos^2(\psi) + \eta^4\cos^2(\psi)] \cdot [P - \eta^2\sin^2(\psi)] \\
&\quad - S\eta^4\sin^2(\psi)\cos^2(\psi) + \eta^6\sin^2(\psi)\cos^2(\psi) \\
&\quad - D^2P + D^2\eta^2\sin^2(\psi) \\
\Leftrightarrow \quad 0 &= S^2P - SP\eta^2 - SP\eta^2\cos^2(\psi) + P\eta^4\cos^2(\psi) \\
&\quad - S^2\eta^2\sin^2(\psi) + S\eta^4\sin^2(\psi) \\
&\quad + S\eta^4\sin^2(\psi)\cos^2(\psi) - \eta^6\sin^2(\psi)\cos^2(\psi) \\
&\quad - S\eta^4\sin^2(\psi)\cos^2(\psi) + \eta^6\sin^2(\psi)\cos^2(\psi) \\
&\quad - D^2P + D^2\eta^2\sin^2(\psi) \\
\Leftrightarrow \quad 0 &= [P\cos^2(\psi) + S\sin^2(\psi)] \cdot \eta^4 \\
&\quad - [SP + SP\cos^2(\psi) + S^2\sin^2(\psi) - D^2\sin^2(\psi)] \cdot \eta^2 \\
&\quad + S^2P - D^2P \\
\overset{Eq.1.77,1.78}{\Rightarrow} \quad 0 &= [S\sin^2(\psi) + P\cos^2(\psi)] \cdot \eta^4 \\
&\quad - \left[RL\sin^2(\psi) + SP[1 + \cos^2(\psi)]\right] \cdot \eta^2 \\
&\quad + RLP
\end{aligned} \tag{1.109}$$

This is a quadratic equation in $\eta^2$ and since $\eta = ck/\omega$ this is commonly defined as the *Dispersion Relation of a cold plasma*. Using short hand notations, the dispersion

relation becomes:

$$\boxed{A\eta^4 + B\eta^2 + C = 0}, \tag{1.110}$$

with

$$A := S\sin^2(\psi) + P\cos^2(\psi) \tag{1.111}$$

$$B := -\left[RL\sin^2(\psi) + SP[1+\cos^2(\psi)]\right] \tag{1.112}$$

$$C := RLP \tag{1.113}$$

To find the solutions of the dispersion relation, we first need to solve Eq. 1.110 as a quadratic equation in $\eta^2$, whose solutions are:

$$\eta^2 = -\frac{1}{2A}\left(B \pm \sqrt{B^2 - 4AC}\right) \tag{1.114}$$

Using the definition of the refractive index $\eta$ (Eq. 1.96) we get:

$$k^2 = -\frac{\omega^2}{2Ac^2}\left(B \pm \sqrt{B^2 - 4AC}\right) \tag{1.115}$$

This is now a quadratic relation between $k$ and $\omega$, which acts as the *final form of the dispersion relation*, with

$$A = \left[1 - \sum_\sigma \frac{\omega_{p,\sigma}^2}{\omega^2}\cdot\frac{\omega^2}{(\omega^2-\Omega_\sigma^2)}\right]\cdot\sin^2(\psi) + \left[1 - \sum_\sigma \frac{\omega_{p,\sigma}^2}{\omega^2}\right]\cdot\cos^2(\psi)$$

$$B = \left[\left(1 - \sum_\sigma \frac{\omega_{p,\sigma}^2}{\omega^2}\cdot\frac{\omega^2}{(\omega^2-\Omega_\sigma^2)}\right)^2 - \left(\sum_\sigma \frac{\omega_{p,\sigma}^2}{\omega^2}\cdot\frac{\omega\Omega_\sigma}{(\omega^2-\Omega_\sigma^2)}\right)^2\right]\cdot\sin^2(\psi)$$
$$+\left(1 - \sum_\sigma \frac{\omega_{p,\sigma}^2}{\omega^2}\cdot\frac{\omega^2}{(\omega^2-\Omega_\sigma^2)}\right)\left(1 - \sum_\sigma \frac{\omega_{p,\sigma}^2}{\omega^2}\right)\left(1+\cos^2(\psi)\right)$$

$$C = \left[\left(1 - \sum_\sigma \frac{\omega_{p,\sigma}^2}{\omega^2}\cdot\frac{\omega^2}{(\omega^2-\Omega_\sigma^2)}\right)^2 - \left(\sum_\sigma \frac{\omega_{p,\sigma}^2}{\omega^2}\cdot\frac{\omega\Omega_\sigma}{(\omega^2-\Omega_\sigma^2)}\right)^2\right]\left(1 - \sum_\sigma \frac{\omega_{p,\sigma}^2}{\omega^2}\right)$$

### 1.5.1 Solutions of the Dispersion Relation

The dispersion relation is usually defined as a function $\omega(k)$, but it is easy to see that it is impossible to solve Eq. 1.115 analytically for an arbitrary wave normal angle $\psi$. It is only possible to find analytical solutions for parallel wave propagation ($\psi = 0°$) and electrostatic waves ($\psi = 90°$), but in the case of propagation at an arbitrary wave normal angle, the dispersion relation must be solved numerically. However, it is possible to *plot* the dispersion relation $\omega(k)$, as the inverse function $k(\omega)$, which is directly defined by Eq. 1.115.

In the case of an arbitrary wave normal angle $\psi$ there are usually several "branches" of the dispersion relation, which are a result of the $\pm$ sign. There are only unique relations between $\omega$ and $k$ at specific frequency ranges, separating the dispersion relation into further branches. Furthermore, since the dispersion relation is a quadratic equation for $k$, the solutions for $\omega(k)$ are symmetric around the $\omega$-axis. The solutions where $k^2 < 0$ lead to purely imaginary expressions for the wave vector $\underline{k}$ and hence correspond to evanescent waves, which do not propagate. It is useful to separate the remaining solution(s), where $k^2 \geq 0$, by the polarisation of the corresponding plasma wave. We therefore need to define the wave polarisation.

#### Wave Polarisation

The polarisation of a transverse electromagnetic wave describes how the orientation of the electric and magnetic components of the wave changes over time, due to oscillations of the electric and magnetic components. Both components of an electromagnetic wave oscillate, but conventionally the polarisation is defined by the oscillations of the electric field component. In the most general case, the electric field has two transverse components that span a plane perpendicular to the wave vector $\underline{k}$, known as the polarisation plane. The two components oscillate with phase shift $\vartheta$. As a result, the total electric wave vector usually describes an ellipse in the polarisation plane, known as *elliptical polarisation*. There are two special cases of elliptical polarisation: In the first case, the phase shift is 90° and the magnitude of both components is equal, this means that the ellipse becomes a circle, known as *circular polarisation*. In the second case, one of the

components is zero, which means that the total electrical vector only oscillates in one direction, known as *linear polarisation*.

In an isotropic medium $k$ has to be perpendicular to $E$ and $B$ for an electromagnetic wave and the wave is hence a completely transverse wave. In an anisotropic medium, such as a magnetised plasma, this relation no longer holds because of the shape of the dielectric tensor describing the relation between $D$ and $E$. This means that, depending on the shape of the dielectric tensor, a plasma wave can have transverse and longitudinal components simultaneously. By definition, the polarisation only describes the oscillations of the transverse components, ignoring the longitudinal ones.

The polarisation plane is composed of two vectors of the electric field, which are perpendicular to the wave vector $\underline{k}$ of the plasma wave. By our definition $\underline{k}$ lies in the $x$-$z$ plane, which means that one of the two vectors spanning the polarisation plane is $\underline{E}_y$ and the other one is a superposition of the $x$ and $z$ component of the electric field, called $\underline{E}_\perp$. The superposition of $\underline{E}_x$ and $\underline{E}_z$ has to be in the way that $\underline{E}_\perp$ is perpendicular to $\underline{k}$. The geometry of the $x$-$z$ plane is shown in Figure 1.14.

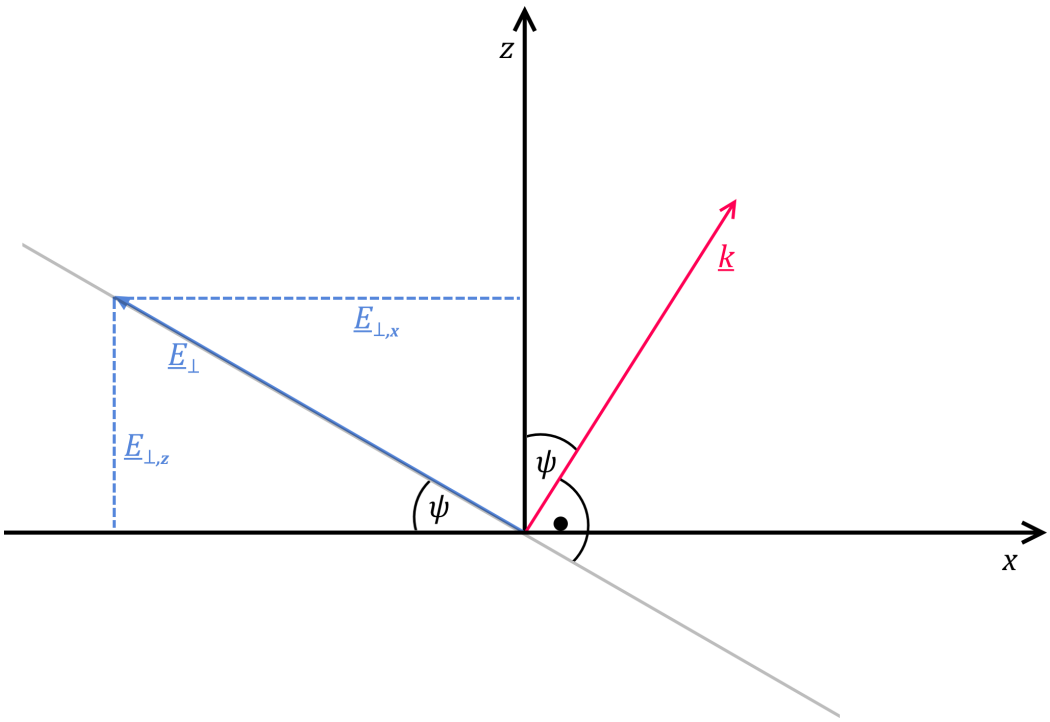


Figure 1.14: Geometry of the $x$-$z$ plane.

Important information about the polarisation of the plasma wave can be deduced from the relation of the two vectors spanning the polarisation plane, i.e. $E_\perp/E_y$. Using basic vector mathematics, the magnitude of $\underline{E}_\perp$ is defined as

$$E_\perp = \sqrt{E_{\perp,x}^2 + E_{\perp,z}^2}\,, \tag{1.116}$$

where $E_{\perp,x}$ and $E_{\perp,z}$ are the magnitudes of the $x$ and $z$ components of $E_\perp$. Furthermore, we can use the geometry of the polarisation plane to specify the condition that has to be fulfilled in order for $E_\perp$ to be perpendicular to $k$, i.e.

$$\tan(\psi) = \frac{E_{\perp,z}}{E_{\perp,x}}\,, \tag{1.117}$$

where $\psi$ is the angle between $k$ and $B_0$ (the $z$-axis), i.e. the *wave normal angle*. If this condition is not fulfilled, $E_\perp$ will have longitudinal components, which ought to be ignored for the polarisation. Without loss of generality we can now let $E_{\perp,x} = E_x$. Using this with Eq. 1.116 and 1.117 we get:

$$E_\perp = E_x \cdot \sqrt{1 + \tan^2\psi} \tag{1.118}$$

This lets us write the ratio of $E_\perp/E_y$ as:

$$\begin{aligned} P :&= \frac{E_\perp}{E_y} \\ &= \frac{E_x}{E_y} \cdot \sqrt{1 + \tan^2\psi} \end{aligned} \tag{1.119}$$

The ratio of $E_x/E_y$ can be obtained by writing out Eq. 1.107:

$$\Big(S - n^2\cos^2(\psi)\Big) \cdot E_x + iD \cdot E_y + \Big(n^2\sin(\psi)\cos(\psi)\Big) \cdot E_z = 0 \tag{1.120}$$

$$-iD \cdot E_x + \Big(S - n^2\Big) \cdot E_y = 0 \tag{1.121}$$

$$\Big(n^2\sin(\psi)\cos(\psi)\Big) \cdot E_x + \Big(P - n^2\sin^2(\psi)\Big) \cdot E_z = 0 \tag{1.122}$$

And hence:

$$\frac{E_x}{E_y} \overset{\text{Eq.1.121}}{=} -i \cdot \frac{S - n^2}{D} \tag{1.123}$$

The ratio $E_x/E_y$ is in general a complex number, and thus the ratio $P$ of the electric field components in the polarisation plane is a complex number as well. Since each of the components of the electric fields oscillates, this means that the total transverse electric field rotates in the polarisation plane and hence the plasma waves are elliptically polarised. We can now define *left hand elliptical polarisation* to be when $P$ is positive and *right hand elliptical polarisation* when $P$ is negative.

As mentioned earlier, there are two special cases of polarisation, circular and linear polarisation. A plasma wave becomes circularly polarised, if $P = \pm i$. For parallel wave propagation ($\psi = 0$) this is the case if the amplitudes of $E_x$ and $E_y$ are identical, except for a phase shift of 90° where $E_x/E_y$ is still a complex number. If $E_x/E_y$ is a real number, the plasma wave becomes linearly polarised. Likewise, plasma waves can become linearly polarised, if either $E_x/E_y \to 0$ or $E_x/E_y \to i\infty$. The former case means that $E_y \gg E_x$ and hence the wave is linearly polarised with $E$ along $E_y$. The latter case means that $E_x \gg E_y$ and the wave is linearly polarised with $E$ along $E_x$.

### Illustration of the Dispersion Relation

Now that we have defined left- and right-hand polarised waves, we are able to distinguish between the solutions of the dispersion relation (Eq. 1.115) in each branch. The resulting dispersion relation covering a wide frequency range is shown for a plasma containing 94 % $H^+$, 5 % $He^+$, and 1 % $O^+$ in Figure 1.15. The electron gyrofrequency was set to $f_{ce} = 5230\,\text{Hz}$, which corresponds to the electron gyrofrequency at $L = 4.5$ near the equator. The ratio of $f_{pe}/f_{ce}$ was set to 10 and the left panel shows the dispersion relation for a wave normal angle of $\psi = 0°$, while the right panel is for $\psi = 45°$.

There are left-hand and right-hand polarised waves above the plasma frequency $\omega_{pe}$, which are known as Z-mode, L-O-mode, and R-X-mode waves. If $\omega_{pe}$ is greater than $\Omega_e$, which is the case inside the Earth's magnetosphere most of the time, there exists a gap between $\omega_{pe}$ and $\Omega_e$, where no waves are able to propagate.

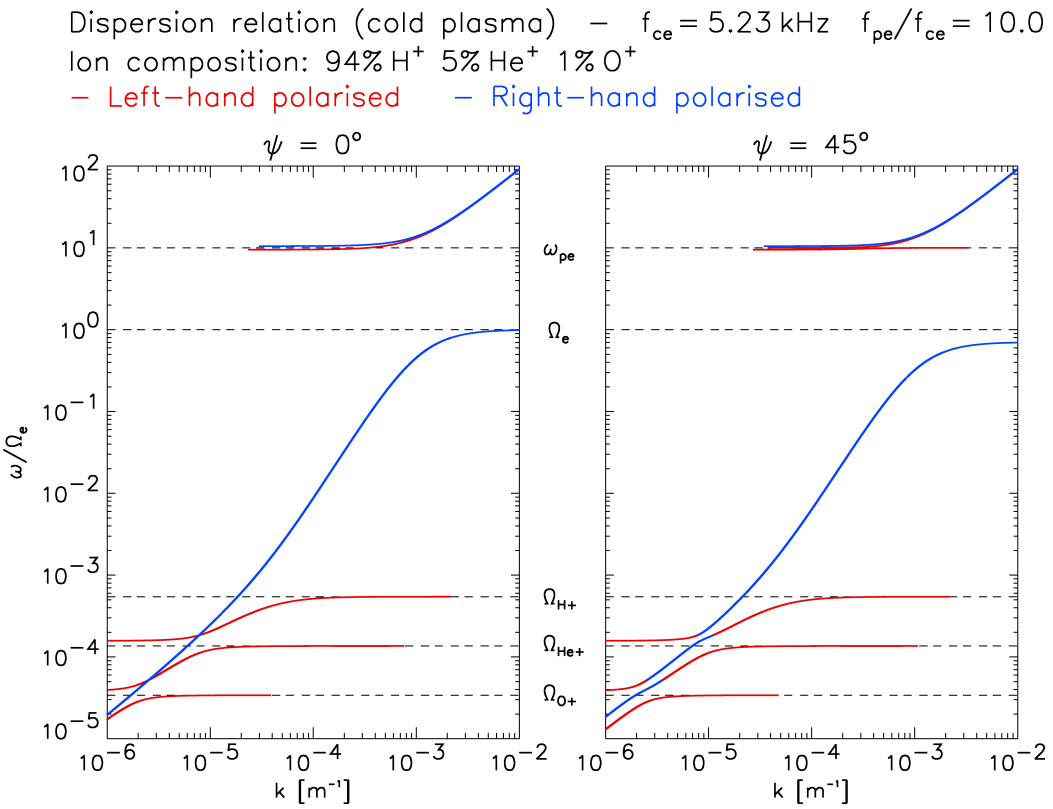


Figure 1.15: Examples of the dispersion relation in a plasma containing 94 % $H^+$, 5 % $He^+$, and 1 % $O^+$. The electron gyrofrequency was set to $f_{ce} = 5230$ Hz and the ratio of $f_{pe}/f_{ce}$ was set to 10. The left panel shows the dispersion relation for completely field aligned waves ($\psi = 0°$), while the right panel is for oblique waves with $\psi = 45°$.

Furthermore, it can be seen that for frequencies below the electron gyrofrequency $\Omega_e$ and above the hydrogen ion cyclotron frequency $\Omega_{H+}$ there are only right-hand polarised waves, known as *whistler mode waves*. Of particular interest in this thesis are the *plasmaspheric hiss*, with frequencies between about 100 Hz and 4000 Hz and the *whistler mode chorus waves*, which lie above the lower hybrid frequency $f_{lhr} = \sqrt{f_{ce} \cdot f_{cp}} \approx 0.022\,\Omega_e$. An example of the dispersion relation of whistler mode chorus waves can be found in Section 4.5.1, in particular Figure 4.12. For more details about these waves see the corresponding chapters. Note that there is a gap between the plasma frequency and the electron cyclotron frequency, where no waves can propagate. If the wave normal angle is increased, the shape of the whistler mode branch is slightly changed in a way that it is shifted to slightly lower frequencies and converges to the electron gyrofrequency at a larger wave vector $k$.

For frequencies below the hydrogen ion cyclotron frequency, both left-hand and right-

hand polarised waves can be found. These wave are known as electromagnetic ion cyclotron (EMIC) waves. It is interesting to note that although both right- and left-hand polarised waves can be found for most of the frequency range, there is a gap in the distribution of the left-hand polarised waves just above the helium and oxygen ion cyclotron frequency, where only right-hand polarised waves can propagate. The frequency above the corresponding ion cyclotron frequency, at which wave propagation for both branches is allowed again is the so-called cross-over frequency $f_{cr}$. Furthermore, it can be seen that for field aligned wave propagation the left- and right-hand polarised EMIC wave branches of the dispersion relation cross each other, while for oblique propagation, the branches of the EMIC waves split up creating a gap in $k$ for a specific frequency. Thereby no gap in frequency can be found for either left- or right-hand polarised waves and hence, no cross-over frequency can be defined for oblique wave propagation.

### 1.5.2 Phase Velocity

As established earlier, electromagnetic plasma waves are a superposition of infinite plane waves (i.e. wave packets). Each individual plane wave is of the form $\underline{E} = \underline{E}_0 \cdot \exp[i(\underline{k} \cdot \underline{r} - \omega t)]$. The *phase velocity* $v_{ph}$ of a plane wave is defined as the velocity $\mathrm{d}r/\mathrm{d}t$ of the waves with a constant phase, i.e.

$$\underline{k} \cdot \underline{r} - \omega t = \text{const}\,. \tag{1.124}$$

Rearranging Eq. (1.124) for $r$ allows us to directly calculate the phase velocity by differentiating with respect to time as:

$$v_{ph} = \frac{\omega}{k} \tag{1.125}$$

If the phase velocity is positive, the wave moves in the positive direction, i.e. as $t$ increases, $r$ increases to keep $kr - \omega t$ constant. Equivalently, if $v_{ph}$ is negative, the wave moves in the negative direction.

### 1.5.3 Group Velocity

Since plasma waves are a superposition of infinite plane waves, there is usually a multitude of waves with different wave vectors $k$ and frequencies $\omega$, resulting in a large variety of phases and hence phase velocities. It is therefore useful to specify the velocity of the wave packet itself, which is called the *group velocity* $v_{gr}$, which is defined as:

$$v_{gr} = \frac{\mathrm{d}\omega}{\mathrm{d}k} \tag{1.126}$$

## 1.6 Wave-Particle Interaction

Plasma waves can interact with the charged particles that are trapped by the geomagnetic field, if they are in resonance with each other. During resonance the plasma wave can transfer energy to the particle or take energy from the particle, depending on the phase of the wave. Since resonance is given if the refractive index becomes infinite [e.g. *Chen*, 1984], the wave vector $k$ has to become very large, for a wave of fixed frequency. This behaviour can be found in the dispersion relation (see Figure 1.15), where $\underline{k}$ tends to become very large, if $\omega$ gets close to one of the gyrofrequencies.
The objective of this thesis is to calculate electron acceleration and losses due to wave-particle interactions, or in other words the energy transfer between charged particles and plasma waves due to resonance. Therefore, we will derive the condition that needs to be fulfilled for wave-particle resonance in the next section and discuss the various possible types of resonances.

### 1.6.1 The Resonance Condition

If we characterise the plasma as a dielectric medium, the plasma is defined by the dielectric tensor. For a hot plasma, the dielectric tensor $\underline{\underline{\varepsilon}}_h$ is given by [*Ichimaru*, 1973]:

$$\begin{aligned}\underline{\underline{\varepsilon}}_h &= \left(1-\sum_\sigma \frac{\omega_{p,\sigma}^2}{\omega^2}\right)\underline{\underline{\mathbf{1}}} \\ &+ \sum_\sigma \frac{\omega_{p,\sigma}^2}{\omega^2}\sum_{-\infty}^{\infty}\int \mathrm{d}\underline{v}\left(\frac{n\Omega_\sigma}{v_\perp}\frac{\partial f_\sigma}{\partial v_\perp}+k_{\shortparallel}\frac{\partial f_\sigma}{\partial v_{\shortparallel}}\right)\frac{\underline{\underline{\mathbf{\Pi}}}_\sigma(v_\perp,v_{\shortparallel};n)}{\omega-n\Omega_\sigma/\gamma-k_{\shortparallel}v_{\shortparallel}}\,,\end{aligned} \tag{1.127}$$

where

$$\underline{\underline{\mathbf{\Pi}}}_\sigma(v_\perp,v_{\shortparallel};n)=\begin{bmatrix} \frac{n^2{\Omega_\sigma}^2}{k_\perp^2}J_n^2 & iv_\perp\frac{n\Omega_\sigma}{k_\perp}J_nJ_n' & v_{\shortparallel}\frac{n\Omega_\sigma}{k_\perp}J_n^2 \\ -iv_\perp\frac{n\Omega_\sigma}{k_\perp}J_nJ_n' & v_\perp^2(J_n')^2 & -iv_{\shortparallel}v_\perp J_nJ_n' \\ v_{\shortparallel}\frac{n\Omega_\sigma}{k_\perp}J_n^2 & iv_{\shortparallel}v_\perp J_nJ_n' & v_{\shortparallel}^2J_n^2 \end{bmatrix}, \tag{1.128}$$

and

$$\int \mathrm{d}\underline{v}=2\pi\int_0^\infty v_\perp \mathrm{d}v_\perp\int_{-\infty}^{\infty}\mathrm{d}v_{\shortparallel}\,. \tag{1.129}$$

Hence, each element of the dielectric tensor for a hot plasma is a function of the angular wave frequency $\omega$, the wave vector $\underline{k}$, the particle velocity $\underline{v}$, and the plasma distribution function $f_\sigma(\underline{r},\underline{v},t)$ of the particle of the species $\sigma$. The cyclotron frequency is $\Omega_\sigma$ and $\omega_{p,\sigma}$ is the plasma frequency of the particle of the species $\sigma$. The functions $J_n$ are Bessel functions with the argument $z=k_\perp v_\perp/\Omega_\sigma$, where $J_n'=\mathrm{d}J_n/\mathrm{d}z$ and $n$ is an integer number.

The integral over $v_{\shortparallel}$ in the dielectric tensor of a hot plasma (Eq. 1.127) has singularities when

$$\omega-\frac{n\Omega_\sigma}{\gamma}-k_{\shortparallel}v_{\shortparallel}=0 \tag{1.130}$$

$$\Leftrightarrow \qquad v_{\shortparallel}=\frac{\omega}{k_{\shortparallel}}\left(1-\frac{n\Omega_\sigma}{\gamma\omega}\right) \tag{1.131}$$

which is known as the *resonance condition* for a (relativistic) particle of species $\sigma$. Here, $n=0,\pm1,\pm2,...$ is an integer number and $\gamma$ is the Lorentz factor defined as:

$$\gamma=\frac{1}{\sqrt{1-\frac{v^2}{c^2}}} \tag{1.132}$$

Note that for non-relativistic particles ($v \ll c \Leftrightarrow \gamma \approx 1$) the resonance condition is independent of $v_\perp$ and hence usually only the particle velocity parallel to the external magnetic field has to be considered. In the relativistic case, $\gamma$ introduces both components of the particle velocity and the resonance condition defines an ellipse in $v_\perp$ and $v_{\shortparallel}$ for the resonance velocity.

The resonance condition defines the frequency $\omega$ for which resonance happens at a given resonance number $n$, wave vector $k$, and particle velocity $v$ (and hence the particle's kinetic energy $E_{kin}$). While $n$ and $E_{kin}$ can easily be defined, the wave vector $k$ is not directly accessible. In order to calculate the resonance frequency, we therefore need to evaluate the dispersion relation, which provides a relation between $k$ and $\omega$. As it is difficult to solve the dispersion relation and the resonance condition simultaneously, it is common to write the resonance condition in the form of a dispersion relation, allowing the resonance frequencies to be found graphically as the intersections of the resonance condition and the dispersion relation:

$$\begin{aligned} & v_{\shortparallel} = \frac{\omega}{k_{\shortparallel}} \left(1 - \frac{n\Omega_\sigma}{\gamma\omega}\right) \\ \Leftrightarrow \quad & v_{\shortparallel} = \frac{\omega}{k_{\shortparallel}} - \frac{n\Omega_\sigma}{k_{\shortparallel}\gamma} \\ \Leftrightarrow \quad & \omega = v_{\shortparallel} k_{\shortparallel} + \frac{n\Omega_\sigma}{\gamma} \\ \Leftrightarrow \quad & \omega = v_{\shortparallel} \cdot k \cdot \cos(\psi) + \frac{n\Omega_\sigma}{\gamma}\,, \end{aligned} \tag{1.133}$$

where $\psi$ denotes the wave normal angle.

Usually one is interested to know the resonance frequency at a particular particle energy and wave normal angle for the various resonance numbers. In order to rewrite Eq. 1.133 in terms of these quantities, we first need to replace $v_{\shortparallel}$ using the definition of the pitch-angle $\alpha$:

$$v_{\shortparallel} = v \cdot \cos(\alpha)\,, \tag{1.134}$$

Furthermore we need to utilise the ratio of the relativistic velocity and the speed of light $c$:

$$\frac{v}{c} = \beta = \left(\frac{\gamma^2 - 1}{\gamma^2}\right)^{1/2} . \tag{1.135}$$

If we use the Lorentz factor as

$$\gamma = \frac{E_{kin}}{E_0} + 1 \,, \tag{1.136}$$

with $E_{kin}$ being the relativistic kinetic energy and $E_0 = m_0 c^2$ the rest energy, this yields:

$$\begin{aligned} & \omega = v\cos(\alpha) \cdot k\cos(\psi) + \frac{n\Omega_\sigma}{\gamma} \\ \Leftrightarrow \qquad & \omega = \frac{n\Omega_\sigma}{\gamma} + ck \cdot \cos(\alpha) \cdot \cos(\psi) \cdot \left(\frac{\gamma^2 - 1}{\gamma^2}\right)^{1/2} \end{aligned} \tag{1.137}$$

This equation now defines the resonance condition in the form of a dispersion relation only depending on the resonance number $n$, the particle's energy, the particle's pitch-angle $\alpha$, and the wave normal angle $\psi$.

#### Landau Resonance

In the case where the resonance number $n = 0$, the resonant particle velocity has to be equal to the parallel phase velocity of the electromagnetic wave, i.e. $v_{\shortparallel} = \omega/k_{\shortparallel}$. This case is known as *Landau resonance*. Particles that experience Landau resonance hence move with the same velocity as the phase velocity of the wave they interact with. As a consequence, they are in phase with the wave and the wave frequency seen by the particles is zero, allowing them to strongly interact with the wave electric field.

Note that, as the elements of the tensor in the integral (Eq. 1.128) depend on the parallel and perpendicular components of $\underline{k}$, the resonance condition (Eq. 1.131) for the case of $n = 0$ only causes a singularity, if the electric field of the resonating electromagnetic wave has components parallel to the external magnetic field, i.e. $k_{\shortparallel} \neq 0$. This is not necessarily the case, for example, whistler mode and electromagnetic ion

cyclotron waves propagating exactly field aligned, have no parallel electric field component. Hence there is no energy exchange between these plasma waves and charged particles due to Landau resonance.

#### Doppler Shifted Cyclotron Resonance

In the frame of reference of the particle, for the cases of $n = \pm 1, \pm 2, ...$, the particle sees the frequency of the electromagnetic wave being Doppler shifted towards multiples of its gyrofrequency $\Omega_\sigma$. This allows the particle to resonate with the wave, which either accelerates or decelerates the particle, depending on the phase of the wave. This is called *Doppler shifted cyclotron resonance*. As long as the electromagnetic wave field is perpendicular to $B_0$, it allows for changes of both the particle's energy and pitch-angle, which are called *pitch-angle scattering* and *energy scattering*, respectively. The net growth or damping of the wave can only be determined by evaluating all the elements of the dielectric tensor of the hot plasma distribution numerically.

An example of the resonance condition for the case of whistler mode waves is presented in Figure 1.16. The solid blue line is the whistler mode branch of the dispersion relation (right-hand polarised) and the resonance condition are the orange to red dashed lines. The resonances were calculated for $n = -10, ..., 10$ but only the Landau resonance ($n = 0$) and resonances with negative $n$ are visible. The resonances with $n \geq 1$ lie outside the frequency range of the plot. The dispersion relation and resonance condition were calculated for a pure proton-electron plasma, where the electron gyrofrequency was set to $f_{ce} = 5230\,\text{Hz}$, which is about the electron gyrofrequency at $L = 4.5$ near the equator. The ratio of $f_{pe}/f_{ce}$ was set to 10. The resonance condition was calculated for electrons with an equatorial pitch-angle of $\alpha = 15°$ and an energy of 500 eV. The left panel shows the results for completely field aligned waves ($\psi = 0°$), while the right panel is for oblique waves with $\psi = 45°$. It can be seen that the Landau resonance crosses the dispersion curve twice, while the higher order resonances only cross the dispersion curve once, if at all. The horizontal dashed lines show the so-called lower and upper cutoff frequencies, which define the frequency range inside which the calculations of the wave-particle interactions are performed. These frequencies try to model the effective frequency range at which waves are observed and they depend on the case that is

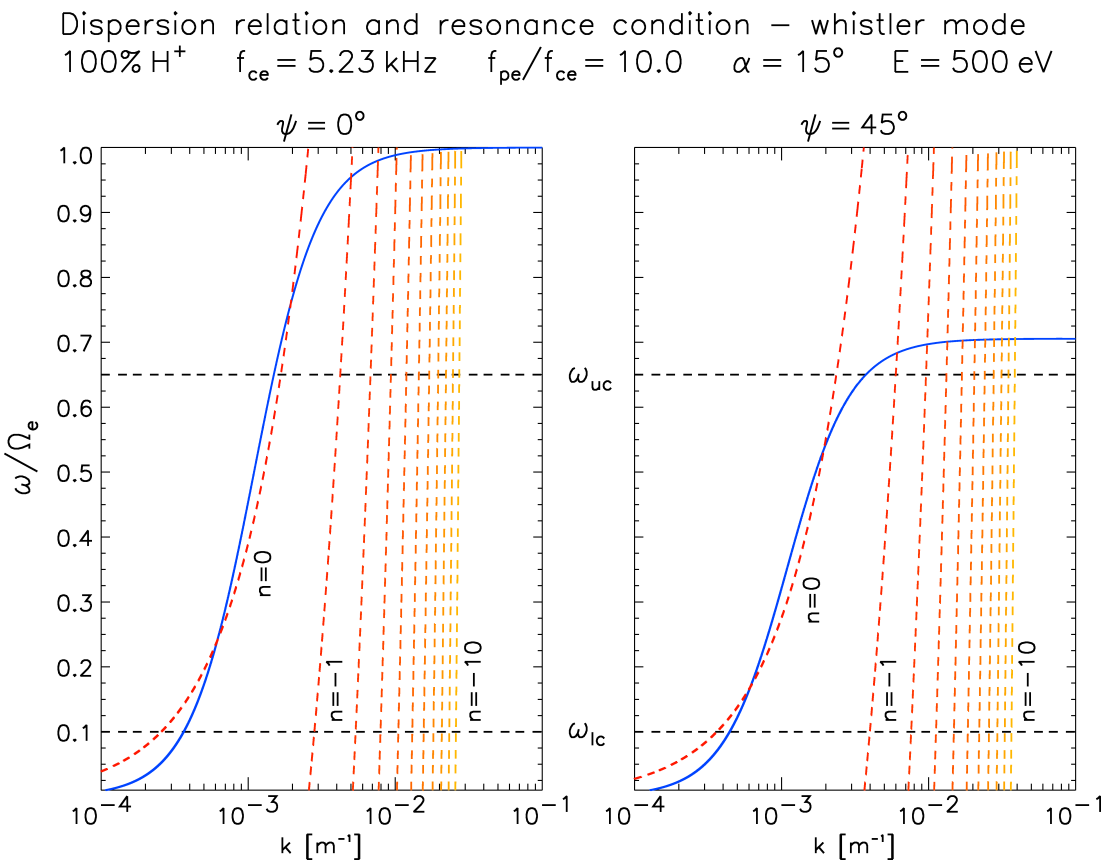


Figure 1.16: Dispersion relation of the whistler mode branch (solid blue line) and resonance condition (orange to red dashed lines) for $n = 0, ..., 10$ calculated for a pure proton-electron plasma with $f_{ce} = 5230\,\mathrm{Hz}$ and $f_{pe}/f_{ce} = 10$. The resonance condition was calculated for electrons with an equatorial pitch-angle of $\alpha = 15°$ and an energy of 500 eV. The left panel shows the results for $\psi = 0°$, while the right panel is for $\psi = 45°$.

studied. They will be defined separately for each type of wave studied in this thesis in the corresponding chapter. For now, it is important to note that only the Landau resonance intersects with the dispersion curve inside the limits of the cutoff frequencies, and hence only this resonance can be found in the presented example. It is easy to construct other examples, where higher or lower order resonances become relevant, and therefore a careful definition of the included resonances is important. For example, plasmaspheric hiss is known to show relevant resonances up to $n = 30$ and more, while for chorus waves usually $n = 10$ suffices.

### 1.6.2 Resonance Cone

Going back to the dispersion relation in terms of the refractive index $\eta$ (Eq. 1.114), we can see that the equation has a singularity for the case that $A \to 0$. In the limit of $A = 0$ this yields:

$$S \sin^2(\psi) + P \cos^2(\psi) \overset{1.111}{=} 0\,,$$

or equivalently if

$$\tan^2(\psi) = -\frac{P}{S}\,. \tag{1.138}$$

If this condition is fulfilled, the refractive index $\eta$ becomes infinite. In order to study the effect of $\eta \to \infty$, we use the definition of the refractive index 1.96 in the Helmholtz equation 1.106:

$$\underline{k}(\underline{k} \cdot \underline{E}) - |\underline{k}|^2 \underline{E} + \frac{|\underline{k}|^2}{\eta^2} \underline{\underline{\varepsilon}}_{\mathbf{r}} \cdot \underline{E} = 0 \tag{1.139}$$

In general, the electric field of an electromagnetic wave can be written as the sum of the transverse component $\underline{E_T}$ perpendicular to $\underline{k}$ and the longitudinal component $\underline{E_L}$ parallel to $\underline{k}$, so that

$$\underline{E} = \underline{E_T} + \underline{E_L}\,. \tag{1.140}$$

Furthermore, we can express $\underline{E_L}$ as the projection of $\underline{E}$ along $\underline{k}$ as:

$$\underline{E_L} = \frac{\underline{k}(\underline{k} \cdot \underline{E})}{|\underline{k}|^2} \tag{1.141}$$

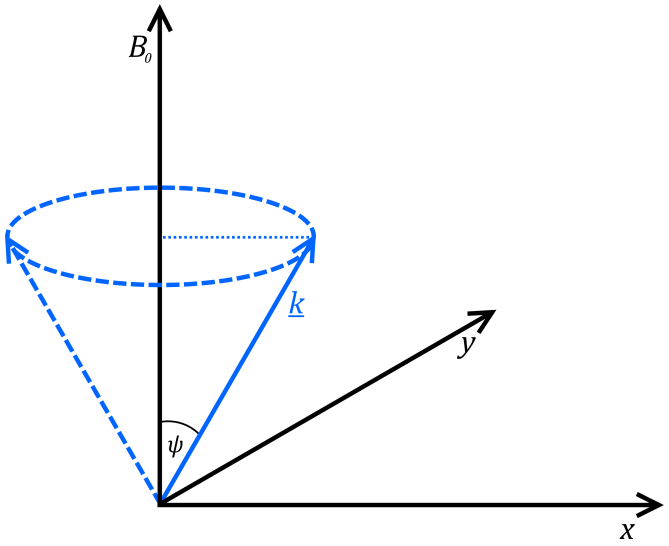


Figure 1.17: Geometry of the resonance cone.

Inserting Eq. 1.141 into Eq. 1.139 yields:

$$
\begin{aligned}
& |\underline{k}|^2 \cdot \underline{E_L} - |\underline{k}|^2 \underline{E} + \frac{|\underline{k}|^2}{\eta^2} \underline{\underline{\varepsilon}}_{\mathbf{r}} \cdot \underline{E} = 0 \\
\overset{\eta \to \infty}{\Rightarrow} \quad & |\underline{k}|^2 \cdot \underline{E_L} - |\underline{k}|^2 \underline{E} + 0 = 0 \\
\Leftrightarrow \quad & \underline{E_L} - \underline{E} = 0 \\
\overset{\text{Eq.1.140}}{\Leftrightarrow} \quad & \underline{E_T} = 0
\end{aligned}
\tag{1.142}
$$

We can now see that if the refractive index becomes infinite, the transverse component of the electric field has to become zero. Therefore, Eq. 1.138 defines the wave normal angle $\psi$, for which the electromagnetic wave becomes purely electrostatic. As resonance is usually studied for waves with an electromagnetic component, the angle $\psi_{res}$ defined by Eq. 1.138 is called the *resonance cone angle*. The volume enclosed by the resonance cone angle effectively forms a cone around the Earth's magnetic field $B_0$, which is called the *resonance cone*, which is illustrated in Figure 1.17. In a cold plasma, whistler mode wave propagation is possible for $\psi \leq \psi_{res}$, but not $\psi > \psi_{res}$, and a similar expression can be found for EMIC waves. Note that for z-mode waves (not studied here), wave propagation is possible for $\psi > \psi_{res}$, but not for $\psi \leq \psi_{res}$.

### 1.6.3 Resonance Ellipse

So far we have derived the physics of plasma waves resonating with charged particles and used the dispersion relation and resonance condition to define the resonance frequencies. We showed that the wave-particle interaction can result in a change of the particle's pitch-angle or kinetic energy (or usually a mixture of both). Since the pitch-angle is defined by the particle's velocity relative to the magnetic field (or, in other words, the direction of the particle's motion) and the kinetic energy is proportional to the magnitude of the velocity, we need to derive an equation for the particle velocity components in order to be able to predict and *quantify* the pitch-angle and energy changes. Unfortunately, it is not possible to find a simple set of equations for the velocity components, but instead a so-called *resonance ellipse* relating the parallel and the perpendicular velocity components can be derived. The resonance ellipse is obtained by rearranging the resonance condition (Eq. 1.131)

$$v_{\shortparallel} = \frac{\omega}{k_{\shortparallel}} \left(1 - \frac{n\Omega_\sigma}{\gamma\omega}\right) \tag{1.143}$$

into the form of an ellipse, which is given by:

$$\frac{v_\perp^2}{a^2} + \frac{(v_{\shortparallel} - d)^2}{b^2} = 1 \tag{1.144}$$

The parameters $a$, $b$, and $d$ are given for parallel wave propagation as [*Horne et al.*, 2003a]:

$$a^2 = c^2 \left[1 - \frac{(\omega/\Omega_\sigma)^2}{(n^2 + h^2)}\right] \tag{1.145}$$

$$b^2 = \frac{n^2 a^2}{(n^2 + h^2)} \tag{1.146}$$

$$d = \frac{\omega}{\Omega_\sigma} \frac{ch}{(n^2 + h^2)} \tag{1.147}$$

with

$$h = \frac{ck_{\shortparallel}}{\Omega_\sigma}\,, \tag{1.148}$$

where $c$ is the speed of light. Since the resonance ellipse is a rearranged form of the resonance condition, it specifies the relation between $v_{\shortparallel}$ and $v_{\perp}$ during resonance.

It was shown by *Lyons et al.* [1971] that the dominant contribution to particle scattering is the first order cyclotron resonance. In order to plot the resonance ellipse, we first need to find a solution for $k_{\shortparallel}$ from the dispersion relation (Eq. 1.115), which was presented for parallel propagating waves in Section 1.5.1. For oblique waves, the dispersion relation for $k_{\shortparallel}$ needs to be derived numerically, which is not presented here, since the effects of oblique waves play a minor role in this thesis.

The resonance ellipse is a function relating $v_{\shortparallel}$ and $v_{\perp}$ for given $\Omega_{\sigma}$ and $\omega_{ce}$, for a specific resonance number $n$. Let us first study the case of Landau resonance ($n = 0$). To illustrate this, we rewrite the resonance ellipse into the following form:

$$\begin{aligned} & 1 - \frac{v_{\perp}^2}{a^2} = \frac{(v_{\shortparallel} - d)^2}{b^2} \\ \Leftrightarrow \qquad & b^2 \left(1 - \frac{v_{\perp}^2}{a^2}\right) = (v_{\shortparallel} - d)^2 \end{aligned} \tag{1.149}$$

Using $n = 0$, we directly get for the parameters of the ellipse:

$$a^2 = \frac{\omega^2}{k_{\shortparallel}^2} \qquad b^2 = 0 \qquad d = \frac{\omega}{k_{\shortparallel}} \tag{1.150}$$

And hence, in case of Landau resonance, the resonance ellipse becomes

$$v_{\shortparallel} = \frac{\omega}{k_{\shortparallel}}\,, \tag{1.151}$$

which is a constant of $\omega$ and $k_{\shortparallel}$.

For the other resonances the resonance ellipse becomes an ellipsoid in $v_{\shortparallel}$-$v_{\perp}$ space (or equivalently, in momentum space), that depends on the various plasma parameters introduced before, as well as the frequency of the plasma wave that resonates with a charged particle of a given energy. It was shown that the wave-particle interactions force the particles to move on trajectories that are defined by the plasma conditions and the interacting waves [*Gendrin*, 1981]. *Summers et al.* [1998] derived the trajectories in velocity space along which electrons will move when they interact with whistler mode

waves inside a specified frequency band. Their solutions are derived in parametric form assuming field aligned waves and are called *diffusion surfaces*. In the general case, where we have a multitude of waves propagating in different directions, the theory becomes more complex and the diffusion surfaces can only be derived numerically.

When electrons and plasma waves resonate with each other, the electrons change their velocity components in such a way that they move from regions with high phase space density to regions of low phase space density (for details about the phase space density, see chapter 2). If this corresponds to the direction of decreasing energy, the electrons will transfer part of their energy onto the waves. Conversely, if this corresponds to the direction of increasing energy, the electrons will gain energy from the waves.

Let us now summarise these complex processes: The wave modes of a plasma wave that are allowed to propagate in the plasma are defined by the dispersion relation. The resonance condition specifies the frequencies at which an electron of a certain energy can resonate with the plasma wave. The resonance ellipses are a rearranged form of the resonance condition, specifying the region in velocity space at which the plasma wave can resonate with the electrons. Thereby, the wave-particle interactions can only happen in such a way that the electrons move on the diffusion surfaces, defining the trajectories of the electron. The change of the velocity of the electron will always be directed from regions with high phase space density to regions with low phase space density.

An example, summarising these processes is given in Figure 1.18 for the case of whistler mode waves. Here the electron phase space density is shown as a contour plot as a function of normalised momentum for the case of $f_{pe} = f_{ce} = 10.4\,\mathrm{kHz}$. The bold solid blue, green and red lines show the resonance ellipses for the frequencies $\omega/\omega_{ce} = 0.1, 0.3,$ and 0.6. The solid white lines represent the diffusion surfaces, i.e. the trajectories at which the electrons are allowed to move, while the dashed white lines represent contours of constant total energy, with the energy increasing radially outwards.

Let us now look at one example in detail. Let's assume that the plasma wave is allowed within the frequency range between $\omega/\omega_{ce} = 0.1 - 0.3$, i.e. between the blue and the green lines. Let us furthermore take the electron moving along the line starting at

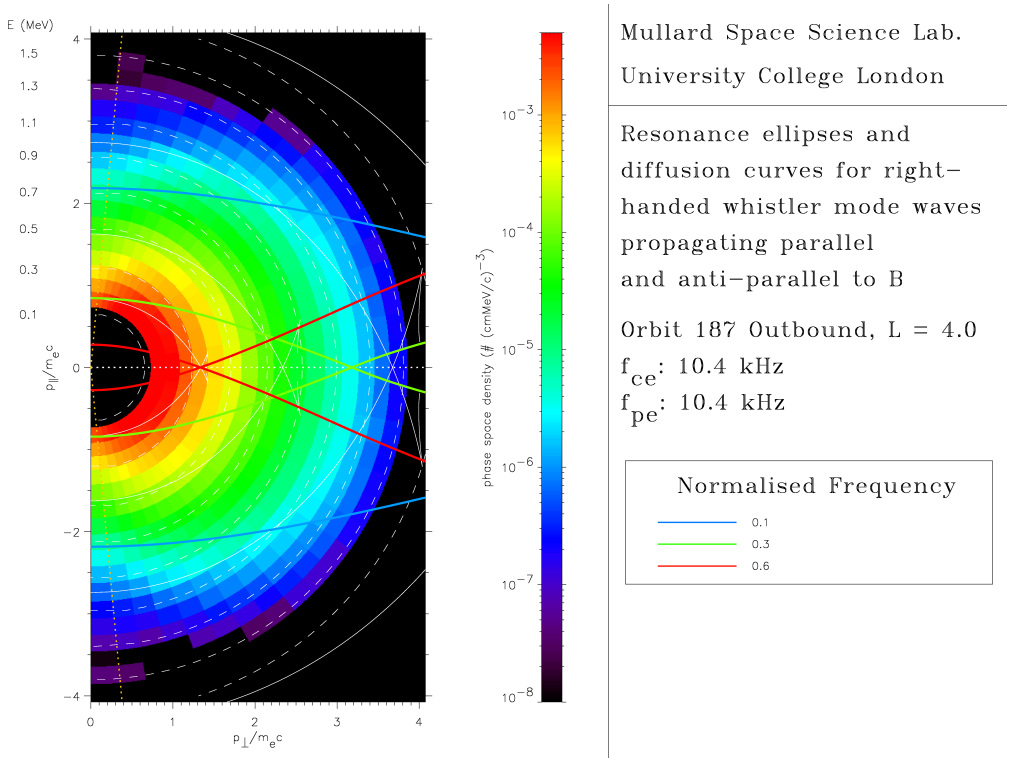


Figure 1.18: Electron phase space density (contour) as a function of normalised momentum for the case of $f_{pe} = f_{ce} = 10.4\,\text{kHz}$. The bold solid blue, green and red lines show the resonance ellipses for the frequencies $\omega/\omega_{ce} = 0.1, 0.3$, and 0.6. The solid white lines represent the diffusion surfaces, while the dashed white lines represent contours of constant total energy, increasing radially outwards. From [*Meredith et al.*, 2002].

$p_{||}/m_e c = 2.75$ and $p_\perp/m_e c = 0$. Coming from high values of $p_{||}$, we can see that just below the lower frequency limit of the resonant plasma wave interaction (blue line) the gradient of the phase space density is decreasing towards the top-left of the plot. The wave-particle interaction would hence force the electron to move to the left along its trajectory (the white line), and therefore towards smaller energies. In contrast, resonance with waves at a larger frequency, i.e. close to the green line, the gradient of the phase space density decreases to the right of the plot, which would force the electron to move further down on its trajectory, corresponding to an increase in electron energy.

## 1.7 Electron flux

We have now developed the theoretical framework to describe how charged particles can get trapped by the geomagnetic field and how their motion is determined by the

electromagnetic fields of the Earth. Furthermore, we defined the propagation of plasma waves and explained how they can interact with the trapped particles, changing their pitch-angle and energy. The objective of this thesis is to study the interactions between plasma waves and the electrons that form the Van Allen electron radiation belts. It is usually difficult to measure individual electrons, so instead the macroscopic multitude of them in specific regions of space is studied. Therefore, a concept describing the electron distribution in space, pitch-angle and energy needs to be developed, namely the concept of the *electron flux*, which is the quantity most often provided by spacecraft. The differential, directional electron flux $j(\theta, E)$ at a given location $r$, and for a given direction and energy is the number of particles $\mathrm{d}N$ with energy $\mathrm{d}E$ crossing the area $\mathrm{d}A$ that is perpendicular to the direction specified by the solid angle $\mathrm{d}\Omega$ (per second). It is usually given in units of $\mathrm{cm}^{-2}\mathrm{s}^{-1}\mathrm{sr}^{-1}\mathrm{keV}^{-1}$ and defined by:

$$\mathrm{d}N(r, \theta, E) = j(\theta, E)\,\mathrm{d}A\,\mathrm{d}E\,\mathrm{d}\Omega \tag{1.152}$$

If we, as usual, use the geomagnetic field as a reference vector for the direction, the flux direction can automatically expressed by the pitch-angle $\alpha$. A typical distribution of the electron flux is shown in Figure 1.19 as contours of the flux around the Earth. It can be seen that there are two distinct torus shaped regions of high electron fluxes, which form the previously mentioned Van Allen electron radiation belts.

Satellite measurements have shown that the electron flux at energies below about 100 keV shows a significant MLT dependence, with the flux being significantly stronger between about 00 and 12 MLT [*Meredith et al.*, 2016]. Furthermore, it was found that, independent of the electron energy, the flux is not constant with magnetic latitude. The electron flux is usually strongest at a pitch-angle of $\alpha = 90°$ and mirrored around this maximum. It was found that the distribution can often be approximated by a $\sin^n$ function, where $n$ ranges between $> 0$ and about 9, depending on geomagnetic conditions and varying significantly with $L$ [*Shi et al.*, 2016]. Furthermore, the electron flux decreases significantly with geomagnetic latitude [*Horne et al.*, 2003a], and for all distributions a minimum pitch-angle can be found, at which electrons can remain

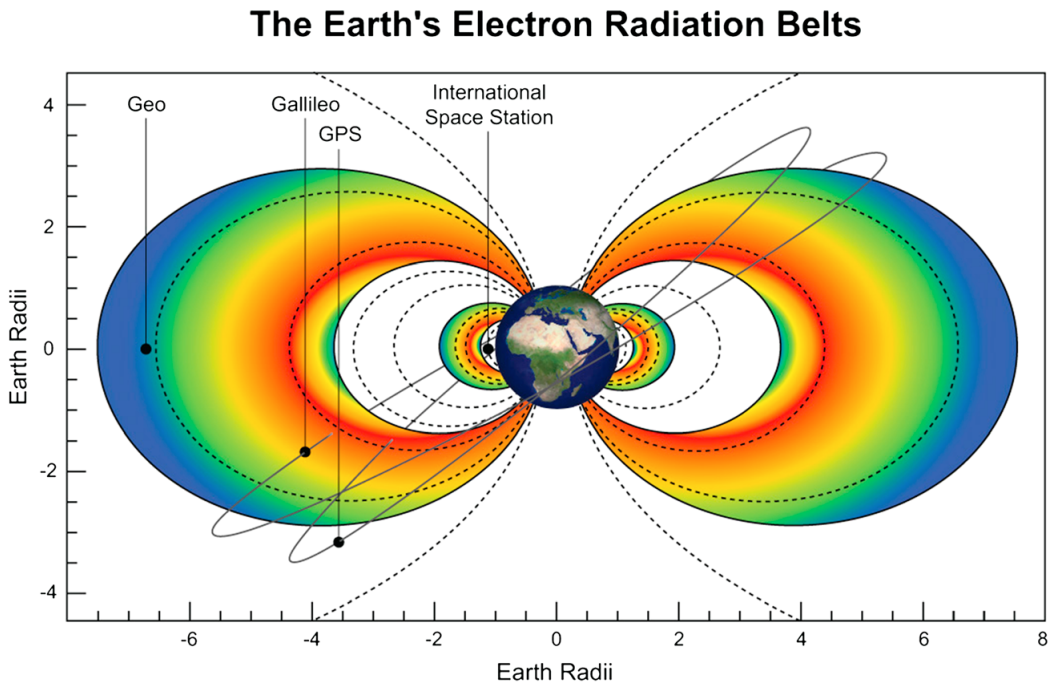


Figure 1.19: Artists representation of the electron fluxes around the Earth forming the Van Allen electron radiation belts. From [*Horne et al.*, 2013a].

trapped. This is the bounce loss cone angle, which was discussed in section 1.3.4.

Satellite measurements of electron fluxes are usually given as local electron fluxes at a specific location (including the latitude). According to Equation 1.38, the local pitch-angle $\alpha_{loc}$ of an electron moving along a field line changes with the local magnetic latitude $\lambda_{m,loc}$, because the magnetic field changes with latitude. Therefore, the flux of electrons at a given local pitch-angle also changes with magnetic latitude.

At the same time, the local flux of electrons with a certain local pitch-angle $\alpha_{loc,1}$ at the corresponding magnetic latitude $\lambda_{m,1}$ is equivalent to the flux at another latitude $\lambda_{m,2}$ for electrons with a corresponding local pitch-angle $\alpha_{loc,2}$. Therefore, it is common to take electron flux at the geomagnetic equator ($\lambda_m = 0°$) as a reference and to translate the electron fluxes at other magnetic latitudes to the equatorial flux. The relation can be derived from Equation 1.38, and we find that the electron flux at a given latitude $\lambda_m$ and pitch-angle $\alpha_{loc}$ is equal to the equatorial electron flux with the equatorial pitch-angle $\alpha_{eq}$, where

$$\alpha_{eq} = \arcsin\left(\sqrt{\frac{B_{eq}}{B(\lambda_m)}} \cdot \sin(\alpha_{loc})\right) . \tag{1.153}$$

# CHAPTER 2
# *Modelling the Radiation Belts*

## 2.1 Introduction

In the last chapter it was shown that charged particles can get trapped by the Earth's magnetic field, leading to a complex particle motion. They gyrate around field lines, bounce back and forth between the mirror points in the northern and southern hemisphere, and slowly drift around the Earth. Due to wave-particle interactions the charged particles can interchange energy with various kinds of electromagnetic waves in the plasma that surrounds the Earth. Thereby, they can change their pitch-angle and (kinetic) energy, leading to particle acceleration (or deceleration) and potentially particle losses. The collective of charged particles form the particle flux, which is the number of particles with a certain energy and direction that move through a specific area at a given location. In this thesis, the spatial and temporal variations of the flux of electrons is of interest. The above mentioned changes of the pitch-angle and energy distribution of the electrons directly affect the electron flux.

The evolution of the Earth's radiation belts can be described by the three-dimensional *Fokker-Planck Equation*, defined as [*Schulz and Lanzerotti*, 1974]:

$$\frac{\partial f(q,p,t)}{\partial t} = \sum_{i,j} \frac{\partial}{\partial J_i} \left[ D_{ij} \frac{\partial f(q,p,t)}{\partial J_i} \right] \tag{2.1}$$

This equation is in the form of a diffusion equation of the phase-averaged *phase space density* $f(q,p,t)$, which is the density of electrons in the phase space, i.e. the space of spatial coordinates $q$ and their canonical conjugate momenta $p$. The coefficients $D_{ij}$ are the so-called *diffusion coefficients* and $J_i$ are the three action integrals $J_1 = 2\pi m_e \mu / e$, $J_2 = J$, and $J_3 = e\Phi$, with $\mu$, $J$, and $\Phi$ being the adiabatic invariants as described in section 1.3.4, and $m_e$ the mass of an electron and $e$ the electron charge.

The phase space density can directly be related to the (electron) flux by:

$$f(q,p,t) = j(\theta, E, t)/p^2 \tag{2.2}$$

Since the adiabatic invariants are not intuitive to visualise and it can be difficult to apply boundary conditions, it is common to transform the Fokker-Planck Equation to other coordinates. The model used in this thesis uses pitch-angle $\alpha$, energy $E$, and $L^*$ as the three independent variables. Following the derivations of *Schulz and Lanzerotti* [1974], neglecting some cross derivatives and assuming a dipole magnetic field, Eq. 2.1 becomes [*Glauert et al.*, 2014]:

$$\begin{aligned}\frac{\partial f(r,p,t)}{\partial t} = & \frac{1}{g(\alpha)}\frac{\partial}{\partial \alpha}\bigg|_{E,L} g(\alpha)\left(D_{\alpha\alpha}\,\frac{\partial f(r,p,t)}{\partial \alpha}\bigg|_{E,L} + D_{\alpha E}\,\frac{\partial f(r,p,t)}{\partial E}\bigg|_{\alpha,L}\right) \\ & + \frac{1}{A(E)}\,\frac{\partial}{\partial E}\bigg|_{\alpha,L} A(E)\left(D_{EE}\,\frac{\partial f(r,p,t)}{\partial E}\bigg|_{\alpha,L} + D_{E\alpha}\,\frac{\partial f(r,p,t)}{\partial \alpha}\bigg|_{E,L}\right) \\ & + L^2\,\frac{\partial}{\partial L}\bigg|_{\mu,J}\left(\frac{D_{LL}}{L^2}\,\frac{\partial f(r,p,t)}{\partial L}\bigg|_{\mu,J}\right), \end{aligned} \tag{2.3}$$

where

$$g(\alpha) = T(\alpha)\sin(2\alpha) \tag{2.4}$$

and

$$A(E) = (E + E_0)\cdot[E(E + 2E_0)]^{1/2}\,. \tag{2.5}$$

Here, $T(\alpha)$ is related to the bounce period in a dipole field and can be approximated by $T(\alpha) = 1.3802 - 0.3198(\sin(\alpha) + \sin(\alpha)^{1/2})$ [*Lenchek et al.*, 1961], and $E_0$ is the electron rest mass energy. The diffusion coefficients have now become the drift and bounce averaged pitch-angle diffusion coefficient $D_{\alpha\alpha}$, energy diffusion coefficient $D_{EE}$, mixed pitch-angle and energy diffusion coefficient $D_{\alpha E} = D_{E\alpha}$, and radial diffusion coefficient $D_{LL}$. Note that for simplicity, in this equation the drift and bounce averaged diffusion coefficients have been written in the given form, and $L^*$ has been written as $L$. For the remainder of this study, they will be explicitly written as $\langle D_{\alpha\alpha}\rangle^d$, $\langle D_{\alpha E}\rangle^d$, $\langle D_{EE}\rangle^d$, and $\langle D_{LL}\rangle^d$ to emphasise that they are drift and bounce averaged. The bounce averaged

pitch-angle and energy diffusion rates are thereby defined as [*Glauert et al.*, 2014]

$$\langle D_{\alpha\alpha} \rangle = \left\langle \frac{(\Delta\alpha)^2}{2\Delta t} \right\rangle \tag{2.6}$$

$$\langle D_{\alpha E} \rangle = \left\langle \frac{\Delta\alpha \Delta E}{2\Delta t} \right\rangle \tag{2.7}$$

$$\langle D_{EE} \rangle = \left\langle \frac{(\Delta E)^2}{2\Delta t} \right\rangle \tag{2.8}$$

in units of $s^{-1}$, J $s^{-1}$, and $J^2$ $s^{-1}$, respectively. As mentioned above, the Fokker-Planck Equation models the radiation belt in the form of a diffusion equation with the diffusion coefficients mentioned before. These diffusion coefficients hence describe the change of a physical property of the collection of electrons forming the phase space density per unit time. For example, the pitch-angle diffusion coefficient describes the change of the electron phase space density with respect to the pitch-angle per unit time. If the initial phase space density distribution $f(r, p, t_0)$ at a given location in phase space defined by $r$ and $p$ was such that all particles had a pitch-angle of 45° and the pitch-angle diffusion coefficient was constant over all pitch-angles (and times), then the pitch-angles of all electrons would change to smaller and larger values over time, until the pitch-angle distribution became flat. This process can be characterised as a diffusion process of the pitch-angle, quantified by the pitch-angle diffusion coefficient. Similarly, the energy diffusion coefficient specifies the change of the phase space density with respect to energy per unit time.

In this thesis the electron fluxes were calculated using the `British Antarctic Survey Radiation Belt Model` (`BAS-RBM`), which essentially solves a modified version of Eq. 2.3. The required diffusion coefficients were calculated with the `PADIE` diffusion code. Both are presented in the following sections.

## 2.2 PADIE Diffusion Code

The first pitch-angle and energy diffusion coefficients were calculated based on quasi-linear theory by *Lyons et al.* [1971] and subsequently by others *Albert* [e.g. 2003]; *Summers and Thorne* [e.g. 2003]. All these calculations assumed a high density approx-

imation, where the plasma frequency was much larger than the electron gyrofrequency. Furthermore, most cases were restricted to waves propagating parallel to the magnetic field and with small amplitudes. The first code that was developed for any plasma density and arbitrary wave propagation was the Pitch Angle and Energy Diffusion of Ions and Electrons (`PADIE`) code by *Glauert and Horne* [2005]. This diffusion code is described in the following, where all definitions and equations are taken from [*Glauert and Horne*, 2005].

In order to obtain expressions for the diffusion coefficients using the `PADIE` diffusion code, the distribution of the wave normal angles $\psi$ of the plasma waves as well as the frequency distribution of the power spectral density (PSD) need to be specified. The distribution of the wave normal angle is assumed to be of Gaussian form defined as:

$$g(X) = \begin{cases} \exp\left[-\left(\frac{X-X_m}{X_w}\right)^2\right] & X_{lc} \leq X \leq X_{uc} \\ 0 & \text{otherwise}\,, \end{cases} \tag{2.9}$$

where $X$ =tan($\psi$), $X_m$ is the peak, and $X_w$ is the angular width of the wave normal angle distribution, and $X_{lc}$ and $X_{uc}$ define the so-called lower and upper cut-offs of the wave normal angle distribution.

### 2.2.1 Power Spectral Density Distribution

There are two general modes of operation in the `PADIE` code available, distinguished by the way the frequency distribution of the power spectral density is supplied . In the first mode, the frequency distribution of the PSD has to be of Gaussian form as defined as:

$$B^2(\omega) = \begin{cases} A_\omega^2 \cdot \exp\left[-\left(\frac{\omega-\omega_m}{\delta\omega}\right)^2\right] & \omega_{lc} \leq \omega \leq \omega_{uc} \\ 0 & \text{otherwise}\,, \end{cases} \tag{2.10}$$

where $A_\omega^2$ is a normalisation constant (or the peak intensity of the PSD) given by

$$A_\omega^2 = \frac{|B_W|^2}{\delta\omega} \cdot \frac{2}{\sqrt{\pi}} \cdot \left[\mathrm{erf}\left(\frac{\omega_m - \omega_{lc}}{\delta\omega}\right) + \mathrm{erf}\left(\frac{\omega_{uc} - \omega_m}{\delta\omega}\right)\right]^{-1} \tag{2.11}$$

Here, $B_W$ is the wave amplitude in nT, while $\omega_m$ is the angular peak frequency, and $\delta\omega$ the angular frequency width (both in rad $s^{-1}$) of the power spectral density. Furthermore, the angular lower and upper cut-off frequencies $\omega_{lc}$ and $\omega_{uc}$, outside which the wave power is zero, need to be specified. In this mode of operation, the user has to provide these five parameters ($B_W$, $\omega_m$, $\delta\omega$, $\omega_{lc}$, and $\omega_{uc}$) from which `PADIE` determines $B^2(\omega)$. Since the wave intensity $B_W$ is by definition given in units of Tesla, the PSD must be in units of $\mathrm{nT^2\,rad^{-1}\,Hz^{-1}}$.

The datasets used in this thesis commonly provide the power spectral density in units of $\mathrm{nT^2\,Hz^{-1}}$ (non-angular frequency), labelled as $B^2(f)$. If the PSD is of Gaussian form, it can hence be expressed by:

$$B^2(f) = A_f^2 \cdot \exp\left[-\left(\frac{f - f_m}{\delta f}\right)^2\right], \tag{2.12}$$

where $A_f^2$ is the amplitude in units of $\mathrm{nT^2\,Hz^{-1}}$, $f_m$ is the frequency of the peak, and $\delta f$ is the width of the Gaussian distribution. Note that the frequencies are now in non-angular units of frequency. Analogously to Equation 2.11, $A_f^2$ can be expressed as:

$$A_f^2 := \frac{|B_W|^2}{\delta f} \cdot \frac{2}{\sqrt{\pi}} \cdot \left[\mathrm{erf}\left(\frac{f_m - f_{lc}}{\delta f}\right) + \mathrm{erf}\left(\frac{f_{uc} - f_m}{\delta f}\right)\right]^{-1}. \tag{2.13}$$

Note that since $A_f^2$ has to be in units of $\mathrm{nT^2\,Hz^{-1}}$, the angular frequencies $\omega$ need to be replaced by non-angular frequencies $f$. The wave power $|B_W|^2$ can be obtained from the distribution of the PSD in the non-angular frequency domain, by rearranging Equation 2.13 for $|B_W|^2$, i.e.:

$$|B_W|^2 = \frac{1}{2} A_f^2 \cdot \delta f \sqrt{\pi} \cdot \left[\mathrm{erf}\left(\frac{f_m - f_{lc}}{\delta f}\right) + \mathrm{erf}\left(\frac{f_{uc} - f_m}{\delta f}\right)\right]. \tag{2.14}$$

The wave power $|B_W|^2$ derived in this way can now be used as an input parameter for the `PADIE` code. The required angular frequency parameters ($\omega_m$, $\delta\omega$, $\omega_{lc}$, and $\omega_{uc}$) can be obtained from $f_m$, $\delta f$, $f_{lc}$, and $f_{uc}$ by using the relation $\omega = 2\pi f$.

In the second mode of operation, the frequency distribution of the power spectral density is provided as tabulated data, where for any given set of frequencies the cor-

responding values of the PSD are provided. The `PADIE` diffusion code calculates the PSD at any given frequency by a linear interpolation between the provided values of the PSD. This operational mode allows the use of measured wave data directly, since no Gaussian power spectral density distribution is required.

### 2.2.2 Definition of the Diffusion Coefficients

Following the approach of *Lyons* [1974], the pitch-angle and momentum diffusion coefficients in units of $s^{-1}$ and momentum$^2$ $s^{-1}$, respectively, are defined as:

$$D_{\alpha\alpha} = \sum_{n=n_l}^{n_h} \int_{X_{lc}}^{X_{uc}} X \mathrm{d}X D_{\alpha\alpha}^{nX} \tag{2.15}$$

$$D_{pp} = \sum_{n=n_l}^{n_h} \int_{X_{lc}}^{X_{uc}} X \mathrm{d}X D_{pp}^{nX}\,, \tag{2.16}$$

where $D_{\alpha\alpha}^{nX}$ and $D_{pp}^{nX}$ are short-hand notations defined as

$$D_{\alpha\alpha}^{nX} = \sum_i \frac{q_\sigma^2 \omega_i^2}{4\pi\,(1+X^2)\,N(\omega_i)} \cdot \left[\frac{n\Omega_\sigma/(\gamma\omega_i) - \sin^2(\alpha)}{\cos(\alpha)}\right]^2 \cdot B^2(\omega_i) g(X)\, \frac{|\Phi_{n,k}|^2}{|v_{\shortparallel} - \frac{\partial\omega}{\partial k_{\shortparallel}}|}\bigg|_{k_{\shortparallel i}} \tag{2.17}$$

$$D_{pp}^{nX} = D_{\alpha\alpha}^{nX} \left[\frac{\sin(\alpha)\cos(\alpha)}{n\Omega_\sigma/(\gamma\omega_i) - \sin^2(\alpha)}\right]^2_{k_{\shortparallel i}} \tag{2.18}$$

The integrands in Eqs. 2.15 and 2.16 are evaluated at the resonant parallel wave number $k_{\shortparallel i}$, which is determined from the resonance condition (Eq. 1.131) and the dispersion relation (Eq. 1.114), that are described in Chapter 1. There, it was shown that for a given pitch-angle, energy, and resonance number $n$ there could be more than one resonant frequency corresponding to the same wave number $k$. Therefore, the summation over $i$ takes the possibility of multiple resonant frequencies into account. The terms $|\Phi_{n,k}|^2$ and $N(\omega)$ are both defined in *Glauert and Horne* [2005]. The former depends on the wave refractive index, while the latter is a normalisation factor which ensures that the wave energy per unit frequency is given by $B^2(\omega)$.

In order to reflect the timescale for energisation and to incorporate the diffusion co-

efficients into radiation belt models such as the BAS-RBM, the momentum diffusion coefficients are then converted into energy diffusion coefficients in units of $J^2 s^{-1}$ by:

$$D_{EE} = \frac{c^2 E(E + 2E_0)}{(E + E_0)^2} D_{pp} \tag{2.19}$$

### 2.2.3 Method of Calculation

#### Input Parameter

In order to calculate the diffusion coefficients, various parameters need to be specified. First, the frequency distribution of the wave power spectral density needs to given, either in tabulated form, or as a set of the Gaussian parameters $\omega_m$, $\delta\omega$, $\omega_{lc}$, $\omega_{uc}$, and $|B_W|$. Furthermore, the parameters $X_m$, $X_w$, $X_{lc}$, and $X_{uc}$ of the wave normal angle distribution have to be provided. Additionally, the conditions of the plasma need to specified, in particular the ion composition and the plasma density in the form of $f_{pe}/f_{ce}$ (see below). In order to evaluate the resonance condition, it is further required to specify the number of resonances $n$. An overview of the required input parameters is presented in Table 2.1.

Based on these parameters, PADIE calculates the bounce averaged diffusion rates at location defined by the McIlwain $L$ parameter and the geomagnetic latitude $\lambda_m$. The magnetic field $B(L, \lambda_m)$at this location is thereby evaluated from a dipole magnetic

| Input Parameter | Description |
|---|---|
| $B_W$ | Wave magnetic field intensity |
| $\omega_m$ | Wave Gaussian peak frequency |
| $\delta\omega$ | Wave Gaussian frequency width |
| $\omega_{lc}$ | Lower cut-off frequency |
| $\omega_{uc}$ | Upper cut-off frequency |
| $X_m$ | Wave normal angle peak |
| $X_w$ | Wave normal angle width |
| $X_{lc}$ | Wave normal angle lower cut-off |
| $X_{uc}$ | Wave normal angle upper cut-off |
| $n$ | Number of resonances included |
| $f_{pe}/f_{ce}$ | Plasma density |
| Ion composition | Hydrogen, Helium, and Oxygen fraction |

Table 2.1: Boundary conditions used in the BAS-RBM.

field model, and hence:

$$B(L, \lambda_m) = \frac{M_0\sqrt{1 + 3\,\sin^2(\lambda_m)}}{L^3 R_E^3 \cos^6(\lambda_m)}\,, \tag{2.20}$$

where $M_0 = 8.0334 \cdot 10^{15}$ Tm$^3$ is the mean value of the magnetic moment at the magnetic equator on the Earth's surface and $R_E$ is the Earth's radius.
The ratio of the plasma frequency to the electron cyclotron frequency $f_{pe}/f_{ce}$ is a widely used parameter to characterise the plasma density, since $f_{pe}/f_{ce}$ is directly proportional to the square root of the plasma density. Using the definitions of the plasma frequency (Eq. 1.50) and the cyclotron frequency (Eq. 1.10), $f_{pe}/f_{ce}$ can be expressed as:

$$\frac{1}{2\pi}\left(\frac{n_e e^2}{m_e \epsilon_0}\right)^{1/2} / \left(\frac{eB_0}{2\pi m_e}\right) \tag{2.21}$$

Note that, since the magnetic field changes with $L$ and $\lambda_m$ (see Eq. 2.20), the local electron gyrofrequency is also location dependent.

#### Computational Details

The diffusion coefficients are found by evaluating the integrals in Eqs. 2.15 and 2.16 over $\tan(\Psi) = X$ between the lower and upper wave-normal angle cut-offs $X_{lc}$ and $X_{uc}$. At each value of $X$ the dispersion relation and resonance condition need to be solved simultaneously in order to determine $\omega$ and $k$. Thereby solutions will be rejected, where $\omega$ lies outside the frequency cut-offs $\omega_{lc}$ and $\omega_{uc}$, or where the solution is complex, or where the solution lies on the wrong branch of the dispersion relation. The integrand is evaluated at as many values of $X$ between the cut-offs, as necessary for the calculation to converge. This is repeated for all number of resonances $n$.
Numerically, the equations are solved using adaptive numerical integration schemes and a polynomial root finder. It was shown in Section 1.6.1 that a careful definition of the resonances included in the calculations of the diffusion coefficients is important. In principle, all resonances should be included, however this would be computationally not feasible and hence the number of resonances has to be limited in a careful way between $n_l$ and $n_h$, which are the last set of parameters that need to be specified.

The equations for the diffusion rates are derived using quasi-linear theory. There are two important assumptions that are being made in quasi-linear theory, namely that the wave amplitudes of the wave field are small and that the waves are broadband and incoherent. If the wave amplitude is small, only second order non-linear effects are required to be included in the calculation of the bounce averaged diffusion rates, while broadband and incoherent waves allow a stochastic description of the particle motion. In the case of monochromatic waves, the particle motion becomes entirely deterministic, which allows for the nonlinear effect of phase-trapping to modify the particle's motion.

Chorus waves in particular are known to be highly nonlinear due to their short duration rising tone frequency structure [e.g. *Omura et al.*, 2009; *Santolík et al.*, 2014a], but it is not yet computationally feasible to simulate chorus waves using nonlinear models over the duration and spatial dimensions required by global models. It has been demonstrated by *Albert* [2010] and *Tao et al.* [2012] that there is remarkable agreement between fully nonlinear and quasi-linear simulations for waves with a wave power less than about 0.1 nT. If the wave power is below this threshold, there is only linear phase-trapping and nonlinear phase trapping effects can be neglected.

Whistler mode waves can acquire a large electrostatic component, if the refractive index is large and for wave normal angles close to the resonance cone [*Glauert et al.*, 2014]. If the wave normal angle distribution of the wave power spectral density is such that there is a too large contribution near the resonance cone, the electrostatic wave components become unrealistically large, leading to inaccurate simulation results. In order to prevent this, the electrostatic components were reduced, by scaling the wave magnetic field down, according to the ratio of the square of the electromagnetic component over the square of the total wave electric field. This approach ensures that the contribution of electrostatic components to the calculations of the diffusion rates are small. Since `PADIE` is only designed to calculate electromagnetic diffusion rates, this procedure is used within this thesis and therefore there could be an electrostatic component that is omitted.

### Calculation of the Bounce Averaged Diffusion Rates

As described in Section 1.3.3, charged particles that are trapped by the Earth's magnetic field bounce back and forth between the northern and southern hemisphere. During this bounce motion towards higher or lower latitudes, their local pitch-angle changes, as well as the plasma density, ion composition, the magnetic field, and the distribution of the wave power spectral density. To take these variations into account, `PADIE` calculates the bounce averaged pitch-angle and energy diffusion rates, whose pitch-angle is mapped back to the equator, denoted by $\langle D_{\alpha_{eq}\alpha_{eq}} \rangle$ and $\langle D_{pp} \rangle$. They are defined as [*Glauert and Horne*, 2005]:

$$\langle D_{\alpha_{eq}\alpha_{eq}} \rangle = \frac{1}{T(\alpha_{eq})} \int_{\lambda_{m,0}}^{\lambda_{m,m}} D_{\alpha\alpha} \frac{\cos(\alpha)}{\cos^2(\alpha_{eq})} \cos^7(\lambda) \mathrm{d}\lambda \tag{2.22}$$

$$\langle D_{pp} \rangle = \frac{1}{T(\alpha_{eq})} \int_{\lambda_{m,0}}^{\lambda_{m,m}} D_{pp} \frac{\cos(\lambda) \left(1 + 3\sin^3(\lambda)\right)^{1/2}}{\cos(\lambda)} \mathrm{d}\lambda \,, \tag{2.23}$$

where $T(\alpha_{eq})$ defines the variation of the bounce period $\tau_b$ and is approximated by [*Hamlin et al.*, 1961]

$$T(\alpha_{eq}) = 1.30 - 0.56 \sin(\alpha_{eq}) \,. \tag{2.24}$$

The bounce averaging is usually performed from the equator $\lambda_{m,0} = 0°$ to the mirror point $\lambda_{m,m}$, which, in `PADIE` is found by solving the polynomial

$$C_l^6 + 3C_l \sin^4(\alpha_{eq}) - 4\sin^4(\alpha_{eq}) = 0 \tag{2.25}$$

for $C_l = \cos^2(\lambda_{m,m})$.

However, the latitudinal limits of the integration can also be changed by the user, if waves are only present within a limited range of latitudes.

The drift and bounce averaged diffusion rates that are needed for the `BAS-RBM` are not directly obtained from `PADIE`, since only bounce averaged diffusion coefficients can be calculated. The drift averaging over a particle's drift orbit is performed by averaging the bounce averaged diffusion rates at a given $L$ over the electron's drift orbit. It

was shown that the drift average approach is only valid above electron energies of about 100 keV, since the electron flux is not uniform for all MLT at energies below this threshold [*Meredith et al.*, 2016].

## 2.3 British Antarctic Survey Radiation Belt Model

The electron radiation belts can be modelled by solving the three-dimensional Fokker-Planck Equation (Eq. 2.3) and there have been several programs developed to do so. The first one that was developed for high-energy radiation belt electrons by *Beutier and Boscher* [1995] is called `Salammbô`. *Varotsou et al.* [2005] included chorus waves at low latitudes up to 15° based on data from the CRRES mission into the model of Beutier and Boscher, showing that chorus can be a relevant acceleration and loss process. An extension of this chorus model to latitudes up to 30° was subsequently included in another 3d-code by *Albert et al.* [2009]. The first model to include the effects of (parametrised) chorus waves, plasmaspheric hiss, and EMIC waves was the `Versatile Electron Radiation Belts` (`VERB`) [*Subbotin and Shprits*, 2009]. Using the same parametrised wave models, *Su et al.* [2010] developed a similar model. Four dimensional models that include the MLT dependence of the wave-particle interactions have been developed by *Jordanova et al.* [2008] and *Fok et al.* [2008]. Nevertheless, most models use diffusion rates that are drift averaged over all MLT, since drift averaged simulations are able to accurately predict the overall shape of the electron pitch angle distribution [*Shprits et al.*, 2009a].

In this thesis, the `British Antarctic Survey Radiation Belt Model` (`BAS-RBM`) [*Glauert et al.*, 2014] is used, which utilises diffusion coefficients that are based on a careful modelling of available satellite data throughout the radiation belts instead of parametrised diffusion coefficients. The `BAS-RBM` solves a modified and simplified version of the Fokker-Planck Equation (Eq. 2.3), where a term of the form $f/\tau_L$ that represents electron losses to the atmosphere due to collisions was added. Inside the loss cone, the loss timescale $\tau_L$ was set to be one quarter of the bounce period, while it is set to be infinite outside the loss cone. Furthermore, the cross diffusion terms $\langle D_{\alpha E} \rangle^d$

and $\langle D_{E\alpha} \rangle^d$ were omitted, since it was shown that the cross diffusion terms only have a small effect on equatorially mirroring particles [*Albert and Young*, 2005; *Subbotin et al.*, 2010]. Nevertheless it is important to note that it was shown that the cross terms might have a significant effect for electrons with energies greater than about 2 MeV and equatorial pitch-angles below 60° *Tao et al.* [2008, 2009], but including the cross diffusion terms is outside the scope of the model at this stage. Using these modifications (and the short-hand notations for $L^*$ and the drift and bounce averaged diffusion rates), the Fokker-Planck Equation, as used in the `BAS-RBM`, becomes:

$$\begin{aligned}\frac{\partial f(r,p,t)}{\partial t} = & \frac{1}{g(\alpha)} \frac{\partial}{\partial \alpha}\Big|_{E,L} \left( g(\alpha) D_{\alpha\alpha} \frac{\partial f(r,p,t)}{\partial \alpha}\Big|_{E,L} \right) \\ & + \frac{1}{A(E)} \frac{\partial}{\partial E}\Big|_{\alpha,L} \left( A(E) D_{EE} \frac{\partial f(r,p,t)}{\partial E}\Big|_{\alpha,L} \right) \\ & + L^2 \frac{\partial}{\partial L}\Big|_{\mu,J} \left( \frac{D_{LL}}{L^2} \frac{\partial f(r,p,t)}{\partial L}\Big|_{\mu,J} \right) - \frac{f}{\tau_L} \end{aligned} \tag{2.26}$$

Up until the late 1990s, it was believed that radial diffusion was the main cause for the variability of the outer electron radiation belt. However, important observations of peaks in the phase space density at medium L suggested that there must be an additional acceleration process that happens locally. It was found that this process was the wave-particle interactions between plasma waves and radiation belt electrons, causing acceleration and loss [*Summers et al.*, 1998; *Horne and Thorne*, 1998]. These interactions lead to pitch-angle and energy diffusion and, in contrast to radial diffusion, break the first and second adiabatic invariants [e.g. *Kennel and Petschek*, 1966]. In this thesis, the diffusion rates due to wave-particle interactions between electrons and whistler mode chorus, plasmaspheric hiss, and EMIC waves are included in the `BAS-RBM`. They are obtained from the `PADIE` code and are drift and bounce averaged, and hence don't include a MLT resolution. Furthermore, radial diffusion is utilised by the model, and a brief discussion of the diffusion coefficients is given in the following section. Since the wave-particle interactions between electrons and chorus, hiss, and EMIC waves with play the major role in this study, their diffusion rates and effects on the radiation belts

are studied in detail and presented in individual chapters, while a literature review of these is presented separately in Chapter 3.

### 2.3.1 Radial Diffusion Coefficients

The two most important processes driving the variability of the outer electron radiation belt are the so-called *radial diffusion* of electrons, and electron acceleration and loss due to the wave-particle interaction between plasma waves and electrons. Radial diffusion transports electrons across the geomagnetic field from regions of high phase space density into regions of lower phase space density. It is driven by large-scale fluctuations of the magnetic and electric fields with frequencies near the electron drift period of a few mHz [*Fälthammar*, 1965]. Assuming conservation of the first and second adiabatic invariant, it was shown that radial diffusion may be enhanced by ultra low frequency (ULF) waves [*Hudson et al.*, 2013; *Elkington*, 2013]. If the first and second adiabatic invariants are conserved, electrons being transported radially outward lose energy, while electrons being transported towards the Earth gain energy, since the Earth's magnetic field decreases with the radial distance to the Earth. Phase space density measurements from the Van Allen Probes satellites suggests that outward radial diffusion is possible at $L^* > 5.5$, while inward radial transport is possible at $L^* < 5.5$ [*Reeves et al.*, 2013]. Therefore, if the outward transport diffuses electrons out of the magnetosphere, radial diffusion can act as a loss process [e.g. *Shprits et al.*, 2006].

The first radial diffusion coefficients $D_{LL}$ were calculated by *Fälthammar* [1965], and many different models have followed. The current de facto standard are the radial diffusion coefficients by *Brautigam and Albert* [2000], which are parametrised by the geomagnetic activity using the $Kp$ index with values between 1 and 6, and defined between $L = 3.0$ - 6.5. They are of the form

$$D_{LL}^{M} + D_{LL}^{E}\,, \tag{2.27}$$

where $D_{LL}^{M}$ represents the radial diffusion coefficients due to the fluctuations of the magnetic field, defined as

$$D_{LL} = D_{LL}^{M} = 10^{0.506Kp-9.325} \cdot (L^*)^{10}\,, \tag{2.28}$$

and $D_{LL}^{E}$ represents the diffusion coefficients due to the fluctuations of the electric field. Since these diffusion rates are well studied and widely used in radiation belt modelling [e.g. *Varotsou et al.*, 2005; *Albert et al.*, 2009; *Subbotin and Shprits*, 2009], they are employed in the present study. However, since it was shown that the use of the electrostatic component leads to unrealistically high fluxes in the slot region [*Kim et al.*, 2011], the component $D_{LL}^{E}$ will be omitted, as done in other studies as well [e.g. *Miyoshi et al.*, 2006].

### 2.3.2 Numerical Method

#### Computational Grids

In order to solve Eq. 2.26 a numerical method was employed. The terms of this equation have to be evaluated at five different constant quantities ($E$, $L^*$, $\alpha$, $\mu$, and $J$), and in order to take them into account, computational grids were created. At first, a regularly spaced grid in $L^*$ is defined between the minimum and maximum values $L^*_{min}$ and $L^*_{max}$, specified by the user. At $L^*_{max}$ the user furthermore specifies the minimum and maximum energies $E_{min}(L^*_{max})$ and $E_{max}(L^*_{max})$, which are then used to derive a grid in equatorial pitch-angle $\alpha$ and the natural logarithm of the electron energy $E$. This ($\alpha$-$E$) grid is created to be regularly spaced, both in pitch-angle with $0° \leq \alpha \leq 90°$, and $\log(E)$, where $E_{min}(L^*_{max}) \leq E \leq E_{max}(L^*_{max})$. Following *Schulz and Lanzerotti* [1974], assuming a dipole field for the Earth's magnetic field, all points of this ($\alpha$-$E$) grid (defined at $L^*_{max}$) have associated values of $\mu$ and $J$, with

$$\mu = \frac{p^2 (L^*)^3 \sin^2(\alpha)}{2 m_e B_d} \tag{2.29}$$

$$J = 2pR_E \cdot L^* \cdot Y(\sin(\alpha))\,. \tag{2.30}$$

Here, $p$ is the electrons momentum, $m_e$ is the electron mass, $R_E$ is the Earth's radius, and $B_d$ is the mean value of the Earth's dipole magnetic field at the magnetic equator on the Earth's surface, while the function $Y(\sin(\alpha))$ is defined in *Schulz and Lanzerotti* [1974]. The function ranges between $Y(0°) \approx 2.76$ and $Y(90°) = 0$. The values obtained from Equations 2.29 and 2.30 are used to define the ($\mu$-$J$) grid at all $L^*$ that is used for the computation, since radial diffusion has to take place at constant values of $\mu$ and $J$ at all $L^*$. The ($\mu$-$J$) grid is hence irregular at each $L^*$, but regular in $L^*$.
The ($\alpha$-$E$) grid that is required for the computation is then defined at all $L^*$ between $L^*_{min}$ and $L^*_{max}$ by

$$0° \leq \alpha \leq 90°$$
$$E_{min}(L^*) \leq E \leq E_{max}(L^*)\,,$$

where $E_{min}(L^*)$ is the minimum energy corresponding to any $\mu$ and $J$ grid point, and $E_{max}(L^*)$ is the maximum energy corresponding to any $\mu$ and $J$ grid point. The ($\alpha$-$E$) grid is hence regular in $\alpha$ and $\log(E)$. An illustration of the resulting computational grid is shown in Figure 2.1.

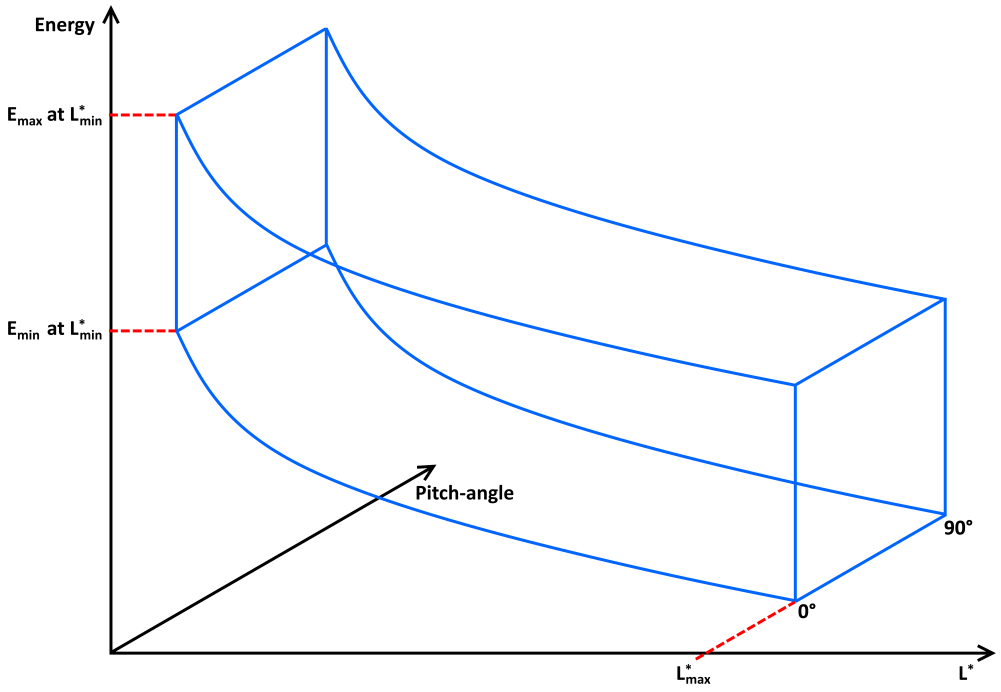


Figure 2.1: Illustration of the ($\alpha$-$E$) computational grid.

### Boundary Conditions

Following the explanations of the previous section, there are six computational boundaries that need to be specified for the BAS-RBM. These are the minimum pitch-angle ($\alpha = 0°$), maximum pitch-angle ($\alpha = 90°$), minimum $L^*$, maximum $L^*$, and the minimum and maximum energy boundaries (for all $L^*$). Both the pitch-angle and the maximum energy boundary conditions are fixed, such that the phase space density is equal to zero at the maximum energy boundary, and the gradient of the phase space density with respect to the pitch-angle ($\partial f/\partial\alpha$) is equal to zero at the pitch-angle boundaries. In this study, the minimum and maximum $L^*$ and the minimum energy boundary conditions are derived directly from data from either the CRRES satellite or the Van Allen probes satellites. Hereby, the measured phase space density at specified minimum and maximum values of $L^*$ and the phase space density of the minimum energy at all values of $L^*$ are used as a boundary condition. The method to derive the boundary conditions from the Van Allen probes is presented in Chapter 7, while the boundary conditions based on the CRRES data were directly taken from [*Glauert et al.*, 2014]. An overview of these boundary conditions is presented in Table 2.2.

| Boundary | Location | Boundary Condition |
|---|---|---|
| Minimum pitch-angle | $\alpha = 0°$ | $\partial f/\partial\alpha = 0$ |
| Maximum pitch-angle | $\alpha = 90°$ | $\partial f/\partial\alpha = 0$ |
| Maximum energy | $E = E_{max}$ at $L_{max}$ | $f = 0$ |
| Minimum energy | $E = E_{min}$ at $L_{max}$ | From satellite data |
| Minimum $L^*$ | $L = L_{min}$ | From satellite data |
| Maximum $L^*$ | $L = L_{max}$ | From satellite data |

Table 2.2: Boundary conditions used in the BAS-RBM.

### Initial Condition

The initial condition specifies the phase space density for the ($\alpha$-$E$) grid for all values of $L^*$ at the beginning of the simulation period. In this study, the initial condition is either derived directly from the CRRES or the Van Allen probes data around the beginning of the simulation period. The phase space density is thereby provided for the ($\alpha$-$E$) grid for all values of $L^*$ by the user, and the BAS-RBM derives the corresponding initial values for the ($\mu$-$J$) grid.

The distribution of the phase space density in the initial condition usually does not satisfy the Fokker-Planck diffusion equation. During the first few timesteps, the electron distribution will therefore adjust in such a way that it will fulfil the diffusion equation. The resulting flux thereby strongly depends on the utilised diffusion coefficients, meaning that even small differences of the diffusion rates can result in significantly different electron fluxes after this period, which is from now on referred to as the "adjustment period".

### Solution Procedure

The Fokker-Planck Equation is solved in three steps using an operator splitting technique [*Strang*, 1968]. The first two steps are to model the pitch-angle and energy diffusion terms, and are hence performed on the ($\alpha$-$E$) grid for each value of $L^*$. In the third step the radial diffusion is modelled and it is therefore performed on the ($\mu$-$J$) grid. The equations are solved using an unconditionally stable implicit finite difference scheme and the solutions are interpolated onto the ($\mu$-$J$) grid using a cubic spline interpolation technique. For the next timestep, the order of the steps is reversed, i.e. the radial diffusion equation is solved first on the ($\mu$-$J$) grid and the solutions are then interpolated onto the ($\alpha$-$E$) grid, where first the energy diffusion is calculated and lastly the pitch-angle diffusion.

# CHAPTER 3
# *Plasma Waves - A Review*

## 3.1 Introduction

One of the most important processes for the variability of the outer electron belt is the electron acceleration and loss caused by wave-particle interactions between electrons and plasma waves. There are many different plasma waves, characterised by their properties including the frequency range, their location in space relative to the plasmapause, and their polarisation. For instance, there are the ultra low frequency (ULF) waves, which drive radial diffusion, as explained in detail in Section 2.3.1. Furthermore, there are left-hand and right-hand polarised waves above the plasma frequency $\omega_{pe}$, which are known as Z-mode, L-O-mode, and R-X-mode waves, as well as the so-called magnetosonic waves, which are a natural, often intense electromagnetic emission observed at frequencies between the lower hybrid frequency and the proton cyclotron frequency. They are observed at radial distances between $L = 2$ and 8 and are mostly confined to the equatorial region [*Meredith et al.*, 2008]. Magnetosonic waves may lead to local acceleration, and may particularly energise electrons with energies between 10 keV up to a few MeV in the outer radiation belt [*Horne et al.*, 2007]. They are thought to be generated by proton ring distributions at energies of about 10 keV [*Boardsen et al.*, 1992] and can propagate both inside and outside the plasmapause [*Meredith et al.*, 2008; *Ma et al.*, 2013].

So far, little work has been done on diffusion caused by either Z-mode, L-O-mode, and R-X-mode, or magnetosonic waves and they are not routinely included in 3d models, such as the `BAS-RBM`. Of greater interest are the right-hand polarised whistler mode chorus waves, and plasmaspheric hiss, as well as the Electromagnetic Ion Cyclotron (EMIC) waves. Since these waves are well studied and they are known to interact with radiation belt electrons, this thesis focuses on building reliable wave models for these waves. In the following sections an overview of the published research on these waves is presented. As an example, a typical spectrogram showing the wave spectral intensity

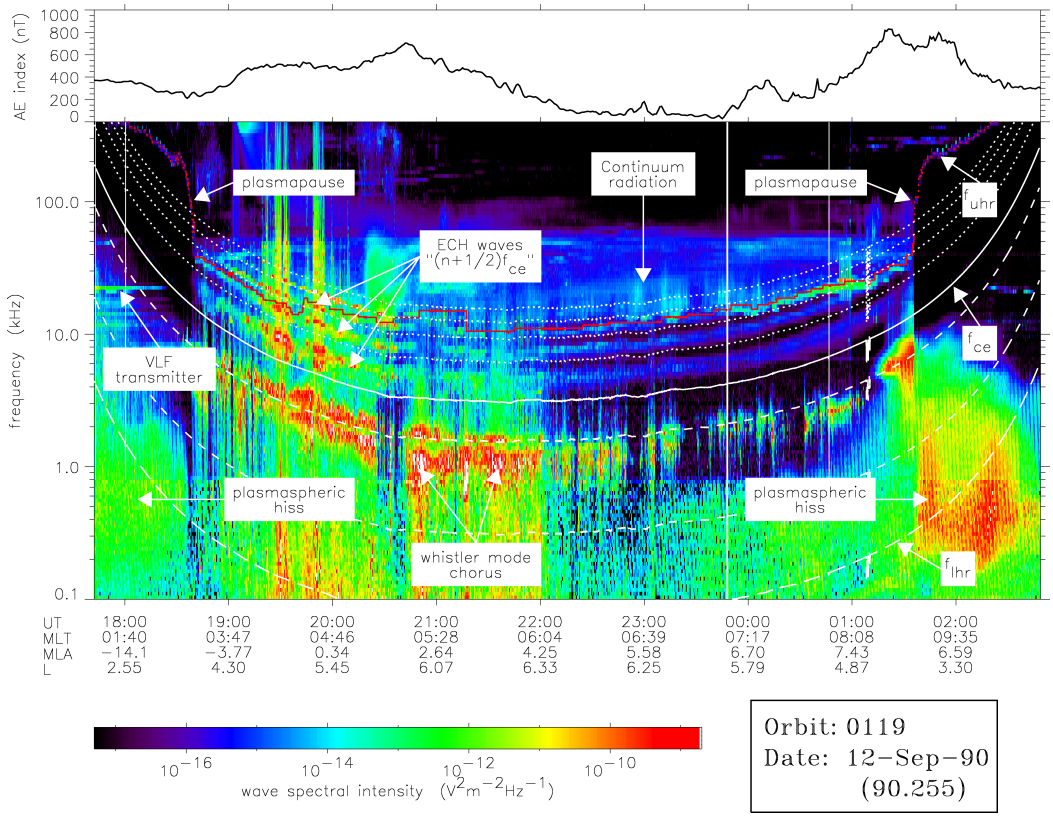


Figure 3.1: Spectrogram of the wave spectral intensity measured by the CRRES satellite on orbit 119. The solid white line denotes the local electron cyclotron frequency, while the dashed and dotted lines are relevant multiples of it. The plasmapause is indicated by the red line, and the *AE* index is given in the top panel. Taken from [*Meredith et al.*, 2004]

of common plasma waves observed by the CRRES satellite is shown in Figure 3.1. The improvements made within this thesis to the various wave models and their impact on the global electron acceleration and loss rates are presented for each type of plasma wave in the following chapters. They are ordered chronologically to reflect the progress that was made during the research for this thesis.

## 3.2 Whistler Mode Chorus Waves

Whistler mode chorus waves are short bursts of electromagnetic waves below the electron cyclotron frequency. They can be observed outside the plasmapause with frequencies ranging from a few hundred Hertz up to a few kHz. The short bursts rise or fall rapidly in frequency [*Burtis and Helliwell*, 1969; *Tsurutani and Smith*, 1974; *Tsurutani*

*et al.*, 2013] and last for a few milliseconds, often overlapping and occurring for periods of many hours [*Santolík et al.*, 2003].

Chorus waves usually show a clear separation into two frequency bands below and above half of the electron cyclotron frequency [*Tsurutani and Smith*, 1974]. The so-called lower band chorus is hence defined to lie in the frequency range of $0.1 < f_{ce} < 0.5$, while the upper band chorus lies in the frequency range of $0.5 < f_{ce} < 1.0$, with a gap between about $0.4\, f_{ce}$ and $0.55\, f_{ce}$. During geomagnetically active conditions chorus waves tend to be most significant on the dawn-side, but can be found over a wide range of MLT ranging from about $22 - 12$ MLT [*Meredith et al.*, 2001, 2012; *Li et al.*, 2011], and observations have shown that they are strongest during substorms [*Meredith et al.*, 2001]. The average wave amplitude of lower band chorus emissions were found to be about 100 pT, while the wave amplitude of upper band chorus is about 20 pT [*Horne et al.*, 2013b]. The amplitude of chorus waves typically takes about 5 h to decay after a substorm [*Meredith et al.*, 2000].

There were several theories proposed to explain the origin of chorus waves. It is generally believed that chorus waves are generated by linear wave growth due to a temperature anisotropy formed by plasma that is injected towards the Earth during geomagnetic substorms [e.g. *Trakhtengerts*, 1999; *Nunn et al.*, 1997; *Omura et al.*, 2007, 2009]. According to nonlinear theory these waves cause electrons to be phase trapped, which can then act as a resonant current, allowing the propagating waves to re-radiate the electrons with a nonlinear growth rate at a different frequency giving rise to chorus waves [*Nunn*, 1974; *Omura et al.*, 1991, 2009; *Katoh and Omura*, 2007]. *Katoh and Omura* [2007] used a self-consistent particle simulation with a dipole magnetic field model to show that chorus waves are discrete whistler mode emissions generated close to the equator by cyclotron resonant interactions with suprathermal electrons, which are injected into the inner magnetosphere during (sub)storms.

Ray tracing methods predict that whistler mode waves are field aligned near the equator and become oblique with latitude due to refraction [*Horne and Thorne*, 2003]. The earliest wave normal angle observations of lower band chorus waves support these simulations, as they have shown that the waves were field aligned within a cone of 20° near

the equator and became more oblique towards higher latitudes [*Burton and Holzer*, 1974; *Hayakawa et al.*, 1984; *Goldstein and Tsurutani*, 1984]. There are however several case events where the wave normal angle was found to be between $30° - 45°$ close to the resonance cone [*Hayakawa et al.*, 1984]. Furthermore, *Lauben et al.* [2002] showed that the wave normal angle can vary significantly between $5° - 50°$over a short period of 0.5 s near $L = 3.7$. More recent studies of the Cluster spacecraft data have found that chorus waves near $L = 4.5$ were quasi field aligned within 5° of the equator and became more oblique towards higher latitudes [*Santolík et al.*, 2003]. A recent more systematic analysis of the Cluster data showed that the wave normal angle is of Gaussian shape and field aligned, while the width of the wave normal angle was measured to lie between 10° and 20° [*Santolík et al.*, 2014b]. However, other studies of the Cluster data found that the wave normal angle of lower band chorus shows two peaks near 20° and 50°, while the upper band chorus peaks near 30° [*Breneman et al.*, 2009] and a statistical analysis showed that the wave normal angle can lie between $0° - 30°$. Lower band chorus wave normal angle measurements from the Cluster spacecraft evaluated by *Agapitov et al.* [2013] show that $\psi = 0°$ - 10° for $|\lambda_m| < 5°$, which slightly increases for latitudes up to $|\lambda_m| = 15°$, although the distribution of the wave normals extend up to about $\psi = 30°$. The distribution tends to be peaked in the field aligned direction. These results agree with a statistical analysis of THEMIS data [*Li et al.*, 2011]. Overall, there seems to be no consensus on the wave normal angle distribution yet, with measurements showing field aligned propagation over a wide range of latitudes, while others show that chorus waves become more oblique at higher latitudes.

Chorus waves are thought to be a major source of electron acceleration and loss due to wave-particle interactions [*Horne et al.*, 2005a,b]. They are able to resonate with electrons through Doppler-shifted cyclotron resonance over a wide range of energies from a few hundred eV up to a few MeV [*Horne and Thorne*, 2003]. They are known to cause pitch-angle diffusion and thereby scatter electrons into the loss cone, and due to their bursty nature it is believed that they are a dominant reason for electron precipitation observed by satellites and balloons at low altitudes [*Rosenberg et al.*, 1971; *Imhof et al.*, 1992; *Tsurutani et al.*, 2013]. The pitch-angle scattering is believed to be a major rea-

son for both the diffuse and the pulsating aurora [*Thorne et al.*, 2010; *Nishimura et al.*, 2010]. Furthermore, chorus waves are known to cause substantial energy diffusion as well as acceleration of trapped electrons [*Horne and Thorne*, 1998; *Summers et al.*, 1998; *Horne et al.*, 2005a,b], especially in regions with a low plasma density [*Horne et al.*, 2003b; *Meredith et al.*, 2002]. Since chorus waves can cause electron acceleration inside geostationary orbit it was suggested that they play a major role in the formation of the outer radiation belt [*Horne et al.*, 2007]. Moreover, chorus waves are thought to be a significant process for the built-up of the radiation belts in general during the recovery phase of geomagnetic storms [*Horne et al.*, 2005a, 2006].

Various efforts to model the diffusion rates caused by chorus waves were made over the last decade. For example, *Horne et al.* [2003b] used the average observed properties of chorus emissions [*Tsurutani and Smith*, 1974] to create a fixed Gaussian chorus model. This model was used to test the effects of chorus waves at various energies during different plasma densities. *Shprits et al.* [2007] developed a chorus model that is parametrised for geomagnetic activity based on CRRES data. The model was initially only valid between $6-15$ MLT, but eventually extended to a day- and nightside model, parametrised for latitude and activity as well. *Horne et al.* [2005a] calculated electron diffusion rates based on their fixed chorus model for three MLT sectors, where the wave power was taken from CRRES measurements. Full MLT dependence with a 1 h MLT resolution and 3 levels of geomagnetic activity within latitudes up to 15°was introduced by *Varotsou et al.* [2005], also based on the CRRES high-energy electron data. They also introduced an activity dependent model for the plasma density, interpolating between 5 levels of $f_{pe}/f_{ce}$ between $1 < f_{pe}/f_{ce} < 10$. This study was extended to higher latitudes up to 30° by *Albert et al.* [2009].

## 3.3 EMIC Waves

Wave-particle interactions with electromagnetic waves with a frequency of typically a few Hertz, known as **E**lectro**m**agnetic **I**on **C**yclotron (EMIC) waves, are thought to be a significant process for electron loss [*Horne and Thorne*, 1998]. Since their frequency

is much lower than the electron cyclotron frequency, the frequency of the EMIC waves needs to be Doppler-shifted to the electron cyclotron frequency by the relative motion of the waves and electrons along a field line. This allows the EMIC waves to resonate with high energy electrons at energies greater than about 500 keV [*Meredith et al.*, 2003a], causing losses of the electrons into the loss cone due to pitch-angle scattering. *Cornwall et al.* [1970] suggested the temperature anisotropy in the energetic proton distribution of ring current ions with energies between a few tens of keV to 100 keV as a source of EMIC waves close to equator. EMIC waves occur in short bursts and tend to be observed only in a fraction of any given observation period [e.g. *Posch et al.*, 2010; *Turner et al.*, 2014a].

EMIC waves are typically separated by their frequency relative to the hydrogen, helium, and oxygen ion cyclotron frequency. *Hydrogen band EMIC waves* are electromagnetic waves with a frequency between the hydrogen ion (or proton) cyclotron frequency $f_{cp}$ and the helium ion cyclotron frequency $f_{cHe}$, *Helium band EMIC waves* are waves with a frequency between $f_{cHe}$ and the oxygen ion cyclotron frequency $f_{cO}$, while *Oxygen band EMIC waves* are waves with a frequency below $f_{cO}$. Hydrogen band EMIC waves are typically observed outside the plasmapause, while helium band EMIC waves can be found both inside and outside the plasmapause [*Fraser and Nguyen*, 2001]. Oxygen band EMIC waves occur very rarely and are difficult to detect against a noisy background.

Previous studies of EMIC waves have observed them over a wide range of L-shells, ranging from about $L = 3$ up to $L = 10$, while their percentage occurrence increases towards larger L shells [e.g. *Anderson et al.*, 1992a; *Usanova et al.*, 2012]. They were found to be strongest in the afternoon sector from about $12 - 16$ MLT [*Bossen et al.*, 1976; *Roux et al.*, 1982; *Meredith et al.*, 2014]. The percentage occurrence of hydrogen band waves tends to be higher than the percentage occurrence of helium band EMIC waves, with hydrogen band EMIC waves occurring about 10 % of the time in the region of $L = 7 - 9$ [*Keika et al.*, 2013], while helium band EMIC waves tend to occur about $5 - 10$ % of the time between $L = 4$ and 7 [*Keika et al.*, 2013].

*Summers and Thorne* [2003] have shown that EMIC waves are able to cause strong

pitch-angle scattering for wave amplitudes of about 1 nT and more. They are hence very effective at diffusing electrons into the loss cone at energies greater than about $1-2$ MeV [*Albert*, 2003; *Summers and Thorne*, 2003], which suggests that they may be a significant contribution to the decay of the radiation belts [*Horne and Thorne*, 1998]. The minimum energy at which EMIC waves can resonate with electrons strongly depends on the parameters used to simulate the EMIC waves. In particular, the upper cut-off frequency seems to be a vital parameter determining the scattering caused by EMIC waves [*Li et al.*, 2014]. Furthermore, *Ukhorskiy et al.* [2010] showed that individual events with peak frequencies close to the helium ion cyclotron frequency were able to scatter electrons of energies less than 2 MeV into the loss cone. This suggests that rather than just the upper cut-off frequency, the relation between the peak frequency and the upper cut-off frequency is critical for the effectiveness of EMIC waves.
EMIC waves were shown to only affect electrons with small pitch-angles lower than about 60°, which means the that the bulk of the electron distribution will be unaffected by EMIC waves [*Kersten et al.*, 2014; *Usanova et al.*, 2014]. Nevertheless, flux dropout events were measured during periods of high EMIC wave occurrence, where the electron flux was significantly reduced even for electrons with an equatorial pitch-angle of 90° [e.g. *Turner et al.*, 2014a,b]. One suggested mechanism for these results is that EMIC waves could indirectly increase the losses for all pitch-angles by creating large gradients in the pitch-angle distribution and thereby facilitating losses caused by other waves present, namely chorus and hiss, [*Li et al.*, 2007] and [*Albert and Shprits*, 2009].

## 3.4 Plasmaspheric Hiss

Plasmaspheric hiss is a broadband and structureless electromagnetic emission usually observed in the frequency range between a few tens of Hz and several kHz. Hiss waves are observed inside the plasmasphere and the strongest emissions have a wave power peaked at the order of 2000 $pT^2$ at a peak frequency near a few hundred Hz. Up until recently, it was believed that plasmaspheric hiss was limited to the frequencies above 100 Hz with a peak frequency near a few kHz. However, using recent data from the

Van Allen Probes, it was found that the peak of plasmaspheric hiss is usually found at lower frequencies of about a few hundred Hz and that hiss waves extend to lower frequencies of about 20 Hz [*Li et al.*, 2015]. The comparison between Gaussian wave profiles peaked at 550 Hz and the measured wave peaks at a few hundred Hz showed an energy and L-shell dependent change of the diffusion rates. For instance, at $L = 3$ the pitch-angle diffusion coefficients increased by a factor of about 5 for energies at tens of keV, and a factor of about 2 for energies between $0.3 - 1$ MeV, while the diffusion rates decreased by a factor of about 3 for energies between 70 and 200 keV. Including the wave power at frequencies below 100 Hz changed the diffusion rates by up to a factor of about 1.5 at $L = 5$, but only insignificantly at $L \leq 3$.

There have been a number of different theories to explain the origin of plasmaspheric hiss. Up until recently the two leading theories were in situ growth of wave turbulences in space [*Thorne et al.*, 1973] and lightning-generated whistlers [*Sonwalkar and Inan*, 1989] as a source of hiss. However, the former theory was unable to achieve the observed power levels [*Church and Thorne*, 1983] and the latter was unable to explain the lack of a correlation between landmass, where most of the lightning storms happen, and measurements of plasmaspheric hiss below 2 kHz [*Meredith et al.*, 2006a]. Recently it was shown by *Bortnik et al.* [2008] using ray tracing modelling that plasmaspheric hiss could originate from bursts of short duration chorus waves that were excited outside the plasmapause and travelled into the plasmasphere, where they got trapped inside the high density plasma. This new theory was able to reproduce most of the observed characteristics of plasmaspheric hiss, including the observed frequency band and the day-night asymmetry of the intensity of hiss, but it underestimated the typical plasmaspheric hiss wave power by $10 - 20$ dB [*Chen et al.*, 2012a]. This problem was resolved by *Chen et al.* [2012b], when they included cyclotron resonance wave growth inside the plasmapause in the model. Further support for this theory has been gained by recent observational studies that show a strong correlation between the amplitude modulation of chorus waves and plasmaspheric hiss as measured by the two THEMIS spacecraft [*Bortnik et al.*, 2009] and the Cluster mission [*Wang et al.*, 2011]. Furthermore, the Polar spacecraft has observed downward propagating chorus and upward propagating

hiss on the dayside, supporting the model. Also, there is statistical evidence that chorus extends to high latitudes in the pre-noon sector and that there is a clear gap of about 1-2 Earth radii between chorus and hiss near the equator [*Meredith et al.*, 2013], which is predicted by the ray tracing model.

*Meredith et al.* [2004] presented the global distribution of plasmaspheric hiss, which was derived from a detailed study of the CRRES satellite data. They found that hiss has a strong day-night asymmetry, with hiss being the strongest between noon and dusk and overall increasing with magnetic activity. Unfortunately their study was not able to present a complete global map of hiss, since CRRES had limited coverage on the dayside. Since the code used to calculate the diffusion rates utilises the wave power of the magnetic field and CRRES only measured the electric field component, they needed to convert the wave power of the electric field to the wave power of the magnetic field. For this E to B conversion they assumed a parallel wave propagation. The wave normal angle of plasmaspheric hiss has been studied by *Agapitov et al.* [2013] using measurements from the Cluster mission. They found that near the equator plasmaspheric hiss is nearly field aligned, with a wave normal angle peaked near 10°. With increasing latitude the wave normal angle increases roughly linearly with the waves becoming electrostatic at a latitude of about 45°. This poses a conceptional problem for the hiss wave power calculated by *Meredith et al.* [2004] at higher latitudes, since the E to B conversion assumes parallel wave propagation and hence that hiss is electromagnetic. As a result, it is likely that the hiss wave power was overestimated due to the E to B conversion.

Inside the plasmapause, plasmaspheric hiss acts as an important loss process, since the formation of the slot region between the inner and the outer radiation belt is mainly due to resonant pitch angle scattering of energetic electrons with plasmaspheric hiss [*Lyons and Thorne*, 1973; *Meredith et al.*, 2007, 2009]. Furthermore, resonant wave-particle interactions with plasmaspheric hiss contribute to electron loss in the outer radiation belt [*Summers et al.*, 2007; *Meredith et al.*, 2006b].

A first analysis of the role of plasmaspheric hiss in diffusion was demonstrated by *Lyons et al.* [1972]. This work was then extended to show the contribution of hiss to pitch-

angle diffusion, assuming constant and field aligned waves [*Abel and Thorne*, 1998]. Since various studies found that plasmaspheric hiss propagates with a wide range of wave normal angles, starting mainly parallel near the geomagnetic equator and shifting towards highly oblique wave normal angles at higher latitudes [*Parrot and Lefeuvre*, 1986; *Hayakawa et al.*, 1986; *Santolík et al.*, 2001; *Agapitov et al.*, 2013], *Meredith et al.* [2006a, 2007] studied the effects of the wave-normal angle on the diffusion rates using different models for the wave-normal angle. They showed that only waves with a small or medium wave-normal angle were causing a significant effect on the diffusion rates. They furthermore used a 3 component Gaussian fit to model the wave power of the hiss. So far, most of the recent calculations of the diffusion caused by plasmaspheric hiss either assumed purely field aligned waves [*Summers et al.*, 2007, 2008] or a wave-normal angle and wave power which were independent of the radial distance towards the Earth [*Subbotin and Shprits*, 2009]. Recently, *Glauert et al.* [2014] calculated new diffusion rates based on *Meredith et al.* [2007], but with a variable wave-normal angle that depended on the latitude. They also used a MLT dependent wave power, but still based on the 3 component fitted wave power spectra. They found that plasmaspheric hiss is crucial to reduce the peak flux of simulations in order to achieve better agreement with the data, in particular in the slot region and the inner edge of the outer radiation belt. Furthermore, they showed that the wave-normal angle distribution is a critical parameter and best results were achieved for wave-normal angles varying with latitude.

# CHAPTER 4

# *Whistler Mode Chorus Waves*

## 4.1 Introduction

One of the main objectives of this thesis is to assess the importance of wave-particle interactions on radiation belt dynamics. As discussed in the previous chapter, whistler mode chorus waves are one of the most important waves, known to cause both electron acceleration and loss. The focus of this chapter is to develop a novel statistical model for chorus waves in order to calculate pitch-angle and energy diffusion rates and to include them into the `BAS-RBM` to assess the effects of chorus on a global scale.

Previous models were mostly based on the data from a single satellite, and therefore have limited data coverage. The models presented here are based on a statistical analysis of the data from 7 different satellites, considerably improving the coverage and resolution of existing wave models. The initial focus of this work was to develop a technique to fit the wave spectral data in order to obtain the wave parameters, required by the `PADIE` diffusion code, which is used to calculate the diffusion rates. During the course of the work, a separate new technique was developed that allowed to use the wave spectral data directly, without requiring the fitting of wave parameters. As a consequence, wave power at frequencies below $0.1\, f_{ce}$, that had to be excluded in the fitting process, could then be included into the chorus wave model.

In the following, the different techniques are presented and evaluated. The corresponding wave models are then used to calculate drift and bounce averaged pitch-angle and energy diffusion rates. These diffusion rates are compared against each other and their effect is studied on a global scale by employing them into the `BAS-RBM` individually. Part of this work was published in [*Horne et al.*, 2013b].

## 4.2 Whistler Mode Wave Database

### 4.2.1 Instrumentation and Data Analysis

The wave data that was used to derive a statistical model for the chorus waves presented here was obtained from seven different satellites, namely the Combined Release and Radiation Effects Satellite (CRRES), Dynamics Explorer 1 (DE 1), Cluster 1, Double Star TC1, and Time History of Events and Macroscale Interactions during Substorms (THEMIS A, D, and E). A full description of the processing of the data from various instruments that were incorporated into the wave model is presented in *Meredith et al.* [2012]. A summary of the spatial coverage, the frequency ranges of the measured plasma waves, as well as the period from which the data was used, are given in the following paragraphs and in Table 4.1.

CRRES was launched into a highly elliptical, geosynchronous transfer orbit with a low inclination. It covered the range of $L^*$ from about 1.1 up to $L^* = 6$ near the equator and $L^* = 8$ at high latitudes [*Meredith et al.*, 2001]. The magnetic local times (MLT) were covered from 14 - 08 MLT, leaving a gap of coverage between 08 - 14 MLT for latitudes up to 30°. The wave data was derived from the Plasma Wave Experiment (PWE), which ran from 20 August 1990 to 11 October 1991, when the satellite failed. Reliable measurements were only available for the electric field components and therefore a conversion of the wave electric field spectral intensity to the magnetic field spectral intensity was performed assuming field aligned propagation of the waves and the appropriate electron density as shown in *Meredith et al.* [2003b].

The Plasma Wave Instrument (PWI) on board the NASA Dynamics Explorer 1 (DE1) spacecraft measured one component of the magnetic field and two components of the electric field. It was launched into a high altitude elliptical polar orbit, enabling it to cover latitudes from the equator up to about $\lambda_m = 60°$. Thereby, waves were sampled in the range of $L^*$ from about 1.5 up to about $L^* = 9$ at the highest latitudes. The MLT coverage of DE1 shows a gap at the dusk side for $L^* < 4$ and $\lambda_m < 30°$, while all MLT are covered at larger latitudes. The complete PWI dataset between September 1981 and June 1984 was incorporated into the wave database.

Cluster 1 is one of the four spacecraft of the ESA Cluster mission and it was launched

into a highly elliptical polar orbit, generally covering the range of $L$ = 1.5 - 9.0 and $0° < \lambda_m < 60°$ for all MLT. However, coverage at high geomagnetic activity is limited. There were three instruments on board Cluster 1, whose data were incorporated into the wave database covering the period from 1 January 2001 to 31 December 2010. The Spatiotemporal Analysis of Field Fluctuations (STAFF), which provided three dimensional measurements of the wave magnetic field, was combined with the two electric field components measured by the Electric Fields and Waves (EFW) experiment. From this dataset, the sum of the three orthogonal components of the magnetic power spectral densities were incorporated into the wave database. The third instrument was the WHISPER instrument, which provided measurements of the wave electric field spectral intensities, which were converted into magnetic field spectral intensities.

The Double Star TC1 spacecraft is a joint ESA and China National Space Administration mission and it was launched into a highly elliptical equatorial orbit, covering magnetic latitudes up to about 45°, for $L$ = 1.1 to about 7.0. The coverage is evenly distributed along magnetic local times, but there is slightly less data on the night side inside the plasmapause. The data taken from the STAFF experiment between 5 January 2004 and 31 December 2004 were incorporated into the wave database.

The five NASA THEMIS spacecraft were launched into near-equatorial orbits with high apogees and low perigees. On THEMIS A, D, and E whistler mode waves were sampled by the Search Coil Magnetometer (SCM) in the range of 5-10 Earth radii. Thereby, geomagnetic latitudes from the equator up to about 15° were sampled for $L$ = 1.1 to about 10.0 on the night side and 8.0 on the day side. The SCM data collected between 1 May 2010 and 1 October 2010 were incorporated into the wave database.

As the data of each satellite is provided in different frequency bands, which only partly overlap, the data needed to be combined to form a joint whistler mode wave database. As a first step, the wave magnetic field data of each satellite was integrated within its corresponding frequency bands to obtain the wave intensity $\mathrm{pT}^2$ (also known as the wave power $B_w^2$). Since the CRRES data only contained the wave electric field measurements, these were converted into wave magnetic field data by assuming field aligned propagation of the waves and the appropriate electron density as shown in [*Meredith*

*et al.*, 2003b]. An analysis of the wave database has shown that there may be enhancement of the wave power due to the E-to-B-conversion for wave normal angles greater than about 50° and at higher latitudes. Since chorus waves are believed to be field aligned near the equator but become more oblique towards higher latitudes, the E-to-B-conversion might introduce an error at larger latitudes. As CRRES measurements were taken only up to about 30° in magnetic latitude, where the wave normal angle of chorus waves is still rather small, the error introduced by the E-to-B-conversion is expected to be negligible.

| Satellite | Perigee [km] | Apogee [km] | Inc. [deg] | Used period | Instrument | Frequency range |
|---|---|---|---|---|---|---|
| CRRES | 350 | 33,584 | 18.1 | Aug/1990 - Oct/1991 | PWE | 100 Hz - 400 kHz |
| DE1 | 568 | 23,289 | 89.9 | Sep/1981 - Jun/1984 | PWI | 1.78 Hz - 410 kHz |
| Cluster 1 | 17,200 | 120,500 | 90.7 | Jan/2001 - Dec/2010 | STAFF | 8 Hz - 4 kHz |
| Cluster 1 | 17,200 | 120,500 | 90.7 | Jan/2001 - Jun/2010 | WHISPER | 2 kHz - 80 kHz |
| TC1 | 562 | 78,970 | 28.2 | Jan/2004 - Dec/2004 | STAFF | 8 Hz - 4 kHz |
| THEMIS | 470 | 87,330 | 16.0 | May/2010 - Oct/2011 | SCM | 0.1 Hz - 4 kHz |

Table 4.1: Summary of the satellite's initial orbits and the instrument whose data was incorporated into the SPACECAST whistler mode wave database, as well as the frequency range and the time period covered.

### 4.2.2 Chorus Wave Database

In order to create a unified chorus wave database, the data was first quality controlled to remove false data and then reorganised into 11 frequency bands in terms of the local electron cyclotron frequency $f_{ce}$. The bands range from 0.0117 $f_{ce}$ - 1.0 $f_{ce}$ and are given in Table 4.2. Usually chorus appears in two frequency bands with a gap near 0.5 $f_{ce}$, which is why it is common to separate chorus into lower band chorus with a frequency below 0.5 $f_{ce}$ and upper band chorus with a frequency above 0.5 $f_{ce}$. The integrated wave intensity in $pT^2$ for each frequency band was stored together with the satellite's position in magnetic coordinates, given by the magnetic latitude $\lambda_m$, magnetic local time (MLT), and the Roederer $L^*$ parameter, as well as the geomagnetic activity defined by the $AE$ index at the corresponding time of each measurement.

| Lower Band Chorus | Upper Band Chorus |
|---|---|
| $0.0117 - 0.02333$ | $0.5 - 0.6$ |
| $0.02333 - 0.1$ | $0.6 - 0.7$ |
| $0.1 - 0.2$ | $0.7 - 0.8$ |
| $0.2 - 0.3$ | $0.8 - 0.9$ |
| $0.3 - 0.4$ | $0.9 - 1.0$ |
| $0.4 - 0.5$ | |

Table 4.2: Frequency bands used in the chorus wave database given relative to local electron cyclotron frequency $f_{ce}$.

### 4.2.3 Separating Chorus from Hiss

In the frequency range covered by the whistler mode wave database presented above two types of waves are present, namely whistler mode chorus and plasmaspheric hiss. However, chorus is expected to be found only outside the plasmapause, while hiss is mainly found inside the plasmapause. Therefore, in order to distinguish between chorus and hiss, a reliable definition of the plasmapause location is required. For the data measured by the CRRES satellite, the ECH criterion can be used [*Meredith et al.*, 2004]. This criterion uses the fact that Electron Cyclotron Harmonic (ECH) waves with a frequency between 1.0 $f_{ce}$ and 2.0 $f_{ce}$ are only observed outside the plasmapause. If ECH waves were measured by the CRRES satellite with an electric field amplitude greater than $0.5\,\mu\mathrm{Vm}^{-1}$ the satellite was assumed to be outside the plasmapause. For the data measured by THEMIS the plasmapause was defined by *Li et al.* [2010] as the location where the total electron density $N_c = 5 \cdot 10^7\,\mathrm{m}^{-3}$ for $L^* > 4.4$ and $N_c = 10 \cdot (6.6/L^*)^4$ for $L^* < 4.4$. For Dynamics Explorer 1 (DE 1), Cluster 1, Double Star TC1 no direct or indirect measurements of the plasmapause were provided and hence the plasmapause model by *Carpenter and Anderson* [1992] was used to define the plasmapause.

Since the methods to define the plasmapause for the CRRES and THEMIS satellites are directly linked to data measured on the corresponding spacecraft, they allow the determination of the plasmapause position for every individual measurement, and hence they are likely to provide accurate results. In contrast, the Carpenter & Anderson plasmapause model used for DE 1, Cluster 1, and Double Star TC1 is only parametrised by the maximum geomagnetic activity in the preceding 24 hours and does not include any MLT resolution. Therefore, it only allows the separation of chorus and hiss in an

average sense and it is likely that contributions of hiss can be falsely identified as chorus, if the plasmapause location changed considerably within the preceding 24 hours.
The data processed in this way forms the chorus wave database, which is part of the SPACECAST whistler mode wave database, stored at the BAS Polar Data Centre.

## 4.3 Chorus Wave Models

Based on the chorus database, statistical models for lower and upper band chorus were developed. In order to have sufficient data for a statistical model, the chorus wave data was separated into 18 equally spaced $L^*$ bins ranging from $L^* = 1.5 - 10.0$ with a width of $\Delta L^* = 0.5$. They were further separated into 10 bins of magnetic latitude in the range of $0^\circ \leq |\lambda_m| \leq 60^\circ$, each $6^\circ$ wide, into 8 bins of MLT, each 3 h wide, and into five levels of geomagnetic activity in terms of $AE$, where $AE < 50$ nT, $50 \leq AE < 100$ nT, $100 \leq AE < 200$ nT, $200 \leq AE < 400$ nT, and $AE \geq 400$ nT.

### 4.3.1 Fitted Chorus Wave Model

#### Fitting Method

As described in chapter 2, the initial version of the `PADIE` diffusion code required the power spectral density (PSD) $B^2(f)$ in $\mathrm{pT}^2/Hz$ of the wave magnetic field to be provided in order to calculate the diffusion rates. $B^2(f)$ has to be provided in Gaussian form given by (see section 2.2):

$$B^2(f) = A_f^2 \cdot \exp\left[-\left(\frac{f - f_m}{\delta f}\right)^2\right] \tag{4.1}$$

where $A$ is a normalisation constant (or the peak intensity of the PSD) given by

$$A_f^2 = \frac{|B_w|^2}{\delta f} \cdot \frac{2}{\sqrt{\pi}} \cdot \left[\mathrm{erf}\left(\frac{f_m - f_{lc}}{\delta f}\right) + \mathrm{erf}\left(\frac{f_{uc} - f_m}{\delta f}\right)\right]^{-1} \tag{4.2}$$

or rearranged for $B_w^2$

$$|B_w|^2 = \frac{1}{2} \cdot \delta f \cdot \sqrt{\pi} \cdot A_f^2 \cdot \left[\mathrm{erf}\left(\frac{f_m - f_{lc}}{\delta f}\right) + \mathrm{erf}\left(\frac{f_{uc} - f_m}{\delta f}\right)\right] \tag{4.3}$$

Here, $B_w$ is the wave amplitude in Tesla, while $f_m$ is the peak frequency, and $\delta f$ is the frequency width of the power spectral density. Furthermore, the lower and upper cut-off frequencies $f_{lc}$ and $f_{uc}$, outside which the wave power is set to zero, need to be specified. In order to obtain the peak intensity $A$, peak frequency, and frequency width of the power spectral density, a Gaussian profile was fitted to the average spectral intensity data inside each $L^*$, MLT, $\lambda_m$, and $AE$ bin (as specified above) for lower and upper band chorus individually. This was performed using the nonlinear least squares fitting procedure called `MPFIT` [*Markwardt*, 2009], which proved to be the most robust of various methods that were tested.

In order to improve the quality of the fits, noisy data had to be removed before performing the fit. The dataset proved to be already well corrected for most of the obvious outlying data, but still some sharp peaks remained and fitting these would result in undesired results. A second challenge was to filter out the noisy background. Setting a general threshold for the power spectral density would exclude potential wave power that is caused by a very wide but flat power spectral density profile, which is also undesired. In order to overcome these two problems, a threshold for the wave amplitude $B_w$ integrated over the whole lower (or upper) chorus frequency band was set for the lower band (and upper) band chorus individually, since the diffusion rates are proportional to $B_w^2$. The measured wave amplitudes of chorus waves vary up to about 100 pT for lower band chorus and about 20 pT for upper band chorus and hence, in order to capture the significant wave power, the threshold value was set to $B_w > 0.1$ pT, above which fits were performed. The fitting was performed for each individual spectral profile in every $L^*$, MLT, $\lambda_m$, and $AE$ bin by performing five nonlinear least squares fits using five different step sizes for the numerical derivatives. As initial parameters for the fitting function, the peak intensity was set to the highest intensity inside the spectral profile, the peak frequency was set to the frequency corresponding to the peak intensity, and the frequency width was set to $\delta f = 0.1\, f_{ce}$. The quality of each of the five fits was quantified using the Pearson $\chi^2$ parameter, where a value closer to zero indicates a better fit. Hence, for each case the fit with the lowest value of $\chi^2$ was selected as the final fit to the corresponding spectral profile.

The individual evaluation of the fits showed that in general better fits were achieved when the spectral data was distributed in a Gaussian shape. Nevertheless many cases were found, where there appeared to be two peaks within each spectral profile at lower latitudes. For lower band chorus this second peak was found to lie below $0.1\,f_{ce}$, while for upper band chorus the second peak lay above $0.9\,f_{ce}$. Depending on the individual intensity of the two peaks, the fitting routine was fitting the second peak, if its intensity was larger.

In the case of lower band chorus fitting the second peak below $0.1\,f_{ce}$ instead of the peak above $0.1\,f_{ce}$, often resulted in a very narrow Gaussian spectrum, where most of the wave power was present at the lowest frequencies and most of the wave power above $0.1\,f_{ce}$ was not captured by the fit, especially when the spectral intensity was very large at the two lowest frequencies compared to frequencies above $0.1\,f_{ce}$. Since two peaks were mainly found at lower latitudes it is unlikely that the measured wave power is due to chorus waves. Therefore, it is undesirable to use these fits, as it would correspond to large electron diffusion at higher energies that is not caused by chorus waves. At low $L^*$ this spectral intensity is most likely to be associated with plasmaspheric hiss or, close to the equator, magnetosonic waves, while at larger $L^*$ strong chorus is generally not expected below $0.1\,f_{ce}$. However, at latitudes greater than about 30° wave power below $0.1\,f_{ce}$ can be associated with chorus, since chorus waves are usually generated near to the equator. While they propagate to higher latitudes, their absolute frequency remains constant, but their frequency relative to the local $f_{ce}$ decreases, since $f_{ce}$ increases with latitude. Since the number of fits was too large to perform a manual correction for these cases, it was decided to only fit to the spectral wave intensity above $0.1\,f_{ce}$ and hence ignore the measured data at the two lowest frequency bands.

In the cases where the omitted wave power actually corresponded to chorus waves below $0.1\,f_{ce}$ the calculated diffusion coefficients would be underestimated at large electron energies of a few MeV, resulting in a reduced electron acceleration and loss rates. The effects of the lower frequency chorus is therefore investigated in the improved chorus models discussed in Section 4.3.2.

In the case of upper band chorus, fitting to the peak above $0.9\,f_{ce}$ caused similar prob-

lems as for the lower band chorus. Since chorus is usually observed at frequencies below $0.7\,f_{ce}$, finding large spectral intensity close to the electron cyclotron frequency is unexpected. The cases where large wave intensity was found near $f_{ce}$ could be due to the way data was processed in the Cluster Whisper and CRRES PWE frequency channels. Here, wave power corresponding to other wave modes such as ECH waves above $f_{ce}$ were translated to frequency channels just below $f_{ce}$. Due to the additional binning process that was performed on the data to create the frequency bands used here, the data very close to $f_{ce}$ is included in the chorus wave database. This spectral wave power is unlikely to be due to chorus, since waves near the harmonic resonances should be strongly damped. Therefore, the last frequency channel ($0.9\,f_{ce} < f < 1.0\,f_{ce}$) was dropped in the presented chorus model.

If the spectral intensity above $0.9\,f_{ce}$ was actually due to chorus, omitting it would result in less electron diffusion at very low energies of tens of keV, and hence the electron acceleration and loss at these low energies would be underestimated. Since the energy range is well below the energy range of the radiation belts, which is typically above about 100 keV, omitting this spectral intensity is unlikely to have a significant effect on the results.

A typical example of the fitted power spectra is shown in Figure 4.1 for the 8 MLT sectors at $L^* = 5.5$, $0^\circ < |\lambda_m| < 6^\circ$ and a medium geomagnetic activity of $200 \leq AE < 400$. The power spectral density data are indicated by the crosses and dotted line, while the resulting Gaussian fits are shown as the solid lines, where the blue line corresponds to the fit of the lower band chorus data ($0.1\,f_{ce} < f < 0.5\,f_{ce}$), and the red line corresponds to the fit of the upper band chorus data ($0.5\,f_{ce} < f < 0.9\,f_{ce}$). It can be seen that in both the data and the fit two clear peaks can be distinguished, one in each frequency band associated with lower and upper band chorus, which is most evident 00-12 MLT. Generally the fit agrees well with the data, but note that there are cases where the fit to the data are distributed over a wide frequency range, for example the lower band chorus at 12-15 MLT and the upper band chorus at 15-18 MLT. In these cases the wave power that is used in the calculation of the diffusion rates is restricted by the lower and upper cut-off frequencies $f_{lc}$ and $f_{uc}$.

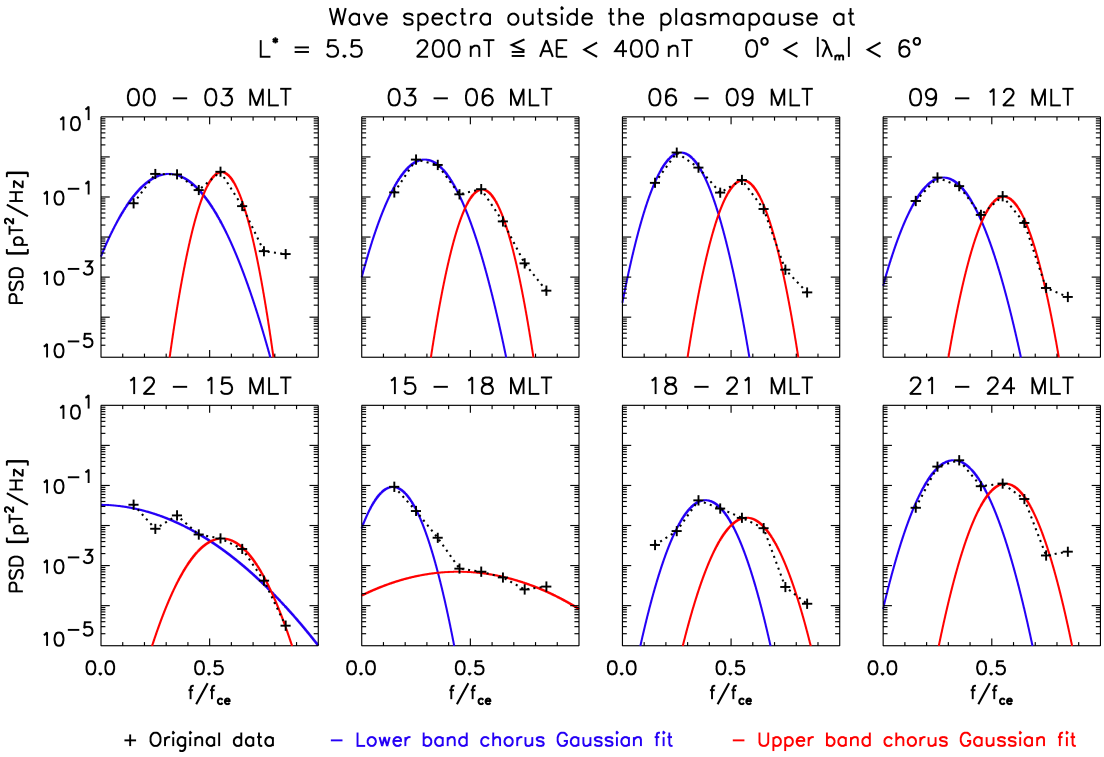


Figure 4.1: Comparison of the observed power spectral density (crosses and dotted line) and the fitted Gaussian power spectrum (solid lines) for lower band (blue) and upper band chorus waves (red) for all 8 MLT sectors in the region of $L^* = 5.5$, $0° < |\lambda_m| < 6°$, and at $200 \leq AE < 400$.

A summary of the statistics for fitting lower and upper band chorus is presented in Table 4.3. In total, there are 7,200 data bins for each chorus band, and out of these 3660 spectra were successfully fitted for lower band chorus and 2120 for upper band chorus, while in only 98 cases the fitting routine could not perform a successful fit to the data. The remaining bins were either lacking data or the integrated wave power was below the threshold of 0.1 pT.

### Wave Power

The wave power $B_w^2$ of the lower or upper band chorus over the whole frequency band can be calculated using Eq. 4.3, where the parameters $A_f$, $f_m$, and $\delta f$ were obtained by the fitting process described above. For the wave power calculated in this way, the short hand "fitted wave power" will be used from now on. The fitted wave power in the defined MLT, $L^*$, and $AE$ bins is shown in Figure 4.2 for lower band (a) and upper band (b) chorus waves near the equator ($0° < |\lambda_m| < 6°$).

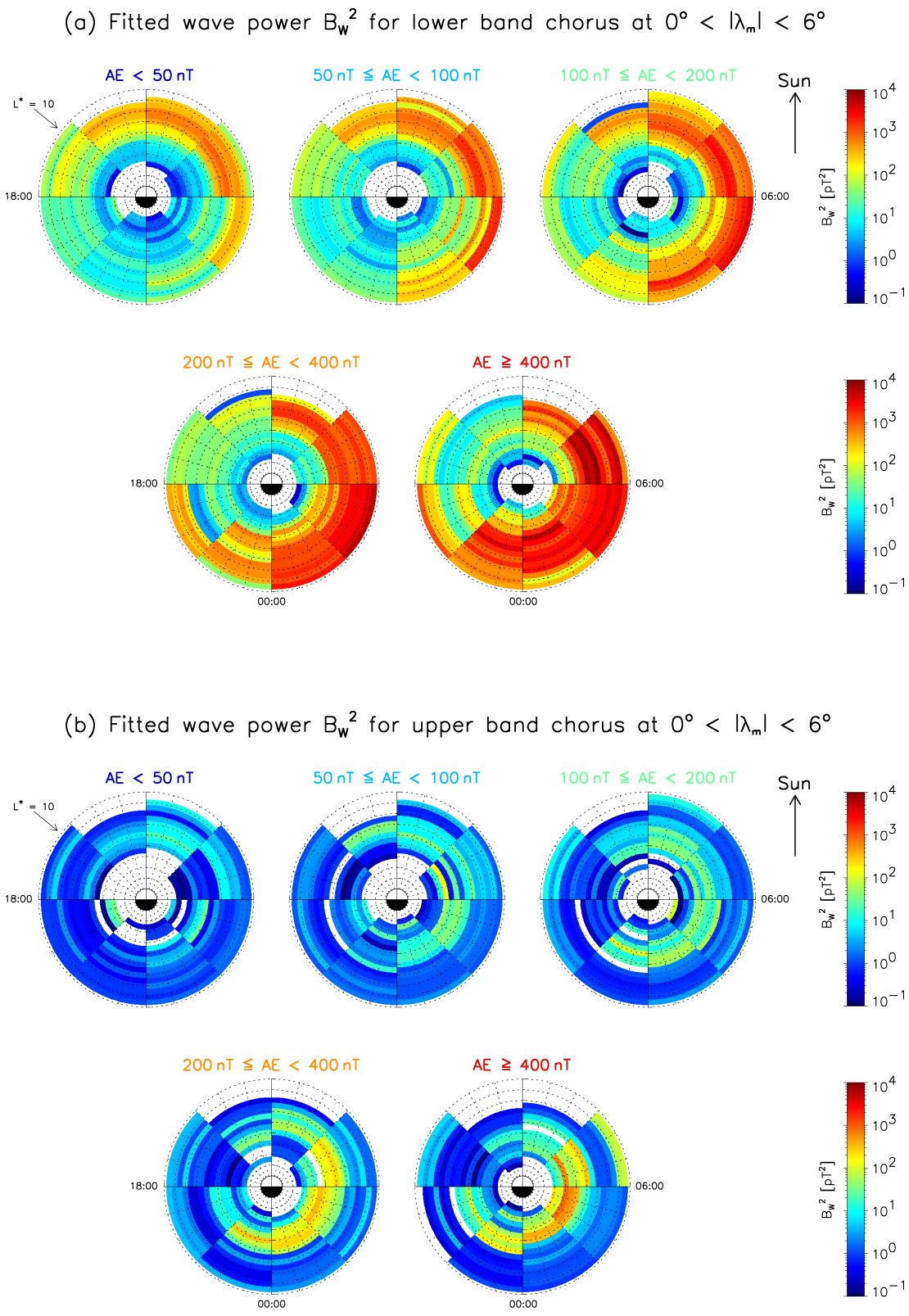


Figure 4.2: Fitted wave power $B_w^2$ for lower band chorus (a) and upper band chorus waves (b) in the region $0° < |\lambda_m| < 6°$.

| | Lower Band Chorus | | | | Upper Band Chorus | | | |
|---|---|---|---|---|---|---|---|---|
| Latitude | No Data | $< 0.1\,\mathrm{pT}$ | No Fits | Fits | No Data | $< 0.1\,\mathrm{pT}$ | No Fits | Fits |
| 0° - 6° | 149 | 3 | 0 | 568 | 158 | 29 | 12 | 521 |
| 6° - 12° | 155 | 8 | 1 | 556 | 168 | 53 | 0 | 499 |
| 12° - 18° | 191 | 5 | 2 | 522 | 194 | 134 | 6 | 386 |
| 18° - 24° | 216 | 8 | 0 | 496 | 219 | 207 | 7 | 287 |
| 24° - 30° | 262 | 10 | 0 | 448 | 263 | 258 | 7 | 192 |
| 30° - 36° | 307 | 35 | 0 | 378 | 342 | 243 | 35 | 100 |
| 36° - 42° | 331 | 86 | 0 | 303 | 357 | 295 | 14 | 54 |
| 42° - 48° | 409 | 139 | 0 | 172 | 451 | 243 | 4 | 22 |
| 48° - 54° | 507 | 135 | 0 | 78 | 514 | 171 | 2 | 33 |
| 54° - 60° | 559 | 111 | 1 | 49 | 575 | 112 | 7 | 26 |
| Total | | | | 3660 | | | | 2120 |

Table 4.3: Summary of the statistics for fitting lower and upper band chorus. The columns show the number of bins that were lacking data ("No Data"), bins where $B_w < 0.1\,\mathrm{pT}$, and the bins with unsuccessful ("No Fits") and successful fits ("Fits") at the corresponding latitude and chorus band.

The lower band chorus is dominant from the night sector starting at 21 MLT all the way through to the early afternoon sector ($12 - 15\,\mathrm{MLT}$) outside the plasmapause at $L^*$ greater than about 4.5 extending up to about $L^* = 10.0$. The fitted wave power increases noticeably with geomagnetic activity. At $AE < 50\,\mathrm{nT}$ the strongest lower band chorus waves are of the order of about $B_w^2 = 1,000\,\mathrm{pT}^2$ in the morning sectors, while for $AE > 400\,\mathrm{nT}$ the wave power can reach up to $10,000\,\mathrm{pT}^2$.
The upper band chorus is dominant in the same MLT region as the lower band chorus, and can also be found outside of $L^* = 4.5$, but it is confined to smaller $L^*$ of up to about 6.5. Furthermore, the fitted wave power of the upper band chorus is generally about one decade lower than the lower band chorus wave power. The wave power of upper band chorus is increasing with geomagnetic activity as well.

### Spectral Properties

The fitted Gaussian wave parameters generally vary with $L^*$, MLT, latitude, and geomagnetic activity. As an example, Figure 4.3 shows the wave amplitude $B_w$ (top row), the fitted normalised peak frequency $f_m/f_{ce}$ (middle row), and the fitted normalised frequency width $\delta f/f_{ce}$ (bottom row) as a function of $L^*$ for lower band chorus in a selected region, where chorus is known to be strong, namely 06 - 09 MLT and $0° < |\lambda_m| < 6°$. It can be seen that as $AE$ increases the wave amplitude increases as well, while the value of $L^*$, at which the amplitude of lower band chorus waves

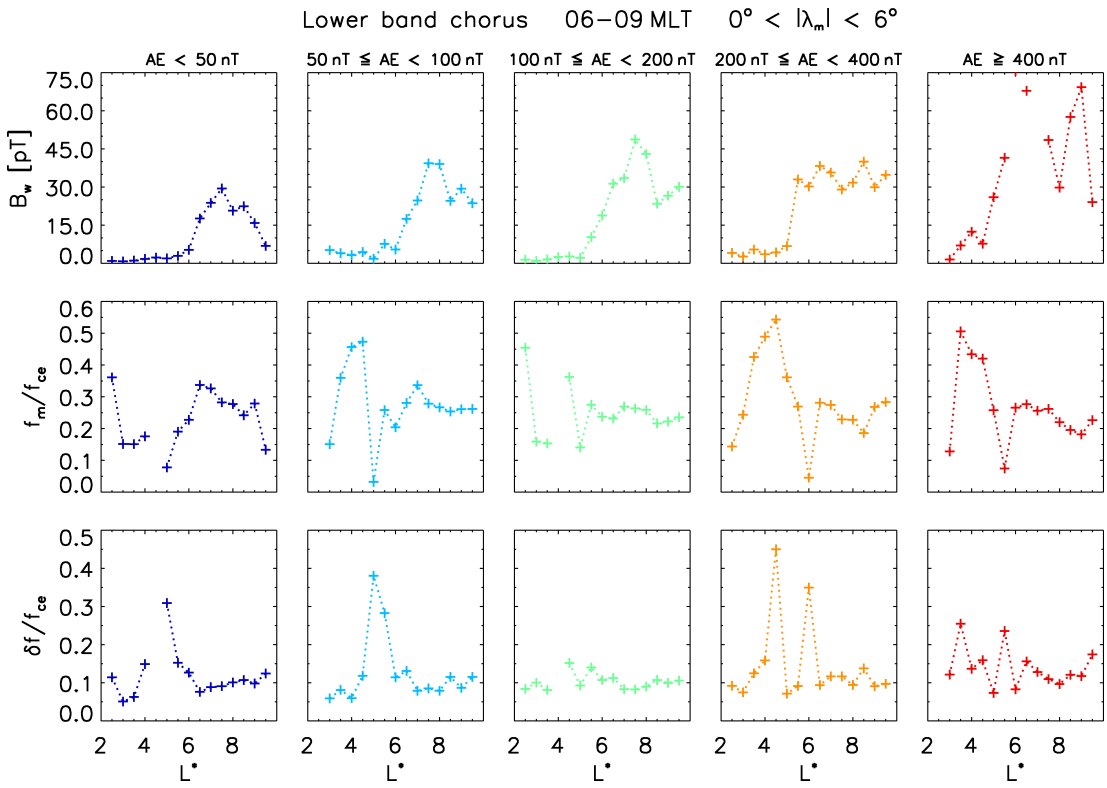


Figure 4.3: Example for parameters derived from fitting the power spectra of lower band chorus waves in the region of 06 - 09 MLT and $0° < |\lambda_m| < 6°$ for the 5 levels of geomagnetic activity defined by $AE$. The parameters are the wave amplitude $B_w$ (top row), the fitted normalised peak frequency $f_m/f_{ce}$ (middle row), and the fitted normalised frequency width $\delta f/f_{ce}$ (bottom row).

reaches significant values above the noise level, decreases with increasing $AE$. For the lowest geomagnetic activity ($AE < 50$ nT) the amplitude becomes significant for about $L^* > 6.0$, while for $AE > 400$ nT lower band chorus amplitudes become significant at about $L^* > 3.5$, which is expected since the plasmapause moves further inwards with increasing geomagnetic activity. Hence, since the diffusion rates are proportional to $B_w^2$, the contribution of the lower activities to the diffusion rates will be small and they will be dominated by the waves of larger wave power at higher activities. Finding significant chorus wave amplitudes for as low as $L^* = 3.5$ for the largest geomagnetic activity level is not surprising, since it was shown that the plasmapause can reach values as low as $L^* = 2.0$ during strong geomagnetic storms [*Baker et al.*, 2004].

The normalised peak frequency slightly tends to decrease with $L^*$, if the wave amplitudes are significant, while there seems to be no trend if the wave amplitudes are very

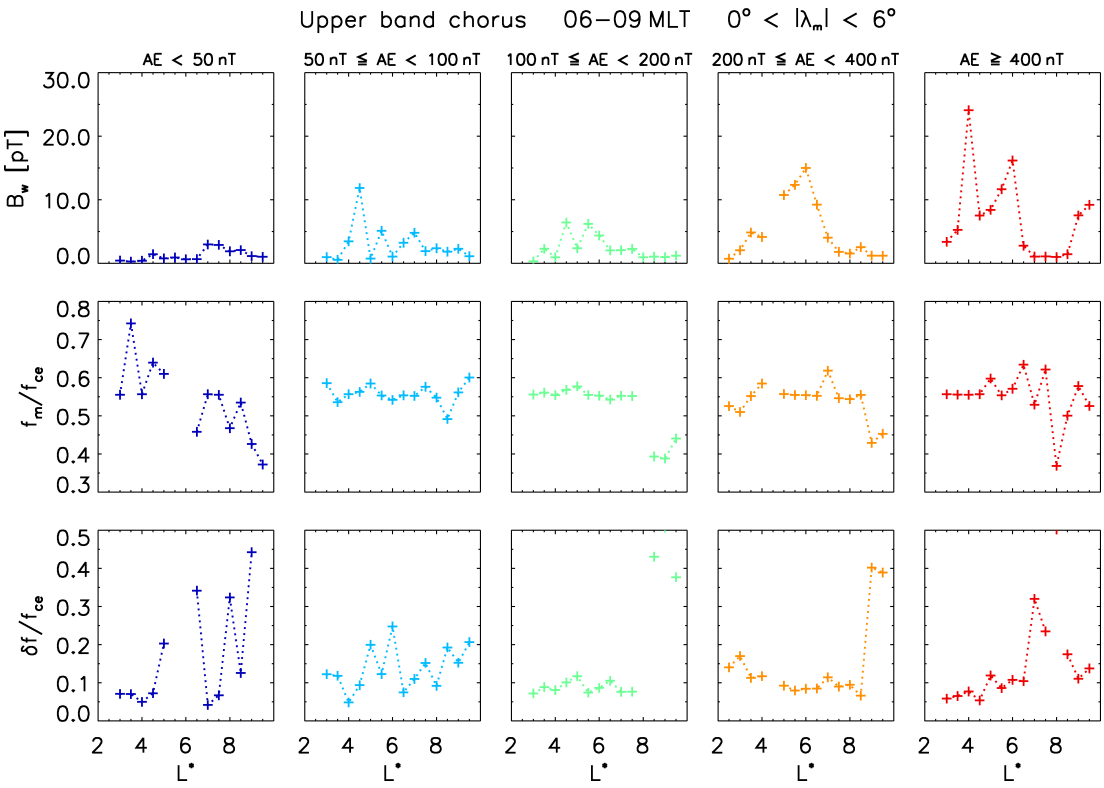


Figure 4.4: Example for parameters derived from fitting the power spectra of upper band chorus waves in the region of 06 - 09 MLT and $0° < |\lambda_m| < 6°$ for the 5 levels of geomagnetic activity defined by $AE$. The parameters are the wave amplitude $B_w$ (top row), the fitted normalised peak frequency $f_m/f_{ce}$ (middle row), and the fitted normalised frequency width $\delta f/f_{ce}$ (bottom row).

low, which is due to the fitting technique. Generally $f_m/f_{ce}$ tends to range from about 0.45 near $L^* = 3.5$ down to about 0.2 for $L^* > 8.0$. In contrast, the normalised frequency width tends to be constant with $\delta f/f_{ce} \approx 0.1$ for all activities and $L^*$, as long as there is significant wave amplitude associated with it. The diffusion rates published prior to this model were mostly calculated using a fixed frequency model, where the peak frequency was set to $f_m/f_{ce} = 0.35$ [*Albert et al.*, 2009; *Fok et al.*, 2008; *Shprits et al.*, 2009b; *Varotsou et al.*, 2005, 2008]. The results of the statistical model suggest that, since the frequencies drop with increasing $L^*$, the diffusion rates should be higher at larger energies.

The fitted parameters in the same region for upper band chorus (Figure 4.4) show mostly a different behaviour. While the wave amplitude also increases with $AE$, upper band chorus waves tend to be confined to $L^* < 6.5$, with the exception of $AE > 400$ nT.

The reason for the confinement to lower values of $L^*$ is not clear, while the exceptions at large geomagnetic activities are most likely due to the fitting of sparse data that represent an extreme event. The latter is also most likely to be the reason for the spike that can be found at $L^* = 4.0$ and $AE > 400\,\mathrm{nT}$. The normalised peak frequency tends to be almost constant with $L^*$ and $AE$ at about $f_m/f_{ce} \approx 0.55$, if the wave intensity is greater than about 5 pT. Similar to the lower band chorus, the normalised frequency width tends to be constant with $\delta f/f_{ce} \approx 0.1$, although some significant variation for the lowest geomagnetic activities, where the wave power is low, is present. This indicates that the fitting algorithm is likely to pick up wave power that is inside the noise level. However, since the corresponding wave power is low, the effect on the diffusion rates is negligible.

#### Wave Normal Angle

The wave normal angle $\psi$ is the angle between the ambient magnetic field and the wave vector $\underline{k}$ of the wave. As explained in Section 3.2, the wave normal angle of chorus waves was found to be mainly field aligned for all latitudes, but can be spread over a range of up to about 40° - 50°. There is no consensus on the distribution yet, with measurements showing field aligned propagation over a wide range of latitudes, while others show that chorus waves become more oblique at higher latitudes. Therefore it was decided to adopt the wave normal angle model that was most agreed on at the time of the study, which were based on Cluster and THEMIS data [*Agapitov et al.*, 2013; *Li et al.*, 2011]. The `PADIE` code assumes a Gaussian distribution in $X$, where $X = \tan(\psi)$. Based on these publications, the peak of the wave normal angle for both the fitted lower and upper band chorus, was set to $\psi_m = 0°$ with a spread of $\delta\psi = 30°$, and hence $X_m = \tan(0°)$ and $X_w = \tan(30°)$. In order to include waves at larger wave normal angles, the cut-offs for the wave normal angle were set to $X_{cut} = 2X_w$, outside which the wave power is set to zero.

#### Evaluation of the Fitting Method

In order to evaluate the obtained wave power, the fitted wave power $B_w^2(\mathrm{fit})$ is compared with the integrated wave power $B_w^2(\mathrm{data})$ (as presented in Section 4.3.1, in par-

ticular Figure 4.2). The ratio of the fitted wave power and the integrated wave power $B_w^2(\text{fit})/B_w^2(\text{data})$ is shown in Figure 4.5. If the fitted wave power was identical with the integrated wave power, the data and the fit would agree perfectly and the ratio would be equal to 1, while values greater than 1 would correspond to the fit overestimating the measured wave power and values smaller than 1 correspond to the fit underestimating the measured wave power.

The results show that for lower band chorus the fitted wave power typically captures at least 80 % of the wave power with most of the fits capturing more than 90 %. There are however cases, where the fitted wave power was significantly lower than the measured data, capturing only about 50 % of the wave power, while only in very few cases the wave power was overestimated by the fits. The wave power of the upper band chorus is generally captured better than the lower band chorus wave power. Typically about 90 - 95 % of the upper band wave power is captured by the fitting process, with only few cases where the wave power was significantly underestimated and no cases where the wave power was overestimated. The cases where the fitting fails to capture the wave power well are typically associated with a power spectral density distribution that is not of Gaussian form and it is therefore difficult to capture the wave power with a Gaussian fitting method. This problem is particularly prominent for the cases where there was significant wave power at very low or high frequencies. Overall, the fitted chorus wave model presents a reliable statistical model for lower and upper band chorus waves, although some cases remain where fitting a Gaussian distribution to the PSD is not the best approach. Therefore improved chorus models were developed, which are described in the next subsection.

### 4.3.2 Improved Chorus Models

As described in the previous subsection, the method of fitting the power spectra, while being reliable and creating valid results, still has some problems, especially when the power spectra are not distributed in a Gaussian shape, where the fitting underestimates the wave power. During the course of this PhD a new version of `PADIE` was developed that allows the use of the integrated wave intensity data from the chorus wave database

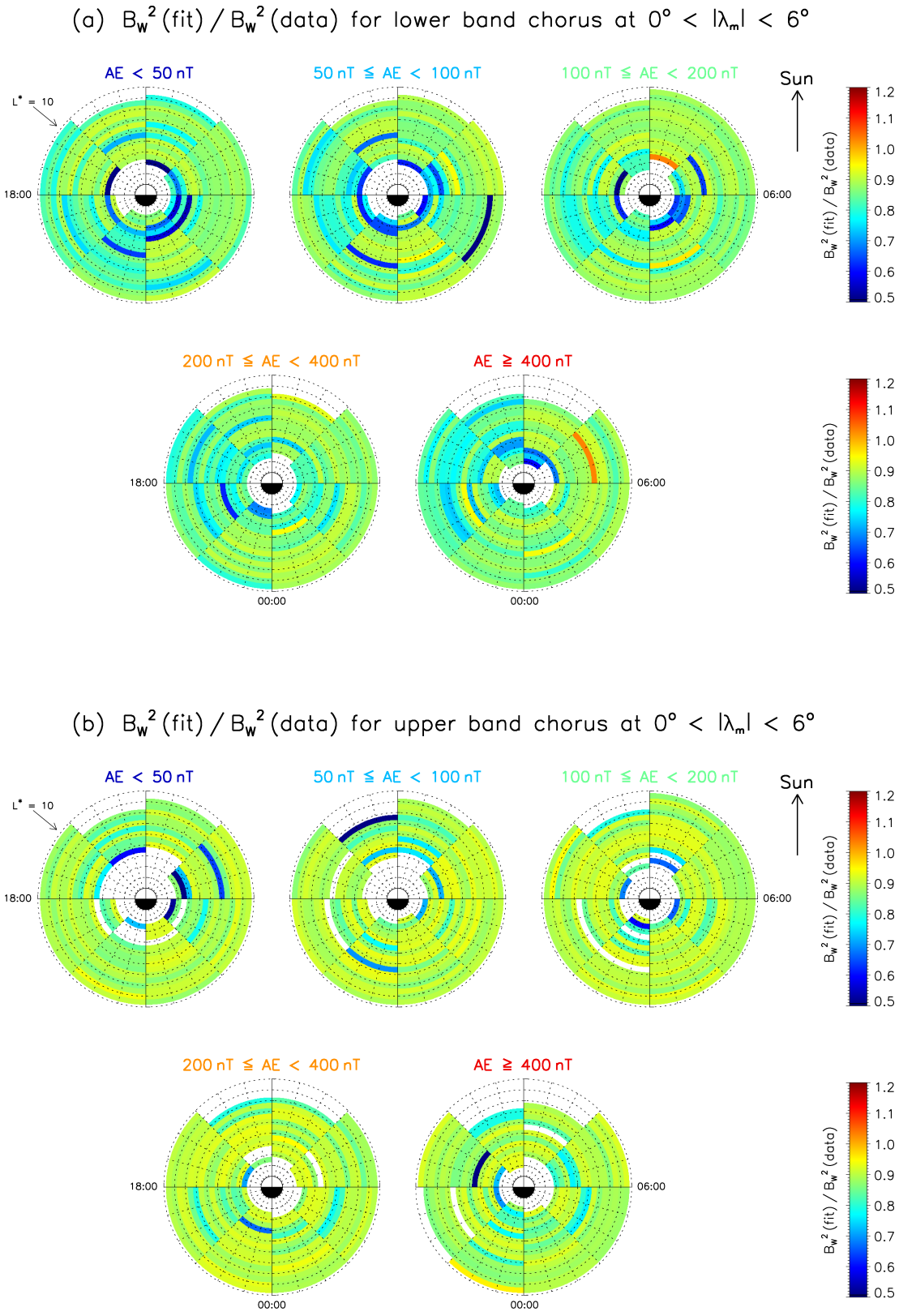


Figure 4.5: Ratio of the fitted wave power $B_w^2$(fit) and the integrated wave power $B_w^2$(data) for lower and upper band chorus in the region $0° < |\lambda_m| < 6°$.

directly, instead of requiring a Gaussian profile for the wave data (see section 2.2). Therefore, as a first improvement of the chorus wave model, a model entirely based on the tabulated wave data was created. The frequency range and all other parameters (cut-off frequencies, wave normal angle, and $f_{pe}/f_{ce}$) of this model were set to be identical to the fitted chorus model, in order to allow for a direct comparison of the results, which is shown in section 4.6. In plots and tables the short-hand "directly from data" will be used for this model.

As explained in Section 3.2, there is no consensus about the wave normal angle of chorus waves yet. Since the creation of the fitted chorus model, there were indications that the wave normal angle of chorus waves are distributed over a slightly narrower range than used in the presented models. Therefore a new chorus model was created, where the width of the wave normal angle for both lower and upper band chorus was set to be $\delta\psi = 15°$. As in the previous model, the wave spectral data are provided directly instead of using a Gaussian fit. For this model the short-hand notation "from data ($\delta\psi = 15°$)" will be used.

Using the tabulated wave data allows the inclusion of the wave power at frequencies lower than $0.1\, f_{ce}$, which were dropped for the fitted model, since they were causing issues for the fitting process. This allowed the creation of a new lower band chorus model that includes the data in the frequency range from $0.02333\, f_{ce} - 0.1\, f_{ce}$, which were not included in any previous chorus models. Consequently, the lower cut-off frequency was set to $f_{lc} = 0.022\, f_{ce}$, in order to model the wave power at lower frequencies. Since the upper band chorus is not affected by these changes, the model for the upper band chorus remains unchanged. Furthermore, the smaller wave normal angle distribution ($\delta\psi = 15°$) was used for this model for both lower and upper band chorus. From here on, this chorus model will be called the "lower frequency chorus model". An overview of the different chorus models is given in Table 4.4

| Chorus Wave Model | Wave power, $f_m$, and $\delta f$ | Frequency Range (lower & upper band) | Wave Normal Angle |
|---|---|---|---|
| **Fitted Model** | fitted | $0.1\,f_{ce} - 0.5\,f_{ce}$<br>$0.5\,f_{ce} - 0.9\,f_{ce}$ | $\delta\psi = 30°$ |
| **Data Driven Model ($\delta\psi = 30°$)** | from data | $0.1\,f_{ce} - 0.5\,f_{ce}$<br>$0.5\,f_{ce} - 0.9\,f_{ce}$ | $\delta\psi = 30°$ |
| **Data Driven Model ($\delta\psi = 15°$)** | from data | $0.1\,f_{ce} - 0.5\,f_{ce}$<br>$0.5\,f_{ce} - 0.9\,f_{ce}$ | $\delta\psi = 15°$ |
| **Lower frequency chorus ($\delta\psi = 15°$)** | from data | $0.022\,f_{ce} - 0.5\,f_{ce}$<br>$0.5\,f_{ce} - 0.9\,f_{ce}$ | $\delta\psi = 15°$ |

Table 4.4: Overview of the different chorus wave models derived from the chorus wave database.

## 4.4 The Ratio of $f_{pe}/f_{ce}$

In order to calculate the diffusion rates using `PADIE` the plasma density at the location where the calculation should be performed is required. In particular, the ratio of $f_{pe}/f_{ce}$ needs to be provided, which is often used to describe the plasma density, since it is proportional to the square root of the plasma density (See Eq. 2.21).

For chorus waves, a new plasma density model was derived entirely from observations of the CRRES and THEMIS satellites. The plasma density measurements were obtained from the CRRES wave instrument directly and in the case of the THEMIS satellite they were inferred from measurements of the electron thermal speed and the spacecraft potential [*Li et al.*, 2010]. For the other satellites, measurements of the plasma density were not easily available and hence they were not included. Only the data outside the plasmapause (defined by the criteria described in Section 4.2) were stored, since chorus waves are mainly found outside the plasmapause. The plasma densities obtained in this way were then converted into $L^*$ and arranged into the same $L^*$ and geomagnetic activity levels as the chorus model, but with a 1h MLT resolution. In order to increase the data coverage, the data inside the latitude range of $0° < |\lambda_m| < 9°$ were combined, while data at larger latitudes were not included to minimise latitudinal effects.

The resulting measurements of $f_{pe}/f_{ce}$ are presented in Figure 4.6 (a). It can be seen that the data coverage of $f_{pe}/f_{ce}$ has no gaps, except close to the Earth, especially

for $AE < 50\,\mathrm{nT}$, and at higher $L^*$ for $AE > 400\,\mathrm{nT}$. The coverage tends to move closer to the Earth with increasing geomagnetic activity, which generally agrees with the observed shape of the plasmapause [*O'Brien and Moldwin*, 2003; *Carpenter and Anderson*, 1992], which moves closer to the Earth with increasing activity. Nevertheless, the data presented here extends much closer to the Earth than expected, especially for $AE < 100\,\mathrm{nT}$ where the plasmapause typically lies near $L^* = 4$ and above, while $f_{pe}/f_{ce}$ data can be found as low as $L^* = 2.0$. Since the presented $f_{pe}/f_{ce}$ data was only measured outside the plasmapause, this suggests that the previously explained criteria used to distinguish between data inside and outside the plasmapause are not perfect and hence some events might be incorrectly associated with chorus. However, the diffusion rates are directly proportional to the measured wave power, which is very low at low $L^*$ and hence the calculated diffusion coefficients are unlikely to have a significant contribution to the overall diffusion rates.

In order to use the measured plasma density as a model for the chorus wave models presented here, the $f_{pe}/f_{ce}$ data inside the latitude range of $0° < |\lambda_m| < 9°$ were interpolated to fill all gaps and cover all $L^*$. Furthermore, the data were averaged to 3h MLT bins, rather than 1h MLT bins, in order to increase the sample size and to match the MLT resolution of the chorus wave model. The interpolation was performed in a number of steps for each level of $AE$ individually. First, the largest $L^*$ for which there were at least 8 MLT sectors containing data, without missing data in two adjacent sectors, was determined for the dayside and nightside individually. The resulting value of $L^*_{max}$ hence represents the largest $L^*$ where at least 66 % of data were still available without large gaps. Within $L^* = 1.5$ and the determined $L^*_{max}$ a linear interpolation using the nearest neighbours, weighted by the number of samples at each neighbour, was performed to fill in the missing data. In the next step, the missing values between $L^*_{max}$ and $L^* = 10.0$ were filled using a linear extrapolation along $L^*$. As a last step, the $f_{pe}/f_{ce}$ model was reduced to a 3h MLT resolution by calculating the average, weighted by the number of samples in each bin.

The resulting model for the plasma density represents $f_{pe}/f_{ce}$ at the equator, for 18 levels of $L^*$, 8 MLT sectors, and 5 levels of geomagnetic activity determined by $AE$

and is presented in Figure 4.6 (b). For higher latitudes, $f_{pe}/f_{ce}$ was recalculated using a dipole magnetic field model to cover the full range of the chorus model ($0° < |\lambda_m| < 60°$). This recalculation is entirely based on the equatorial density model that contains data within $0° < |\lambda_m| < 9°$ and any possible variation of (measured) $f_{pe}/f_{ce}$ with latitude is hence excluded in this model.

## 4.5 Bounce Averaged Diffusion Rates

The effect of lower and upper band chorus waves on the electron flux can be predicted from the pitch-angle and energy diffusion rates, which provide a measure of the change in electron pitch-angle and electron energy caused by the corresponding waves. The `BAS-RBM` uses the drift and bounce averaged diffusion rates, which are calculated from the bounce averaged diffusion rates, by (drift) averaging them over all MLT. In order to understand how the drift and bounce averaged diffusion rates are composed, the bounce averaged diffusion rates are presented for the fitted chorus model in this section first. The comparison of the different chorus models is presented in the next section on the basis of the drift and bounce averaged diffusion rates.

All diffusion rates for all models were calculated from individual runs of the `PADIE` diffusion code for 111 energy levels evenly spread over a logarithmic energy range from 100 eV to 10 MeV. Each run was performed with a pitch-angle resolution of 1°, covering all equatorial pitch-angles between 0° and 90°. The runs included the dominant resonances from $n = -10...10$ and the diffusion rates were only calculated if the integrated wave amplitude was greater than the threshold of 0.1 pT.

Within each of the 6° latitude bins specified for the model, the bounce averaging was performed by `PADIE` directly assuming a dipole magnetic field. The full bounce averaged diffusion rates covering the whole latitude range at each $L^*$, MLT, energy, and geomagnetic activity sector were calculated by adding the bounce averaged diffusion rates of the 6° latitude sectors inside the corresponding $L^*$, MLT, energy, and activity sectors. In order to save computational time, the total latitude range covered was restricted to geomagnetic latitudes $< 42°$ for lower band chorus and $< 12°$ for upper

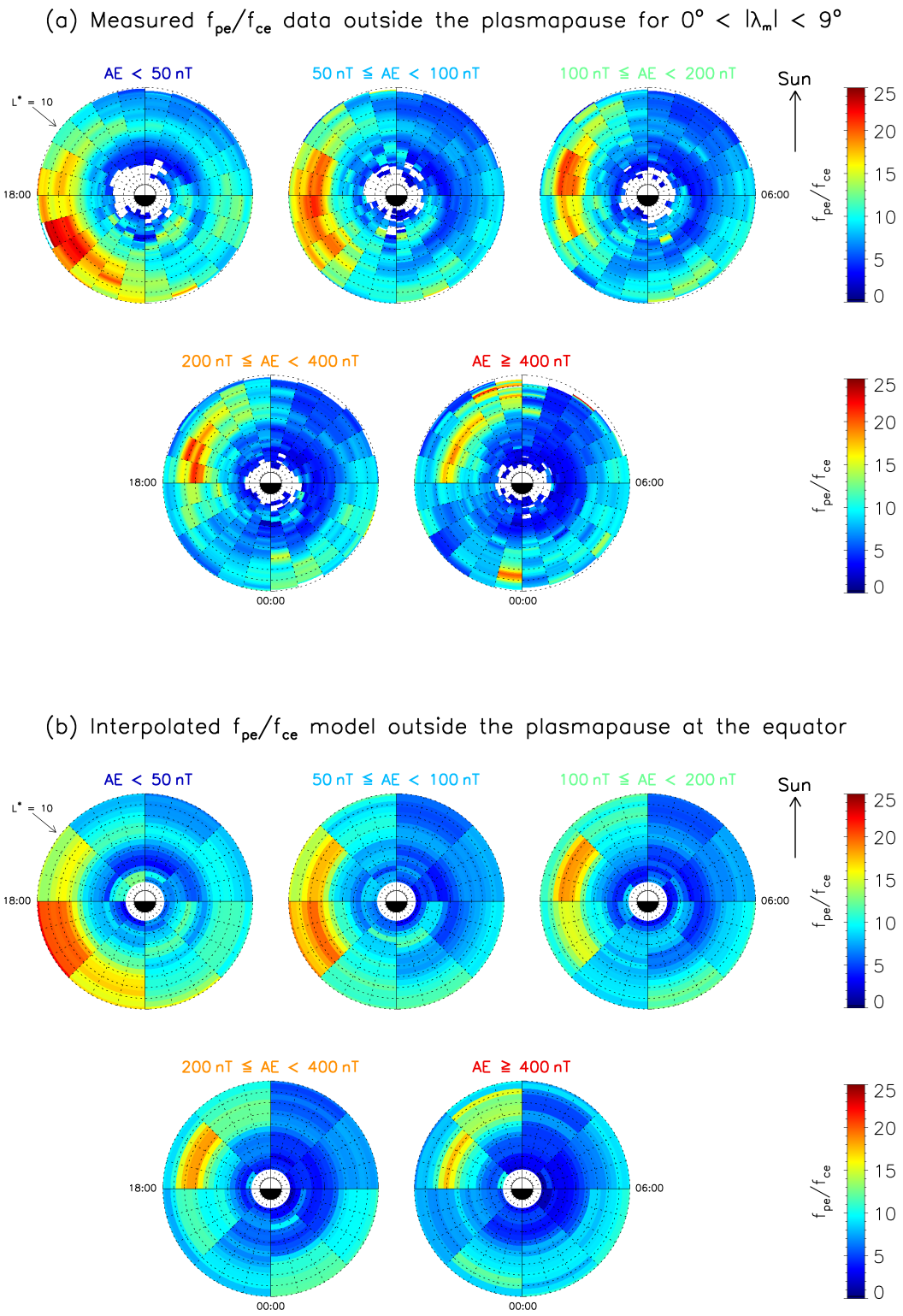


Figure 4.6: (a) $f_{pe}/f_{ce}$ derived from the CRRES and THEMIS satellites outside the plasmapause for $0° < |\lambda_m| < 9°$ and five levels of $AE$. (b) Final $f_{pe}/f_{ce}$ model at the equator, achieved through weighted interpolation and extrapolation of the CRRES and THEMIS data.

band chorus, since studies have shown that the most of the wave intensity can be found within these limits.

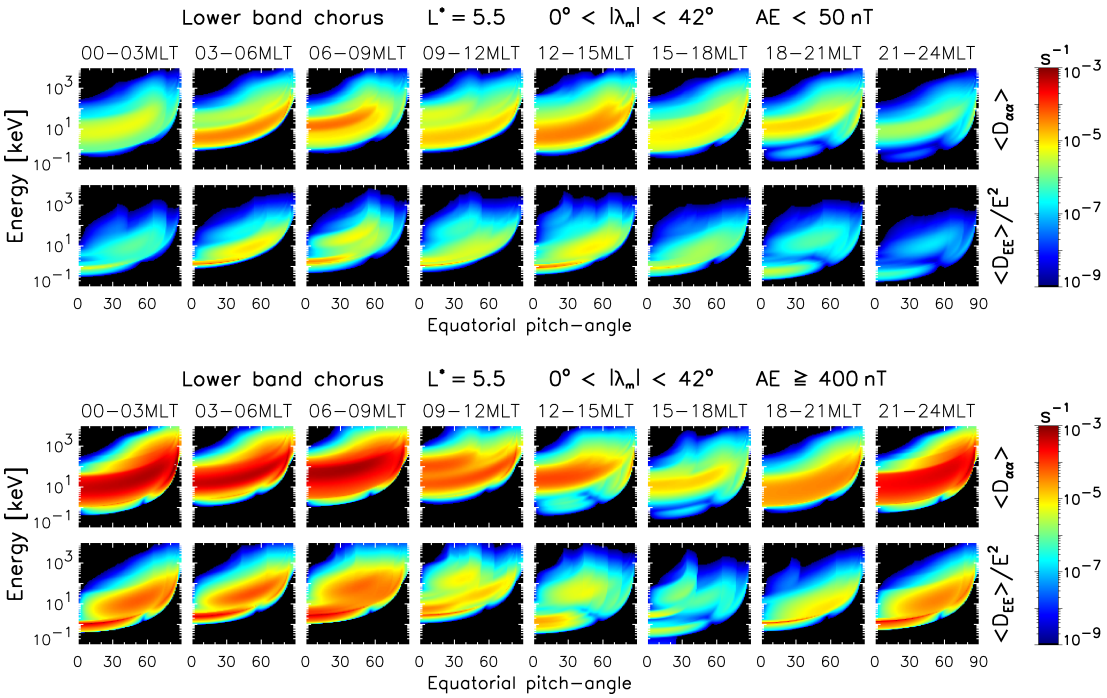


Figure 4.7: Bounce averaged pitch-angle $\langle D_{\alpha\alpha}\rangle$ and energy $\langle D_{EE}\rangle/E^2$ diffusion rates for lower band chorus (fitted model) at $L^* = 5.5$ within $0° < |\lambda_m| < 42°$ as a function of equatorial pitch-angle and energy. MLT increases from left to right and the top rows are for $AE < 50\,\mathrm{nT}$, while the bottom rows are for $AE > 400\,\mathrm{nT}$.

As an example, the bounce averaged pitch-angle diffusion rates $\langle D_{\alpha\alpha}\rangle$ and the bounce averaged energy diffusion rates $\langle D_{EE}\rangle/E^2$ of the fitted lower band chorus model are presented in Figure 4.7 for all 8 MLT sectors at $L^* = 5.5$ for the quietest and most active geomagnetic activity levels ($AE < 50\,\mathrm{nT}$ and $AE > 400\,\mathrm{nT}$). During the quiet period, both the pitch-angle and energy diffusion rates are generally weaker than during the active period. At small equatorial pitch-angles the stronger pitch-angle diffusion coefficients typically extend from about 1 keV to 100 keV, and with increasing equatorial pitch-angles the condition for stronger pitch-angle diffusion widens and shifts to higher energies, covering the energy range from about 10 keV to about 1 MeV at about 60°. For pitch-angles close to 90°, the covered energy range becomes narrower again and only covers high electron energies between about 100 keV and about 1 MeV.

For $AE < 50\,\mathrm{nT}$ there is little variation with MLT, where the maximum pitch-angle

diffusion rates are of the order of $10^{-4}\,s^{-1}$ in the strongest MLT sector and $10^{-5}\,s^{-1}$ in the weakest MLT sector. For $AE > 400\,nT$ the pitch-angle diffusion rates are generally significantly stronger than during quiet conditions with pitch-angle diffusion rates of up to about $10^{-3}\,s^{-1}$. There is also a clear trend in MLT, where the lower band chorus diffusion rates are generally strong between about 21 - 09 MLT, and weak in the afternoon and evening sector (12 - 21 MLT) with a minimum between 15 - 18 MLT, where the pitch-angle diffusion rates are of the order of $10^{-5}\,s^{-1}$.

The energy diffusion rates show a similar trend in MLT and geomagnetic activity, i.e. no clear MLT dependence during quiet conditions, as opposed to active conditions, and much stronger energy diffusion during active conditions than during quiet conditions. The energy diffusion is typically strong at slightly lower electron energies compared to the pitch-angle diffusion. At small equatorial pitch-angles the energy diffusion is strong at about 0.5 - 50 keV and 1 - 500 keV at 60°. The energy diffusion rates are generally about one decade lower than the pitch-angle diffusion rates, and are strongest at smaller energies than the pitch-angle diffusion rates, indicating that a particle of a particular energy and pitch-angle is either predominantly scattered in pitch-angle, or predominantly accelerated.

An example of the bounce averaged diffusion rates of the fitted upper band chorus model is shown at the same $L^*$, MLT sectors, and geomagnetic activities in Figure 4.8. In this case the much higher frequencies of the upper band chorus result in diffusion at much lower energies. Upper band chorus pitch-angle and energy diffusion rates are significant at energies as low as a few 100 eV, which is lower than the energies where lower band chorus is effective. The energy range covered at each equatorial pitch-angle is generally much smaller than the one of the lower band chorus. The trends in MLT and $AE$ are similar to the ones found for lower band chorus, where the diffusion rates increase with geomagnetic activity and are weakest between noon and the evening sector. The peaks of the upper band chorus diffusion rates are of the same order as the lower band chorus diffusion rates. Note that the lower diffusion rates at 00 - 03 MLT are due to the relatively high $L^*$ chosen. At lower $L^*$ the upper band diffusion rates are strong all the way through 21 - 09 MLT.

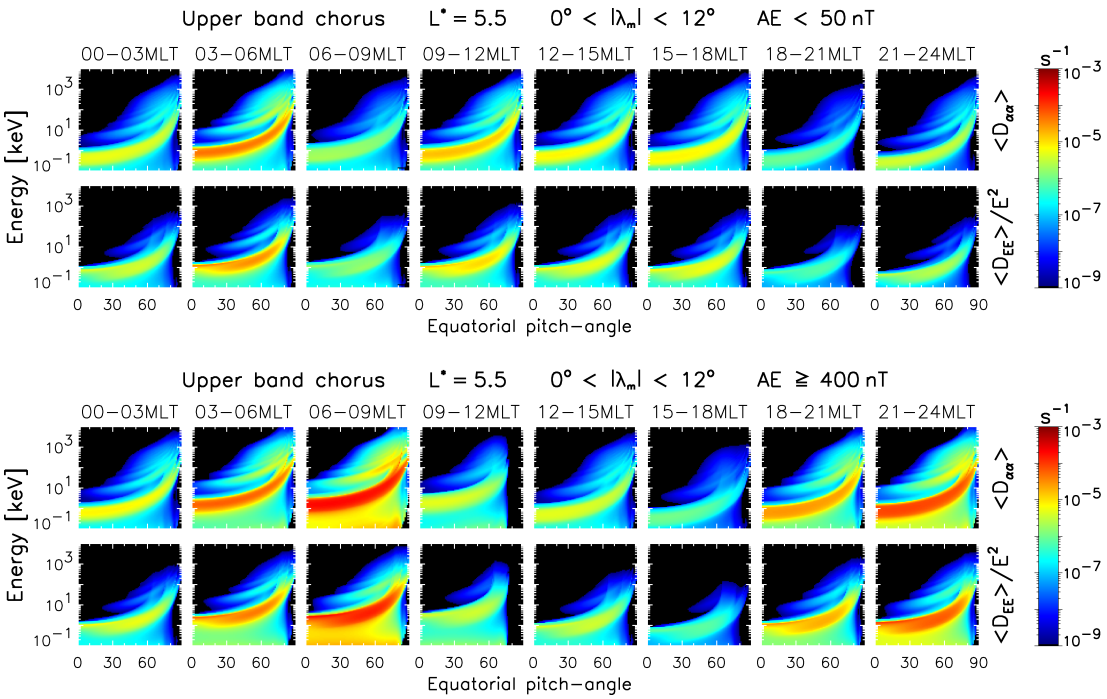


Figure 4.8: Bounce averaged pitch-angle $\langle D_{\alpha\alpha} \rangle$ and energy $\langle D_{EE} \rangle / E^2$ diffusion rates for upper band chorus (fitted model) at $L^* = 5.5$ within $0° < |\lambda_m| < 12°$ as a function of equatorial pitch-angle and energy. MLT increases from left to right and the top rows are for $AE < 50\,\mathrm{nT}$, while the bottom rows are for $AE > 400\,\mathrm{nT}$.

Overall the lower and upper band chorus diffusion rates tend to complement each other, covering a wide range of energies and pitch-angles. As a result, it can be expected that chorus waves are effective at scattering particles into the loss cone and accelerate electron at energies ranging from a couple hundred eV up to about 1 MeV. At energies above about 1 keV these processes are likely to be dominated by lower band chorus. The MLT distribution of the diffusion rates show that the electrons will be affected the most between about 21 - 12 MLT during their drift orbits around the Earth.

### 4.5.1 Comparison of the Chorus Models

As discussed in Section 4.3.2 the model for lower and upper band chorus waves were improved over time resulting in four successive chorus models (see Table 4.4). In this section the different chorus models are compared against each other by studying the effects of the change made in each model on the bounce averaged pitch-angle and energy diffusion rates. Since each change is incremental, the comparison is only made between

the succeeding and preceding model. The comparison will be presented at one value of $L^*$, where chorus is strong and which is representative for the results that are shown. The variation of the diffusion rates with $L^*$ will be shown in Section 4.6.

Although lower and upper band chorus waves were calculated independently, the `BAS-RBM` expects the diffusion rates of chorus waves to be one set of diffusion coefficients, rather than using lower and upper band chorus waves independently. Therefore, the bounce averaged diffusion rates of lower and upper band chorus waves were combined by adding them in each individual $L^*$, energy, and geomagnetic activity bin.

### Fitted Chorus Model

The combined lower and upper band chorus pitch-angle and energy diffusion rates of the fitted chorus model are presented as a reference in Figure 4.9 for the region $L^* = 5.5$, $200\,\mathrm{nT} < AE < 400\,\mathrm{nT}$, and for all MLT. As before, the bounce averaging was performed between $0° < |\lambda_m| < 42°$ for the lower band chorus diffusion rates and $0° < |\lambda_m| < 12°$ for the upper band chorus diffusion rates. Combining the diffusion rates allows the chorus waves to cause diffusion in the combined energy and pitch-angle range of lower and upper band chorus. Note that the striped structure in the diffusion rates are due to the combination of the diffusion rates.

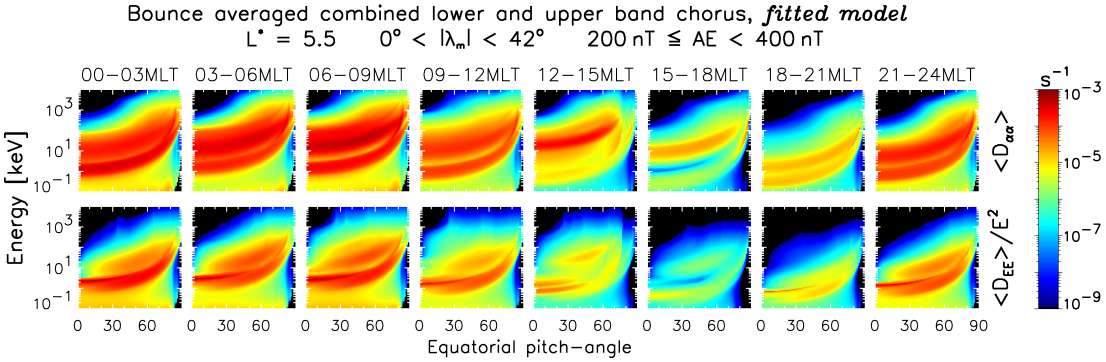


Figure 4.9: Bounce average pitch-angle and energy diffusion rates of combined lower and upper band chorus waves of the fitted chorus model in the region of $L^* = 5.5$, $0° < |\lambda_m| < 42°$, and $200\,\mathrm{nT} < AE < 400\,\mathrm{nT}$ for 8 levels of MLT.

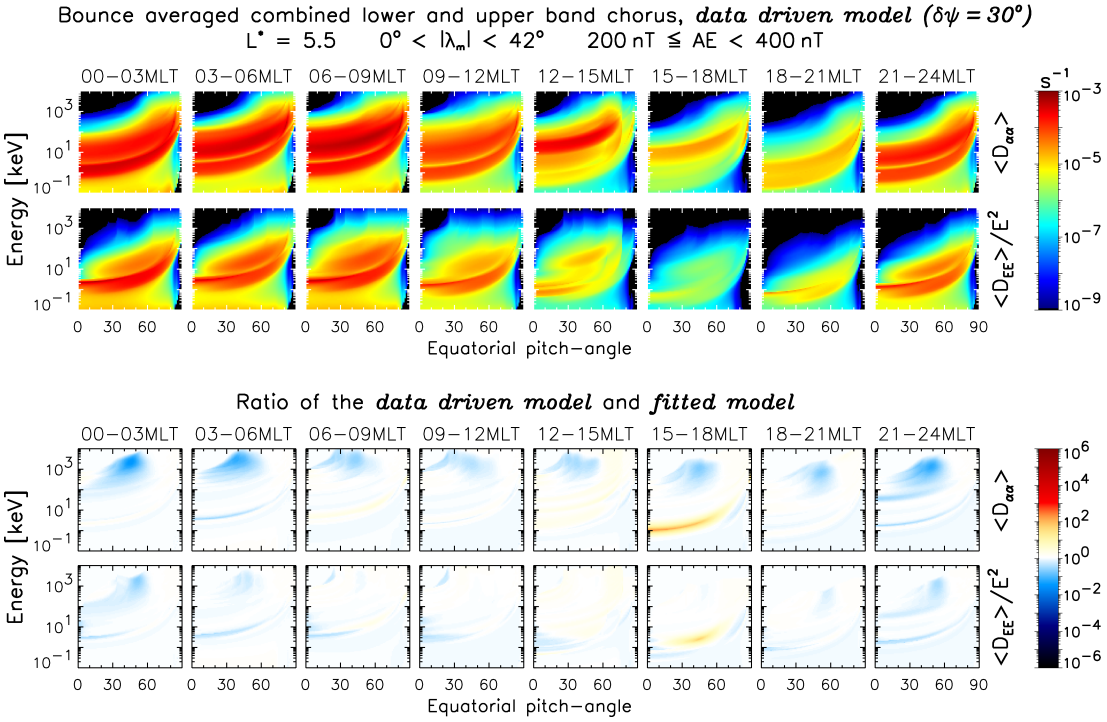


Figure 4.10: Bounce average pitch-angle and energy diffusion rates of combined lower and upper band chorus waves of the data driven chorus model with a wave normal angle width of $\delta\psi = 30°$ (top) in the region of $L^* = 5.5$, $0° < |\lambda_m| < 42°$, and 200 nT $< AE <$ 400 nT for 8 levels of MLT. The bottom panel shows the ratio of the diffusion rates of the data driven chorus model and the fitted chorus model.

### Directly from Data Chorus Model

The first improvement made to the chorus models was to use the integrated wave intensity data directly instead of fitting the data first and providing Gaussian spectral profiles. Comparing this "data driven" model with the "fitted model" allows further evaluation of the quality of the fitting process, since the resulting diffusion rates of the two chorus models should be similar. However, it is expected that there will be differences due to bad fits. For instance, if the fitting process was unable to capture the wave intensity data properly, the resulting diffusion rates could either be underestimated or overestimated, depending on the fit. The bounce averaged pitch-angle and energy diffusion rates of the "data driven" model are shown in the top panel of Figure 4.10 for the same region as before, while the bottom panel of the same figure shows the ratio of the diffusion rates of the data driven model and the fitted chorus model.

The results show that using the data driven model overall produces diffusion rates

that are close the ones of the fitting process. In the MLT regions where the overall wave power is strong and the fitting generally agrees well with the data, the ratio of the diffusion rates is close to 1, indicating that the two models are identical in this region. The largest differences between the two models can generally be found at energies greater than about 100 keV and pitch-angles between about 35 - 55°, where the pitch-angle diffusion rates of the data driven model are decreased by about one decade compared to the fitted model. Furthermore, there is an increase of the pitch-angle diffusion rates in the region of 15-18 MLT at low energies, where the wave power (and hence the diffusion rates) are low compared to the other MLT sectors. In these regions the corresponding spectral profiles of the data are usually difficult to fit. Overall, the largest differences of the diffusion rates usually occur in an energy region or pitch-angle region where the diffusion rates are low, and hence the absolute values of the diffusion rates are insignificant for the fluxes.

Overall, the comparison of the data driven model and the fitted model shows that the fitting method reliably captures most of the wave power at all times, except in regions of low wave power. Conversely, the data driven model does not deviate significantly from the fitted model, and as a consequence, the data driven approach can be used to further improve the chorus wave models, by including spectral information that had to be excluded in the fitting process.

#### From Data ($\delta\psi = 15°$) Chorus Model

The effects of the change of the wave normal angle on the pitch-angle and energy diffusion rates are presented in Figure 4.11. Here, the top panel shows the bounce averaged diffusion rates of the "data driven" chorus model with a width of the wave normal angle of $\delta\psi = 15°$ in the same range as before. The bottom panel shows the ratio of the data driven chorus model with $\delta\psi = 15°$ and the data driven chorus model with $\delta\psi = 30°$.

It can be seen that reducing the wave normal angle generally decreases both the pitch-angle and energy diffusion rates. At energies greater than about 10 keV the diffusion rates are decreased to a minor degree by up to about 1 decade, with the largest decrease

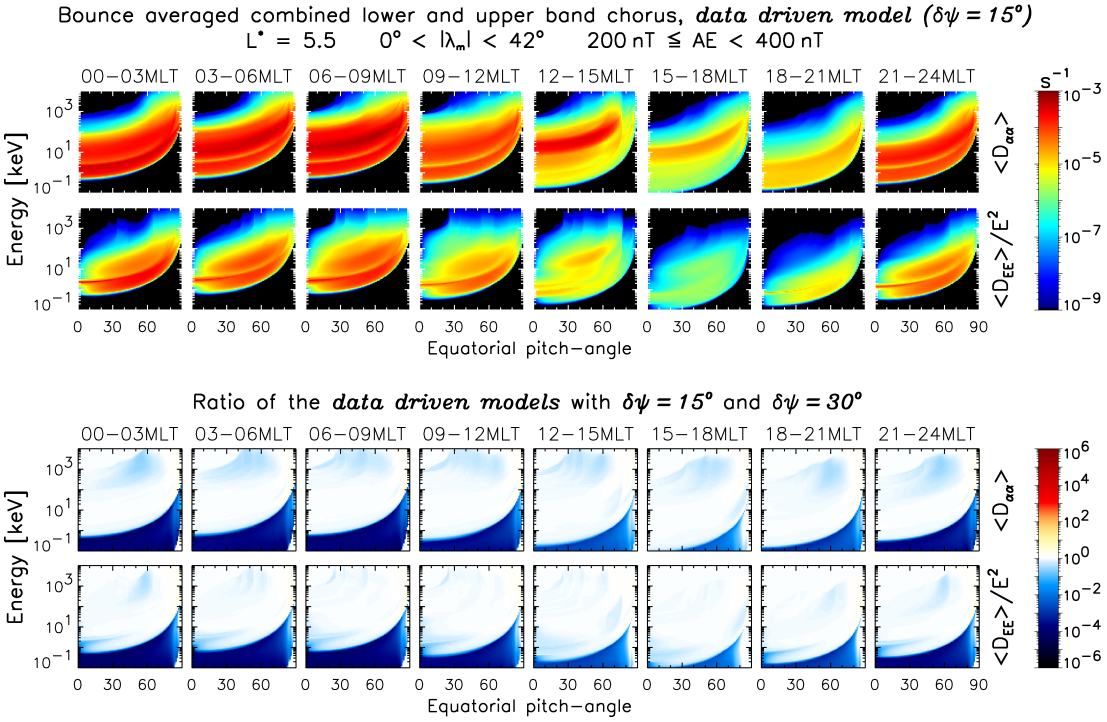


Figure 4.11: Bounce average pitch-angle and energy diffusion rates of combined lower and upper band chorus waves of the data driven chorus model with a wave normal angle with of $\delta\psi = 15°$ (top) in the region of $L^* = 5.5$, $0° < |\lambda_m| < 42°$, and 200 nT $< AE <$ 400 nT for 8 levels of MLT. The bottom panel shows the ratio of the diffusion rates of the data driven chorus model with $\delta\psi = 15°$ and data driven chorus model with $\delta\psi = 30°$.

for pitch-angle diffusion occurring at pitch-angles between about 30° and 60°. In this region, the absolute diffusion rates of the data driven model decreased from about $10^{-6}\mathrm{s}^{-1}$ down to $10^{-7}\mathrm{s}^{-1}$, which are both significantly lower than the diffusion rates at lower energies and hence the pitch-angle scattering of electrons is only affected insignificantly by the change in wave normal angle at energies greater than about 10 keV.

However, at energies below about 10 keV a significant reduction of both the pitch-angle and energy diffusion rates can be found. The diffusion rates decrease from about $10^{-5}\mathrm{s}^{-1}$ down below the minimum value. A further investigation showed that this drastic change is only prominent in the upper band chorus diffusion rates and it is due to the wider wave normal angle distribution, which allows the waves to resonate with the particles, while a smaller wave normal angle distribution doesn't. An illustration of this effect is shown in Figure 4.12, which presents the dispersion relation of the

upper band chorus waves for a case that represents the conditions near $L^* = 5.5$ and 06-09 MLT. The wave normal angle has been chosen to be slightly below the upper cut-off of the wave normal angle distribution $X_{uc} = 2\tan(\delta\psi)$. It can be seen that for a wave normal angle of $\psi = 25°$ the dispersion relation does not intersect with the resonance condition within the frequency limits imposed by the lower and upper cut-off frequencies $f_{lc}$ and $f_{uc}$. In contrast, a wave normal angle of $\psi = 50°$ changes the dispersion relation so that all resonances $n \leq 0$ can intersect with the dispersion relation, allowing for pitch-angle and energy diffusion.

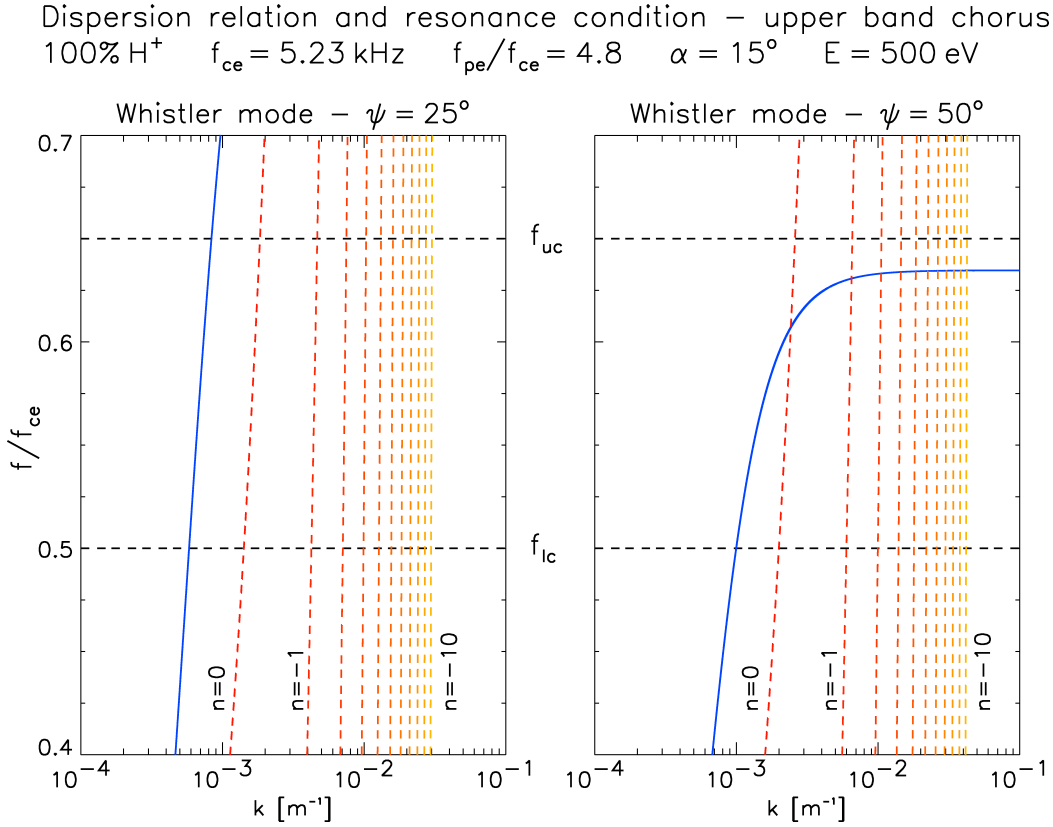


Figure 4.12: Dispersion relation for the whistler mode branch (blue line) of upper band chorus waves in proton-electron plasma with $f_{ce} = 5.23\,\text{kHz}$ and $f_{pe}/f_{ce} = 4.8$ for a wave normal angle of $\psi = 25°$ (left) and $\psi = 50°$ (right). The dashed lines show the resonance condition for the resonance numbers $n = 0...-10$ for an electron with energy $E = 500\,\text{eV}$ and pitch-angle $\alpha = 15°$ at the corresponding wave normal angle.

### Lower Frequency Chorus Model

Using the tabulated wave data directly allows modelling the effects of wave intensity below $0.1\,f_{ce}$, which could not be done reliably using the fitting process. Contributions

of waves at lower frequencies are expected to result in larger diffusion rates at larger energies. The bounce averaged pitch-angle and energy diffusion rates of the combined lower and upper band chorus waves of the "lower frequency chorus" model, which includes the chorus wave power at frequencies as low as $0.022\,f_{ce}$, are shown in Figure 4.13 (top) in the same range as in the previous figures. Similarly, the bottom panel of the same figure shows the ratio of the diffusion rates of the lower frequency chorus model and the data driven model (both calculated with $\delta\psi = 15°$).

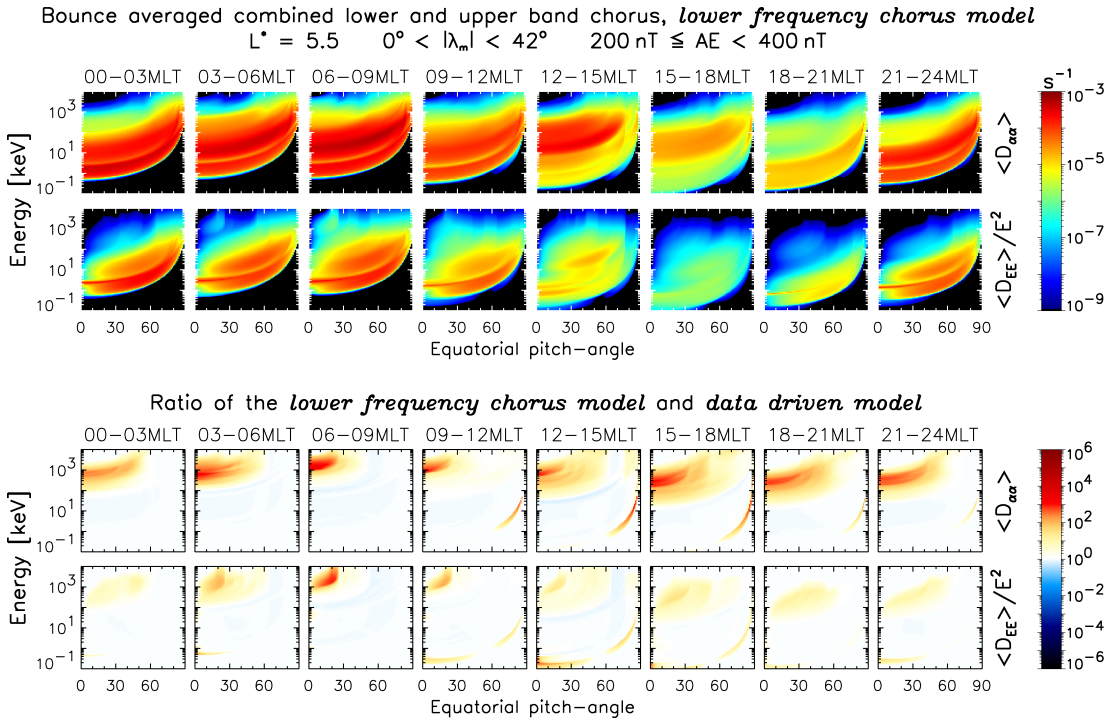


Figure 4.13: Bounce average pitch-angle and energy diffusion rates of combined lower and upper band chorus waves of the lower frequency chorus model (top) in the region of $L^* = 5.5$, $0° < |\lambda_m| < 42°$, and $200\,\text{nT} < AE < 400\,\text{nT}$ for 8 levels of MLT. The bottom panel shows the ratio of the diffusion rates of the lower frequency chorus model and data driven chorus model with $\delta\psi = 15°$.

The results show that for energies less than about 100 keV both the pitch-angle and energy diffusion rates are virtually unaffected, with the ratio of the diffusion rates being close to unity. As expected, at energies greater than about 100 keV the pitch-angle and energy diffusion rates increase up to 5 decades, in particular close to about 1 MeV. The new absolute values of the diffusion rates are in the region of $10^{-5}\text{s}^{-1}$. In comparison with the diffusion rates without the lower frequency component, it can be seen that

in particular the pitch-angle diffusion rates at lower pitch-angles are significantly increased, closing the gap to the diffusion rates at larger pitch-angles, allowing chorus waves to be effective at scattering particles over all pitch-angles for energies as high as about 1 MeV, instead of just a few hundred keV. In this energy range, this allows electrons of all pitch-angles to be diffused to lower equatorial pitch-angles and hence reach much higher latitudes during their bounce period. Consequently, they can reach the loss cone, where they can be scattered into the atmosphere and are removed from the radiation belts. Therefore it can be expected that the resulting distribution of the electron flux will most likely be decreased between 100 keV and 1 MeV, if the lower frequency components of the chorus waves are included. Furthermore, the similar increase of the energy diffusion coefficients is expected to allow for increased electron acceleration in this energy range.

## 4.6 Drift and Bounce Averaged Diffusion Rates

Most models to calculate the electron fluxes in the Earth's radiation belts, including the `BAS-RBM`, do not include a MLT resolution, and there are very few models that are able to do so. Instead, most models use diffusion rates that are drift averaged over all MLT, since drift averaged simulations are able to predict the overall shape of the pitch angle distribution accurately.

Here, the drift and bounce averaged pitch-angle diffusion rates $\langle D_{\alpha\alpha}\rangle^d$ and the drift and bounce averaged energy diffusion rates $\langle D_{EE}\rangle^d/E^2$ at a given $L^*$, geomagnetic latitude, and $AE$ were computed by adding the bounce averaged diffusion rates of all MLT sectors at the same location and dividing them by the number of MLT sectors, i.e. eight. There are gaps in the coverage of the chorus wave model at high $L^*$ of typically about $L^* > 8.5$ between 09 and 15 MLT, especially during geomagnetic active conditions. Since the drift averaging is always performed by dividing by the total number of MLT sectors instead of only the sectors that contain data, this approach is likely to underestimate the diffusion rates at very large $L^*$ and geomagnetic activities. Since the drift average approach is only valid for electron energies greater than about

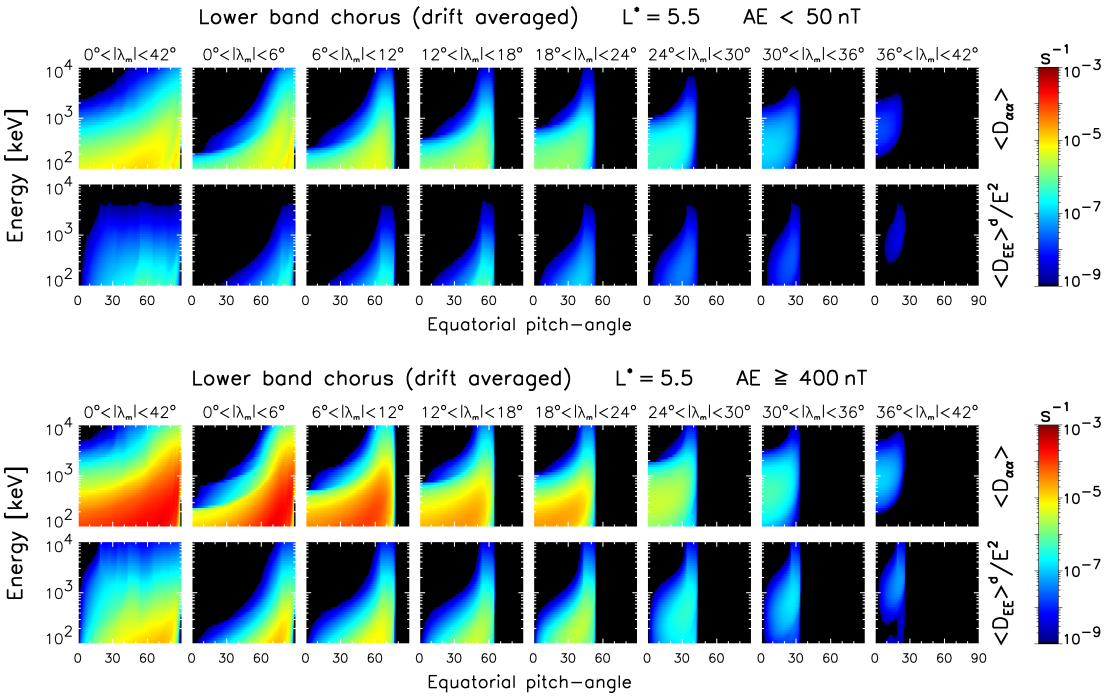


Figure 4.14: Latitudinal distribution of the drift and bounce averaged pitch-angle and energy diffusion rates of the lower band chorus of the lower frequency chorus model at $L^* = 5.5$ for $AE < 50\,\text{nT}$ (top) and $AE > 400\,\text{nT}$ (bottom). The first column shows the diffusion rates in the range of $0° < |\lambda_m| < 42°$, while the other columns show the diffusion rates at each individual 6° latitude bin, with increasing latitude from left to right.

100 keV (see Section 2.2.3), the drift and bounce averaged diffusion rates are presented only for energies between 100 keV and 10 MeV.

### 4.6.1 Latitudinal Distribution

To evaluate the influence of each contributing latitudinal sector to the drift and bounce averaged diffusion rates, the latitudinal distribution of the drift and bounce averaged pitch-angle and energy diffusion rates of the lower band chorus of the lower frequency chorus model are presented in Figure 4.14 for geomagnetic quiet and active conditions at $L^* = 5.5$. The first column shows the diffusion rates over the complete latitude range of $0° < |\lambda_m| < 42°$, while the other columns show each contributing 6° latitude sector, increasing in latitude from left to right.

The results show that the drift and bounce averaged diffusion rates are dominated by the diffusion due to waves near the equator, i.e. $0° < |\lambda_m| < 6°$ and the contribution

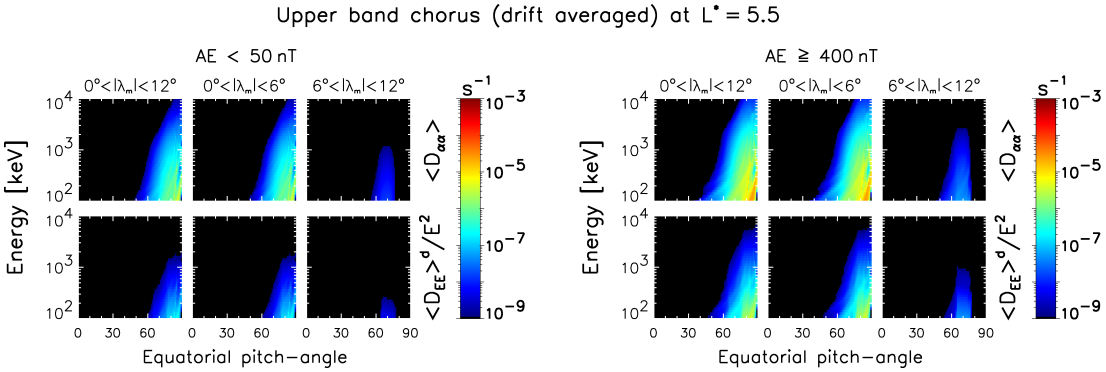


Figure 4.15: Latitudinal distribution of the drift and bounce averaged pitch-angle and energy diffusion rates of the data driven ($\delta\psi = 15°$) upper band chorus model at $L^* = 5.5$ for $AE < 50\,\text{nT}$ (left) and $AE > 400\,\text{nT}$ (right). The first column shows the diffusion rates in the range of $0° < |\lambda_m| < 12°$, the second covers $0° < |\lambda_m| < 6°$, and the third shows the diffusion rates in the range of $6° < |\lambda_m| < 12°$.

decreases with each consecutive latitude range. For latitudes greater than about 24° the diffusion rates are more than two decades lower than near the equator and for latitudes greater than 36° there is no significant pitch-angle and energy diffusion caused by lower band chorus waves. Furthermore, it can be seen that the equatorial pitch-angle range where the diffusion rates are effective decreases with latitude, which is due to the fact that electrons with a larger pitch-angles mirror at lower latitudes. While the lower band chorus waves near the geomagnetic equator cover the whole pitch-angle range, the diffusion rates at higher latitudes only extend to smaller equatorial pitch-angles, reaching as low as about 30° for $|\lambda_m| > 36°$. This suggests that pitch-angle and energy diffusion to larger pitch-angles must take place near the equator

The latitudinal distribution of the data driven ($\delta\psi = 15°$) upper band chorus wave model (Figure 4.15) shows a similar behaviour, where the strongest contribution is due to the waves near the equator. The diffusion rates calculated for $6° < |\lambda_m| < 12°$ are at least two decades lower than the diffusion rates near the equator. Therefore, these results indicate that limiting the calculations to latitudes up to 42° and 12° for lower and upper band chorus respectively is unlikely to have a noticeable effect on the drift and bounce averaged diffusion rates and hence the calculated electron fluxes.

Furthermore, it can be seen that, inside the energy range relevant for the drift averaged approach, the upper band chorus diffusion rates are only significant at large pitch-angles

and they are generally only significant in a very limited energy and pitch-angle range, compared to the lower band chorus. Hence, the electron acceleration and pitch-angle scattering are dominated by lower band chorus waves.

### 4.6.2 Combined Lower and Upper Band Diffusion Rates

The drift and bounce averaged pitch-angle and energy diffusion rates of the combined lower and upper chorus of the lower frequency chorus model are presented in Figure 4.16 for all five levels of $AE$ and for three selected $L^*$, namely $L^* = 4.5$, $L^* = 6.0$, and $L^* = 8.0$, which represent the range of $L^*$ where chorus is effective.

It can be seen that both the pitch-angle and the energy diffusion rates increase with $AE$, where peak diffusion rates are usually one to two decades higher at large geomagnetic activity compared to the peak diffusion rates at low activity. Furthermore, the diffusion rates significantly increase with $L^*$, even during geomagnetic active conditions. As a consequence, even the pitch-angle diffusion rates during quiet conditions ($AE < 50\,\mathrm{nT}$) at $L^* = 8.0$ are larger than the pitch-angle diffusion rates during active conditions ($200\,\mathrm{nT} < AE \leq 400\,\mathrm{nT}$) at $L^* = 6.0$. The pitch-angle and energy diffusion rates are generally high for $L^* > 6.0$ and even at $L^* = 4.5$ the diffusion rates are significant during active times. Since the peak in the electron phase space density is usually observed between $L^* = 4.0$ - $6.0$ [*Green and Kivelson*, 2004] this suggests that acceleration due to chorus waves play an important role in creating this peak.

For energies between a few hundred keV up to about 500 keV the pitch-angle diffusion rates are strong over all equatorial pitch-angles up to the loss cone. Hence, combined lower and upper band chorus waves will be effective at diffusing electrons of all pitch-angles into the loss cone in this energy range. For electron energies greater than about 500 keV chorus waves are only effective at larger pitch-angles, and hence electrons are unlikely to be scattered into the loss cone and electron loss should be reduced with increasing energy. Therefore, chorus waves are expected to create an energy dependent structure of the electron flux.

The drift and bounce averaged energy diffusion is generally more peaked at lower energies than the drift and bounce averaged pitch-angle diffusion rates. The peak

of $\langle D_{EE}\rangle^d/E^2$ is normally found at about 100 keV, while $\langle D_{\alpha\alpha}\rangle^d$ is peaked at about 200 keV.

Note that the contribution of the upper band chorus waves is restricted to $L^*$ less than about 6.0, because the upper band chorus wave power becomes much smaller at larger $L^*$.

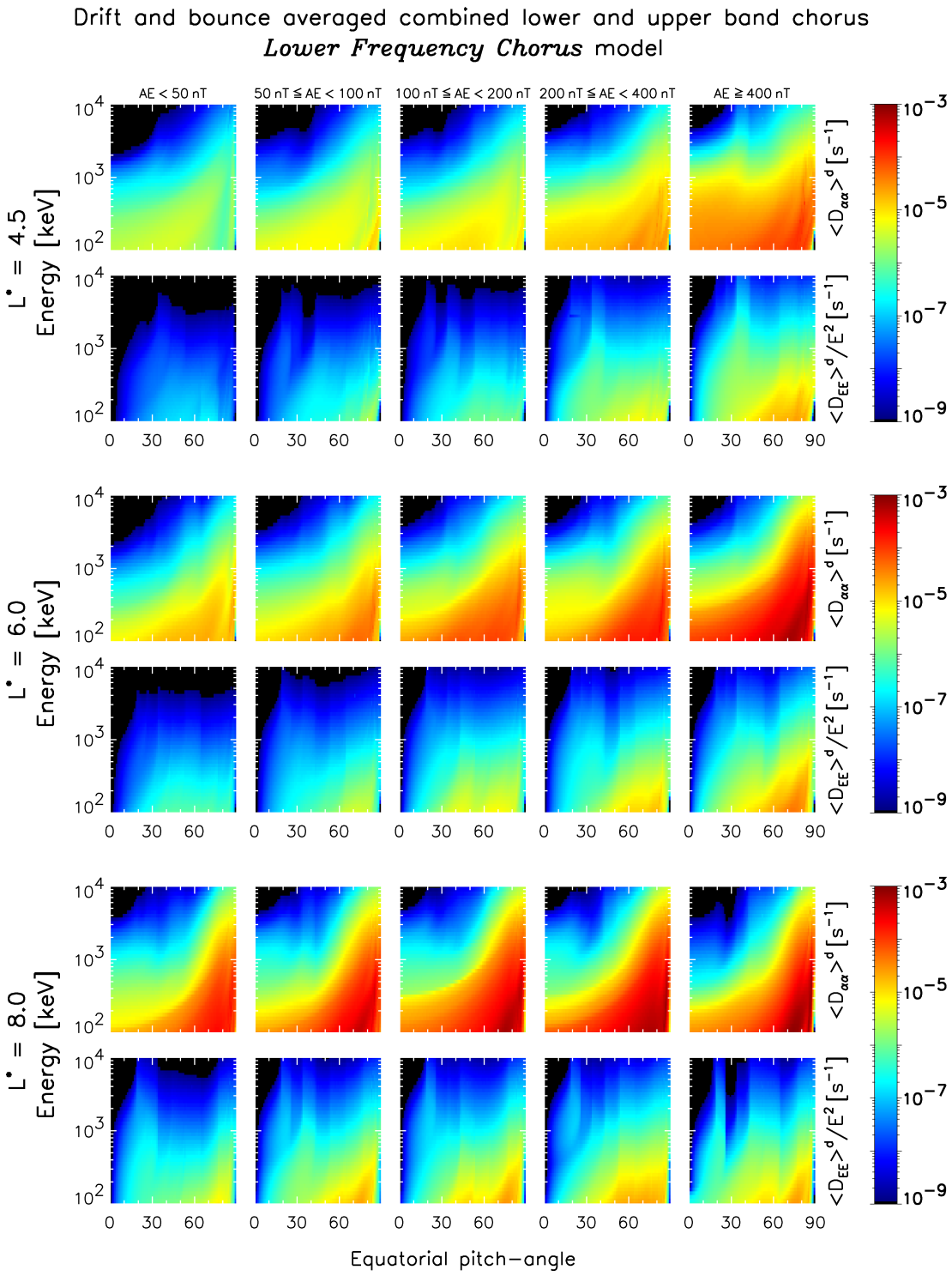


Figure 4.16: Drift and bounce averaged pitch-angle and energy diffusion rates for combined lower and upper band chorus of the *lower frequency chorus* model for five levels of $AE$ at $L^* = 4.5$, $L^* = 6.0$, and $L^* = 8.0$.

## 4.7 Global Simulations of the Electron Flux

So far the differences of the various chorus models were studied on the basis of (drift and) bounce averaged diffusion rates. It was shown that using the spectral wave data directly instead of fitting Gaussian profiles caused only minor differences in the diffusion rates. Similarly, changing the wave normal angle width had only an insignificant effect with slightly reduced pitch-angle and energy diffusion rates. Including the lower frequency chorus components however, resulted in a significant increase of the pitch-angle and energy diffusion rates at lower pitch-angles and electron energies between about 200 keV and 1 MeV, peaked around 500 keV. In order to study the influence of the lower frequency chorus component on the distribution of the electron flux on a global scale, the drift and bounce averaged diffusion rates of the *lower frequency chorus* model and the *data driven chorus* model (with $\delta\psi = 15°$) were utilised in the `BAS-RBM`. The model was run for a 100 day period in 1990 during which the boundary conditions were derived from the CRRES satellite. For the simulations a $60 \times 60 \times 60$ pitch-angle, energy, and $L^*$ grid with a timestep of 300 seconds was used. The energy ranged from $E_{min} = 153.0\,\text{keV}$ to $E_{max} = 20.0\,\text{MeV}$ at $L_{max} = 5.55$ and $L_{min} = 2.05$. In addition to the chorus diffusion rates, the model utilised the hiss diffusion rates by *Glauert et al.* [2014], which are presented in Chapter 6 (the so-called "G14 hiss model"), and the radial diffusion coefficients by *Brautigam and Albert* [2000]. The chorus and hiss diffusion rates were driven by the $AE$ index, while the radial diffusion was driven by the $Kp$ index.

Figure 4.17 shows the electron flux for electrons with an equatorial pitch-angle of 90° and an energy of 976 keV. Panel (a) shows the flux as measured by the CRRES satellite, while panel (b) shows the results of the `BAS-RBM`, using the data driven chorus model without the lower frequency chorus components included ($f_{lc} = 0.1\,f_{ce}$), and panel (c) shows the results using the data driven chorus model including the lower frequency chorus components ($f_{lc} = 0.022\,f_{ce}$). The location of the plasmapause as defined by *Carpenter and Anderson* [1992] is indicated by the white line.

The flux measured by the CRRES satellite shows small variations during the initial period near $L^* = 4$ with the slot region increasing from about $L^* = 2.5$ at the begin-

ning of the period up to about $L^* = 3.0$ at day 285. At this time a major increase of the electron flux, $AE$, and $Kp$ can be seen. The inner boundaries of the flux start to move inwards at about day 290 and the flux eventually returns back to the initial level at about day 315. Further periods of increased flux followed by a slow reduction to previous levels can be found around days 310, 315, 322, and 330, although they are less intense than the first major event. All these flux increases are driven by a rapid increase of $AE$ and $Kp$ and directly preceded by a flux dropout, where the flux is significantly reduced on a timescale of hours. Furthermore, it can be seen that each increase of the flux is associated with the plasmapause rapidly moving inwards to lower $L^*$.

The simulation results in panel (b) reproduce the general variability of the outer belt, but does not reproduce the flux dropout events mentioned before. During the beginning of the simulation period the simulation overestimates the measured fluxes, while they are similar after the first major flux increase at day 285. Comparing the results of panels (b) and (c) it can be seen that the lower frequency components of the chorus waves generally reduce the electron flux by a factor between about $2 - 4$, particularly between $L^* = 3.5 - 4.5$, and the difference decreases with increasing $L^*$.

In order to quantify the differences more accurately, the electron flux is presented for the same period as a set of line plots at constant values of $L^*$ in Figure 4.18. The CRRES data are shown as the dotted lines, while the simulations utilising the chorus model with ($f_{lc} = 0.1\, f_{ce}$) and without ($f_{lc} = 0.022\, f_{ce}$) the lower frequency chorus component are shown as the blue and red lines, respectively. The results are presented at $L^* = 3.57$, $L^* = 3.97$, and $L^* = 4.44$, in order to highlight the differences between the chorus models. The results show that during the whole simulation period the flux is decreased by a factor of about 2-4 at $L^* = 3.57$ and about 2 at $L^* = 4.44$, when the lower frequency chorus components are included in the chorus diffusion rates. The difference is created during the adjustment period of the simulation, where the model adjusts the initial state of the flux to fulfil the diffusion equation for the different chorus diffusion rates. The resulting offset after the adjustment period shows that there is a stronger net loss rate when the lower frequency chorus components are included. This could be the result of either less acceleration or stronger losses, or a combination of

the two. Since the comparison of the diffusion rates indicates that both the pitch-angle and energy diffusion rates increase it must be concluded that the net loss is the result of a comparably stronger pitch-angle diffusion. The variations of the flux in the two models during the simulation period are generally small and only have an insignificant effect on the overall difference between the two fluxes.

During the beginning of the simulation up to the first major flux increase around day 285 the flux calculated with the data driven chorus model overestimates the measured flux by up to a factor of 8 at $L^* = 3.57$ and a factor of about 2 at $L^* = 4.44$, while there is much better agreement between data and simulation if the lower frequency chorus is included. After day 285, the simulation without the lower frequency chorus agrees better with the measured flux at all $L^*$ during the flux increases, but since the loss rates are not high enough to follow the data, the flux tends to be overestimated by about a factor of 2 during the phases of decreasing flux. In these periods the simulations including the lower frequency chorus components begin to show better agreement, while they are unable to reproduce the data during the first days of a flux increase.

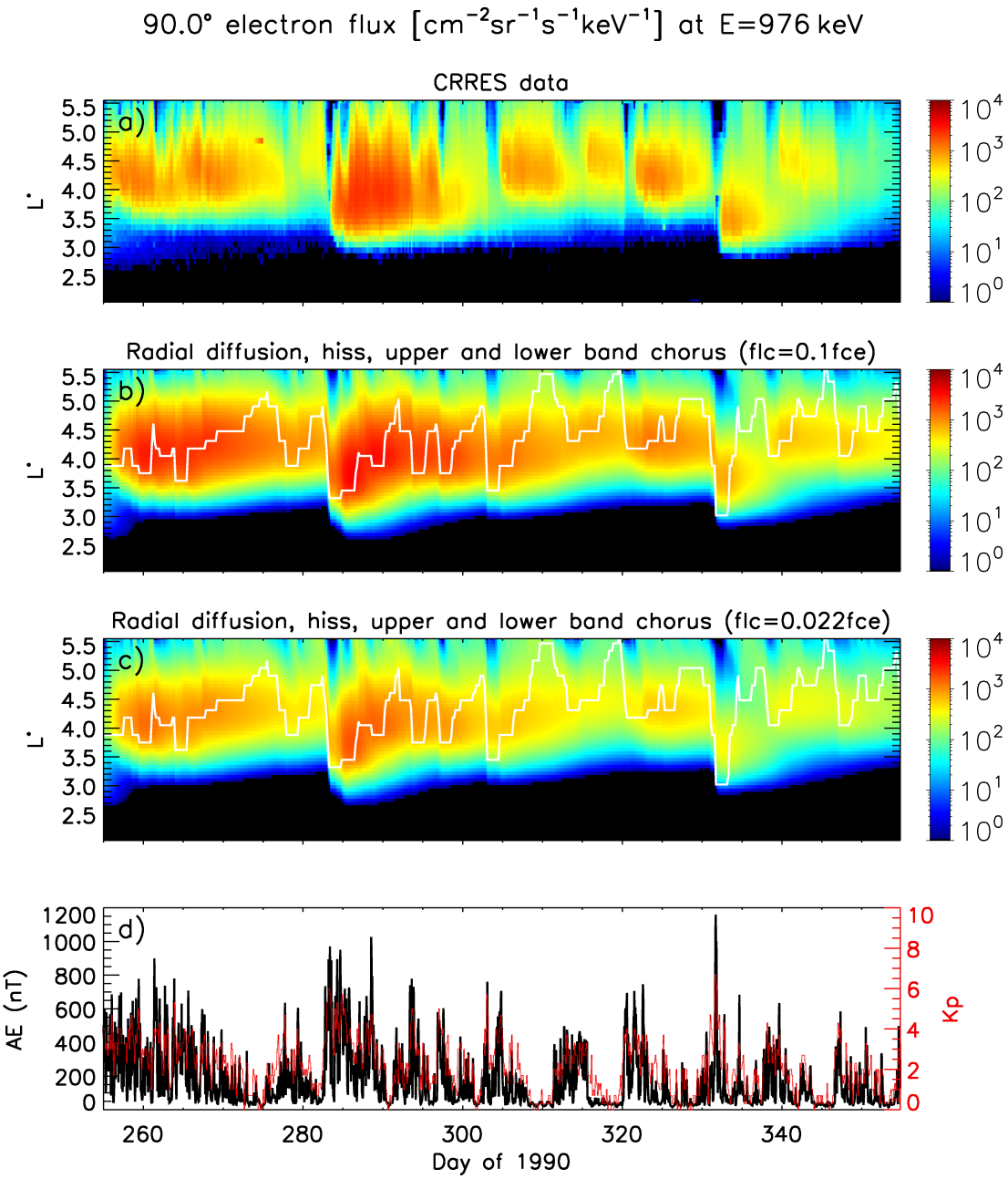


Figure 4.17: Contour plot of the flux as a function of time and $L^*$ of electrons with an equatorial pitch-angle of 90° and energy $E = 976\,\text{keV}$ (a) as measured by the CRRES satellite, and calculated by the BAS-RBM using radial diffusion, the G14 hiss model, and additionally the *data driven chorus* model including lower band chorus from (b) $0.1\,f_{ce}$ or (c) the *lower frequency chorus* model, including chorus from $0.022\,f_{ce}$. The model was driven by the $AE$ and $Kp$ indices shown in panel (d), while the white line indicates the plasmapause location as defined by *Carpenter and Anderson* [1992].

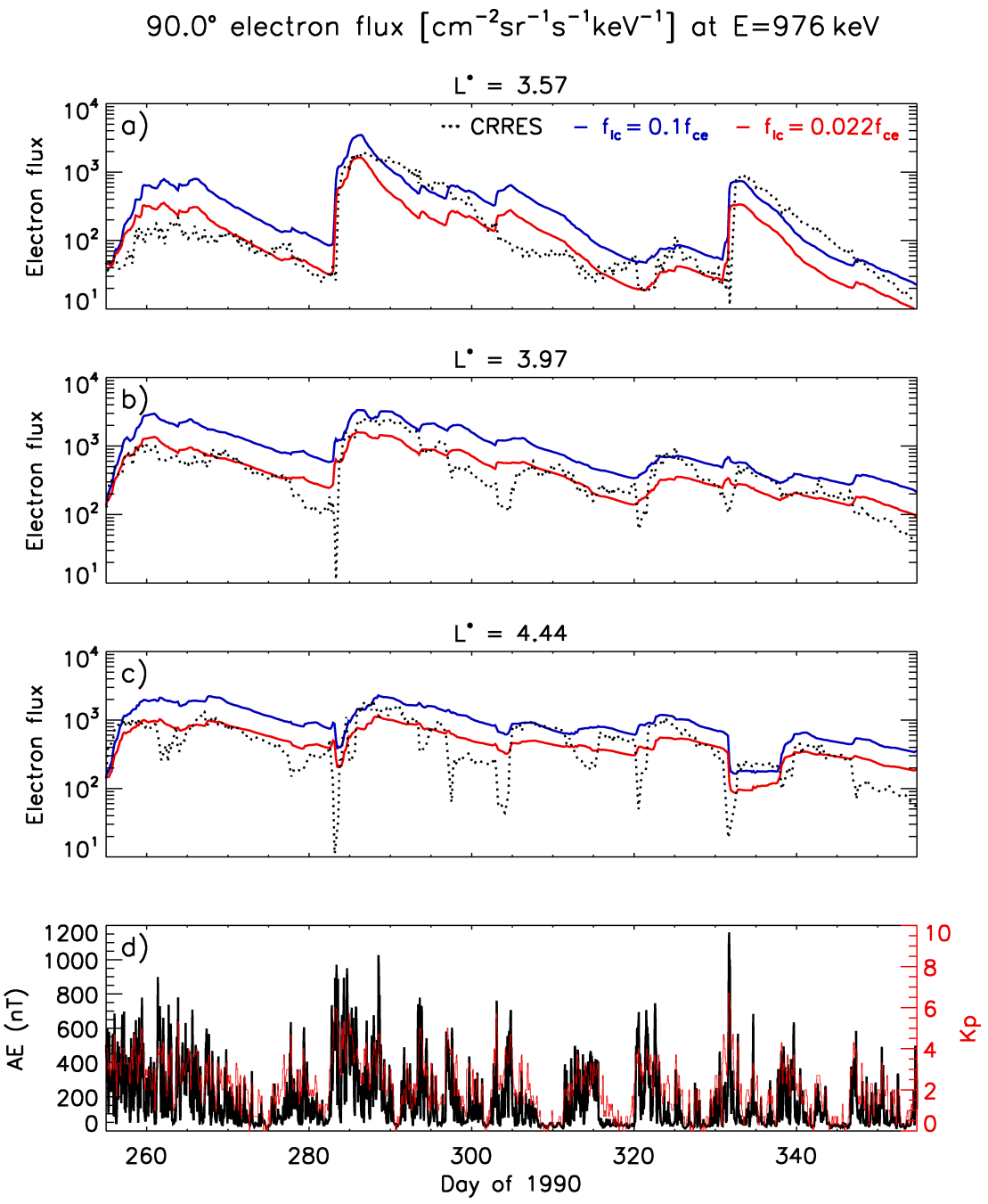


Figure 4.18: Flux of electrons with an equatorial pitch-angle of 90° and energy $E = 976\,\text{keV}$ at (a) $L^* = 3.57$, (b) $L^* = 3.97$, and (c) $L^* = 4.44$. The dotted lines show the flux as measured by the CRRES satellite, while the solid lines were calculated by the `BAS-RBM` using radial diffusion, the G14 hiss model, and additionally the *data driven chorus* model with a wave normal angle width of $\delta\psi = 15°$ including lower band chorus waves from 0.1 $f_{ce}$ (blue line) or the lower frequency chorus waves starting from 0.022 $f_{ce}$ (red line). The $AE$ and $Kp$ indices driving the model are shown in panel (d).

## 4.8 Discussion

The chorus wave models presented in this chapter were derived from the data from 7 different satellites. As these are statistical models and as such average the data into defined levels of $L^*$, MLT, geomagnetic latitude, and activity, rare and extreme events will always be averaged out and are hence not represented in statistical models. Since both the pitch-angle and energy diffusion rates tend to increase with activity, it is difficult to predict the electron flux during severe geomagnetic storms from the presented chorus models. A possible solution would be to add an additional level of geomagnetic activity above the last level ($AE > 400\,\mathrm{nT}$), in order to represent extreme events. Generally the reliability of the statistical model will increase, when the amount of data included in the model is increased, for instance by adding the VAP wave data. The comparison of the diffusion rates suggested that including the lower frequency chorus components into the 3d model should produce noticeable differences compared to simulations without the lower frequency components. However, most differences are due to the offset created during the adjustment period of the simulations, while variation between the two chorus models at later times was smaller. Nevertheless, the offset after the adjustment period shows that there is a stronger net loss rate due to increased pitch-angle diffusion when the lower frequency component is included.

There are indications that the lower frequency chorus model performs better in the regions that are inside the plasmapause, while the model without it achieves better agreement with the data outside the plasmapause. However, the provided plasmapause location is based on a crude model and in order to draw viable conclusions a more reliable model of the plasmapause needs to be included in the model first. Furthermore, the plasmapause moves close to the Earth when the geomagnetic activity is increased. Since currently the highest activity level is $AE > 400\,\mathrm{nT}$, a further refinement of the resolution of the model in terms of $AE$ might help to understand this situation. It would be interesting to investigate a chorus model that includes the lower frequency component only during the most intense storms or at lower $L^*$.

The chorus diffusion rates were calculated using quasi-linear theory since it is not yet computationally feasible to simulate chorus waves using nonlinear models over the

duration and spatial dimensions required by the `BAS-RBM`. Although chorus waves are known to be highly nonlinear due to their short-duration rising-tone frequency structure [e.g. *Omura et al.*, 2009; *Santolík et al.*, 2014a], it has been demonstrated by *Albert* [2010] and *Tao et al.* [2012] that there is remarkable agreement between fully nonlinear and quasi-linear simulations for waves with a wave power less than about 0.1 nT. Since the chorus wave power presented here only reaches this magnitude in rare cases during the highest geomagnetic activity, it can be assumed that nonlinear effects can be neglected here.

The model for the plasma density (defined by $f_{pe}/f_{ce}$) was based on the CRRES and THEMIS data within 9° of the geomagnetic equator, but used to represent the plasma density for all latitudes, since data at higher latitudes was sparse. The ratio of $f_{pe}/f_{ce}$ defines the resonant energies for wave-particle interactions and is therefore a critical parameter in determining the diffusion rates. However, since the chorus diffusion is dominated by the waves between $\lambda_m = 0°$ and about 12°, the effects of possibly different plasma densities at higher latitudes should be insignificant. An alternative would be to use published models for $f_{pe}/f_{ce}$ that are defined at higher latitudes, such as *Carpenter and Anderson* [1992], but these are based on fewer data and use fewer and different levels of geomagnetic activity. The plasma density model presented here hence provides an improvement over the other models, although limited to lower latitudes.

## 4.9 Conclusions

In this chapter novel statistical chorus wave models were developed based on the analysis of wave data from seven different satellites. The resulting models cover the range from $L^* = 2.0 - 10.0$ in steps of 0.5, the latitude range from $0° < |\lambda_m| < 42°$ in steps of 6°, and the whole MLT range in steps of 3 h for 5 levels of geomagnetic activity measured by the $AE$ index. Hence, the models extend the coverage of previous models, particularly for large $L^*$ between $L^* = 7.0 - 10.0$, for the MLT regions of the dayside, and for the various geomagnetic activities. Furthermore, these model include the upper band chorus waves, which are rarely modelled. The models themselves differed in the

way the data was evaluated, the width of the wave normal angle, and whether the lower frequency chorus components were included or not. Additionally, an improved model of the plasma density in the form of the ratio of $f_{pe}/f_{ce}$ was developed based on the CRRES and THEMIS satellite data. The plasma density is provided in the form of a statistical model in the same $L^*$, MLT, and activity region as the chorus model.

Drift and bounce averaged pitch-angle diffusion rates were calculated for each model and compared against each other. It was found that the lower band chorus is dominant at energies above about 1 keV, while upper band chorus dominated the diffusion rates below about 1 keV. In this study, the lower band chorus is therefore more relevant for the calculation of the electron flux, since this was only performed for energies greater than 100 keV. Furthermore, the latitudinal distribution showed that most diffusion takes place within about 12° of the equator. The comparison between the various models showed that the fitting process is reliable and that the diffusion rates are relatively insensitive to changes of the wave normal angle in the energy range, where the drift averaging will be performed. More importantly, it was found that including the low frequency chorus components resulted in an increase of both pitch-angle and energy diffusion predominantly at pitch-angles less than about 30°.

The most advanced chorus model with and without the lower frequency components included were then utilised in the `BAS-RBM` to study their effects on a global scale. It was found that the lower frequency chorus created a larger net loss rate compared to the model without the lower frequency component. As a result, including the lower frequency chorus at $L^* = 3.57$ achieved better agreement with the CRRES data for most times, while at larger $L^*$ either of the two models was able to reproduce the data during different times. At periods of increased geomagnetic activity including the lower frequency chorus components showed better agreement with the data, while during times of medium and low geomagnetic activity excluding these components resulted in better agreement.

Overall, the chorus models developed here provide a valuable extension of the radiation belt model, that allows to include the lower frequency chorus components into the global modelling of the electron flux.

# CHAPTER 5

# *Electromagnetic Ion Cyclotron Waves*

## 5.1 Introduction

Wave-particle interactions with electromagnetic waves with a frequency of typically a few Hertz, known as **E**lectro**m**agnetic **I**on **C**yclotron (EMIC) waves, are thought to be a significant process for electron loss at electron energies greater than about 500 keV. EMIC waves are typically separated by their frequency relative to the hydrogen, helium, and oxygen ion cyclotron frequency. *Hydrogen band EMIC waves* are electromagnetic waves with a frequency between the hydrogen ion (or proton) cyclotron frequency $f_{cp}$ and the helium ion cyclotron frequency $f_{cHe}$, *Helium band EMIC waves* are waves with a frequency between $f_{cHe}$ and the oxygen ion cyclotron frequency $f_{cO}$, while *Oxygen band EMIC waves* are waves with a frequency below $f_{cO}$ that occur very rarely and are difficult to detect against a noisy background.

This chapter presents an in depth study of the effects of EMIC waves on electron loss. It starts with a description of the EMIC wave database used to derive a model for EMIC waves, followed by an analysis of the wave properties. Diffusion rates, based on the derived model, are then presented. In order to understand the influence of the derived wave parameters, case studies are performed. The chapter concludes by using the diffusion coefficients to model global simulations of the electron fluxes and by assessing the importance of the EMIC waves on a global scale.

The EMIC wave model, diffusion rates and global simulation results presented in this chapter were published in *Kersten et al.* [2014], while the EMIC wave database, from which the EMIC wave model was derived, was published in a companion paper by *Meredith et al.* [2014].

## 5.2 EMIC Wave Data Analysis

The wave data used to derive a model for EMIC waves in this thesis is based on the three-component fluxgate magnetometer data from the CRRES satellite. CRRES was launched on 25 July 1990 into a highly elliptical ($350 \times 35,548$ km) geosynchronous transfer orbit with a low inclination of 18.1° [*Johnson and Kierein*, 1992]. It operated for about 15 months, during which it covered the range of $L^*$ from about 1.1 up to $L^* = 6$ near the equator and $L^* = 8$ at high latitudes [*Meredith et al.*, 2001]. The magnetic local times (MLT) were covered from $14 - 08$ MLT, leaving a gap of coverage between $08 - 14$ MLT. One orbit took about 10 hours, allowing for good coverage of the radiation belts during the mission period.

The fluxgate magnetometer data were analysed orbit by orbit by *Meredith et al.* [2014], providing EMIC wave spectra covering the frequency range from $0 - 8$ Hz in steps of 10 mHz. An excerpt of a typical spectrogram during a time of active EMIC waves is shown in Figure 5.1. Here the wave power spectral density in $\mathrm{nT^2Hz^{-1}}$ is plotted as a function of frequency versus time, as well as the corresponding MLT, magnetic latitude, and the calculated value of $L^*$ of the satellite's position. The solid white line denotes the proton (or hydrogen ion) cyclotron frequency, the dashed white line the helium ion cyclotron frequency, and the dashed-dotted line the oxygen ion cyclotron frequency. It can be seen that the EMIC wave events are short bursts lasting a few minutes that are well defined in the hydrogen and helium EMIC wave bands, limited by the corresponding ion cyclotron frequencies. Most detected EMIC wave events were in the range of ±20° of geomagnetic latitude.

### 5.2.1 EMIC Wave Database

In order to create the EMIC wave database, a Gaussian fit was performed for each of the 830 EMIC wave event intervals, as defined in a study by *Fraser and Nguyen* [2001], at the 25.6 s resolution of the data set. The fitted peak spectral intensity, the frequency of the peak spectral intensity (from here on referred to as the peak frequency $f_m$), the frequency width $df$, as well as the average wave intensity integrated over the wave band (also known as the wave power $B_w^2$) were stored for hydrogen and helium band EMIC

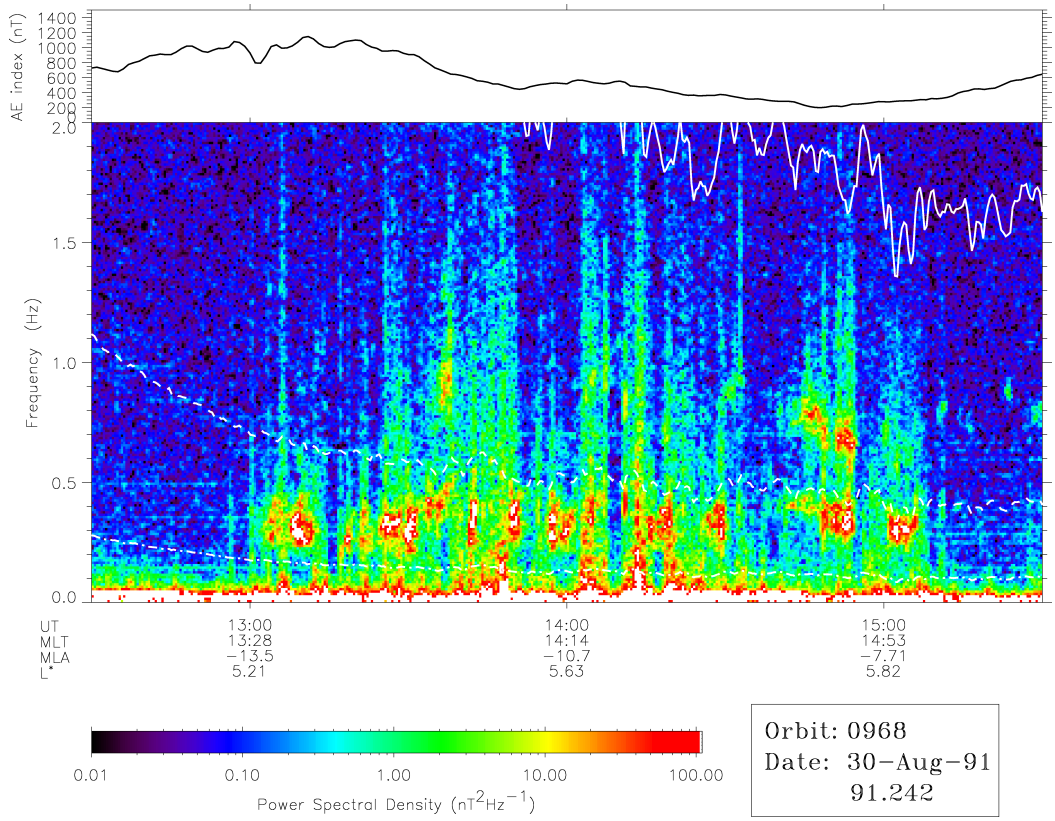


Figure 5.1: Wave power spectral density from 12:30 - 15:30 UT on 30 Aug 1991 during CRRES orbit 968 as a function of frequency and UT. The solid white line denotes the hydrogen ion cyclotron frequency, the dashed line the helium ion cyclotron frequency, and the dash-dotted line the oxygen ion cyclotron frequency, while the $AE$ index is given in the top panel. Taken from *Meredith et al.* [2014].

events separately. Due to the orbital coverage of the CRRES satellite, EMIC wave events were only found in the region between $L^* = 3.5 - 7.0$ with a gap in the pre-noon MLT sector, thereby excluding EMIC waves at higher $L^*$, as found by e.g. *Anderson et al.* [1992a] and *Usanova et al.* [2012]. For each spectral profile the satellite position in magnetic coordinates, the proton cyclotron frequency $f_{cp}$, the plasma frequency $f_{pe}$, as well as the geomagnetic activity given by the $AE$ and $Kp$ indices were stored at the 25.6 s resolution of the data set, for times when EMIC waves were present as well as times where EMIC waves were not detected.

Initially the data were arranged into 24 MLT bins, 35 bins of $L^*$ ranging from $3.5-7.0$ in steps of 0.1 $L^*$, and 5 levels of geomagnetic activity ($AE < 50$ nT, $50 \leq AE < 100$ nT, $100 \leq AE < 200$ nT, $200 \leq AE < 400$ nT, $AE \geq 400$ nT). Figures 5.2 and 5.3 show the time-averaged wave power of the hydrogen and helium band EMIC waves, respectively,

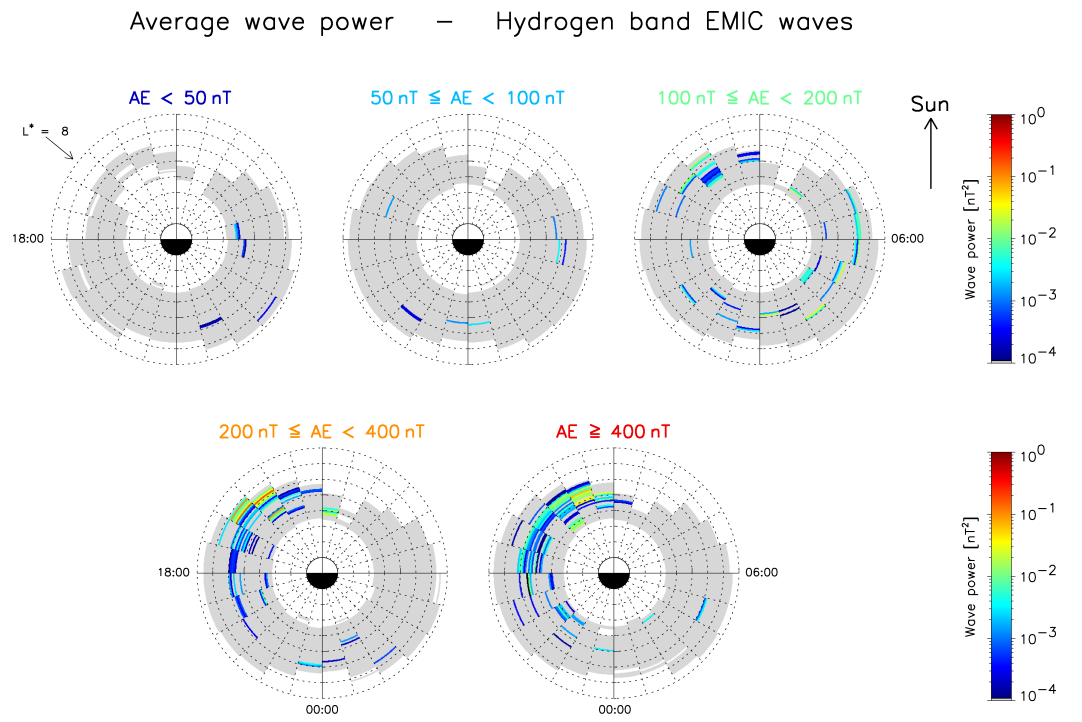


Figure 5.2: Time-averaged wave power of hydrogen band EMIC waves as measured by the CRRES satellite. Grey areas show the area covered by the satellite where no hydrogen band EMIC waves were measured.

as a function of $L^*$, MLT and $AE$. The grey areas show regions that were sampled by the CRRES satellite, but no EMIC waves were detected. Most of the strong EMIC wave events can be detected in the afternoon sector ($12-18$ MLT) with a clear increase of the wave power and occurrence rate with geomagnetic activity, for both hydrogen and helium band EMIC waves. The strongest events, with a wave power of up to about $0.5\,\mathrm{nT}^2$, occurred in the region of $5 < L^* < 6$, but EMIC wave events can be found for the whole range of $L^*$ that was covered by CRRES. The number of events outside the afternoon sector is insignificant and the corresponding wave power is weak compared to the afternoon events.

The EMIC peak power spectral density measured by the CRRES satellite ranges typically between 1 and $100\,\mathrm{nT}^2\mathrm{Hz}^{-1}$ and might also reach up to $1,000\,\mathrm{nT}^2\mathrm{Hz}^{-1}$for very strong helium band events [*Meredith et al.*, 2014], while the wave power reaches about $10\,\mathrm{nT}^2$ occasionally. Compared to a previous analysis of the AMPTE data, which found that the average power spectral density lies between 1 and $10\,\mathrm{nT}^2\mathrm{Hz}^{-1}$ and the wave power can reach up to $2.5\,\mathrm{nT}^2$ [*Anderson et al.*, 1992a,b], the values measured

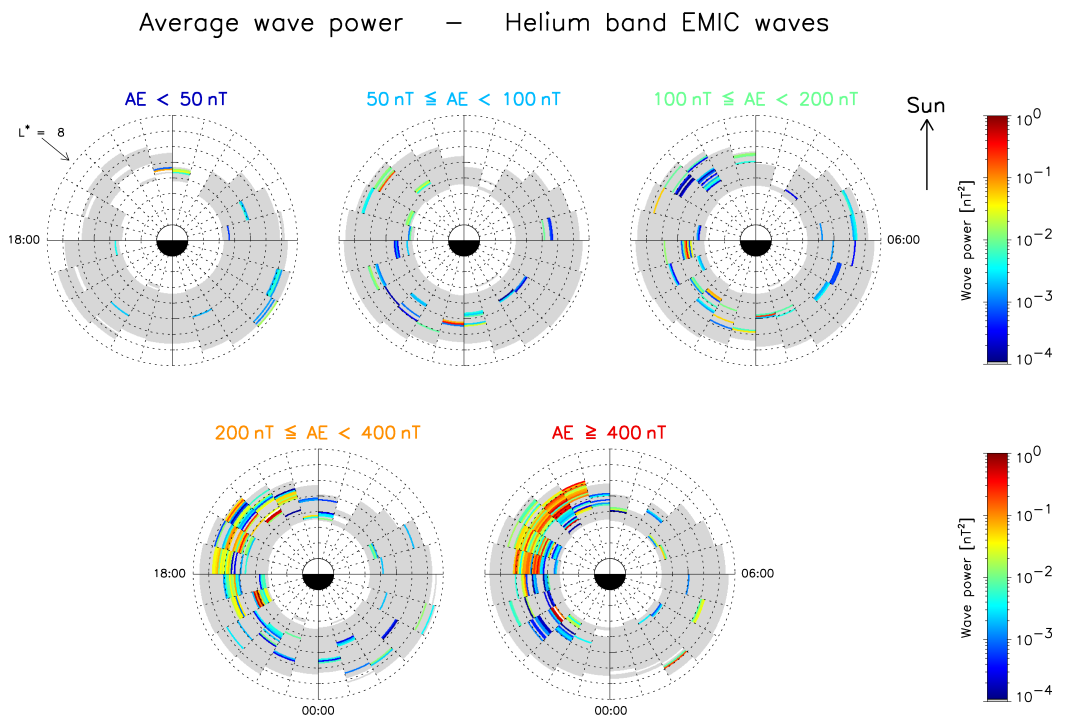


Figure 5.3: Time-averaged wave power of helium band EMIC waves as measured by the CRRES satellite. Grey areas show the area covered by the satellite where no helium band EMIC waves were measured.

by the CRRES satellite are a little larger, but generally still agree with the AMPTE observations.

### 5.2.2 Spectral Properties and Nominal Wave Model

#### Characteristic Frequencies

Since the number of detected EMIC wave events in the EMIC wave database is sparse, a statistical event based wave model as used for chorus and hiss waves is not viable. Instead, a nominal wave model for EMIC waves based on the properties stored in the global wave database is used. In order to define this model, a separate analysis of the frequency spectra of the hydrogen band and helium band EMIC waves was performed. Since EMIC waves mainly occur in the afternoon sector, only waves in this sector were taken into account, and furthermore a threshold for the peak power spectral density of $0.1\,\mathrm{nT}^2/\mathrm{Hz}$ was introduced, to only include EMIC waves of significant wave power. The normalised peak frequency $f_m/f_{cp}$, normalised frequency width $\mathrm{d}f/f_{cp}$ and the ratio of the electron plasma frequency to the electron cyclotron frequency $f_{pe}/f_{ce}$ of the EMIC

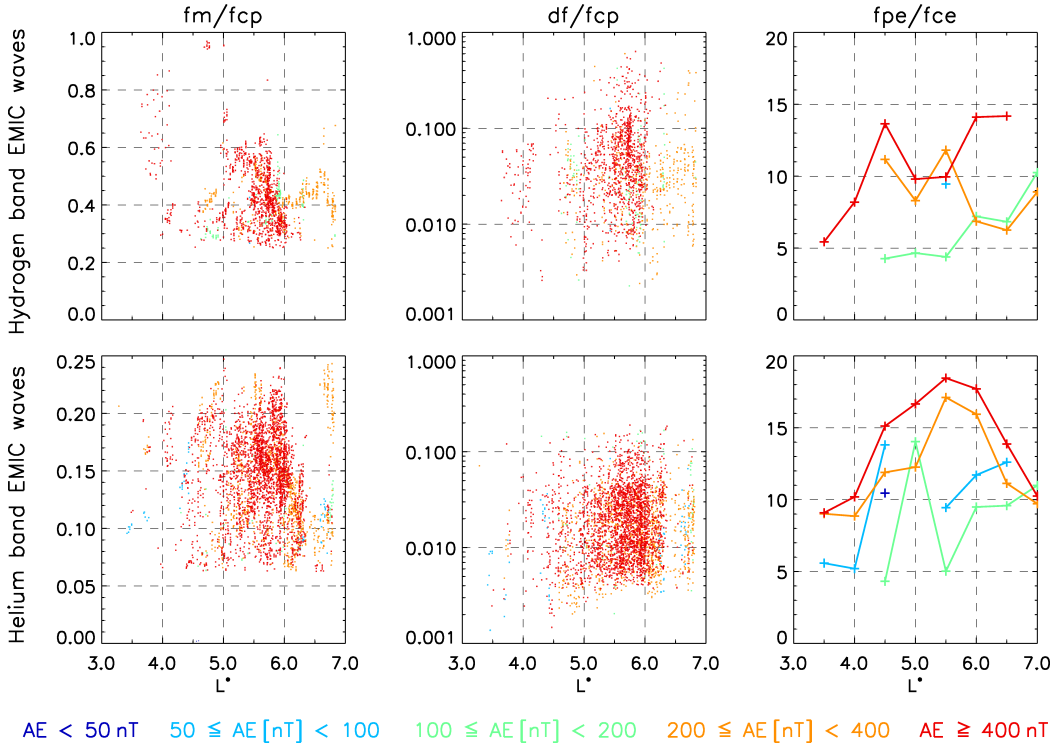


Figure 5.4: Scatterplots of the normalised peak frequency $f_m/f_{cp}$ (left column), normalised frequency width $\mathrm{d}f/f_{cp}$ (middle column), and the ratio $f_{pe}/f_{ce}$ (right column) for hydrogen band (top row) and helium band (bottom row) EMIC events with a peak power spectral density greater than $0.1\,\mathrm{nT}^2/\mathrm{Hz}$.

waves fulfilling the defined criteria are shown as scatterplots in Figure 5.4.

For hydrogen band EMIC waves the bulk of the normalised peak frequency varies from $f_m/f_{cp} \approx 0.25$ to $f_m/f_{cp} \approx 0.6$ with some outliers at larger frequencies. Most hydrogen band EMIC events can be found close to $f_m/f_{cp} = 0.4$ with no obvious trend in geomagnetic activity given by $AE$. Therefore the peak frequency of hydrogen band EMIC waves is set to $f_m/f_{cp} = 0.4$.

The bulk of the frequency width varies by an order of magnitude from $\mathrm{d}f/f_{cp} = 0.01$ to $\mathrm{d}f/f_{cp} = 0.1$ with some outliers spreading to larger and smaller frequency widths. Again, no clear trend in $AE$ can be found. Since the wave power should not extend into the cut-off frequencies (see below), a value of $\mathrm{d}f/f_{cp} = 0.02$ was be chosen for the hydrogen band EMIC wave frequency width and studies on the influence of this parameter is performed in section 5.3.3.

The frequency width of helium band EMIC waves varies on a similar scale as $\mathrm{d}f/f_{cp}$ of the hydrogen band EMIC waves and hence, the same frequency width was chosen.

The peak frequency of helium band EMIC waves varies considerably, filling the whole helium EMIC waves frequency band ($0.0625 f_{cp} \leq f \leq 0.25 f_{cp}$). In order to represent all helium band EMIC waves, the value $f_m/f_{cp} = 0.15$ was chosen for the peak frequency of helium band EMIC waves.

As described in section 2.2 `PADIE` requires a lower and upper cut-off frequency to be specified, outside which the wave power is set to zero. Since the wave power of a Gaussian spectrum falls off rapidly with frequency, the lower and upper cut-off frequencies were set to lie at twice the frequency width around the peak frequency, for each hydrogen and helium band EMIC waves individually.

#### The Ratio of $f_{pe}/f_{ce}$

As detailed in section 2.2.3, the ratio of the plasma frequency to the electron cyclotron frequency is an important parameter that defines the resonant energies at which electron diffusion are most effective. It is often used to describe the plasma density, as according to Eq. 2.21 it is proportional to the square root of the plasma density.

The right hand panels of Figure 5.4 show that $f_{pe}/f_{ce}$ varies significantly with $L^*$ and geomagnetic activity, ranging from about $5 < f_{pe}/f_{ce} < 13$ for hydrogen band EMIC wave events and $5 < f_{pe}/f_{ce} < 18$ for helium band wave events. The former are clustered around $f_{pe}/f_{ce} \approx 10$, while the latter are clustered around $f_{pe}/f_{ce} \approx 15$. The large variation is due to the low number of $f_{pe}/f_{ce}$ measurements taken during the short bursts of EMIC waves. Building a complete plasma density model for the EMIC waves is therefore not possible. Instead, a fixed value for $f_{pe}/f_{ce}$ needs to be used. Since one important part of this investigation is to study EMIC waves while chorus waves are present at the same time, the plasma densities used for EMIC waves and chorus waves need to be of the same order. The average value of $f_{pe}/f_{ce}$ in the afternoon sector outside the plasmapause was $f_{pe}/f_{ce} = 10$, which is why this value is used to model the hydrogen and helium band EMIC waves. In order to understand the effects of this generalisation, in depth studies of the influence of $f_{pe}/f_{ce}$ on the diffusion rates is performed in section 5.3.3.

### Latitudinal Distribution

It is believed that EMIC waves are generated close the geomagnetic equator by a temperature anisotropy in the energetic proton distribution of ring current ions. These EMIC waves then propagate along the magnetic field to higher latitudes. Although there have been hardly any satellite measurements of EMIC waves at latitudes above 15°, EMIC waves can be observed on the ground and hence at higher latitudes. The MLT distribution is usually similar to the one measured at lower latitudes by satellites, although there can be significant differences [*Posch et al.*, 2010].
Therefore, for the nominal model it will be assumed that EMIC waves are present at all latitudes.

### Wave Normal Angle

The wave normal angle $\psi$ is the angle between the ambient magnetic field and the wave vector $\underline{k}$ of the wave. Generally, there is very limited information about the wave normal angle of EMIC waves available. Wave polarisation experiments have shown that near the equator EMIC waves exhibit a wide range of wave normal angles. They range from left hand circularly polarised waves to highly elliptical or even linear polarised waves, with a trend to becoming more linearly polarised towards higher latitudes [*Anderson et al.*, 1992b]. This mixture of wave polarisations suggests that EMIC waves are either not strictly field aligned or that there are two distributions of EMIC waves, where the first one is field aligned and circularly polarised propagating away from the equator and the second distribution consists of EMIC waves that were reflected at high latitudes and have a large wave normal angle, which could account for the linear polarisation at the equator [*Horne and Thorne*, 1994].
The `PADIE` code assumes a Gaussian distribution in $X$, where $X = \tan\psi$. In order to model the mixture of wave normal angles of EMIC waves, the Gaussian distribution was chosen to be peaked in the field aligned direction, i.e. $X_m = \tan 0°$ with a width of $X_w = \tan 15°$. In order to include waves at larger wave normal angles, the cut-offs for the wave normal angle were set to $X_{cut} = 2X_w$. Outside of the cut-offs the wave power is set to zero.

### Ion Composition

The ion composition of the plasma through which an electromagnetic wave propagates sets limits on the characteristic wave frequencies of a multi-ion plasma. Therefore, the ion composition is a very important parameter for the modelling of EMIC waves. Unfortunately, it is extremely difficult to measure the ion composition in space, because the ion distribution is dominated by thermal ions with energies of about 1 eV. In this energy region, the plasma detectors used on satellites are hindered by problems associated with the satellites potential and by sheath effects around the satellite. Efforts to estimate an ion composition were made by *Albert* [2003] and *Summers and Thorne* [2003], who estimated both the helium fraction and oxygen fraction to lie between 5 and 10 %, while the rest are hydrogen ions. It is believed that the oxygen fraction is usually significantly lower and only reaches high fractions during very strong geomagnetic storms. During storm times the hot $O^+$ concentration might increase substantially [*Daglis et al.*, 1999] but this is beyond the scope of capability of the computational tools used in this thesis, since only cold plasma theory is used. Therefore, an oxygen fraction of 1 % $O^+$ was chosen for the nominal EMIC model.

Additionally, it is possible to estimate the helium ion concentration by using observed EMIC wave frequencies and exploiting properties of the dispersion relation. As shown in Figure 5.5 hydrogen band EMIC waves are right hand polarised for parallel propagation, if their frequency lies between the helium ion cyclotron frequency and the so-called (hydrogen) cross-over frequency $f_{cr,H^+}$ [*Horne and Thorne*, 1993], while they are left hand polarised, if their frequency lies above $f_{cr,H^+}$. Theory shows that EMIC waves are generated as left hand (circularly) polarised waves near the equator and that very high energies are required to change the polarisation [*Kozyra et al.*, 1984] and hence hydrogen band EMIC waves should very rarely be observed below $f_{cr,H^+}$. For a plasma consisting only of hydrogen and helium ions, which is a valid approximation for the case of the nominal model, the cross-over frequency can be estimated as

$$f_{cr}/f_{cp} = 1/4 \cdot \sqrt{1 + 15\eta}\,, \tag{5.1}$$

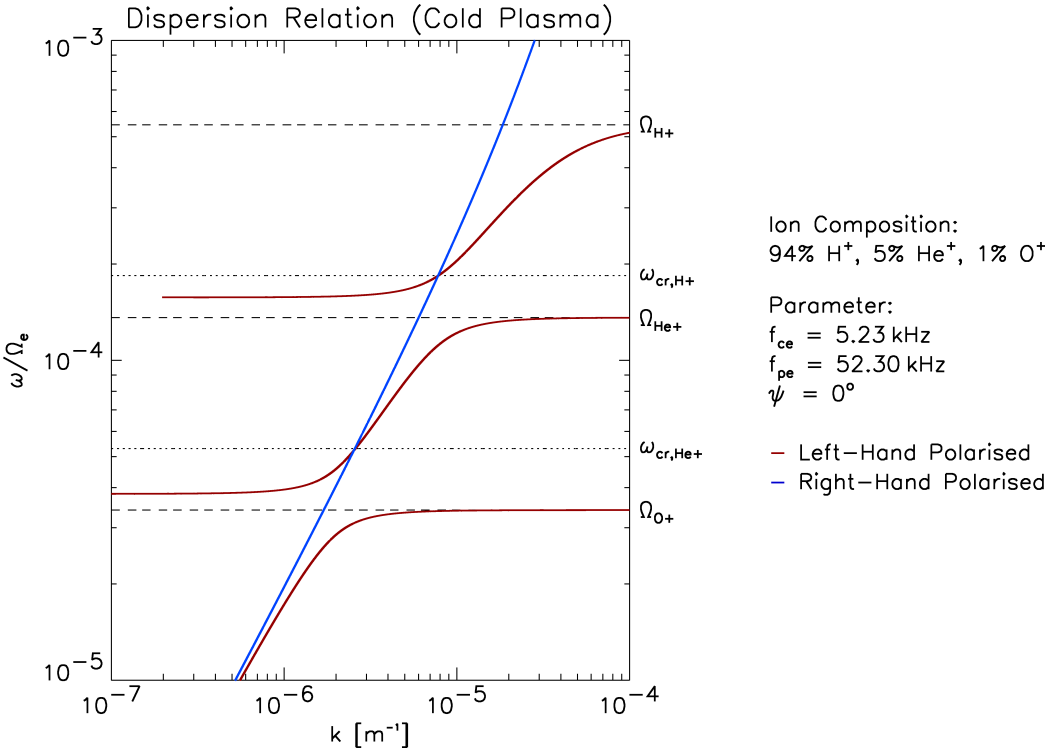


Figure 5.5: Dispersion relation of EMIC waves in a plasma containing 94 % $H^+$, 5 % $He^+$, and 1 % $O^+$. The electron gyrofrequency was set to $f_{ce} = 5230\,\text{Hz}$ and the ratio of $f_{pe}/f_{ce}$ was set to 10. The waves are completely field aligned ($\psi = 0°$).

where $\eta$ is the ratio of the helium number density to the total number density, and defines the helium fraction of a $H^+$-$He^+$ plasma. Since hydrogen band EMIC waves should not be present below $f_{cr,H^+}$, Eq. 5.1 can be used to estimate the concentration of helium ions by finding the upper limit of the frequency where EMIC waves are observed.

As shown in Figure 5.4, hydrogen band EMIC waves can be observed with peak frequencies as low as about $f_m \approx 0.28\,f_{cp}$. Taking the frequency width into account a helium fraction between 2 and 3 % can be derived from Eq. 5.1. However, most of the hydrogen band EMIC waves can be found at larger frequencies and therefore a slightly larger helium concentration must be present on average. Since the average peak frequency of hydrogen band waves lies at about $f_m = 0.4\,f_{cp}$, which corresponds to a helium concentration of about 10 %, the helium fraction must lie between $2-10$ %, with a tendency to a lower fraction. Therefore, a fraction of 5 % $He^+$ is estimated for the nominal model. As a consequence, the resulting ion composition of the nominal

| Parameter | Hydrogen band waves | Helium band waves |
|---|---|---|
| $B_W$ | $1\,\mathrm{nT}^2$ | $1\,\mathrm{nT}^2$ |
| $f_m/f_{cp}$ | 0.4 | 0.15 |
| $df/f_{cp}$ | 0.02 | 0.02 |
| $f_{lc}/f_{cp}$ | $(f_m - 2df)/f_{cp} = 0.36$ | $(f_m - 2df)/f_{cp} = 0.11$ |
| $f_{uc}/f_{cp}$ | $(f_m + 2df)/f_{cp} = 0.44$ | $(f_m + 2df)/f_{cp} = 0.19$ |
| $f_{pe}/f_{ce}$ | 10.0 | |
| $X_m$ | 0.0 | |
| $X_w$ | $\tan 15^\circ$ | |
| $X_{cut}$ | $2 \cdot X_w$ | |
| Latitude | All latitudes | |
| Resonances | $-10 \leq n \leq 10$ | |
| Ion composition | 94 % $H^+$, 5 % $He^+$, 1 % $O^+$ | |

Table 5.1: Parameters of the EMIC waves nominal model used to calculate the pitch-angle diffusion rates using `PADIE`.

EMIC model is 94 % $H^+$, 5 % $He^+$, and 1 % $O^+$.

All the parameters of the nominal model discussed here are summarised in Table 5.1. Note that for the nominal model a wave power of $B_w = 1\,\mathrm{nT}^2$ was chosen. Since the diffusion rates are proportional to $B_w^2$ the actual diffusion rates at any given location can easily be derived from the nominal model, without the need to perform the computationally expensive calculations of the diffusion rates using `PADIE` for each location. The method and model used for the wave power are detailed in the following section.

### 5.2.3 Wave Power

Since the EMIC wave data are sparse, a statistical model for each $L^*$ and MLT sector could not be developed. Instead, in order to only model the significant wave power of EMIC waves, the average wave power of each $L^*$ sector taken over the whole afternoon sector (in MLT) was used, derived for each range of $AE$ individually. During the averaging, the wave power was averaged over all times, including times where no EMIC waves were present, and hence the wave power used is significantly lower than a single event, which will in effect restrict the model to capture only average EMIC events, although sporadically short burst EMIC events exist that can cause strong diffusion even at wave powers of about $1\,\mathrm{nT}^2$ [e.g. *Summers and Thorne*, 2003]. The wave power outside the afternoon sector was set to zero, as there were hardly any EMIC events

detected in these regions.

The resulting average wave power as a function of $L^*$ is shown for the five levels of geomagnetic activity used for the model in Figure 5.6. It can be seen that the average wave intensity of hydrogen band EMIC waves is usually lower than the intensity of helium band EMIC waves. For $AE > 200\,\mathrm{nT}$, helium band waves are usually about a decade stronger than hydrogen band EMIC waves, while for $100\,\mathrm{nT} < AE < 200\,\mathrm{nT}$ the wave intensity of both types of waves are more or less the same. There is no clear trend of the average intensity with geomagnetic activity and $L^*$. The variations in $L^*$ are rather small, where the average intensity seems to be more or less constant for $L^* > 4.5$ for larger geomagnetic activity. For $AE < 100\,\mathrm{nT}$ the data above the noise level was so sparse that only a limited region in space was covered, with only one data point being left at $AE < 50\,\mathrm{nT}$. It was decided that this single data point is dropped and not used in the calculation of the diffusion rates.

Due to the way in which the wave intensity was processed, the resulting EMIC wave model has no MLT resolution and instead models the EMIC waves in the complete afternoon sector ($12 - 18\,\mathrm{MLT}$) as one sector. The intensity for the other sectors is set to zero. The wave model has 5 levels of geomagnetic activity measured by $AE$ and covers the range $L^* = 3.5 - 7.0$.

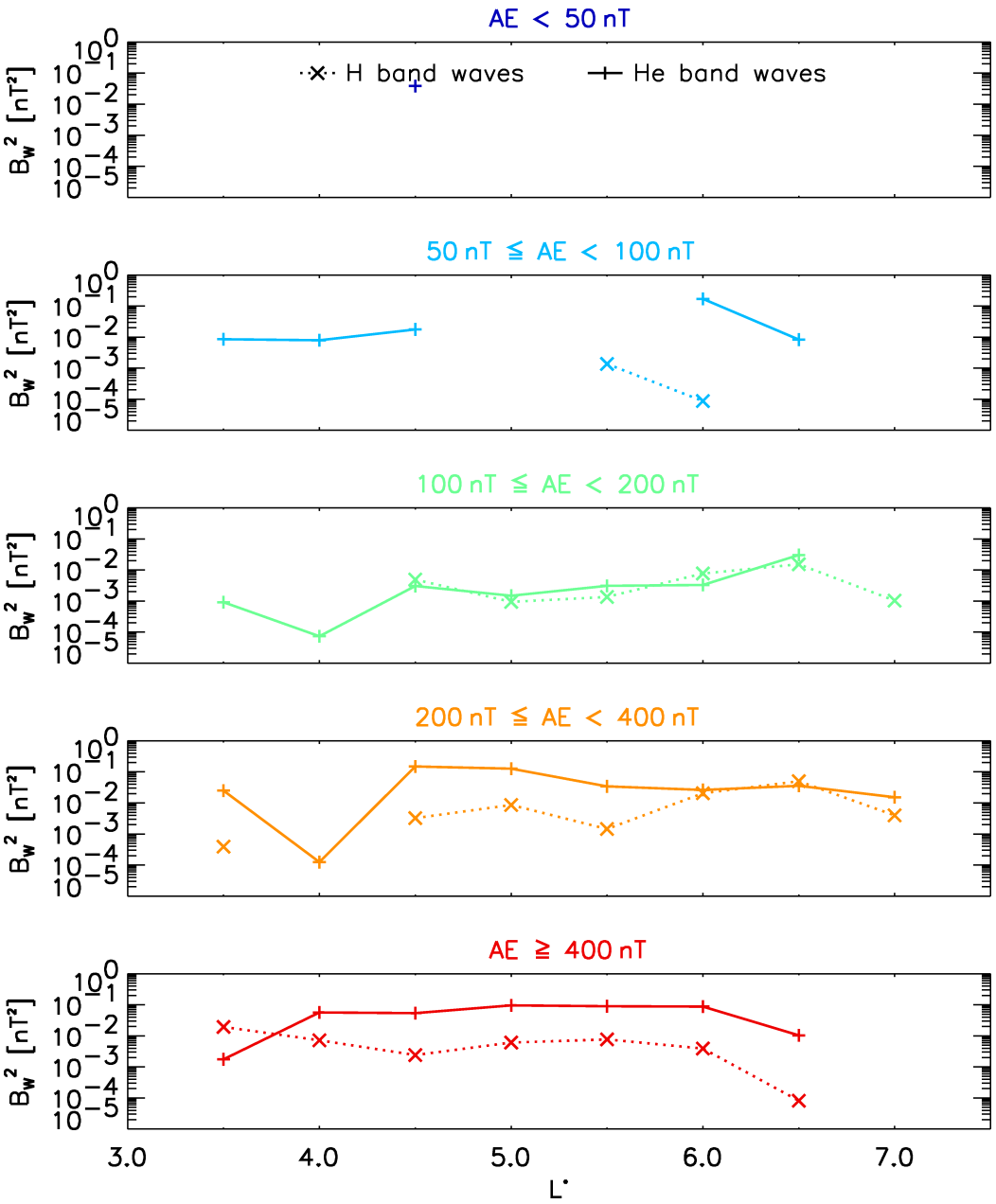


Figure 5.6: Average wave intensity used to model the EMIC waves as function of $L^*$ and $AE$. The dotted line shows the intensity of the hydrogen band EMIC waves, while the solid line shows the intensity of the helium band EMIC waves.

## 5.3 Diffusion Rates

### 5.3.1 Bounce Averaged Diffusion Rates

EMIC waves are expected to only be effective at scattering electrons into the loss cone at energies greater than a couple of MeV. In order to illustrate the dependence of the electron distribution on the EMIC wave energy, Figure 5.7 shows the bounce averaged EMIC pitch-angle diffusion rates $\langle D_{\alpha\alpha} \rangle$ for both hydrogen (left) and helium band EMIC waves (right) for $AE \geq 400\,\mathrm{nT}$ calculated using `PADIE` and the nominal EMIC wave model. Furthermore, the strong diffusion rate $D_{SD}$, as given in [*Summers and Thorne*, 2003], at an energy of 10 MeV is plotted as the dotted line. Since the diffusion rates are proportional to the wave power, the largest geomagnetic activity level ($AE \geq 400\,\mathrm{nT}$) was chosen, as the wave power is comparably strong there.

In the case of hydrogen band EMIC waves, the bounce averaged diffusion rates extend from the loss cone, which is typically located at about 4°, up to larger equatorial pitch-angles. At an energy-dependent pitch-angle the diffusion rates rapidly drop to zero. This angle increases with energy, from about 45° at 5.5 MeV to slightly above 65° at 10 MeV. Even for energies above the limit usually studied, the pitch-angle at which the diffusion rates drop to zero does not extend all the way up to 90°.

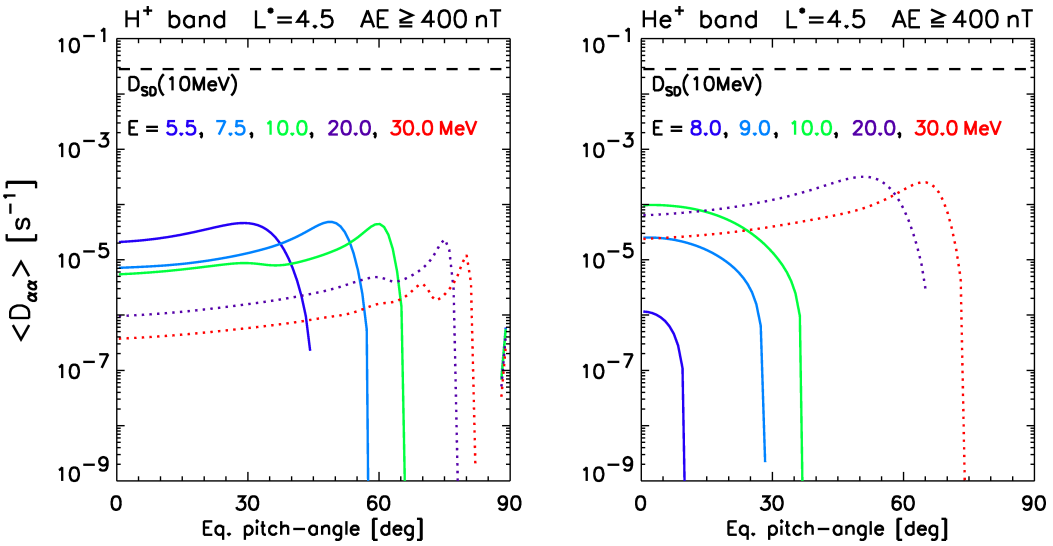


Figure 5.7: Bounce averaged pitch-angle diffusion rates as a function of the equatorial pitch-angle for hydrogen band EMIC waves (left) and helium band EMIC waves (right). The diffusion rates were calculated for different energies at $L^* = 4.5$ and $AE \geq 400\,\mathrm{nT}$ using the `PADIE` code. Also shown is the strong diffusion rate $D_{SD}$ at $E = 10\,\mathrm{MeV}$.

In contrast to the hydrogen band EMIC waves, helium band EMIC waves become effective at even larger energies, starting at about 8.0 MeV. The diffusion rates show a similar behaviour, as they are also not able to diffuse electrons with large equatorial pitch-angles. The effective pitch-angle range of helium band EMIC waves is much smaller, with the diffusion rates dropping to zero at about 35° at 10 MeV. The diffusion rates of helium band EMIC waves are peaked between 10 and 20 MeV, while the diffusion rates of hydrogen band EMIC waves peak at about 5.5 MeV.

Overall, this suggests that EMIC waves can indeed diffuse electrons into the loss cone, which are then lost into the atmosphere, but since the diffusion rates do not extend all the way to 90°, EMIC waves cannot diffuse electrons with a large pitch-angle into the loss cone. Therefore, electrons with large pitch-angles are unaffected and hence remain trapped in the magnetosphere, resulting in a so-called "pancake distribution" of the electrons. The diffusion rates of both types of EMIC waves are on average about 3 decades lower than the strong diffusion rate.

The relative importance of the pitch-angle diffusion coefficients and energy diffusion coefficients is shown in Figure 5.8. It can be seen that even at the largest energy and geomagnetic activity where the effects of EMIC waves are relatively strong, the energy diffusion rates are at least 6 decades lower than the pitch-angle diffusion rates. This suggests that there will be no significant electron acceleration caused by either hydrogen or helium band EMIC waves.

To confirm this hypothesis, Figure 5.9 shows the energy dependence of the energy diffusion coefficients for both hydrogen (left) and helium band (right) EMIC waves at $L^* = 4.5$ and $AE \geq 400$ nT. It can be seen that larger electron energies allow EMIC waves to resonate at larger pitch-angles, but they do not reach all the way up to 90°. More importantly, even the largest energy diffusion rates are insignificant compared to the pitch-angle diffusion rates, and they do not increase significantly for larger electron energies.

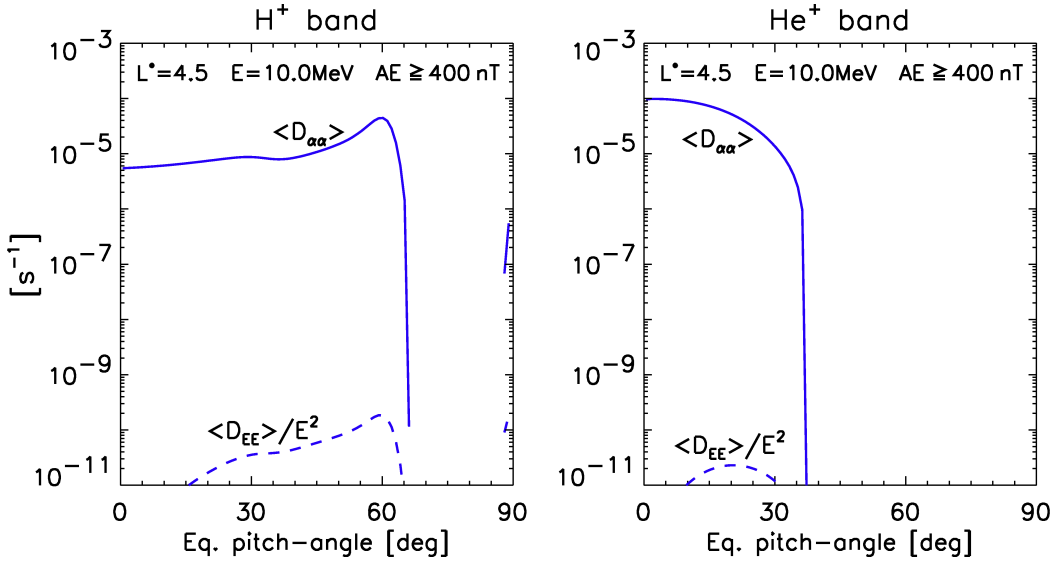


Figure 5.8: Bounce averaged pitch-angle and energy diffusion rates as a function of the equatorial pitch-angle for hydrogen band EMIC waves (left) and helium band EMIC waves (right). The diffusion rates were calculated for $E = 10\,\mathrm{MeV}$ at $L^* = 4.5$ and $AE \geq 400\,\mathrm{nT}$ using `PADIE`.

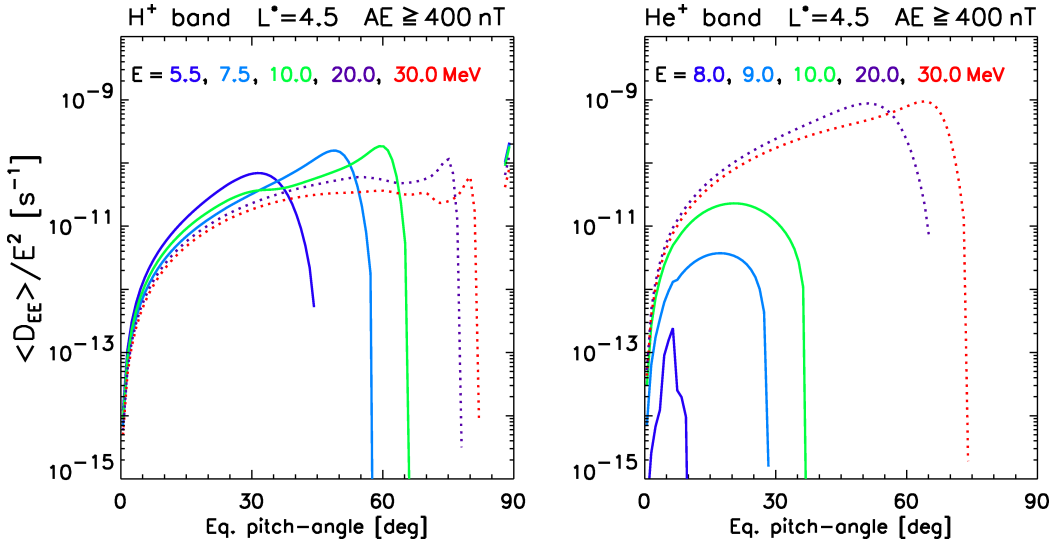


Figure 5.9: Bounce averaged energy diffusion rates as a function of the equatorial pitch-angle for hydrogen band EMIC waves (left) and helium band EMIC waves (right). The diffusion rates were calculated for different energies at $L^* = 4.5$ and $AE \geq 400\,\mathrm{nT}$ using the `PADIE` code.

### 5.3.2 Drift and Bounce Averaged Diffusion Rates

As detailed in Section 5.2.3 the presented EMIC wave model has no MLT resolution and instead covers the whole 6 h afternoon sector as one large bin. Since the wave power in the other MLT regions is set to zero, the drift and bounce averaged diffusion rates are calculated by simply dividing the bounce averaged diffusion rates of the afternoon sector by four. The drift and bounce averaged pitch-angle diffusion rates $\langle D_{\alpha\alpha}\rangle^d$ are shown in Figure 5.10 for both hydrogen (top) and helium (middle) band EMIC waves for all 5 levels of $AE$ as a contour plot as a function of the equatorial pitch-angle and all electron energy levels, ranging from 100 eV to 10 MeV. In order to assess the importance of EMIC waves compared to other loss processes, the bottom panel shows the hydrogen and helium EMIC wave diffusion rates combined with the chorus diffusion rates with a wave normal angle spread of $\delta\psi = 15°$ and including the lower frequency chorus, as presented in Chapter 4.

Naturally, the drift and bounce averaged diffusion rates show an equivalent behaviour

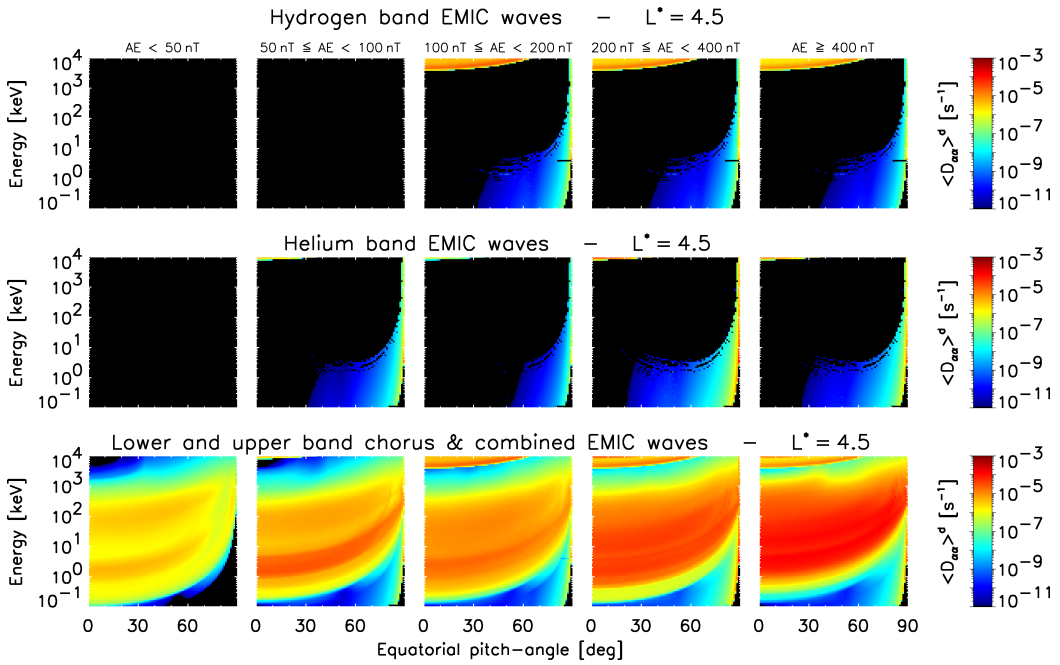


Figure 5.10: Drift and Bounce averaged pitch-angle diffusion rates for hydrogen band (top) and helium band (middle) EMIC waves at $L^* = 4.5$ for the 5 levels of geomagnetic activity used. The bottom panel shows the pitch-angle diffusion rates of hydrogen and helium band EMIC waves combined with lower and upper band chorus (including the very low frequency chorus with a wave normal angle of $\delta\psi = 15°$).

to the bounce averaged diffusion rates, since they are only scaled down by a factor of four. Overall, the most important feature of the EMIC diffusion rates is that EMIC waves only cause significant pitch-angle diffusion at energies greater than about 4 MeV. The contribution at the lower MeV energies are mainly due to hydrogen band EMIC waves, while helium band EMIC waves become important at energies of about 7 MeV. Since they only cover a narrower pitch-angle region than the hydrogen band EMIC waves, they only significantly contribute at small pitch-angles and large energies. At the selected $L^*$ the wave power of the hydrogen band EMIC waves only slightly varies with $AE$ and hence there is no clear trend in the diffusion rates with geomagnetic activity. In contrast, the pitch-angle diffusion rates caused by helium band waves increase significantly with $AE$. Since there was no wave power measured above the background level for $AE < 100$ nT for hydrogen band EMIC waves and $AE < 50$ nT for helium band EMIC waves (see Figure 5.6), there is no pitch-angle diffusion caused by EMIC waves at these activity levels.

Additionally there is pitch-angle diffusion caused at lower electron energies that extend from very close to 90° at large energies down to pitch-angles as low as about 30° for electron energies lower than about 5 keV. At these low energies the diffusion rates cover a wide range of pitch-angles but do not extend up to 90° anymore. More importantly, the diffusion rates are only significantly strong at a very narrow pitch-angle range of a few degrees.

In contrast to the EMIC waves, the diffusion rates caused by lower and upper band chorus are present at all pitch-angles and cover a wide range of energies, except very large energies and small pitch-angles, which is the region that is dominated by the effects of the EMIC waves. Generally the pitch-angle diffusion rates caused by chorus are between one and two decades larger than the one caused by EMIC waves. It can be seen that chorus diffusion rates generally fill the areas where EMIC waves are ineffective and hence EMIC waves complement the chorus waves allowing diffusion of particles at a wide range of energies and all pitch-angles.

The energy diffusion due to EMIC waves, and combined chorus and EMIC waves are shown in Figure 5.11. As expected, there is no significant energy diffusion caused by

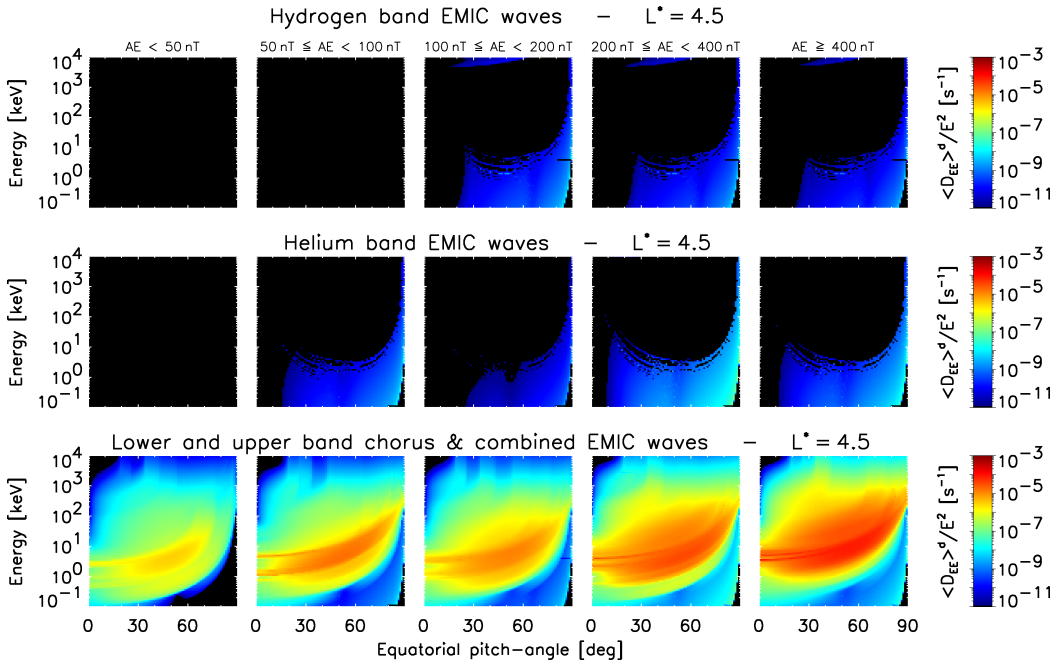


Figure 5.11: Drift and Bounce averaged energy diffusion rates for hydrogen band (top) and helium band (middle) EMIC waves at $L^* = 4.5$ for the 5 levels of geomagnetic activity used. The bottom panel shows the energy diffusion rates of hydrogen and helium band EMIC waves combined with lower and upper band chorus (including the very low frequency chorus with a wave normal angle of $\delta\psi = 15°$).

neither hydrogen nor helium band EMIC waves. When compared to the energy diffusion caused by lower and upper band chorus, the EMIC energy diffusion is negligible. Therefore, it is highly unlikely that EMIC waves are able to accelerate electrons at any energies or pitch-angles.

### 5.3.3 Parameter Studies

The spectral properties of the EMIC waves are important parameters that determine the minimum energy at which electrons can resonate with the waves. This can be shown theoretically by using the resonance condition (see section 1.6.1), which was derived as (Eq. 1.131)

$$v_{\shortparallel} = \frac{\omega}{k_{\shortparallel}} \left(1 - \frac{n\Omega_\sigma}{\gamma\omega}\right) . \tag{5.2}$$

In the case of wave resonance with an electron, $\Omega_\sigma$ is the electron cyclotron frequency, i.e. $\Omega_\sigma = \Omega_e = eB/m$. The frequency of EMIC waves is roughly of the order of the

hydrogen ion cyclotron frequency $\Omega_{cH}$ which is much smaller than the electron cyclotron frequency, i.e. $\omega \approx \Omega_{cH} \ll \Omega_e$. Using this approximation for mildly relativistic electrons ($\gamma \approx 1$) and the dominant resonance number $n = \pm 1$ it directly follows that

$$\frac{n\Omega_e}{\gamma\omega} \gg 1\,. \tag{5.3}$$

Therefore the resonance condition for EMIC waves with electrons can be approximated by

$$v_{\shortparallel} \approx \frac{\omega}{k_{\shortparallel}} \left( \frac{n\Omega_e}{\gamma\omega} \right) \approx \frac{n\Omega_e}{k_{\shortparallel}\gamma}\,. \tag{5.4}$$

From the dispersion relation it can be seen that an increase of the wave frequency $\omega$ results in an increase of $k_{\shortparallel}$, and according to Eq. 5.4 a decrease of $v_{\shortparallel}$. Thus the minimum resonant energy is reduced, and the waves are therefore able to diffuse electrons at lower energies, resulting in increased diffusion rates at lower electron energies.

Equivalently, an increase of the ratio $f_{pe}/f_{ce}$ reduces the phase velocity $\omega/k_{\shortparallel}$. Therefore, an increase of the plasma density causes waves at a given frequency $\omega$ to be able to resonate with electrons of lower energies, since an increase of $f_{pe}/f_{ce}$ results in an increase of $k_{\shortparallel}$ and hence decrease of $v_{\shortparallel}$.

Therefore, the spectral properties of the Gaussian distribution of the EMIC waves, as well as the ratio $f_{pe}/f_{ce}$ are vital in defining the minimum resonant energies of EMIC waves. Since these parameters had to be set to average values for the nominal model, although the underlying data varied significantly, case studies of the influence of these parameters are presented here. The spectral properties are determined by the Gaussian profile of the wave model, defined by the peak frequency, the frequency width and the lower and upper cutoff frequencies, outside which the wave power is set to zero.

As shown in the previous sections, the (drift and) bounce averaged energy diffusion rates caused by hydrogen and helium band EMIC waves are insignificant compared to the pitch-angle diffusion rates as well as the diffusion rates caused by chorus waves and hence unlikely to cause any significant energy diffusion. Therefore, the case studies are be presented for the pitch-angle diffusion rates.

### Peak Frequency

The peak frequency $f_m$ specifies the peak of the wave power spectral density, which is then distributed in a Gaussian form defined by the frequency width. The dependence of the bounce-averaged pitch-angle diffusion coefficients on the peak frequency is shown in Figure 5.12 for hydrogen band (left) and helium band EMIC waves (right). The diffusion rates were calculated at a representative value of $L^* = 4.5$, and at the largest geomagnetic activity ($AE \geq 400\,\mathrm{nT}$), as well as the highest energy value used in the model ($E = 10\,\mathrm{MeV}$). The pitch-angle diffusion rates of both wave bands show a clear increase of the maximum equatorial pitch-angle at which the EMIC waves are still effective. For hydrogen band EMIC waves the maximum pitch-angle at which diffusion is still possible increases from about 45° at $f_m = 0.30\,f_{cp}$ to about 75° at $f_m = 0.55\,f_{cp}$. The maximum pitch-angle diffusion rate and the overall shape are unaffected by the change of the peak frequency, only the position in pitch-angle of the peak of the diffusion rates moves towards larger pitch-angles. Hence, using a larger peak frequency in the nominal model for the hydrogen band EMIC waves allows hydrogen band EMIC waves to be effective up to slightly larger pitch-angles, while still not covering the whole pitch-angle range.

In the case of helium band EMIC waves it can be seen that the peak frequency of the nominal model is the lowest peak frequency that produces significant pitch-angle diffusion. In contrast to the hydrogen band EMIC waves, the peak of the helium band pitch-angle diffusion rates increases by about a factor of 5 at larger peak frequencies than the one used in the nominal model. The equatorial pitch-angle at which the pitch-angle diffusion rates drop to zero increases from about 36° at $f_m = 0.15\,f_{cp}$ up to about 79° at $f_m = 0.225\,f_{cp}$.

Therefore, the peak frequency chosen for the nominal model of helium band EMIC waves might underestimate the effects of helium band EMIC waves at larger pitch-angles. Since the presented model was built on a statistical evaluation of the data, it is therefore only able to represent an average case of helium band EMIC waves and the diffusion rates of some events with a larger peak frequency could be increased significantly at larger pitch-angles. Nevertheless, helium band EMIC waves are still

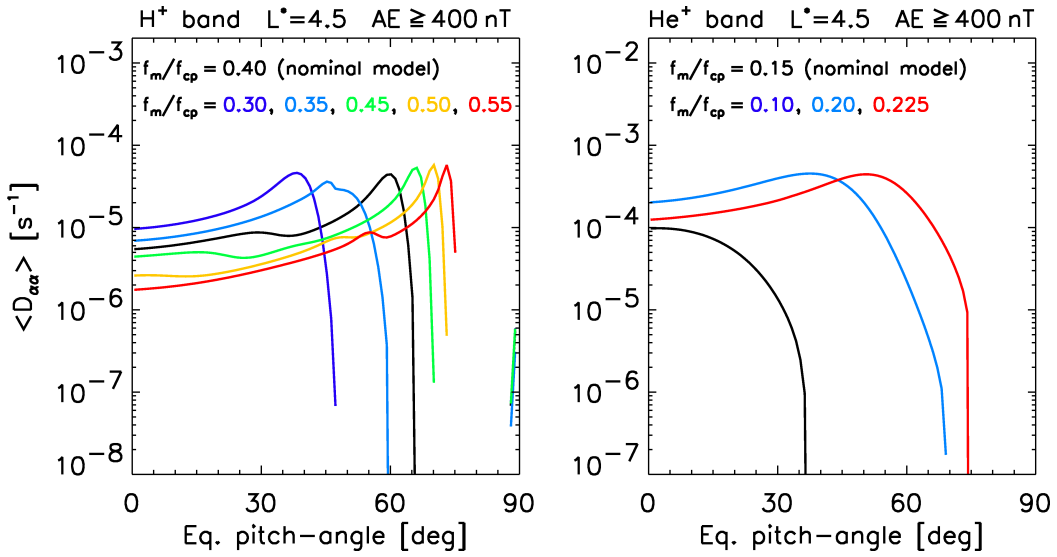


Figure 5.12: Bounce-averaged pitch-angle diffusion rates for hydrogen band (left) and helium band (right) EMIC waves at an electron energy of $E = 10\,\text{MeV}$ for a variable peak frequency $f_m$. All other parameters are the same as the one of the nominal model. The wave power has been set to the value corresponding to $L^* = 4,5$ and $AE \geq 400\,\text{nT}$.

unable to cover the whole pitch-angle range using a large peak frequency and are therefore not able to diffuse all particles into the loss cone.

To assess the influence of the peak frequency on the minimum energy at which EMIC waves can be effective at scattering electrons into the loss cone, Figure 5.13 shows the pitch-angle rates for a variety of energies using the highest peak frequency of the previous studies ($f_m = 0.55$ and $f_m = 0.225$) for both hydrogen (left) and helium band EMIC waves (right). It can be seen that setting the peak of the wave power to very large frequencies allows both hydrogen and helium band EMIC waves to become effective at energies as low as about 3 MeV, but not at lower electron energies, suggesting that even an extreme value of $f_m$ does not enable EMIC waves to resonate with electrons at lower energies.

### Frequency Width

In the nominal model the EMIC wave power spectral density is distributed in a Gaussian form, which is defined by the peak frequency $f_m$ and the frequency width $df$ of the Gaussian distribution. The frequency width determines how quickly the wave power is reduced from its peak value at the peak frequency. Since the width varies significantly

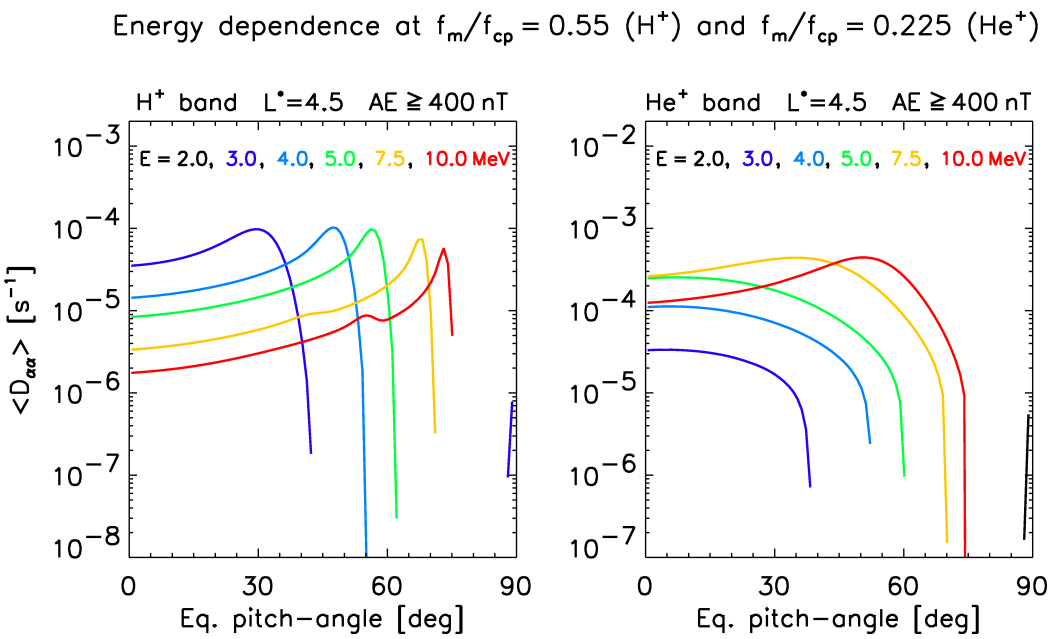


Figure 5.13: Bounce-averaged pitch-angle diffusion rates for hydrogen band (left) and helium band (right) EMIC waves for various electron energies at a peak frequency of $f_m = 0.55 f_{cp}$ and $f_m = 0.225 f_{cp}$, respectively. All other parameters are the same as the one of the nominal model. The wave power has been set to the value corresponding to $L^* = 4, 5$ and $AE \geq 400\,\mathrm{nT}$

for EMIC wave events, this section studies the influence of the frequency width on the pitch-angle and energy diffusion coefficients. The wave power of an EMIC wave must lie between the corresponding ion cyclotron frequencies and since the peak frequency has been set to average values in the centre of the bands for the nominal model, only frequency widths that allow the wave power to tail off within these frequency bands are studied here, namely $df = 0.01\, f_{cp}$, $df = 0.03\, f_{cp}$, $df = 0.04\, f_{cp}$, and $df = 0.02\, f_{cp}$, which is the value used in the nominal model.

The results of these studies are shown in Figure 5.14 for hydrogen band (left) and helium band EMIC waves (right). It can be seen that for hydrogen band EMIC waves the pitch-angle diffusion rates are only affected to a minor degree. The peak of diffusion rate is located at the same equatorial pitch-angle and the diffusion rates decrease by about a factor of five close to the peak for increasing frequency width, while the maximum pitch-angle at which the hydrogen band EMIC waves are still effective is varying by a few degrees.

In contrast, changing the frequency width for the helium band EMIC waves causes

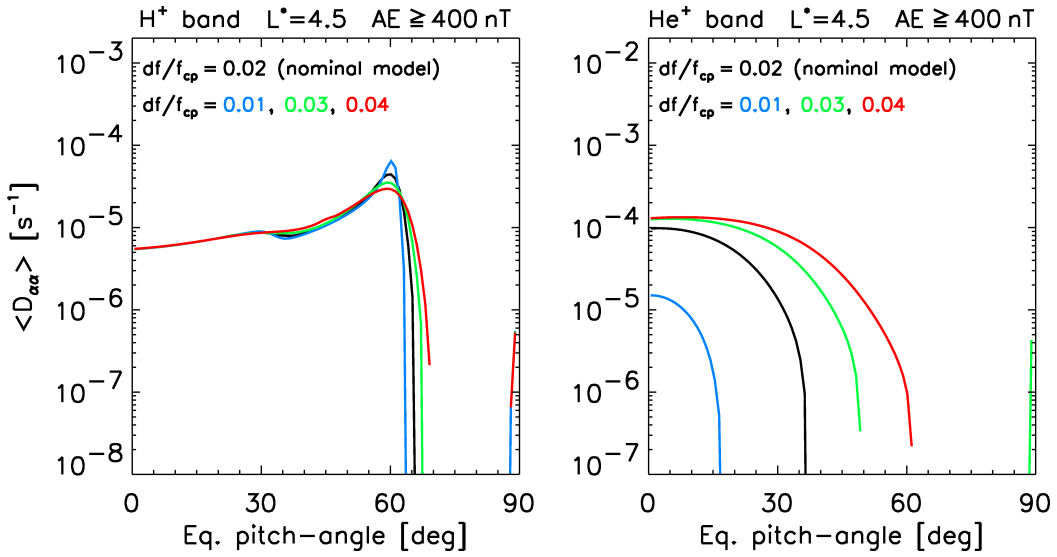


Figure 5.14: Bounce-averaged pitch-angle diffusion rates for hydrogen band (left) and helium band (right) EMIC waves at an electron energy of $E = 10\,\mathrm{MeV}$ for a variable frequency width $df$. All other parameters are the same as the one of the nominal model. The wave power has been set to the value corresponding to $L^* = 4,5$ and $AE \geq 400\,\mathrm{nT}$.

large changes of the pitch-angle diffusion rates. They increase up to a decade when the frequency width is increased from $df = 0.01\,f_{cp}$ to the value of the nominal model ($df = 0.02\,f_{cp}$), with only minor increases of the diffusion rates at larger frequency widths. The angle at which the pitch-angle diffusion rate drops to zero also depends strongly on the frequency width, increasing from about 16° at $df = 0.01\,f_{cp}$ up to about 61° at $df = 0.04\,f_{cp}$.

The energy dependence of the pitch-angle diffusion rates for hydrogen and helium band EMIC waves in the case of a very wide frequency distribution ($df = 0.04\,f_{cp}$) is shown in Figure 5.15. It can be seen that the minimum effective energy for hydrogen band EMIC waves is at a value of about 4 MeV, while the minimum energy at which helium band EMIC waves can be effective about 5 MeV, where the pitch-angle diffusion rates start to become effective at low pitch-angles.

Overall, these results show that the frequency width can be an important parameter, but only if the peak frequency is close to the ion cyclotron frequencies, in which case a wider Gaussian frequency distribution of the wave power shows significant effects.

As a last study of the frequency distribution of the wave power, the two cases showing the strongest effects on the diffusion rates are combined, namely a frequency width of

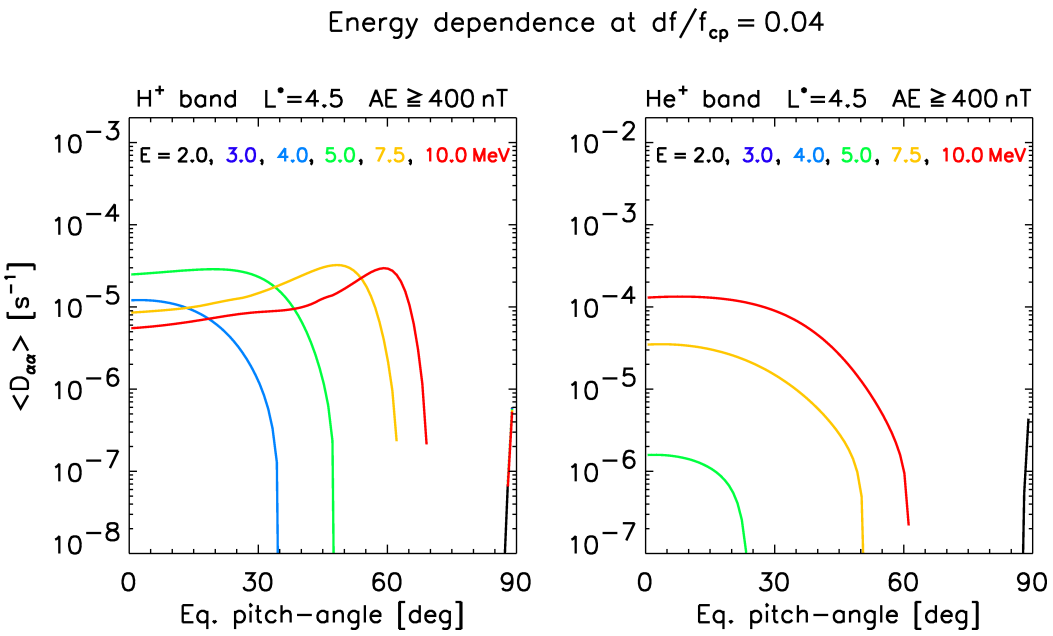


Figure 5.15: Bounce-averaged pitch-angle diffusion rates for hydrogen band (left) and helium band (right) EMIC waves for various electron energies at a frequency width of $df = 0.04 f_{cp}$. All other parameters are the same as the one of the nominal model. The wave power has been set to the value corresponding to $L^* = 4,5$ and $AE \geq 400\,\mathrm{nT}$.

$df = 0.04\, f_{cp}$, and the largest peak frequency for hydrogen and helium band EMIC waves, $f_m = 0.55\, f_{cp}$ and $f_m = 0.225\, f_{cp}$, respectively. The results are shown in Figure 5.16 as a function of energy. Setting these maximum values allows hydrogen band and helium band EMIC waves to become effective at electron energies as low as about 2 MeV and 3 MeV, respectively. Since this is an extreme case modelling an highly unlikely event, EMIC waves usually won't reach such low energies and these values therefore define a lower boundary for very extreme cases of EMIC wave events.

### Cut-Off Frequency

The lower and upper cut-off frequencies of the Gaussian distribution were set to $2 \cdot df$ in the nominal model in order to include most of the wave power. *Li et al.* [2014] and *Ukhorskiy et al.* [2010] have shown that the upper cut-off frequency $f_{uc}$ is an important parameter for the scattering of electrons, as wave power close to the hydrogen or helium ion cyclotron frequency is known to be able to cause significant diffusion rates. Since this parameter was not taken from CRRES measurements in the nominal model, additional tests of the upper cut-off frequency are performed here.

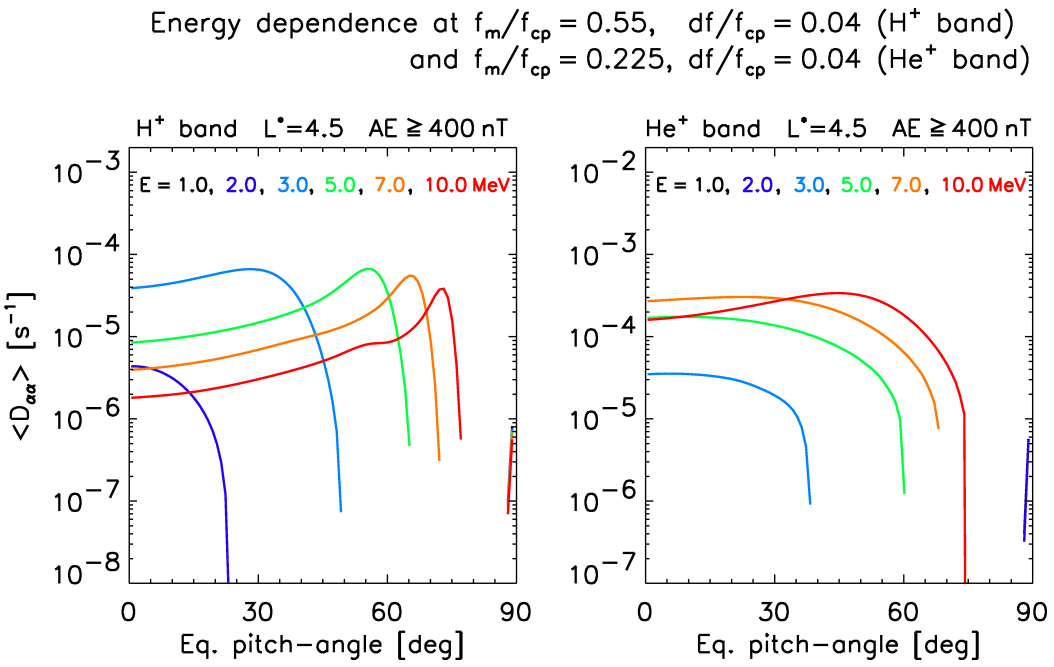


Figure 5.16: Bounce-averaged pitch-angle diffusion rates for hydrogen band (left) and helium band (right) EMIC waves for various electron energies at the maximum peak frequency ($f_m = 0.55\, f_{cp}$ and $f_m = 0.225\, f_{cp}$) and frequency width of $df = 0.04 f_{cp}$. All other parameters are the same as the one of the nominal model. The wave power has been set to the value corresponding to $L^* = 4, 5$ and $AE \geq 400\,\mathrm{nT}$.

For the hydrogen band EMIC waves the upper cut-off frequency was varied between $f_{uc} = 0.41\, f_{cp}$ and $f_{uc} = 0.50\, f_{cp}$, where the latter corresponds to $5 \cdot df$ at which point the wave power is significantly lower than at the peak. In the case of helium band EMIC waves, $f_{uc}$ was varied between $f_{uc} = 0.16\, f_{cp}$ and $f_{uc} = 0.24\, f_{cp}$, where the latter allows wave power very close to the helium ion cyclotron frequency $f_{cHe} = 0.25 f_{cp}$. The resulting pitch-angle diffusion rates are shown in Figure 5.17 for an electron energy of $E = 10\,\mathrm{MeV}$ at $L^* = 4, 5$ and $AE \geq 400\,\mathrm{nT}$. It can be seen that in the case of hydrogen band EMIC waves the effect of an increased upper cut-off frequency is marginal, while in the case of helium band EMIC waves the pitch-angle diffusion rates extend to larger pitch-angles when the upper cut-off frequency is increased. While the diffusion rate drops to zero close to 16° for $f_{uc} = 0.16\, f_{cp}$ it extends to about 46° for $f_{uc} = 0.24\, f_{cp}$, and drops to zero near 36° for the value used in the nominal model ($f_{uc} = 0.19\, f_{cp}$). Overall these results show that the choice for the upper cut-off frequency of the nominal model was sufficient to capture the effects of both hydrogen and helium band EMIC

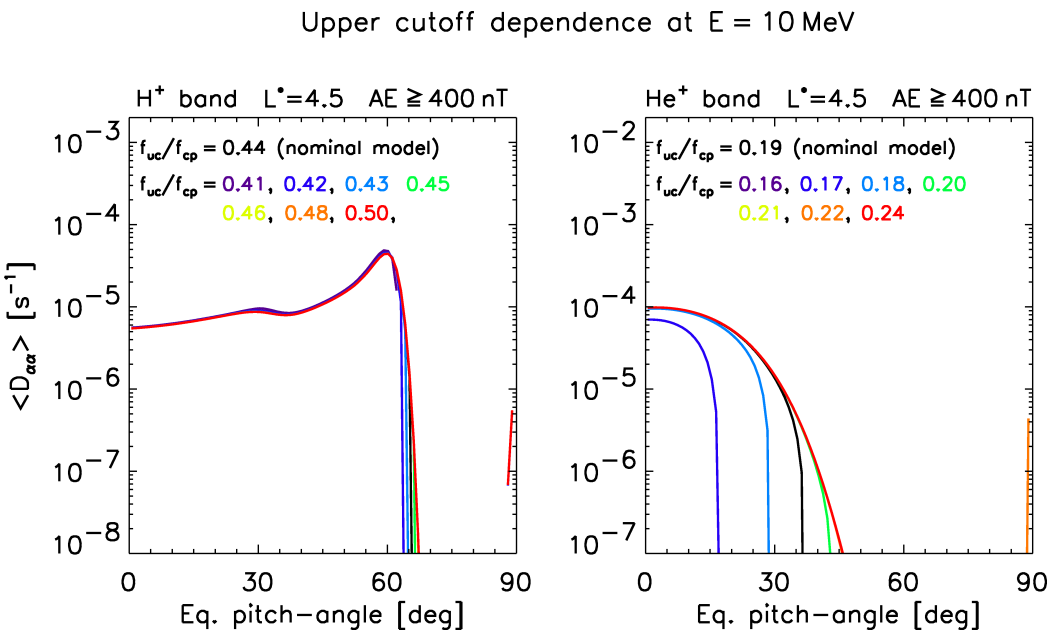


Figure 5.17: Bounce-averaged pitch-angle diffusion rates for hydrogen band (left) and helium band (right) EMIC waves for a variable upper cut-off frequency $f_{uc}$ at an electron energy of $E = 10\,\mathrm{MeV}$. All other parameters are the same as the one of the nominal model. The wave power has been set to the value corresponding to $L^* = 4,5$ and $AE \geq 400\,\mathrm{nT}$.

waves well, since a larger upper cut-off would only slightly increase the maximum pitch-angle at which helium band EMIC waves are effective. This result does not contradict the findings of *Li et al.* [2014], since the peak helium band frequency used in this thesis is much lower and hence further away from the helium ion cyclotron frequency.

### The ratio $f_{pe}/f_{ce}$

As explained at the beginning of this section, the ratio of $f_{pe}/f_{ce}$ defines the minimum resonant energy for EMIC waves, where an increase of $f_{pe}/f_{ce}$ allows waves to resonate with electrons of lower energies. In order to study the effects of $f_{pe}/f_{ce}$, Figure 5.18 shows the bounce-averaged pitch-angle diffusion rates for hydrogen band (left) and helium band (right) EMIC waves for different values of $f_{pe}/f_{ce}$ ranging from $f_{pe}/f_{ce} =$ 5 to 17 at an electron energy of 10 MeV. It can be seen that the choice of $f_{pe}/f_{ce}$ determines the maximum pitch-angle at which EMIC waves are effective. For instance, if $f_{pe}/f_{ce} = 5$ for hydrogen band EMIC waves, the maximum equatorial pitch-angle lies at about 35°, while for the nominal model value $f_{pe}/f_{ce} = 10$ the diffusion rates drop to

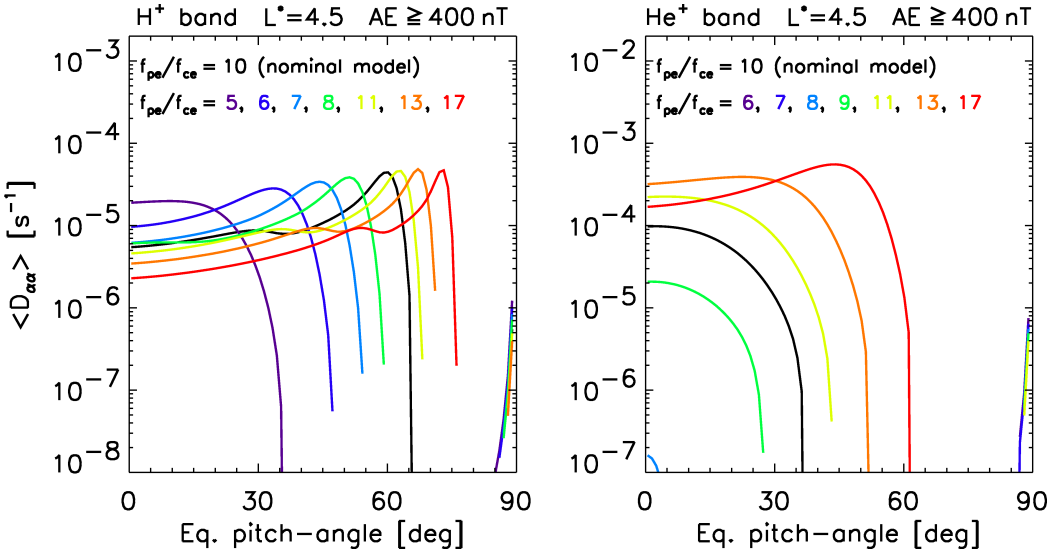


Figure 5.18: Bounce-averaged pitch-angle diffusion rates for hydrogen band (left) and helium band (right) EMIC waves for various values of $f_{pe}/f_{ce}$ at an electron energy of $E = 10\,\text{MeV}$. All other parameters are the same as the one of the nominal model. The wave power has been set to the value corresponding to $L^* = 4,5$ and $AE \geq 400\,\text{nT}$.

zero at about 65°. At larger values, for instance $f_{pe}/f_{ce} = 17$, the diffusion rates drop to zero at about 75°. Helium band EMIC waves start to resonate with 10 MeV electrons at about $f_{pe}/f_{ce} = 8$ and they show a similar increase of the maximum equatorial pitch-angle at which they cause diffusion.

The maximum value of the diffusion rate is only slightly affected by the choice of $f_{pe}/f_{ce}$ for hydrogen band EMIC waves, while larger values of $f_{pe}/f_{ce}$ can increase the diffusion rates for helium band EMIC waves about a decade compared to the value of the nominal model.

The effects of $f_{pe}/f_{ce}$ on the minimum resonant energy can be seen in Figure 5.19 for hydrogen (left) and helium band (right) EMIC waves. Since the minimum resonant energy is determined by the highest value of $f_{pe}/f_{ce}$, for these plots the ratio was set to $f_{pe}/f_{ce} = 17$, which represents a rather extreme case. In this case, the minimum resonant energy for hydrogen band waves reaches values as low as about 3 MeV, while the minimum resonant energy for helium band EMIC waves reaches about 5 MeV. These results show that a reliable plasma density model for the EMIC waves is important, since it affects the minimum resonant energy. Comparing these results with the results of the nominal model, it can be seen that the minimum resonant energy of the nominal

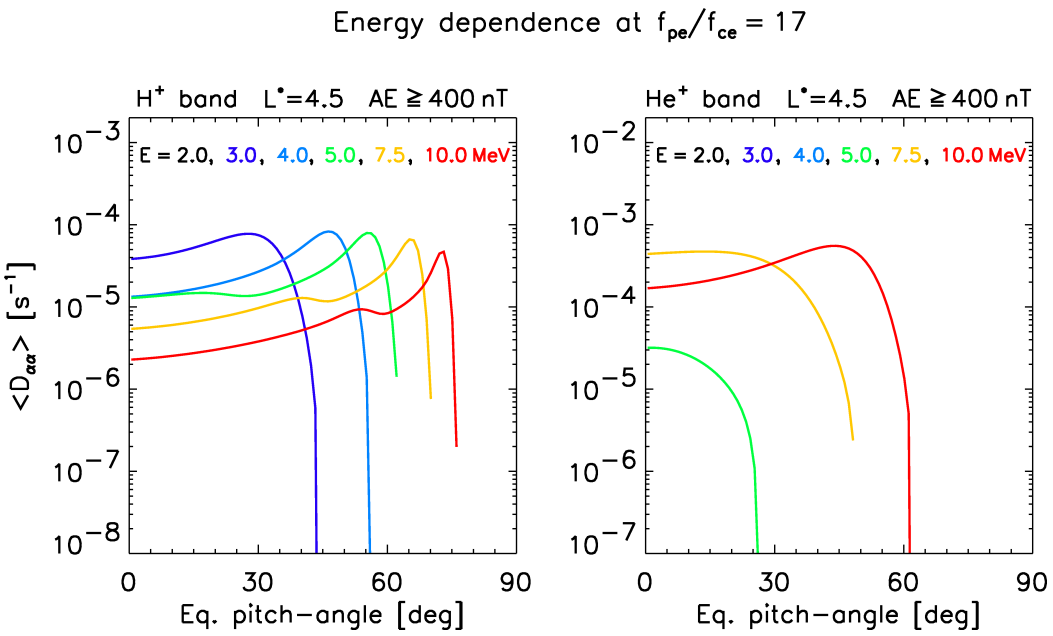


Figure 5.19: Bounce-averaged pitch-angle diffusion rates for hydrogen band (left) and helium band (right) EMIC waves for various electron energies at $f_{pe}/f_{ce} = 17$. All other parameters are the same as the one of the nominal model. The wave power has been set to the value corresponding to $L^* = 4,5$ and $AE \geq 400\,\mathrm{nT}$.

model is of the same order for hydrogen band EMIC waves and slightly larger for helium band EMIC waves, where the minimum resonant energy lies at about 7 MeV, showing that the choice of $f_{pe}/f_{ce} = 10$ for the nominal model captures the EMIC effects well.

## 5.4 Global Simulations of the Electron Flux

In order to assess the importance of EMIC waves on a global scale, the `BAS-RBM` was run for the same 100 day period in 1990 that was studied in chapter 4 for chorus waves, driven by the $AE$ index. The model was run on a $60 \times 60 \times 60$ pitch-angle, energy, and $L^*$ grid with a timestep of 300 seconds. The energy ranged from $E_{min} = 153.0\,\mathrm{keV}$ to $E_{max} = 20.0\,\mathrm{MeV}$ at $L^*_{max}$ and $L^*$ ranged from 2.05 to 5.55. The objective of this section is to study the effects of EMIC waves on the electron fluxes by comparing simulations with and without EMIC waves included in the model runs, which allows to assess the relative influence of EMIC diffusion rates on the electron fluxes in the radiation belts. Since EMIC waves are expected to only be effective at energies greater than a few MeV, which is outside the energy range measured by the CRRES satellite,

a comparison to real data cannot be performed.

### 5.4.1 Temporal Distribution

The drift and bounce averaged diffusion rates suggest that EMIC waves are effective at scattering electrons with pitch-angles less than about 60° and ineffective at scattering electrons with larger pitch-angles (see section 5.3.2). To demonstrate these effects on a global scale, the electron flux is studied for a high and a lower pitch-angle case.

In order to study the effects of EMIC waves on the electron distribution at large pitch-angles, a comparison of the electron flux for 10 MeV electrons with an equatorial pitch-angle of 90° for simulations with and without EMIC waves is presented in Figure 5.20. Here the top panel shows the electron flux caused by radial diffusion, hiss, and lower and upper band chorus as a function of time and $L^*$. The second panel shows the electron flux caused by radial diffusion, hiss, and lower and upper band chorus, and hydrogen and helium band EMIC waves. The third panel shows a comparison of the flux between the runs with and without EMIC waves at a constant value of $L^* = 3.97$, while the bottom panel shows the $AE$ and $Kp$ indices which drive the simulation.

The simulations without the EMIC waves show that there are small variations of the electron flux during the initial period near $L^* = 4$ with the slot region increasing from about $L^* = 2.5$ at the beginning of the simulation period up to about $L^* = 3.0$ at day 285. At this time a major increase of the electron flux, $AE$, and $Kp$ can be seen. The inner boundaries of the flux start to move inwards until about day 290 and the flux eventually returns back to the initial level at about day 315. Further periods of increased flux followed by a slow reduction to previous levels can be found around days 310, 315, 322, and 330, although they are less intense than the first major event. All these flux increases are driven by a rapid increase of $AE$ and $Kp$ and directly preceded by a flux dropout, where the flux is significantly reduced on a timescale of hours. Furthermore, it can be seen that each increase of the flux is associated with the plasmapause rapidly moving inwards to lower $L^*$.

The comparison between the results of the simulation with and without EMIC waves shows that the flux of 90° electrons is nearly unaffected by EMIC waves at most $L^*$, but

the line plots show that there is a difference noticeable at very low $L^*$ (e.g. $L^* = 2.98$). At these very low $L^*$ the electron flux is reduced by about 15% if EMIC waves are present in the simulations. The diffusion rates indicate that EMIC waves alone cannot be responsible for electron loss at large pitch-angles, especially since the model is only defined at $L^* > 3.5$. *Li et al.* [2007] and *Albert and Shprits* [2009] have shown that EMIC waves may be able to facilitate losses by hiss and chorus over all pitch-angles by creating large gradients in pitch-angle, and the results presented here are an indication that changes of the electron flux at lower $L^*$ could be caused by EMIC waves indirectly, although the changes are small compared to the direct effects of EMIC waves at smaller pitch-angles.

In contrast, the results of the simulations of the 10 MeV electron flux for electrons with an equatorial pitch-angle of 45°, as presented in Figure 5.21, show a significant reduction of the electron flux caused by EMIC waves up to about a factor of 5. The reduction is especially strong during day 285 and 310 for $L^* > 3.5$, because the EMIC model is only defined for $L^* > 3.5$, as explained in section 5.2.3. For $L^* < 3.5$ the (indirect) losses caused by EMIC waves are of the same order as for the 90° electron flux.

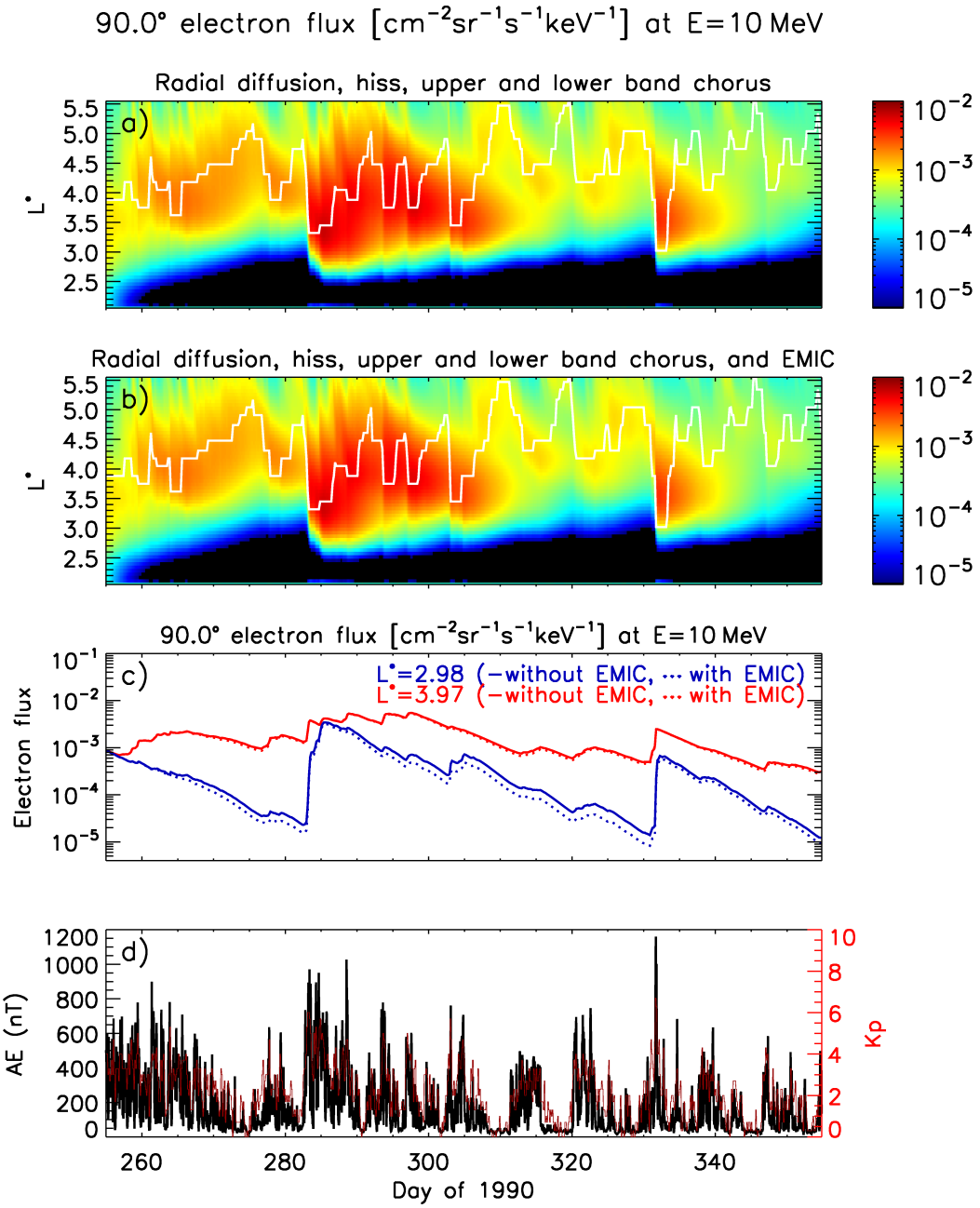


Figure 5.20: Temporal distribution of the flux of 10 MeV electrons with an equatorial pitch-angle of 90° as a function of $L^*$. The flux was calculated using the BAS-RBM driven by (a) radial diffusion, hiss, and lower and upper band chorus, and (b) additionally by hydrogen and helium band EMIC waves. Panel (c) shows the electron flux at constant $L^* = 2.98$ and $L^* = 3.97$ without (solid lines) and with EMIC waves being present (dotted lines). The location of the plasmapause is indicated by the white line, while the geomagnetic activity given by the $AE$ and $Kp$ indices during the simulation period is presented in panel (d).

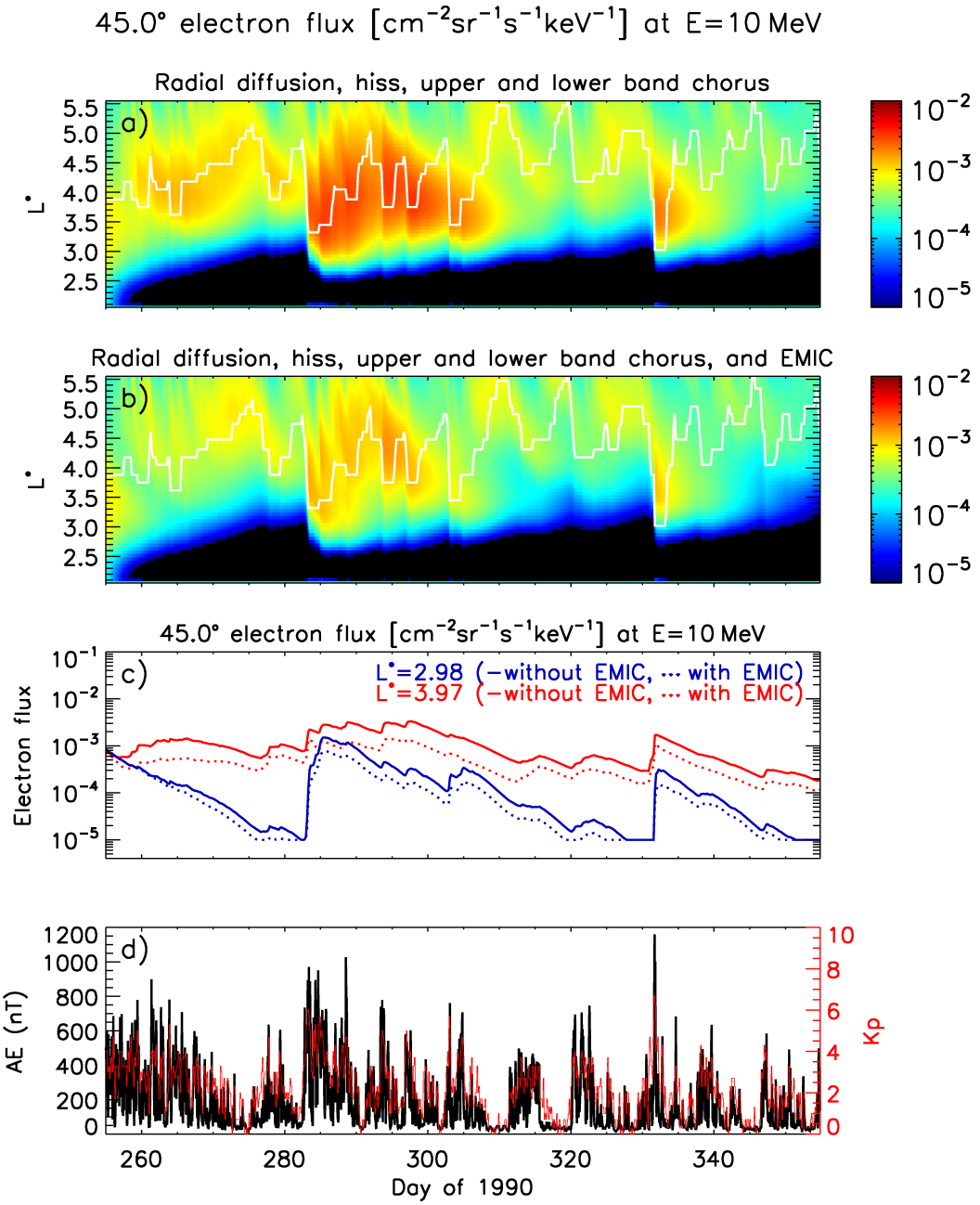


Figure 5.21: Temporal distribution of the flux of 10 MeV electrons with an equatorial pitch-angle of 45° as a function of $L^*$. The flux was calculated using the `BAS-RBM` driven by (top) radial diffusion, hiss, and lower and upper band chorus, and (second panel) additionally by hydrogen and helium band EMIC waves. Panel (c) shows the electron flux at $L^* = 2.98$ and $L^* = 3.97$ without (solid lines) and with EMIC waves being present (dotted lines). The location of the plasmapause is indicated by the white line, while the geomagnetic activity given by the $AE$ and $Kp$ indices during the simulation period is presented in panel (d)

### 5.4.2 Pitch-angle Distribution

So far only the fluxes at two selected pitch-angles were presented as a function of time and $L^*$. In order to show how the electron flux changes with pitch-angle, Figure 5.22 shows the pitch-angle distribution of the electron flux for $E = 6.0\,\text{MeV}$ (panels a and (b), and $E = 10.0\,\text{MeV}$ (panels c and d) during the same simulation period as before, with and without EMIC waves being present (panels b and d). The pitch-angle distribution is shown at $L^* = 4.00$ since the differences between the simulations with and without EMIC waves are large in this region. Note that the simulations were performed for equatorial pitch-angles up to 90°, while the presented pitch-angles range up to 180°, since this is a common way to present pitch-angle distributions. The full range of the electron flux is shown by mirroring the calculated results at 90°.

As expected from the drift and bounce averaged diffusion rates (see section 5.3.2), the EMIC waves are significantly decreasing the electron flux over a range of pitch-angles that increases with the electron energy, but does not go all the way up to 90°. In the case of $E = 6.0\,\text{MeV}$ electrons the reduction of the flux affects pitch-angles between about 0° and 45°, and for $E = 10.0\,\text{MeV}$ electrons the reduction caused by EMIC waves is more pronounced, being effective from about 0° up to about 75°. The effects seen in these pitch-angle distributions are consistent with measurements taken by the Van Allen Probes [e.g. *Usanova et al.*, 2014].

To quantify the effect of EMIC waves on the electron flux and to further demonstrate their effect on the pitch-angle distribution, a slice through the simulations at day 288 of year 1990 has been taken. The flux at this day for various energy levels where EMIC waves are effective (4.0 MeV, 6.0 MeV, 8.0 MeV, 10.0 MeV) is shown in Figure 5.23. It can be seen that the pitch-angle range at which EMIC waves are able to scatter electrons, increases with the electron energy. At 4.0 MeV the EMIC waves only cause a minor change of the electron flux, mainly at pitch-angles less than about 30°. For 6.0 MeV electrons the effective range in pitch-angle has increased to about 50° and the flux is reduced by up to a factor of 4, while for 10.0 MeV electrons the electron flux can be reduced up to about a factor of 5 over a wide range of pitch-angles up to about 70°. Furthermore, EMIC waves are able to maintain the electron flux at very

low pitch-angles of less than about 10°, where they compensate the electron losses by other processes and actually increase the overall electron flux.

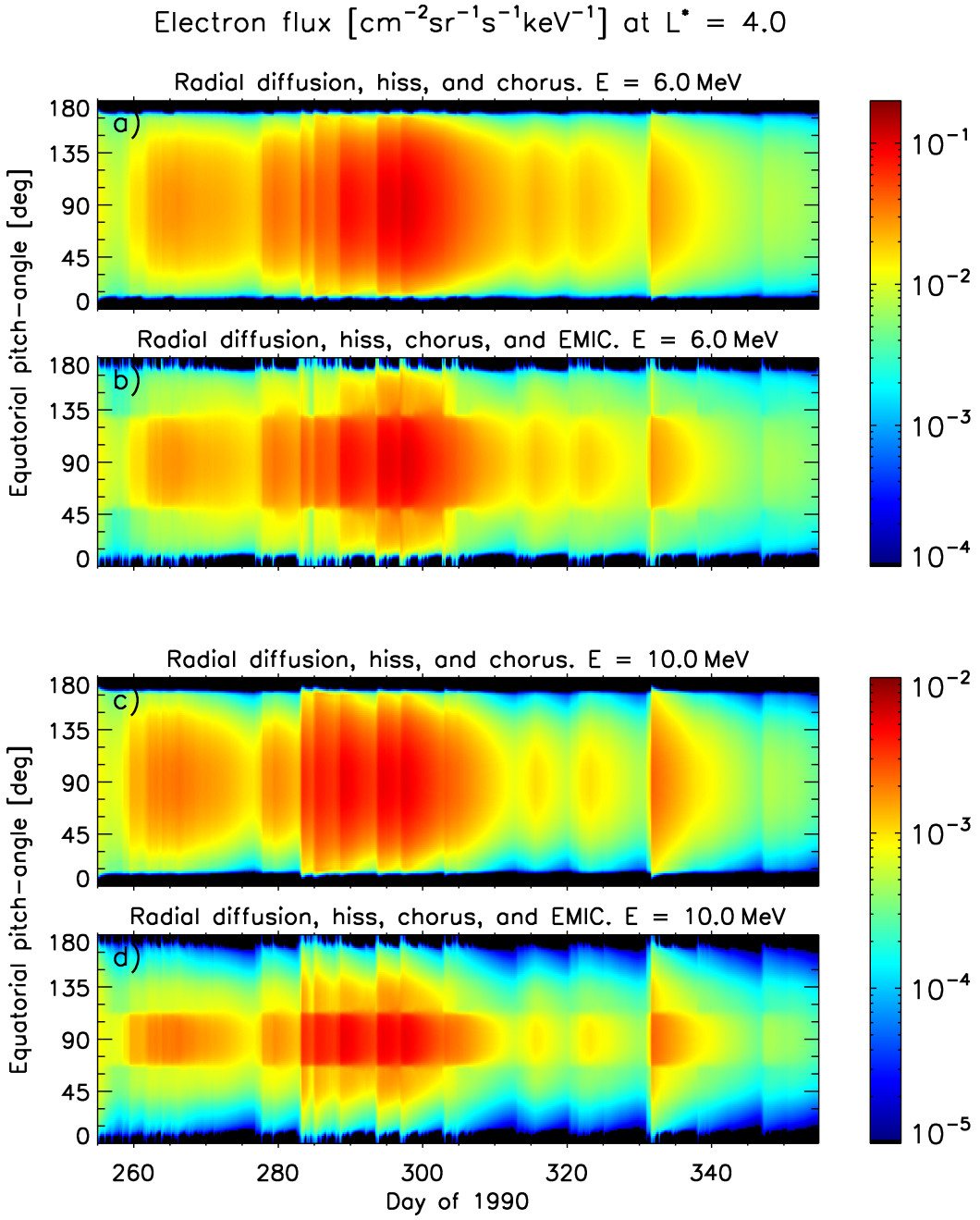


Figure 5.22: Equatorial pitch-angle distribution of the electron flux at $L^* = 4.00$ calculated with the BAS-RBM utilising radial diffusion, hiss, and chorus (panels a and c), and additionally by hydrogen and helium band EMIC waves (panels b and d) for electron energies of $E = 6.0\,\mathrm{MeV}$ (panels a and b) and $E = 10.0\,\mathrm{MeV}$ (panels c and d). The simulation period is the same as in Figures 5.20 and 5.21.

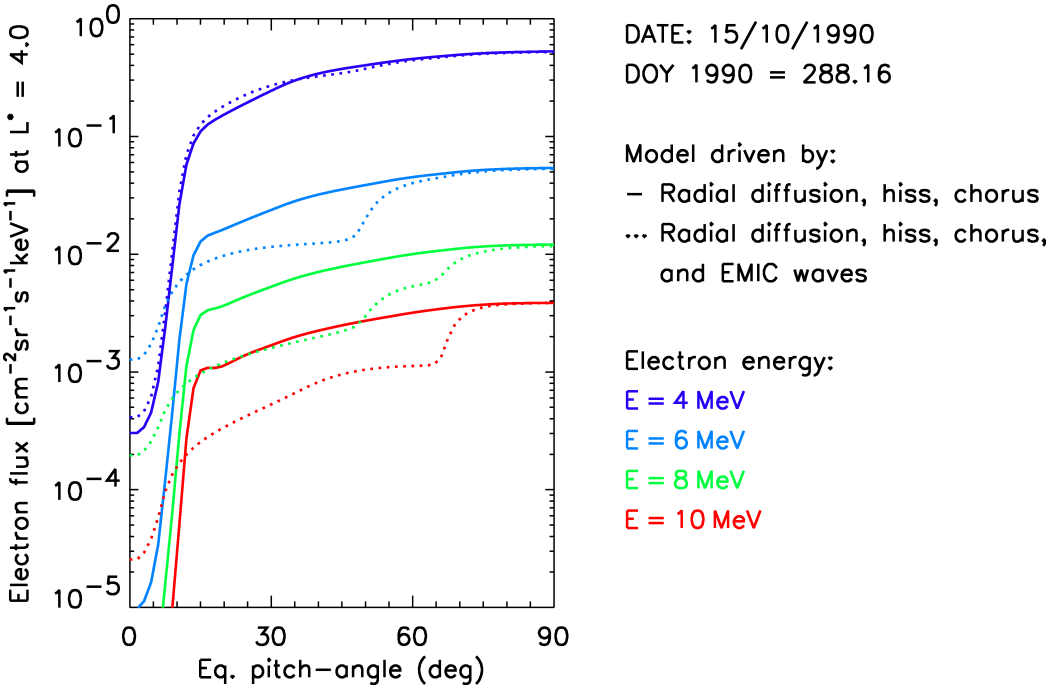


Figure 5.23: Equatorial pitch-angle dependence of the flux at $L^* = 4.00$ for different electron energies calculated with the BAS-RBM utilising radial diffusion, hiss, and chorus (solid lines), and additionally by hydrogen and helium band EMIC waves (dotted lines). The simulation period is the same as in Figures 5.20 and 5.21.

## 5.5 Discussion

The results presented in this chapter are based on a nominal model, which in turn is based on the EMIC wave events measured by the CRRES satellite. Since the data are sparse, the nominal model has some uncertainties, especially in the Gaussian frequency distribution and in the fixed value of the plasma frequency that was used. The parameter studies that were performed showed that, in the case of the frequency distribution, the hydrogen band EMIC waves are only affected to a minor degree by the choice of the peak frequency, frequency width, and the upper cut-off frequency. In contrast, the model for the helium band waves might underestimate the diffusion rates at lower energies significantly. The studies have shown that the combined hydrogen and helium band waves diffusion rates can be roughly doubled at energies between about $3-7\,\mathrm{MeV}$, if larger values for the peak frequency and frequency width were chosen for the helium band EMIC waves. However, choosing these larger values still did not allow EMIC waves to diffusion electrons at large pitch-angles.

Similarly, the parameter study of the ratio of the plasma frequency to the electron cyclotron frequency has shown that high values of $f_{pe}/f_{ce}$ allow EMIC waves to resonate with electrons at larger pitch-angles, but still not up to 90°. Overall, these results underline that the presented model is only a statistical model and it is hence unable to model extreme events with large values of $f_m$, $df$, and $f_{pe}/f_{ce}$, which is not its purpose. Furthermore, the presented simulation results neglect warm plasma effects that could allow EMIC waves to resonate with electrons of lower energies by affecting the resonant energies. The warm plasma effects are expected to be strongest during geomagnetic storms [*Silin et al.*, 2011] particularly when the ring current is strong, which is found during times of low $Dst$. Since EMIC waves show little correlation with $Dst$ and are rather more closely related to substorm activity, it can be assumed that warm plasma effects may not be very important for EMIC waves, especially for a statistical model.

There is evidence from ground observations that EMIC waves result in the precipitation of electrons with energies larger than a couple MeV [*Clilverd et al.*, 2007; *Millan et al.*, 2007; *Rodger et al.*, 2008]. This suggests that EMIC waves might play a role in high energy electron flux dropout events that can be seen during the main phase of

geomagnetic storms [e.g. *Blake et al.*, 2001; *Green et al.*, 2004]. On the other hand, satellite observations could not find any evidence for strong precipitation of high energy electrons during the main phase of geomagnetic storms [*Horne et al.*, 2009; *Meredith et al.*, 2011; *Turner et al.*, 2012]. The simulations based on the presented EMIC wave model support these results, since it was shown that EMIC waves can cause precipitation of high energy electrons with energies greater than about 3 MeV near the loss cone, but the bulk of the electron population at larger pitch-angles was unaffected by EMIC waves. Therefore, it seems unlikely that EMIC waves are directly responsible for flux dropout events of high energy electrons.

It needs to be noted that EMIC waves usually appear in short strong bursts that might be able to cause strong diffusion. Since the presented model is using time-averaged wave power, including times when no EMIC waves were present, the model is unable to capture the strongest EMIC bursts. The calculated pitch-angle diffusion rates are on average about 3 decades lower than the strong diffusion rate. It was shown by *Meredith et al.* [2014] that the time-averaged intensity of EMIC wave events is about $30-50$ times lower than the event-averaged intensity, which means that even if event-averaged intensities were used instead of time-averaged intensities the diffusion rates caused by EMIC wave events would still be at least one decade lower than the strong diffusion rate, indicating that the measured EMIC wave events are unlikely to cause strong diffusion.

## 5.6 Conclusions

In this chapter a global, average, statistical model for hydrogen and helium band EMIC waves was developed based on the CRRES satellite data. The resulting model covers the range of $L^* = 3.5-7.0$ in the afternoon sector ($12-18$ MLT) covering all latitudes for 5 levels of geomagnetic activity defined by the $AE$ index. The model was used to calculate pitch-angle and energy diffusion rates which were then used to calculate the electron fluxes during a 100 day period in 1990. The results show that EMIC waves can be a significant loss process for the high energy electron flux with energies greater

than about 3 MeV and equatorial pitch-angles ranging from the loss cone up to about 60°. EMIC waves are hence able to scatter all electrons with a pitch-angle less than 60° into the loss cone over time.

The remaining distribution therefore looks like a pancake distribution, which means it is depleted between the loss cone and an energy-dependent pitch-angle and constant afterwards up to 90°. Since EMIC waves are unable to cause this effect at energies lower than about 3 MeV and the highest energy channel of the CRRES MEA instrument, that provides measurements of the electron flux, is at $E = 1582\,\mathrm{keV}$, no comparison of the simulated electron fluxes with real data could be performed. Nevertheless, a recent study by *Usanova et al.* [2014] showed that evidence of electron loss of ultrarelativistic electrons with pitch-angles below about 45° caused by EMIC waves can be found in the Van Allen Probes data, which supports the results predicted by the presented EMIC wave model.

Lastly, the presented results suggest that EMIC waves are unlikely to set an upper limit on the energy flux of the radiation belt electrons, since even at very large electron energies of 30 MeV EMIC waves are not able to cause diffusion for all pitch-angles and still leave the high pitch-angle electron distribution unaffected. Finding the upper energy limit of the electron flux is an important issue in space weather research and of high interest for satellite operators and engineers, since the shielding of the electronic components of the satellite needs to be designed to withstand the high energy electrons, in order to prevent internal charging that could damage the satellite.

# CHAPTER 6

# *Plasmaspheric Hiss*

## 6.1 Introduction

Plasmaspheric hiss is a broadband and structureless electromagnetic emission that is typically found at frequencies between a few tens of Hz and several kHz. Resonant wave-particle interactions with plasmaspheric hiss are known to be an important loss process for electrons in the outer radiation belt [*Summers et al.*, 2007; *Meredith et al.*, 2006b] and the main cause for the formation of the slot region between the inner and the outer radiation belt [*Lyons and Thorne*, 1973; *Meredith et al.*, 2007, 2009]. Previous studies of plasmaspheric hiss analysed the effects of individual wave profiles representing average or extreme geomagnetic conditions in order to determine the importance of hiss on the electron distribution in the radiation belts. While existing statistical wave models of plasmaspheric hiss are able to represent the variability with $L^*$, MLT, and geomagnetic activity, they are usually based on data from a single satellite and hence lack in spatial or temporal resolution.

In this chapter a novel, statistical model for plasmaspheric hiss is presented, that is derived from the wave spectral data of 7 different satellites, considerably improving the resolution of existing statistical wave models. Furthermore, a new technique to separate chorus waves from plasmaspheric hiss was developed, based on the spatial distribution of the two kinds of whistler mode waves. Additionally, a corresponding plasma density model was derived from the data of the CRRES satellite, replacing existing parametrised plasma density models. The wave model is used to calculate drift and bounce averaged pitch-angle and energy diffusion rates. These diffusion rates are compared to the previously published hiss diffusion rates and their effect is studied on a global scale by employing them into the `BAS-RBM` individually.

## 6.2 Plasmaspheric Hiss Wave Database

The wave data that was used to derive the novel statistical model for the plasmaspheric hiss presented here is part of the SPACECAST whistler mode wave database, which is based on the data from seven different satellites, namely CRRES, DE 1, Cluster 1, Double Star TC1, and THEMIS A, D, and E. The instrumentation and data analysis is presented in detail in Section 4.2.

### 6.2.1 Separating Hiss from Chorus

Plasmaspheric hiss and lower band chorus are both whistler mode waves and hence their frequency range overlaps. Hiss is typically found between 100 Hz and about 4 kHz, although recent research based on the Van Allen probes mission data suggests that hiss can be found at frequencies starting as low as a few tens of Hz. The plasmaspheric hiss wave power is peaked at a few hundred Hz, while lower band chorus waves are typically peaked near $0.3\,f_{ce}$. Using Eq. 1.9, the peak of the chorus wave power can be determined in the frequency domain as about 2.8 kHz at $L^* = 4.5$, 1.2 kHz at $L^* = 6.0$, and 510 Hz at $L^* = 8.0$ (all at $\lambda_m = 3°$). At lower $L^*$ and higher latitudes, the peak of the lower band chorus corresponds to frequencies above 4 kHz, while hiss is usually not found outside of $L^* = 6.0$. Therefore, hiss and chorus waves share the same frequency range but are mostly separated by $L^*$, although some overlap exists. However, plasmaspheric hiss and chorus waves are typically separated by their location relative to the plasmapause, as chorus can only be found outside of it, while hiss is confined to higher density regions inside the plasmapause. Furthermore, chorus is usually strong in the night sector starting at about 22 MLT all the way through to the early afternoon sector (about 14 MLT), while hiss is dominant from about 6 MLT to 22 MLT. Hence, the greatest overlap between chorus and hiss is expected to be found on the dayside between 6 and 14 MLT.

In order to define a plasmapause location based on the satellite data, a method using the CRRES measurements of electron cyclotron harmonic (ECH) waves that are found at frequencies between harmonics of the electron cyclotron frequency $f_{ce}$ was used. Since ECH waves are usually only found outside the plasmapause, simultaneous

measurements of ECH and whistler mode waves can be used to specify whether the CRRES satellite was inside (no ECH waves present) or outside (ECH waves are present) the plasmapause. The ECH criterion was used to create a parametrised plasmapause location for 6 levels of geomagnetic activity defined by $AE$ within $3° < \lambda_m < 15°$. As a similar method is not available for the other satellites, this template based on the ECH CRRES measurements (from now on referred to as the CRRES template) was applied to the whistler mode wave data of all satellites. Because of the statistical nature of the whistler mode wave model, there are times where a satellite has been either inside or outside the plasmapause at the same spatial position. Applying the CRRES plasmapause template to the data of all satellites other than CRRES hence can include times where chorus waves and hiss waves overlap.

Figure 6.1 (a) shows the average intensity in the frequency band from 200 - 500 Hz with the CRRES template for the plasmapause location superposed (red line). It can be seen that there are two regions of high intensity, clearly separated by their location in $L^*$, corresponding to waves inside and outside the plasmapause. The CRRES ECH plasmapause criterion performs reasonably well to separate chorus and hiss in this frequency range, where chorus can only be found at very large $L^*$. However, at larger absolute frequencies, chorus moves further inwards, due to the $L^*$ dependence of the electron cyclotron frequency. At the same time, the CRRES plasmapause location is fixed. As an example, Figure 6.1 (b) shows the average intensity in the frequency band from 1 - 2 kHz with the CRRES template for the plasmapause location superposed (red line). While there are still two regions of high intensity, separated by their location in $L^*$, it can be seen that at this frequency range the CRRES template starts to include both chorus and hiss waves, particularly at larger geomagnetic activities, where the plasmapause is closer to the Earth. Nevertheless, the ECH criterion captures the outer boundary of the plasmaspheric hiss reasonably well in the MLT regions where no chorus is present (14 - 22 MLT). Therefore, using the ECH criterion as a template for the data of all satellites does not work well enough if both chorus and hiss are present, and another method to separate the two wave modes needs to be derived.

An individual study of all the chorus and hiss wave data solely based on the CRRES

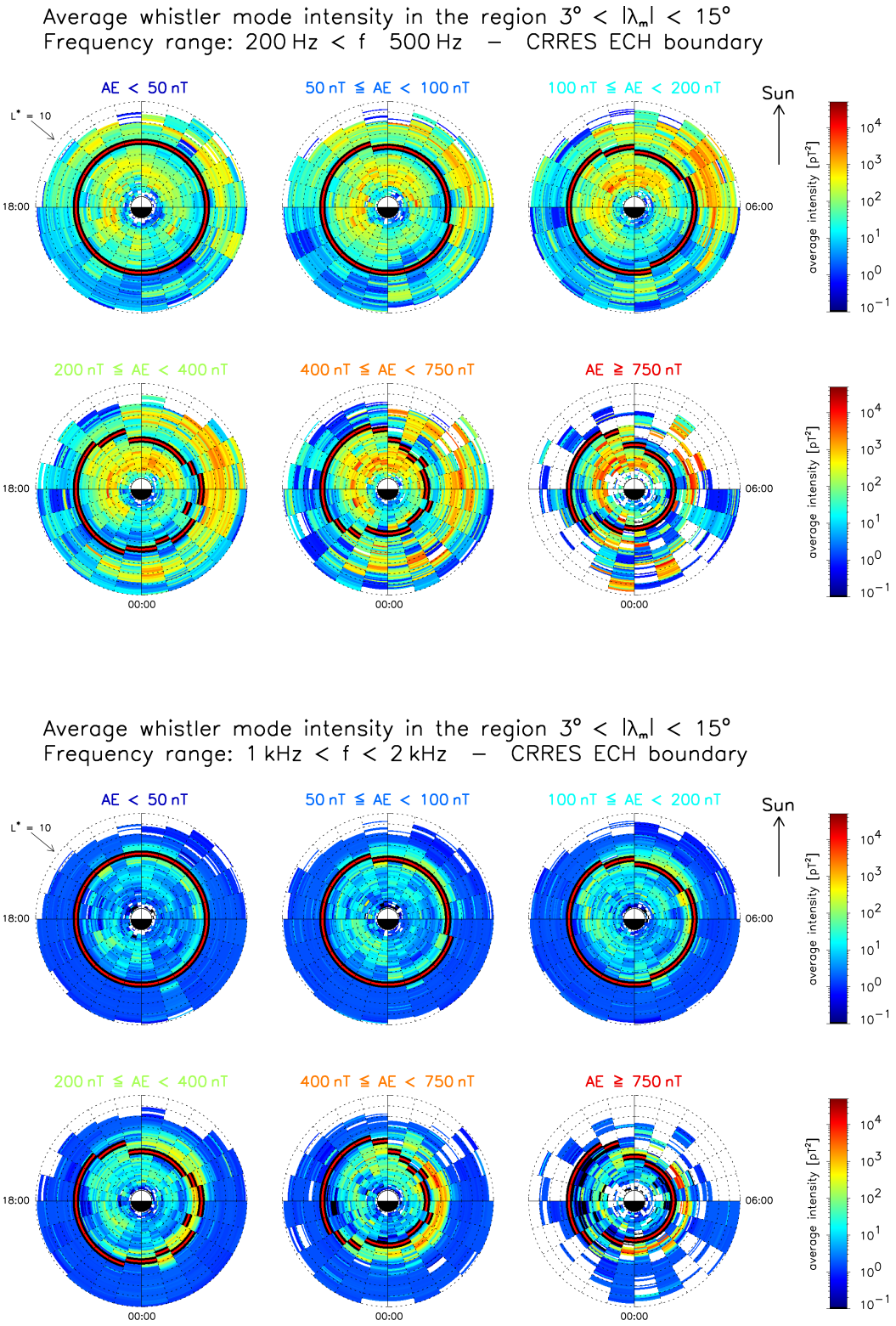


Figure 6.1: Average wave intensity of whistler mode waves in the frequency range of 200 Hz - 500 Hz (top) and 1 kHz - 2 kHz (bottom) in the region $3° < |\lambda_m| < 15°$ for the 6 activity levels of the wave database. The red line indicates the CRRES plasmapause location derived using the ECH wave criterion.

satellite showed that, at fixed frequencies, there are two regions of high intensity at different $L^*$. These regions are usually separated by a gap of low intensity. The ECH criterion furthermore shows that the inner region of high intensity is clearly inside the plasmapause, while the outer region is always outside the plasmapause. The frequency distributions showed that the inner region is strongest at frequencies of a couple hundred Hz, while the outer region is strongest at the largest frequency band (3kHz - 4kHz). Due to the individual shape of the two frequency distributions and since chorus waves are expected to be present mainly outside the plasmapause, while hiss is located inside the plasmapause, it is assumed here that the waves in the inner region are hiss and the outer region is the inner edge of lower band chorus waves.

Similar patterns of the $L^*$ distribution of the average wave intensity can be found in the data from the other satellites, and hence this feature can be exploited to derive a method to separate hiss from chorus. An analysis showed that the chorus and hiss intensity distribution in $L^*$ can be represented by a Gaussian form, where the peak moved to smaller values of $L^*$ for increasing geomagnetic activity. It was found that hiss peaked between 200 - 500 Hz for $AE < 200$ nT and between 500 - 1000 Hz for $AE > 200$ nT, while chorus generally peaked in the largest frequency bin between 3 - 4 kHz. However, chorus could be identified more accurately at slightly lower frequency ranges of 1 - 2 kHz for $AE < 200$ nT and between 2 - 3 kHz for $AE > 200$ nT. In the first two mentioned frequency bands (associated with hiss) the $L^*$ distribution of the wave intensity is usually strongest at lower $L^*$ and quickly tails off with no significant wave intensity found at higher $L^*$. Similarly, the $L^*$ distribution of the wave intensity in the two frequency bands associated with chorus is strongest at larger $L^*$, with comparably low wave intensity at lower $L^*$. In order to identify the boundary between hiss and chorus as well as possible, the $L^*$ distributions of the intensity for hiss and chorus were fitted with a Gaussian profile separately for the specified individual frequency bands. To exclude any potential wave intensity associated with chorus while fitting hiss and vice versa, all wave intensity above a specific cut-off value $L^*_{cut}$ were set to zero while fitting hiss. Similarly, the intensities below $L^*_{cut}$ were set to zero in the case of fitting to chorus. The value of $L^*_{cut}$ was set to $L^*_{cut} = 4.0$ for all activities with $AE < 400$ nT

and to $L^*_{cut} = 3.0$ for $AE > 400\,\mathrm{nT}$. The fits were performed using the nonlinear least squares fitting procedure called `MPFIT` [*Markwardt*, 2009]. In the case of chorus waves, fits where the peak was identified below $L^* = 3.5$ were disregarded, as this is typically inside the plasmapause and hence not chorus. Furthermore, unreasonably wide distributions of the wave intensity were excluded in order to be able to distinguish between chorus and hiss at all times.

This method was performed for all 6 levels of geomagnetic activity, but since chorus is not present or only weak between 14 - 22 MLT, only the MLT range from 22 - 14 MLT was included. For these activity and MLT levels most of the peaks of the wave intensity were well identified in the $L^*$ distribution. The boundary to separate plasmaspheric hiss and chorus waves was then defined as the $L^*$ value where the two Gaussian fits intersected. An example illustrating this process is shown in Figure 6.2 for $100\,\mathrm{nT} \leq AE < 200\,\mathrm{nT}$ (top row) and $400\,\mathrm{nT} \leq AE < 750\,\mathrm{nT}$ (bottom row) for four different MLT. The average intensity of plasmaspheric hiss and chorus waves in the corresponding frequency bands is shown as a function of $L^*$, where the dotted lines left of the vertical green line are the satellite data inside the hiss frequency band, while the dotted lines right of the vertical green line are the satellite data inside the chorus frequency band. The solid blue and red lines are the Gaussian profiles fitted to the $L^*$ distribution inside the individual frequency bands associated with hiss and chorus, respectively. The intersection between the two Gaussian fits that define the boundary to separate plasmaspheric hiss from chorus waves is shown as the dashed line.

Based on the Gaussian boundary, a template to identify plasmaspheric hiss was created, where it is assumed that all wave power inside the $L^*$ value defined by the boundary corresponds to hiss, rather than chorus. Since this method was only applied to waves within 22 - 14 MLT, and chorus is weak outside this region, the ECH criterion was used as the outer boundary between 14 - 22 MLT. This includes hiss in plumes, which otherwise would be excluded. The boundary defined in this way is from now on called the "***hiss boundary***". Between 22 - 14 MLT this method identifies hiss from $L^* = 1.5$ up to about $L^* = 4.5$ during geomagnetically quiet conditions and to about $L^* = 3.0$ during very active times. Furthermore, between 14 - 22 MLT hiss extends to larger values of

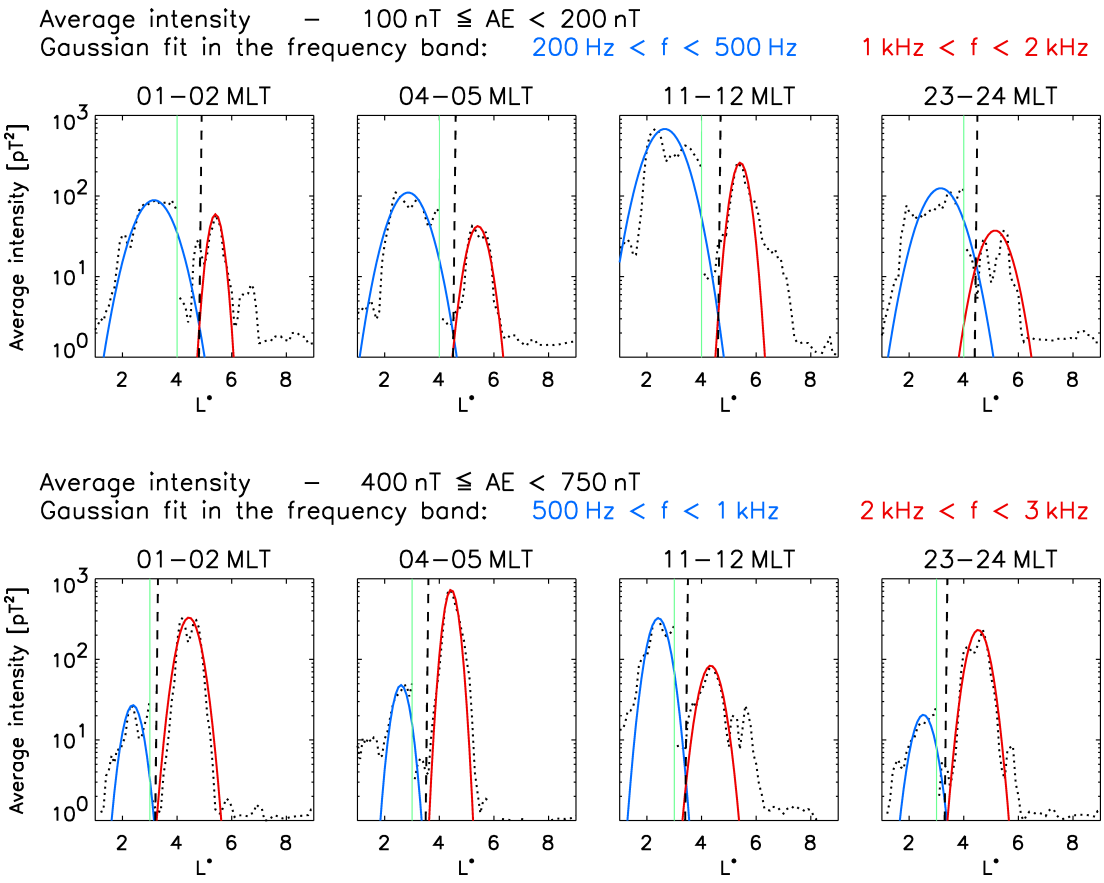


Figure 6.2: $L^*$ distribution of the average wave intensity (dotted line) for 100 nT $\leq$ $AE$ < 200 nT (top row) and 400 nT $\leq$ $AE$ < 750 nT (bottom row) for four different MLT. The data left of the green line corresponds to the hiss frequency band (top: 200 Hz < $f$ < 500 Hz, bottom: 500 Hz < $f$ < 1 kHz), while the data right of the green line corresponds to the chorus frequency band (top: 1 kHz < $f$ < 2 kHz, bottom: 2 kHz < $f$ < 3 kHz). The Gaussian fits to the $L^*$ distribution in each band are indicated by the blue and red lines.

$L^*$ up to about $L^* = 6.0$ for all activities showing the bulge representing the plumes. Global maps of the average intensity with the derived hiss boundary superposed as a red line are shown in Figure 6.3. The derived method is able to capture the outer edge of plasmaspheric hiss at 200 - 500 Hz well, while the inner edge of chorus at 1 - 2 kHz is still well outside the hiss boundary. Even at 3 - 4 kHz only very few contributions of chorus waves are included (not shown).

Note that this hiss boundary is not to be confused with a definition of a plasmapause, since this concept is based on the $L^*$ distribution of the wave intensity of plasmaspheric hiss and chorus waves, while a plasmapause model needs to be defined by a rapid change of the plasma density. Measurements of the plasma density were not available for all

satellites, however. For details about the plasma density, see Section 6.4.

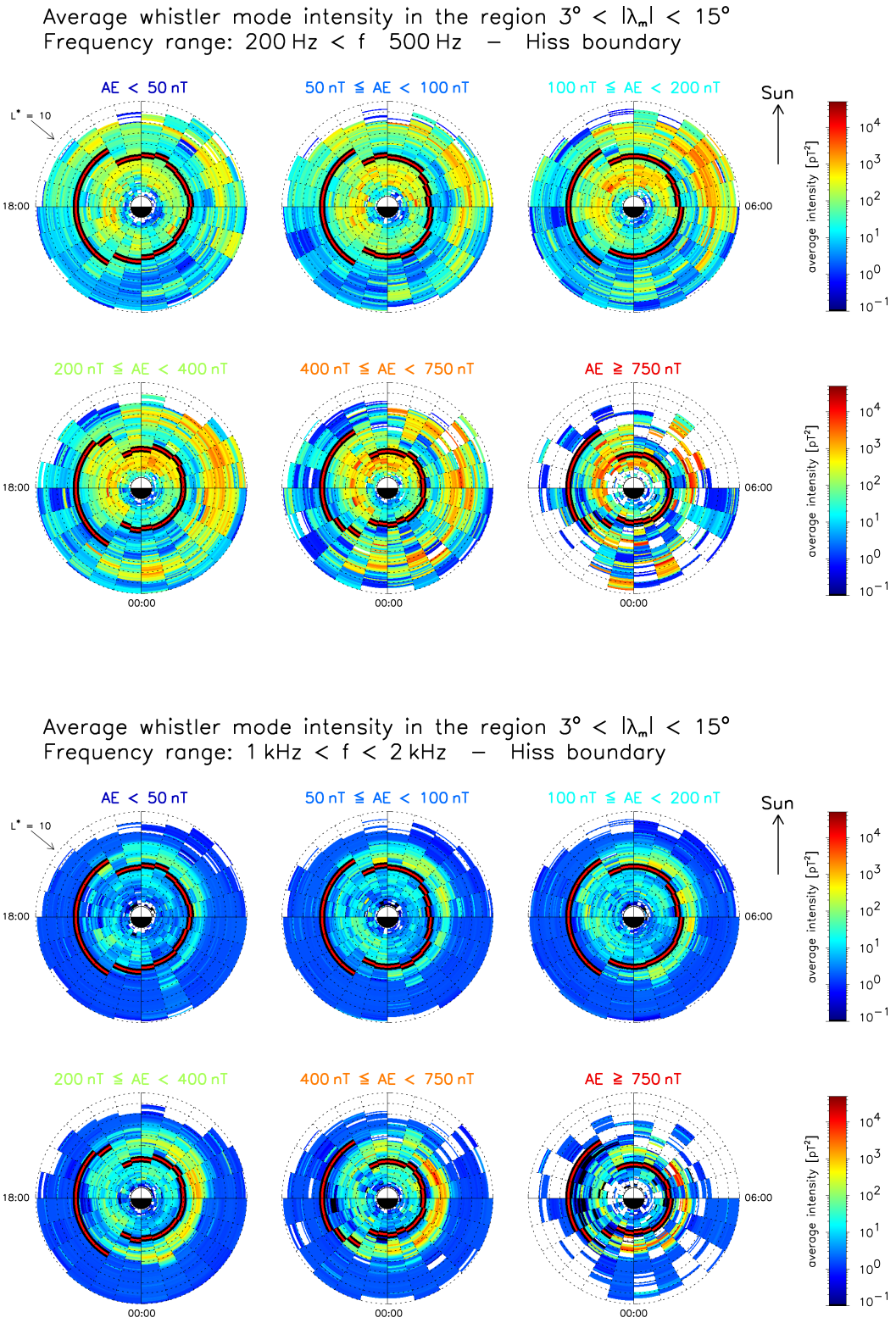


Figure 6.3: Average wave intensity of whistler mode waves in the frequency range of 200 Hz - 500 Hz (top) and 1 kHz - 2 kHz (bottom) in the region $3° < |\lambda_m| < 15°$ for the 6 activity levels of the wave database. The red line indicates the derived hiss boundary that separates plasmaspheric hiss and chorus waves.

## 6.3 Wave Model

The plasmaspheric hiss model was derived from the SPACECAST whistler mode wave database described in Section 4.2. As explained, a boundary to separate chorus from hiss was derived and applied to the database, resulting in a statistical, parametrised model for plasmaspheric hiss. The resulting model covers the frequency range from 100 Hz to 4 kHz in the frequency bands 100 - 200 Hz, 200 - 500 Hz, 500 Hz - 1 kHz, 1 - 2 kHz, 2 - 3 kHz, 3 - 4 kHz. The $L^*$ range covered extends from $L^* = 1.5$ to $L^* = 4.0$ on the dawn side, and up to about $L^* = 6.0$ inside the plumes on the dayside, with a bin size of $\Delta L^* = 0.5$. The model's magnetic local time resolution is 1 hour, and it is defined for six levels of geomagnetic activity, defined by the $AE$ index, i.e. $AE < 50$ nT, $50\,\text{nT} \leq AE < 100$ nT, $100\,\text{nT} \leq AE < 200$ nT, $200\,\text{nT} \leq AE < 400$ nT, $400\,\text{nT} \leq AE < 750$ nT, and $AE \geq 750$ nT. The covered latitude range extends from 3° above the geomagnetic equator up to $\lambda_m = 60°$, distributed over 10 latitude sectors, each in steps of 6°. The first sector thereby ranges from 3° to 9°, while the second starts at 6° geomagnetic latitude. The waves close to the equator were omitted in order to exclude magnetosonic waves, which overlap with the lower hiss frequency bands inside the plasmapause. The parametrisation is summarised in Table 6.1.

| | | | |
|---|---|---|---|
| Frequency bands | 100 Hz - 200 Hz<br>1 kHz - 2 kHz | 200 Hz - 500 Hz<br>2 kHz - 3 kHz | 500 Hz - 1 kHz<br>3 kHz - 4 kHz |
| Activity Levels | $AE < 50$ nT<br>$200\,\text{nT} \leq AE < 400$ nT | $50\,\text{nT} \leq AE < 100$ nT<br>$400\,\text{nT} \leq AE < 750$ nT | $100\,\text{nT} \leq AE < 200$ nT<br>$AE \geq 750$ nT |
| MLT levels | 24 with 1 h MLT resolution | | |
| $L^*$ lvl (dawn side) | Ranging from 1.5 - 4.0 with $\Delta L^* = 0.5$ | | |
| $L^*$ lvl (dusk side) | Ranging from 1.5 - 6.0 with $\Delta L^* = 0.5$ | | |
| Latitude levels | $3° < \lvert\lambda_m\rvert < 9°$, $6° < \lvert\lambda_m\rvert < 12°$, $12° < \lvert\lambda_m\rvert < 18°$, ..., $54° < \lvert\lambda_m\rvert < 60°$ | | |

Table 6.1: Frequency bands, maximum covered $L^*$ range at dawn and dusk, MLT resolution, latitude levels, and geomagnetic activity levels of the plasmaspheric hiss model.

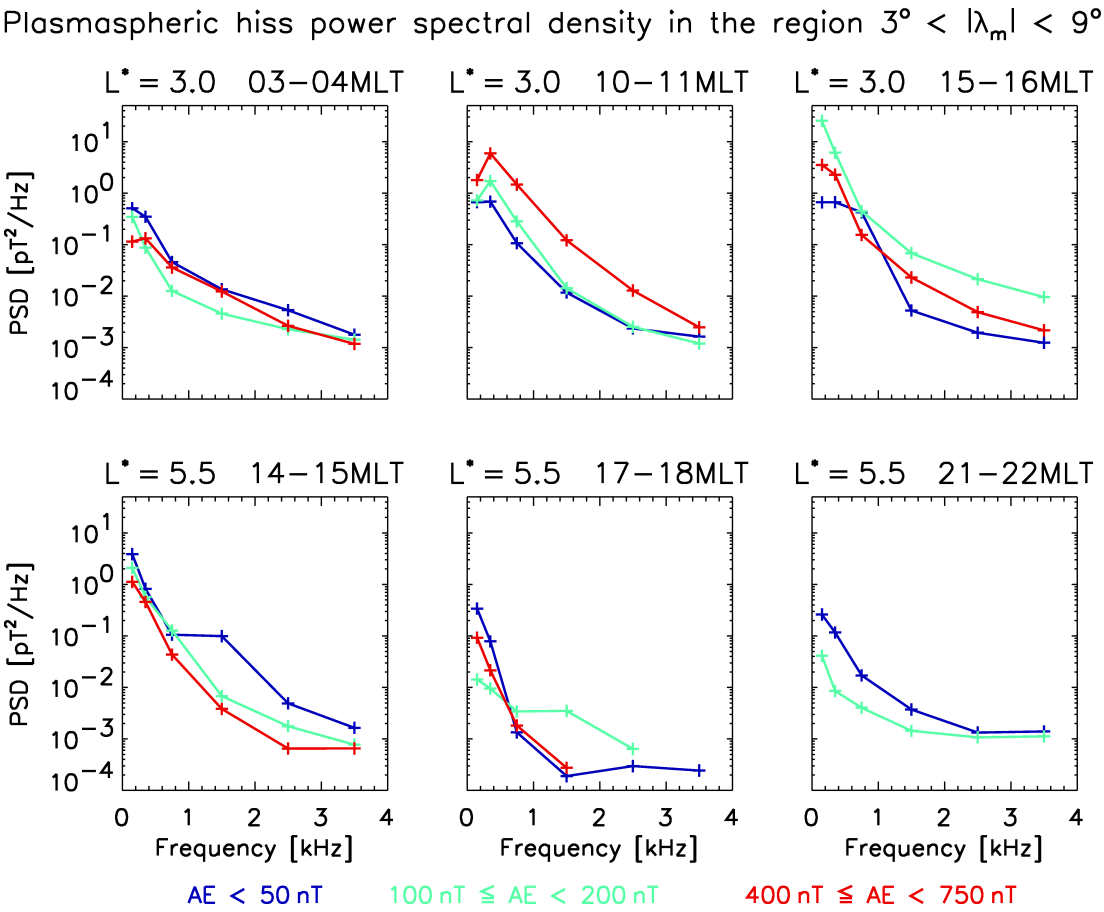


Figure 6.4: Frequency distribution of the power spectral density of plasmaspheric hiss at $L^* = 3.0$ (top) and $L^* = 5.5$ (bottom) for various levels of MLT in the region $3° < \lambda_m < 9°$. The blue line is for $AE < 50\,\text{nT}$, the green line for $100\,\text{nT} \leq AE < 200\,\text{nT}$, and the red line for $400\,\text{nT} \leq AE < 750\,\text{nT}$.

### 6.3.1 Spectral Properties

Plasmaspheric hiss is typically found in the frequency range between about 100 Hz and 4 kHz. A few typical frequency spectra at various MLT and $L^* = 3.0$ (top) and $L^* = 5.5$ (bottom) for $AE < 50\,\text{nT}$, $100\,\text{nT} \leq AE < 200\,\text{nT}$, and $400\,\text{nT} \leq AE < 750\,\text{nT}$ in the region $3° < \lambda_m < 9°$ are shown in Figure 6.4. It can be seen that hiss is strong in the frequency range between 100 Hz - 1 kHz and is usually peaked between 200 Hz - 500 Hz. In contrast to chorus waves, hiss is usually not distributed in a Gaussian form and hence it is difficult to represent hiss by individual Gaussian spectra. Therefore, in this study, the average wave intensity inside each frequency band is used directly to model the plasmaspheric hiss.

The MLT and $L^*$ dependence of the frequency distribution is shown in Figure 6.5 for

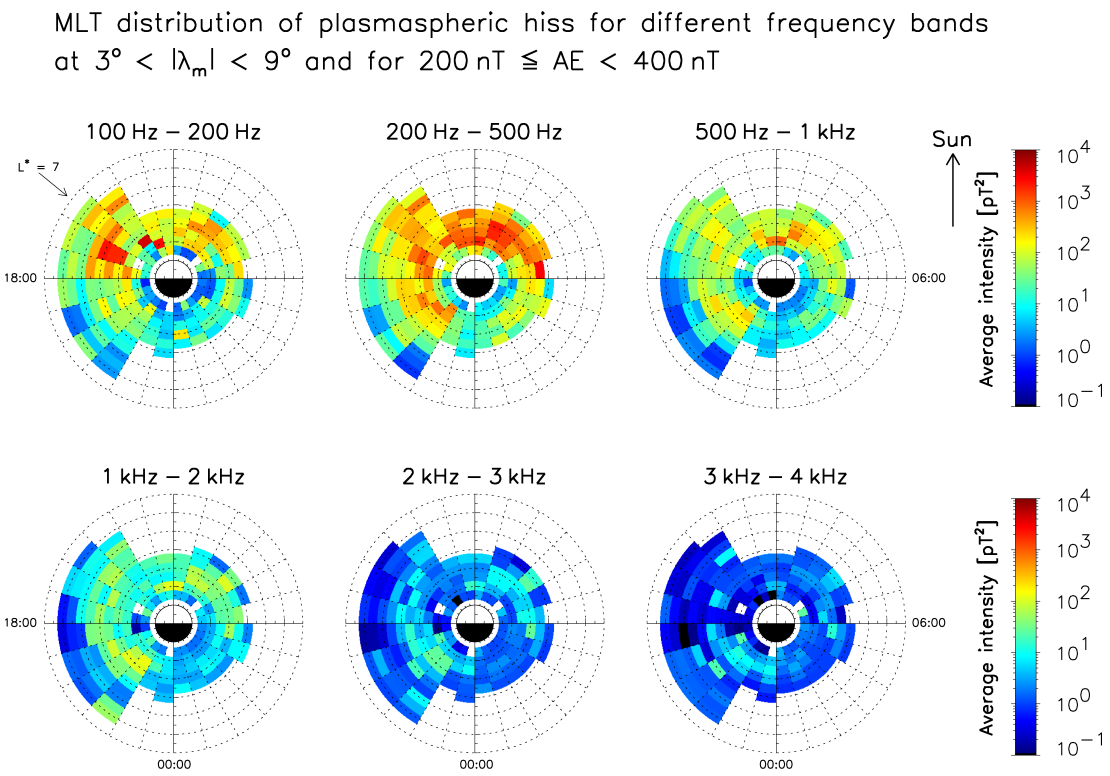


Figure 6.5: Frequency distribution of the average intensity of plasmaspheric hiss in the 6 hiss frequency bands of the model in the region $3° < \lambda_m < 9°$ and medium geomagnetic activity ($200\,\mathrm{nT} \leq AE < 400\,\mathrm{nT}$).

plasmaspheric hiss near the equator. As before, hiss is usually peaked between 200 Hz - 500 Hz and occasionally between 100 Hz - 200 Hz, where the average peak intensity is of the order of about $1000\,\mathrm{pT}^2$. It is strongest on the dayside, ranging from about 6 - 22 MLT, and at $2 < L^* < 4$. The waves found inside the plumes region are usually dominant in the region between 14 - 16 MLT, where the average wave intensity is of the same order as in other regions. At later MLT, the peak wave intensity in the plumes is at least one decade lower than at the other regions where hiss is strong.

The latitudinal distribution of the average wave power in the frequency band, where hiss is usually the strongest (200 Hz - 500 Hz), is shown in Figure 6.6 for medium geomagnetic activity of $200\,\mathrm{nT} \leq AE < 400\,\mathrm{nT}$. There is no obvious change in the distribution or average intensity of the plasmaspheric hiss with geomagnetic latitudes up to about 30°, where all satellites except the THEMIS spacecraft contributed to the data set. Above 30° the coverage gets sparse, and especially above 48° large gaps of coverage inside $L^* = 4$ are found. There are indications that the average intensity of

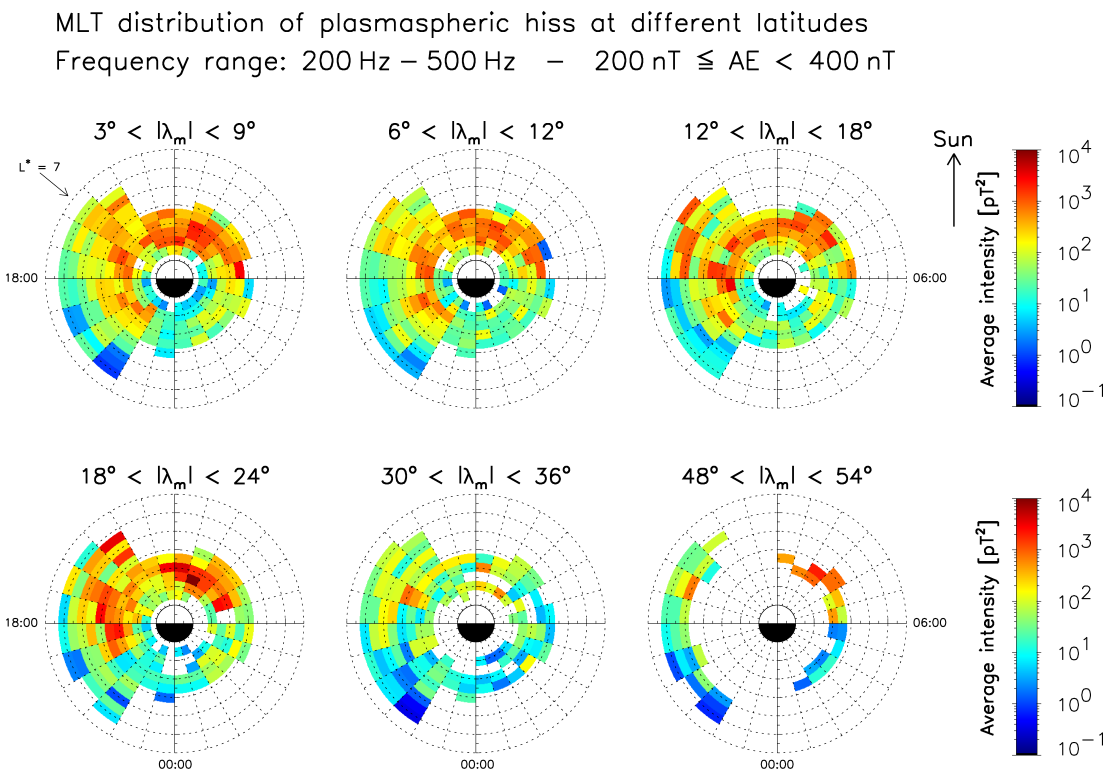


Figure 6.6: Latitudinal distribution of the average intensity in the frequency band 200 Hz - 500 Hz of plasmaspheric hiss at 6 selected latitude ranges of the model covering the region $3° < \lambda_m < 54°$ at medium geomagnetic activity ($200\,\mathrm{nT} \leq AE < 400\,\mathrm{nT}$).

hiss at high latitudes are lower than at lower latitudes.

### 6.3.2 Wave Power

The wave power $B_w^2$ of the plasmaspheric hiss was obtained by integrating the peak spectral intensity inside each wave band with respect to the frequency. The results for the hiss wave power between 100 Hz and 4 kHz are shown for the near equatorial waves as a function of $L^*$, MLT, and geomagnetic activity in Figure 6.7. It can be seen that the wave power increases with geomagnetic activity, while the covered $L^*$ decreases with activity on the dawn side, since the plasmapause is moving inwards. The hiss in plumes however, extends to the same value of $L^*$ for all activities, but the wave power inside the plumes is peaked at medium geomagnetic activity and weak for high activities. Generally $B_w^2$ is strongest at the dayside, reaching a few $\mathrm{pT}^2$, and weaker on the night side (about 22 - 6 MLT), where $B_w^2$ is typically of the order of about $100\,\mathrm{pT}^2$.

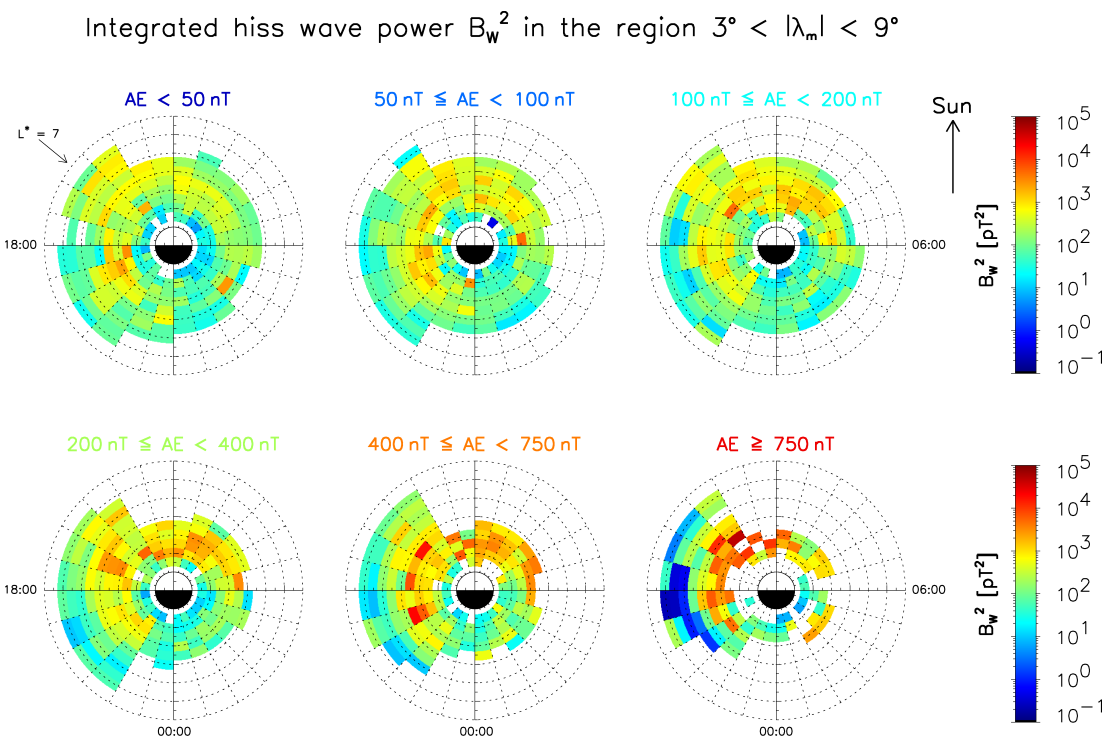


Figure 6.7: Integrated wave power $B_w^2$ of plasmaspheric hiss, identified using the *hiss boundary*. The integration was performed in the frequency range of 100 Hz - 4 kHz in the region $3° < |\lambda_m| < 9°$.

### 6.3.3 Wave Normal Angle Model

The wave normal angle $\psi$ is known to be an important wave parameter with significant influence on the resonance condition and hence the diffusion rates. The `PADIE` code, which is used to calculate the diffusion coefficients, assumes a Gaussian distribution of the wave normal angle in $X$, where $X = \tan(\psi)$ (see Section 2.2.3). Based on observations, previous studies mostly assumed parallel wave propagation near the equator with an increasing wave normal angle at higher latitudes. *Ni et al.* [2011] improved the precision of these assumptions by modelling the wave normal angle using ray tracing techniques, presenting a set of wave normal angle distributions up to 45° in latitudinal steps of 5°, which are consistent with the observations from e.g. *Santolík et al.* [2001]; *Agapitov et al.* [2012, 2013]. Instead of assuming values for the wave normal angle, this study exploits the actual wave normal angle data derived from the Cluster measurements as presented in *Agapitov et al.* [2013]. In order to use the data together with the statistical wave model, the data has been recalculated into steps of 6° in latitude, and

furthermore has been parametrised for low and high geomagnetic activity, as well as day- and nightside. The data are used in the statistical model with the dayside defined to be between 06-18 MLT, while the nightside is between 18-06 MLT. Low geomagnetic activity is assumed to be for $AE < 200\,\mathrm{nT}$, while high geomagnetic activity is for $AE \geq 200\,\mathrm{nT}$. The data above $\lambda_m = 42°$ is used for all latitude bins above $\lambda_m = 42°$. For each of these MLT, $AE$, and latitude ranges, the peak $\psi_m$ and the width $\delta\psi$ are presented in Table 6.2. In order to include most of the wave power, the cut-offs of the wave normal angle distribution are set to $X_{cut} = 2X_w = 2\tan(\delta\psi)$, outside which the wave power is set to zero.

| $AE < 200\,\mathrm{nT}$ | 06-18 MLT | | 18-06 MLT | |
|---|---|---|---|---|
| Latitude | $\psi_m$ | $\delta\psi$ | $\psi_m$ | $\delta\psi$ |
| $0° \leq \lvert\lambda_m\rvert < 6°$ | 13.4725° | 6.19047° | 17.1324° | 6.54510° |
| $6° \leq \lvert\lambda_m\rvert < 12°$ | 19.6978° | 9.68693° | 23.1888° | 10.0760° |
| $12° \leq \lvert\lambda_m\rvert < 18°$ | 28.9783° | 14.0075° | 32.2230° | 16.7275° |
| $18° \leq \lvert\lambda_m\rvert < 24°$ | 38.6343° | 17.7940° | 40.8107° | 25.2186° |
| $24° \leq \lvert\lambda_m\rvert < 30°$ | 47.1840° | 21.3452° | 46.0278° | 27.4462° |
| $30° \leq \lvert\lambda_m\rvert < 36°$ | 58.3558° | 21.7122° | 60.1125° | 22.5592° |
| $36° \leq \lvert\lambda_m\rvert < 42°$ | 77.9516° | 19.9582° | 88.5431° | 27.4168° |
| $\lvert\lambda_m\rvert \geq 42°$ | 87.4366° | 20.1395° | 94.2141° | 28.1823° |
| $AE \geq 200\,\mathrm{nT}$ | 06-18 MLT | | 18-06 MLT | |
| Latitude | $\psi_m$ | $\delta\psi$ | $\psi_m$ | $\delta\psi$ |
| $0° \leq \lvert\lambda_m\rvert < 6°$ | 13.9093° | 6.38871° | 16.0609° | 7.61205° |
| $6° \leq \lvert\lambda_m\rvert < 12°$ | 21.2528° | 8.62547° | 22.1168° | 11.7368° |
| $12° \leq \lvert\lambda_m\rvert < 18°$ | 26.6015° | 14.1706° | 31.9405° | 18.7053° |
| $18° \leq \lvert\lambda_m\rvert < 24°$ | 31.2622° | 16.7695° | 35.7351° | 17.6968° |
| $24° \leq \lvert\lambda_m\rvert < 30°$ | 39.7995° | 24.9828° | 45.7663° | 22.6379° |
| $30° \leq \lvert\lambda_m\rvert < 36°$ | 58.6850° | 42.6963° | 55.1494° | 22.9673° |
| $36° \leq \lvert\lambda_m\rvert < 42°$ | 70.3578° | 15.3201° | 97.1397° | 28.2361° |
| $\lvert\lambda_m\rvert \geq 42°$ | 70.0240° | 13.4893° | 97.1397° | 28.2361° |

Table 6.2: Distribution of the peak $\psi_m$ and the width $\delta\psi$ of the wave normal angle for dayside (06-18 MLT) and nightside (18-06 MLT) during low ($AE < 200\,\mathrm{nT}$) and high ($AE \geq 200\,\mathrm{nT}$) geomagnetic activity.

### 6.3.4 Comparison with the Glauert et al. [2014] Hiss Model

In this study the effects of the presented novel statistical model for plasmaspheric hiss (from now on referred to as "***new hiss model***") is evaluated by a comparison with the preceding hiss model used at the British Antarctic Survey. This model (from now on referred to as "***G14 hiss model***") was first presented in *Glauert et al.* [2014] and it includes whistler mode waves in the frequency range between 100 Hz and 5 kHz measured by the CRRES satellite. Whistler mode chorus and plasmaspheric hiss were separated using the ECH criterion for ECH waves in the frequency range $f_{ce} < f < 2\,f_{ce}$, while magnetosonic waves were excluded by restricting hiss to magnetic latitudes outside of $\pm 5°$.

In order to calculate the drift and bounce averaged pitch-angle and energy diffusion rates, the wave spectral intensities were separated into bins of $0.5\,L^*$ ranging from $L^* = 2.0$ - $L^* = 6.5$ and into three levels of geomagnetic activity, namely $AE^* < 100\,\mathrm{nT}$, $100\,\mathrm{nT} \leq AE^* < 500$ , and $AE^* \geq 500\,\mathrm{nT}$, where $AE^*$ is the maximum value of the $AE$ index in the preceding 3 hours. The wave spectral intensities were then first averaged over the magnetic latitude from $5° < |\lambda_m| < 30°$ and then over magnetic local time. The calculation of the diffusion rates was performed using the `PADIE` code, which required a Gaussian frequency distribution of the wave power. Since the resulting spectral profiles of the plasmaspheric hiss were not of Gaussian form, it was shown that the best approach was to fit three individual Gaussians to separated frequency ranges. The first of these ranges from 100 Hz to the frequency where the fit departed from the data. The second frequency range extends to 2 kHz, while the third covers the lightning-generated whistlers in the range between 2 kHz - 5 kHz. For the calculation of the diffusion rates the resonances between $-5 \leq n \leq +5$ were included and the average spectral profiles were assumed to be the same for all latitudes. The plasma density was defined as the mean value of $f_{pe}/f_{ce}$ at the defined levels of $L^*$ and geomagnetic activity derived from the CRRES data. The wave normal angle was defined by a variable wave normal angle model derived from ray tracing that assumes field aligned wave propagation close to the magnetic equator and highly oblique waves at larger latitudes. The peak wave normal angle is 0° at the equator and increases to about 80° at $\lambda_m = 40°$.

The new hiss model therefore gives a much more detailed representation of the plasmaspheric hiss, in particular a 24 hour MLT and 6° latitude resolution is now available. Furthermore it doubles the resolution of the geomagnetic activity and includes significantly higher resonances, that are important when modelling plasmaspheric hiss. And lastly, no fits to the wave spectral data are required anymore.

## 6.4 The Ratio of $f_{pe}/f_{ce}$

In order to calculate pitch-angle and energy diffusion rates using the `PADIE` diffusion code, the plasma density must be provided in the form of the ratio of the plasma frequency to the electron cyclotron frequency $f_{pe}/f_{ce}$. It was shown (See Eq. 2.21) that this ratio is proportional to the square root of the plasma density.

For this study of plasmaspheric hiss a novel plasma density model was derived entirely from satellite data in order to complement the new hiss model. Initially a similar approach to derive the plasma density model as presented in Chapter 4 for chorus waves was tested. Hence, plasma density measurements were obtained from the CRRES wave instrument and also inferred from measurements of the electron thermal speed and the spacecraft potential of the THEMIS satellite [*Li et al.*, 2010]. In both cases, only the data from inside the plasmapause were stored, in order to represent the plasma densities in regions where plasmaspheric hiss is found. The data within $0° < |\lambda_m| < 9°$ were combined in order to increase the data coverage, while still minimising latitudinal effects. The plasma densities were then converted into $L^*$ and arranged into the same $L^*$ and geomagnetic activity levels as the chorus model.

However, analysis of the individual satellite data showed that the ratio of $f_{pe}/f_{ce}$ derived from the THEMIS satellite was consistently about a factor of 2 - 3 larger than the CRRES data, where the latter are in good agreement with published plasma density models [e.g. *Carpenter and Anderson*, 1992; *O'Brien and Moldwin*, 2003]. Therefore, it was decided to discard the THEMIS $f_{pe}/f_{ce}$ data and build a plasma density model entirely based on CRRES measurements instead.

In order to create a good coverage for the plasma density model, the data was inter-

polated in MLT and $L^*$ inside the hiss boundary as defined in Section 6.2.1. As a first step, an interpolation weighted by the number of samples was performed for every $L^*$ and MLT sector between $L^* = 1.5$ - 9.0, as long as the number of neighbours that contained data was at least 6. All remaining gaps were then closed in two further steps. First by a weighted interpolation at all $L^*$ and MLT using the values of $f_{pe}/f_{ce}$ of the adjacent activity bins, and second, if gaps were still present, by calculating the weighted average in MLT at fixed $L^*$. In order to keep the shape of the plumes intact, these last two steps were performed only within the plasmapause location as defined by *O'Brien and Moldwin* [2003].

The resulting model for the plasma density is specified to represent $f_{pe}/f_{ce}$ at the equator, for up to 11 levels of $L^*$ within $L^* = 1.5$ - 6.5, 24 MLT sectors, and 6 levels of geomagnetic activity determined by $AE$ and is presented in Figure 6.8. For higher latitudes, $f_{pe}/f_{ce}$ was recalculated using a dipole magnetic field model to cover the range of the hiss model ($0° < |\lambda_m| < 60°$).

The model shows a clear increase of $f_{pe}/f_{ce}$ with $L^*$, while it seems to be rather constant with geomagnetic activity. On the dawn side the model extends out to about $L^* = 5.0$ at low activity and about $L^* = 4.0$ during most active conditions. While these values are mostly determined by the plasmapause location as defined by *O'Brien and Moldwin* [2003], the model extends into plumes, which are found on the dusk side. There, the model extends from $L^* = 1.5$ up to about $L^* = 6.5$ during quiet conditions, while the plumes become less pronounced during higher activities.

On the dawn side, $f_{pe}/f_{ce}$ of the hiss model is generally slightly larger than $f_{pe}/f_{ce}$ in the chorus model, with values between $f_{pe}/f_{ce} = 5$ - 15. Similar values can be found on the dusk side, and hence $f_{pe}/f_{ce}$ of the chorus model is greater than in the hiss model in this region. This is because the chorus plasma density model is defined outside the plasmapause, while the hiss model is defined inside. Since the plasmapause is defined as the region where the plasma density rapidly decreases by more than one decade and $f_{pe}/f_{ce}$ is proportional to the square root of the plasma density, this ratio must hence be higher for chorus than for hiss. The ratio $f_{pe}/f_{ce}$ defines the resonant energies at which electron diffusion is most effective, where larger values allow waves to resonate

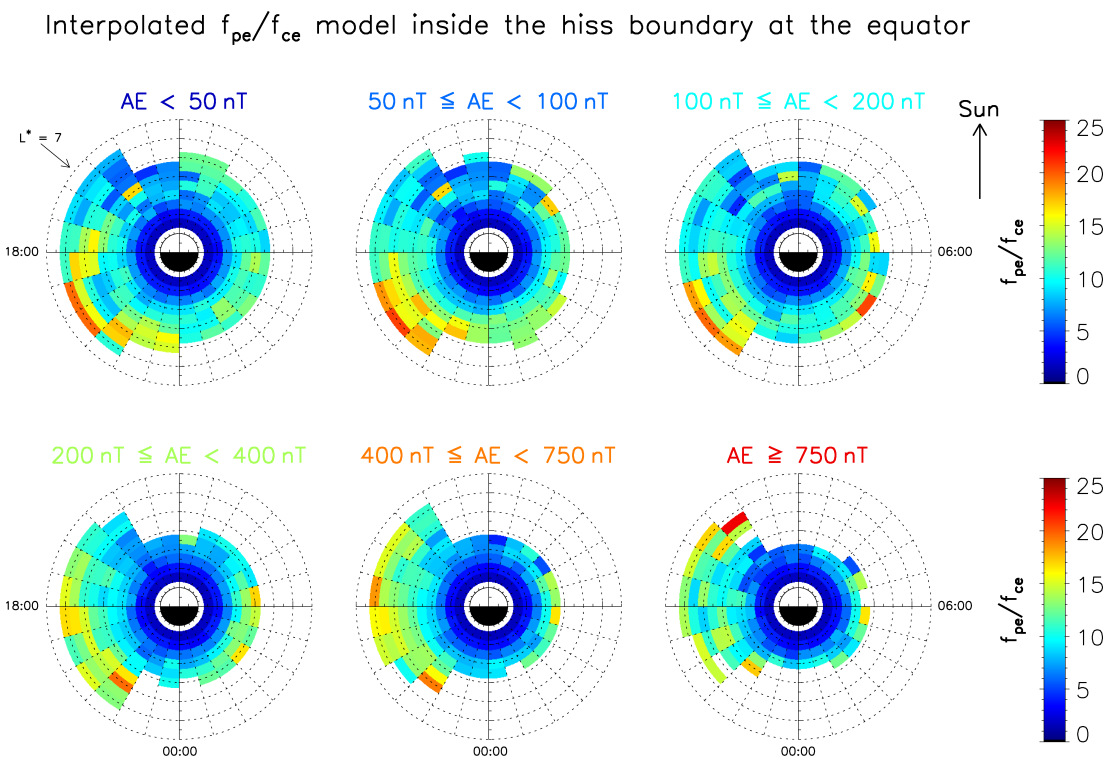


Figure 6.8: Interpolated model for the ratio of $f_{pe}$ over $f_{ce}$ inside the hiss boundary for the 6 levels of geomagnetic activity of the hiss model.

with electrons of lower energies. As a consequence, it is expected that the diffusion rates due to plasmaspheric hiss are most effective at slightly higher electron energies than the diffusion rates due to chorus waves.

## 6.5 Bounce Averaged Diffusion Rates

The effect of plasmaspheric hiss on the distribution of the electron flux in the radiation belts can be predicted from the pitch-angle and energy diffusion rates, since they provide a measure of the change of the electron pitch-angle and electron energy caused by the corresponding waves. The `BAS-RBM` uses drift and bounce averaged diffusion rates, that are calculated from the bounce averaged diffusion rates, by averaging them over a whole drift orbit (i.e. all MLT). In this section, the bounce averaged diffusion rates are presented, in order to understand the contribution of each MLT sector to the drift averaged diffusion rates.

The pitch-angle and energy diffusion rates at all $L^*$ and MLT sectors at each level of

geomagnetic activity of the plasmaspheric hiss model were calculated from individual runs of the `PADIE` diffusion code. The diffusion rates were calculated for 111 electron energy levels evenly spread over a logarithmic energy range from 100 eV to 10 MeV. Each run covered equatorial pitch-angles between 0° and 90° in steps of 1° and no threshold for the integrated wave amplitude was set. For the dominant resonances an adaptive model was developed, allowing the inclusion of resonances from $n = 0$ up to $n = \pm 30$. The details and justification of this model are discussed in the next section. The bounce averaging within each of the 6° latitude bins specified for the model was directly performed by `PADIE` assuming a dipole magnetic field. The bounce averaged diffusion rates covering the complete geomagnetic latitude range from 0° to 60° at each $L^*$, MLT, energy, and geomagnetic activity sector were calculated by adding the bounce averaged diffusion rates of the 6° latitude sectors inside the corresponding $L^*$, MLT, energy, and activity sectors.

As an example, the bounce averaged pitch-angle diffusion rates $\langle D_{\alpha\alpha} \rangle$ and the bounce averaged energy diffusion rates $\langle D_{EE} \rangle / E^2$ during medium geomagnetic activity (200 nT $\leq AE <$ 400 nT) are presented in Figure 6.9 for 8 different MLT sectors. The top panels show the diffusion rates well inside the plasmapause at $L^* = 3.0$, while the bottom panels show the diffusion rates at $L^* = 5.0$, which corresponds to a region where hiss is only found inside the plumes. In the first case, the MLT sectors were spread evenly among all MLT, while they are focused on the plumes region in the last case.

In the case of $L^* = 3.0$ the pitch-angle diffusion rates, as well as the energy diffusion rates, are strong between about 4 - 19 MLT, where the peak of the pitch-angle diffusion rate is up to 100 times larger than in the MLT region where hiss is weak. The pitch-angle diffusion rates are strong between a few tens of keV and about 3 MeV, where they cover the whole pitch-angle range. The pitch-angle diffusion rates are usually peaked between a few hundred keV and 1 MeV. At lower energies, the hiss diffusion rates are restricted to large pitch-angles around 80°. Similarly to the chorus diffusion rates, the stripy features are due to latitudinal effects, where the diffusion rates are peaked at different equatorial pitch-angles and combining them results in stripes of slightly increased diffusion rates.

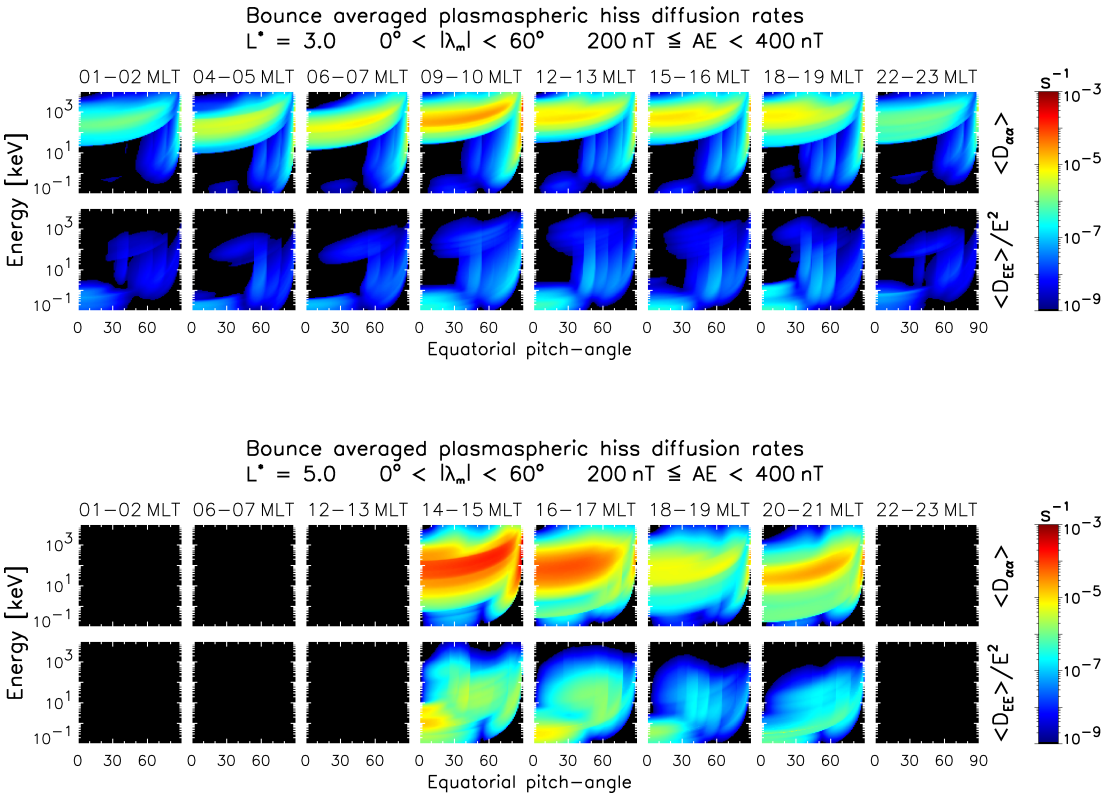


Figure 6.9: Bounce average pitch-angle and energy diffusion rates of plasmaspheric hiss at $L^* = 3.0$ (top) and $L^* = 5.0$ (bottom) for $200\,\text{nT} \leq AE < 400\,\text{nT}$ in the region $0° < |\lambda_m| < 60°$. In the top panels the values of MLT have been spread evenly among all MLT, while the MLT values in the bottom panel where chosen to highlight the diffusion in the plumes region.

In contrast, the pitch-angle diffusion rates due to hiss in plumes only cause significant diffusion between 14 - 21 MLT, where the model allows for hiss wave-power. The pitch-angle diffusion rates are strongest between 14 - 15 MLT, where the diffusion rate is peaked around about 100 keV and covers all pitch-angles. Between 14 - 17 MLT the pitch-angle diffusion rates are at least one decade stronger than the maximum diffusion rate at $L^* = 3.0$. Generally, the pitch-angle diffusion rates are strong at lower electron energies, between a few tens of keV and up to less than 1 MeV.

In both cases, the pitch-angle diffusion rates suggest that plasmaspheric hiss is able to affect particles of all pitch-angles. However, this is limited to electron energies between a few hundred keV and about 1 MeV at $L^* = 3.0$ and about a few tens of keV up to about 1 MeV inside the plumes region. Furthermore, the scattering of electrons is possible at all MLT for $L^* = 3.0$, but restricted to the plumes region at larger $L^*$.

The energy diffusion rates are generally much weaker compared to the pitch-angle diffusion rates, in particular at $L^* = 3.0$, where the maximum energy diffusion rate is of the order of $10^{-7}\,s^{-1}$, which is at least 4 decades lower than the highest pitch-angle diffusion rates. At $L^* = 5.0$ the energy diffusion rates are much stronger than at $L^* = 3.0$, but they are still significantly lower than the pitch-angle diffusion rates in the corresponding sectors. At both levels of $L^*$ the energy diffusion rates are peaked at very low electron energies below 1 keV. The distribution of the energy diffusion rates in MLT is similar to the distribution of the pitch-angle diffusion rates. Therefore, it is unlikely that there will electron acceleration caused by hiss at lower $L^*$, while only a small distribution of electrons with low pitch-angles and low energies can be slightly accelerated inside the plumes.

### 6.5.1 Included Number of Resonances

It was shown in Section 1.6.1 that a careful definition of the resonances included in the calculations of the diffusion coefficients is important. In principle, all resonances should be included, however this would not be computationally feasible and hence the number of resonances has to be limited carefully. In contrast to chorus waves, plasmaspheric hiss usually has significant contributing higher resonances. Therefore, the principal resonances between the Landau resonance and $n = \pm 10$, $n = \pm 30$, or even $n = \pm 50$ [e.g. *Thorne et al.*, 2013; *Li et al.*, 2015] are routinely included into the calculation of the hiss diffusion rates.

In order to determine the relevant resonances for this study, calculations of the diffusion rates were performed that include the resonances of the chorus model ($-10 < n < +10$), as well as separate calculations including only the higher resonances ranging from $-30 < n < -11$ and $11 < n < 30$. The latter range was split into two sets, including the resonances $n = \pm 11, \pm 12, ..., \pm 20$ and $n = \pm 21, \pm 22, ..., \pm 30$. The resulting bounce averaged pitch-angle and energy diffusion rates of the different simulations at 15 - 16 MLT in the region $0° < |\lambda_m| < 60°$ and at the geomagnetic activity of 200 nT $\leq AE < 400$ nT are presented in Figure 6.10. The top panels show the diffusion rates including the resonances between $-10 < n < +10$ for all levels of $L^*$ between 2.5 and

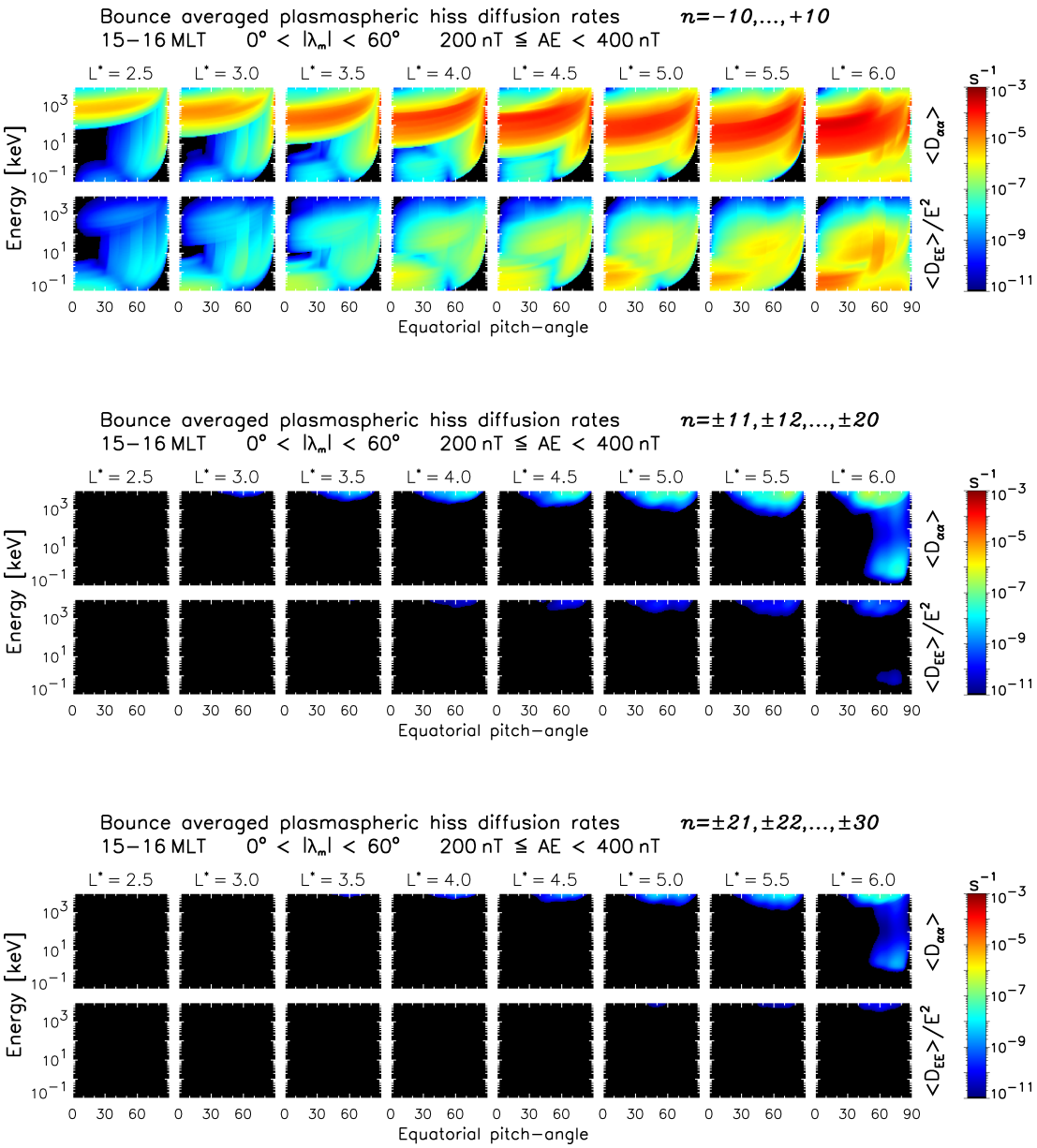


Figure 6.10: Bounce averaged plasmaspheric hiss pitch-angle and energy diffusion rates at 15 - 16 MLT and 200 nT $\leq AE <$ 400 nT in the region $0° < |\lambda_m| < 60°$ for all levels of $L^*$ between 2.5 and 6.0. The top panels show the pitch-angle and energy diffusion rates for the resonances between $-10 \leq n \leq +10$. The middle panels show the diffusion rates for the resonances $-20 \leq n \leq -11$ and $+11 \leq n \leq +20$, while the bottom panels are for $-30 \leq n \leq -21$ and $+21 \leq n \leq +30$.

6.0, increasing from left to right. The middle panels show the diffusion rates due to the higher order resonances with $-20 < n < -11$ and $11 < n < 20$, while the bottom panel shows the diffusion rates due to the highest resonances between $-30 < n < -21$ and $21 < n < 30$.

It can be seen that the diffusion rates caused by the higher order resonances ($n > \pm 10$) are generally much weaker than the diffusion rates of the resonances between $-10 < n < +10$. Furthermore, at larger resonance numbers, the energy range where diffusion can be found increases with $L^*$. At $L^* = 3.0$ diffusion can only be found at energies greater than about 6 MeV, while at $L^* = 5.5$ diffusion is found at energies as low as a few hundred keV. At $L^* = 6.0$, pitch-angle and energy diffusion due to resonances outside of $n = \pm 10$ covers the complete energy range. However, the diffusion at the highest resonances between $-30 < n < -21$ and $21 < n < 30$ is already very low and insignificant compared to the diffusion rates due to resonances with $-10 < n < +10$. Therefore, the contribution above $n = \pm 30$ are assumed to be negligible, and hence these can safely be discarded, while significantly decreasing the computational effort. In order to only calculate the relevant resonances, a $L^*$ and energy dependent model for the included resonance numbers was developed. This model specifies the minimum value of the energy, above which the principal resonances between $-30 < n < +30$ are included. At energies below the minimum energy, the calculations are performed including the resonances between $-10 < n < +10$. The resulting minimum energies are presented in Table 6.3.

| $L^*$ | Minimum energy | $L^*$ | Minimum energy |
|---|---|---|---|
| 1.5 | - | 4.0 | 300 keV |
| 2.0 | - | 4.5 | 200 keV |
| 2.5 | 3000 keV | 5.0 | 60 keV |
| 3.0 | 1000 keV | 5.5 | 20 keV |
| 3.5 | 600 keV | $\geq 6.0$ | 0.1 keV |

Table 6.3: Minimum energy at each level of $L^*$ above which diffusion rates were calculated with $n = -30, ..., +30$ instead of $n = -10, ..., +10$.

## 6.6 Drift and Bounce Averaged Diffusion Rates

Since the `BAS-RBM`, as well as most other radiation belt models, does not include a MLT resolution, the bounce averaged diffusion rates need to be averaged over a full drift orbit. Here, the drift and bounce averaged pitch-angle diffusion rates $\langle D_{\alpha\alpha} \rangle^d$ and the drift and bounce averaged energy diffusion rates $\langle D_{EE} \rangle^d / E^2$ at a given $L^*$, geomagnetic

latitude, and $AE$ were computed by adding the bounce averaged diffusion rates of all MLT sectors at the same location and dividing them by the number of all MLT sectors, i.e. 24. Inside of about $L^* < 4.0$ the coverage of plasmaspheric hiss is mostly complete for latitudes less than 48° and hence the drift averaging is able to capture the effects of hiss waves well in an average sense. However, outside of $L^* = 4.0$ the hiss is mainly present inside the plumes between 14 - 22 MLT. Since the drift averaging is always performed by dividing by the total number of MLT sectors instead of only the sectors that contain data, this approach therefore is likely to underestimate the diffusion rates inside the plumes. In the 3d model, the overall diffusion rates of the plumes region are applied in an average sense at values of $L^*$ that correspond to the plumes, since there is no MLT resolution in the model available.

The drift and bounce averaged diffusion rates are presented only for energies between 100 keV and 10 MeV, since the drift average approach is only valid for electron energies greater than about 100 keV (see Section 2.2.3) and the minimum energy used for the simulations of the radiation belts is therefore usually set to values greater than about 150 keV.

### 6.6.1 Latitudinal Distribution

To assess the influence of each contributing latitudinal sector to the drift and bounce averaged diffusion rates, the latitudinal distribution of the drift and bounce averaged pitch-angle and energy diffusion rates of plasmaspheric hiss are presented in Figure 6.11 for moderate geomagnetic activity of $200\,\text{nT} \leq AE < 400\,\text{nT}$. The latitudinal distribution is presented inside the plasmapause at $L^* = 3.0$ (top panels) and in the region associated with hiss in plumes at $L^* = 5.0$ (bottom panels). The first column shows the diffusion rates over the complete latitude range covered by the model ($0° < |\lambda_m| < 60°$), while the other columns show the contributing 6° latitude sectors, increasing from left to right. The rightmost latitude sector ranges from $42° < |\lambda_m| < 48°$ and since there is no significant diffusion at these high latitudes, no higher latitudes are presented. In this section, only the latitudinal distribution of the diffusion rates is discussed, a detailed analysis of the features of the diffusion rates are presented in the next section.

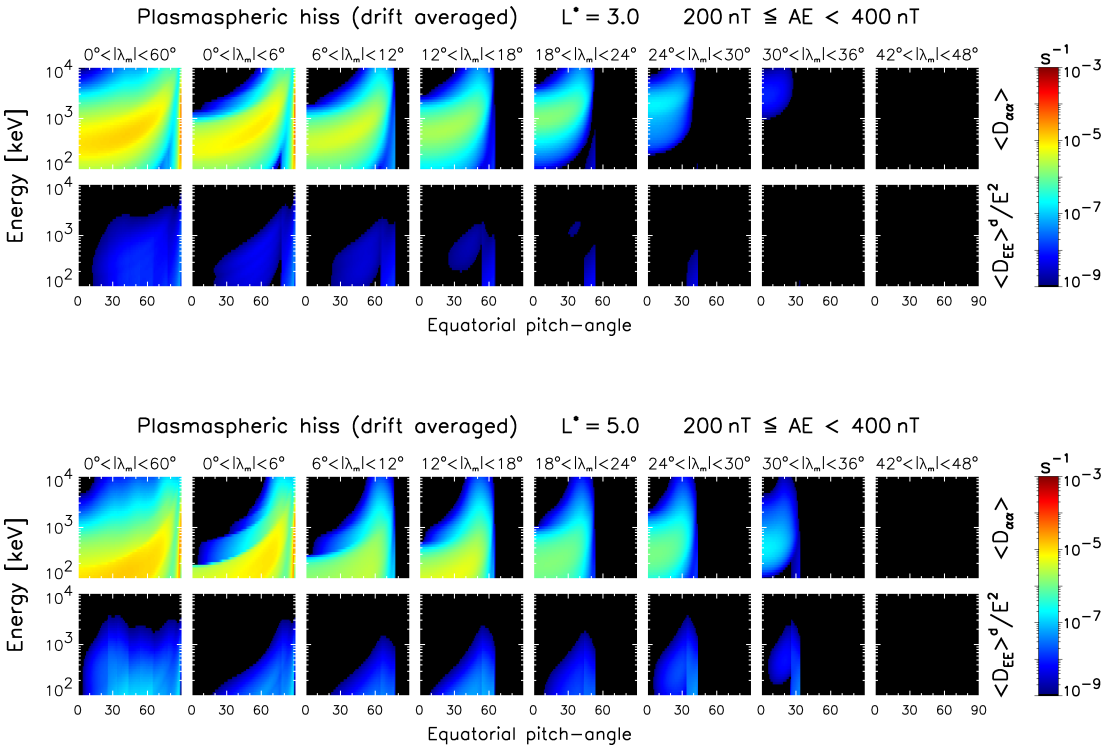


Figure 6.11: Latitudinal distribution of the drift and bounce averaged pitch-angle and energy diffusion rates of plasmaspheric hiss at $L^* = 3.0$ (top) and $L^* = 5.0$ (bottom) for $200\,\mathrm{nT} \leq AE < 400\,\mathrm{nT}$. The first column shows the diffusion rates in the range of $0° < |\lambda_m| < 60°$, while the other columns show the diffusion rates at individual 6° latitude bins, with increasing latitude from left to right.

The results show that the contribution of the plasmaspheric hiss near the equator is the strongest, but in contrast to chorus waves, the equatorial diffusion rates do not dominate the overall diffusion rates, since the pitch-angle diffusion rates at geomagnetic latitudes up to 18° are only between 2 and 5 times lower. Nevertheless, the diffusion rates do not cover the whole pitch-angle range. With increasing latitude, the maximum pitch-angle, at which significant pitch-angle and energy diffusion can be found, decreases. For instance, at the latitude range $12° < |\lambda_m| < 18°$ the diffusion rates cover equatorial pitch-angles from $\alpha_{eq} = 0°$ to about $\alpha_{eq} = 65°$. At latitudes greater than about 18° the diffusion rates slowly decrease with increasing latitude, in comparison with the diffusion rates near the equator. Above 30° only small contributions can be found and above 42° the diffusion rates become insignificant. More importantly, it can be seen that the contribution to the diffusion rates at small pitch-angles and energies greater than a few MeV are only due to the plasmaspheric hiss at higher latitudes. For

instance, there is no pitch-angle diffusion in the equatorial region above about 1 MeV at pitch-angles less than about 30°, while the hiss at higher latitudes causes diffusion in this region. All these features are generally similar at $L^* = 3.0$ and $L^* = 5.0$, showing that the hiss in plumes contributes in the same latitude range as the hiss at lower $L^*$.

### 6.6.2 Comparison of the G14 and the New Hiss Model

Most models to calculate the electron fluxes in the Earth's radiation belts, including the `BAS-RBM`, don't include a MLT resolution, and there are very few models that are able to do so. Instead, most models use diffusion rates that are drift averaged over all MLT, since drift averaged simulations are able to predict the overall shape of the pitch angle distribution accurately.

Here, the drift and bounce averaged pitch-angle diffusion rates $\langle D_{\alpha\alpha}\rangle^d$ and the drift and bounce averaged energy diffusion rates $\langle D_{EE}\rangle^d/E^2$ at a given $L^*$, geomagnetic latitude, and $AE$ were computed by adding the bounce averaged diffusion rates of all MLT sectors at the same location and dividing them by the number of MLT sectors, i.e. 24. Since the drift averaging is always performed by dividing by the total number of MLT sectors instead of only the sectors that contain data, the averaged diffusion rates at higher $L^*$, where the hiss can only be found in plumes, are lower than the bounce averaged diffusion rates in the plumes region. This might lead to underestimated electron fluxes at large $L^*$ and can only be circumvented using a 4d radiation belt model. Since the drift average approach is only valid for electron energies greater than about 100 keV (see Section 2.2.3), the drift and bounce averaged diffusion rates are presented only for energies between 100 keV and 10 MeV.

As an example, the drift and bounce averaged pitch-angle and energy diffusion rates at $L^* = 3.5$, $L^* = 4.0$, and $L^* = 5.5$ are presented in Figures 6.12 - 6.14. The latter therefore represents hiss in plumes at larger geomagnetic activity. The pitch-angle diffusion rates are shown for the new (first row) and the G14 hiss model (second row), while the energy diffusion rates are shown for the new (third row) and the G14 hiss model (fourth row). The new diffusion rates are shown for the 6 levels of geomagnetic activity of the model, measured by the $AE$ index, while the G14 model is presented for

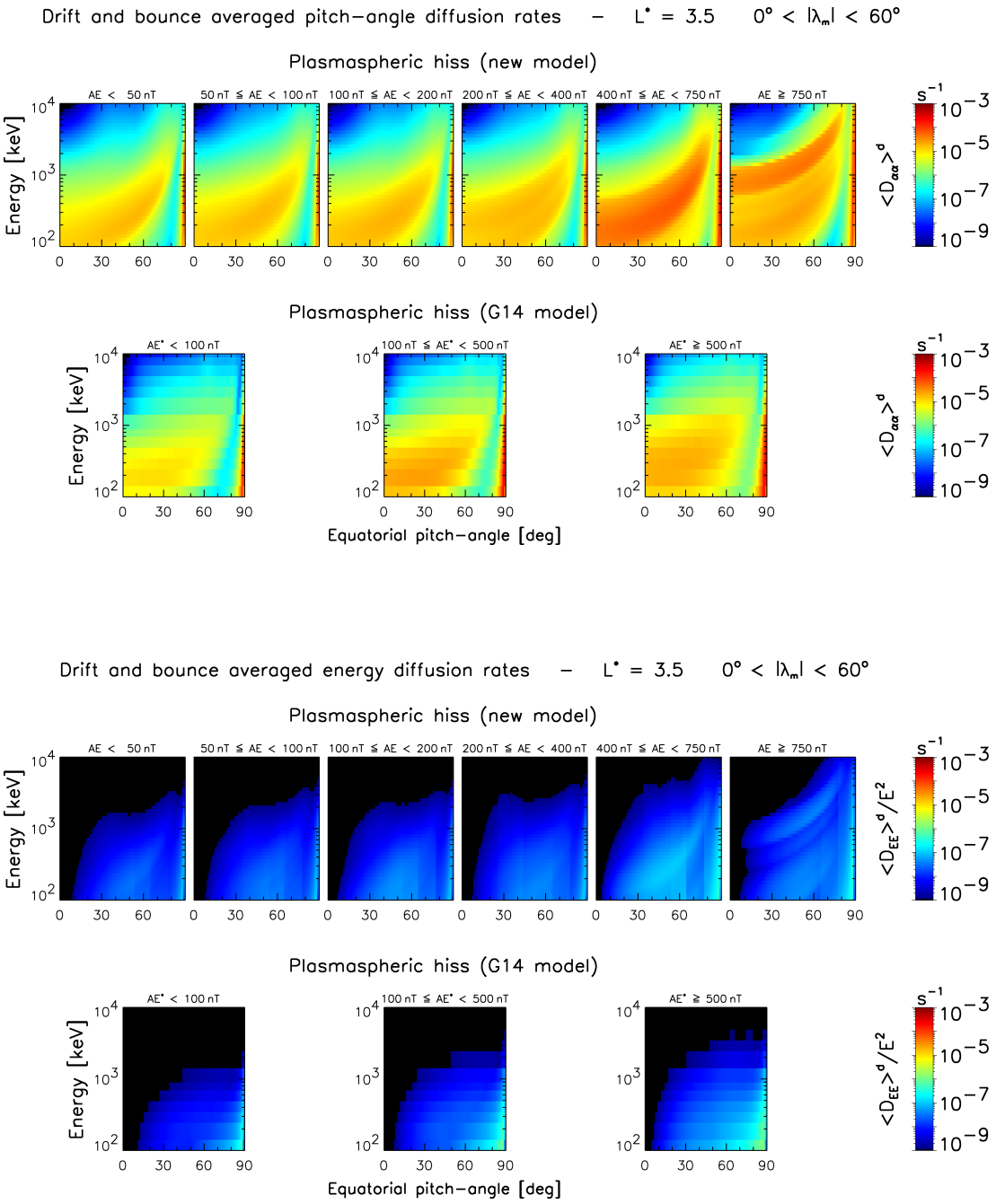


Figure 6.12: Drift and bounce averaged pitch-angle (top) and energy diffusion rates (bottom) of the new hiss model (first and third row) and the G14 hiss model (second and fourth row) at $L^* = 3.5$ and $0° < |\lambda_m| < 60°$ for the activity levels of each model.

3 levels of $AE^*$.

For $L^* = 3.5$ there is a clear increase of the diffusion rates with geomagnetic activity for both models. Generally, the pitch-angle diffusion rates are peaked at energies of a few hundred keV and strong from about 100 keV to about 1 MeV. However, there is a

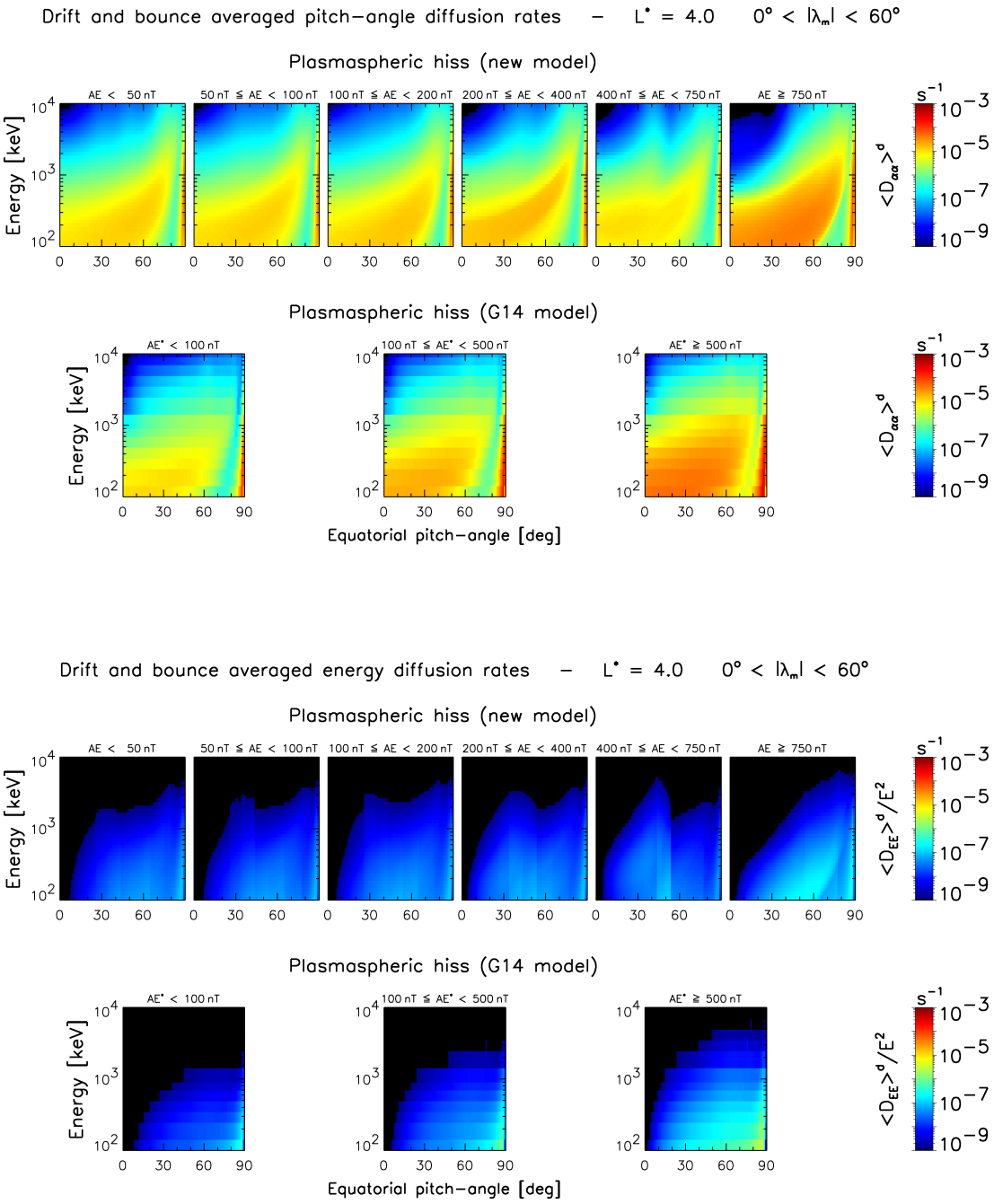


Figure 6.13: Drift and bounce averaged pitch-angle (top) and energy diffusion rates (bottom) of the new hiss model (first and third row) and the G14 hiss model (second and fourth row) at $L^* = 4.0$ and $0° < |\lambda_m| < 60°$ for the activity levels of each model.

gap of low diffusion rates at large pitch-angles greater than about 65° at 100 keV and increasing towards about 80° for higher energies. The diffusion rates might still be large enough to scatter particles into the loss cone, but it indicates that the strongest losses should be expected for pitch-angles of about 60° (and less).

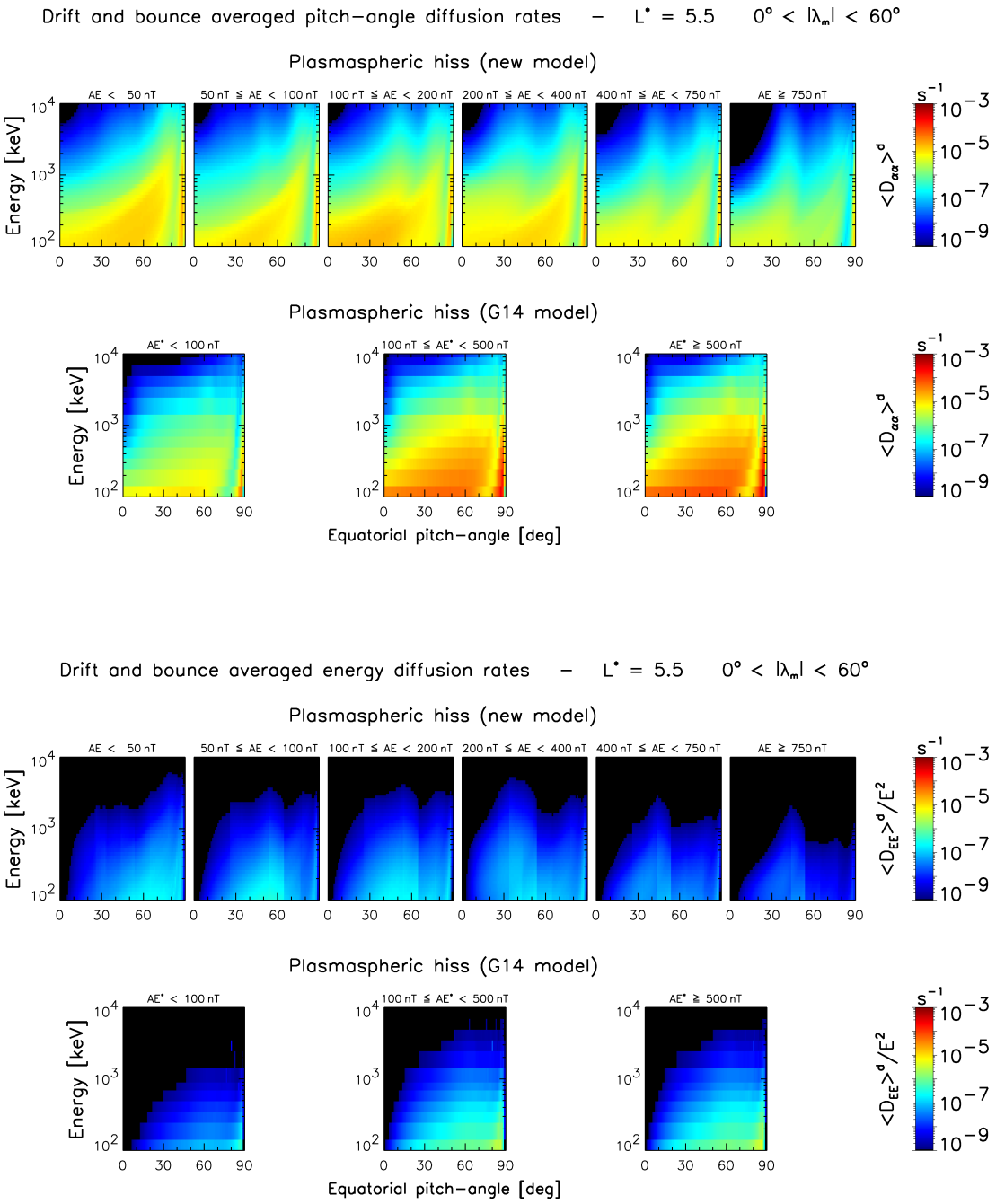


Figure 6.14: Drift and bounce averaged pitch-angle (top) and energy diffusion rates (bottom) of the new hiss model (first and third row) and the G14 hiss model (second and fourth row) at $L^* = 5.5$ and $0° < |\lambda_m| < 60°$ for the activity levels of each model.

During very quiet conditions, the pitch-angle diffusion rates of the G14 and the new hiss model are of the same order of magnitude, while for medium and high geomagnetic activity, the pitch-angle diffusion rates of the new model are at least one order of magnitude larger than the ones of the G14 hiss model. In contrast, the energy diffusion

rates of the G14 hiss model are generally about one decade larger than the ones of the new model, although the energy diffusion is very low compared to the pitch-angle diffusion and hence it is unlikely that either model would cause significant electron acceleration.

However, since the G14 hiss model was calculated for $AE^*$ rather than $AE$, conclusions for the comparison of the effect of the new hiss model and the G14 hiss model on the global electron fluxes can not be drawn directly. Using the fact that $AE^*$ is the maximum value of $AE$ in the previous 3 hours, the comparison can still give indications to the effect on the fluxes, though. It is expected that due to the use of $AE^*$, short periods of high $AE$ result in overestimating the effects of the G14 hiss model at high geomagnetic activity. During prolonged periods of high $AE$ however, it should be possible to compare the two hiss models directly, since $AE$ and $AE^*$ are equivalent for an extended period.

At $L^* = 4.0$ the peak of the pitch-angle diffusion rates of the G14 and the new hiss model is shifted towards lower energies, and they are about the same as at $L^* = 3.5$, while the diffusion rates of the G14 and the new hiss model are now of the same order. However, inside the plumes at $L^* = 5.5$ the pitch-angle diffusion rates of the G14 hiss model become much stronger than the ones of the new model at medium and high geomagnetic activities and the peak of the diffusion rates is reduced to even lower electron energies. This effect is the same for the energy diffusion rates, which are stronger for both models, but still too small, to cause acceleration, except at energies of about 100 keV for the G14 hiss model.

Overall, the diffusion rates of the G14 hiss model tend increase with $L^*$, while they are constant for the new model until the regions where hiss is only present in the plumes region. These differences of the diffusion rates are due to the difference of the way the two models were computed. The G14 hiss model is a statistical model that varies with $L^*$, it has no MLT resolution, while the new model is much more sophisticated. At very high geomagnetic activity, the plasmapause is likely to move further in to about $L^* < 4.5$ at most MLT, but there might be plumes in the afternoon sector. The hiss in plumes is captured by the new hiss model, and the drift averaging of the diffusion rates

includes hiss only at the MLT sectors, if it is present, reducing the overall diffusion rates in the regions of larger $L^*$. The G14 hiss model however, assumes hiss to be present at all magnetic local times and hence overestimates the diffusion rates significantly at larger $L^*$. This effect is most likely to be even more pronounced in the electron fluxes, because of the differences between $AE$ and $AE^*$ discussed above.

## 6.7 Global Simulation of the Electron Flux

In order to assess the influences of the changes made in the new plasmaspheric hiss model on the electron fluxes in the Van Allen radiation belts, the `BAS-RBM` was run for the same 100 day period in 1990 that was studied in chapter 4 for chorus waves, driven by the $AE$ index. As this period is well understood and comprehensively studied by other authors, it is appropriate to evaluate the differences between the G14 and the new plasmaspheric hiss model. The model was run on a $60 \times 60 \times 60$ pitch-angle, energy, and $L^*$ grid with a timestep of 300 seconds. The energy was ranging from $E_{min} = 153.0\,\text{keV}$ to $E_{max} = 20.0\,\text{MeV}$ at $L^*_{max}$ and $L^*$ ranges between 2.05 and 5.55. In addition to the new plasmaspheric hiss model or the G14 hiss model, the EMIC waves, as presented in Chapter 5, as well as lower and upper band chorus waves, in particular the lower frequency chorus model presented in Chapter 4, were included in the 3d model runs. Furthermore, the radial diffusion coefficients by *Brautigam and Albert* [2000], driven by the $Kp$ index, were included. Here, the chorus and EMIC waves, as well as the plasmaspheric hiss represented by the new hiss model were driven by the $AE$ index, while the plasmaspheric hiss defined by the G14 model, was driven by the $AE^*$ index. As explained earlier, it is difficult to predict the effects of the drift and bounce averaged diffusion rates of the different hiss models on the electron flux at lower $L^*$, since two different geomagnetic indices were used. However, at larger $L^*$ of about 4.5 the diffusion rates of the G14 hiss model are significantly stronger than the ones of the new hiss model during the most active conditions. Therefore, it is expected that during prolonged times of high geomagnetic activity, the electron fluxes driven by the new model, decay less quickly, and hence the overall fluxes of the new hiss model should be higher, due to

less pitch-angle scattering of the new hiss model.

The results of the simulations are shown as contour plots in Figure 6.15 for the flux of electrons with an equatorial pitch-angle of 90° and an energy of $E = 418\,\text{keV}$. Panel (a) shows the CRRES data, panel (b) shows the simulations that include radial diffusion, lower and upper band chorus, EMIC waves, and plasmaspheric hiss defined by the G14 hiss model, and panel (c) shows the simulations that include the same waves as panel (b), but with plasmaspheric hiss defined by the new hiss model. The geomagnetic indices driving the simulations are shown in panel (d), while the white line indicates the location of the plasmapause as defined by *Carpenter and Anderson* [1992]. The data below $L^* = 3.0$ is not plotted, since it is below the minimum energy of the simulation at this energy level. It can be seen that simulations of the new hiss model and G14 hiss model are similar. At $L^* < 3.75$ the flux of the new model is slightly lower than the fluxes of the G14 hiss model at nearly all times. On the other hand, the fluxes at larger $L^*$ tend to be slightly larger for the new model. Overall, the fluxes of both models tend to underestimate the fluxes as measured by the CRRES satellite, but they are able to reproduce the general shape of the electron belt at most times, while the fine structure and sharp dropouts are not reproduced well by the model. Overall, the results show that the differences between the G14 and the new hiss model are subtle, indicating that the G14 hiss model already captured most effects of plasmaspheric hiss well.

In order to quantify the differences more accurately, the electron flux is presented for the same period and parameters as a set of line plots at constant values of $L^*$ in Figure 6.16. The CRRES data are shown as the dotted lines, while the simulations based on the G14 hiss model are the blue lines and the ones based on the new hiss model are the red lines. The results are presented at $L^* = 3.65$, $L^* = 4.25$, and $L^* = 5.05$, in order to represent the effects of hiss well inside the plasmapause, at medium $L^*$, and in a region where hiss in plumes is already present.

The results show that at $L^* = 3.65$ the fluxes calculated with the new hiss model decay much faster than the fluxes calculated with the G14 hiss model, during periods of low geomagnetic activity, while the decay rates are similar during enhanced geomagnetic

activity. The resulting flux of the new hiss model can be up to 5 times smaller than the fluxes calculated utilising the G14 hiss model. The differences of the flux caused by the different hiss decay rates are evened out during the phases of a strong increase of the electron flux, where both models reach the same flux levels. However, both models underestimate the measured flux by about a factor of 5 to 10 during all times. This difference is mainly due to a difference during the adjustment period of the simulation, where the data and simulation quickly depart from each other, resulting in a permanent shift between data and simulation. If this shift was adjusted for, the decay rates of the new hiss model would represent the data better than the ones of the G14 hiss model at $L^* = 3.65$.

At larger $L^*$ this behaviour is inverted. For example, at $L^* = 4.25$ the fluxes of the new hiss model tend to be always larger than the ones of the G14 hiss model, with differences up to about a factor of 2-3. The decay rates of the new hiss model tend to be slightly smaller than the decay rates of the G14 hiss model, resulting in higher fluxes of the new hiss model. The comparison with the CRRES data shows mixed results. While the G14 model tends to underestimate the measured fluxes by up to a factor of 3 during most times, there are times when the simulation agrees with the data, in particular around flux dropout events around days 284, 305, and 330. The simulations utilising the new hiss model however, tend to achieve better agreement during and after times of enhanced fluxes (around days 260, 286, and 310), but tend to overestimate the flux at other times. As a result, there are indications that a combination of the two hiss models, with the diffusion rates from the new model during quiet times and G14 during active times, might be able to reproduce the measured fluxes better.

At $L^* = 5.05$ this effect is the same, while the differences between data and both simulations are much smaller, which is most likely due to imposed fluxes from the $L^*_{max}$ boundary. Similarly to $L^* = 4.25$ there are times where the G14 hiss model agrees better with the data, and times where the new hiss model achieves better agreement. The decay times of both models tend to be of the same order, with only minor differences less than a factor of 2.

The results for electrons with an energy of 976 keV are shown in the same format in

Figures 6.17 and 6.18. The contour plots show that the flux calculated utilising the G14 model tends to underestimate the measured electron flux during most times, while the flux calculated with the new hiss model achieves better agreement with the data. Similarly to the lower energy level presented, the model is able to reproduce the general structure of the measured electron flux, but is lacking the fine structure, in particular the flux dropout events around days 284, 304, and 322. The lineplots at constant $L^*$ confirm these observations, showing that the G14 hiss model underestimates the measured flux at all $L^*$ up to a factor of 10 at $L^* = 3.65$, a factor of about 5 at $L^* = 4.25$ and $L^* = 5.05$. At all $L^*$ the fluxes calculated with the G14 and the new hiss model diverge during the adjustment period of the model. While the decay rates of the two models tend to be similar at $L^* = 4.25$ and $L^* = 5.05$, they are larger for the new hiss model at $L^* = 3.65$, resulting in more loss caused by the new hiss model at this $L^*$. As a result, the measured flux tends to be overestimated by the new hiss model during most times, while it is always underestimated by the G14 hiss model. Both models are unable to fully reproduce the flux dropout events at the larger $L^*$. Overall these results are similar to the ones at 418 keV.

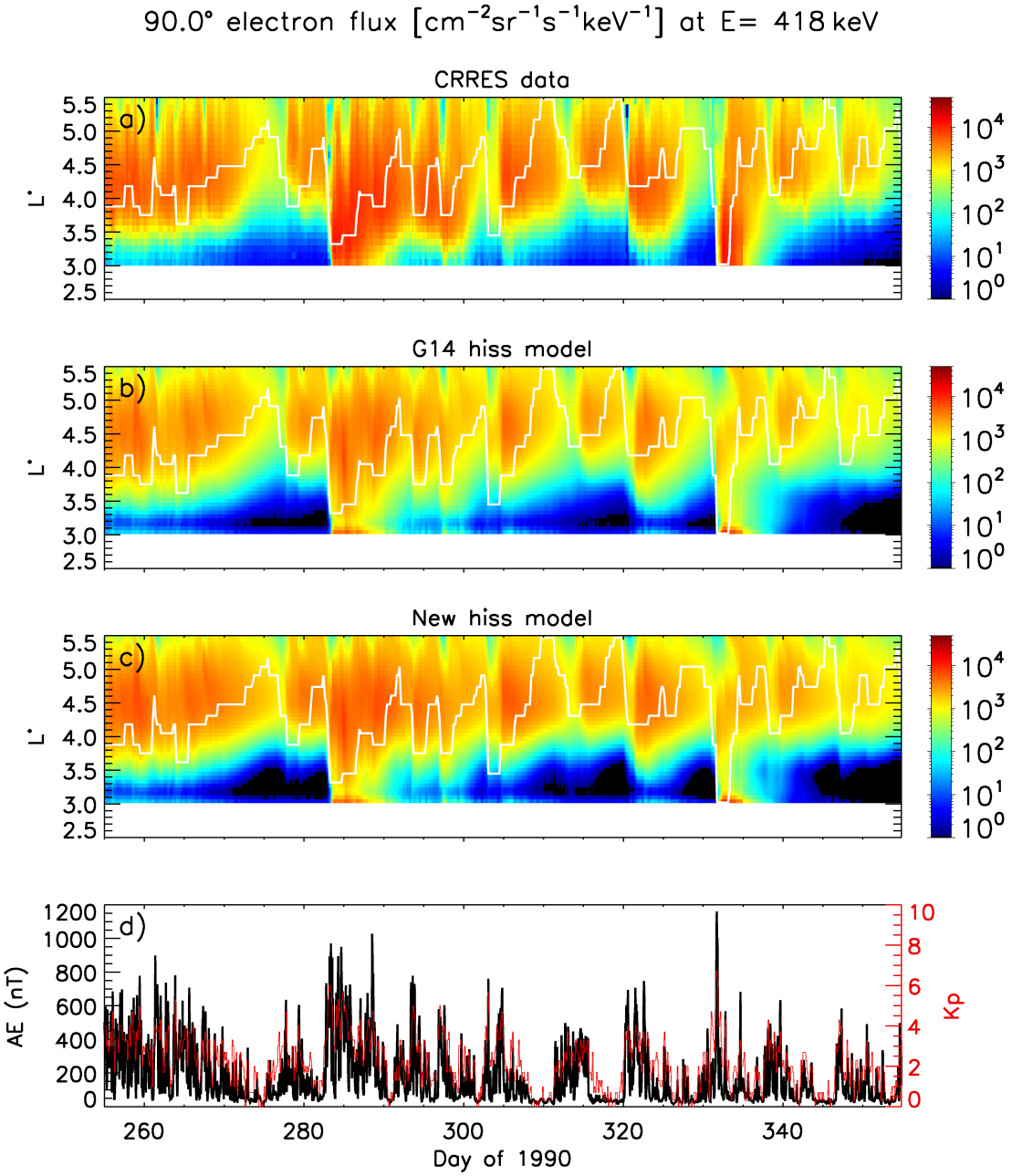


Figure 6.15: Flux of electrons with an equatorial pitch-angle of 90° and energy of $E = 418\,\mathrm{keV}$ as measured by the CRRES satellite (a), and calculated by the `BAS-RBM` using radial diffusion, lower and upper band chorus waves, EMIC waves, and additionally the G14 hiss model (b) or new hiss model (c). The model was driven by the $AE$ and $Kp$ indices shown in panel (d). The flux is presented as a function of the simulation period time and $L^*$.

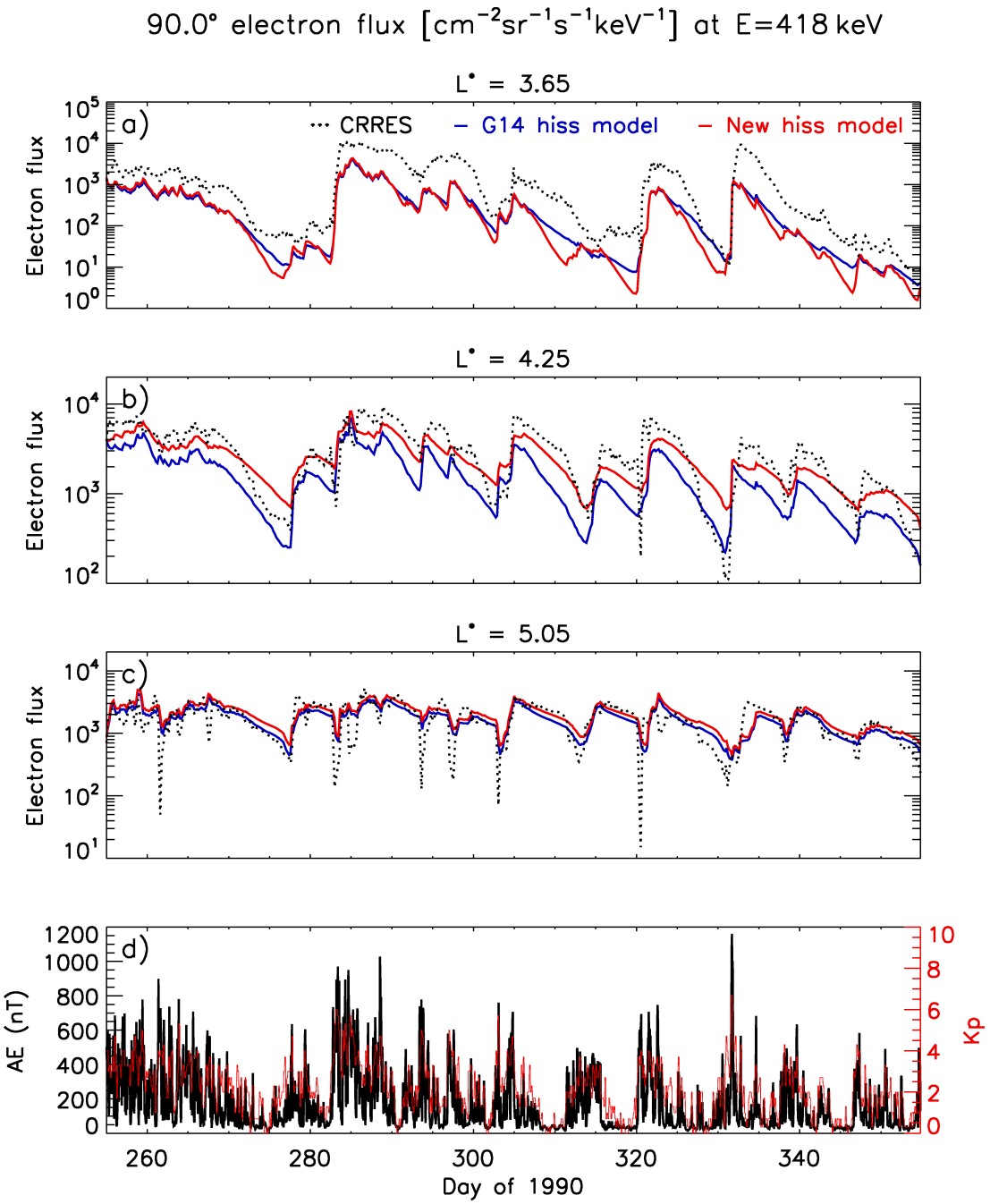


Figure 6.16: Flux of electrons with an equatorial pitch-angle of 90° and energy of $E = 418\,\mathrm{keV}$ at the constant values of (a) $L^* = 3.65$, (b) $L^* = 4.25$, (c) $L^* = 5.05$. The blue line shows the fluxes calculated by the `BAS-RBM` using radial diffusion, lower and upper band chorus waves, EMIC waves, and the G14 hiss model, the red line the results of the same calculation but with the new hiss model instead. The dotted line shows the electron flux as measured by the CRRES satellite, and the driving $AE$ and $Kp$ indices are shown in panel (d).

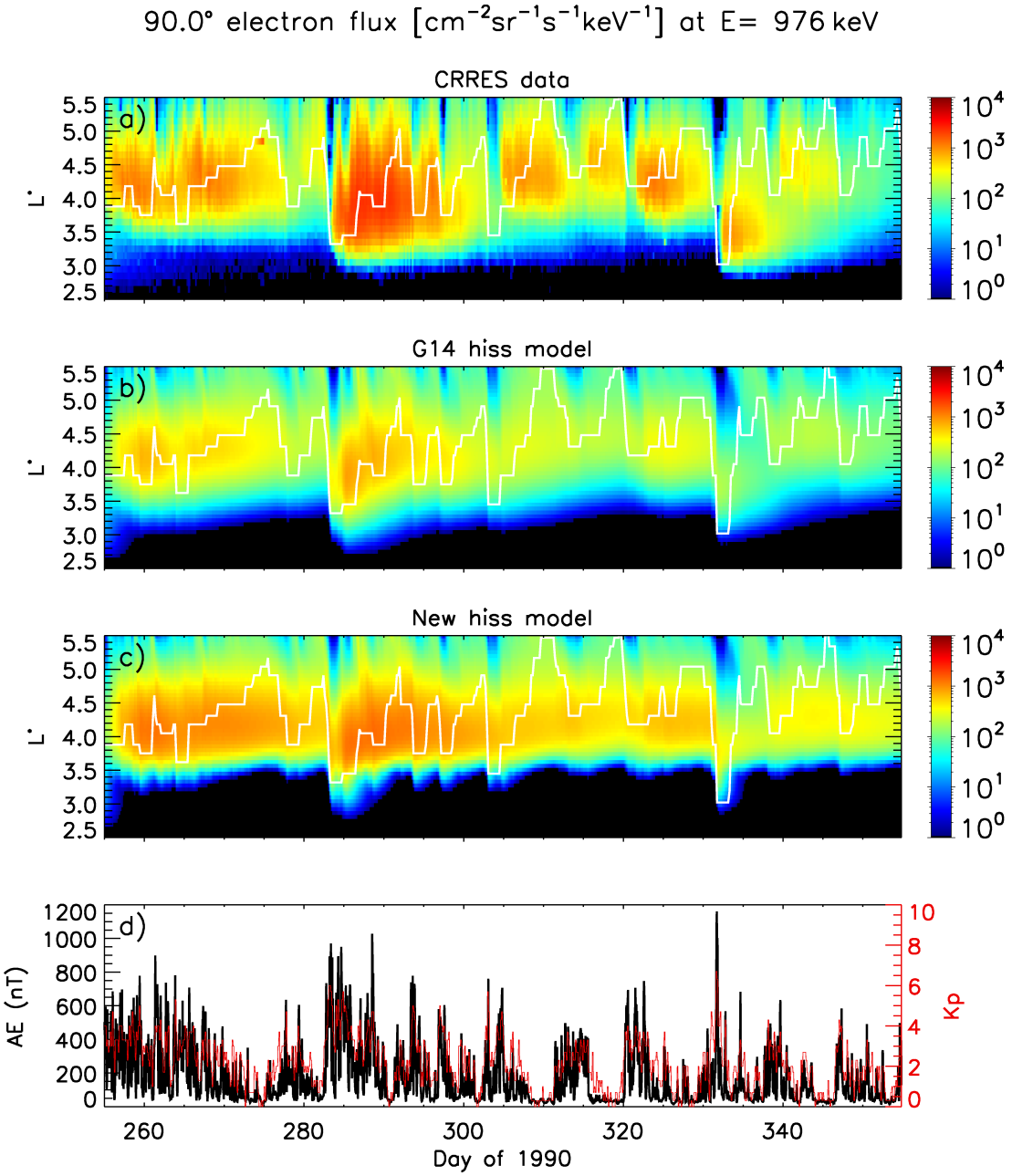


Figure 6.17: Flux of electrons with an equatorial pitch-angle of 90° and energy of $E =$ 976 keV (a) as measured by the CRRES satellite, and calculated by the BAS-RBM using radial diffusion, lower and upper band chorus waves, EMIC waves, and additionally the (b) the G14 hiss model or (c) new hiss model. The model was driven by the $AE$ and $Kp$ indices shown in panel (d). The flux is presented as a function of the simulation period time and $L^*$.

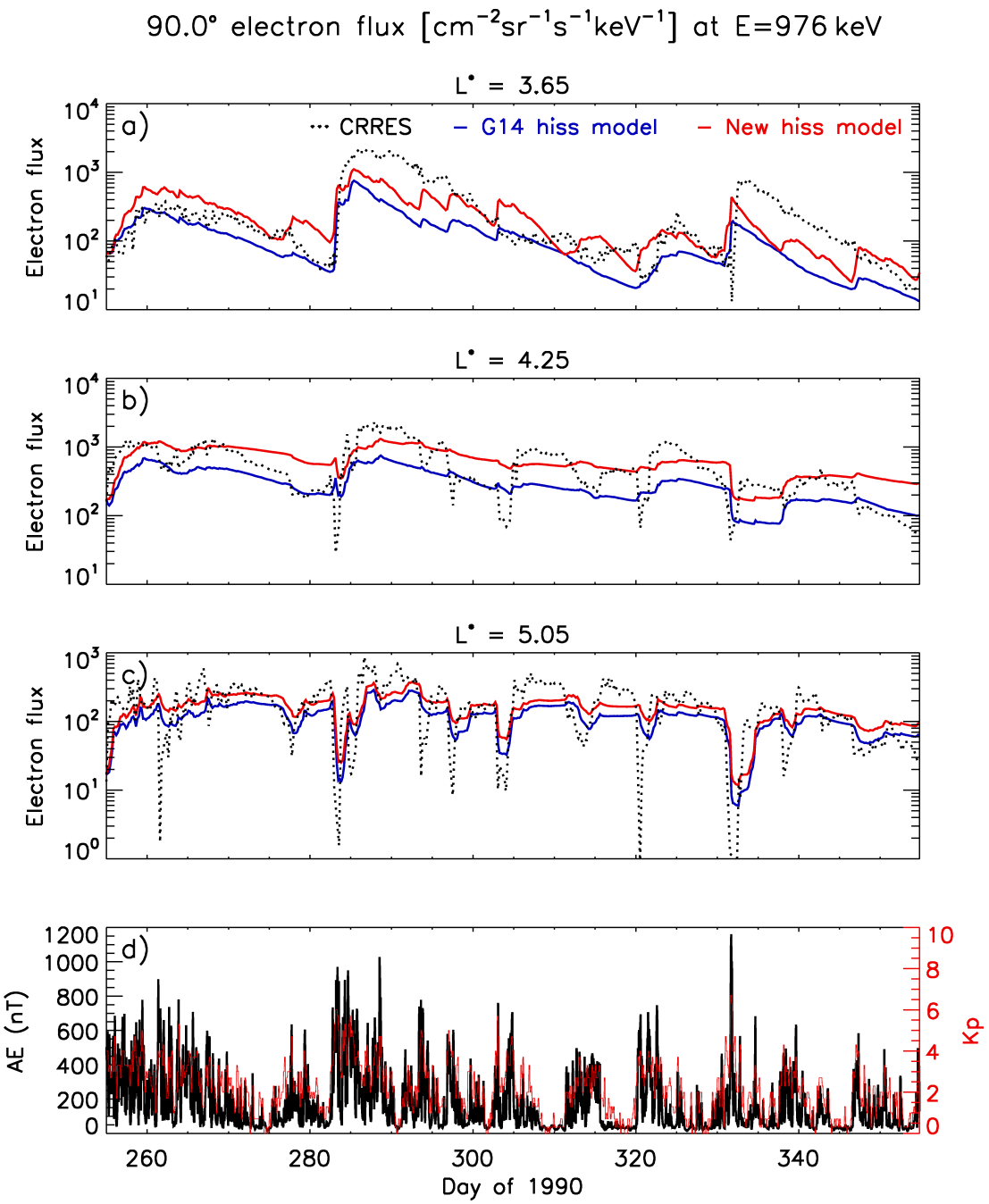


Figure 6.18: Flux of electrons with an equatorial pitch-angle of 90° and energy of $E = 976\,\mathrm{keV}$ at the constant values of (a) $L^* = 3.65$, (b) $L^* = 4.25$, (c) $L^* = 5.05$. The blue line shows the fluxes calculated by the `BAS-RBM` using radial diffusion, lower and upper band chorus waves, EMIC waves, and the G14 hiss model, the red line the results of the same calculation but with the new hiss model instead. The dotted line shows the electron flux as measured by the CRRES satellite, and the driving $AE$ and $Kp$ indices are shown in panel (d).

## 6.8 Discussion

The presented wave model for the plasmaspheric hiss is based on a statistical analysis of the average spectral intensity of the wave magnetic field component from seven different satellites covering a wide range of latitudes. Since the CRRES satellite only provided reliable measurements of the wave electric field components, a conversion of the electric field to the magnetic field was performed assuming field aligned wave propagation. However, plasmaspheric hiss is known to become highly oblique for increasing geomagnetic latitudes. Therefore, the E-to-B conversion of the CRRES data might produce wave intensities that are greater than the physically present waves at larger latitudes. This effect should be most significant near the highest latitudes covered by the CRRES satellite ($\lambda_m = 30°$). Since there is still good coverage of most satellites at these latitudes, it is believed that possible errors of the CRRES data are averaged out by the data of the other satellites. Nevertheless, a revised version of the plasmaspheric hiss wave database should be created at a later time, where the E-to-B conversion is based on a more realistic wave normal angle distribution. However, this would require a lot of additional work, since the complete raw satellite data needs to be recalculated. Lower band chorus waves and plasmaspheric hiss can be found in the same frequency ranges and are separated by being outside or inside the plasmapause, respectively. A method to separate chorus from hiss was presented, where two individual Gaussian profiles were fitted to the distribution in $L^*$ of the wave intensity. The intersection of these Gaussians was used to define the boundary separating hiss from chorus between 22 - 14 MLT, while a plasmapause model was used between 14 - 22 MLT, in order to include hiss in plumes. While this method captures the hiss reasonably well and excludes chorus from the model, there is no physical reason to assume a Gaussian distribution of the peak wave power with respect to $L^*$. However, this method was not trying to model the distribution of the wave power, but rather trying to identify the regions where hiss and chorus are strong and then separate the two types of waves. Consequently, the presented method does not describe or replace a definition of the plasmapause, instead it is only used to define a boundary region between chorus and hiss.

Plasmaspheric hiss is usually found inside the plasmapause, which can extend into

plumes on the afternoon side. The technique to separate chorus from hiss was chosen in such a way that hiss in plumes is included into the wave model. Since the BAS-RBM does not include MLT resolution, the diffusion rates had to be averaged over a drift orbit. Since the averaging includes all MLT sectors, even the ones without data, the drift averaged diffusion rates at values of $L^*$ that correspond to a plumes region are significantly lower than the bounce averaged diffusion rates at the individual contributing MLT sectors. The effects of hiss in plumes is therefore only applied in an average sense and hence affects the electron fluxes at all MLT, instead of only inside the plumes. In order to be able to simulate the hiss in plumes correctly, a 4d model that includes full MLT resolution is needed, which unfortunately is outside the scope of the capabilities of the available models at this time.

## 6.9 Conclusions

In this chapter a new global, statistical model for plasmaspheric hiss inside the plasmapause and the plumes was developed based on the data from seven different satellites. The resulting model covers the range between $L^* = 1.5 - 4.0$ between 22 - 14 MLT and $L^* = 1.5 - 7.0$ between 14 - 22 MLT with a one hour MLT resolution for geomagnetic latitudes between $0° < \lambda_m < 60°$ for 6 levels of geomagnetic activity defined by the $AE$ index. The model was used to calculate drift and bounce averaged pitch-angle and energy diffusion coefficients, which were compared with a previously published hiss model. The models were used to calculate the electron fluxes during a 100 day period in 1990 that was covered by the CRRES satellite. The results show that plasmaspheric hiss is a significant loss process that can cause electron loss due to pitch-angle scattering over all pitch-angles for electron energies between about 100 keV and about 1 MeV. At the same time, hiss will only cause insignificant electron acceleration. The comparison between the G14 and the new hiss model shows that the largest differences can be found at $L^* < 4.0$, where the new hiss model is causing significantly more electron loss. At larger values of $L^*$, the losses of the new hiss model are less than those of the G14 hiss model, resulting in fluxes that are about a factor of 3 higher. The comparison

with the CRRES data showed that the decay rates of the new hiss model might result in better agreement between model and data than the G14 hiss model at $L^* = 3.65$, if the shift between data and simulation was accounted for. This could be achieved by increased electron acceleration due to chorus waves, for example. At larger values of $L^*$, the new hiss model showed better agreement with the data during times of low geomagnetic activity, while the G14 hiss model produced better agreement during more active times. Conversely, the loss rates of the new hiss model were too large during times of high geomagnetic activity, while they were too low for the G14 hiss model during quiet times. This indicates that a mix of the two diffusion models might be able to reproduce the measured fluxes better.

In order to separate chorus and plasmaspheric hiss, which can be found in the same frequency ranges, a novel technique was developed. From the seven satellites whose data are included into the hiss wave database, only the CRRES satellite provides (reliable) measurements that allow to determine the plasmapause location, in particular the measurements of ECH waves, which are only found outside the plasmapause. It was shown that applying the ECH criterion to the data from all of the satellites includes chorus wave power at large $L^*$. Therefore, a different method to separate chorus from hiss was presented, where two individual Gaussian profiles were fitted to the distribution in $L^*$ of the wave intensity and the intersection of the two was used to define the boundary between hiss and chorus waves between 22 - 14 MLT. In order to include hiss in plumes, a plasmapause model was used between 14 - 22 MLT. The method is able to separate chorus and hiss well, while allowing the modelling of hiss in plumes.

Furthermore, a global, statistical plasma density model was derived entirely from CRRES measurements that has the same resolution as the hiss wave model, but is only based on measurements between $3^\circ < \lambda_m < 15^\circ$.

The calculation of the diffusion rates requires knowledge of the wave normal angle distribution of the waves. Previous studies have used different assumptions for the wave normal angle, while this study uses a parametrised model derived from the THEMIS data. The resulting wave normal angle model distinguishes between day and nightside and provides the wave normal angle profiles for two different geomagnetic activity levels

and all latitudes in steps of 6°.

Although the comparison with the CRRES data showed mixed results, the significant increase of the volume of data used for the presented new hiss model considerably improves the confidence in the statistical model and hence provides a valuable extension of the current radiation belt model.

# CHAPTER 7
# *Model Evaluation*

## 7.1 Introduction

In the previous chapters novel and improved models for lower and upper band chorus, EMIC waves, and plasmaspheric hiss were presented. Their effects were discussed based on simulations of the electron flux during a selected period of the CRRES satellite. However, the CRRES satellite only reliably measured the electron flux up to energies of around 1 MeV and failed after about 15 months of operation. In August 2012 the NASA Van Allen Probes mission was launched, whose main objective was to considerably extend the knowledge of the radiation belts. Of particular interest for this study were the key objectives to "understand and quantify the conditions that control the production and propagation of waves (e.g. EMIC, whistler-mode chorus and hiss)" and to "determine the types and characteristics of plasma waves causing particle energisation and loss: including wave growth rates; energisation and loss mechanisms; diffusion coefficients and loss rates" [*Mauk et al.*, 2012]. In order to achieve these goals, the Van Allen Probes cover a wide range of $L^*$ and more importantly, they measure the fluxes of ultrarelativistic electrons with energies up to 20 MeV. These high energy electron fluxes are known to have a significant impact on spacecraft, as they can cause internal charging that can damage the electronics of satellites. For instance, *Iucci et al.* [2005] found a significant correlation between satellite anomalies and the ultrarelativistic electron flux at geosynchronous orbit. Therefore, the Van Allen Probes data currently represent the best dataset available to evaluate the `BAS-RBM` against, and to identify remaining problems.

In order to be able to compare the results of the simulations with the Van Allen Probes data, the `BAS-RBM` will be driven by boundary and initial conditions derived directly from the VAP data. An overview of the Van Allen Probes mission is presented in the first section, followed by a description of the method to generate the boundary and initial conditions. The results of the `BAS-RBM` utilising the models for lower and upper

band chorus, EMIC waves, and plasmaspheric hiss presented in the previous chapters are then evaluated by a comparison with the electron fluxes measured by the Van Allen Probes. This chapter concludes with a detailed analysis and discussion of the results as well as encountered problems.

## 7.2 The BAS Van Allen Probes Database

The NASA Radiation Belt Storm Probes (RBSP) mission was launched at the end of August 2012 and on the 9th of November 2012 it was officially renamed to the Van Allen Probes (VAP) mission. The mission is comprised of two identical spacecraft, RBSP-A and RBSP-B. The two satellites were launched into highly elliptical orbits ($1.1\,R_E \times 5.8\,R_E$) with a low inclination of about 10° [*Mauk et al.*, 2012]. The orbital period is about nine hours and the orbits of the two satellites are slightly different, allowing one spacecraft to lap the other about every 2.5 months. After small adjustments to the orbits, the Van Allen Probes now cover the range of about $L^* = 1.1$ - 6.5 at geomagnetic latitudes between about $0° < \lambda_m < 20°$. There are a variety of instruments on board of the spacecraft specifically designed to measure the physical processes inside the Earth's radiation belts. In this study, the data from the Magnetic Electron Ion Spectrometer (MagEIS) and the Relativistic Electron Proton Telescope (REPT) instruments of the Energetic Particle, Composition, and Thermal Plasma Suite (ECT) are used to evaluate the `BAS-RBM` and to derive the boundary and initial conditions for a selected period of the Van Allen Probes mission. Among other data, MagEIS and REPT provide measurements of the electron flux in various pitch-angle channels that are different for each instrument ranging between 0° and 90°. The electron energies covered by MagEIS range between about 30 keV and 4 MeV, while REPT covers electrons between about 2 - 20 MeV.

The datasets provided by NASA were revised significantly over the last few years. Not only was erroneous data removed, but also the available pitch-angle and energy channels, as well as the corresponding data coverage were changed. The Polar Data Centre at the British Antarctic Survey created the BAS RBSP database, which is a local

copy of the publicly available VAP datasets (Level 3, Version 7.2) extended with useful additional data. For instance, the satellites position in $L^*$ was calculated using both the Olson-Pfitzer Quiet Time [*Olson et al.*, 1977] and the Tsyganenko '89 [*Tsyganenko*, 1989] magnetic field model. Furthermore, the magnetic field at the mirror point, as well as the equatorial field strength were calculated using both field models. The resulting datasets were stored for each instrument and satellite individually. For the MagEIS instrument they provide the electron flux in 17 energy channels for 6 values of the average local electron pitch-angle, while for the REPT instrument the flux is provided in 12 energy channels for 9 values of the average local electron pitch-angle. A summary of the pitch-angle and energy channels of MagEIS and REPT as defined in the database is given in Table 7.1. The electron fluxes are provided on a 11 second time resolution, but due to the instrumentation data are not provided for all pitch-angles and all energy channels at every timestep. The interval between each individual measurement is not uniform with data missing for minutes in individual channels, and there are even longer gaps covering the whole dataset.

| **MagEIS** | | | | | | |
|---|---|---|---|---|---|---|
| Local pitch-angle channels [deg] | 8.18182 | | 24.5455 | | 40.9091 | |
| | 57.2727 | | 73.6364 | | 90.0000 | |
| Electron energy channels [keV] | 31.5 | 53.8 | 79.8 | 108.3 | 143.5 | 183.4 |
| | 226.1 | 231.8 | 342.1 | 464.4 | 593.0 | 741.6 |
| | 901.8 | 999.0 | 1077.7 | 1547 | 1701 | |

| **REPT** | | | | | | |
|---|---|---|---|---|---|---|
| Local pitch-angle channels [deg] | 5.29412 | | 15.8824 | | 26.4706 | |
| | 37.0588 | | 47.6471 | | 58.2353 | |
| | 68.8235 | | 79.4118 | | 90.0000 | |
| Electron energy channels [MeV] | 1.8 | 2.1 | 2.6 | 3.4 | 4.2 | 5.2 |
| | 6.3 | 7.7 | 9.9 | 12.3 | 15.2 | 20.0 |

Table 7.1: Summary of the energy channels and pitch-angle channels covered by the MagEIS and REPT instrument of the Van Allen Probes satellites.

## 7.3 Boundary and Initial Conditions

The BAS-RBM solves the Fokker-Planck equation using two computational grids, the ($\alpha$-$E$) and the ($\mu$-$J$) grid, where $\mu$ and $J$ are the first and second adiabatic invariants, $\alpha$ is the electron pitch-angle, and $E$ the electron energy, which depends on $L^*$ (see Section 2.3). In order to determine the temporal evolution of the electron flux using the Fokker-Planck equation, the boundaries of the computational grids need to be defined. As detailed in Section 2.3.2, there are six boundaries, the minimum pitch-angle ($\alpha = 0°$) and maximum pitch-angle ($\alpha = 90°$) boundary, the minimum $L^*$ ($L^*_{min}$) and maximum $L^*$ ($L^*_{max}$) boundary, and the minimum and maximum energy boundary. For both pitch-angle boundaries, the gradient of the phase space density with respect to the pitch-angle is defined to be zero, i.e.:

$$\left.\frac{\partial f}{\partial \alpha}\right|_{\alpha=0°} = 0\,, \qquad \left.\frac{\partial f}{\partial \alpha}\right|_{\alpha=90°} = 0\,. \tag{7.1}$$

Furthermore, the phase space density at the maximum energy is zero, i.e.:

$$f|_{E=E_{max}} = 0\,. \tag{7.2}$$

The phase space density on the $L^*_{min}$, $L^*_{max}$, and $E_{min}$ boundaries is provided to the BAS-RBM by the user. In this chapter, these boundary conditions are directly derived from the Van Allen Probes data during the simulation period.
Likewise, the initial state of the phase space density needs to be specified at the beginning of the simulation period. In this study, the initial condition is derived directly from the Van Allen probes data around the beginning of the simulation period.

### 7.3.1 Minimum and Maximum $L^*$ Boundary Conditions

The minimum and maximum $L^*$ boundary conditions specify a time series of the phase space density of electrons with an equatorial pitch-angle of 90° at user defined values of $L^*_{min}$ and $L^*_{max}$ during the simulation period. Thereby the phase space density is provided for a constant set of energy levels between the parameters $E_{min}$ and $E_{max}$, for both the $L^*_{min}$ and $L^*_{max}$ boundary condition. In order to specify these boundaries based

on the Van Allen Probes data, the phase space density of 90° electrons (converted from the measured electron fluxes) at all energy levels of the MagEIS and REPT instruments is provided each time either RBSP-A or RBSP-B passes through $L^*_{min}$ or $L^*_{max}$ and intermediate timesteps are interpolated by the `BAS-RBM`. Since MagEIS and REPT do not provide measurements for all energy channels at every single timestep of the 11 s time resolution, the data of RBSP-A and RBSP-B is time averaged over a period of 60 seconds in order to be able to derive the boundary conditions for all energy levels at the same time. The averaging is performed for each energy channel, instrument, and satellite individually, taking only existing data into account, while missing data are ignored. Consequently, the satellites position provided in $L^*$ is also averaged, but due to the elliptical orbit of the satellites, $L^*$ does not vary uniformly during an orbit. However, an analysis has shown that the maximum change of $L^*$ within the 60 s averaging period is of the order of about $\Delta L^* = 0.06$ and hence negligible.

The electron fluxes measured by the Van Allen probes are provided in fixed *local* pitch-angle channels rather than the required *equatorial* pitch-angles. Therefore, the flux of electrons with a local pitch-angle $\alpha_{loc} = 90°$ needs to be converted to the flux corresponding to electrons with an equatorial pitch-angle $\alpha_{eq} = 90°$. When an electron moves along a field line, the local magnetic field $B_{loc}(\lambda_m)$ changes with the geomagnetic latitude $\lambda_m$. According to Eq. 1.153 the equatorial pitch-angle corresponding to the local pitch-angle at a given latitude can be calculated as

$$\alpha_{eq} = \arcsin\left(\sqrt{\frac{B_{eq}}{B(\lambda_m)} \cdot \sin(\alpha_{loc})}\right) . \tag{7.3}$$

In this study, the magnetic field at the equator $B_{eq}$ and the magnetic field at the electrons position $B(\lambda_m)$ calculated with the Olson Pfitzer Quiet field model are extracted from the BAS RBSP database. In order to calculate the flux of electrons with an equatorial pitch-angle of $\alpha_{eq} = 90°$ from the flux of electrons with an equatorial pitch-angle $\alpha_{eq}$, knowledge of the pitch-angle distribution of the equatorial electron flux is required. Pitch-angle distributions are highly variable and there is no consensus or reliable model available. Recent studies found a $\sin^n(\alpha)$ pitch-angle distribution, where $n$

ranges between $> 0$ and about 9 [e.g. *Shi et al.*, 2016; *Horne et al.*, 2003a]. Since both MagEIS and REPT measure the electron flux at various constant pitch-angle channels, attempts were made to derive a pitch-angle distribution from this data. Unfortunately, it was found that the pitch-angle distributions of the electron fluxes measured by the Van Allen Probes were unsuitable to calculate valid $\alpha_{eq} = 90°$ fluxes for the model. Discussions with the MagEIS PI made clear that the current $\alpha$ values of the pitch-angle channels, except for the 90° channel, are debated and effectively should not be used at the time, and that they will be updated soon. Therefore, and since the current version of the `BAS-RBM` assumes a pitch-angle distribution proportional to $\sin(\alpha)$ for the initial condition, it was decided to use a $\sin(\alpha)$ pitch-angle distribution of the electron flux for the boundary conditions as well.

The $\alpha_{eq} = 90°$ electron fluxes derived from the MagEIS and REPT instruments in this way were then combined into one dataset, spanning the combined energy range covered by MagEIS and REPT. During this step, the MagEIS energy channels from 31.5 keV to 1701 keV, and the REPT energy channels from 1.8 MeV to 15.2 MeV were used, while the overlapping higher energy channels of the MagEIS instrument and the 20.0 MeV REPT channel were discarded, since they proved to only provide data on rare occasions. At every timestep of the 60 s time resolution of the time averaged dataset, missing data of the energy channels were interpolated using a linear interpolation of the $\log_{10}$ of the electron flux for each satellite individually. Lastly, the data of the two satellites are interleaved timewise, creating the final data set used for the boundary conditions and the initial condition.

The $L^*_{min}$ and $L^*_{max}$ boundary condition are derived from this dataset as the fluxes at all energies at the timesteps where the two satellites passed through $L^*_{min}$ or $L^*_{max}$, respectively. An illustration of this procedure is presented in Figure 7.1, where the orbits of the two Van Allen Probes are represented by the green and blue line. In this example, the $L^*_{min}$ and $L^*_{max}$ data are taken at all blue and red circles, respectively. The electron fluxes $j$ obtained by this method are then converted to phase space densities

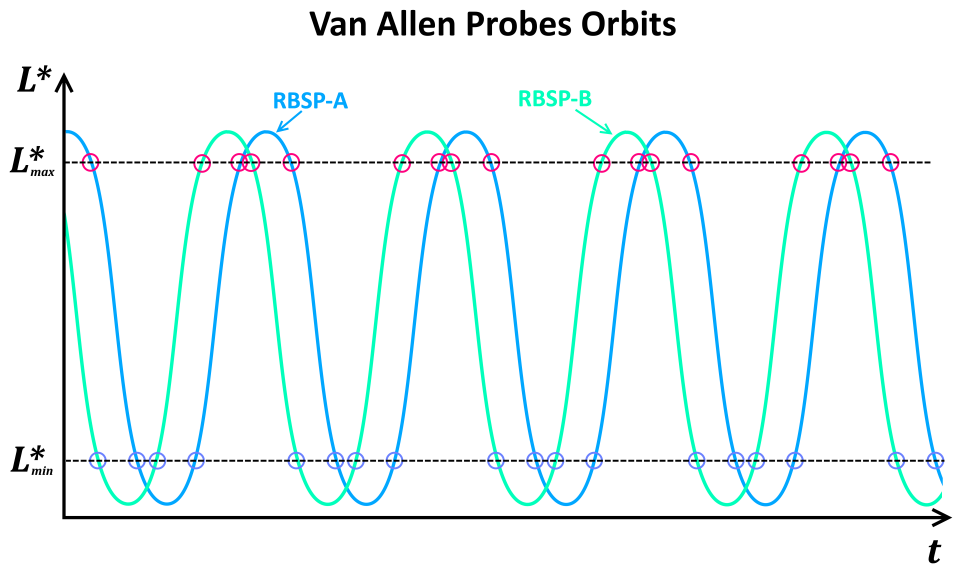


Figure 7.1: Illustration of the method used to define the times at which the $L^*_{min}$ and $L^*_{max}$ boundary condition are derived as the time when either RBSP-A or RBSP-B passes of through $L^*_{min}$ or $L^*_{max}$ (not to scale).

$f$ using the definition (see Chapter 2):

$$f = j/p^2\,, \tag{7.4}$$

where $p$ is the relativistic momentum, which can be related to the relativistic particle energy by

$$p^2 = \frac{E(E+2E_0)}{c^2}\,, \tag{7.5}$$

with rest energy $E_0$ and the speed of light $c$. Hence:

$$f = \frac{c^2 \cdot j(E,t)}{E(E+2E_0)}\,. \tag{7.6}$$

In order to avoid discontinuities between the $L^*$ boundaries and the $E_{max}$ boundary, where the phase space density has to be equal to zero, additional energy levels were added above the maximum energy level of the dataset (15.2 MeV) up to the maximum energy, which was set to $E_{max} = 30$ MeV here. In order to minimise potential discontinuities, the phase space density is tailed off to zero within these additional levels by

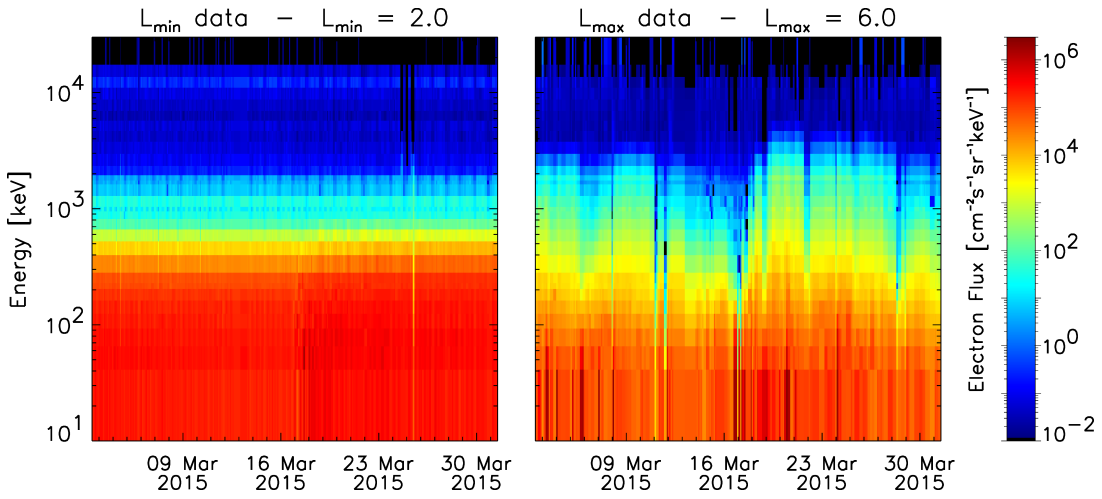


Figure 7.2: Electron flux at the minimum and maximum $L^*$ boundary at $L^*_{min} = 2.0$ and $L^*_{max} = 6.0$ as a contour plot as a function of time and energy derived from the Van Allen Probes data in the period between 3 March 2015 and 1 April 2015.

a linear interpolation from the PSD at 15.2 MeV to zero at 30 MeV.

The resulting $L^*_{min}$ and $L^*_{max}$ boundary conditions are presented in Figure 7.2 between 3 March 2015 and 1 April 2015. In these examples, the values $L^*_{min} = 2.0$ and $L^*_{max} = 6.0$ were chosen. It can be seen that the electron flux at the $L^*_{min}$ boundary is distributed evenly along time with only small variations and the flux gradually decreases with increasing energy. In contrast, the flux at the $L^*_{max}$ boundary is much more variable over time, and the flux also decreases with increasing energy. The `BAS-RBM` is generally able to cope with variations of the electron flux, as long as they are not too large or show discontinuities between two boundaries that share a common border.

### 7.3.2 Minimum Energy Boundary Condition

The minimum energy boundary condition specifies the phase space density at $E_{min}$ for all values of $L^*$ between $L^*_{min}$ and $L^*_{max}$. More specifically, for all values of $E_{min}$ that correspond to the energy values defined within $L^*_{min}$ and $L^*_{max}$ (see Section 2.3.2). These values of the phase space density on the minimum energy boundary needs to be provided continuously throughout the selected simulation period. At every timestep, where the $E_{min}$ boundary is specified, the phase space density for all levels of $L^*$ needs to be provided. Since the satellite can not physically be present at all positions at the same time, the data need to be interpolated.

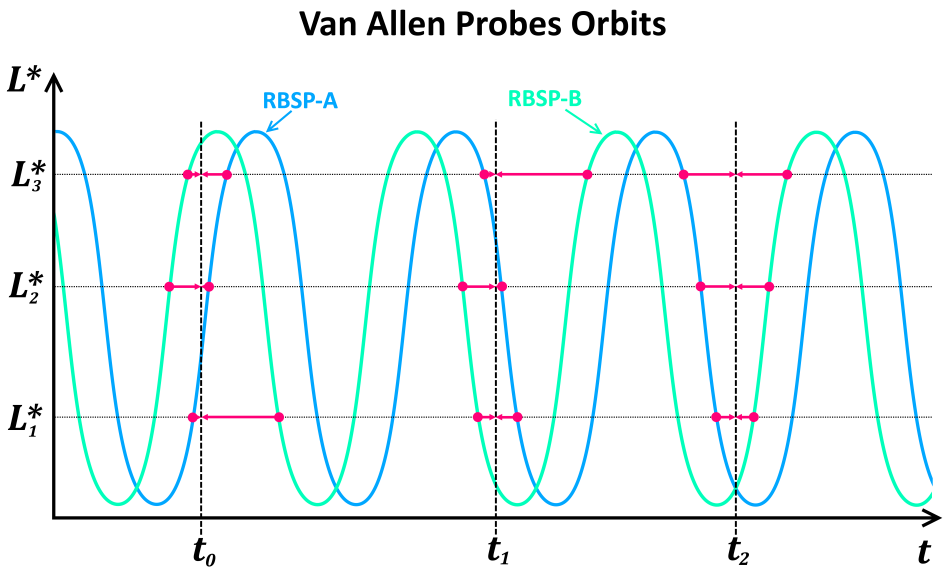


Figure 7.3: Illustration of the method to derive the $E_{min}$ boundary condition (not to scale).

The method used here provides the $E_{min}$ boundary every 5 minutes. For each of these timesteps the closest datapoints before and after any given timestep are stored for each value of $L^*$ individually. The $\log_{10}$ of the electron flux is then averaged for each value of $L^*$, weighted by the time distance of the flux to the timestep of the $E_{min}$ boundary. This process is illustrated in Figure 7.3 for three representative time steps $t_i$ and three levels of $L^*$.

Since the $L^*$ values of the orbits of RBSP-A and RBSP-B can intersect at times, this method might include data from just one satellite at the same timestep, but it is not restricted to it. Depending on the satellites position at any given timestep, certain values of $L^*$ always contain a larger uncertainty than others. But since the $E_{min}$ boundary is defined every 5 minutes, which is much shorter than the about 9 hours of one RBSP orbit, the affected values of $L^*$ change all the time, resulting in a small average error of the fluxes at the $E_{min}$ boundary. The resulting fluxes are then converted into the corresponding phase space densities using Eq. 7.6, creating the final structure of the $E_{min}$ boundary.

The flux of the minimum energy boundary condition during the period of 3 March 2015 to 1 April 2015 is shown in Figure 7.4. The minimum energy at the maximum $L^*$ is set

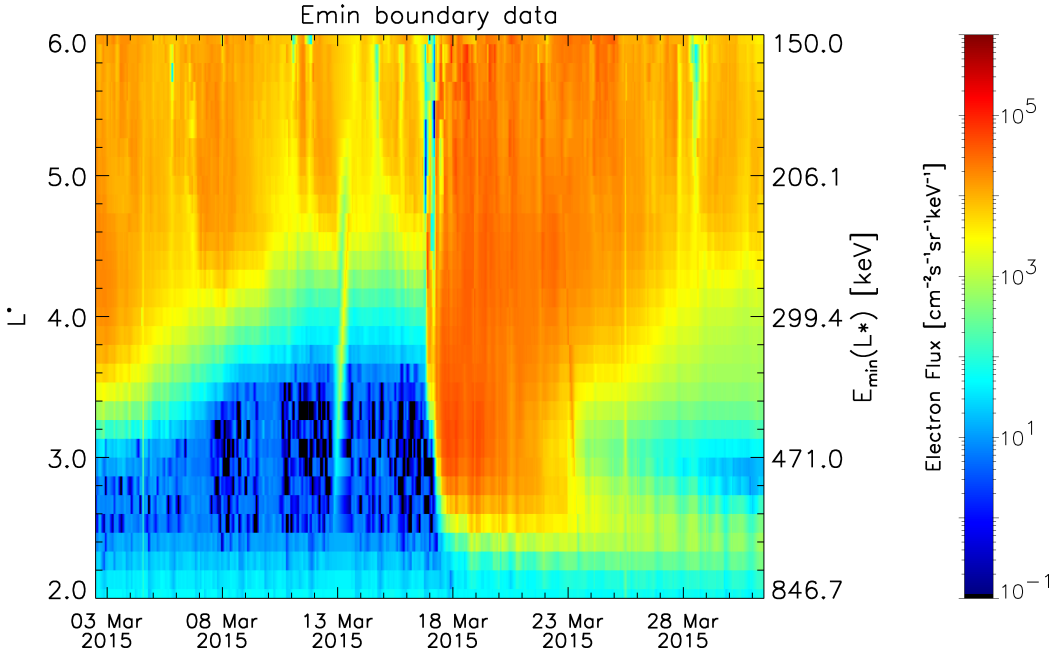


Figure 7.4: Electron flux at the minimum energy boundary derived from the Van Allen Probes data in the period between 3 March 2015 and 1 April 2015. Here, $E_{min}(L^*_{max}) = 150\,\text{keV}$, with $L^*_{max} = 6.0$.

to 150 keV and $L^*$ covers the range between $L^*_{min} = 2.0$ and $L^*_{max} = 6.0$ (left y-axis). The energies corresponding to the values of $L^*$ are shown on the right y-axis.

### 7.3.3 Initial Condition

The initial condition specifies the electron flux for all values of $L^*$, energy, and all pitch-angles of the ($\alpha$-$E$) grid. As explained earlier, all MagEIS pitch-angle channels, except $\alpha = 90°$, ought not be used at the moment and therefore, the electron fluxes at pitch-angles other than 90° must be calculated from these assuming a pitch-angle distribution. Here a $\sin(\alpha)$ distribution is used to calculate the electron flux for each value of $L^*$ and energy individually. The fluxes are directly derived from the interpolated and interleaved dataset created for the boundary conditions, similar to the $E_{min}$ boundary derivation. But instead of providing the data every 5 minutes, only the data at the initial time of the simulation is provided. In order to avoid discontinuities between the initial condition and the maximum energy boundary, one additional energy level at 20 MeV was introduced in the initial condition, where the flux is set to zero.

The resulting fluxes of the initial condition on 3 March 2015 (midnight) are shown

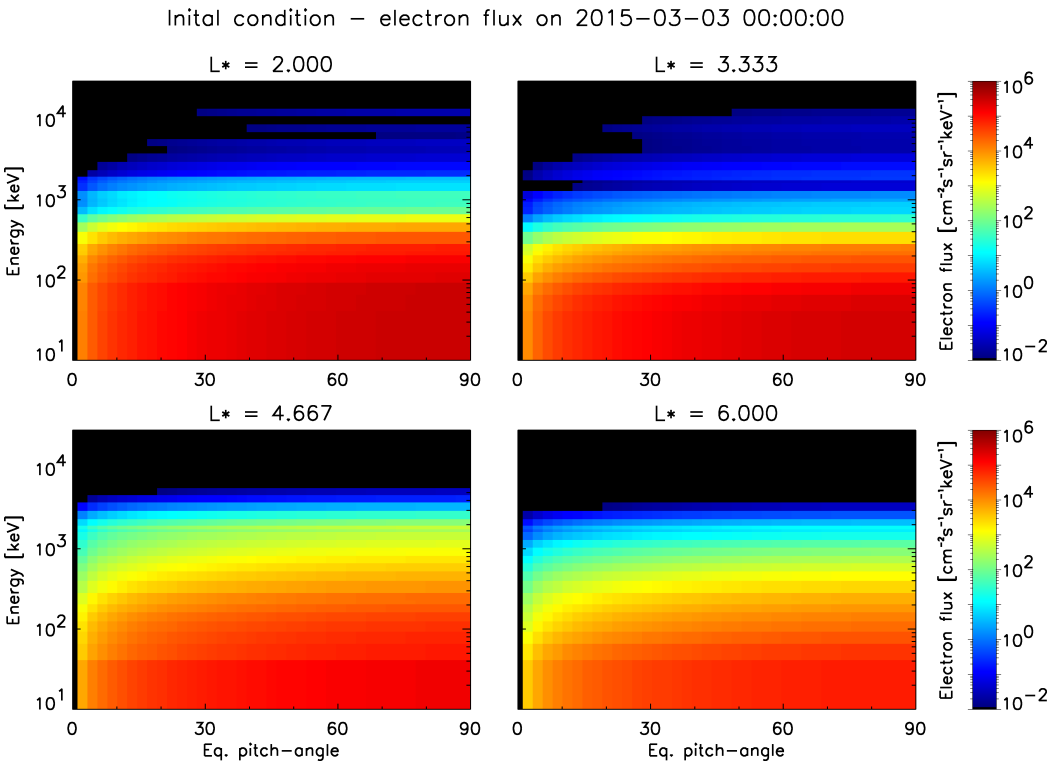


Figure 7.5: Electron flux of the initial condition on 3 March 2015 (midnight) as a contour plot of equatorial pitch-angle and energy for four different values of $L^*$.

in Figure 7.5 as contours as a function of equatorial pitch-angle and electron energy. The initial fluxes are presented for $L^* = 2.0$, $L^* = 3.33$, $L^* = 4.67$, and $L^* = 6.0$. The initial fluxes decrease smoothly with increasing energy and also smoothly with decreasing pitch-angle, due to the employed $\sin(\alpha)$ pitch-angle distribution.

## 7.4 Results

In order to evaluate the BAS-RBM and the utilised wave models, the Van Allen Probes period between 3 March 2015 and 1 April 2015 was chosen, since it provides a large variation of the geomagnetic conditions and the measured electron fluxes. Quiet times are followed by high geomagnetic activity with $AE > 1000\,\mathrm{nT}$, resulting in a large flux dropout event followed by significantly increased electron fluxes that slowly decay over the period of about two weeks. This period therefore poses a demanding challenge for any radiation belt model, while providing the variability that allows the study of the effects of different plasma waves.

### 7.4.1 VAP Electron Flux

The MAGEIS and REPT instruments on board the two Van Allen Probes (RBSP-A and RBSP-B) measure the flux of electrons with an equatorial pitch-angle inside a small range around the nominal pitch-angle. Here, it is assumed that the stated value of any given pitch-angle channel represents the centre of the channel. Therefore, the electrons measured in the 90° channel cover the pitch-angle range half way between this and the next pitch-angle channel ($\approx 78°$), i.e. 84° - 90°. The flux measured by the Van Allen Probes satellites in the period between 3 March 2015 and 1 April 2015 for electrons with an equatorial pitch-angle of $\alpha_{eq} = 84° - 90°$ and with an electron energy of $E = 593\,\mathrm{keV}$ are shown in Figure 7.6 (a), while Figures 7.7 (a) and 7.8 (a) are for electron energies of 1547 keV and 4200 keV, respectively. The two lower energy levels were chosen to cover the regions where the chorus and hiss wave-particle interactions are most effective, while the highest energy level was chosen to study a range that is rarely covered by previous satellites. The location of the plasmapause, as defined by *Carpenter and Anderson* [1992] is indicated as the white line.

At the beginning of the period, the fluxes at all energies are moderately raised after a preceding geomagnetic storm on 28 February 2015. They slowly decrease during the recovery phase of about 14 days until 17 March 2015 where $AE$ and $Kp$ are at moderate levels of about $100\,\mathrm{nT} < AE < 400\,\mathrm{nT}$ and $Kp < 4$. While the range of the 593 keV electron flux narrows in $L^*$ with the inner edge of the outer radiation belt

moving towards higher $L^*$, the 1547 keV and 4200 keV electron fluxes are slowly shifted towards smaller $L^*$ moving the lower edge of the 1547 keV electron flux from about $L^* = 3.8$ on 3 March to $L^* = 3.6$ on 16 March, and the 4200 keV electron flux from about $L^* = 4.0$ to about $L^* = 3.5$. On 17 March a significant geomagnetic storm with $AE > 1200$ nT and $Kp \approx 8$ causes a flux dropout that rapidly decreases the electron flux to below noise level at all $L^*$ over a period of about 18 hours. During this time the plasmapause moves from about $L^* = 4.5$ to $L^* = 2.6$. The dropout is followed by a phase of significantly increased electron fluxes during enhanced geomagnetic activity, lasting until about 22 March after which the fluxes start to decrease again. During the geomagnetic storm, the inner edge of the outer radiation belt is moved inwards to lower $L^*$ for all electron energies. During the recovery phase, the 593 keV electron flux is reduced to pre-storm levels within about 7 days, while the 1547 keV and 4200 keV fluxes stay enhanced at medium $L^*$, but slowly decrease at $L^* > 5.0$ ($E = 1547$ keV) and $L^* > 4.6$ ($E = 4200$ keV).

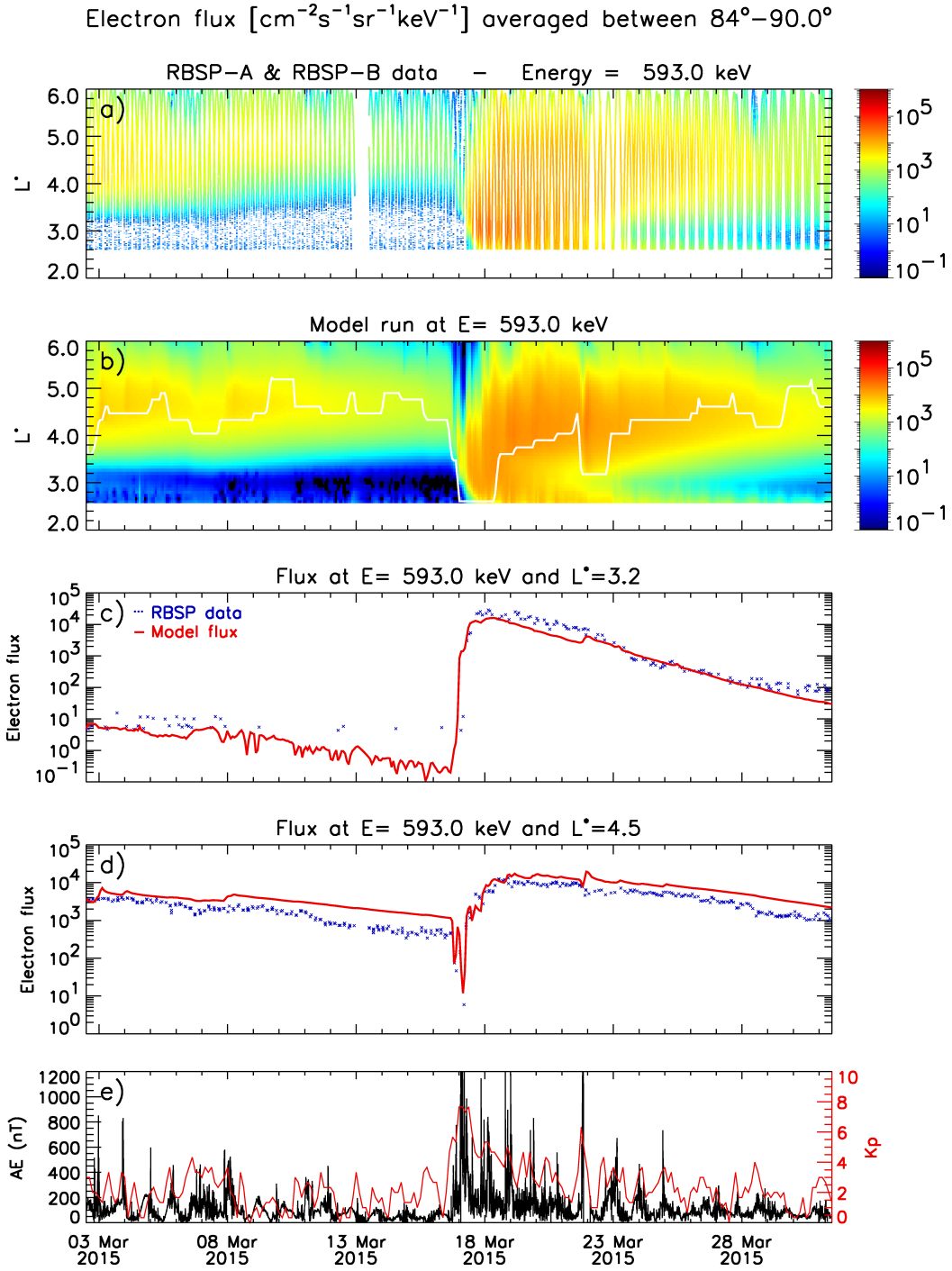


Figure 7.6: Flux of 593 keV electrons with an equatorial pitch-angle averaged between $84° - 90°$ measured by RBSP-A and RBSP-B (a) and calculated using the `BAS-RBM` utilising radial diffusion, hiss, lower and upper band chorus, and EMIC waves (b). The electron flux of the simulation (solid lines) and the VAP data (dotted lines) at constant $L^* = 3.2$ and $L^* = 4.5$ is shown in (c) and (d), respectively. The $AE$ and $Kp$ indices are presented in panel (e).

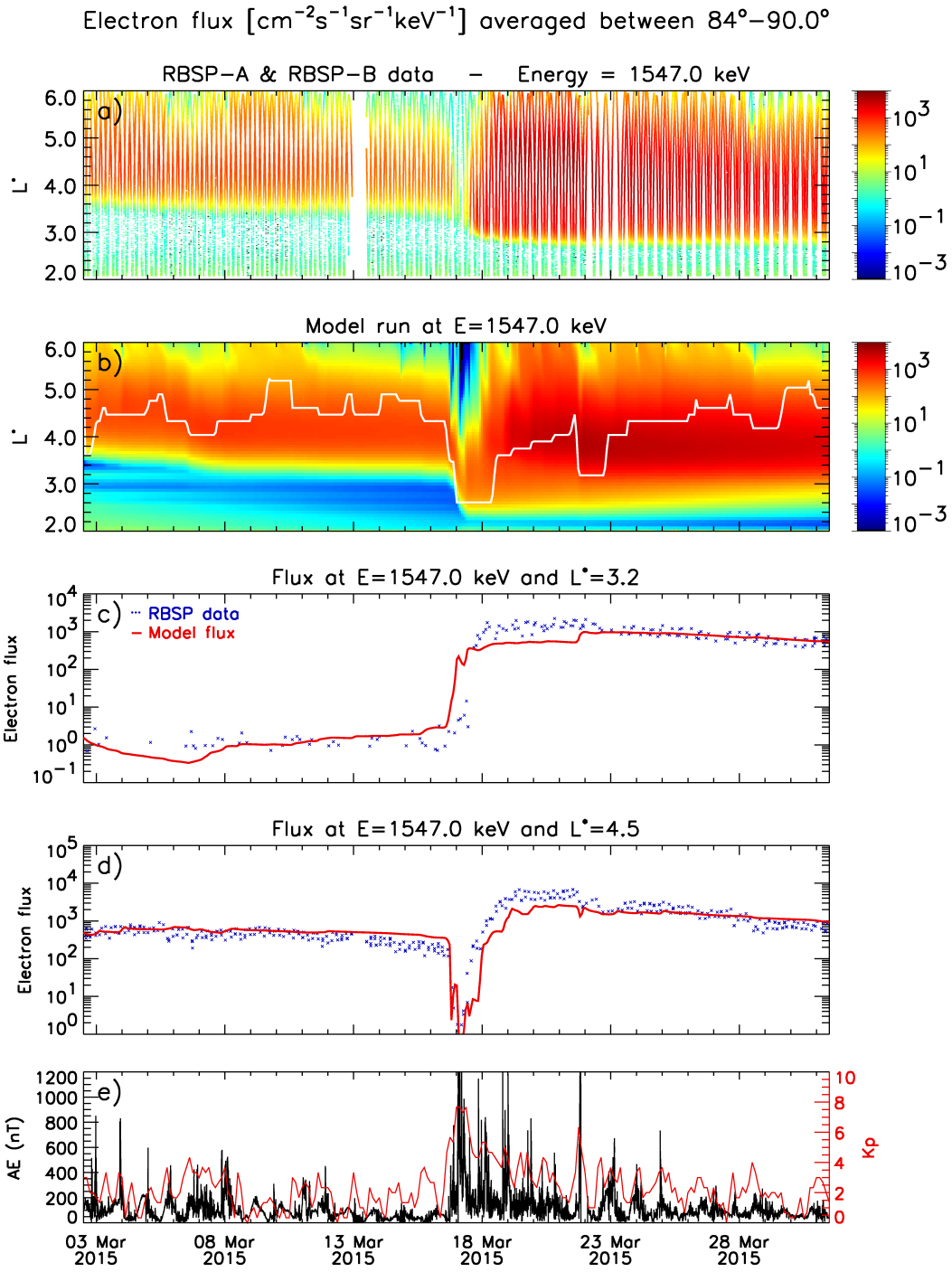


Figure 7.7: Flux of 1547 keV electrons with an equatorial pitch-angle averaged between $84° - 90°$ measured by RBSP-A and RBSP-B (a) and calculated using the BAS-RBM utilising radial diffusion, hiss, lower and upper band chorus, and EMIC waves (b). The electron flux of the simulation (solid lines) and the VAP data (dotted lines) at constant $L^* = 3.2$ and $L^* = 4.5$ is shown in (c) and (d), respectively. The $AE$ and $Kp$ indices are presented in panel (e).

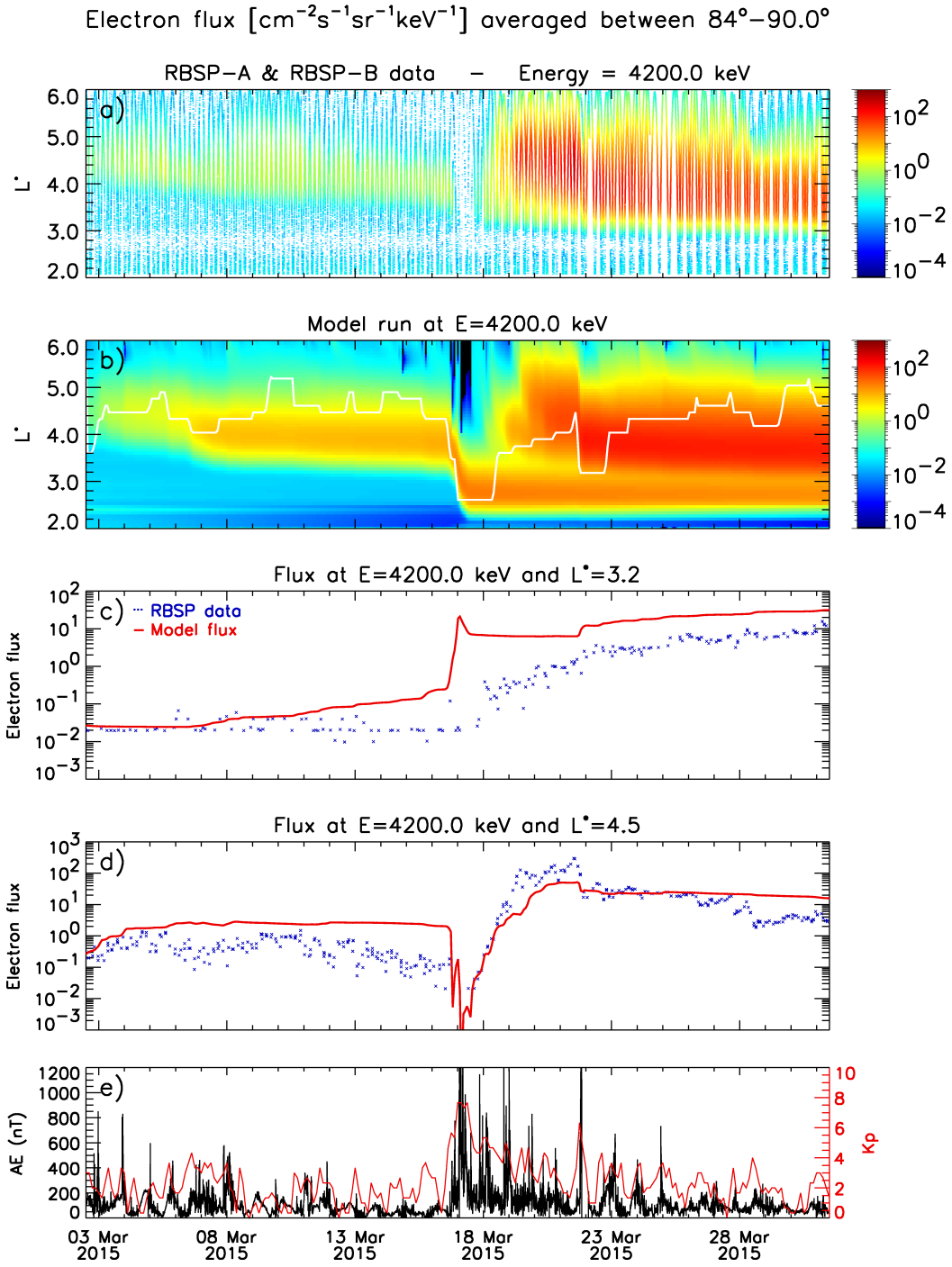


Figure 7.8: Flux of 4200 keV electrons with an equatorial pitch-angle averaged between $84° - 90°$ measured by RBSP-A and RBSP-B (a) and calculated using the `BAS-RBM` utilising radial diffusion, hiss, lower and upper band chorus, and EMIC waves (b). The electron flux of the simulation (solid lines) and the VAP data (dotted lines) at constant $L^* = 3.2$ and $L^* = 4.5$ is shown in (c) and (d), respectively. The $AE$ and $Kp$ indices are presented in panel (e).

### 7.4.2 Model Results

The BAS-RBM was run for the period between 3 March 2015 and 1 April 2015 discussed above using the initial and boundary conditions derived from the Van Allen Probes data, as described in Section 7.3. The simulations were run between $L_{min} = 2.0$ and $L_{max} = 6.0$, while the minimum energy was set to $E_{min} = 150\,\text{keV}$ at $L_{max}$ and the maximum energy to $E_{max} = 30\,\text{MeV}$ at $L_{max}$. The model was run on a $60 \times 60 \times 60$ (pitch-angle, energy, $L^*$)-grid utilising lower and upper band chorus waves of the "lower frequency chorus model" presented in Section 4.3.2, EMIC waves of the EMIC wave model presented in Chapter 5, plasmaspheric hiss of the "new hiss model" presented in Section 6.3, and the magnetic radial diffusion coefficients by Brautigam & Albert presented in Section 2.3.1. As defined in the corresponding sections, the chorus, hiss, and EMIC wave models are parametrised by the $AE$ index, while the radial diffusion coefficients are parametrised by the $Kp$ index. The resulting flux of the simulation is shown as contours as a function of time and $L^*$ for electrons with an energy of 593 keV and an equatorial pitch-angle averaged between $84° - 90°$ in Figure 7.6 (b). The electron fluxes at $L^* = 3.2$ and $L^* = 4.5$, representing the inner edge of the outer radiation belt and a region well inside the outer belt, are compared to the Van Allen Probes data in panels (c) and (d) of the same figure. Here, the red line is the flux of the simulation and the blue dots are the measured data. The $AE$ and $Kp$ indices driving the simulation are shown in panel (e). The fluxes of electrons with an energy of 1547 keV and 4200 keV are presented in the same format in Figures 7.7 and 7.8, respectively.

At first glance, the 593 keV electron flux calculated by the model agrees reasonably well with the measured satellite data. At most times, the data and simulation are of the same order and most of the shape and variability of the radiation belt is reproduced, only lacking the fine structure at some times. The line plots show that the rapid increases of the electron flux during the main storm are captured reasonably well. During the beginning of the simulation until about 9 March the simulated flux underestimates the measured data by about a factor of 1.5 at $L^* = 3.2$. During the following days up to the storm on 17 March the difference between simulation and measured data increases up to about two decades, as the simulated flux decreases, while the data resides at

the same flux level. However, the number of data are extremely sparse and indicates that the measured flux is in the noise level. The mismatch between model and data is therefore unsurprising. After the storm, the data and simulation are nearly identical at $L^* = 3.2$. In contrast, the measured 593 keV flux at $L^* = 4.5$ (Figure 7.6 (d) ) is overestimated by about a factor of 1.5 by the simulation, while the decay times are still comparable, resulting in general agreement between data and simulation after 17 March.

However, there are some important differences between model and simulation. First of all, the model decay rates during the recovery phase between 3 March and 16 March are slightly too low at $L^* = 4.5$, resulting in overestimated electron fluxes inside the main region of the outer belt (see panel (b) ). Furthermore, the first short high peak in $AE$ on 4 March causes the flux at $L^* = 4.5$ to increase above the measured electron flux, causing a difference of about a factor of 4. Due to the too low loss rates, this difference increases over time, reaching about a factor of 8 shortly before the main storm on 16 March. Furthermore, the reduction of the flux of the inner edge of the electron belt between about 7 March and 17 March in Figure 7.6 (b) is not fully reproduced. Although, the inner edge of the simulation moves inward, the losses at about $L^* = 3.5$ are not large enough to reduce the flux to the necessary degree. As a result, the inner edge of the data moves quicker to larger $L^*$ than the simulation. It needs to be noted that the features found around $L^* < 2.8$ are primarily driven by the $L_{min}$ boundary condition that is derived from the VAP data and lies at about $L^* = 2.6$. The reproduction of the connection of the inner and outer belt during the main storm is hence forced by the boundary condition.

It can also be seen that the flux dropout on 17 March is reproduced by the model at 593 keV, as well as the increased flux after the dropout. The decay rates after 17 March are of the correct order, however, due to a small increase on 22 March, the simulated flux is shifted to a slightly too large value, but decreasing at the same rate as the measured flux until about 29 March. Overall, the model is able to reproduce the measured flux reasonably well, with only small differences in the decay rates that accumulate to minor differences over time.

The electron flux calculated with the BAS-RBM at 1547 keV presented in Figure 7.7 also tends to reproduce most of the measured VAP data. Between 3 March and 17 March the flux at all $L^*$ is reproduced by the model, in particular at larger $L^*$. The line plots at $L^* = 4.5$ show that the fluxes of simulation and data are of the same order, except between 14 March and 16 March, where the decay rates are slightly too low and therefore the measured flux is overestimated by about a factor of 3. Similarly, the flux at $L^* = 3.2$ is also overestimated as the simulated flux increases more strongly than the measured flux.

However, the flux dropout during the main storm is not captured completely, as the flux of the simulation is only reduced down to about $L^* = 3.5$, but is unaffected at lower $L^*$, while the RBSP data shows that the flux dropout penetrates through all $L^*$. Consequently, it looks like a large number of electrons are transported from about $L^* = 3.8$ down to about $L^* = 2.4$ within a couple of hours. Hence, instead of being completely eradicated, the flux seems to move to lower regions of $L^*$. The increased electron population at $L^* < 3.5$ consequently defines the inner edge of the simulated outer belt, located at about $L^* = 2.4$, while the measured inner edge is located at about $L^* = 2.9$. However, at larger $L^*$ the simulation and the data tend to be of the same order after about 22 March, while the simulation underestimates the measured flux by about a factor of 5 before this date. Furthermore, the decay rates of data and simulation after 22 March tend to be similar at $L^* = 3.2$ and $L^* = 4.5$.

Unlike at the lower energy levels, the flux of 4200 keV electrons (Figure 7.8) shows large differences between simulation and the Van Allen Probes data. One of the major differences is the deficit in modelling the flux dropout on 17 March, resulting in the before mentioned increased fluxes at very low $L^*$. The second main difference is the significantly overestimated electron flux during the initial quiet period leading up to 16 March, where the electron flux of the simulation steadily increases, while the measured flux resides at the same level, leading to a difference of more than a decade just before the main storm event. At this energy level the model is unable to reproduce the flux at $L^* = 3.2$, where there is either too much acceleration or the losses are too low at nearly all times. However, at $L^* = 4.5$ the model is able to reproduce the data during some

periods, especially during and after the main storm. Even before 16 March the decay rates of the model and the data tend to be of the same order, although the fluxes are shifted against each other due to the times of larger geomagnetic activity during the first few days of the simulation period.

## 7.5 Evaluation

The presented electron fluxes obtained with the `BAS-RBM` are the result of a complex simulation, utilising the diffusion rates of several different plasma waves. In order to evaluate the results and identify and quantify the contribution of each plasma wave, as well as to understand the presented shortcomings of the `BAS-RBM` and identify their underlying problems, each contributing wave-particle interaction, including radial diffusion, needs to be assessed individually. Therefore, the lower and upper band chorus wave model, plasmaspheric hiss wave model, and radial diffusion model are investigated in this section. An evaluation of EMIC waves is excluded, since it was shown that they are only effective at equatorial pitch-angles less than about 60°, and hence do not contribute to the presented electron flux at 90°. A comparison of the RBSP data at pitch-angles where EMIC waves are effective is currently not reasonable, as the pitch-angle channels other than 90° are reported to be unreliable in the dataset used here. Furthermore, the simulation of lower pitch-angles is known to require cross diffusion terms in order to reproduce the data, but these are not included in the current version of the `BAS-RBM`.

In all following results, the `BAS-RBM` was run for the same simulation period between 3 March 2015 and 1 April 2015 with $L_{min} = 2.0$ and $L_{max} = 6.0$. The minimum energy was set to $E_{min} = 150\,\text{keV}$ at $L_{max}$ and the maximum energy to $E_{max} = 30\,\text{MeV}$ at $L_{max}$, and the model was run on a $60 \times 60 \times 60$ (pitch-angle, energy, $L^*$)-grid. The utilised wave models were changed, depending on the case that is illustrated. In order to be concise, from now on it is implied that all simulations are run utilising the lower and upper band chorus waves as defined by the "lower frequency chorus model" presented in Section 4.3.2, the EMIC waves of the wave model presented in Chapter 5,

the plasmaspheric hiss defined by the "new hiss model" presented in Section 6.3, and the magnetic radial diffusion coefficients by Brautigam & Albert presented in Section 2.3.1. Deviations from this are explicitly specified. For example, if it is said that the model is run without chorus waves, it is implied that all other plasma waves are still included, which in this case are radial diffusion, hiss, and EMIC waves.

### 7.5.1 Chorus Waves

It was shown in Chapter 4 that whistler mode chorus waves are most effective in accelerating electrons as well as scattering electrons into the loss cone at energies between about 100 keV and 1 MeV. At larger energies, the diffusion rates became low and the contribution of chorus to electron acceleration and loss decreased. Lower energies were not included in the study of the electron flux, due to the drift averaging approach. In order to understand the contribution of the chorus waves to the electron fluxes of the selected Van Allen Probes period, the `BAS-RBM` is run with and without chorus waves being present.

The resulting electron fluxes are presented as a contour plot of time and $L^*$ in Figure 7.9 for electrons with an energy of 593 keV and averaged between pitch-angles of 84°-90°. Panel (a) shows the electron flux as measured by the two VAP satellites, panel (b) shows the simulated flux where chorus waves are not present, and panel (c) shows the flux with chorus waves present. The $AE$ and $Kp$ indices driving the simulations are shown in panel (d). The electron flux at the same energy and pitch-angle range is shown as a function of time at $L^* = 3.0$, $L^* = 4.0$, and $L^* = 5.2$ in Figure 7.10. Here, the fluxes of the simulation where chorus is present are shown as the red lines, while the fluxes of the simulation without chorus are shown as the blue lines. The fluxes measured by RBSP-A and RBSP-B are indicated by the black dots. The results for electrons with an energy of 1547 keV are presented in the same format in Figures 7.11 and 7.12, while the results for electrons with an energy of 4200 keV are presented in Figures 7.13 and 7.14.

Figures 7.9 and 7.10 show that the measured flux at 593 keV is generally underestimated if chorus waves are excluded from the simulation. This effect is most notable between

18 March and 22 March in the region of about $L^* = 3.0$, where the flux is reduced by at least two decades if chorus waves are excluded. If chorus waves are included in the simulation, the results agree much better with the measured VAP electron fluxes, particularly after 18 March. Before this date at $L^* = 3.0$, there is no difference between simulations with and without chorus, and the large mismatch between simulation and the data is not corrected. However, since the data are sparse and there are no measurements of fluxes with lower values, the measurements are most likely to be in the noise level. The small difference between the simulation with and without chorus is due to the fact that chorus is mainly found outside the plasmapause and hence at larger $L^*$. The results therefore show that at 593 keV chorus is a significant acceleration process that is vital in order to reproduce the measured electron flux.

Similar results can be found for 1547 keV electrons, although the differences between the simulations with and without chorus become less pronounced, particularly at low $L^*$ before the main storm on 17 March, where both simulations are more or less identical. Before the main storm, the simulated flux is about one decade lower than the measured flux, but as before, it is expected that the measurements are most likely in the noise level of the instrument.

At 4200 keV (Figures 7.13 and 7.14) the influence of chorus waves on the electron flux is reduced, although there are still differences between the simulations with and without chorus. After 17 March the electron flux of the simulations with chorus waves present are increased by about a factor of two compared to the simulations without chorus waves, but only at $L^* \leq 4.0$. Since the diffusion rates at these energies are too low to cause a significant effect directly and the differences are minimal at $L^* = 5.2$, it is expected that the main reason for the deviation between the measured flux at $L^* = 3.0$ at 4200 keV and the simulation results after 18 March is radial transport of electrons from larger $L^*$ and hence lower energies to lower $L^*$.

Before 17 March, the reduction of the electron flux is more pronounced with differences of up to a decade. Since in this period the electron flux of the simulation with chorus waves included significantly overestimates the measured flux, a better agreement between data and simulation might be reached for $L^* > 4.0$ and 4200 keV, if chorus waves

are excluded. Therefore, one possible reason for the disagreement between data and simulation might be overestimated chorus diffusion at large electron energies. However, the simulated electron flux without chorus waves still overestimates the measured flux by about a decade. Therefore, decreased chorus diffusion alone would not suffice to reproduce the high energy electron fluxes.

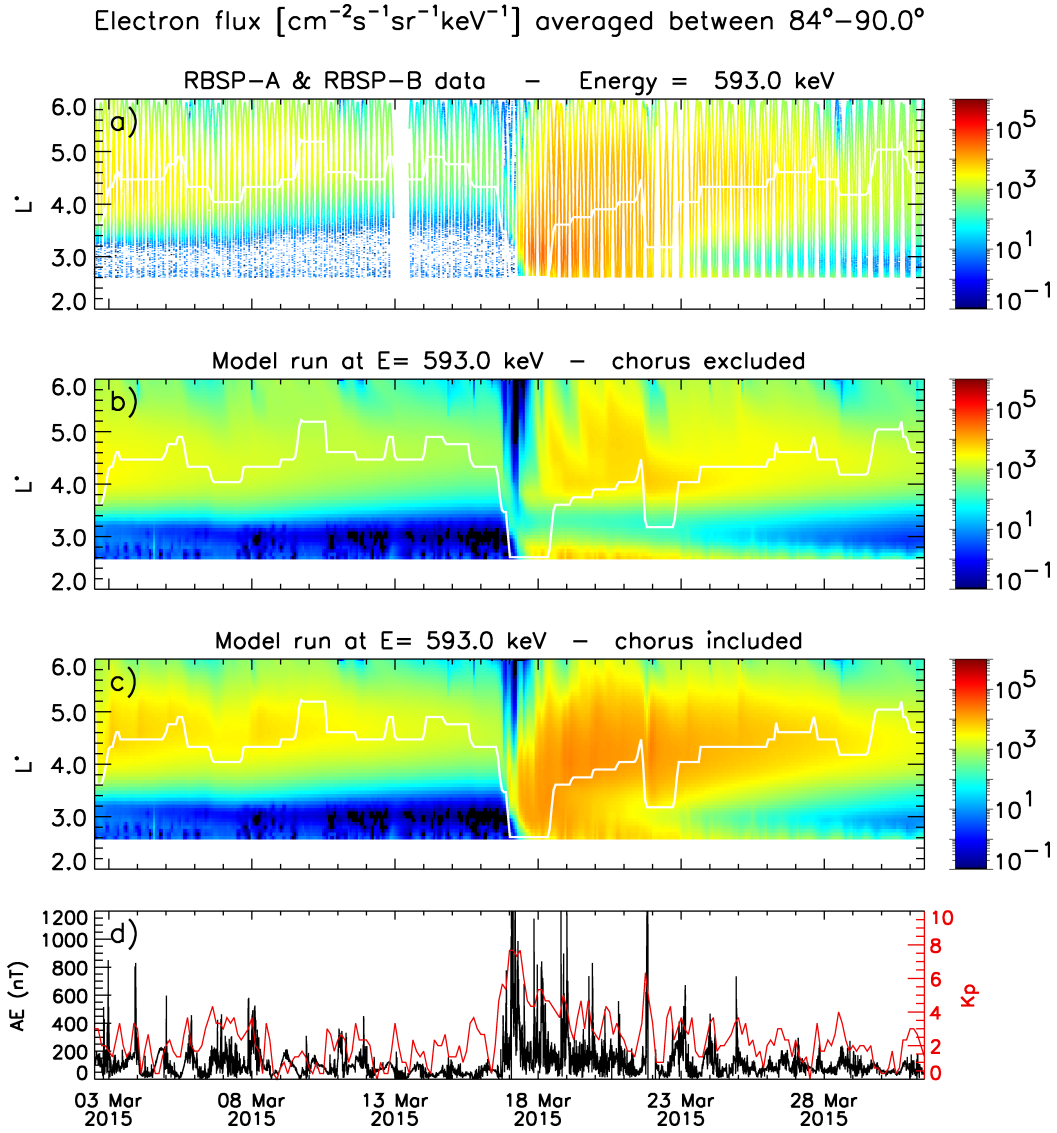


Figure 7.9: Flux of 593 keV electrons with an equatorial pitch-angle averaged between $84° - 90°$ measured by RBSP-A and RBSP-B (a). The flux calculated with the `BAS-RBM` utilising radial diffusion and hiss, but without chorus waves are shown in panel (b), while panel (c) shows the simulation results where chorus waves were included. The $AE$ and $Kp$ indices are presented in panel (d).

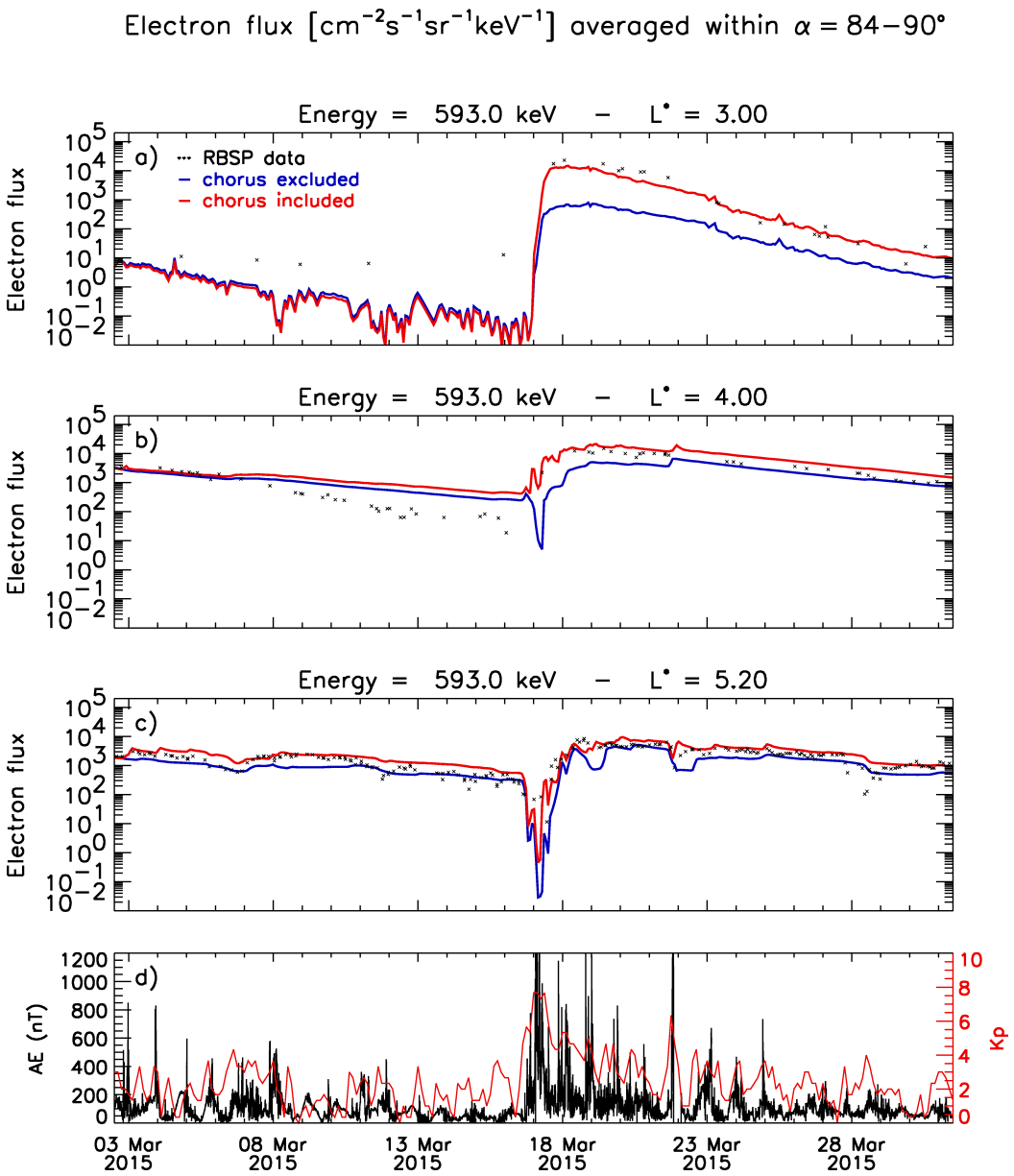


Figure 7.10: Flux of 593 keV electrons with an equatorial pitch-angle averaged between $84° - 90°$ at three constant values of $L^*$. The flux measured by RBSP-A and RBSP-B is indicated by the black dots. The blue line is the flux calculated with the `BAS-RBM` utilising radial diffusion and hiss, but without chorus waves, while the red line is the flux calculated with chorus waves included in the simulation. The $AE$ and $Kp$ indices are presented in panel (d).

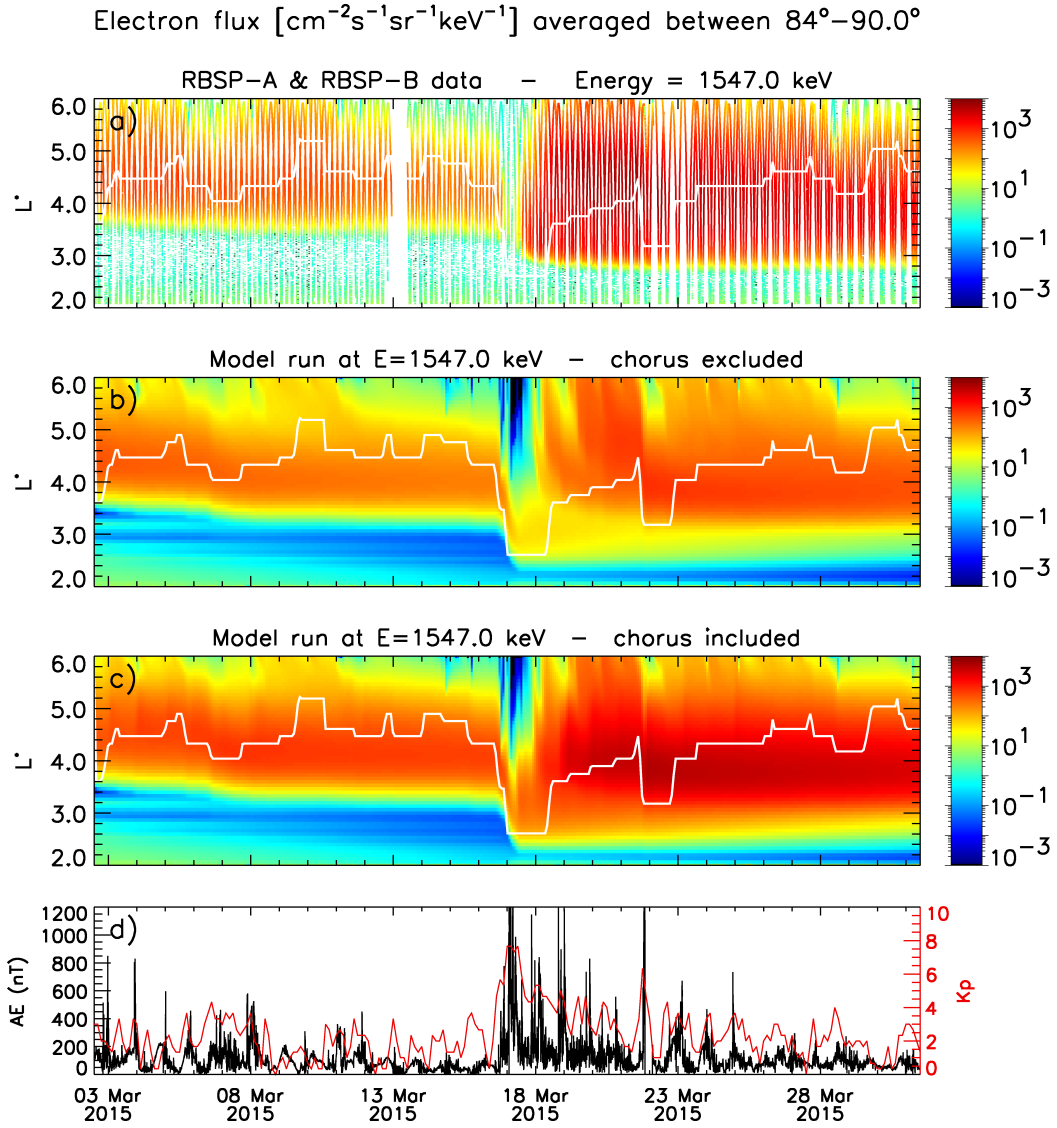


Figure 7.11: Flux of 1547 keV electrons with an equatorial pitch-angle averaged between $84° - 90°$ measured by RBSP-A and RBSP-B (a). The flux calculated with the `BAS-RBM` utilising radial diffusion and hiss, but without chorus waves are shown in panel (b), while panel (c) shows the simulation results where chorus waves were included. The $AE$ and $Kp$ indices are presented in panel (d).

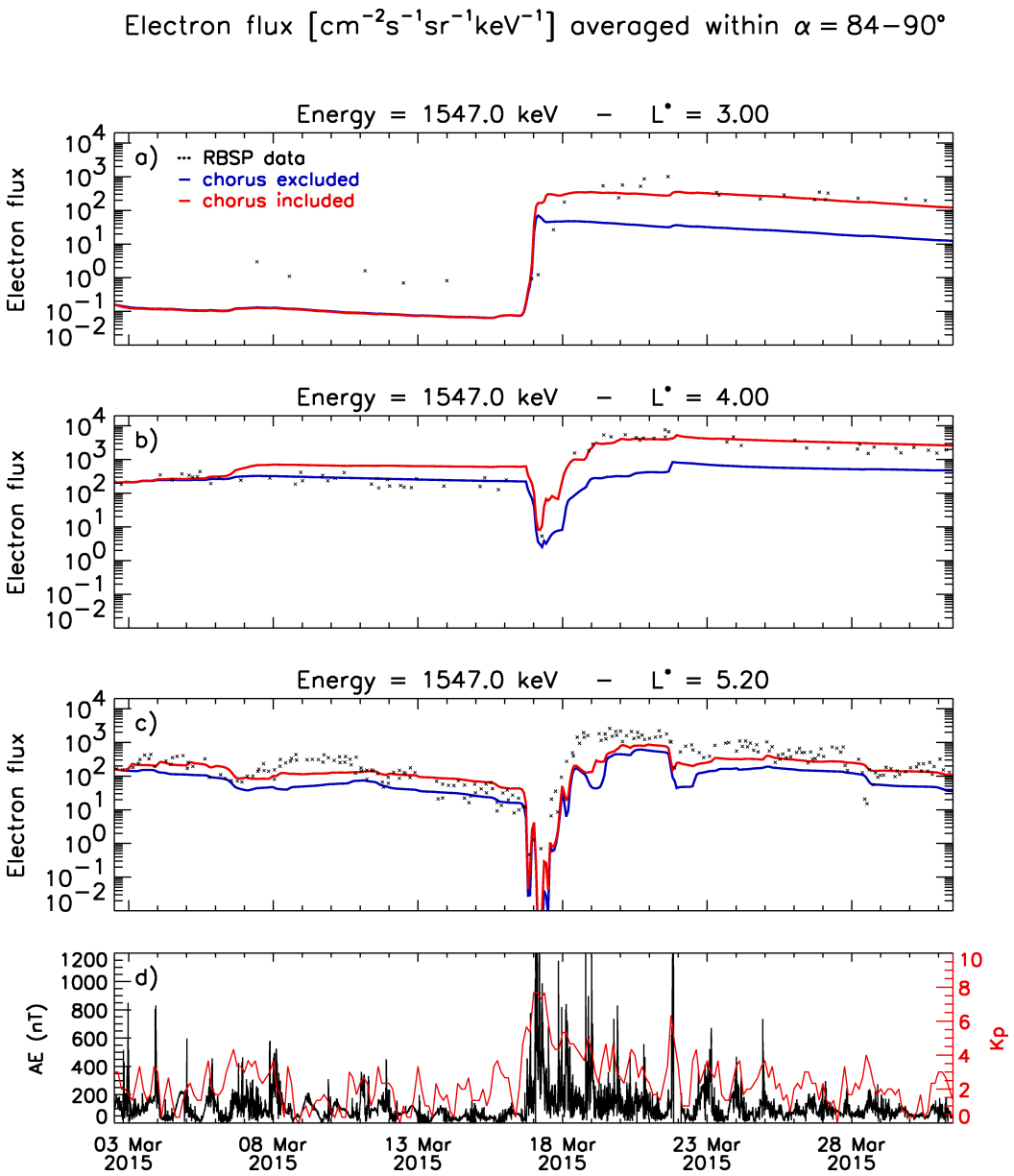


Figure 7.12: Flux of 1547 keV electrons with an equatorial pitch-angle averaged between $84° - 90°$ at three constant values of $L^*$. The flux measured by RBSP-A and RBSP-B is indicated by the black dots. The blue line is the flux calculated with the `BAS-RBM` utilising radial diffusion and hiss, but without chorus waves, while the red line is the flux calculated with chorus waves included in the simulation. The $AE$ and $Kp$ indices are presented in panel (d).

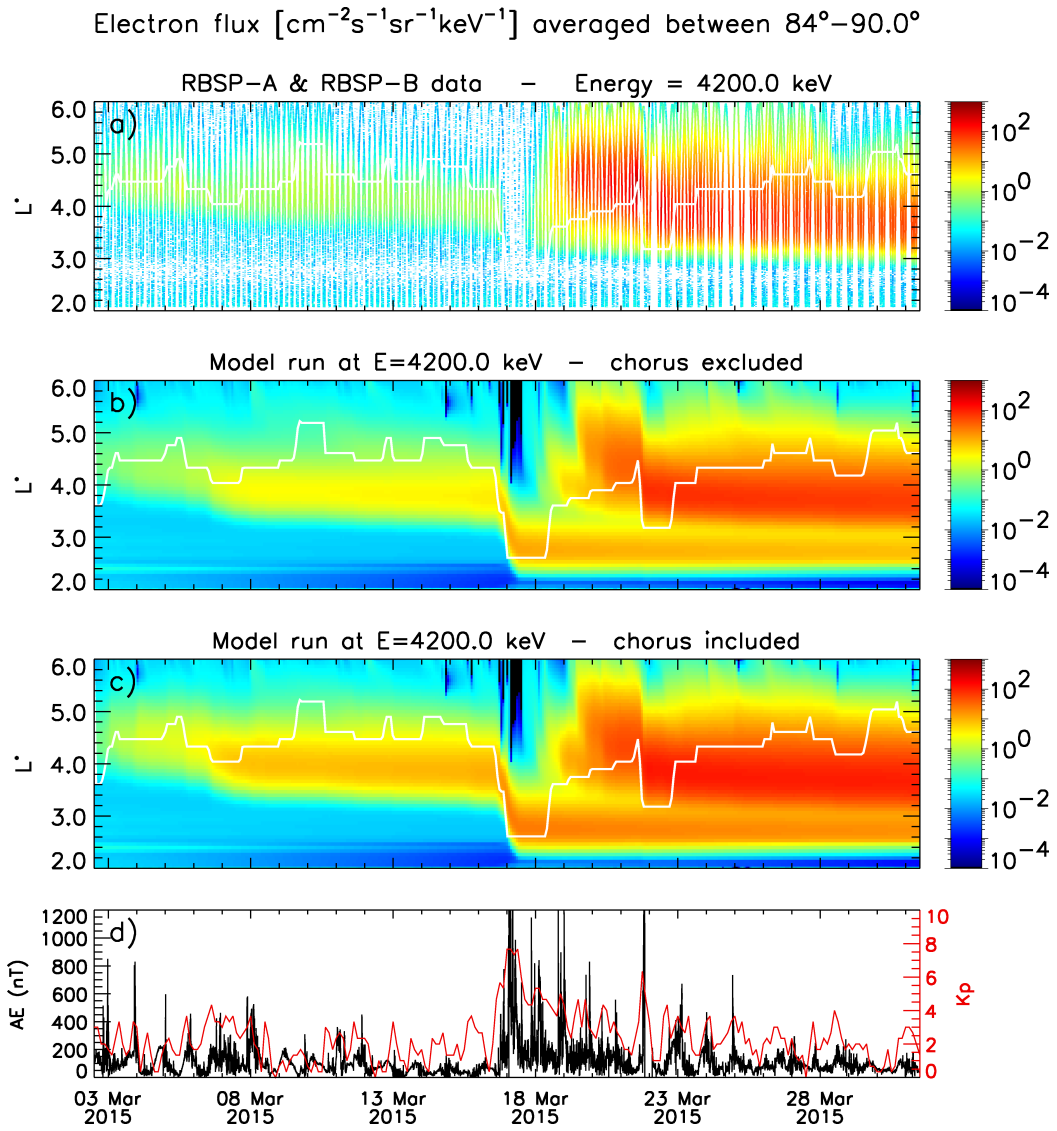


Figure 7.13: Flux of 4200 keV electrons with an equatorial pitch-angle averaged between $84° - 90°$ measured by RBSP-A and RBSP-B (a). The flux calculated with the `BAS-RBM` utilising radial diffusion and hiss, but without chorus waves are shown in panel (b), while panel (c) shows the simulation results where chorus waves were included. The $AE$ and $Kp$ indices are presented in panel (d).

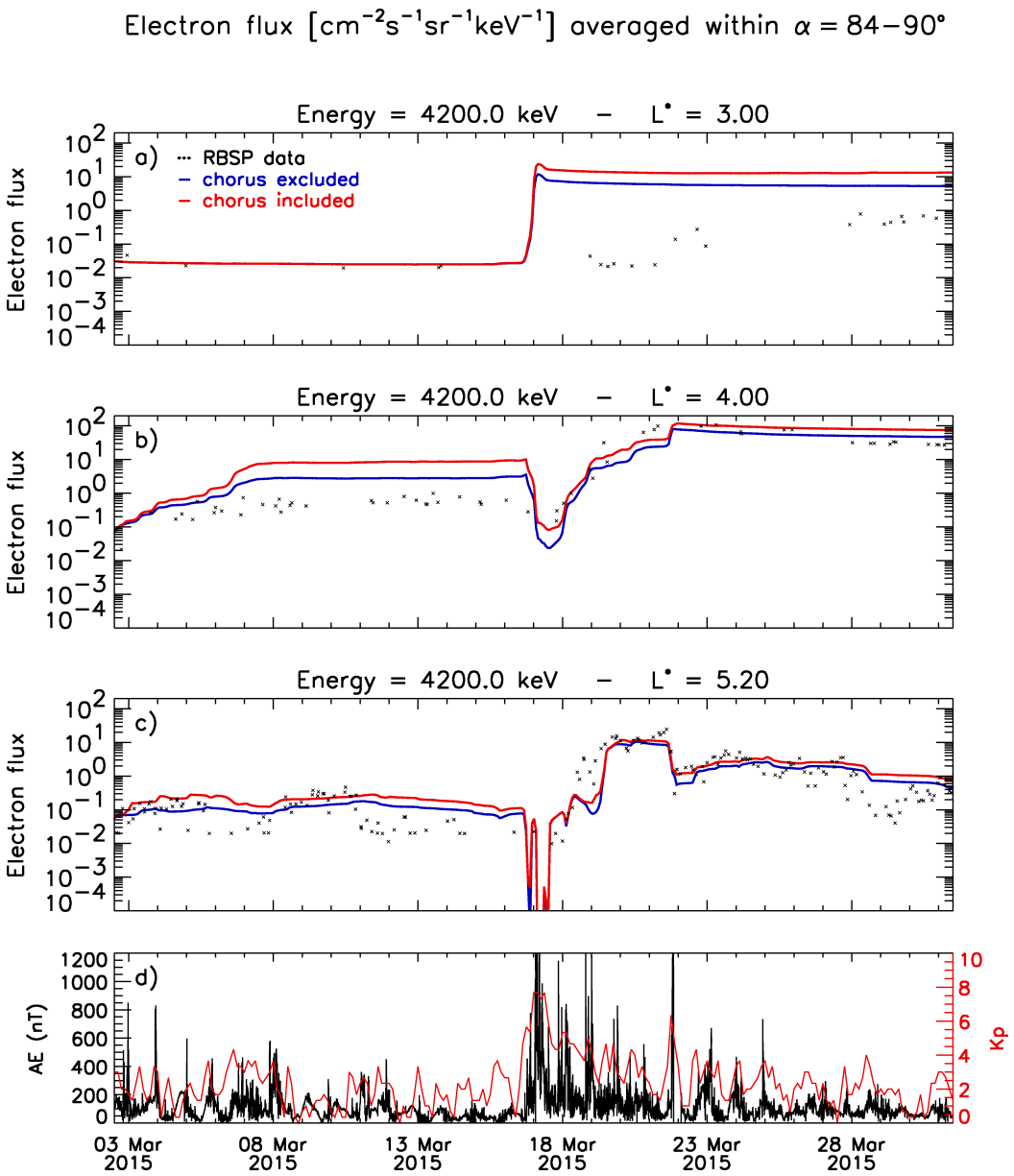


Figure 7.14: Flux of 4200 keV electrons with an equatorial pitch-angle averaged between $84° - 90°$ at three constant values of $L^*$. The flux measured by RBSP-A and RBSP-B is indicated by the black dots. The blue line is the flux calculated with the `BAS-RBM` utilising radial diffusion and hiss, but without chorus waves, while the red line is the flux calculated with chorus waves included in the simulation. The $AE$ and $Kp$ indices are presented in panel (d).

### 7.5.2 Plasmaspheric Hiss

Plasmaspheric hiss is known to cause electron loss due to pitch-angle scattering of electrons into the loss cone, but no significant electron acceleration. It was shown in Chapter 6 that the pitch-angle diffusion is most effective for electron energies between about 100 keV and 1 MeV, while there was no significant energy diffusion. Hiss is therefore expected to decrease the electron flux inside this energy range, due to pitch-angle scattering and consequent losses of electrons to the atmosphere. In order to quantify the effect of plasmaspheric hiss on the global electron flux of the selected Van Allen Probes period, simulations using the `BAS-RBM` are performed with and without hiss being present.

The flux of electrons with an equatorial pitch-angle between 84° and 90° is presented as a contour plot of time and $L^*$ for electron energies of 593 keV, 1547 keV, and 4200 keV in Figures 7.15, 7.17, and 7.19, respectively. Here, panel (a) shows the electron flux as measured by the two VAP satellites, panel (b) shows the simulated flux where hiss is not present, and panel (c) shows the flux with hiss present. The plasmapause is indicated by the white line, and the $AE$ and $Kp$ indices driving the simulations are shown in panel (e). The electron fluxes are shown as line plots at constant values of $L^*$ as a function of time at $L^* = 3.0$, $L^* = 4.0$, and $L^* = 5.2$ for electron energies of 593 keV, 1547 keV, and 4200 keV in Figures 7.16, 7.18, and 7.20, respectively. Here, the Van Allen Probes data are indicated by the black dots, while the solid lines show the results of the simulations with hiss included (red) and hiss excluded (blue).

Figures 7.15 and 7.16 first of all show that plasmaspheric hiss is causing significant losses for 593 keV at $L^* \leq 4.0$, while the losses caused by hiss are small at $L^* = 5.2$. Figure 7.16 (a) shows that including hiss in the simulation causes the measured flux to be underestimated by up to two decades between 3 March and 17 March at $L^* = 3.0$, but the measured flux is likely to be in the noise level, as mentioned before. After 17 March, there is much better agreement between data and simulation, if hiss is included. Panel (b) also shows much better agreement if hiss is included after 17 March at $L^* = 4.0$. Before 17 March, the agreement between data and simulation now also improves if hiss is included, although the measured flux is still overestimated by up to a decade.

This shows that plasmaspheric hiss is an important loss process that is required to reproduce the flux during the decay periods. However, the loss caused by hiss is not strong enough to achieve agreement between data and simulation before 16 March at all $L^*$. It is surprising that, since the geomagnetic activity in the decay periods before and after the main event on 16 March are similar, there is much better agreement of the decay after the main event than before the event.

However, the flux at $L^* = 4.0$ on about 07 March shows a small increase of the simulated electron flux on a period of about one day that is not found in the measured flux. At this time, both $AE$ and $Kp$ are moderately enhanced. One reason for the overestimated flux might be too much acceleration caused by chorus waves or too few losses caused by plasmaspheric hiss during this time. However, the simulations where chorus waves were excluded from the simulation (see Figures 7.9 - 7.14), still show an increase of the flux around 07 March, albeit smaller than if chorus waves were present. This therefore indicates that additionally the model for radial diffusion might be wrong during this period.

Figures 7.17 and 7.18 shows that at an electron energy of 1547 keV the influence of hiss on the electron flux is much smaller. At $L^* = 4.0$ and above, the difference between the simulations with and without hiss are about a factor of 2, and better agreement between data and simulation is achieved when hiss is included. Nevertheless, the flux is slightly overestimated after 16 March, while the difference between data and simulation becomes even larger before the main event, with a difference up to a factor of 5 at $L^* = 4.0$. This indicates that the hiss diffusion rates might not be large enough at this value of $L^*$. However, most of the disagreement between data and simulation is due to an increase of the flux around 07 March, similar to the results at 593 keV. Without this increase, data and simulation might agree much better. At 1547 keV the simulations where chorus waves are excluded (See Figure 7.12) indicate that the increased electron flux around 07 March is most likely to be due to chorus waves that cause too much acceleration or too few losses at this energy range.

In contrast to these results, the simulation tends to underestimate the flux at $L^* = 3.0$ before 16 March. However, at these low $L^*$ the data are likely to be in the noise

level. After the main storm on 17 March the agreement between data and simulation improved significantly, where the loss times caused by hiss result in an electron flux that is nearly identical with the measured data.

Figures 7.19 and 7.20 show that the electron flux at $E = 4200\,\mathrm{keV}$ has an intensification of the problematic increase around 07 March, particularly at medium $L^*$. While the measured flux resides more or less at the same level, the simulated flux increases by over two decades, resulting in a strongly overestimated flux before the main storm. While there tends to be better agreement between simulation and data after 17 March on larger $L^*$, the flux is overestimated by about 3 decades at $L^* = 3.0$. The difference between the simulations with and without plasmaspheric hiss are small, with the largest difference of a factor of about 2.5 at $L^* = 3.0$. The decay times of the simulations with and without hiss are similar and the main difference of the fluxes is caused at the main storm. This indicates that at very high energies hiss is only having a minor effect on the variability of the electron flux and only during the most intense storm times. Furthermore, there is no indication that plasmaspheric hiss could significantly improve the disparity between simulation and data at large electron energies, and hence another processes must be the cause for the overestimated fluxes at high energies.

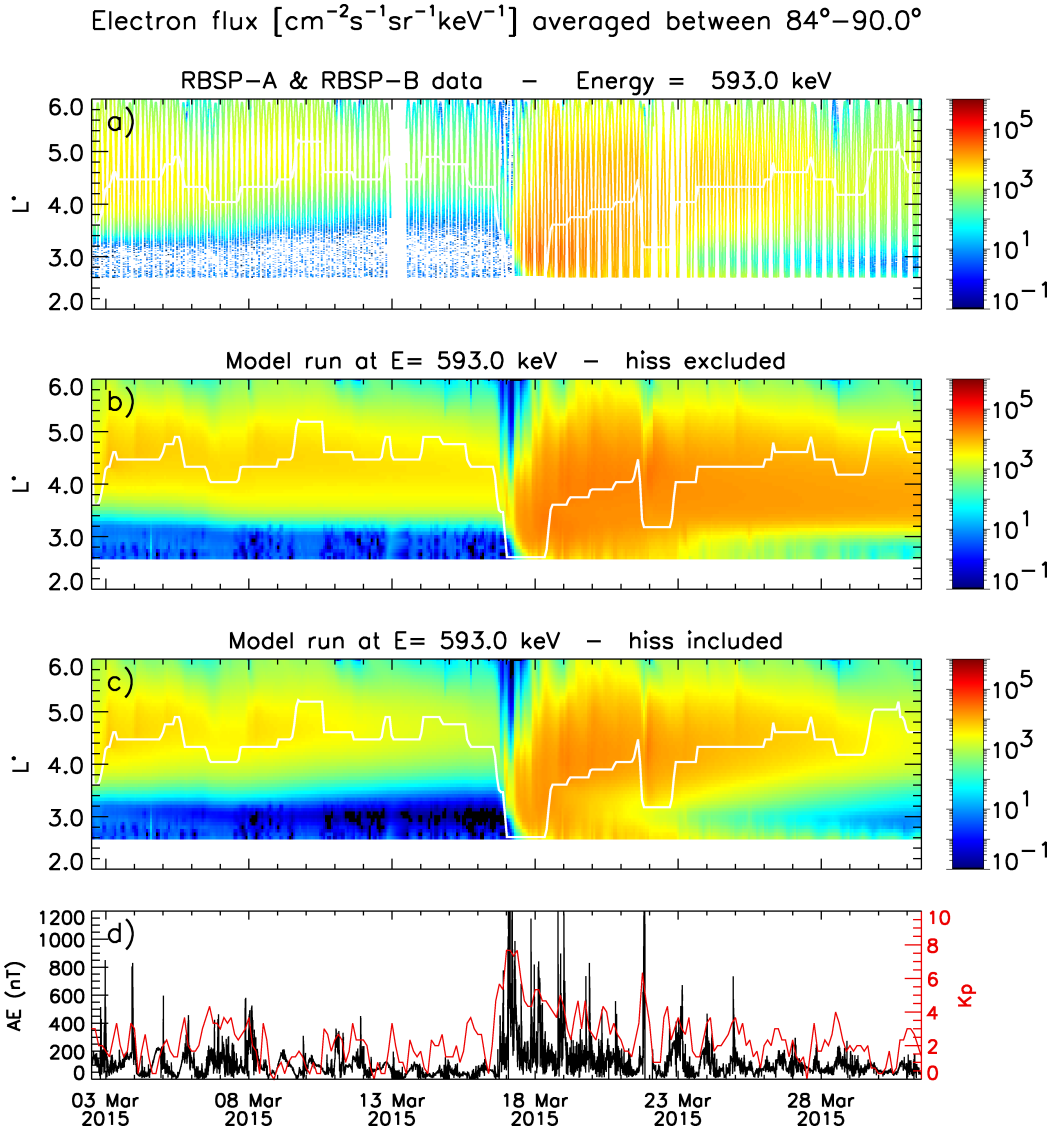


Figure 7.15: Flux of 593 keV electrons with an equatorial pitch-angle averaged between $84° - 90°$ measured by RBSP-A and RBSP-B (a). The flux calculated with the BAS-RBM utilising radial diffusion, chorus, and EMIC waves, but without hiss are shown in panel (b), while panel (c) shows the simulation results where hiss is included. The *AE* and *Kp* indices are presented in panel (d).

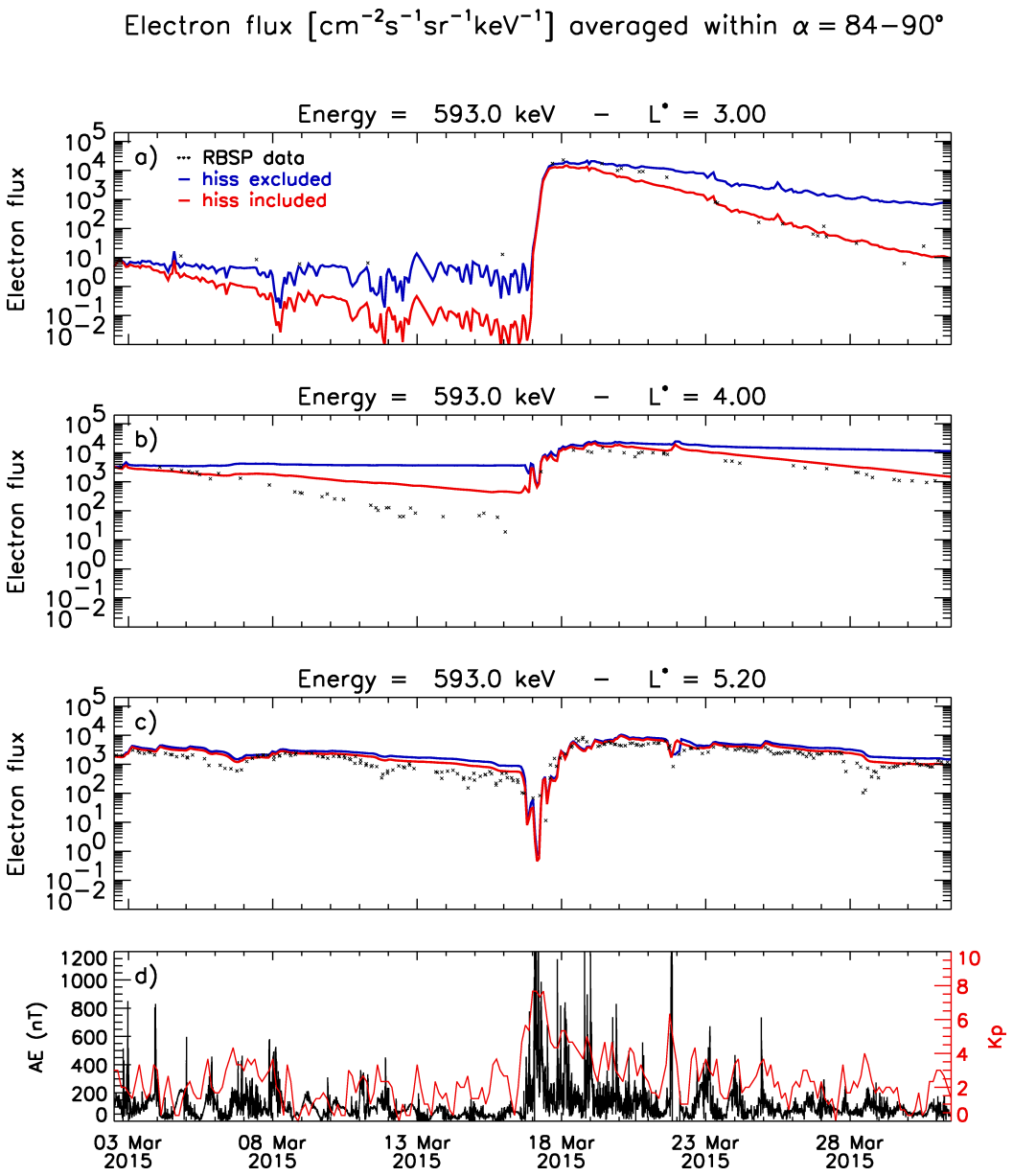


Figure 7.16: Flux of 593 keV electrons with an equatorial pitch-angle averaged between $84° - 90°$ at three constant values of $L^*$. The flux measured by RBSP-A and RBSP-B is indicated by the black dots. The blue line is the flux calculated with the `BAS-RBM` utilising radial diffusion, chorus, and EMIC waves, but without hiss, while the red line is the flux calculated with hiss included in the simulation. The $AE$ and $Kp$ indices are presented in panel (d).

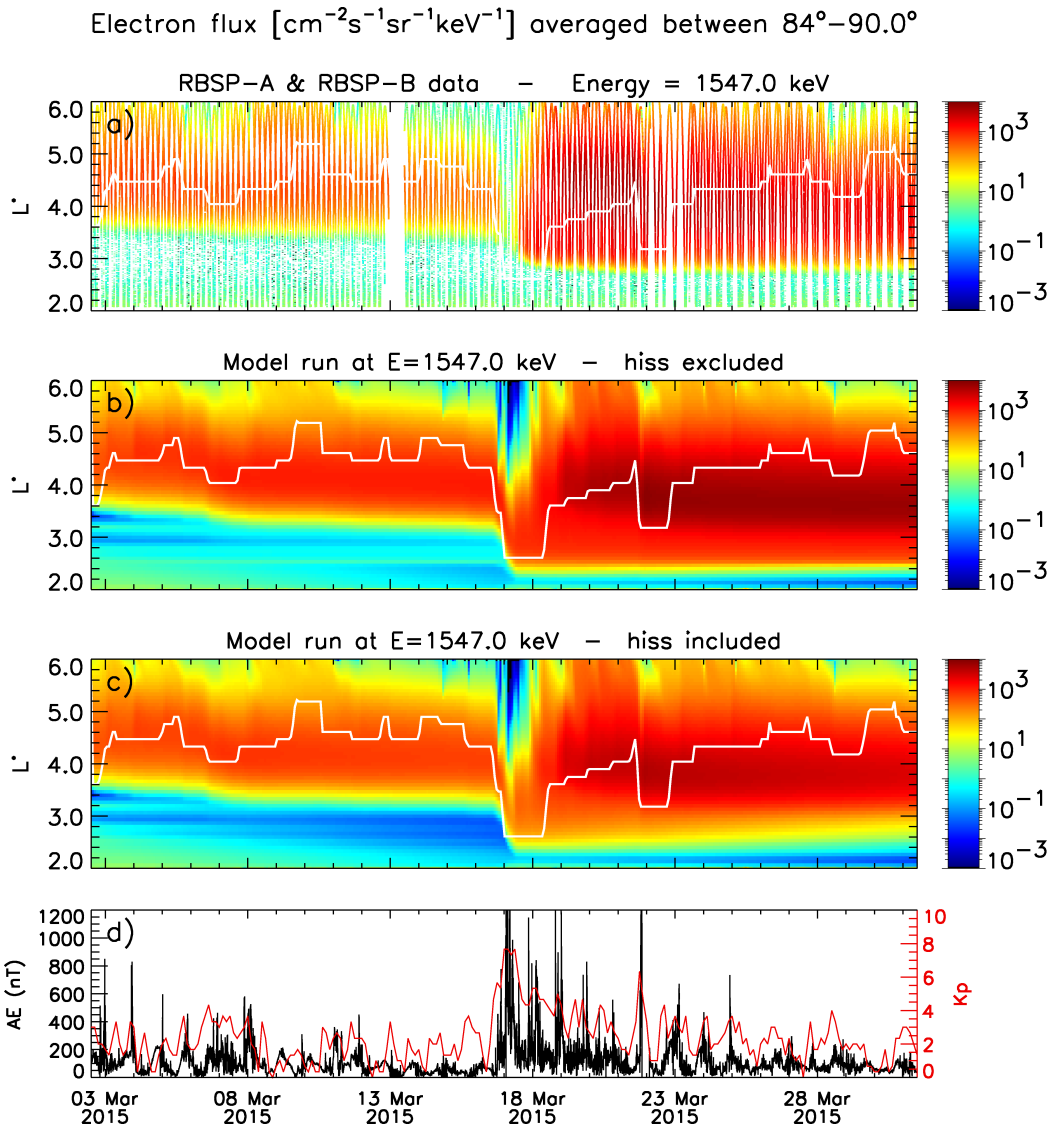


Figure 7.17: Flux of 1547 keV electrons with an equatorial pitch-angle averaged between $84° - 90°$ measured by RBSP-A and RBSP-B (a). The flux calculated with the `BAS-RBM` utilising radial diffusion, chorus, and EMIC waves, but without hiss are shown in panel (b), while panel (c) shows the simulation results where hiss is included. The *AE* and *Kp* indices are presented in panel (d).

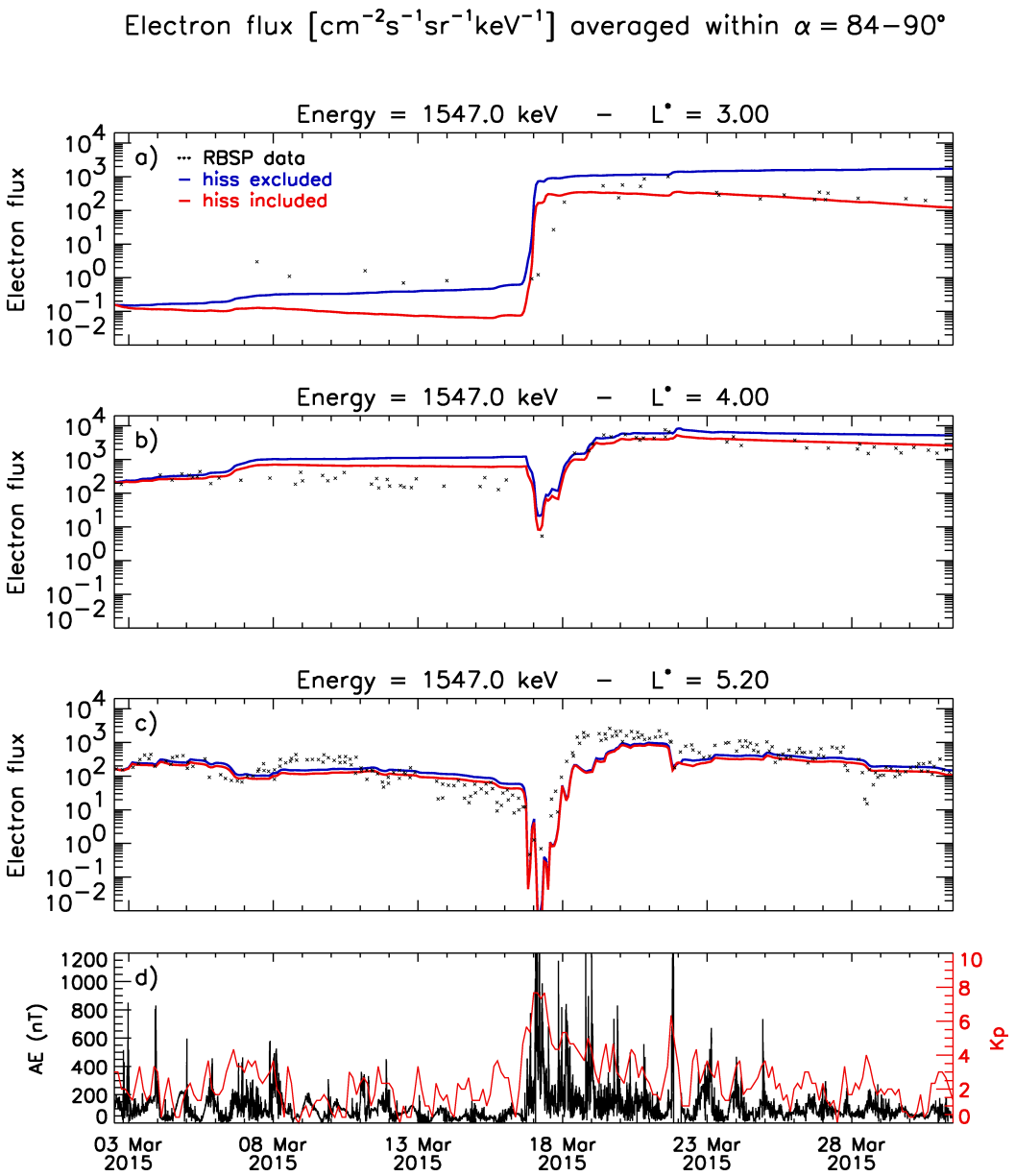


Figure 7.18: Flux of 1547 keV electrons with an equatorial pitch-angle averaged between $84° - 90°$ at three constant values of $L^*$. The flux measured by RBSP-A and RBSP-B is indicated by the black dots. The blue line is the flux calculated with the `BAS-RBM` utilising radial diffusion, chorus, and EMIC waves, but without hiss, while the red line is the flux calculated with hiss included in the simulation. The $AE$ and $Kp$ indices are presented in panel (d).

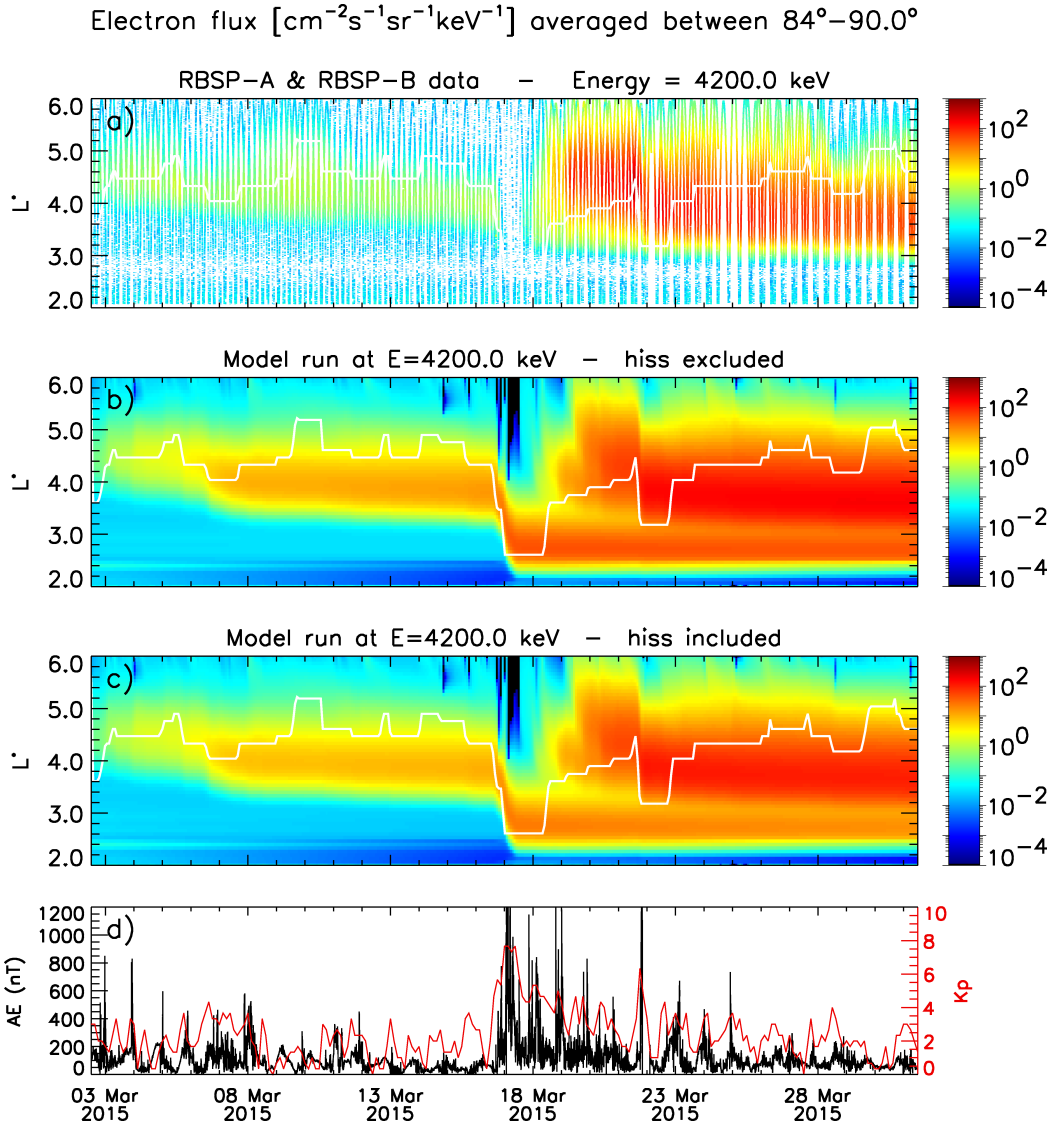


Figure 7.19: Flux of 4200 keV electrons with an equatorial pitch-angle averaged between $84° - 90°$ measured by RBSP-A and RBSP-B (a). The flux calculated with the `BAS-RBM` utilising radial diffusion, chorus, and EMIC waves, but without hiss are shown in panel (b), while panel (c) shows the simulation results where hiss is included. The *AE* and *Kp* indices are presented in panel (d).

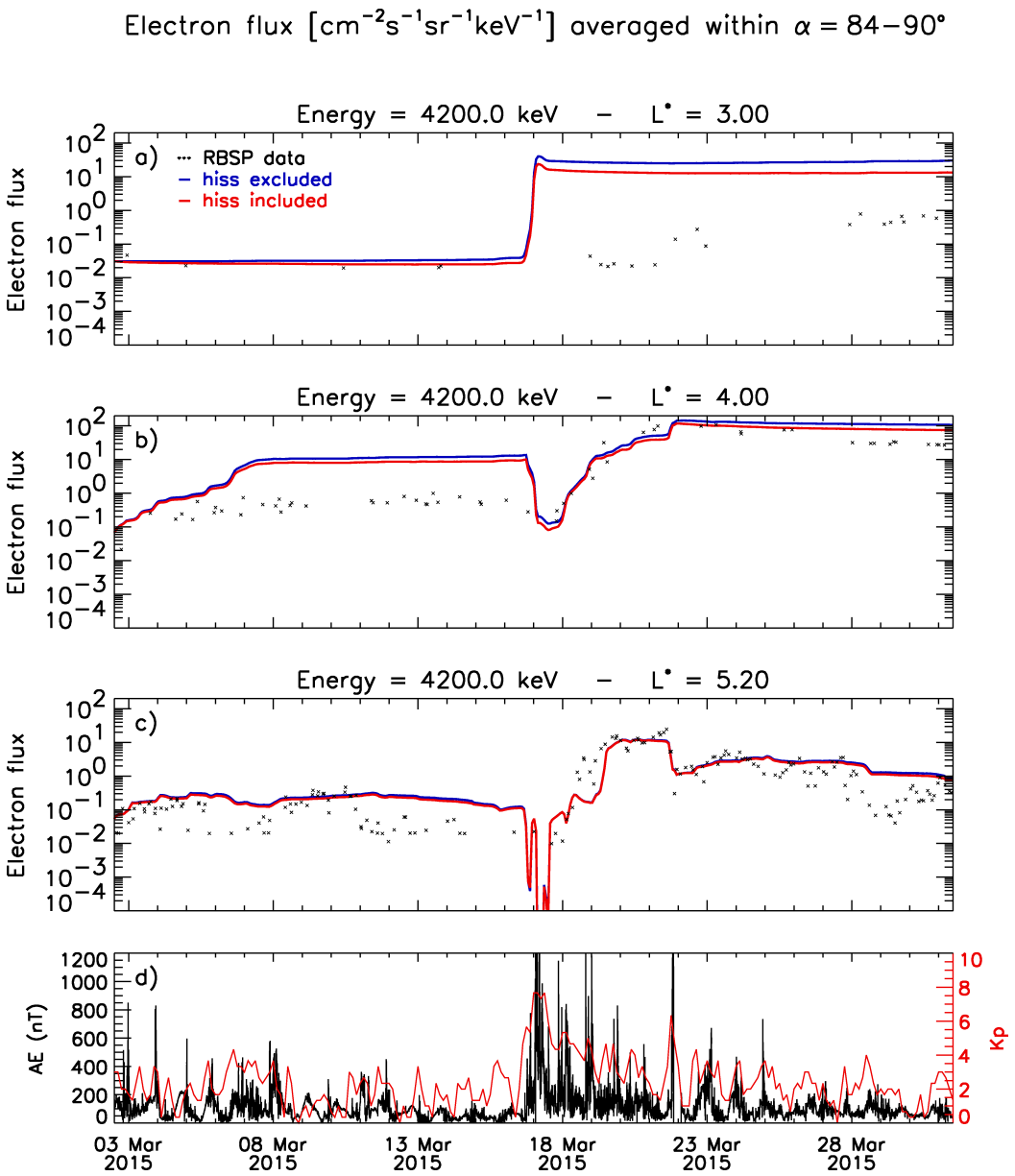


Figure 7.20: Flux of 4200 keV electrons with an equatorial pitch-angle averaged between $84° - 90°$ at three constant values of $L^*$. The flux measured by RBSP-A and RBSP-B is indicated by the black dots. The blue line is the flux calculated with the `BAS-RBM` utilising radial diffusion, chorus, and EMIC waves, but without hiss, while the red line is the flux calculated with hiss included in the simulation. The $AE$ and $Kp$ indices are presented in panel (d).

### 7.5.3 Radial Diffusion

Radial diffusion transports electrons across the geomagnetic field from regions of high phase space density (PSD) into regions of lower PSD. Assuming conservation of the first and second adiabatic invariant, electrons being transported radially outward lose energy, while electrons being transported towards the Earth gain energy, since the Earth's magnetic field decreases with the radial distance to the Earth. In this thesis, the radial diffusion coefficients of *Brautigam and Albert* [2000] are used, since they are the de-facto standard for radiation belt models (For details see Section 2.3.1).
However, the results presented in the previous sections show that at large energies and low $L^*$ the electron flux of the simulation is considerably overestimated. One likely reason for this might be that radial diffusion is too strong at low $L^*$. In the `BAS-RBM` radial diffusion has to take place at constant values of $\mu$ and $J$ at all $L^*$, where $\mu$ and $J$ are related to $L^*$ and the pitch-angle $\alpha$ by (for details see Section 2.3.2):

$$\mu = \frac{p^2 (L^*)^3 \sin^2(\alpha)}{2 m_e B_d} \tag{7.7}$$

$$J = 2 p R_E \cdot L^* \cdot Y(\sin(\alpha)) \,. \tag{7.8}$$

#### Phase Space Density Distribution

In order to evaluate the influence of the radial diffusion model on the electron flux, the phase space density distribution with respect to $L^*$ needs to be studied at relevant values of $\mu$ and $J$. Since only fluxes of electrons with $\alpha \approx 90^\circ$ are studied here, it follows from Eq. 7.8 that $J \approx 0\,\mathrm{kgm^2s^{-1}}$. In order to cover a wide range of energies, all following results will be presented at $\mu = 400\,\mathrm{MeV/G}$, $1000\,\mathrm{MeV/G}$, and $3000\,\mathrm{MeV/G}$. At $L^*_{max} = 6.0$ these values correspond to $E \approx 400\,\mathrm{keV}$, $800\,\mathrm{keV}$, and $1.7\,\mathrm{MeV}$, while at $L^*_{min} = 2.0$ they correspond to $E \approx 3.5\,\mathrm{MeV}$, $5.8\,\mathrm{MeV}$, and $10.4\,\mathrm{MeV}$. A comparison of the phase space density of electrons measured by the VAP satellites with the results calculated with the `BAS-RBM` utilising chorus, EMIC waves, plasmaspheric hiss, and radial diffusion at $J = 0\,\mathrm{kgm^2s^{-1}}$ and $\mu = 400\,\mathrm{MeV/G}$, $1000\,\mathrm{MeV/G}$, and $3000\,\mathrm{MeV/G}$ are shown in Figures 7.21, 7.22, and 7.23, respectively. Here, panel (a) shows the PSD obtained from the VAP data as a contour plot of time and $L^*$, while panel (b) shows

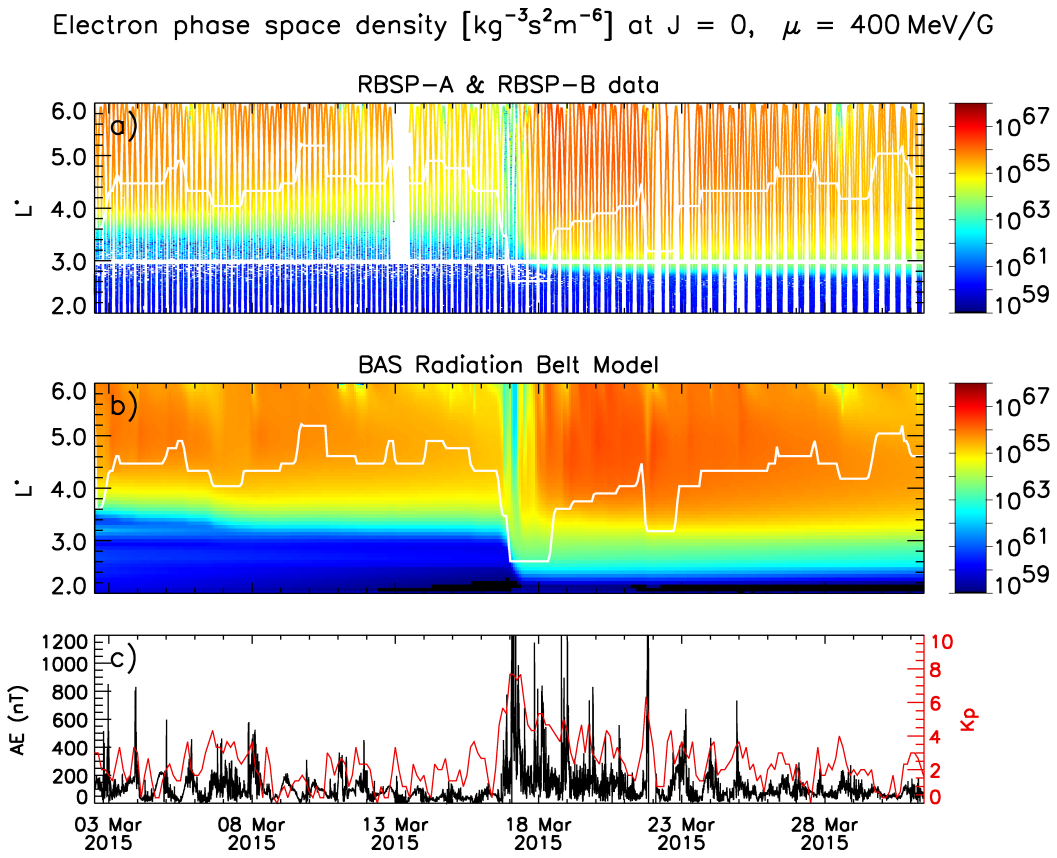


Figure 7.21: Phase space density of electrons at $J = 0$ and $\mu = 400\,\mathrm{MeV/G}$ measured by RBSP-A and RBSP-B (a) and calculated using the `BAS-RBM` utilising by radial diffusion, hiss, lower and upper band chorus, and EMIC waves (b). The $AE$ and $Kp$ indices are presented in panel (c).

the model results in the same format. In order to obtain the VAP PSD at the desired values of $\mu$, the data was interpolated. First, the values of $\mu$ corresponding to all energy channels of MagEIS and REPT of both VAP satellites at all timesteps (and corresponding values of $L^*$) were calculated using Eq. 7.7. Then the PSD at the desired value of $\mu$ was obtained by a linear interpolation of the $\log_{10}$ of the PSD of all determined VAP $\mu$ channels at each timestep. A remnant of this process is the horizontal white stripe, which corresponds to the energy gap between MagEIS and REPT.

The phase space densities measured by the Van Allen Probes are generally peaked at larger values of $L^* > 4.0$ for all values of $\mu$. There is a slight decrease of the overall PSD from the beginning of the period up until the main storm around 17 March. Around this time, the PSD significantly reduces for about half a day and then increases by more than a decade compared to the time before the storm. While the inner edge of

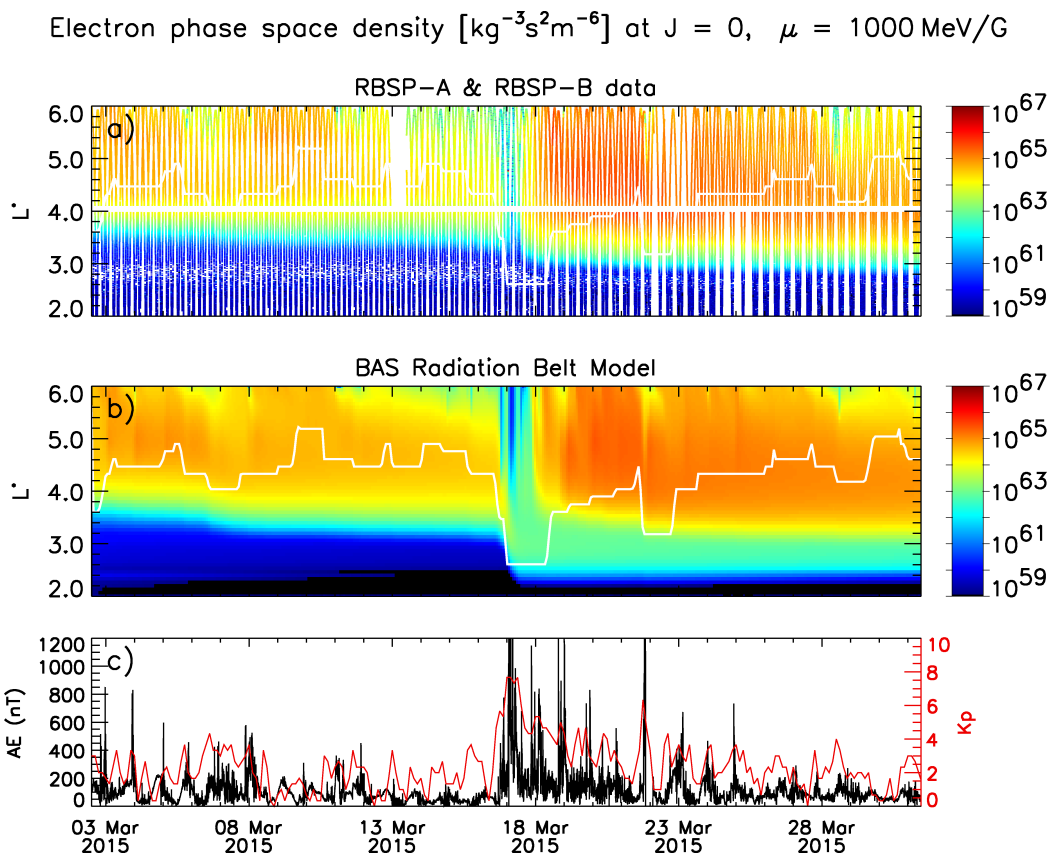


Figure 7.22: Phase space density of electrons at $J = 0$ and $\mu = 1000\,\mathrm{MeV/G}$ measured by RBSP-A and RBSP-B (a) and calculated using the `BAS-RBM` utilising by radial diffusion, hiss, lower and upper band chorus, and EMIC waves (b). The $AE$ and $Kp$ indices are presented in panel (c).

the measured outer belt moves from about $L^* = 3.8$ on 3 March to $L^* = 4.2$ before 17 March for all $\mu$, it moves from $L^* = 3.8$ to $L^* = 3.6$ in the simulation. After the main storm on 17 March the inner edge of the PSD is moved to lower values of $L^*$ and the PSD slowly reduces until the end of the period. The $L^*$ distribution of the PSD seems to be rather flat for $L^* > 4.2$ at nearly all times, while the PSD is decreasing for $L^* < 4.2$. Therefore, radial transport should be mostly inward for $L^* < 4.2$, and small at larger $L^*$. Except for the inner edge of the outer belt, the `BAS-RBM` tends to be able to reproduce the measured PSD for all $\mu$, particularly during the first 13 days of the simulation. However, during and after the storm around 17 March, the PSD tends to be overestimated at lower $L^*$ for both $\mu = 400\,\mathrm{MeV/G}$ and $\mu = 1000\,\mathrm{MeV/G}$, and the resulting gradients with respect to $L^*$ are likely to be different between simulation and measured data.

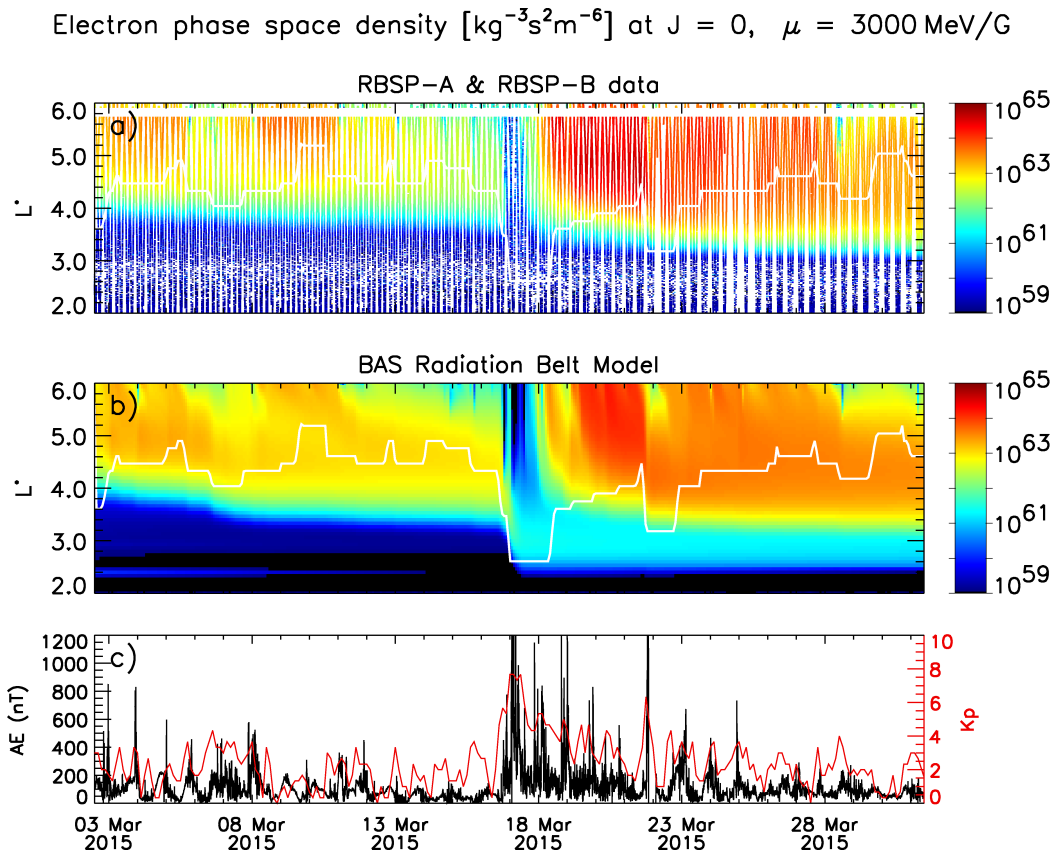


Figure 7.23: Phase space density of electrons at $J = 0$ and $\mu = 3000\,\mathrm{MeV/G}$ measured by RBSP-A and RBSP-B (a) and calculated using the `BAS-RBM` utilising by radial diffusion, hiss, lower and upper band chorus, and EMIC waves (b). The $AE$ and $Kp$ indices are presented in panel (c).

Since the gradients are one important factor to determine the strength of the radial diffusion, a detailed analysis of the $L^*$ distribution of the phase space densities is presented in Figure 7.24 at noon of 07 March, 17 March, 18 March, and 22 March (left to right) for the same three values of $\mu$ (top to bottom). The VAP data in the half-orbit around the four dates are presented as the dots, where blue and red are the MagEIS RBSP-A and RBSP-B data and the green and yellow dots are the REPT RBSP-A and RBSP-B data. The solid line is the PSD calculated with the `BAS-RBM` at the stated time.

The results show that the model is able to reproduce the measured data at $\mu = 400\,\mathrm{MeV/G}$ and $1000\,\mathrm{MeV/G}$ in the period before the main storm (first column, 07 March), and there is reasonable agreement for $\mu = 3000\,\mathrm{MeV/G}$. The data are overestimated by about a factor of two, but more importantly, the gradients are reproduced for

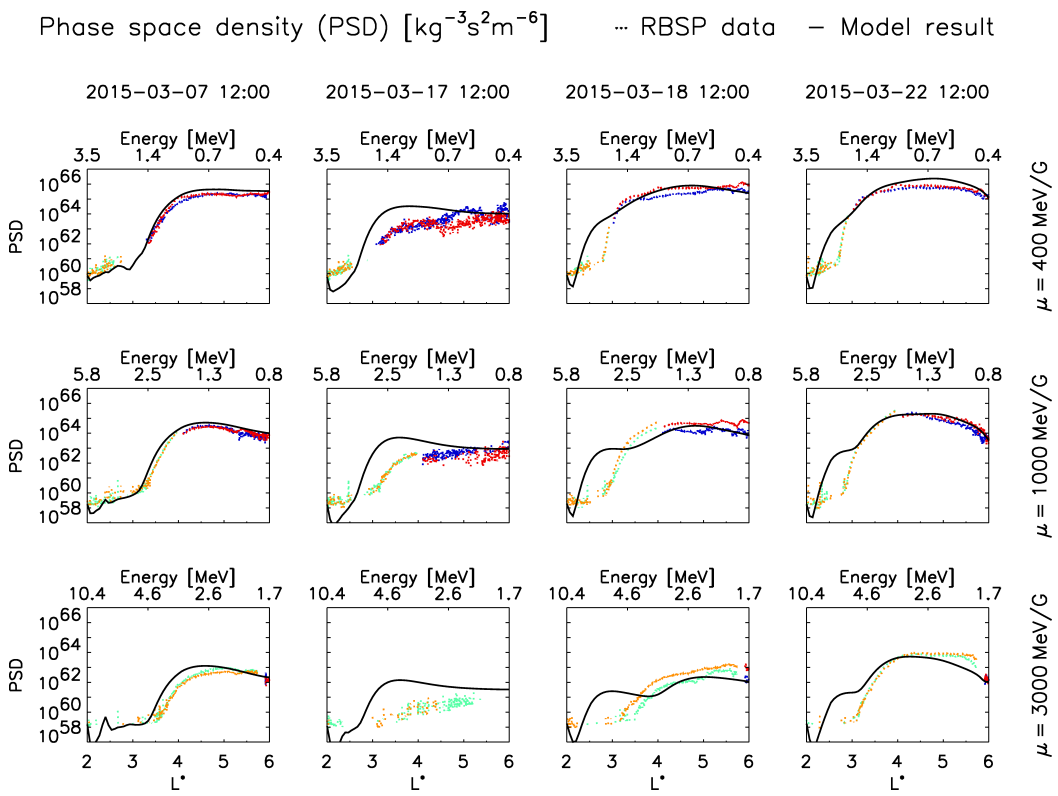


Figure 7.24: Phase space density of electrons at $J = 0$ and $\mu = 400\,\mathrm{MeV/G}$ (top), $1000\,\mathrm{MeV/G}$ (middle), and $3000\,\mathrm{MeV/G}$ (bottom) at four different times $t_i$ from left to right. The dots are the RBSP data of the half-orbit around $t_i$, and the solid lines are the `BAS-RBM` results at $t_i$ utilising chorus, EMIC, hiss, and radial diffusion.

all $L^*$ and $\mu = 400\,\mathrm{MeV/G}$ and $1000\,\mathrm{MeV/G}$. However, at $\mu = 3000\,\mathrm{MeV/G}$ the PSD distribution of the simulation is shifted to lower $L^*$ by about $0.3\,L^*$ and decreasing for $L^* > 4.2$, where the measured PSD is flat. As a consequence, radial diffusion will be slightly overestimated between about $L^* = 3.2 - 3.6$ where the simulation gradient is steeper. Furthermore, the model will diffuse ultrarelativistic electrons radially outward for $L^* > 4.2$.

During the main storm around 17 March (second column) the PSD of model and VAP data only agree for $L^* > 5.5$. For smaller $L^*$, the model is generally unable to reproduce the measured data, and instead overestimates it by up to 3.5 decades around $L^* = 3.0 - 4.0$. The observed PSD has decreased, particularly near $L^* = 3$-$4$ compared to 7 March. Furthermore, the gradient of the observed PSD is now positive for $L^* > 2.5$, whereas before there was a peak in PSD. The model has not been able to reproduce this feature and the change in gradient is significant. At large $L^*$, and hence

on the outer boundary of the simulation, there is a drop in PSD which drives outward radial diffusion and loss, but it has not been possible to remove all the electrons in the model at lower $L^*$. Also, since the PSD drops more at about $L^* = 4.0$ that at $L^* = 6.0$, it is difficult to understand how all the losses could be due to outward radial diffusion alone.

The gradients of the model are much larger than the measured ones for $L^* < 3.3$ and consequently electrons are diffused radially inward from about $L^* < 3.3$ down to about $L^* = 2.2$. The corresponding energies are in the MeV range, and since the electron energy is increased for inward diffusion, the flux of ultrarelativistic electrons is likely to be increased significantly between $L^* = 2.2 - 3.3$ in the model, which is exactly what was identified as one of the fundamental problems of the 4.2 MeV electron flux discussed in the previous sections.

On the day following the main storm (18 March) the model tends to reproduce the observed PSD for $L^*$ with corresponding energies less than about 1.4 MeV. At larger energies however, the PSD profiles for $\mu = 1000$ MeV/G and 3000 MeV/G show local minima at $L^* = 3.5$ and $L^* = 4.0$, respectively. These will cause the overestimated high energy electron fluxes to be decreased slightly through radial diffusion towards these local minima, but the simulations show that this is not sufficient.

The plots during the recovery phase of the storm (22 March) show that the PSD tends to be reproduced by the model for all values of $\mu$ for about $L^* > 3.0$. However, at lower $L^*$, the measured PSD is still overestimated considerably by the model. Consequently, the electron flux at $L^* < 3.0$ is likely to remain overestimated by the model, at least for ultrarelativistic electrons.

In summary, the phase space density distribution with respect to $L^*$ shows that the overestimated electron fluxes at electron energies greater than about 1.5 MeV, discussed in the previous, sections are most likely due to the inability of the model to reproduce the PSD profile correctly which affects radial diffusion. At lower values of $L^*$, the gradients, which drive the radial diffusion, are overestimated by the model, particularly during storm times. Therefore, too many electrons will be radially diffused to lower $L^*$ and thereby gaining energy, resulting in too high fluxes of ultrarelativistic electrons.

Possible reasons for this problem are not enough electron precipitation, which will be discussed later, or overestimated radial diffusion rates at lower $L^*$ and MeV energies of the Brautigam & Albert radial diffusion model. In the following section, the radial diffusion model will therefore be analysed.

### Variation of the Radial Diffusion Model

In order to test the hypothesis mentioned above that reduced diffusion rates at lower $L^*$ and MeV energies might solve the presented problems, a new radial diffusion model developed by *Liu et al.* [2016] based on seven years of data from the THEMIS satellite will be adopted. Under the assumption of a dipole magnetic field they define the radial diffusion coefficients in this model (from now on "THEMIS $D_{LL}$") as

$$D_{LL}^{[THEMIS]} = 1.115 \cdot 10^{0.281Kp-6.0} \cdot (L^*)^{8.184} \cdot \mu^{-0.608}, \tag{7.9}$$

where the model is valid for $Kp$ between 0 and 5, and $L^*$ = 3.5 - 7.5. In contrast to the radial diffusion rates by Brautigam & Albert (from now on "Brautigam & Albert $D_{LL}$") the THEMIS $D_{LL}$ depends on $\mu$, and the model is valid for 400 MeV/G $\leq \mu \leq$ 4000 MeV/G. A comparison between the Brautigam & Albert $D_{LL}$ (dotted lines) and the THEMIS $D_{LL}$ (solid lines) is shown in Figure 7.25 for $Kp = 1$ (blue) and $Kp = 5$ (red), and the three values of $\mu$ used before.

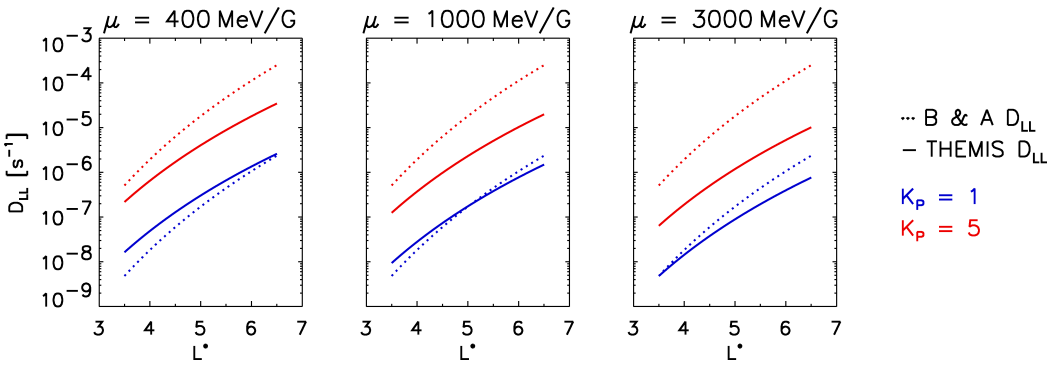


Figure 7.25: Comparison of the Brautigam & Albert $D_{LL}$ (dotted lines) and the THEMIS $D_{LL}$ (solid lines) for $Kp = 1$ (blue) and $Kp = 5$ (red) and different values of $\mu$.

It can be seen that for high geomagnetic activity the THEMIS $D_{LL}$ are up to one decade smaller than the Brautigam & Albert $D_{LL}$, and the difference increases with $\mu$ and therefore energy. At low geomagnetic activity and $\mu = 400\,\mathrm{MeV/G}$, the THEMIS $D_{LL}$ are about a factor of 2 larger than the Brautigam & Albert $D_{LL}$ at low $L^*$, while they are the same at $L^* = 6.5$. With increasing $\mu$ the THEMIS $D_{LL}$ are overall reduced, while the Brautigam & Albert $D_{LL}$ are independent of $\mu$. As a consequence, the THEMIS $D_{LL}$ become up to a factor of 2 smaller than the Brautigam & Albert $D_{LL}$ at larger $\mu$ and $L^*$. Overall, the THEMIS $D_{LL}$ therefore should be sufficient to study the effects of reduced diffusion rates at lower $L^*$ and MeV energies.

The effects of the THEMIS $D_{LL}$ are studied in Figures 7.26, 7.27, and 7.28, which show a comparison of the flux calculated with the `BAS-RBM` utilising the Brautigam & Albert $D_{LL}$ or the THEMIS $D_{LL}$ for electrons with energies of 593 keV, 1547 keV, and 4200 keV, respectively. Panel (a) shows the electron flux measured by the Van Allen Probes as a contour plot of time and $L^*$, while panel (b) shows the results of the model run utilising the Brautigam & Albert $D_{LL}$ (as well as chorus, EMIC, and hiss), and panel (c) shows the results calculated using the THEMIS $D_{LL}$. The $AE$ and $Kp$ indices driving the simulations are shown in panel (d).

The results show that the THEMIS radial diffusion coefficients and Brautigam & Albert radial diffusion coefficients produce similar fluxes at $E = 593\,\mathrm{keV}$ and $E = 1547\,\mathrm{keV}$, although the inner edge of the outer radiation belt as measured by the Van Allen Probes is not reproduced by either model.

At $E = 4200\,\mathrm{keV}$ however, the difference between the two models are much more pronounced at all $L^*$. The significantly overestimated flux around $L^* = 4.0$ before 16 March is reduced by up to 2 decades if the THEMIS $D_{LL}$ are used instead of the Brautigam & Albert $D_{LL}$. The resulting flux reaches values similar to the measured flux until about 9 March, while it is still overestimated by about one decade afterwards. After the main storm event around 18 March the flux at all $L^*$ is reduced considerably by the THEMIS model. As a result, the flux below $L^* = 3.5$ now agrees better with the data. While the inner edge of the outer radiation belt is still not reproduced, the THEMIS radial diffusion model provides a way to reduce the overestimated flux at low

$L^*$, at least to some extent. However, above $L^* = 3.5$ the THEMIS radial diffusion rates result in an underestimated flux, while the Brautigam & Albert diffusion rates produce better agreement with the data. This indicates that revisions of the radial diffusion model might result in considerably improved simulation results, although the THEMIS model itself is not appropriate, since a better agreement at large energies and low $L^*$ is achieved in exchange for worse agreement at lower energies and larger $L^*$.

Overall, two key issued were identified so far: The significantly overestimated electron flux at high electron energies and low $L^*$ during and after the main storm on 17 March, and the increasingly overestimated flux around $L^* = 4.0$ before 16 March. We now consider the case that if there were better agreement between the data and the simulation just before the dropout, whether this would lead to a better simulation of the dropout event. In order to test this hypothesis, a set of simulations was performed between 16 March 2015 and 31 March 2015. Since the simulation was initialised with the Van Allen Probes data, the simulated flux just before the dropout agrees with the data. The results for the most problematic energy range of $E = 4200\,\mathrm{keV}$ are shown in Figure 7.29 in the same format as before, comparing the THEMIS and Brautigam & Albert radial diffusion models with the data measured by the Van Allen Probes.

The simulations show that the flux transported to $L^* < 3$ is considerably reduced, because less flux is transported as low in $L^*$ compared to the results of the full simulation period (e.g. Figure 7.28). However, it is not sufficient to reproduce the observation, since the flux is still overestimated at low $L^*$ by both radial diffusion models. Therefore, while it is still necessary to achieve better agreement between the measured and the simulated flux before 16 March, no sufficient improvement after 16 March can be achieved thereby.

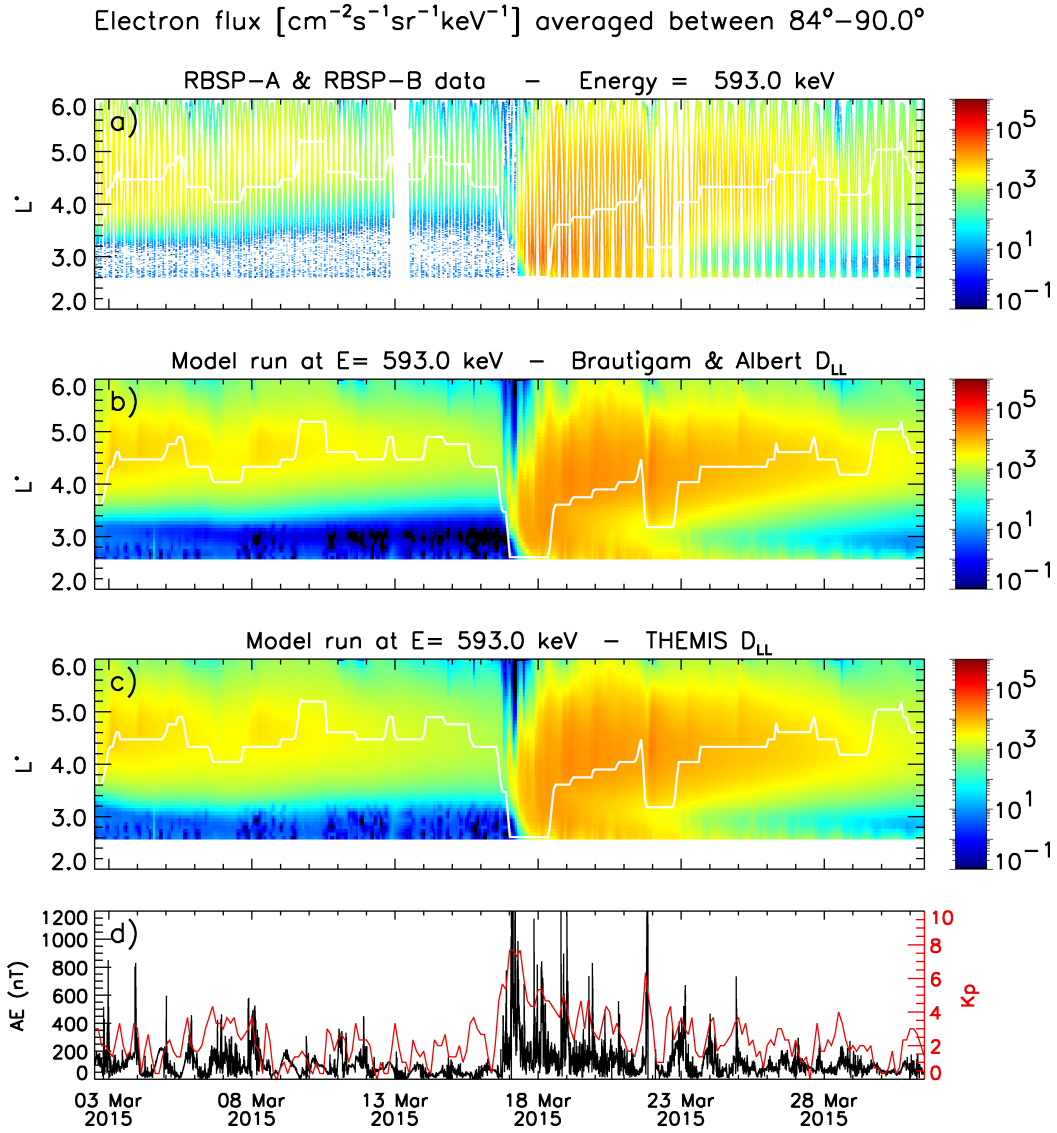


Figure 7.26: Flux of 593 keV electrons with an equatorial pitch-angle averaged between $84° - 90°$ measured by RBSP-A and RBSP-B (a). The flux calculated with the `BAS-RBM` utilising chorus, EMIC, hiss, and the radial diffusion rates by Brautigam & Albert is shown in panel (b), while panel (c) shows the simulation result using the THEMIS radial diffusion model instead. The *AE* and *Kp* indices are presented in panel (d).

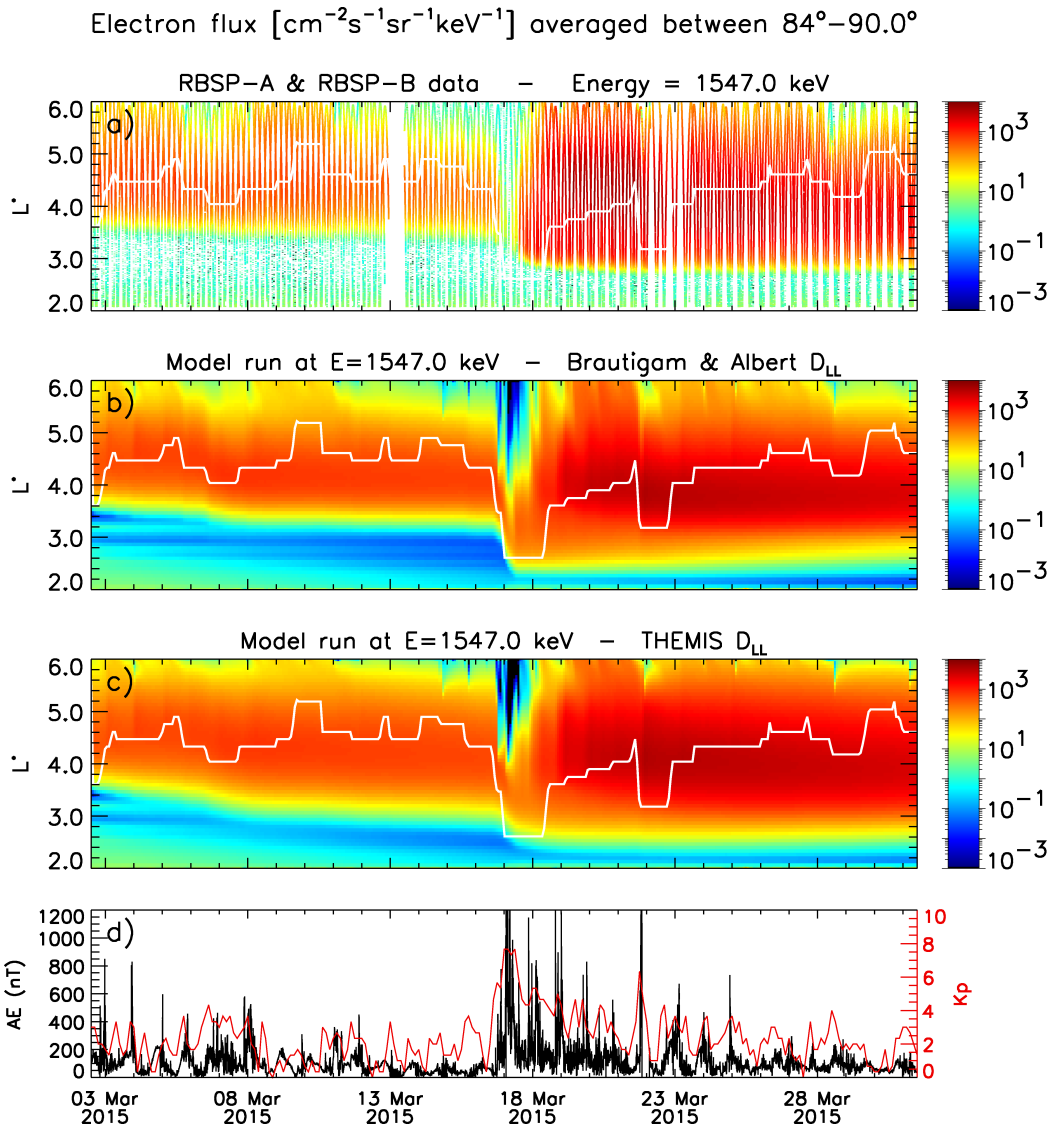


Figure 7.27: Flux of 1547 keV electrons with an equatorial pitch-angle averaged between $84° - 90°$ measured by RBSP-A and RBSP-B (a). The flux calculated with the `BAS-RBM` utilising chorus, EMIC, hiss, and the radial diffusion rates by Brautigam & Albert is shown in panel (b), while panel (c) shows the simulation result using the THEMIS radial diffusion model instead. The $AE$ and $Kp$ indices are presented in panel (d).

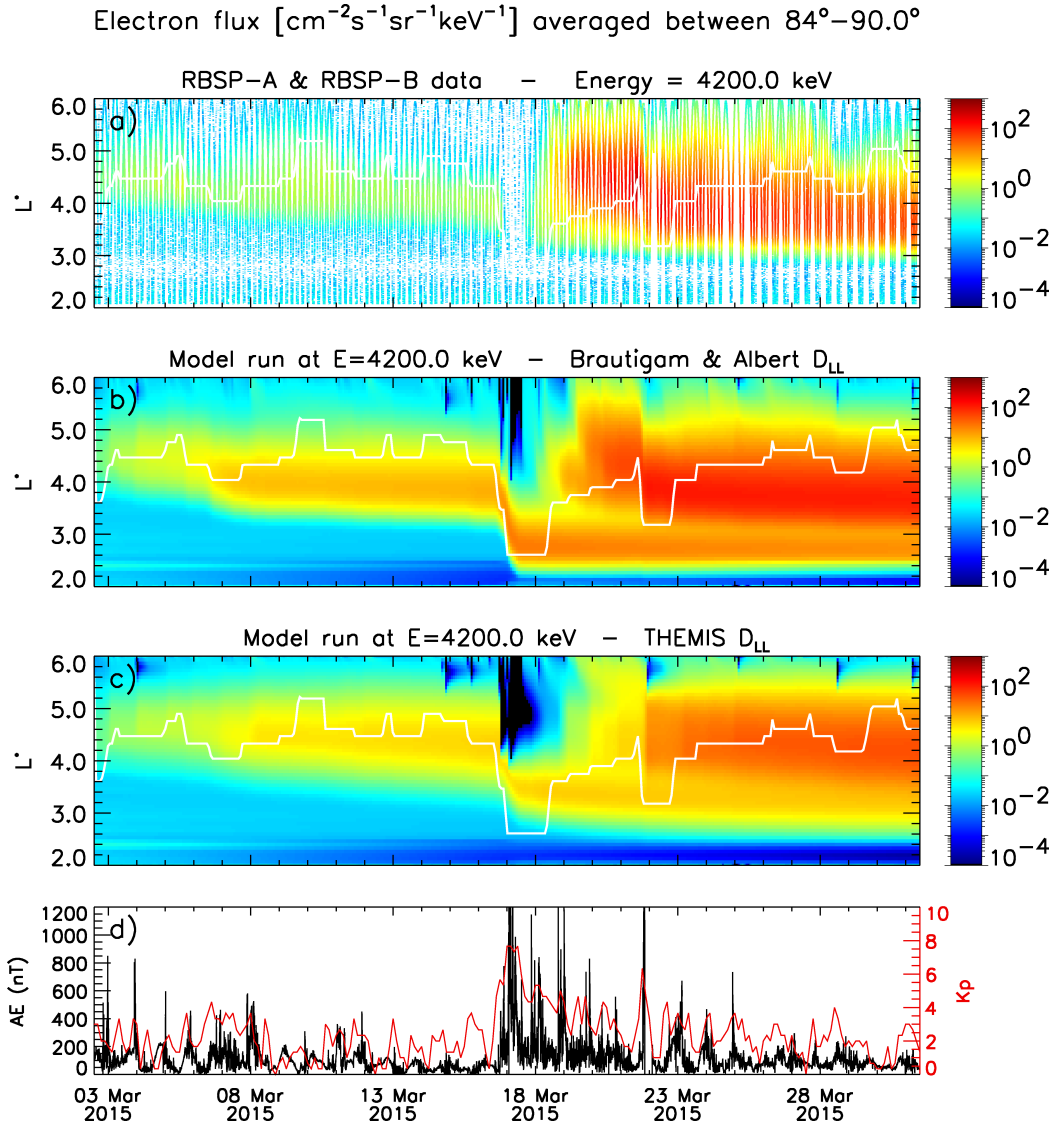


Figure 7.28: Flux of 4200 keV electrons with an equatorial pitch-angle averaged between $84° - 90°$ measured by RBSP-A and RBSP-B (a). The flux calculated with the `BAS-RBM` utilising chorus, EMIC, hiss, and the radial diffusion rates by Brautigam & Albert is shown in panel (b), while panel (c) shows the simulation result using the THEMIS radial diffusion model instead. The $AE$ and $Kp$ indices are presented in panel (d).

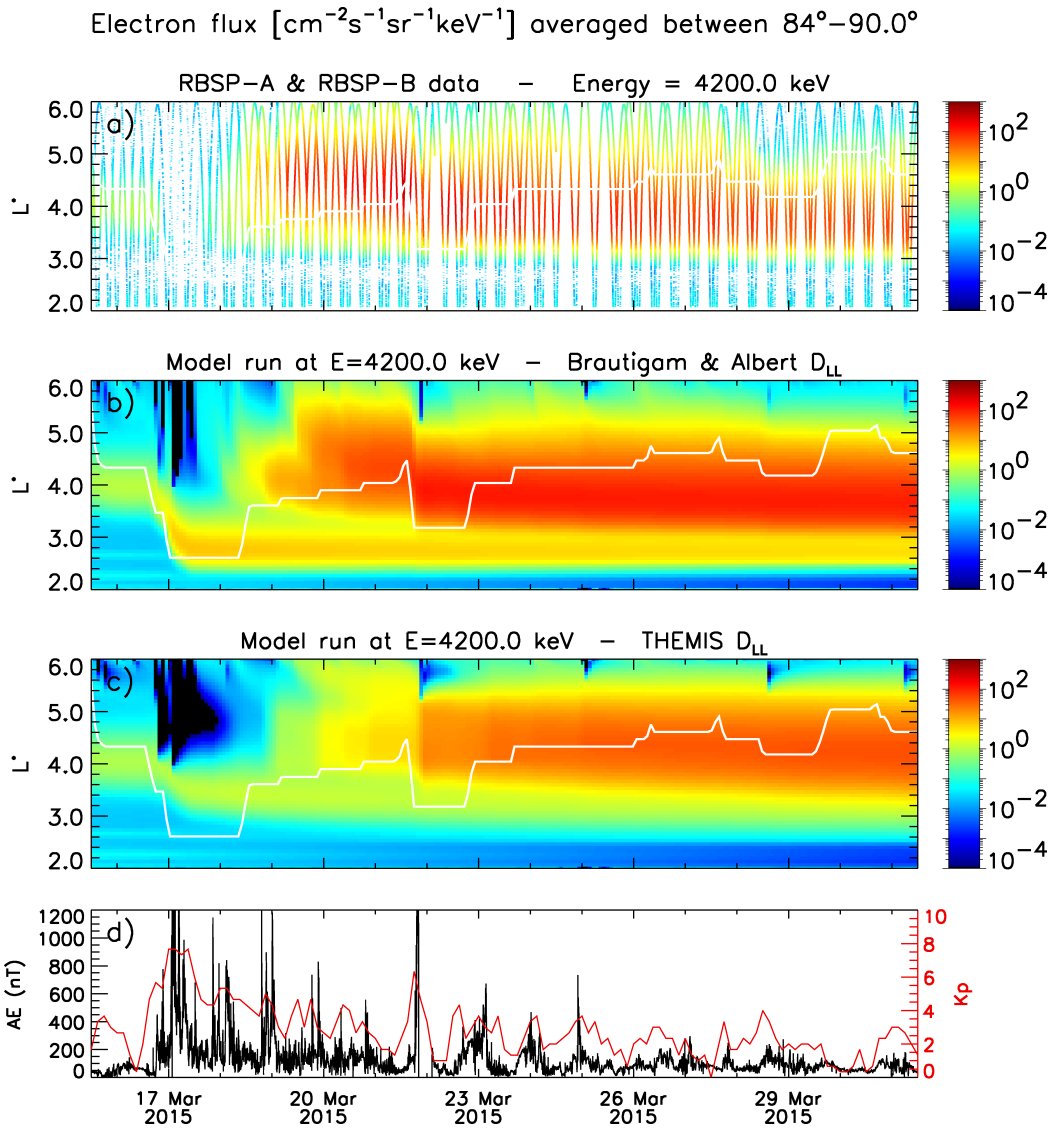


Figure 7.29: Flux of 4200 keV electrons with an equatorial pitch-angle averaged between $84° - 90°$ in the period between 16 March and 31 March 2015 measured by RBSP-A and RBSP-B (a). The flux calculated with the `BAS-RBM` utilising chorus, EMIC, hiss, and the radial diffusion rates by Brautigam & Albert is shown in panel (b), while panel (c) shows the simulation result using the THEMIS radial diffusion model instead. The *AE* and *Kp* indices are presented in panel (d).

## 7.6 Discussion

The presented results show that the electron flux calculated with the BAS-RBM tends to agree reasonably well with the flux measured by the Van Allen Probes at electron energies below about 1.5 MeV, except for very low values of $L^*$ (e.g. $L^* = 3.0$) before the main storm on 17 March. At these low values of $L^*$ the simulations are likely to underestimate the measured electron fluxes by at least one decade. However, the sparse number of data and the lack of any lower flux measurements indicate that the measured flux is likely to be in the noise level. In contrast to the reasonably good agreement of electron energies up to about 1.5 MeV, there is a large discrepancy between data and simulation at higher energies, and two main issues were identified. Firstly, an overestimated increase of the simulated flux around the 7th of March, particularly at high energies, resulting in too large fluxes before the main storm, and secondly the considerably overestimated fluxes after 17 March at lower $L^*$. A detailed analysis identified overestimated radial diffusion rates at low $L^*$ and energies greater than a few MeV as the main reason for these problems. In situ studies indicate that ULF waves might be reduced inside the plasmapause [*Takahashi and Anderson*, 1992], and hence radial diffusion rates based on improved ULF wave models could be able to considerably improve the electron flux at large electron energies inside the plasmapause.

Furthermore, these issues indicate that the models for wave-particle interactions at ultrarelativistic energies need to be improved, and also plasma waves that are not routinely included in the simulations of the radiation belts might be relevant. One cause of the overestimated fluxes could be the lack of magnetosonic waves in the simulation. However, it was shown that they are most effective at pitch-angles between about 40° - 80° [*Horne et al.*, 2007] and ineffective at larger pitch-angles. Therefore, it is unlikely that they are able to reduce the problems of the 90° electron flux.

Similarly, EMIC waves were shown to cause significant losses at ultrarelativistic electron energies, but only at pitch-angles less than about 60° (See Chapter 5). There were also indications that improved statistics of the EMIC wave model might increase the losses at higher pitch-angles, but unfortunately only up to about $\alpha_{eq} = 80°$. In combination with other plasma waves these losses might still be able to indirectly affect

the losses at larger pitch-angles, improving the simulation.

The presented results tend to provide better agreement between simulation and data at 4.2 MeV, if chorus waves are excluded, indicating that the chorus diffusion rates might be too large at high electron energies. Recent discussions indicate that the values for the ratio of $f_{pe}/f_{ce}$ used in the present chorus wave model might be too large. It was suggested by *Li et al.* [2014] that chorus may be able to accelerate electrons locally to energies of the order of 6 MeV, while *Shprits et al.* [2013] showed that the chorus waves might not, at least directly, contribute to the acceleration at 6 MeV. [*Kersten et al.*, 2014] showed that the increased acceleration at 6 MeV is mainly due to much lower values of $f_{pe}/f_{ce}$ in the study by *Li et al.* [2014]. Improving and hence reducing the ratio of $f_{pe}/f_{ce}$ will therefore shift the diffusion rates to higher energies and hence result in increased energy and pitch-angle diffusion rates at larger electron energies. While this will result in more acceleration, the losses due to pitch-angle scattering are increased as well, and the overall distribution of the 90° electron flux might be reduced, improving the results.

The presented plasmaspheric hiss wave model includes waves in the frequency range between 100 Hz - 4 kHz. A recent study of the VAP wave data showed that plasmaspheric hiss can be found at frequencies as low as a few tens of Hz [*Li et al.*, 2015], but the contribution to the pitch-angle diffusion rates were shown to be insignificant. The presented wave model also does not include all of the lightning-generated whistlers, as they are usually found at frequencies between 2 - 5 kHz and above. However, since the resonant energy decreases with increasing frequency, the diffusion rates of lightning-generated whistlers at frequencies larger than 4 kHz are unlikely to contribute significantly to the diffusion rates.

Another possible loss process that could positively affect the electron flux are collisions of particles with each other. In the current model the loss timescale $\tau_L$ was set to be one quarter of the bounce period inside the loss cone, while it was set to be infinite outside the loss cone (See 2.3). In principle, larger loss rates outside the loss cone can be studied. However, physically collisions between particles depend on the particle density, which is strongest close to the atmosphere. In order to be scattered into the loss cone,

particles therefore need to have a low equatorial pitch-angle. Hence, increased collision loss rates will mostly affect the distribution of particles with small pitch-angles, while the fluxes presented here are for particles with an equatorial pitch-angle close to 90°, and therefore increased collision rates are not expected to affect the presented results sufficiently.

One particular problem for the mismatch between model and data was that the observed flux was wiped out completely during the dropout at ultrarelativistic energies (for example 4.2 MeV), while the model was unable to reproduce this. Modelling the dropout correctly is likely to involve several complex processes. It was shown that outward radial diffusion and loss play a significant role, but are unable to solve the issue alone. As a consequence, higher loss rates, due to precipitation, are needed, but neither hiss, nor chorus are strong enough at 4.2 MeV. However, it was shown in Chapter 4 that chorus diffusion is strong at 4.2 MeV, but only at very large pitch-angles. Combining these with increased EMIC wave diffusion, which could be found for extreme events of high activity as during the dropout event, might be able to facilitate sufficient losses together. Another reason for the insufficient modelling of the dropout could be adiabatic effects, which are currently not included in the `BAS-RBM`. An extreme event might cause the Earth's magnetic field to be significantly reduced during a geomagnetic storm, and in order to conserve the third adiabatic invariant (the flux enclosed by a particle's drift shell), the electrons have to move to much larger $L^*$. Thereby, the flux of electrons at low $L^*$ would be significantly reduced, resulting in the desired flux dropout.

Lastly, it needs to be noted that the current version of the `BAS-RBM` does not include the cross diffusion terms in the calculation of the electron flux. While it was shown that these do not have a significant effect on equatorially mirroring electrons, the cross terms might have a significant effect for electrons with energies greater than about 2 MeV and equatorial pitch-angles below 60° *Tao et al.* [2008, 2009]. Since all electron fluxes were presented for electrons with an equatorial pitch-angle close to $\alpha_{eq} = 90°$, they are therefore unlikely to be affected by the lack of the cross terms.

## 7.7 Conclusion

In this chapter the BAS-RBM was evaluated during a recent period of the Van Allen Probes mission, which allows the comparison of data and the model results at energies of up to about 10 MeV, which were not reliably measured by other satellites before. The most important part of the BAS-RBM are the drift and bounce averaged diffusion rates describing the electron acceleration and loss due to wave-particle interactions, which were presented in the previous chapters. The influence of these interactions on the electron fluxes were studied by performing simulations where each type of wave was individually excluded from the simulation.

The results show that the BAS-RBM is generally able to reproduce the measured electron fluxes at energies of 593 keV over all $L^*$ during the selected simulation period. The general structure, as well as the inner edge of the outer radiation belt is captured well, and the simulated fluxes are generally of the same order as the measured electron flux. At larger electron energies, in particular at 4.2 MeV, the fluxes are of the same order only after the main storm on 17 March and only above about $L^* = 3.2$. Before the main storm, the fluxes are generally overestimated by about one decade, in the $L^*$ region where the measured flux is enhanced. After 17 March, the flux below about $L^* = 3.2$ is overestimated by at least two decades by the simulation. It was discussed that there are several likely reasons for this difference, including an insufficient radial diffusion model and the lack of the ability to model the flux dropout correctly. Since it is not possible to model these currently, the understanding of the variability of the outer belt is not complete.

At $E = 4.2$ MeV the wave models for chorus and plasmaspheric hiss were shown to have a negligible effect on the electron flux, while using a more recent, advanced model for the radial diffusion is able to significantly reduce the electron fluxes in the critical regions. Unfortunately, the fluxes that were initially simulated correctly are reduced by the advanced radial diffusion model as well. This indicates that the radial diffusion rates are a critical component in improving the differences at large electron energies, and more research on these needs to be done.

Overall, the results show that the BAS-RBM utilising the presented chorus, EMIC, and

hiss diffusion models, performs well at electron energies below about 1 MeV, suggesting that the presented wave models capture most of the underlying physics of the plasma waves, at least in an average, statistical sense. At larger electron energies, which were not commonly studied before, due to a lack of measurements, important problems with the wave models remain, in particular with the ULF waves that drive radial diffusion.

# CHAPTER 8
# *Summary and Conclusions*

In this study, novel statistical models for lower and upper band chorus waves, electromagnetic ion cyclotron (EMIC) waves, and plasmaspheric hiss were presented. The models were derived from a statistical analysis of the data from up to seven different satellites and they were used to calculate the drift and bounce averaged pitch-angle and energy diffusion rates. These were in turn utilised in the `BAS-RBM` to study their effects on a global scale.

In the first part of this study, a novel statistical model for lower and upper band whistler mode chorus waves was developed based on the data from seven different satellites, which significantly improved the resolution of the parametrisation of previous models. The results showed that chorus waves can be a significant electron acceleration and loss process at energies lower than a few MeV. Initially the model was calculated by performing a Gaussian fit to the wave spectral data, but improvements of the code to calculate the diffusion rates allowed it to use the wave spectral data directly. It was shown that these two methods produce similar results, proving that the initial fitting method was reliable. Furthermore, improvements to the wave normal angle model were made that affected the diffusion rates insignificantly in the energy range, where the drift averaging approach, that is used to calculate the electron fluxes, is valid. Using the wave spectral data directly led to the most important result of the chorus studies, namely the development of a model that includes chorus waves at frequencies as low as $0.022\,f_{ce}$. It was shown that including the lower frequency chorus into the calculation of the global electron fluxes improved the results leading to a better agreement between the modelled electron fluxes and the data measured by the CRRES satellite.

In the case of EMIC waves, a global, average, and statistical model based on the wave data from the CRRES satellite was developed. The results showed that EMIC waves can be a significant loss process for the high energy electron flux with energies greater than about 3 MeV and equatorial pitch-angles ranging from the loss cone up to about 60°. EMIC waves are hence able to scatter all electrons with a pitch-angle less than

60° into the loss cone over time. The remaining distribution therefore looked like a "pancake distribution".

Using a similar analytical technique as for the chorus wave model, a novel statistical wave model for plasmaspheric hiss was developed that considerably improved the resolution of the parametrisation of previous hiss models. Furthermore, a novel method to separate hiss from chorus was presented that allowed the identification of plasmaspheric hiss inside the plasmapause. More importantly this method also includes hiss in plumes in a statistical sense, representing plasmaspheric hiss in this important region. The results showed that plasmaspheric hiss is an important loss process for energies up to a few MeV, and that it is vital to reproduce the measured fluxes.

Lastly, all these new wave models were included into the `BAS-RBM` to calculate the electron flux during a recent Van Allen Probes period, and to evaluate the `BAS-RBM`, as well as each wave model. The results showed that the simulation is able to reproduce the measured data well at electron energies less than about 1 MeV where the effects of hiss and chorus are most important. The variability of the fluxes are reproduced reasonably well and the general shape, including the inner edge of the radiation belt, as well as periods of acceleration and loss are captured by the model and tend to agree with the data.

However, at higher energies the results of the model and the data start to disagree, where the fluxes tend to be overestimated by the model. It was shown that the overestimation is due to too much acceleration or too low loss rates. Various possible causes were investigated, and it was shown that this issue is not caused by one individual process, but rather a complex interaction between various waves. The most uncertainties remain in the radial diffusion model that was used, and significant improvements of the radial diffusion rates are likely to considerably improve the results.

This bears the general question how accurate the utilised wave models are. In the case of the chorus, EMIC, and hiss wave models that were developed during this thesis, there are still large uncertainties, since they are statistical models based on limited satellite data, covering only a few solar cycles. This is particularly problematic for the presented model of the EMIC waves, since data of less than one year including only 830 events

were used. Furthermore, the coverage during times of high geomagnetic activity was low, since extreme events are rare. Additionally, the high geomagnetic activities are resolved insufficiently in the case of the chorus and EMIC wave database, as the largest level is defined as $AE > 400\,\mathrm{nT}$. Therefore, it is proposed to add a second activity level above $AE > 750\,\mathrm{nT}$, reaching a similar resolution of the geomagnetic activity as for the presented plasmaspheric hiss wave model. Generally, all statistical wave models will improve significantly, if the number of data included into the wave models was increased considerably. For instance, the data of the EMFISIS instrument on board the Van Allen Probes satellites might be included in the wave database, which is currently being worked on.

As, the presented models remain statistical wave models, that capture the wave spectral data in an average sense, excluding uncommon wave properties and extreme events, it is therefore mandatory to perform case studies of rarely occurring wave parameters, in order to identify the limits of each wave model.

The dispersion relation is an important component in the calculation of the diffusion rates. The `PADIE` diffusion code is based on cold plasma theory and it neglects warm plasma effects. While the plasma inside the plasmasphere is dominated by cold plasma, the fraction of hot plasma increases considerably outside the plasmapause. Since whistler mode chorus waves and EMIC waves are mainly found outside the plasmapause, hot plasma effects may become important for them. The difference between hot and cold plasma theory becomes relevant at large values of the wave vector $k$. For chorus waves this corresponds to waves with a large electrostatic component, and hot plasma effects can therefore be neglected for the electromagnetic waves that were studied here. In the case of EMIC waves, large $k$ are associated with wave frequencies close to the ion cyclotron frequencies. Since the frequencies of the EMIC wave model presented here are well below the ion cyclotron frequencies, hot plasma effects should also be small for them. Furthermore, waves with frequencies close to the ion cyclotron frequencies are affected by significant cyclotron and Landau damping in hot plasma theory, and would hence be considerably reduced anyway. Overall, the uncertainties of the cold plasma approximation are therefore believed to be small.

All the diffusion coefficients presented in this thesis were calculated using quasi-linear theory, since it is yet not computationally feasible to employ fully nonlinear models. Studies show that in particular chorus waves are highly nonlinear due to their short duration rising or falling tone frequency structure [e.g. *Omura et al.*, 2009; *Santolík et al.*, 2014a] and it is difficult to predict, whether the quasi-linear theory over- or underestimates the diffusion rates, since the nonlinear theory depends on whether the chorus elements are falling or rising in frequency. However, it was demonstrated by *Albert* [2010] and *Tao et al.* [2012] that there is remarkable agreement between fully nonlinear and quasi-linear simulations for waves with a wave power less than about 0.1 nT, which is higher than the wave power found in any wave model presented here. Like most radiation belt models, the `BAS-RBM` currently does not include a magnetic local time resolution, and hence drift averaged diffusion rates need to be utilised. Although it was shown that drift averaged simulations are able to accurately predict the overall shape of the electron pitch angle distribution [*Shprits et al.*, 2009a], the drift average approach is only valid for electron energies above about 100 keV [*Meredith et al.*, 2016]. Therefore, valid simulations are currently limited to electrons with energies of 100 keV and above, which excludes potentially interesting effects at lower electron energies. Furthermore, most plasma waves show an asymmetry in their MLT distribution, and these effects are therefore only included in an average sense. Employing a radiation belt model with full MLT resolution would therefore not only allow the study of the effect of wave-particle interactions on the electron distribution at lower energies, but it would also considerably improve the accuracy of wave-particle interactions due to waves with a strong MLT dependence, for instance hiss in plumes.

Despite these remaining issues, considerable improvements of the wave models were achieved during this study. Furthermore, a method of using the highly-valued Van Allen Probes data as boundary and initial conditions for the `BAS-RBM` was presented. Implementing this method and the enhanced wave models into the BAS Space Weather forecast, will therefore further improve the capability to provide reliable predictions of dangers to satellites and humans in space, as well as strengthen our knowledge about space weather effects.

# References


Abel, B., and R. M. Thorne (1998), Electron scattering loss in Earth's inner magnetosphere: 1. Dominant physical processes, *Journal of Geophysical Research: Space Physics*, *103*(A2), 2385–2396, doi:10.1029/97JA02919.

Agapitov, O., V. Krasnoselskikh, Y. V. Khotyaintsev, and G. Rolland (2012), Correction to "A statistical study of the propagation characteristics of whistler waves observed by Cluster", *Geophysical Research Letters*, *39*(24), doi:10.1029/2012GL054320.

Agapitov, O., A. Artemyev, V. Krasnoselskikh, Y. V. Khotyaintsev, D. Mourenas, H. Breuillard, M. Balikhin, and G. Rolland (2013), Statistics of whistler mode waves in the outer radiation belt: Cluster STAFF-SA measurements, *Journal of Geophysical Research: Space Physics*, *118*(6), 3407–3420, doi:10.1002/jgra.50312.

Albert, J., and Y. Shprits (2009), Estimates of lifetimes against pitch angle diffusion, *Journal of Atmospheric and Solar-Terrestrial Physics*, *71*(16), 1647 – 1652, doi:10.1016/j.jastp.2008.07.004.

Albert, J. M. (2003), Evaluation of quasi-linear diffusion coefficients for EMIC waves in a multispecies plasma, *Journal of Geophysical Research: Space Physics*, *108*(A6), doi:10.1029/2002JA009792.

Albert, J. M. (2010), Diffusion by one wave and by many waves, *Journal of Geophysical Research: Space Physics*, *115*(A3), doi:10.1029/2009JA014732.

Albert, J. M., and S. L. Young (2005), Multidimensional quasi-linear diffusion of radiation belt electrons, *Geophysical Research Letters*, *32*(14), doi:10.1029/2005GL023191.

Albert, J. M., N. P. Meredith, and R. B. Horne (2009), Three-dimensional diffusion simulation of outer radiation belt electrons during the 9 October 1990

magnetic storm, *Journal of Geophysical Research: Space Physics*, *114*(A9), doi: 10.1029/2009JA014336.

Anderson, B. J., R. E. Erlandson, and L. J. Zanetti (1992a), A statistical study of Pc 1-2 magnetic pulsations in the equatorial magnetosphere: 1. Equatorial occurrence distributions, *Journal of Geophysical Research: Space Physics*, *97*(A3), 3075–3088, doi:10.1029/91JA02706.

Anderson, B. J., R. E. Erlandson, and L. J. Zanetti (1992b), A statistical study of Pc 1-2 magnetic pulsations in the equatorial magnetosphere: 2. Wave properties, *Journal of Geophysical Research: Space Physics*, *97*(A3), 3089–3101, doi:10.1029/91JA02697.

Baker, D. N., J. B. Blake, R. W. Klebesadel, and P. R. Higbie (1986), Highly relativistic electrons in the Earth's outer magnetosphere: 1. Lifetimes and temporal history 1979-1984, *Journal of Geophysical Research: Space Physics*, *91*(A4), 4265–4276, doi: 10.1029/JA091iA04p04265.

Baker, D. N., J. B. Blake, L. B. Callis, J. R. Cummings, D. Hovestadt, S. Kanekal, B. Klecker, R. A. Mewaldt, and R. D. Zwickl (1994), Relativistic electron acceleration and decay time scales in the inner and outer radiation belts: SAMPEX, *Geophysical Research Letters*, *21*(6), 409–412, doi:10.1029/93GL03532.

Baker, D. N., S. G. Kanekal, X. Li, S. P. Monk, J. Goldstein, and J. L. Burch (2004), An extreme distortion of the Van Allen belt arising from the Halloween solar storm in 2003, *Nature*, *432*(7019), 878–881, doi:10.1038/nature03116.

Baker, D. N., S. G. Kanekal, R. B. Horne, N. P. Meredith, and S. A. Glauert (2007), Low-altitude measurements of 2-6 MeV electron trapping lifetimes at $1.5 \leq L \leq 2.5$, *Geophysical Research Letters*, *34*(20), doi:10.1029/2007GL031007.

Baker, D. N., S. G. Kanekal, V. C. Hoxie, M. G. Henderson, X. Li, H. E. Spence, S. R. Elkington, R. H. W. Friedel, J. Goldstein, M. K. Hudson, G. D. Reeves, R. M. Thorne, C. A. Kletzing, and S. G. Claudepierre (2013), A Long-Lived Relativistic Electron Storage Ring Embedded in Earth's Outer Van Allen Belt, *Science*, *340*(6129), 186–190, doi:10.1126/science.1233518.

Bartels, J., N. H. Heck, and H. F. Johnston (1939), The three-hour-range index measuring geomagnetic activity, *Terrestrial Magnetism and Atmospheric Electricity*, *44*(4), 411–454, doi:10.1029/TE044i004p00411.

Beutier, T., and D. Boscher (1995), A three-dimensional analysis of the electron radiation belt by the Salammbô code, *Journal of Geophysical Research: Space Physics*, *100*(A8), 14,853–14,861, doi:10.1029/94JA03066.

Bittencourt, J. A. (2004), *Fundamentals of Plasma Physics*, 679 pp., Springer-Verlag New York, doi:10.1007/978-1-4757-4030-1.

Blake, J. B., R. S. Selesnick, D. N. Baker, and S. Kanekal (2001), Studies of relativistic electron injection events in 1997 and 1998, *Journal of Geophysical Research: Space Physics*, *106*(A9), 19,157–19,168, doi:10.1029/2000JA003039.

Boardsen, S. A., D. L. Gallagher, D. A. Gurnett, W. K. Peterson, and J. L. Green (1992), Funnel-shaped, low-frequency equatorial waves, *Journal of Geophysical Research: Space Physics*, *97*(A10), 14,967–14,976, doi:10.1029/92JA00827.

Bortnik, J., R. M. Thorne, and N. P. Meredith (2008), The unexpected origin of plasmaspheric hiss from discrete chorus emissions, *Nature*, *452*(7183), 62–66, doi:10.1038/nature06741.

Bortnik, J., W. Li, R. M. Thorne, V. Angelopoulos, C. Cully, J. Bonnell, O. Le Contel, and A. Roux (2009), An Observation Linking the Origin of Plasmaspheric Hiss to Discrete Chorus Emissions, *Science*, *324*(5928), 775–778, doi:10.1126/science.1171273.

Boscher, D., and S. Bourdarie (2004), ONERA-DESP library V4.2, unpublished.

Bossen, M., R. L. McPherron, and C. T. Russell (1976), A statistical study of Pc 1 magnetic pulsations at synchronous orbit, *Journal of Geophysical Research*, *81*(34), 6083–6091, doi:10.1029/JA081i034p06083.

Brautigam, D. H., and J. M. Albert (2000), Radial diffusion analysis of outer radiation belt electrons during the October 9, 1990, magnetic storm, *Journal of Geophysical Research: Space Physics*, *105*(A1), 291–309, doi:10.1029/1999JA900344.

Breneman, A. W., C. A. Kletzing, J. Pickett, J. Chum, and O. Santolik (2009), Statistics of multispacecraft observations of chorus dispersion and source location, *Journal of Geophysical Research: Space Physics*, *114*(A6), doi:10.1029/2008JA013549.

Burtis, W. J., and R. A. Helliwell (1969), Banded chorus - A new type of VLF radiation observed in the magnetosphere by OGO 1 and OGO 3, *Journal of Geophysical Research*, *74*(11), 3002–3010, doi:10.1029/JA074i011p03002.

Burton, R. K., and R. E. Holzer (1974), The origin and propagation of chorus in the outer magnetosphere, *Journal of Geophysical Research*, *79*(7), 1014–1023, doi:10.1029/JA079i007p01014.

Carpenter, D. L., and R. R. Anderson (1992), An ISEE/whistler model of equatorial electron density in the magnetosphere, *Journal of Geophysical Research: Space Physics*, *97*(A2), 1097–1108, doi:10.1029/91JA01548.

Chen, A., and R. Wolf (1972), Effects on the plasmasphere of a time-varying convection electric field, *Planetary and Space Science*, *20*(4), 483 – 509, doi:10.1016/0032-0633(72)90080-3.

Chen, F. F. (1984), *Introduction to Plasma Physics and Controlled Fusion*, Introduction to Plasma Physics and Controlled Fusion, 421 pp., Springer US, doi:10.1007/978-1-4757-5595-4.

Chen, L., J. Bortnik, W. Li, R. M. Thorne, and R. B. Horne (2012a), Modeling the properties of plasmaspheric hiss: 1. Dependence on chorus wave emission, *Journal of Geophysical Research: Space Physics*, *117*(A5), doi:10.1029/2011JA017201.

Chen, L., W. Li, J. Bortnik, and R. M. Thorne (2012b), Amplification of whistler-mode hiss inside the plasmasphere, *Geophysical Research Letters*, *39*(8), doi:10.1029/2012GL051488.

Church, S. R., and R. M. Thorne (1983), On the origin of plasmaspheric hiss: Ray path integrated amplification, *Journal of Geophysical Research: Space Physics*, *88*(A10), 7941–7957, doi:10.1029/JA088iA10p07941.

Clilverd, M. A., C. J. Rodger, R. M. Millan, J. G. Sample, M. Kokorowski, M. P. McCarthy, T. Ulich, T. Raita, A. J. Kavanagh, and E. Spanswick (2007), Energetic particle precipitation into the middle atmosphere triggered by a coronal mass ejection, *Journal of Geophysical Research: Space Physics*, *112*(A12), doi: 10.1029/2007JA012395.

Cornwall, J. M., F. V. Coroniti, and R. M. Thorne (1970), Turbulent loss of ring current protons, *Journal of Geophysical Research*, *75*(25), 4699–4709, doi:10.1029/JA075i025p04699.

Daglis, I. A., R. M. Thorne, W. Baumjohann, and S. Orsini (1999), The terrestrial ring current: Origin, formation, and decay, *Reviews of Geophysics*, *37*(4), 407–438, doi:10.1029/1999RG900009.

Darrouzet, F., D. L. Gallagher, N. André, D. L. Carpenter, I. Dandouras, P. M. E. Décréau, J. Keyser, R. E. Denton, J. C. Foster, J. Goldstein, M. B. Moldwin, B. W. Reinisch, B. R. Sandel, and J. Tu (2009), *The Earth's Plasmasphere: A CLUSTER and IMAGE Perspective*, chap. Plasmaspheric Density Structures and Dynamics: Properties Observed by the CLUSTER and IMAGE Missions, pp. 55–106, Springer New York, doi:10.1007/978-1-4419-1323-4_4.

Davis, T. N., and M. Sugiura (1966), Auroral electrojet activity index AE and its universal time variations, *Journal of Geophysical Research*, *71*(3), 785–801, doi:10.1029/JZ071i003p00785.

Dungey, J. W. (1965), The length of the magnetospheric tail, *Journal of Geophysical Research*, *70*(7), 1753–1753, doi:10.1029/JZ070i007p01753.

Elkington, S. R. (2013), *A Review of ULF Interactions with Radiation Belt Electrons*, pp. 177–193, American Geophysical Union, doi:10.1029/169GM12.

ESA/DTU Space (2014), June 2014 magnetic field, Online; released: 19/06/2014 10:18 am, http://www.esa.int/spaceinimages/Images/2014/06/June_2014_magnetic_field.

Fennell, J. F., S. G. Claudepierre, T. P. O'Brien, J. B. Blake, J. H. Clemmons, H. E.

Spence, G. D. Reeves, and J. L. Roeder (2014), Inner Radiation Zone and Slot Region Electron Fluxes: Van Allen Probes ECT/MagEIS Data, in *Geospace revisited: a Cluster/MAARBLE/Van Allen Probes Conference, Rhodes (Greece), September 15-20, 2014*.

Fälthammar, C.-G. (1965), Effects of time-dependent electric fields on geomagnetically trapped radiation, *Journal of Geophysical Research*, *70*(11), 2503–2516, doi:10.1029/JZ070i011p02503.

Fok, M.-C., R. B. Horne, N. P. Meredith, and S. A. Glauert (2008), Radiation Belt Environment model: Application to space weather nowcasting, *Journal of Geophysical Research: Space Physics*, *113*(A3), doi:10.1029/2007JA012558.

Fraser, B., and T. Nguyen (2001), Is the plasmapause a preferred source region of electromagnetic ion cyclotron waves in the magnetosphere?, *Journal of Atmospheric and Solar-Terrestrial Physics*, *63*(11), 1225 – 1247, doi:10.1016/S1364-6826(00)00225-X.

Friedel, R., G. Reeves, and T. Obara (2002), Relativistic electron dynamics in the inner magnetosphere — a review, *Journal of Atmospheric and Solar-Terrestrial Physics*, *64*(2), 265 – 282, doi:10.1016/S1364-6826(01)00088-8.

Friedel, R. H. W., S. Bourdarie, and T. E. Cayton (2005), Intercalibration of magnetospheric energetic electron data, *Space Weather*, *3*(9), doi:10.1029/2005SW000153.

Gallagher, D. L., and R. H. Comfort (2016), Unsolved problems in plasmasphere refilling, *Journal of Geophysical Research: Space Physics*, *121*(2), 1447–1451, doi:10.1002/2015JA022279, 2015JA022279.

Gendrin, R. (1981), General relationships between wave amplification and particle diffusion in a magnetoplasma, *Reviews of Geophysics*, *19*(1), 171–184, doi:10.1029/RG019i001p00171.

Glauert, S. A., and R. B. Horne (2005), Calculation of pitch angle and energy diffusion coefficients with the PADIE code, *Journal of Geophysical Research: Space Physics*, *110*(A4), doi:10.1029/2004JA010851.

Glauert, S. A., R. B. Horne, and N. P. Meredith (2014), Three-dimensional electron radiation belt simulations using the BAS Radiation Belt Model with new diffusion models for chorus, plasmaspheric hiss, and lightning-generated whistlers, *Journal of Geophysical Research: Space Physics*, *119*(1), 268–289, doi:10.1002/2013JA019281.

Goldstein, B. E., and B. T. Tsurutani (1984), Wave normal directions of chorus near the equatorial source region, *Journal of Geophysical Research: Space Physics*, *89*(A5), 2789–2810, doi:10.1029/JA089iA05p02789.

Gonzalez, W. D., B. T. Tsurutani, A. L. C. Gonzalez, E. J. Smith, F. Tang, and S.-I. Akasofu (1989), Solar wind-magnetosphere coupling during intense magnetic storms (1978-1979), *Journal of Geophysical Research: Space Physics*, *94*(A7), 8835–8851, doi:10.1029/JA094iA07p08835.

Grebowsky, J. M. (1970), Model study of plasmapause motion, *Journal of Geophysical Research*, *75*(22), 4329–4333, doi:10.1029/JA075i022p04329.

Green, J. C., and M. G. Kivelson (2004), Relativistic electrons in the outer radiation belt: Differentiating between acceleration mechanisms, *Journal of Geophysical Research: Space Physics*, *109*(A3), doi:10.1029/2003JA010153.

Green, J. C., T. G. Onsager, T. P. O'Brien, and D. N. Baker (2004), Testing loss mechanisms capable of rapidly depleting relativistic electron flux in the Earth's outer radiation belt, *Journal of Geophysical Research: Space Physics*, *109*(A12), doi:10.1029/2004JA010579.

Gusev, A., G. Pugacheva, U. Jayanthi, and N. Schuch (2003), Modeling of low-altitude quasi-trapped proton fluxes at the equatorial inner magnetosphere, *Brazilian Journal of Physics*, *33*, 767 – 774.

Hamlin, D. A., R. Karplus, R. C. Vik, and K. M. Watson (1961), Mirror and azimuthal drift frequencies for geomagnetically trapped particles, *Journal of Geophysical Research*, *66*(1), 1–4, doi:10.1029/JZ066i001p00001.

Hargreaves, J. K. (1979), *The upper atmosphere and solar-terrestrial relations - An*

*introduction to the aerospace environment*, Van Nostrand Reinhold Co, New York London.

Hayakawa, M., Y. Yamanaka, M. Parrot, and F. Lefeuvre (1984), The wave normals of magnetospheric chorus emissions observed on board GEOS 2, *Journal of Geophysical Research: Space Physics*, *89*(A5), 2811–2821, doi:10.1029/JA089iA05p02811.

Hayakawa, M., N. Ohmi, M. Parrot, and F. Lefeuvre (1986), Direction finding of ELF hiss emissions in a detached plasma region of the magnetosphere, *Journal of Geophysical Research: Space Physics*, *91*(A1), 135–141, doi:10.1029/JA091iA01p00135.

Horne, R. B. (2002), The contribution of wave-particle interactions to electron loss and acceleration in the Earth's radiation belts during geomagnetic storms, in *Review of radio science 1999-2002*, edited by W. Stone, pp. 801–828, IEEE Press.

Horne, R. B., and R. M. Thorne (1993), On the preferred source location for the convective amplification of ion cyclotron waves, *Journal of Geophysical Research: Space Physics*, *98*(A6), 9233–9247, doi:10.1029/92JA02972.

Horne, R. B., and R. M. Thorne (1994), Convective instabilities of electromagnetic ion cyclotron waves in the outer magnetosphere, *Journal of Geophysical Research: Space Physics*, *99*(A9), 17,259–17,273, doi:10.1029/94JA01259.

Horne, R. B., and R. M. Thorne (1998), Potential waves for relativistic electron scattering and stochastic acceleration during magnetic storms, *Geophysical Research Letters*, *25*(15), 3011–3014, doi:10.1029/98GL01002.

Horne, R. B., and R. M. Thorne (2003), Relativistic electron acceleration and precipitation during resonant interactions with whistler-mode chorus, *Geophysical Research Letters*, *30*(10), doi:10.1029/2003GL016973.

Horne, R. B., N. P. Meredith, R. M. Thorne, D. Heynderickx, R. H. A. Iles, and R. R. Anderson (2003a), Evolution of energetic electron pitch angle distributions during storm time electron acceleration to megaelectronvolt energies, *Jour-*

*nal of Geophysical Research: Space Physics*, *108*(A1), SMP 11–1–SMP 11–13, doi: 10.1029/2001JA009165.

Horne, R. B., S. A. Glauert, and R. M. Thorne (2003b), Resonant diffusion of radiation belt electrons by whistler-mode chorus, *Geophysical Research Letters*, *30*(9), doi: 10.1029/2003GL016963.

Horne, R. B., R. M. Thorne, S. A. Glauert, J. M. Albert, N. P. Meredith, and R. R. Anderson (2005a), Timescale for radiation belt electron acceleration by whistler mode chorus waves, *Journal of Geophysical Research: Space Physics*, *110*(A3), doi:10.1029/ 2004JA010811.

Horne, R. B., R. M. Thorne, Y. Y. Shprits, N. P. Meredith, S. A. Glauert, A. J. Smith, S. G. Kanekal, D. N. Baker, M. J. Engebretson, J. L. Posch, M. Spasojevic, U. S. Inan, J. S. Pickett, and P. M. E. Decreau (2005b), Wave acceleration of electrons in the Van Allen radiation belts, *Nature*, *437*(7056), 227–230, doi:10.1038/nature03939.

Horne, R. B., N. P. Meredith, S. A. Glauert, A. Varotsou, D. Boscher, R. M. Thorne, Y. Y. Shprits, and R. R. Anderson (2006), Mechanisms for the acceleration of radiation belt electrons, in *Geophys. Monogr. Ser.*, vol. 167, pp. 151–173, AGU, doi: 10.1029/167GM14.

Horne, R. B., R. M. Thorne, S. A. Glauert, N. P. Meredith, D. Pokhotelov, and O. Santolík (2007), Electron acceleration in the Van Allen radiation belts by fast magnetosonic waves, *Geophysical Research Letters*, *34*(17), doi:10.1029/2007GL030267.

Horne, R. B., M. M. Lam, and J. C. Green (2009), Energetic electron precipitation from the outer radiation belt during geomagnetic storms, *Geophysical Research Letters*, *36*(19), doi:10.1029/2009GL040236.

Horne, R. B., S. A. Glauert, N. P. Meredith, D. Boscher, V. Maget, D. Heynderickx, and D. Pitchford (2013a), Space weather impacts on satellites and forecasting the Earth's electron radiation belts with SPACECAST, *Space Weather*, *11*(4), 169–186, doi:10.1002/swe.20023.

Horne, R. B., T. Kersten, S. A. Glauert, N. P. Meredith, D. Boscher, A. Sicard-Piet, R. M. Thorne, and W. Li (2013b), A new diffusion matrix for whistler mode chorus waves, *Journal of Geophysical Research: Space Physics*, *118*(10), 6302–6318, doi: 10.1002/jgra.50594.

Hudson, M. K., S. R. Elkington, J. G. Lyon, C. C. Goodrich, and T. J. Rosenberg (2013), *Simulation of Radiation Belt Dynamics Driven by Solar Wind Variations*, pp. 171–182, American Geophysical Union, doi:10.1029/GM109p0171.

Ichimaru, S. (1973), *Basic Principles of Plasma Physics: A Statistical Approach*, A lecture note and reprint series, W. A. Benjamin.

Imhof, W. L., H. D. Voss, J. Mobilia, D. W. Datlowe, E. E. Gaines, J. P. McGlennon, and U. S. Inan (1992), Relativistic electron microbursts, *Journal of Geophysical Research: Space Physics*, *97*(A9), 13,829–13,837, doi:10.1029/92JA01138.

Iucci, N., A. E. Levitin, A. V. Belov, E. A. Eroshenko, N. G. Ptitsyna, G. Villoresi, G. V. Chizhenkov, L. I. Dorman, L. I. Gromova, M. Parisi, M. I. Tyasto, and V. G. Yanke (2005), Space weather conditions and spacecraft anomalies in different orbits, *Space Weather*, *3*(1), doi:10.1029/2003SW000056.

Johnson, M. H., and J. Kierein (1992), Combined release and radiation effects satellite (CRRES) - Spacecraft and mission, *Journal of Spacecraft and Rockets*, *29*, 556–563, doi:10.2514/3.55641.

Jordanova, V. K., J. Albert, and Y. Miyoshi (2008), Relativistic electron precipitation by EMIC waves from self-consistent global simulations, *Journal of Geophysical Research: Space Physics*, *113*(A3), doi:10.1029/2008JA013239.

Katoh, Y., and Y. Omura (2007), Computer simulation of chorus wave generation in the Earth's inner magnetosphere, *Geophysical Research Letters*, *34*(3), doi:10.1029/2006GL028594.

Keika, K., K. Takahashi, A. Y. Ukhorskiy, and Y. Miyoshi (2013), Global characteristics of electromagnetic ion cyclotron waves: Occurrence rate and its storm dependence,

*Journal of Geophysical Research: Space Physics*, *118*(7), 4135–4150, doi:10.1002/jgra.50385.

Kennel, C. F., and H. E. Petschek (1966), Limit on stably trapped particle fluxes, *Journal of Geophysical Research*, *71*(1), 1–28, doi:10.1029/JZ071i001p00001.

Kersten, T., R. B. Horne, S. A. Glauert, N. P. Meredith, B. J. Fraser, and R. S. Grew (2014), Electron losses from the radiation belts caused by EMIC waves, *Journal of Geophysical Research: Space Physics*, *119*(11), 8820–8837, doi:10.1002/2014JA020366.

Kim, K.-C., Y. Shprits, D. Subbotin, and B. Ni (2011), Understanding the dynamic evolution of the relativistic electron slot region including radial and pitch angle diffusion, *Journal of Geophysical Research: Space Physics*, *116*(A10), doi:10.1029/2011JA016684.

Kivelson, M., and C. Russell (1995), *Introduction to Space Physics*, Cambridge atmospheric and space science series, Cambridge University Press.

Kozyra, J. U., T. E. Cravens, A. F. Nagy, E. G. Fontheim, and R. S. B. Ong (1984), Effects of energetic heavy ions on electromagnetic ion cyclotron wave generation in the plasmapause region, *Journal of Geophysical Research: Space Physics*, *89*(A4), 2217–2233, doi:10.1029/JA089iA04p02217.

Lauben, D. S., U. S. Inan, T. F. Bell, and D. A. Gurnett (2002), Source characteristics of ELF/VLF chorus, *Journal of Geophysical Research: Space Physics*, *107*(A12), SMP 10–1–SMP 10–17, doi:10.1029/2000JA003019.

Lemaire, J., and K. I. Gringauz (1998), *The Earth's plasmasphere*, 312-346 pp., Cambridge University Press.

Lenchek, A. M., S. F. Singer, and R. C. Wentworth (1961), Geomagnetically trapped electrons from cosmic ray albedo neutrons, *Journal of Geophysical Research*, *66*(12), 4027–4046, doi:10.1029/JZ066i012p04027.

Li, W., Y. Y. Shprits, and R. M. Thorne (2007), Dynamic evolution of energetic outer zone electrons due to wave-particle interactions during storms, *Journal of Geophysical Research: Space Physics*, *112*(A10), doi:10.1029/2007JA012368.

Li, W., R. M. Thorne, J. Bortnik, Y. Nishimura, V. Angelopoulos, L. Chen, J. P. McFadden, and J. W. Bonnell (2010), Global distributions of suprathermal electrons observed on THEMIS and potential mechanisms for access into the plasmasphere, *Journal of Geophysical Research: Space Physics*, *115*(A12), doi:10.1029/2010JA015687.

Li, W., J. Bortnik, R. M. Thorne, and V. Angelopoulos (2011), Global distribution of wave amplitudes and wave normal angles of chorus waves using THEMIS wave observations, *Journal of Geophysical Research: Space Physics*, *116*(A12), doi:10.1029/2011JA017035.

Li, W., R. M. Thorne, Q. Ma, B. Ni, J. Bortnik, D. N. Baker, H. E. Spence, G. D. Reeves, S. G. Kanekal, J. C. Green, C. A. Kletzing, W. S. Kurth, G. B. Hospodarsky, J. B. Blake, J. F. Fennell, and S. G. Claudepierre (2014), Radiation Belt Electron Acceleration by Chorus Waves During the 17 March 2013 Storm, *Journal of Geophysical Research: Space Physics*, doi:10.1002/2014JA019945.

Li, W., Q. Ma, R. M. Thorne, J. Bortnik, C. A. Kletzing, W. S. Kurth, G. B. Hospodarsky, and Y. Nishimura (2015), Statistical properties of plasmaspheric hiss derived from Van Allen Probes data and their effects on radiation belt electron dynamics, *Journal of Geophysical Research: Space Physics*, *120*(5), 3393–3405, doi:10.1002/2015JA021048.

Li, X., D. N. Baker, M. Temerin, T. E. Cayton, E. G. D. Reeves, R. A. Christensen, J. B. Blake, M. D. Looper, R. Nakamura, and S. G. Kanekal (1997), Multisatellite observations of the outer zone electron variation during the November 3–4, 1993, magnetic storm, *Journal of Geophysical Research: Space Physics*, *102*(A7), 14,123–14,140, doi:10.1029/97JA01101.

Li, X., M. Temerin, D. N. Baker, G. D. Reeves, and D. Larson (2001), Quantitative pre-

diction of radiation belt electrons at geostationary orbit based on solar wind measurements, *Geophysical Research Letters*, *28*(9), 1887–1890, doi:10.1029/2000GL012681.

Liu, W., W. Tu, X. Li, T. Sarris, Y. Khotyaintsev, H. Fu, H. Zhang, and Q. Shi (2016), On the calculation of electric diffusion coefficient of radiation belt electrons with in situ electric field measurements by THEMIS, *Geophysical Research Letters*, *43*(3), 1023–1030, doi:10.1002/2015GL067398.

Lyons, L., and D. Williams (1984), *Quantitative Aspects of Magnetospheric Physics*, Geophysics and Astrophysics Monographs : an international series of fundamental textbooks, Springer, doi:10.1007/978-94-017-2819-5.

Lyons, L. R. (1974), Pitch angle and energy diffusion coefficients from resonant interactions with ion–cyclotron and whistler waves, *Journal of Plasma Physics*, *12*, 417–432, doi:10.1017/S002237780002537X.

Lyons, L. R., and R. M. Thorne (1973), Equilibrium structure of radiation belt electrons, *Journal of Geophysical Research*, *78*(13), 2142–2149, doi:10.1029/JA078i013p02142.

Lyons, L. R., R. M. Thorne, and C. F. Kennel (1971), Electron pitch-angle diffusion driven by oblique whistler-mode turbulence, *Journal of Plasma Physics*, *6*, 589–606, doi:10.1017/S0022377800006310.

Lyons, L. R., R. M. Thorne, and C. F. Kennel (1972), Pitch-angle diffusion of radiation belt electrons within the plasmasphere, *Journal of Geophysical Research*, *77*(19), 3455–3474, doi:10.1029/JA077i019p03455.

Ma, Q., W. Li, R. M. Thorne, and V. Angelopoulos (2013), Global distribution of equatorial magnetosonic waves observed by THEMIS, *Geophysical Research Letters*, *40*(10), 1895–1901, doi:10.1002/grl.50434.

Markwardt, C. B. (2009), Non-linear Least-squares Fitting in IDL with MPFIT, in *Astronomical Data Analysis Software and Systems XVIII*, *Astronomical Society of*

*the Pacific Conference Series*, vol. 411, edited by D. A. Bohlender, D. Durand, and P. Dowler, p. 251.

Mauk, B. H., N. J. Fox, S. G. Kanekal, R. L. Kessel, D. G. Sibeck, and A. Ukhorskiy (2012), Science Objectives and Rationale for the Radiation Belt Storm Probes Mission, *Space Science Reviews*, *179*(1), 3–27, doi:10.1007/s11214-012-9908-y.

McCollough, J. P., J. L. Gannon, D. N. Baker, and M. Gehmeyr (2008), A statistical comparison of commonly used external magnetic field models, *Space Weather*, *6*(10), doi:10.1029/2008SW000391.

McIlwain, C. E. (1961), Coordinates for mapping the distribution of magnetically trapped particles, *Journal of Geophysical Research*, *66*(11), 3681–3691, doi:10.1029/JZ066i011p03681.

Meredith, N. P., R. B. Horne, A. D. Johnstone, and R. R. Anderson (2000), The temporal evolution of electron distributions and associated wave activity following substorm injections in the inner magnetosphere, *Journal of Geophysical Research: Space Physics*, *105*(A6), 12,907–12,917, doi:10.1029/2000JA900010.

Meredith, N. P., R. B. Horne, and R. R. Anderson (2001), Substorm dependence of chorus amplitudes: Implications for the acceleration of electrons to relativistic energies, *Journal of Geophysical Research: Space Physics*, *106*(A7), 13,165–13,178, doi:10.1029/2000JA900156.

Meredith, N. P., R. B. Horne, D. Summers, R. M. Thorne, R. H. A. Iles, D. Heynderickx, and R. R. Anderson (2002), Evidence for acceleration of outer zone electrons to relativistic energies by whistler mode chorus, *Annales Geophysicae*, *20*(7), 967–979, doi:10.5194/angeo-20-967-2002.

Meredith, N. P., R. M. Thorne, R. B. Horne, D. Summers, B. J. Fraser, and R. R. Anderson (2003a), Statistical analysis of relativistic electron energies for cyclotron resonance with EMIC waves observed on CRRES, *Journal of Geophysical Research: Space Physics*, *108*(A6), doi:10.1029/2002JA009700.

Meredith, N. P., M. Cain, R. B. Horne, R. M. Thorne, D. Summers, and R. R. Anderson (2003b), Evidence for chorus-driven electron acceleration to relativistic energies from a survey of geomagnetically disturbed periods, *Journal of Geophysical Research: Space Physics*, *108*(A6), doi:10.1029/2002JA009764.

Meredith, N. P., R. B. Horne, R. M. Thorne, D. Summers, and R. R. Anderson (2004), Substorm dependence of plasmaspheric hiss, *Journal of Geophysical Research: Space Physics*, *109*(A6), doi:10.1029/2004JA010387.

Meredith, N. P., R. B. Horne, M. A. Clilverd, D. Horsfall, R. M. Thorne, and R. R. Anderson (2006a), Origins of plasmaspheric hiss, *Journal of Geophysical Research: Space Physics*, *111*(A9), doi:10.1029/2006JA011707.

Meredith, N. P., R. B. Horne, S. A. Glauert, R. M. Thorne, D. Summers, J. M. Albert, and R. R. Anderson (2006b), Energetic outer zone electron loss timescales during low geomagnetic activity, *Journal of Geophysical Research: Space Physics*, *111*(A5), doi:10.1029/2005JA011516.

Meredith, N. P., R. B. Horne, S. A. Glauert, and R. R. Anderson (2007), Slot region electron loss timescales due to plasmaspheric hiss and lightning-generated whistlers, *Journal of Geophysical Research: Space Physics*, *112*(A8), doi:10.1029/2007JA012413.

Meredith, N. P., R. B. Horne, and R. R. Anderson (2008), Survey of magnetosonic waves and proton ring distributions in the Earth's inner magnetosphere, *Journal of Geophysical Research: Space Physics*, *113*(A6), doi:10.1029/2007JA012975.

Meredith, N. P., R. B. Horne, S. A. Glauert, D. N. Baker, S. G. Kanekal, and J. M. Albert (2009), Relativistic electron loss timescales in the slot region, *Journal of Geophysical Research: Space Physics*, *114*(A3), doi:10.1029/2008JA013889.

Meredith, N. P., R. B. Horne, M. M. Lam, M. H. Denton, J. E. Borovsky, and J. C. Green (2011), Energetic electron precipitation during high-speed solar wind stream driven storms, *Journal of Geophysical Research: Space Physics*, *116*(A5), doi:10.1029/2010JA016293.

Meredith, N. P., R. B. Horne, A. Sicard-Piet, D. Boscher, K. H. Yearby, W. Li, and R. M. Thorne (2012), Global model of lower band and upper band chorus from multiple satellite observations, *Journal of Geophysical Research: Space Physics*, *117*(A10), doi:10.1029/2012JA017978.

Meredith, N. P., R. B. Horne, J. Bortnik, R. M. Thorne, L. Chen, W. Li, and A. Sicard-Piet (2013), Global statistical evidence for chorus as the embryonic source of plasmaspheric hiss, *Geophysical Research Letters*, *40*(12), 2891–2896, doi:10.1002/grl.50593.

Meredith, N. P., R. B. Horne, T. Kersten, B. J. Fraser, and R. S. Grew (2014), Global morphology and spectral properties of EMIC waves derived from CRRES observations, *Journal of Geophysical Research: Space Physics*, doi:10.1002/2014JA020064.

Meredith, N. P., R. B. Horne, J. D. Isles, and J. C. Green (2016), Extreme Energetic Electron Fluxes in Low Earth Orbit: Analysis of POES E > 30, E > 100 and E > 300 keV Electrons, *Space Weather*, doi:10.1002/2015SW001348.

Millan, R. M., R. P. Lin, D. M. Smith, and M. P. McCarthy (2007), Observation of relativistic electron precipitation during a rapid decrease of trapped relativistic electron flux, *Geophysical Research Letters*, *34*(10), doi:10.1029/2006GL028653.

Miyoshi, Y. S., V. K. Jordanova, A. Morioka, M. F. Thomsen, G. D. Reeves, D. S. Evans, and J. C. Green (2006), Observations and modeling of energetic electron dynamics during the October 2001 storm, *Journal of Geophysical Research: Space Physics*, *111*(A11), doi:10.1029/2005JA011351.

Ni, B., R. M. Thorne, Y. Y. Shprits, K. G. Orlova, and N. P. Meredith (2011), Chorus-driven resonant scattering of diffuse auroral electrons in nondipolar magnetic fields, *Journal of Geophysical Research: Space Physics*, *116*(A6), doi:10.1029/2011JA016453.

Nishimura, Y., J. Bortnik, W. Li, R. M. Thorne, L. R. Lyons, V. Angelopoulos, S. B. Mende, J. W. Bonnell, O. Le Contel, C. Cully, R. Ergun, and U. Auster (2010), Identifying the Driver of Pulsating Aurora, *Science*, *330*(6000), 81–84, doi:10.1126/science.1193186.

Nunn, D. (1974), A Self-Consistent Theory of Triggered VLF Emissions, in *Magnetospheric Physics*, *Astrophysics and Space Science Library*, vol. 44, edited by B. McCormac, pp. 313–321, Springer Netherlands, doi:{10.1007/978-94-010-2214-9_26}.

Nunn, D., Y. Omura, H. Matsumoto, I. Nagano, and S. Yagitani (1997), The numerical simulation of VLF chorus and discrete emissions observed on the Geotail satellite using a Vlasov code, *Journal of Geophysical Research: Space Physics*, *102*(A12), 27,083–27,097, doi:10.1029/97JA02518.

O'Brien, T. P., and M. B. Moldwin (2003), Empirical plasmapause models from magnetic indices, *Geophysical Research Letters*, *30*(4), doi:10.1029/2002GL016007.

Olson, W. P., K. A. Pfitzer, and M. D. A. C.-W. H. B. CALIF. (1977), *Magnetospheric Magnetic Field Modeling*, Defense Technical Information Center.

Omura, Y., D. Nunn, H. Matsumoto, and M. Rycroft (1991), A review of observational, theoretical and numerical studies of VLF triggered emissions, *Journal of Atmospheric and Terrestrial Physics*, *53*(5), 351 – 368, doi:10.1016/0021-9169(91)90031-2.

Omura, Y., N. Furuya, and D. Summers (2007), Relativistic turning acceleration of resonant electrons by coherent whistler mode waves in a dipole magnetic field, *Journal of Geophysical Research: Space Physics*, *112*(A6), doi:10.1029/2006JA012243.

Omura, Y., M. Hikishima, Y. Katoh, D. Summers, and S. Yagitani (2009), Nonlinear mechanisms of lower-band and upper-band VLF chorus emissions in the magnetosphere, *Journal of Geophysical Research: Space Physics*, *114*(A7), doi:10.1029/2009JA014206.

Park, C. G. (1974), Some features of plasma distribution in the plasmasphere deduced from Antarctic whistlers, *Journal of Geophysical Research*, *79*(1), 169–173, doi:10.1029/JA079i001p00169.

Parker, E. N. (1965), Dynamical theory of the solar wind, *Space Science Reviews*, *Volume 4, Issue 5-6*, 666–708, doi:10.1007/BF00216273.

Parrot, M., and F. Lefeuvre (1986), Statistical study of the propagation characteristics of ELF hiss observed on GEOS-1, inside and outside the plasmasphere, *Annales Geophysicae*, *4*, 363–383.

Paulikas, G. A., and J. B. Blake (1979), Effects of the solar wind on magnetospheric dynamics: Energetic electrons at the synchronous orbit, in *Geophys. Monogr. Ser.*, vol. 21, pp. 180–202, AGU, doi:10.1029/GM021p0180.

Posch, J. L., M. J. Engebretson, M. T. Murphy, M. H. Denton, M. R. Lessard, and R. B. Horne (2010), Probing the relationship between electromagnetic ion cyclotron waves and plasmaspheric plumes near geosynchronous orbit, *Journal of Geophysical Research: Space Physics*, *115*(A11), doi:10.1029/2010JA015446.

Reeves, G. D., H. E. Spence, M. G. Henderson, S. K. Morley, R. H. W. Friedel, H. O. Funsten, D. N. Baker, S. G. Kanekal, J. B. Blake, J. F. Fennell, S. G. Claudepierre, R. M. Thorne, D. L. Turner, C. A. Kletzing, W. S. Kurth, B. A. Larsen, and J. T. Niehof (2013), Electron Acceleration in the Heart of the Van Allen Radiation Belts, *Science*, *341*(6149), 991–994, doi:10.1126/science.1237743.

Robert DeMajistre (2014), ENA measurements of the ring current, Online, http://solar.gmu.edu/teaching/CSI769_2005/lect07-09/demajistre_sw_sats.ppt.

Rodger, C. J., T. Raita, M. A. Clilverd, A. Seppälä, S. Dietrich, N. R. Thomson, and T. Ulich (2008), Observations of relativistic electron precipitation from the radiation belts driven by EMIC waves, *Geophysical Research Letters*, *35*(16), doi:10.1029/2008GL034804.

Roederer, J. G., and H. Zhang (2014), *Dynamics of Magnetically Trapped Particles: Foundations of the Physics of Radiation Belts and Space Plasmas*, vol. 403, Springer-Verlag Berlin Heidelberg, doi:10.1007/978-3-642-41530-2.

Rosenberg, T. J., R. A. Helliwell, and J. P. Katsufrakis (1971), Electron precipitation associated with discrete very-low-frequency emissions, *Journal of Geophysical Research*, *76*(34), 8445–8452, doi:10.1029/JA076i034p08445.

Roux, A., S. Perraut, J. L. Rauch, C. de Villedary, G. Kremser, A. Korth, and D. T. Young (1982), Wave-particle interactions near ΩHe+ observed on board GEOS 1 and 2: 2. Generation of ion cyclotron waves and heating of He+ ions, *Journal of Geophysical Research: Space Physics*, *87*(A10), 8174–8190, doi:10.1029/JA087iA10p08174.

Santolík, O., M. Parrot, L. R. O. Storey, J. S. Pickett, and D. A. Gurnett (2001), Propagation analysis of plasmaspheric hiss using Polar PWI measurements, *Geophysical Research Letters*, *28*(6), 1127–1130, doi:10.1029/2000GL012239.

Santolík, O., D. A. Gurnett, J. S. Pickett, M. Parrot, and N. Cornilleau-Wehrlin (2003), Spatio-temporal structure of storm-time chorus, *Journal of Geophysical Research: Space Physics*, *108*(A7), doi:10.1029/2002JA009791.

Santolík, O., C. A. Kletzing, W. S. Kurth, G. B. Hospodarsky, and S. R. Bounds (2014a), Fine structure of large-amplitude chorus wave packets, *Geophysical Research Letters*, *41*(2), 293–299, doi:10.1002/2013GL058889.

Santolík, O., E. Macúšová, I. Kolmašová, N. Cornilleau-Wehrlin, and Y. de Conchy (2014b), Propagation of lower-band whistler-mode waves in the outer Van Allen belt: Systematic analysis of 11 years of multi-component data from the Cluster spacecraft, *Geophysical Research Letters*, *41*(8), 2729–2737, doi:10.1002/2014GL059815.

Schulz, M., and L. J. Lanzerotti (1974), *Particle diffusion in the radiation belts*, Berlin ; New York : Springer-Verlag.

Shi, R., D. Summers, B. Ni, J. F. Fennell, J. B. Blake, H. E. Spence, and G. D. Reeves (2016), Survey of radiation belt energetic electron pitch angle distributions based on the Van Allen Probes MagEIS measurements, *Journal of Geophysical Research: Space Physics*, *121*(2), 1078–1090, doi:10.1002/2015JA021724.

Shprits, Y. Y., R. M. Thorne, R. Friedel, G. D. Reeves, J. Fennell, D. N. Baker, and S. G. Kanekal (2006), Outward radial diffusion driven by losses at magnetopause, *Journal of Geophysical Research: Space Physics*, *111*(A11), doi:10.1029/2006JA011657.

Shprits, Y. Y., N. P. Meredith, and R. M. Thorne (2007), Parameterization of radiation belt electron loss timescales due to interactions with chorus waves, *Geophysical Research Letters*, *34*(11), doi:10.1029/2006GL029050.

Shprits, Y. Y., L. Chen, and R. M. Thorne (2009a), Simulations of pitch angle scattering of relativistic electrons with MLT-dependent diffusion coefficients, *Journal of Geophysical Research: Space Physics*, *114*(A3), doi:10.1029/2008JA013695.

Shprits, Y. Y., D. Subbotin, and B. Ni (2009b), Evolution of electron fluxes in the outer radiation belt computed with the VERB code, *Journal of Geophysical Research: Space Physics*, *114*(A11), doi:10.1029/2008JA013784.

Shprits, Y. Y., D. Subbotin, A. Drozdov, M. E. Usanova, A. Kellerman, K. Orlova, D. N. Baker, D. L. Turner, and K.-C. Kim (2013), Unusual stable trapping of the ultrarelativistic electrons in the Van Allen radiation belts, *Nature Physics*, *9*(11), 699–703, doi:10.1038/nphys2760.

Silin, I., I. R. Mann, R. D. Sydora, D. Summers, and R. L. Mace (2011), Warm plasma effects on electromagnetic ion cyclotron wave MeV electron interactions in the magnetosphere, *Journal of Geophysical Research: Space Physics*, *116*(A5), doi:10.1029/2010JA016398.

Sonwalkar, V. S., and U. S. Inan (1989), Lightning as an embryonic source of VLF hiss, *Journal of Geophysical Research: Space Physics*, *94*(A6), 6986–6994, doi:10.1029/JA094iA06p06986.

Strang, G. (1968), On the Construction and Comparison of Difference Schemes, *SIAM Journal on Numerical Analysis*, *5*(3), 506–517, doi:10.1137/0705041.

Su, Z., F. Xiao, H. Zheng, and S. Wang (2010), STEERB: A three-dimensional code for storm-time evolution of electron radiation belt, *Journal of Geophysical Research: Space Physics*, *115*(A9), doi:10.1029/2009JA015210.

Subbotin, D., Y. Shprits, and B. Ni (2010), Three-dimensional VERB radiation

belt simulations including mixed diffusion, *Journal of Geophysical Research: Space Physics*, *115*(A3), doi:10.1029/2009JA015070.

Subbotin, D. A., and Y. Y. Shprits (2009), Three-dimensional modeling of the radiation belts using the Versatile Electron Radiation Belt (VERB) code, *Space Weather*, *7*(10), doi:10.1029/2008SW000452.

Sugiura, M., and S. Hendricks (1967), Provisional hourly values of equatorial Dst for 1961, 1962 and 1963, *Tech. rep.*, NASA Tech. note D-4047.

Summers, D., and R. M. Thorne (2003), Relativistic electron pitch-angle scattering by electromagnetic ion cyclotron waves during geomagnetic storms, *Journal of Geophysical Research: Space Physics*, *108*(A4), 943–946, doi:10.1029/2002JA009489.

Summers, D., R. M. Thorne, and F. Xiao (1998), Relativistic theory of wave-particle resonant diffusion with application to electron acceleration in the magnetosphere, *Journal of Geophysical Research: Space Physics*, *103*(A9), 20,487–20,500, doi:10.1029/98JA01740.

Summers, D., B. Ni, and N. P. Meredith (2007), Timescales for radiation belt electron acceleration and loss due to resonant wave-particle interactions: 1. Theory, *Journal of Geophysical Research: Space Physics*, *112*(A4), doi:10.1029/2006JA011801.

Summers, D., B. Ni, N. P. Meredith, R. B. Horne, R. M. Thorne, M. B. Moldwin, and R. R. Anderson (2008), Electron scattering by whistler-mode ELF hiss in plasmaspheric plumes, *Journal of Geophysical Research: Space Physics*, *113*(A4), doi:10.1029/2007JA012678.

Takahashi, K., and B. J. Anderson (1992), Distribution of ULF energy ($f < 80$ mHz) in the inner magnetosphere: A statistical analysis of AMPTE CCE magnetic field data, *Journal of Geophysical Research: Space Physics*, *97*(A7), 10,751–10,773, doi:10.1029/92JA00328.

Tao, X., A. A. Chan, J. M. Albert, and J. A. Miller (2008), Stochastic modeling of

multidimensional diffusion in the radiation belts, *Journal of Geophysical Research: Space Physics*, *113*(A7), doi:10.1029/2007JA012985.

Tao, X., J. M. Albert, and A. A. Chan (2009), Numerical modeling of multidimensional diffusion in the radiation belts using layer methods, *Journal of Geophysical Research: Space Physics*, *114*(A2), doi:10.1029/2008JA013826.

Tao, X., J. Bortnik, J. M. Albert, and R. M. Thorne (2012), Comparison of bounce-averaged quasi-linear diffusion coefficients for parallel propagating whistler mode waves with test particle simulations, *Journal of Geophysical Research: Space Physics*, *117*(A10), doi:10.1029/2012JA017931.

Thorne, R. M., E. J. Smith, R. K. Burton, and R. E. Holzer (1973), Plasmaspheric hiss, *Journal of Geophysical Research*, *78*(10), 1581–1596, doi:10.1029/JA078i010p01581.

Thorne, R. M., B. Ni, X. Tao, R. B. Horne, and N. P. Meredith (2010), Scattering by chorus waves as the dominant cause of diffuse auroral precipitation, *Nature*, *467*(7318), 943–946, doi:10.1038/nature09467.

Thorne, R. M., W. Li, B. Ni, Q. Ma, J. Bortnik, D. N. Baker, H. E. Spence, G. D. Reeves, M. G. Henderson, C. A. Kletzing, W. S. Kurth, G. B. Hospodarsky, D. Turner, and V. Angelopoulos (2013), Evolution and slow decay of an unusual narrow ring of relativistic electrons near L˜ 3.2 following the September 2012 magnetic storm, *Geophysical Research Letters*, *40*(14), 3507–3511, doi:10.1002/grl.50627.

Trakhtengerts, V. Y. (1999), A generation mechanism for chorus emission, *Annales Geophysicae*, *17*(1), 95–100, doi:10.1007/s00585-999-0095-4.

Tsurutani, B. T., and E. J. Smith (1974), Postmidnight chorus: A substorm phenomenon, *Journal of Geophysical Research*, *79*(1), 118–127, doi:10.1029/JA079i001p00118.

Tsurutani, B. T., G. S. Lakhina, and O. P. Verkhoglyadova (2013), Energetic electron (>10 keV) microburst precipitation, $5 - 15$ s X-ray pulsations, chorus, and wave-

particle interactions: A review, *Journal of Geophysical Research: Space Physics*, *118*(5), 2296–2312, doi:10.1002/jgra.50264.

Tsyganenko, N. (1989), A magnetospheric magnetic field model with a warped tail current sheet, *Planetary and Space Science*, *37*(1), 5 – 20, doi:10.1016/0032-0633(89)90066-4.

Turner, D. L., Y. Shprits, M. Hartinger, and V. Angelopoulos (2012), Explaining sudden losses of outer radiation belt electrons during geomagnetic storms, *Nat Phys*, *8*(3), 208–212, doi:10.1038/nphys2185.

Turner, D. L., V. Angelopoulos, S. K. Morley, M. G. Henderson, G. D. Reeves, W. Li, D. N. Baker, C.-L. Huang, A. Boyd, H. E. Spence, S. G. Claudepierre, J. B. Blake, and J. V. Rodriguez (2014a), On the cause and extent of outer radiation belt losses during the 30 September 2012 dropout event, *Journal of Geophysical Research: Space Physics*, *119*(3), 1530–1540, doi:10.1002/2013JA019446.

Turner, D. L., V. Angelopoulos, W. Li, J. Bortnik, B. Ni, Q. Ma, R. M. Thorne, S. K. Morley, M. G. Henderson, G. D. Reeves, M. Usanova, I. R. Mann, S. G. Claudepierre, J. B. Blake, D. N. Baker, C.-L. Huang, H. Spence, W. Kurth, C. Kletzing, and J. V. Rodriguez (2014b), Competing source and loss mechanisms due to wave-particle interactions in Earth's outer radiation belt during the 30 September to 3 October 2012 geomagnetic storm, *Journal of Geophysical Research: Space Physics*, *119*(3), 1960–1979, doi:10.1002/2014JA019770.

Ukhorskiy, A. Y., Y. Y. Shprits, B. J. Anderson, K. Takahashi, and R. M. Thorne (2010), Rapid scattering of radiation belt electrons by storm-time EMIC waves, *Geophysical Research Letters*, *37*(9), doi:10.1029/2010GL042906.

Usanova, M. E., I. R. Mann, J. Bortnik, L. Shao, and V. Angelopoulos (2012), THEMIS observations of electromagnetic ion cyclotron wave occurrence: Dependence on AE, SYMH, and solar wind dynamic pressure, *Journal of Geophysical Research: Space Physics (1978-2012)*, *117*(A10), doi:10.1029/2012JA018049.

Usanova, M. E., A. Drozdov, K. Orlova, I. R. Mann, Y. Shprits, M. T. Robertson, D. L. Turner, D. K. Milling, A. Kale, D. N. Baker, S. A. Thaller, G. D. Reeves, H. E. Spence, C. Kletzing, and J. Wygant (2014), Effect of EMIC waves on relativistic and ultrarelativistic electron populations: Ground-based and Van Allen Probes observations, *Geophysical Research Letters*, *41*(5), 1375–1381, doi:10.1002/2013GL059024.

Van Allen, J. A. (1959), The geomagnetically trapped corpuscular radiation, *Journal of Geophysical Research*, *64*(11), 1683–1689, doi:10.1029/JZ064i011p01683.

Van Allen, J. A., and L. A. Frank (1959), Radiation Around the Earth to a Radial Distance of 107,400 km., *Nature*, *183*(4659), 430–434, doi:10.1038/183430a0.

Varotsou, A., D. Boscher, S. Bourdarie, R. B. Horne, S. A. Glauert, and N. P. Meredith (2005), Simulation of the outer radiation belt electrons near geosynchronous orbit including both radial diffusion and resonant interaction with Whistler-mode chorus waves, *Geophysical Research Letters*, *32*(19), doi:10.1029/2005GL023282.

Varotsou, A., D. Boscher, S. Bourdarie, R. B. Horne, N. P. Meredith, S. A. Glauert, and R. H. Friedel (2008), Three-dimensional test simulations of the outer radiation belt electron dynamics including electron-chorus resonant interactions, *Journal of Geophysical Research: Space Physics*, *113*(A12), doi:10.1029/2007JA012862.

Walt, M. (1994), *Introduction to Geomagnetically Trapped Radiation*, Cambridge University Press, doi:10.1017/CBO9780511524981.

Wang, C., Q. Zong, F. Xiao, Z. Su, Y. Wang, and C. Yue (2011), The relations between magnetospheric chorus and hiss inside and outside the plasmasphere boundary layer: Cluster observation, *Journal of Geophysical Research: Space Physics*, *116*(A7), doi:10.1029/2010JA016240.